The Diversity of Neutron Stars: Nearby Thermally Emitting Neutron Stars and the Compact Central Objects in Supernova Remnants

Thesis by
David L. Kaplan

In Partial Fulfillment of the Requirements
for the Degree of
Doctor of Philosophy

California Institute of Technology
Pasadena, California

2004

(Defended May 24, 2004)

Acknowledgements

The past five years have been very exciting and scientifically rewarding. For help on the scientific side, I would like to acknowledge my enormous debt to my advisor, Prof. Shri Kulkarni, whose quirky advice usually turns out to be correct in the long run. While he was not my official advisor, I would also like to thank Prof. Marten van Kerkwijk, whose in-depth involvement in the details of our research and stimulating conversations enabled me to get through the weeks when Shri was traveling.

Of course, I would like to thank all of my collaborators for helping and putting up with me: Jay Anderson, Dale Frail, Derek Fox, and Herman Marshall; and the hollow supernova remnant crowd: Bryan Gaensler, Eric Gotthelf, and Pat Slane.

Very little research would have been possible without the great support from the staffs of Palomar, Keck, and Las Campanas observatories. I would especially like to thank Ray Escoffier, Rich Lacasse, Karen O'Neil, and the staff at NRAO Green Bank for all of their help with the GBT Pulsar Spigot.

For making life at Caltech tolerable, I would like to thank all of the graduate students, but most significantly Edo Berger, Micol Christopher, and Bryan Jacoby. No work would have been possible at all without the great support of Patrick Shopbell, Cheryl Southard, and Anu Mahabal.

My astronomical career began as an undergraduate at Cornell University. Since it has given me so much satisfaction and happiness, I would like to thank Richard Lovelace for introducing me to the Astronomy Department, Jim Cordes (and later Gordon Stacey and Yervant Terzian) for giving me a job, Jim Condon for a fantastic internship at NRAO, and my officemates Joe Lazio (who taught me Unix), Maura McLaughlin, and Shami Chatterjee.

For supporting me through graduate school I would like to thank the Fannie and John Hertz Foundation, whose generous fellowship enabled me to pursue my research without the constant worry over funding.

Nothing at all would have been possible without my parents, Marion and Joel.

And of course Dawn Erb.

Abstract

Neutron stars are invaluable tools for exploring stellar death, the physics of ultra-dense matter, and the effects of extremely strong magnetic fields. The observed population of neutron stars is dominated by the > 1000 radio pulsars, but there are distinct sub-populations that, while fewer in number, can have significant impact on our understanding of the issues mentioned above. These populations are the nearby, isolated neutron stars discovered by *ROSAT*, and the central compact objects in supernova remnants. The studies of both of these populations have been greatly accelerated in recent years through observations with the *Chandra X-ray Observatory* and the *XMM-Newton* telescope. First, we discuss radio, optical, and X-ray observations of the nearby neutron stars aimed at determining their relation to the Galactic neutron star population and at unraveling their complex physical processes by determining the basic astronomical parameters that define the population—distances, ages, and magnetic fields—the uncertainties in which limit any attempt to derive basic physical parameters for these objects. We conclude that these sources are 10^6 year-old cooling neutron stars with magnetic fields above 10^{13} G. Second, we describe the hollow supernova remnant problem: why many of the supernova remnants in the Galaxy have no indication central neutron stars. We have undertaken an X-ray census of neutron stars in a volume-limited sample of Galactic supernova remnants, and from it conclude that either many supernovae do not produce neutron stars contrary to expectation, or that neutron stars can have a wide range in cooling behavior that makes many sources disappear from the X-ray sky.

Contents

List of Figures

List of Tables

We learn wisdom from failure much more than from success. We often discover what will do by finding out what will not do; and probably he who never made a mistake never made a discovery.

— Samuel Smiles (*Self-Help*)

I have found you an argument; I am not obliged to find you an understanding.

— Samuel Johnson

Part I

The Nearby Isolated Neutron Stars

Chapter 1

The Parallax and Proper Motion of RX J1856.5−3754 Revisited[†]

D. L. Kaplan[a], M. H. van Kerkwijk[b‡], & J. Anderson[c*]

[a]Department of Astronomy, 105-24 California Institute of Technology, Pasadena, CA 91125, USA

[b]Sterrenkundig Instituut, Universiteit Utrecht, Postbus 80000, 3508 TA Utrecht, The Netherlands

[c]Astronomy Department, University of California, Berkeley, CA 94720-3411, USA

Abstract

RX J1856.5−3754, a bright soft X-ray source believed to be the nearest thermally emitting neutron star, has commanded and continues to command intense interest from X-ray missions. One of the main goals is to determine the radius of this neutron star. An integral part of the determination is an accurate parallax. Walter (2001) analyzed *Hubble Space Telescope* (*HST*) data and derived a parallax, $\pi = 16.5 \pm 2.3\,$mas. Combining this distance with the angular radius derived from blackbody fits to observations of RX J1856.5−3754 with *ROSAT*, *EUVE*, *HST*, Pons et al. (2002a) derived an observed radius ("radiation radius"), $R_\infty = 7\,$km. This value is smaller than the radii calculated from all proposed equations-of-state (EOS) of dense baryonic matter (Haensel 2001). Here, we have analyzed the same *HST* data and find $\pi = 7 \pm 2$ mas. We have verified our result using a number of different, independent techniques, and find the result to be robust. The implied radius of RX J1856.5−3754 is $R_\infty = 15 \pm 6\,$km, falling squarely in the range of radii, 12–16 km, expected from calculations of neutron star structure for different equations of state. The new distance also implies a smaller age for RX J1856.5−3754 of 0.4 Myr, based on its association with the Upper Sco OB association.

1.1 Introduction

The *ROSAT* all-sky survey identified six neutron stars that are radio-quiet but bright in the soft X-ray band. These sources, unlike the well-studied radio pulsars, lack significant nonthermal emission and are thus excellent candidates for X-ray spectroscopic studies of the atmospheres of neutron stars (for reviews, see Mereghetti 2001; Treves et al. 2000).

[†] A version of this chapter was published in *The Astrophysical Journal*, vol. 571, 447–457.

[‡] Current address: Department of Astronomy and Astrophysics, University of Toronto, 60 St. George Street, Toronto, ON M5S 3H8, Canada.

[*] Current address: Department of Physics and Astronomy, Rice University, Houston, TX 77251, USA

The brightest of these sources is RX J1856.5−3754 (Walter, Wolk, & Neuhäuser 1996). A faint, blue optical counterpart was identified from *Hubble Space Telescope* (*HST*) data (Walter & Matthews 1997). RX J1856.5−3754 has been intensively studied by most major facilities, especially *ROSAT*, *EUVE*, *ASCA* and *HST*. The broadband data can be well fitted by thermal emission from a neutron star, which has resulted in the determination of the effective temperature, $kT_{\rm eff} \approx 50$ eV, and angular radius of the neutron star, $R_\infty/d \approx 0.11$ km pc^{-1} (Pavlov et al. 1996; Pons et al. 2002a).

Walter (2001, hereafter W01) used *HST* data spanning three years to measure the astrometric parameters of RX J1856.5−3754, finding a parallax of 16.5 ± 2.3 mas and a proper motion of 332 ± 1 mas yr^{-1} at a position angle of $100.3^\circ \pm 0.1^\circ$ ($\mu_\alpha = 326.7 \pm 0.8$ mas yr^{-1}, $\mu_\delta = -59.1 \pm 0.7$ mas yr^{-1}).

Combining this parallax with the broadband modeling yields a radiation radius of $R_\infty \approx 7\,$km. For the canonical mass of a neutron star, $1.4\,M_\odot$ this radius is smaller than the minimum radiation radius of $R_\infty^{\rm min} = 10.7$ km allowed by General Relativity (Lattimer & Prakash 2000). For the radius to exceed $R_\infty^{\rm min}$ the mass has to be less than $1\,M_\odot$ (Pons et al. 2002a).

The importance of RX J1856.5−3754 as a laboratory for dense matter physics has motivated deep observations by *Chandra* (Burwitz et al. 2001), *XMM* and the Very Large Telescope (VLT). Results from the first 50 ks Chandra observations[1] can be found in Burwitz et al. (2001); the blackbody fits are similar to those of Pons et al. (2002a). Using the VLT, van Kerkwijk & Kulkarni (2001b) discovered an unusual Hα nebula around RX J1856.5−3754, from which they infer properties of RX J1856.5−3754's energetics and emission characteristics (van Kerkwijk & Kulkarni 2001a).

Parallax or distance is essential to obtaining the radius, the key physical parameter (since it now appears that X-ray and optical observations yield reliable values for $T_{\rm eff}$ and the angular radius). In view of the perplexing radius inferred from the parallax measurement of W01 we undertook an analysis of the publicly available *HST* data. Here we present a detailed description of our analysis followed by our measurement of the parallax.

1.2 Observations, Analysis & Results

We analyzed the publicly available *HST*/WFPC2 observations described by W01 and Walter & Matthews (1997); see Table 1.1 for a log of the observations. As noted by W01, the observations took place near the times of parallactic maximum (3 October and 30 March). RX J1856.5−3754 is always on the Planetary Camera (PC) detector so we only analyzed those data.

1.2.1 Relative Astrometry

We used the effective point-spread function (ePSF) fitting technique to perform the astrometry, as described by Anderson & King (2000, hereafter AK00). We did not have sufficient numbers of stars to derive our own ePSF for each data set, so we used a previously determined ePSF (from archival data) for the *HST*/WFPC2 F555W filter. While the parallax data were taken with the F606W filter, we feel that using the F555W ePSF was appropriate, as it was of superior quality to the F606W ePSF that we have (also derived from other data). The difference in ePSFs should not bias the data, as the wavelength dependence of the ePSF is not strong, especially across the ≈ 50 nm difference in effective wavelength between the filters. Furthermore, the blue color of RX J1856.5−3754 brings its ePSF closer to the F555W ePSFs of normal stars. In any case, we also performed the analysis with the F606W ePSF. Since the latter ePSFs were of inferior quality (owing to a less ideal data set), we obtained larger errors, but the results were entirely consistent with those obtained using the F555W ePSF.

---

[1] In early October, 2001, Chandra observed RX J1856.5−3754 for an additional 450 ks under the aegis of the Director's discretionary program.

Table 1.1. WFPC2 Observation Summary

Epoch (UT)	$t_{\rm exp}$ (s)	$n_{\rm dither}$[a]	Sky Level (DN s^{-1})	Nominal PA (deg)	ΔPA[b] (deg)	Scale (mas pixel^{-1})	x_0[c] pixels	y_0[c] pixels
1996 Oct 6	4800	4	0.006	129.38	0.012(2)	45.5936(8)	408.004(5)	428.143(5)
1999 Mar 30	7200	8	0.006	−51.75	0.0212(7)	45.6028(5)	429.221(3)	437.824(3)
1999 Sep 16[d]	5191	4	0.005	124.97	0	45.5938	417.948	436.803

[a] The dither pattern was in sets of four images, with $(\Delta x,\Delta y)$ =(0,0), (0,0), (5.5,5.5), and (5.5,5.5) pixels.

[b] Defined as the difference between the fitted position angle and the nominal position angle (from the image header and Table 1.1).

[c] x and y pixel coordinates of the pointing center, which has $\alpha = -18^{\rm h}56^{\rm m}35\overset{\rm s}{.}374$ and $\delta = -37^\circ 54' 31\overset{''}{.}71$; see § 1.2.3.

[d] The values for this epoch were assumed to be correct.

Note. — See Eqn. 1.2 for the sense of the transformation.

We fit the F555W ePSF to the raw images, uncorrected for dithering or cosmic rays. For each epoch, we used a χ^2-minimization, as described by AK00, to derive a position for each star in each of the raw images. We corrected this position for the 34th-row anomaly[2] (Anderson & King 1999) and geometric distortions in the PC detector using new coefficients (Anderson 2002, in preparation). For each epoch, this yielded four (or eight) positions for each star.

We then solved for the shifts (due to dithering) between the four (or eight) images in a given epoch; these shifts are given in Table 1.2. We rejected sources which had significantly higher residuals than other sources of their magnitude (see Figure 1.1), ascribable to the source being extended or saturated. For the remaining sources we used an iterative σ-clipping (with threshold at 2.5σ) to reject outlying position determinations. Following this the remaining position measurements were used to derive the average position for each source. The final distortion-corrected source positions in image (x, y) coordinates as well as the number of accepted measurements are listed in Table 1.3.

In the limit of a large number of independent observations that are well dithered, the measured rms would have yielded reliable uncertainties. However, we are limited by the meager number of available frames at each epoch. With a maximum of four (or even eight) measurements of each position we were not able to search for systematic errors. Furthermore, the data were taken with nonoptimal dithering,[3] with the fractional pixel portions of the dither often repeating from one image to the next (Table 1.2). This increases the likelihood of systematic pixel-phase errors. We therefore adopted a semi-empirical approach for the measurement uncertainties along the following lines.

As the first approximation of the uncertainty for each position, we take the rms variation between the positions used to construct the average. As the next level, we used the expected precision in the positions as a function of the signal-to-noise ratio (SNR) of stars. To this end, we utilized an astrometric database that one of us (J.A.) has built up over the last several years. In particular, we used 18 well-dithered PC

---

[2] It is a common error to apply the 34th-row correction *after* shifting and combining the data. This procedure is incorrect, as the 34th-row correction should be applied to the raw image coordinates and not those that have been shifted and rebinned.

[3] For astrometric purposes, a 2 × 2 dithering grid is minimal for optimal removal of pixel-phase errors; a 15-point dither pattern is even better. See AK00.

Table 1.2. Fitted Dither Positions

Epoch	Image Number	Δx (pixels)	Δy
1996 Oct 6	1	0.000	0.000
	2	−0.049	−0.112
	3	5.451	5.417
	4	5.416	5.270
1999 Mar 30	1	0.000	0.000
	2	0.022	0.115
	3	5.456	5.455
	4	5.465	5.476
	5	−0.066	−0.142
	6	−0.097	−0.064
	7	5.368	5.628
	8	5.399	5.532
1999 Sep 16	1	0.000	0.000
	2	−0.159	−0.027
	3	5.515	5.542
	4	5.386	5.422

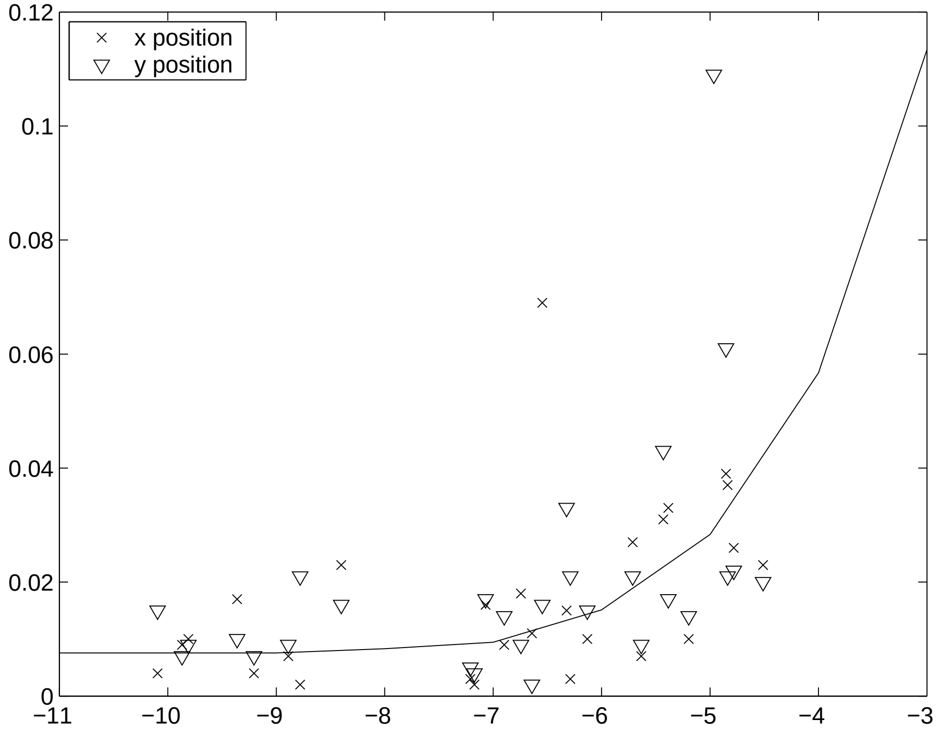

Figure 1.1 1-D position uncertainty (pixels) vs. instrumental magnitude, defined by $m = -2.5\log_{10}(\mathrm{DN})$ within a 5×5 pixel region in a single exposure. The x's are for the raw uncertainties in the x positions of the stars used to register the different epochs, the triangles for the raw y uncertainties, and the solid line is a relation determined from $\sim$ 5000 well-observed stars in other data sets. The sources here are those that are not saturated and were used in the analysis; see Tables 1.4 and 1.3. The data from this paper (x's and triangles) generally follow the trend defined by the line (also given in Eqn. 1.1), but there is considerable spread due to the small number of measurements (3 or 4) used to construct each uncertainty.

images that were obtained under similar conditions (filter, background, crowding) to those discussed here. In Figure 1.1 we display a fit (obtained from the measurements of about 5000 stars) to the astrometric precision as a function of the SNR of stars. The relation from Figure 1.1 is reasonably well fit by

$$\sigma = \frac{1}{\sqrt{2}}\left[\left(2.38e^{0.69m}\right)^3 + (0.02)^3\right]^{1/3} \text{ pixels,} \tag{1.1}$$

where $m = -2.5\log_{10}(\mathrm{DN})$ (within a 5×5 pixel area) is the magnitude measured in a single exposure and σ is the 1-D position uncertainty. For N well-dithered exposures, the uncertainty is $\sigma/\sqrt{N}$, as expected (AK00).

We see that the raw uncertainties generally follow the expected trend, but that there is substantial scatter. This is not surprising, given that we may be computing the uncertainties from four or fewer than four measurements. Therefore, in our analysis we use the maximum of the empirically determined uncertainty for an individual star and the uncertainty from the relation in Figure 1.1 corrected to the appropriate magnitude; the stars that have uncertainties larger than those inferred from this relation do so due to cosmic rays or proximity to bright sources.

The above analysis gives us reliable and accurate measurements of stellar positions, but while these stars are in the background relative to RX J1856.5−3754 they can still have their own motions that will

Table 1.3. Distortion Corrected (x, y) Source Positions

ID	Epoch								
	1996 Oct			1999 Mar			1999 Sep		
	x (pixels)	y (pixels)	N[a]	x (pixels)	y (pixels)	N[a]	x (pixels)	y (pixels)	N[a]
100	269.63(3)	173.83(2)	3	562.43(2)	694.92(2)	8	304.53(2)	170.38(2)	4
102	452.45(1)	132.70(1)	4	379.55(3)	732.33(1)	8	489.55(2)	146.83(1)	4
103	583.81(1)	107.54(1)	4	247.36(2)	755.08(2)	8	623.26(1)	134.02(1)	4
104	612.51(3)	120.50(5)	4	218.50(5)	741.63(7)	8	650.93(5)	149.61(5)	4
105	616.08(4)	295.90(4)	4	218.82(4)	565.99(4)	8	637.53(4)	324.77(4)	3
106	561.03(2)	366.40(2)	4	275.145(9)	496.71(1)	8	576.066(8)	389.601(8)	4
107	84.80(2)	400.36(2)	4	751.80(2)	471.926(9)	8	98.673(9)	378.58(1)	4
108	233.92(33)	725.84(11)	4	609.04(8)	144.08(9)	7	216.36(12)	716.08(11)	4
110	278.43(2)	762.35(2)	4	565.18(2)	106.41(2)	8	257.51(2)	757.17(2)	4
111	738.04(1)	728.20(2)	4	104.91(1)	131.54(1)	8	718.50(2)	766.57(1)	4
112	707.599(9)	519.420(9)	4	131.642(9)	340.811(9)	8	707.46(2)	555.82(2)	4
113	507.48(7)	598.59(2)	4	332.92(2)	265.71(3)	8	501.25(3)	615.74(5)	3
114	523.36(2)	522.78(3)	4	315.58(1)	341.14(1)	8	524.10(1)	541.72(2)	3
116	69.84(2)	146.13(1)	4	761.95(2)	726.29(1)	8	107.72(1)	124.24(2)	1
117	434.37(1)	135.98(1)	4	397.66(3)	729.44(2)	8	471.62(30)	147.99(30)	3
118	452.54(1)	254.49(2)	4	381.66(2)	610.43(2)	8	478.38(1)	268.20(2)	3
119	597.78(3)	375.85(4)	4	238.33(3)	486.51(3)	8	612.02(10)	402.70(13)	3
127	123.33(4)	660.75(6)	4	718.28(4)	210.87(4)	8	112.59(3)	641.37(3)	4
128	130.64(3)	624.33(2)	4	710.32(2)	247.15(2)	7	123.17(2)	605.92(2)	3
129	161.07(4)	534.78(3)	4	677.93(7)	335.92(3)	8	162.31(6)	519.85(5)	4
201	764.454(8)	494.44(2)	4	74.173(8)	364.652(8)	8	766.54(1)	536.370(8)	4
J	450.297(9)	374.648(8)	4	385.946(8)	490.481(8)	8	465.10(1)	387.523(8)	4
19	88.005(8)	303.943(9)	4	746.47(2)	568.192(8)	8	111.311(9)	282.994(8)	4
20	243.62(4)	455.03(3)	4	593.76(3)	414.32(3)	8	252.08(4)	447.98(2)	4
21	235.02(1)	380.065(9)	4	601.15(1)	488.972(9)	8	250.279(9)	372.88(1)	4
23	317.345(9)	444.296(9)	4	520.60(2)	423.45(1)	8	325.671(9)	444.27(3)	4
25	602.610(8)	650.40(2)	4	239.092(8)	211.774(8)	8	590.571(8)	676.538(8)	4
26	698.28(2)	682.24(1)	4	144.40(1)	177.714(8)	8	682.42(1)	717.680(8)	4
28	375.731(8)	290.699(8)	4	458.94(1)	575.797(9)	8	398.67(2)	297.003(8)	4
X	357.93(4)	516.84(4)	4	472.30(4)	333.92(4)	8	368.42(4)	540.08(4)	4

[a] The number of independent measurements used to determine the mean position; see § 1.2.1.

bias our determinations. Therefore, to have some idea of the absolute motion of the stars in the image, we included in the data measurements of the positions of two slightly extended sources (presumed to be galaxies) present on the *HST* images (see Table 1.4). As these sources are nonstellar, we could not use the AK00 technique to measure their positions. Instead we fitted Gaussian profiles and then applied the same distortion corrections as with the other technique. Gaussian fitting is inherently less accurate than ePSF fitting (AK00), but the errors are important primarily for sources that are undersampled by the WFPC2 pixels (i.e., where pixel-phase errors are important). The galaxies were reasonably well resolved (FWHM ≈ 3.2 pixels for source #20, FWHM ≈ 3.6 pixels for source #104), so they should not suffer from systematic errors related to undersampling.

1.2.2 Registration of Epochs

To determine the transformation of the background sources (all sources except for RX J1856.5−3754) between epochs, we proceeded iteratively. Our basic input data set was the 27 stellar sources that had consistent measurements in each epoch plus the two galaxies (§ 1.2.1), given in Table 1.3. The faintest of these sources were as faint as RX J1856.5−3754, and the brightest were ≈ 160 times as bright as RX J1856.5−3754 (the brightest nonsaturated sources on the WFPC2 images). First, we set the fiducial positions of the sources to their measured positions at epoch 1999.7. We chose this epoch as the effects of parallax between it and epoch 1996.8 are minimized (due to similar parallactic angles) and the effects of proper motion between it and epoch 1999.3 are minimized (due to close proximity in time), thus yielding the best matches to the other epochs given the limited information that we have. We assumed that the position angle, scale, and pointing center of this fiducial epoch are known. The pointing center has no impact on the results, and is simply a dummy parameter. The position angle and scale are known to reasonable precision ($< 0.1^\circ$ for the position angle, and $< 0.1\%$ for the scale). For our nominal values, we take the values from the *HST* image headers (listed in Tables 1.1). If these values are wrong at certain levels, they would introduce errors on those levels into our measurements (i.e., if the fiducial scale were wrong by 0.1%, our proper motions would be wrong by the same amount) but these are systematic effects that are well below the measurement precision of the current data.

For our transformation between the epochs, we assumed a simple rotation, scale, and offset. This is valid if the distortion correction (§ 1.2.1) removed all nonlinear terms. The transformation equation between the measured positions of star i at epoch j, $(x_{i,j}, y_{i,j})$, to the celestial position $(\Delta\alpha_{i,j}, \Delta\delta_{i,j})$ is

$$\begin{aligned}\Delta\alpha_{i,j} &= -\mathrm{scale}_j\left((x_{i,j}-x_{0,j})\cos\mathrm{PA}_j-(y_{i,j}-y_{0,j})\sin\mathrm{PA}_j\right)\\ \Delta\delta_{i,j} &= \mathrm{scale}_j\left((x_{i,j}-x_{0,j})\sin\mathrm{PA}_j+(y_{i,j}-y_{0,j})\cos\mathrm{PA}_j\right),\end{aligned}\tag{1.2}$$

where scale_j is the plate scale (arcsec per pixel), $(x_{0,j}, y_{0,j})$ are the offsets, and PA_j is the position angle of epoch j, all of which are given in Table 1.1.

We performed a χ^2 fit between the fiducial positions and the positions at the three measured epochs, varying the scale, position angle, and offsets of the other epochs. This fit gave relatively large χ^2 values, due to proper motion between the epochs.

We then fit for updated fiducial positions and proper motions of the background sources based on a linear least-squares technique (for the galaxies, the proper motion was forced to be 0). These positions and proper motions were used to re-calculate the expected positions in the non reference epochs, which dramatically lowered the χ^2 values. We iterated this procedure (fitting for the transformation between the epochs, then fitting for the individual positions and proper motions) making sure that the solution was converging. After five iterations, χ^2 changed by 0.2; we considered the solution to have converged. The results of the fitting (the fiducial positions and proper motions) are given in Table 1.4.

For our analysis we did not fit for the parallaxes of the background sources as they are primarily at distances of > 1 kpc (see §§ 1.4 and 1.5). Our final χ^2 value for the fit was 228 for 50 degrees of freedom. The reduced χ^2 deviates significantly from 1, indicating that we may be missing some source of error in our analysis. We have determined, though, that the majority of the excess χ^2 comes from four objects: the stars #21 and #201, and the galaxies #20 and #104. Without these sources, we obtain a χ^2 value of 56 for 38 degrees of freedom, or a reduced χ^2 of 1.5. This value is much more acceptable. The question, then, is why these four sources contributed so much to the χ^2. For the galaxies, they were not measured with the ePSF technique of AK00, and are therefore subject to systematic errors not addressed here; we only include them to provide an "inertial" reference frame in the analysis. The stars, #21 and #201, are among the brightest of the sources measured (Table 1.4) and may be among the closest (except for RX J1856.5−3754,

Table 1.4. Reference Sources for Astrometry

ID$^{\mathrm{a}}$	$\alpha^{\mathrm{b}}-18^{\mathrm{h}}56^{\mathrm{m}}$ (s)	$\delta^{\mathrm{b}}+37^\circ54'$ (arcsec)	M_{F606W} (mag)	$\Delta\alpha^{\mathrm{c}}$ (arcsec)	$\Delta\delta^{\mathrm{c}}$	μ_α (mas yr^{-1})	μ_δ
100	34.28	−29.2	25.0	−12.9651(9)	2.4976(9)	0.1(5)	5.6(6)
102	34.60	−21.6	24.5	−9.1416(8)	10.0946(9)	−5.6(3)	−6.6(3)
103	34.85	−16.2	23.9	−6.2193(4)	15.4760(3)	−2.7(2)	1.9(2)
104$^{\mathrm{d}}$	34.96	−15.6	25.2	−4.924(1)	16.117(1)	0	0
105	35.49	−20.6	26.0	1.3560(2)	11.1550(2)	−1.3(7)	−0.9(7)
106	35.56	−24.5	22.4	2.2431(3)	7.1809(3)	−2.7(3)	0.9(3)
107	34.50	−42.3	23.7	−10.3348(4)	−10.5884(4)	−1.8(3)	−1.2(3)
108$^{\mathrm{e}}$	35.83	−46.5	25.0	···	···	···	···
110	36.05	−45.9	25.1	8.0253(7)	−14.2280(7)	−0.9(4)	2.4(4)
111	37.07	−28.7	24.6	20.1264(4)	2.9624(5)	1.5(3)	4.8(3)
112	36.38	−23.8	23.6	11.8772(5)	7.9134(5)	−2.4(2)	−1.0(2)
113	36.12	−33.1	23.8	8.8837(3)	−1.411(1)	0.1(9)	6(1)
114	35.94	−30.4	24.2	6.6715(4)	1.3405(4)	−0.3(5)	4.8(4)
116	33.71	−35.5	24.0	−19.7242(6)	−3.7665(6)	−0.9(3)	−3.3(3)
117$^{\mathrm{e}}$	34.57	−22.4	25.8	···	···	···	···
118	34.97	−25.1	24.6	−4.8365(6)	6.5790(6)	−1.9(3)	−4.9(3)
119$^{\mathrm{e}}$	35.68	−23.6	25.7	···	···	···	···
127	35.37	−48.5	26.3	−0.043(1)	−16.758(1)	−1(1)	1.1(9)
128	35.28	−47.2	24.9	−1.1148(9)	−15.4528(9)	−1.2(5)	−1.2(5)
129	35.09	−43.5	26.3	−3.374(3)	−11.782(2)	4.5(8)	1.8(9)
201	36.44	−21.1	20.4	12.6471(3)	10.6446(3)	−0.7(2)	0.6(2)
J	35.32	−28.7	21.0	−0.6627(4)	3.0372(4)	−0.4(2)	−0.3(2)
19	34.22	−39.4	21.9	−13.6277(4)	−7.6757(4)	2.4(2)	2.4(2)
20$^{\mathrm{d}}$	35.05	−38.3	23.7	−3.8055(8)	−6.5591(8)	0	0
21	34.81	−36.4	21.0	−6.6871(4)	−4.7115(4)	3.9(2)	−2.3(2)
23	35.20	−35.4	23.8	−2.0685(5)	−3.6799(5)	−5.0(3)	−6.1(2)
25	36.51	−31.3	22.0	13.4631(2)	0.4201(2)	0.2(3)	−2.6(3)
26	36.84	−28.9	21.5	17.3585(4)	2.8446(5)	2.2(2)	−11.1(3)
28	34.89	−28.9	21.7	−5.7783(5)	2.8325(5)	−0.4(2)	−2.3(2)
X$^{\mathrm{f}}$	35.60	−36.2	26.1	2.643(2)	−4.504(2)	···	···

[a] ID's are as in W01 where possible; source 201 was not present in W01; X is RX J1856.5−3754.

[b] Positions are measured at equinox J2000, epoch 1999.26.

[c] Position offsets at epoch 1999.7, relative to the pointing center, for which our absolute astrometry yields $\alpha = -18^{\mathrm{h}}56^{\mathrm{m}}35^{\mathrm{s}}.374$ and $\delta = -37^\circ54'31''.71$; see § 1.2.3.

[d] Extended source, probably a galaxy.

[e] Rejected from the analysis due to poor position measurements; see Table 1.3.

[f] For proper motions, see Table 1.5.

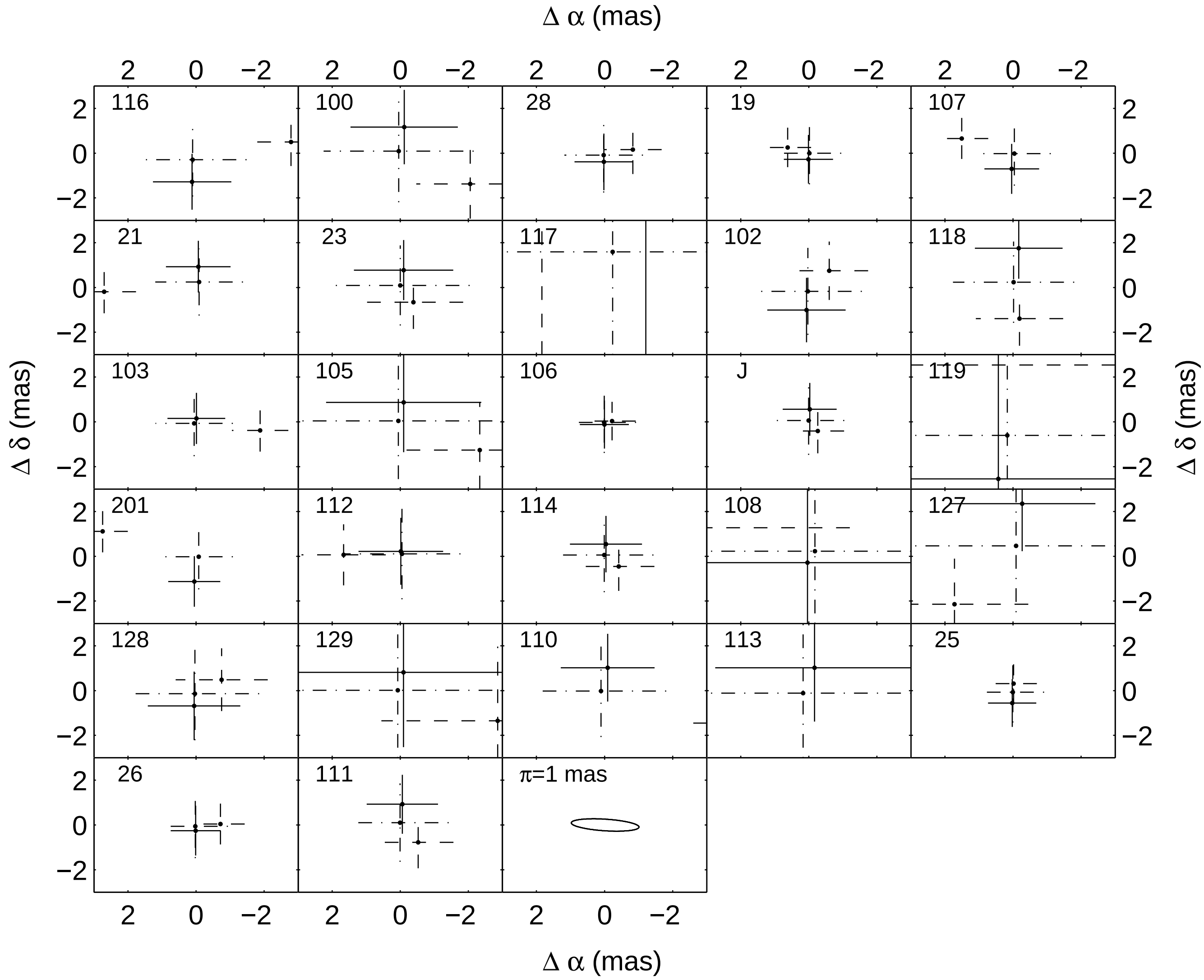

Figure 1.2 Residual positions for background sources with best-fit proper motion removed; see Figure 1.4 for RX J1856.5−3754. Position from 1996 October has dot-dashed cross; position from 1999 March has dashed cross; position from 1999 September has solid cross. All sources are labeled with identifiers from Table 1.4 in the upper-left corners. The last plot in the bottom row shows a parallactic ellipse for $\pi = 1$ mas.

of course). As can be seen from their position residuals (Figure 1.2) they may have parallaxes of ~ 1.5 mas and therefore would not be expected to register well. They are also close to extremely bright stars (Figure 1.6) that may bias the position measurements. Together, these effects (nonzero parallax and mis-measuring positions) significantly increase the χ^2 for the fit. Neither of these effects is important for the majority of the stars, which typically have residuals consistent with zero parallax (also see § 1.5). For the results of the registration, the inclusion or exclusion of these sources does not matter.

We performed additional analyses to determine how robust our measurements are, and included information from these analyses in the final estimates (see §§ 1.2.4 and 1.4).

The deviations of the scales and position angles from the nominal value were small but significant (see Table 1.1), unlike stated by W01. We find that the scale changed by $\approx 0.03\%$ from one epoch to another, and that the position angle changed by $\approx 0^\circ\!.02$. This is reasonable, given the fluctuations seen in other

WFPC2 observations (due to thermal fluctuations in the detector and telescope assembly; AK00).

1.2.3 Absolute Astrometry

Absolute astrometry was done relative to the USNO-A2.0 catalog (Monet 1998). We first determined centroids for all 571 USNO-A2.0 stars that overlapped with the average R-band image obtained in 2000 using FORS2 on UT#2 (Kueyen) at the Very Large Telescope (see van Kerkwijk & Kulkarni 2001b; the image is composed of 29 exposures of 135 s). We rejected 63 objects that were badly overexposed or had widths inconsistent with them being stellar. Next, the pixel coordinates were corrected for instrumental distortion using a cubic radial distortion function provided to us by T. Szeifert and W. Seifert (1999, private communication). Finally, the zero point position, the plate scale, and the position angle on the sky were determined, rejecting iteratively a further 87 objects for which the residuals to the solution were larger than $0\farcs6$ (inspection of the images showed that virtually all of these were visual doubles, which are blended on the sky survey plates on which the USNO-A2.0 coordinates are based). For the 421 stars that pass our cuts, the inferred single-star measurement errors are $0\farcs18$ in each coordinate, which is line with the uncertainties expected for the USNO-A2.0 catalog (Deutsch 1999). Thus, we conclude that our astrometry is tied to the USNO-A2.0 system at about $0\farcs01$ accuracy.

We used the solution to determine the positions in the VLT R-band image of 19 stars from Table 1.4 (for the remaining 7—objects 105, 106, 112, 113, 118, 127, and 128—it was not possible to determine accurate positions, either because they were too faint or because they were too close to brighter stars). Using these epoch 2000.3 positions and the fiducial epoch 1999.7 positions derived from the registration of the *HST* images above, we derived the pointing center for our reference *HST* image (we corrected for the difference in epoch using the observed proper motions). We solved for zero point offsets only, i.e., the scale and orientation were held fixed to the values listed in the header. The inferred single-star measurement errors are $0\farcs025$ in each coordinate, and the zero point should thus be tied to the R-band image to better than $0\farcs01$.[4] With this pointing center, we determined the absolute positions for all stars listed in Table 1.4. These should be on the USNO-A2.0 system to about $0\farcs02$, and on the International Celestial Reference System to about $0\farcs2$.

1.2.4 Determination of Parallax and Proper Motion of RX J1856.5−3754

With the three epochs registered, we compared the positions of RX J1856.5−3754 in each (see Table 1.3). We combined the initial estimates of the position uncertainties in quadrature with the uncertainties introduced by the registration. We fit for the proper motion and parallax of RX J1856.5−3754 using a linear least-squares solution. The locations along the parallactic ellipse at each epoch were determined using the JPL DE200 ephemeris.

As noted in § 1.2.1 and § 1.2.2, our limited number of measurements means that the individual position uncertainties have limited accuracy. Because of this, the uncertainty on the parallax derived from strict statistical considerations (1.7 mas) may not be correct. We have therefore estimated the parallax uncertainty using a variety of techniques (see § 1.4); these techniques have an rms of 0.4 mas, which we add in quadrature to find an rms of 1.8 mas. To be conservative we round this up, finding the overall 1-σ uncertainty to be 2 mas, similar to the value found by W01.

We present the results of the fitting for π, μ_α, and μ_δ in Table 1.5. We also present the values for the derived parameters of distance D and transverse velocity $V_\perp$. The best-fit parallax is 7 ± 2 mas. We can exclude a null-result for the parallax at the 10^{-4} level. Our results are inconsistent with those of W01

---

[4] Leaving the position angle and scale free, we find changes of $0\fdg09$ and 0.07%, respectively. The corresponding change in inferred pointing center is $\sim 0\farcs002$.

Table 1.5. Motion of RX J1856.5−3754

Parameter	Best-fit Values
α^{a}	2.6435 ± 0.0042
δ^{a}	-4.5050 ± 0.0030
μ_α (mas yr^{-1})	328 ± 1
μ_δ (mas yr^{-1})	-58 ± 1
π (mas)	7 ± 2
D (pc)	140 ± 40
μ (mas yr^{-1})	333 ± 1
PA (deg)	100.2 ± 0.2
$V_\perp$ (km s^{-1})	220 ± 60

[a] Fiducial positions at epoch 1999.7, relative to (x_0, y_0) offsets given in Table 1.1.

Note. — Best-fit values for μ_α, μ_δ, π are determined directly from a linear least-squares solution, and errors are 1-σ/68% confidence. Best-fit values and errors for the other parameters are derived from those for μ_α, μ_δ and π.

at the 99.8% level. However, our best-fit values for the proper motions are entirely consistent with those presented in W01, and also agree with the orientation of the Hα nebula (van Kerkwijk & Kulkarni 2001a).

The severe inconsistency between the values of the parallax derived by W01 and that derived by us is puzzling. The most obvious explanation for the discrepancy between our measured parallax and that of W01 is the significant difference in the way the data were processed: we used an ePSF that accounts for pixel phase errors and fit the data without manipulations such as rebinning or resampling. We also use more accurate distortion corrections, account for small changes in the scale and position angle of the observations from their nominal values, and account for the proper motion of the background objects. W01, on the other hand, first resampled the data, then shifted, then rebinned the data, and measured the positions with a PSF that is independent of pixel phase. Such analysis is liable to introduce even more pixel phase errors than those that were originally present. However, even if we follow the general method of W01 (resampling and rebinning, Gaussian fitting, old distortion corrections) we cannot reproduce a parallax of 16.5 mas (see § 1.4).

The surest way to resolve the differences between our analysis and that of W01 will be with the 2001 March *HST*data (not yet publicly available). This should allow further refinement of the proper motion and a more robust measurement of the parallax, with a final uncertainty of ≈ 1.5–2 mas.

As noted by W01, due to the small angle between the proper motion and the major axis of the parallactic

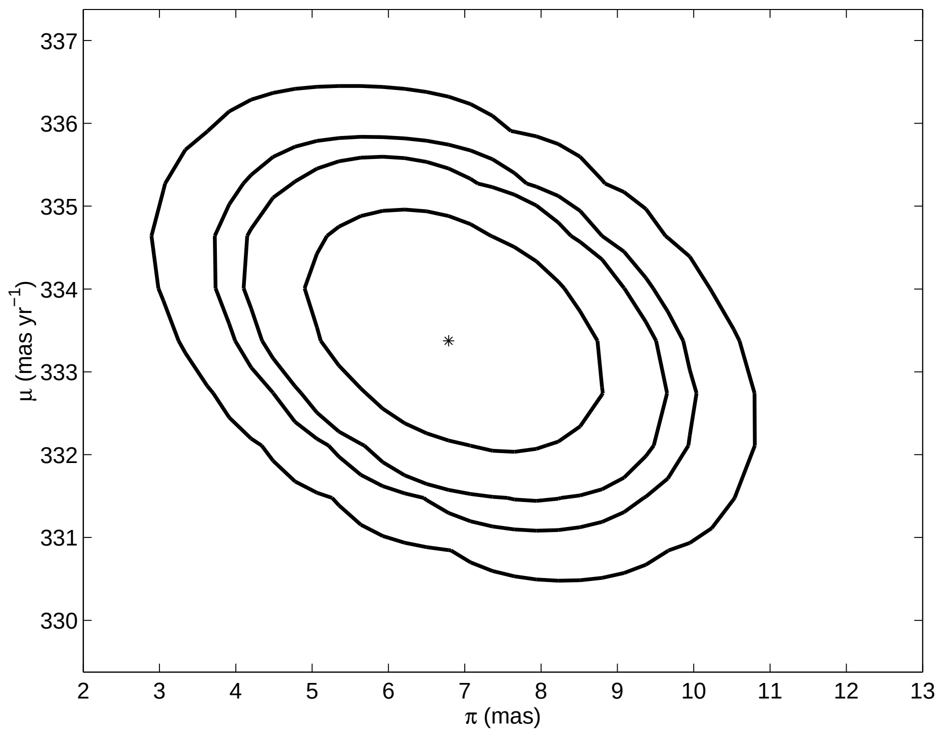

Figure 1.3 Joint confidence contours for the parallax π (mas) and the magnitude of the proper motion μ (mas yr^{-1}) for RX J1856.5−3754, illustrating the covariance between these parameters. Plotted are 68%, 90%, 95%, and 99% confidence contours, with the best-fit values indicated by the star. Note that the contours are for the joint confidence—the 1-D 68%confidence levels are given in Table 1.5. Compare to Fig. 2 from W01.

ellipse, there is significant anti-correlation between the parallax and the magnitude of the proper motion. This is shown in Figure 1.3. We stress, though, that even with the latitude given by this anti-correlation we cannot accommodate a parallax of 16.5 mas.

The position offsets with the proper motion subtracted are shown in Figure 1.4. The offsets are consistent with the best-fit parallax. The correlation between motion due to parallax and due to proper motion is also illustrated in Figure 1.4—the proper motion direction differs from the position angle of the parallactic ellipse by only 20°.

1.3 Discussion

1.3.1 Mass & Radius

The most immediate impact of a revised distance for RX J1856.5−3754 is in the interpretation of its spectrum. Pons et al. (2002a) used spectral fits to X-ray and broadband data to determine a best-fit mass and radius, taking the previously published distance of $d = 61$ pc (W01) to convert the measured angular size R_∞/d to a radius R_∞, where R_∞ is the "radiation" radius determined from blackbody fitting. The best-fit radius for all atmosphere choices was $R_\infty = 6$ km; causality then requires that the mass be less than this (in geometric units), giving $M < 1 M_\odot$ (Haensel 2001). These values are inconsistent with all neutron star equations-of-state (EOS), most of which have radii $R \geq 10$ km (Thorsett & Chakrabarty 1999; Lattimer & Prakash 2000).

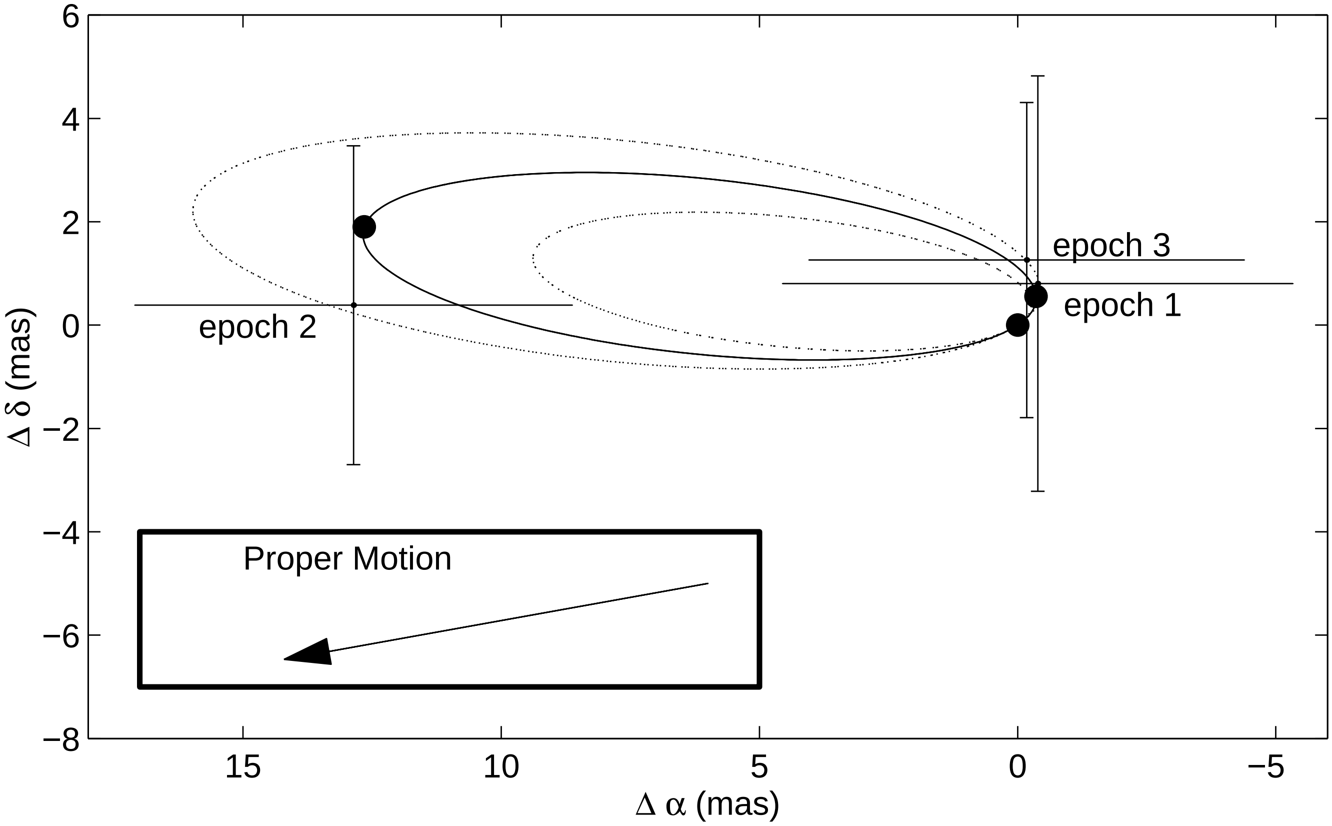

Figure 1.4 Parallactic ellipse for RX J1856.5−3754, showing the measured positions (points with error-bars) and expected positions (filled circles) at each epoch (after subtracting the best-fit proper motion). The inset shows an arrow that indicates the direction of the proper motion. The solid ellipse is for the best-fit parallax of 7 mas, while the dotted ellipses are for the ±1-σ values of 5 and 9 mas. This figure can be compared to Fig. 4 from W01.

Our new distance pushes RX J1856.5−3754 further away, and therefore allows for larger radii and masses. For example, the best-fit uniform temperature blackbody fit (a uniform temperature is preferred by the limits on X-ray pulsations; Burwitz et al. 2001Ransom, Gaensler, & Slane 2002) has $R_\infty/d = 0.11 \pm 0.01$ km pc^{-1} (Pons et al. 2002a), which had implied $R_\infty \approx 6.7$ km for a distance of 61 pc. Using our revised parallax value changes the radius to $R_\infty \approx 15$ km, giving a physical radius of $R \approx 12$ km (for the canonical neutron star mass of $1.4 M_\odot$; Thorsett & Chakrabarty 1999). This is much more in line with the likely values for R determined by equations of state (e.g., Lattimer & Prakash 2000).

Paczyński (2001) has predicted that the passage of RX J1856.5−3754 near star #115 (from W01) in 2003 will cause the apparent position of star #115 to change by ≈ 0.6 mas due to gravitational lensing. Paczyński (2001) goes on to suggest that precise measurement of this deflection, perhaps by the new Advanced Camera for Surveys (ACS) aboard *HST*, could be used to measure the mass of RX J1856.5−3754 and provide an independent estimate to constrain the equation of state. While we do note include star #115 in our analysis because it is fainter than our detection threshold, we were able to estimate its proper motion. As expected from its faintness, the measurement is not very accurate; we find $\mu_\alpha = 1.2 \pm 1.6$ mas yr^{-1}, $\mu_\delta = 3.4 \pm 1.6$ mas yr^{-1}. The closest approach of RX J1856.5−3754 to star #115 is $0\farcs2$ and should occur around April 2004. With the revised distance to RX J1856.5−3754, we find that the Einstein ring radius will be $\varphi_{\rm E} \approx 9$ mas (eq. 2 of Paczyński 2001), giving a displacement of ≈ 0.4 mas. This is somewhat less than the displacement predicted by Paczyński (2001). Based on the current WFPC2 data, it appears impossible to measure (in a reasonable number of orbits) the position of the star with enough precision to perform the suggested measurements (even assuming a displacement of 0.6 mas) with the ACS.

1.3.2 Origin & Age

W01 used the observed proper motion of RX J1856.5−3754 to trace it back toward the Upper Sco OB association, a source of supernovae during the last few million years (de Geus, de Zeeuw, & Lub 1989). He found, for $d = 61$ pc, that RX J1856.5−3754 came within 16 pc of the association 0.9 Myr ago. W01 notes that for an unconstrained distance, the radius of closest approach is minimized for a distance $d = 130$ pc, entirely consistent with our measurement. This then gives a closest-approach 0.4 Myr ago (with a radial velocity of $+30$ km s^{-1} instead of -60 km s^{-1}), making RX J1856.5−3754 half the age given in W01. This revised age resolves the minor discrepancy in the cooling history of RX J1856.5−3754 found by Yakovlev, Kaminker, & Gnedin (2001).

1.3.3 Energetics & Nature

Another area where the distance enters is in modeling of the Hα nebula that surrounds RX J1856.5−3754 (van Kerkwijk & Kulkarni 2001a). In most of the modeling, the distance enters linearly and the factor of ~ 2 difference that we find here will not significantly change the conclusions. However, there are a number of quantities that have steeper dependencies on the distance. We examine each of these.

In their estimate of the minimum pulsar wind energy loss $\dot{E}$ in the bow-shock model, van Kerkwijk & Kulkarni (2001a) find that $\dot{E} \propto d^3$. We are able therefore to revise the limit to $\dot{E} \gtrsim 8 \times 10^{32} d_{140}^3$ ergs s^{-1}, where the distance to RX J1856.5−3754 is $140 d_{140}$ pc. This impacts on the estimates of the inferred spin period P and magnetic field B, giving[5] $P \lesssim 1.5$ s and $B \lesssim 1 \times 10^{13}$ G. The new radial velocity is reasonably consistent with the inclination angle of $60^\circ \pm 15^\circ$ determined for the Hα nebula.

If RX J1856.5−3754 were powered by accretion, van Kerkwijk & Kulkarni (2001a) find an accretion rate $\dot{M} = 3 \times 10^9 d_{60}^{-3.5}$ g s^{-1}, where the distance $d = 60 d_{60}$ pc. For $d_{60} = 2.3$, as we find here, this then implies an available accretion power of $\sim 3 \times 10^{28}$ g s^{-1}. This is now almost four orders of magnitude less than the observed bolometric luminosity of RX J1856.5−3754, which is revised upward to $\sim 2 \times 10^{32} d_{140}^2$ ergs s^{-1}, further supporting the claim that accretion cannot power the source.

The final model for the Hα nebula considered by van Kerkwijk & Kulkarni (2001a) is an ionization nebula. Here, RX J1856.5−3754 can still be a pulsar, but its energy loss $\dot{E}$ must be small enough that any bow-shock nebula is smaller than the observed nebula. This leads to the result $\dot{E} \lesssim 2 \times 10^{34} d_{140}^{3.5}$ ergs s^{-1}, a much less constraining value than that given in van Kerkwijk & Kulkarni (2001a). However, we note that the ionization model has become less likely. With a distance of 140 pc the shape of the ionization nebula cannot be easily reproduced (van Kerkwijk & Kulkarni 2001a).

1.3.4 Local Density of Neutron Stars

Once the emission characteristics and size of one neutron star are well determined, they can be used to calibrate other sources. As an example, we derive a relation between the optical magnitude, X-ray blackbody temperature, and distance for isolated neutron stars, and apply it to the two brightest isolated neutron stars and PSR B0656+14, a nearby radio pulsar.

The optical emission from RX J1856.5−3754 and another isolated neutron star, RX J0720.4−3125 (Haberl et al. 1997; Kulkarni & van Kerkwijk 1998), is very well described by the Rayleigh-Jeans tail of

---

[5] Eqns. 8 & 9 from van Kerkwijk & Kulkarni (2001a) contain a small error: both P and B should go as $d^{-3/2}$, not $d^{3/2}$ as written.

Table 1.6. Implied Distances to Neutron Stars

Name	kT (eV)	V (mag)	d_{100}	Refs.
RX J1856.5−3754	57	25.7	1.4	1,2, this work
RX J0720.4−3125	79	26.6[a]	3.0	3,4
RX J1308.8+2127	118	28.3	6.7	5,6
PSR B0656+14[b]	73	27.3	3.3	7,8,9

References. — 1 – Pons et al. 2002a; 2 – van Kerkwijk & Kulkarni 2001b; 3 – Haberl et al. 1997; 4 – Kulkarni & van Kerkwijk 1998; 5 – Schwope et al. 1999; 6 – Kaplan et al. 2002, in preparation; 7 – Pavlov, Welty, & Córdova 1997; 8 – Koptsevich et al. 2001; 9 – Zavlin et al. 2001, in preparation

[a] B magnitude.

[b] We have taken the temperature of the dominant blackbody component, and extrapolated the V magnitude from the Rayleigh-Jeans tail found in the UV.

Note. — Calibrated using the parallax of RX J1856.5−3754; see § 1.3, Eqn. 1.3.

a blackbody, although at a level slightly above that inferred from blackbody fits to the X-ray data (van Kerkwijk & Kulkarni 2001b). In particular, $f_\nu \propto \nu^2$ in the optical regime. If we assume that the surface compositions of isolated neutron stars are similar, then $f_\nu \propto R^2 kT \nu^2/d^2$, where R is the neutron star radius, kT is the effective temperature of the surface, and d is the distance. If the neutron stars all have the same radii, we can write

$$d_{100} = 1.4\sqrt{\frac{kT}{57\ \mathrm{eV}}}10^{(V-25.7)\ \mathrm{mag}/5} = 1.4\sqrt{\frac{kT}{57\ \mathrm{eV}}}10^{(B-25.3)\ \mathrm{mag}/5}, \tag{1.3}$$

where $d = 100 d_{100}$ pc, and B and V are the observed optical magnitudes. Here we use the best-fit blackbody temperature; while this is not always the best-fit overall to the X-ray emission (Pons et al. 2002a), it is a simple model and the dependence of d_{100} on kT is rather weak, so it suffices. We list the implied distances for the three other neutron stars that have thermally-dominated X-ray emission and optical counterparts in Table 1.6. As a general result of our new parallax, we decrease the local density of isolated neutron stars by a factor of ~ 10 with respect to that inferred from W01.

For the radio pulsar B0656+14 we get a distance of $d_{100} \approx 3.3$, near the low end of the values estimated through other means (250–800 pc; Mignani, De Luca, & Caraveo 2000) but still plausible. We understand that W. Brisken will soon have a VLBA measurement of the parallax, which should provide independent confirmation of our results (W. Brisken 2001, personal communication).

Data are based on observations with the NASA/ESA Hubble Space Telescope, obtained from the data Archive at the Space Telescope Science Institute, which is operated by the Association of Universities for Research in Astronomy, Inc., under NASA contract NAS 5-26555. D.L.K. holds a fellowship from the Fannie and John Hertz Foundation, and his research is supported by NSF and NASA. M.H.v.K. is supported by a fellowship from the Royal Netherlands Academy of Arts and Sciences. J.A. acknowledges support from HST grant GO-8153. We thank S. Kulkarni and D. Frail for valuable discussions.

1.4 Details of Analysis

To test the robustness of our analysis, we performed the same general analysis but with variations on the input data set and analysis method. These variations included combinations of

- Using a six-parameter linear transformation between the epochs (instead of the standard four-parameter transformation involving a shift, scale, and rotation).
- Rejecting the stars with the largest position uncertainties.
- Rejecting the stars whose derived proper motions had the largest uncertainties.
- Rejecting stars #21 and #201, and the galaxies #20 and #104.
- Rejecting the stars more than 300 pixels (15″) from RX J1856.5−3754.
- Rejecting up to 10 stars at random from the sample.
- Using the F606W ePSF instead of the F555W ePSF (see § 1.2.1).

All of these analyses gave entirely consistent results with rms variance of 0.4 mas, showing that our parallax measurements are not biased by any particular data points. Comparison of these parallax determinations allows us to better estimate the uncertainty in the parallax. To the formal error determined from the least-squares fit (1.7 mas), we add (in quadrature) the 0.4 mas rms found above.

As another test, we used the same algorithm to measure the parallaxes of all of the other stellar sources in the *HST* images. As expected from their photometric distances (§ 1.5), there were very few convincing parallax measurements for these sources (Figure 1.2). The measured parallaxes had a mean of −0.3 mas and a variance of 1.2 mas. The variance in the measured parallax was roughly independent of the brightness of the star, down to the brightness of RX J1856.5−3754, and is reasonably consistent with our estimation of the uncertainty of the parallax of RX J1856.5−3754. We therefore believe that a conservative estimate of the 1-σ parallax uncertainty to be 2 mas.

Finally, we performed the same analysis but with the initial astrometry done using more conventional Gaussian fitting and with older WFPC2 distortion coefficients (Holtzman et al. 1995; Trauger et al. 1995), like W01. Again, the results were consistent with those found using the more accurate ePSF fitting.

1.5 Background Sources

Figure 1.5 shows the color-magnitude diagram for the background sources that have reliable VLT photometry (van Kerkwijk & Kulkarni 2001b,a) and the distances implied from main-sequence fitting. Almost all of the sources are bounded by main sequences with distances from 2–25 kpc, with a number at implied distances of 10–15 kpc. Alternately, a number of the sources are consistent with red-giant branch stars at a distance ~ 25 kpc.

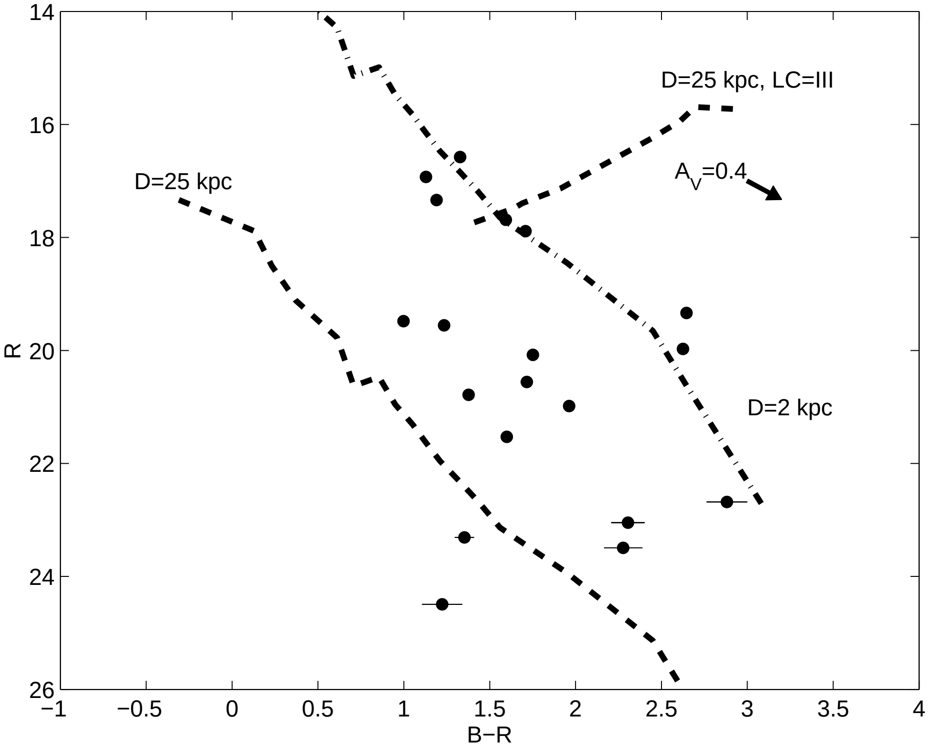

Figure 1.5 Color-magnitude diagram for background sources. R vs. $B-R$, with a $A_V = 0.4$ mag reddening vector and a model main sequences at a distance of 2 kpc (dash-dotted line), a main sequence at a distance of 25 kpc (dotted line), and a giant branch at a distance of 25 kpc (dotted line, marked "LC=III") from Cox (2000, p. 388, p. 392).

The implied distances of some of these sources, up to 25 kpc, places then at the edge of the Milky Way and ≈ 2.5 kpc above the disk, making them unlikely to be part of the Milky Way. The sources may be, however, in the Sgr dwarf galaxy. The heliocentric distance of the Sgr dwarf galaxy is ≈ 25 kpc, and it has a line-of-sight extent of $\lesssim$ 8 kpc (Ibata et al. 1997). The region near RX J1856.5−3754 is ≈ 7.5° from the center of the Sgr dwarf galaxy (Ibata et al. 1997), plausibly within the solid angle subtended by the Sgr dwarf galaxy. Therefore a number of the stars in the field could be main-sequence or giant stars in the Sgr dwarf galaxy.

In Figure 1.6, we show the proper motion vectors for the background sources determined from the fitting. Most of the motions are small, < 5 mas yr^{-1}, with the majority being ≈ 2 mas yr^{-1}. This is consistent with the magnitude of the proper motion of the Sgr dwarf galaxy, 250 km s^{-1} at a distance of 25 kpc. The two galaxies (which were forced to have zero proper motion in our analysis) provide an absolute reference for these proper motions. The net proper motion of the background sources is $\lesssim$ 0.5 mas yr^{-1}. As this is less than the uncertainty in the measured proper motion for RX J1856.5−3754, the motion of the background sources should not bias the parallax of RX J1856.5−3754.

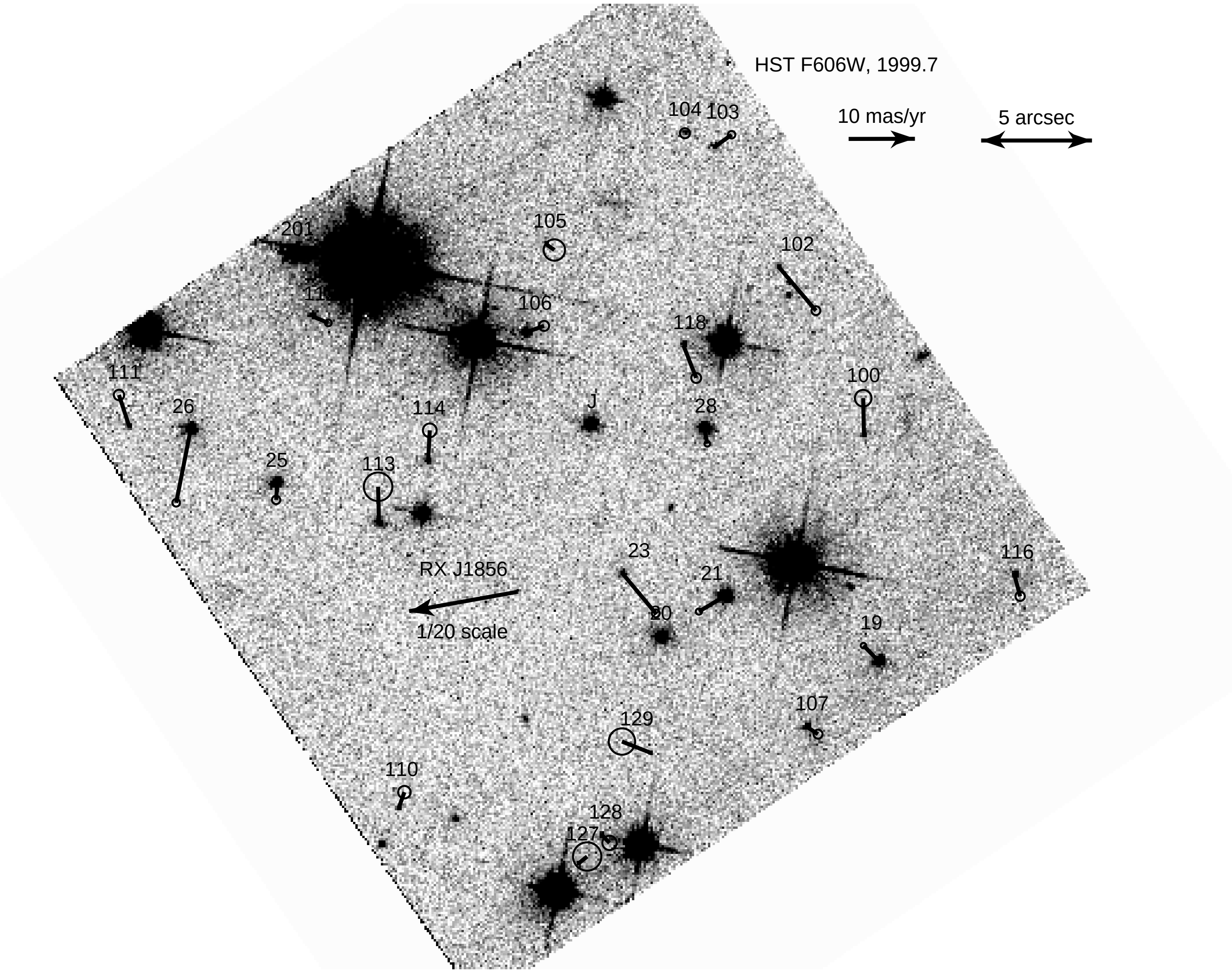

Figure 1.6 Derived proper motions for the background stars and galaxies used to register the three epochs, overlayed on the 1999.7 *HST* image. The lines indicate proper motions going from the stars to the circles. The sizes of the circles indicate the errors in the proper motions. The arrow in the upper right indicates proper motion with a magnitude of 10 mas yr^{-1}; next to it is a $5''$ scale bar. North is up, and east is to the left. The arrow from the position of RX J1856.5−3754 indicates the direction but only 1/20 the magnitude of the source's proper motion (no uncertainties are plotted for RX J1856.5−3754 as its proper motion is scaled such that the uncertainties would be invisible). All sources are labeled with identifiers from Table 1.4.

Chapter 2

A Probable Optical Counterpart for the Isolated Neutron Star RX J1308.6+2127[†]

D. L. Kaplan[a], S. R. Kulkarni[a], & M. H. van Kerkwijk[b‡]

[a]Department of Astronomy, 105-24 California Institute of Technology, Pasadena, CA 91125, USA

[b]Sterrenkundig Instituut, Universiteit Utrecht, Postbus 80000, 3508 TA Utrecht, The Netherlands

Abstract

Using a very deep observation with *HST*/STIS, we have searched for an optical counterpart to the nearby radio-quiet isolated neutron star RX J1308.6+2127 (RBS 1223). We have identified a single object in the 90% *Chandra* error circle that we believe to be the optical counterpart. This object has $m_{50\mathrm{CCD}} = 28.56 \pm 0.13$ mag, which translates approximately to an unabsorbed flux of $F_\lambda = (1.7 \pm 0.3) \times 10^{-20}$ ergs s^{-1} cm^{-2} Å^{-1} at 5150 Å or an X-ray-to-optical flux ratio of $\log(f_{\mathrm{X}}/f_{\mathrm{opt}}) = 4.9$. This flux is a factor of ≈ 5 above the extrapolation of the blackbody fit to the X-ray spectrum, consistent with the optical spectra of other isolated neutron stars. Without color information we cannot conclude that this source is indeed the counterpart of RX J1308.6+2127. If not, then the counterpart must have $m_{50\mathrm{CCD}} > 29.6$ mag, corresponding to a flux that is barely consistent with the extrapolation of the blackbody fit to the X-ray spectrum.

2.1 Introduction

Neutron stars have been regarded as natural laboratories for matter denser than can be obtained by heavy-ion accelerators. The basic physics is summarized by the mass and radius, with larger radii for a given mass favoring stiffer equations-of-state (EOS; Lattimer & Prakash 2000). It is against this backdrop that one recognizes that one of the major outcomes of the all-sky survey undertaken by the X-ray satellite *ROSAT* was the systematic identification of the nearest neutron stars (see reviews by Motch 2001 and Treves et al. 2000).

RX J1308.6+2127 (also known as RBS 1223) was identified as a candidate neutron star from the *ROSAT* Bright Survey by Schwope et al. (1999) on the basis of its soft X-ray spectrum (blackbody with $kT \approx 100$ eV), constant X-ray flux, and lack of optical counterpart. It now joins six other similar objects

---

[†] A version of this chapter was published in *The Astrophysical Journal Letters*, vol. 579, L29–L32.

[‡] Current address: Department of Astronomy and Astrophysics, University of Toronto, 60 St. George Street, Toronto, ON M5S 3H8, Canada.

(RX J1856.5−3754, RX J0720.4−3125, RX J1605.3+3249, RX J2143.0 +0654, RX J0806.4−4123, and RX J0420.0−5022; Walter, Wolk, & Neuhäuser 1996; Haberl et al. 1997; Motch et al. 1999; Haberl, Pietsch, & Motch 1999; Zampieri et al. 2001) and three previously known pulsars (Geminga, PSR B0656+14, and PSR B1055−52) in the sample of nearby 10^6-year old neutron stars detected by the *ROSAT* Bright Survey.

Of these objects, the five brightest (in terms of soft X-ray count rate) have been well studied. PSR 0656+14 and PSR B1055−52 are well known radio pulsars, not particularly remarkable in any other way. Geminga, first identified via is γ-ray emission (and thereby dramatically demonstrating that radio pulsars can lose a large fraction of their energy via γ-rays), is now generally considered to be an ordinary pulsar whose radio beam we happen to miss.

In contrast, RX J1856.5−3754 and RX J0720.4−3125 are mysterious. Both sources have (as expected) faint, blue, optical counterparts (Walter & Matthews 1997; Kulkarni & van Kerkwijk 1998), with X-ray-to-optical flux ratios of $\log(f_{\rm X}/f_{\rm opt}) \sim 5$. RX J1856.5−3754 shows no significant pulsations (Ransom, Gaensler, & Slane 2002) and despite significant investment of *Chandra* time, the X-ray spectrum is featureless (Drake et al. 2002). There is no evidence for any nonthermal emission (van Kerkwijk & Kulkarni 2001b). Conventional models for this source include a weakly magnetized cooling neutron star (van Kerkwijk & Kulkarni 2001a) or an off-beam radio pulsar (like Geminga but without the γ-ray emission; Braje & Romani 2002). In contrast, RX J0720.4−3125 shows 8.4-second pulsations. It too exhibits a featureless X-ray spectrum (largely thermal; Paerels et al. 2001). Again, conventional possibilities include an off-beam radio pulsar but the long period would require that the neutron star was born with either an unusually long period or an unusually large magnetic field (Kaplan et al. 2002b; Zane et al. 2002).

Thus the five brightest (in soft X-rays) and presumably the nearest neutron stars show a stunning diversity. Our understanding of the nature of two (or perhaps even three) of these sources is quite incomplete.

In this *Letter*, we re-determine the position of RX J1308.6+2127 from archival *Chandra* analysis. We present radio observations of RX J1308.6+2127, and we then discuss very deep optical observations aimed at detecting its optical counterpart. This source exhibits long-period pulsations with $P = 5.16$ s. However, unlike RX J0720.4−3125 a large period derivative has been measured (Hambaryan et al. 2002). If this is ascribed to magnetic braking then the implied dipole field strength is $B \gtrsim 10^{14}$ G, and RX J1308.6+2127 is a magnetar. Kulkarni & van Kerkwijk (1998) and Heyl & Kulkarni (1998) advocated the magnetar model for nearby long period pulsators because magnetars have an additional source of heat (their magnetic fields) and thus are warmer than ordinary neutron stars for a longer duration.

2.2 Observations & Data Reduction

2.2.1 X-ray

We used the 10 ks observation of RX J1308.6+2127 from the *Chandra X-ray Observatory* described in Hambaryan et al. (2002) to determine the position of the X-ray source. The main change from the analysis presented by Hambaryan et al. (2002) was that we corrected the spacecraft aspect by $0\farcs23$ according to the CXC prescription.[1] We measured the centroid of the X-ray source to be (J2000): $\alpha = 13^{\rm h}08^{\rm m}48\fs27$, $\delta = +21^\circ27'06\farcs78$, with statistical uncertainties of $\pm0\farcs05$ in each coordinate. This position is consistent with the position determined by Hambaryan et al. (2002) and with the *ROSAT* HRI position, but it has been tied (at least statistically) to the ICRS and is therefore preferable for comparison with other data sets. Overall, the positions of X-ray sources that have been corrected for aspect errors match optical positions (from the ICRS or Tycho) with a 90% confidence radius of $0\farcs6$, with a distribution that is highly

---

[1] `http://asc.harvard.edu/cal/ASPECT/fix_offset/fix_offset.cgi`

non-Gaussian.[2]

2.2.2 Radio

We observed RX J1308.6+2127 with the Very Large Array (VLA) at 1.4 GHz on 2001 February 12 through 2001 February 14, with a total integration time of 173 min. Observations were done in the BnA configuration with 2×50 MHz bandwidths, giving a final beam size of $1\farcs2 \times 3\farcs8$. All data sets independently calibrated using `AIPS` then combined for imaging. Imaging and self-calibration were performed in `difmap`. The data were repeatedly cleaned and self-calibrated (phase corrections only) until the solution converged. After cleaning, we found rms map noise to be 0.032 mJy.

No emission from RX J1308.6+2127 was found, giving a 3σ upper limit to the flux of a point-source of 0.10 mJy. This implies a radio luminosity limit for RX J1308.6+2127 of $0.05d_{700}^2$ mJy kpc^2 where the distance is $d = 700d_{700}$ pc (Kaplan, van Kerkwijk, & Anderson 2002c). Such a limit is a factor of 10 below the luminosity PSR J0205+6449 in 3C 58 (Camilo et al. 2002d) and a factor of 2 above the limit for Geminga (Seiradakis 1992). In fact, it is below virtually all of the radio pulsars younger than 10^6 yr (Motch 2001).

2.2.3 Optical

Schwope et al. (1999) unsuccessfully searched for an optical counterpart to RX J1308.6+2127, and determined limits of $B \gtrsim 26$ mag and $R \gtrsim 26$ mag from observations at Keck. The large X-ray-to-optical flux ratio inferred from the ground based data strongly favored a neutron star origin for RX J1308.6+2127. Accordingly, we obtained data from the Space Telescope Imaging Spectrometer (STIS) aboard *HST*, listed in Table 2.1. The data were taken with the CCD without a filter (50CCD aperture), which gives an extremely broad spectral response from 3000 Å to 9000 Å. For these data, we drizzled (Fruchter & Hook 2002) all the individual exposures onto a single image, for a total exposure of 21,144 s (8 orbits). We used a pixel scale of 0.5, so that the final image had $0\farcs0254$ pixels. For astrometric purposes we also obtained data with the Echelle Spectrograph and Imager (ESI; Sheinis et al. 2002) at the Keck II telescope and the Large Format Camera (LFC) at the Palomar 200-inch telescope. We performed standard reduction of the ground-based data in `IRAF`, subtracting bias images, flat-fielding, and stacking the exposures. We referenced the astrometry to the latest version of the Guide Star Catalog[3] (GSC 2.2). After applying a distortion solution (M. Hunt 2002, personal communication[4]), we identified 142 unsaturated stars on the LFC image, solved for rotation, zero point, and plate scale (the same terms were used for all subsequent astrometric solutions), and got residuals of $0\farcs4$ in each coordinate.

We used 13 sources on the LFC image to transfer the astrometric solution to the ESI image, with residuals of $0\farcs14$ in each coordinate. From the ESI image (Figure 2.1), we identified 10 stars that we used to go to the STIS image, and obtained residuals of $0\farcs06$ in each coordinate. Assuming a $0\farcs3$ intrinsic uncertainty[5] for the GSC 2.2, we then have overall uncertainties of $0\farcs3$ in each coordinate for the STIS image. With the $0\farcs6$ 90% radius for the X-ray astrometry, we estimate a final 90% confidence radius of $\approx 1\farcs0$.

---

[2] `http://asc.harvard.edu/cal/ASPECT/celmon/`

[3] `http://www-gsss.stsci.edu/support/data_access.htm`

[4] `http://wopr.caltech.edu/~mph/lfcred/`

[5] `http://www-gsss.stsci.edu/gsc/gsc2/calibrations/astrometry/astrometry.htm#method`

Table 2.1. Summary of Optical Observations

Telescope	Instrument	Date (UT)	Exposure (s)	Band
Keck II	ESI	2000-May-03	3,500	R
HST	STIS	2001-Jul-22	5,264	50CCD
···	···	2001-Aug-04	15,880	50CCD
P200	LFC	2002-Mar-05	375	*r*

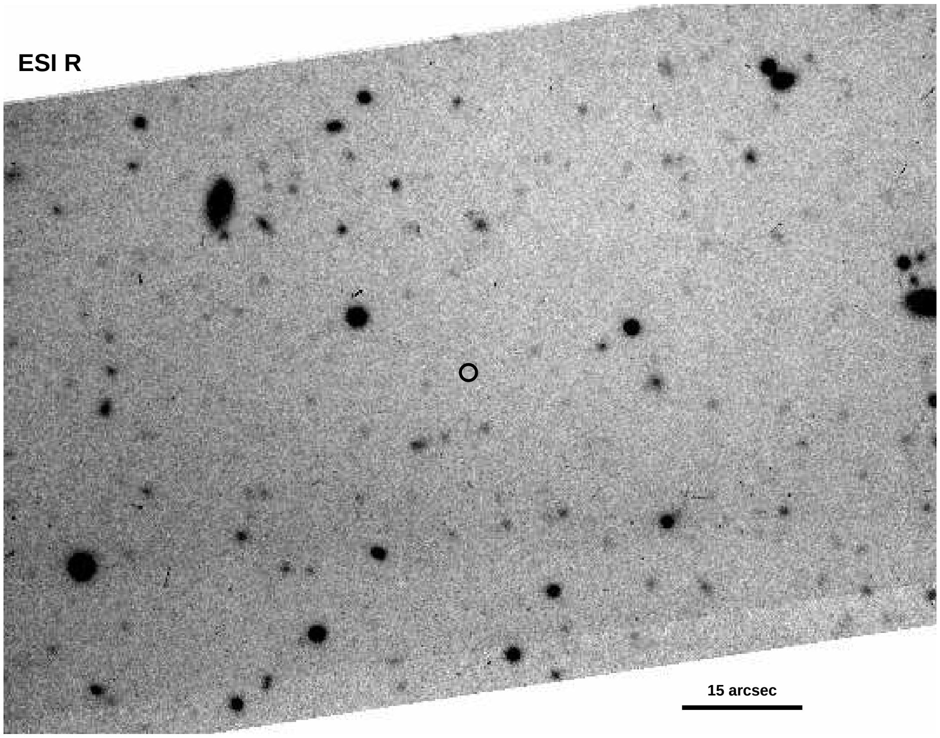

Figure 2.1 Keck ESI image of the field around RX J1308.6+2127. The image is ≈ $2'$ on a side, with north up and east to the left. The $1\farcs0$-radius *Chandra* error circle is shown.

2.3 Analysis & Discussion

In the following, we use the results of the spectroscopic fits of Hambaryan et al. (2002) to the *Chandra* data. Specifically, we take $N_H = (2.4 \pm 1.1) \times 10^{20}$ cm^{-2}, $kT = 91 \pm 1$ eV and $R = (6.5 \pm 0.3) d_{700}$ km, where the normalization comes from the *Chandra* count rate. This spectrum implies an unabsorbed flux of $(3.5 \pm 0.3) \times 10^{-21}$ ergs s^{-1} cm^{-2} Å^{-1} at 5150 Å.

There is only one optical source inside the *Chandra* error circle. This source, marked X in Figure 2.2, is a possible counterpart to RX J1308.6+2127. There are no other potential counterparts visible in Figure 2.2, the next closest unresolved source being ≈ $4''$ from the *Chandra* position (source B in Figure 2.2).

Without color information, it is difficult to accurately photometer the 50CCD data. This is because its

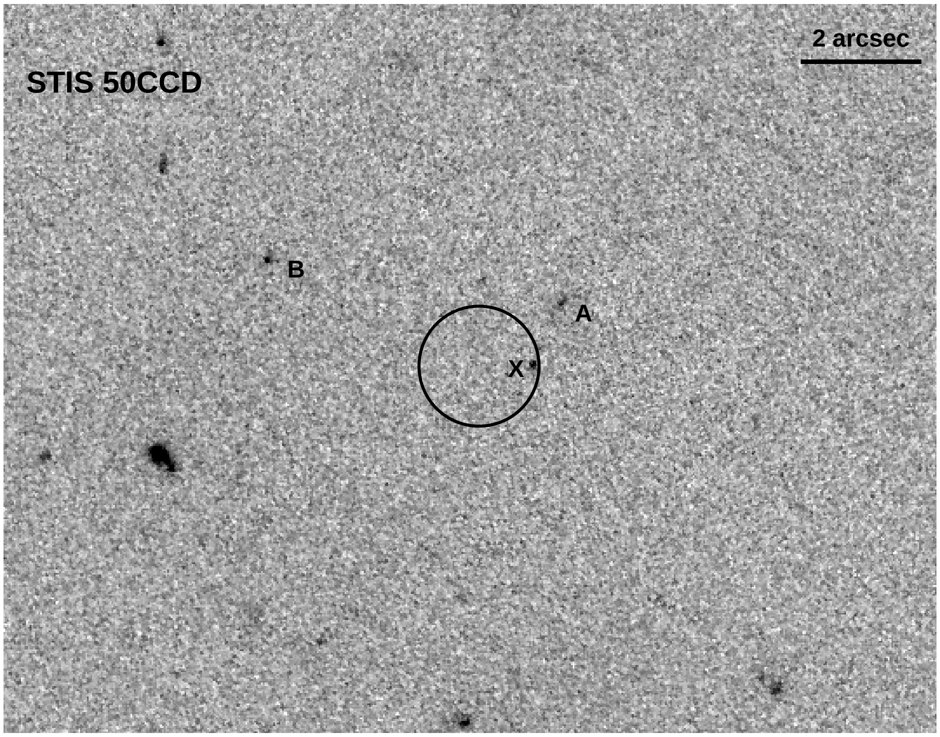

Figure 2.2 *HST*/STIS image of the field around RX J1308.6+2127. The image is $\approx 15''$ on a side, with north up and east to the left. The $1\farcs0$-radius *Chandra* error circle is shown. Source X, the likely counterpart of RX J1308.6+2127, and the unrelated sources A and B, are also indicated. Source A is extended.

wide bandwidth makes the aperture corrections and zero-point fluxes color dependent, leading to uncertainties of greater than a factor of 2 for the flux coming from stars ranging from type M to type O. In what follows, we follow the analysis of Kaplan et al. (2003b) for RX J0720.4−3125. We assumed that X is the counterpart and therefore has blue colors (similar to RX J1856.5−3754 and RX J0720.4−3125; van Kerkwijk & Kulkarni 2001b; Kulkarni & van Kerkwijk 1998). Then we used the bluest of the available aperture corrections: 0.183 mag at $0\farcs254$ radius (T. Brown 2002, personal communication). This correction is for a star with $B-V=-0.09$ mag, compared with an expected $B-V=-0.3$ mag for RX J1308.6+2127, and is therefore not quite right. However, the scattered light that contributes to the color-dependence of the STIS aperture corrections is predominantly red. For blue sources, the dependence of the correction on color is relatively small: for a star with $B-V=0.05$ mag, the correction changes by about 0.01 mag from that for a source with $B-V=-0.09$ mag. So the aperture correction used here should be reasonably appropriate, and to account for any remaining differences we have added a 0.02 mag systematic uncertainty into the photometry for RX J1308.6+2127.

With this correction, we find a magnitude of $m = 28.56 \pm 0.13$ mag for X at infinite aperture. The 3-σ limiting magnitude is ≈ 29.6 mag. These magnitudes are in the STMAG system, where $F_\lambda = 10^{-(m+21.1)/2.5}$ ergs s^{-1} cm^{-2} Å^{-1}. Assuming a spectrum similar to a Rayleigh-Jeans tail, this relation holds at $\lambda \approx 5148$ Å (this is the wavelength at which a Rayleigh-Jeans spectrum has the same flux as a flat spectrum that produces the same number of counts in the 50CCD band; see Appendix A of van Kerkwijk & Kulkarni 2001b).

From this we find $F_\lambda(\mathrm{X}) = (1.4 \pm 0.2) \times 10^{-20}$ ergs s^{-1} cm^{-2} Å^{-1} at 5148 Å. We estimate $A_V = 0.14 \pm 0.06$ mag, using the hydrogen column from above and the relation from Predehl & Schmitt (1995). Again assuming a Rayleigh-Jeans spectrum, we convert A_V to the extinction appropriate for the 50CCD bandpass (again see van Kerkwijk & Kulkarni 2001b) and find $A_{50\mathrm{CCD}} = 0.22 \pm 0.09$ mag. This gives us an unabsorbed flux of $(1.7 \pm 0.3) \times 10^{-20}$ ergs s^{-1} cm^{-2} $\mathrm{\AA}^{-1}$.

The optical flux of X is then a factor of ≈ 5 higher than the extrapolation of the X-ray blackbody of RX J1308.6+2127, smaller than the value of 16 found for RX J1856.5−3754 (van Kerkwijk & Kulkarni 2001b), but very similar to the values found for RX J0720.4−3125 and PSR B0656+14 (Kaplan et al. 2003b; Koptsevich et al. 2001). Likewise, the unabsorbed X-ray-to-optical flux ratio is $\log(f_{\mathrm{X}}/f_{\mathrm{opt}}) = 4.9$ (where the X-ray flux has been integrated over the entirety of the blackbody spectrum). The similarity of these values to those for other isolated neutron stars suggests that source X is the optical counterpart of RX J1308.6+2127.

While a blue color would assure us that X is the counterpart of RX J1308.6+2127, without color information we cannot be certain. Source X is very similar to the counterparts of RX J0720.4−3125 and RX J1856.5−3754, but it is possible that it is an unrelated source and that no counterpart was detected. If that is the case, then any counterpart would have $m_{50\mathrm{CCD}} > 29.6$ mag ($\log(f_{\mathrm{X}}/f_{\mathrm{opt}}) > 5.3$), or an optical flux just consistent with the extrapolation of the X-ray blackbody fit.

Aside from color information (difficult to obtain given its faintness), another good test for the nature of source X is proper motion. Neutron stars have significantly higher proper motions than the stellar population, with velocities of ~ 100 km s^{-1} typical for the general population of neutron stars (Arzoumanian, Chernoff, & Cordes 2002). Such high velocities have been found for the local neutron star population as well (e.g., Mignani et al. 2000; Walter 2001). Assuming a velocity of 100 km s^{-1}, the proper motion of RX J1308.6+2127 would be $30d_{700}^{-1}$ mas yr^{-1}. While the absolute astrometry from the STIS image does not have this precision, we expect to be able to perform relative astrometry with at least ~ 20 mas precision (the limiting factors are distortion correction and modeling of the point-spread-function, which is color-dependent), although this has not been tested for STIS. If this is the case, then in the next few years proper motion of source X may be detectable, and if so source X would almost certainly be a neutron star (if X were instead a star, it would have to be many kpc away and would therefore have negligible proper motion and be out of the galaxy, given its galactic latitude of $b = 83^{\circ}$).

In the P-$\dot{P}$ plane, RX J1308.6+2127 appears very similar to the anomalous X-ray pulsars (AXPs; Mereghetti 2000). However, whether or not we have detected the counterpart of RX J1308.6+2127, the X-ray-to-optical flux ratio is considerably higher than those found for AXPs (Hulleman, van Kerkwijk, & Kulkarni 2000; Hulleman et al. 2001; Wang & Chakrabarty 2002): for 4U 0142+61, $\log(f_{\mathrm{X}}/f_{\mathrm{opt}}) \approx 4.1$ (where the X-ray flux is measured from 0.5–10 keV; Juett et al. 2002). The optical emission from AXPs, which has a nonthermal spectrum, is thought to arise from the magnetosphere. Therefore the lack of an active magnetosphere would significantly decrease the optical flux. Scaling the nonthermal X-ray emission of 4U 0142+61 by the optical flux of RX J1308.6+2127, we would predict an X-ray power-law for RX J1308.6+2127 that would have been easily visible with *Chandra* (2×10^{-3} photons s^{-1} cm^{-2} keV^{-1} at 1 keV). As this power-law is not seen (Hambaryan et al. 2002), it appears that despite its rapid spin-down RX J1308.6+2127 does not have an active magnetosphere. Without an active magnetosphere, the optical emission from RX J1308.6+2127 would likely be similar to those of RX J1856.5−3754 and RX J0720.4−3125, suggesting that we have indeed found the counterpart to RX J1308.6+2127.

We thank A. Mahabal for obtaining the LFC data. D. L. K. is supported by the Fannie and John Hertz Foundation, S. R. K by NSF and NASA, and M.H.v.K. by the Royal Netherlands Academy of Arts and Sciences KNAW. Based on observations made with the NASA/ESA Hubble Space Telescope. Data presented herein were also obtained at the W. M. Keck Observatory, which is operated as a scientific partnership among the California Institute of Technology, the University of California, and the National Aeronautics and Space Administration. The Guide Star Catalog-II is a joint project of the Space Telescope Science Institute and the Osservatorio Astronomico di Torino. The National Radio Astronomy Observatory is a facility of the National Science Foundation operated under cooperative agreement by Associated

Universities, Inc.

Chapter 3

The Optical Counterpart of the Isolated Neutron Star RX J1605.3+3249[†]

D. L. Kaplan[a], S. R. Kulkarni[a], & M. H. van Kerkwijk[b]

[a]Department of Astronomy, 105-24 California Institute of Technology, Pasadena, CA 91125, USA

[b]Dept. of Astronomy & Astrophysics, University of Toronto, 60 St George St., Toronto, ON, M5S 3H8, Canada

Abstract

We have detected the optical counterpart to the nearby isolated neutron star RX J1605.3+3249 using observations from the Space Telescope Imaging Spectrometer aboard the *Hubble Space Telescope*. The counterpart, with $m_{50\mathrm{CCD}} = 26.84 \pm 0.07$ mag and very blue colors, lies close to the *ROSAT* HRI error circle and within the *Chandra* error circle. The spectrum is consistent with a Rayleigh-Jeans tail whose emission is a factor of ≈ 14 above the extrapolation of the X-ray blackbody, and the source has an unabsorbed X-ray-to-optical flux ratio of $\log(f_X/f_{\mathrm{opt}}) = 4.4$, similar to that of other isolated neutron stars. This confirms the classification of RX J1605.3+3249 as a neutron star.

3.1 Introduction

Thanks to *ROSAT*, a half dozen nearby neutron stars that emit no detectable radio emission have been identified (see Treves et al. 2000 for a comprehensive review). These objects have been eagerly studied using facilities such as the *XMM-Newton* Observatory, the *Chandra* X-ray Observatory, the *Hubble Space Telescope* (*HST*), Keck and the Very Large Telescope with the hope of determining the physical parameters, in particular radius and temperature, and to compare these to models of neutron stars. Independently, by their sheer proximity these objects play a pivotal role in assessing the neutron star demographics in the Galaxy. These two considerations highlight the virtue of detailed studies of nearby neutron stars.

RX J1605.3+3249 was identified in the *ROSAT* All-Sky Survey by Motch et al. (1999). The X-ray spectrum is well fitted by a blackbody with $kT \sim 90\,\mathrm{eV}$ and low interstellar column density, $N_H \sim 10^{20}\,\mathrm{cm}^{-2}$, and is quite similar to those of well studied nearby neutron stars such as RX J1856.5−3754 and RX J0720.4−3125. Motch et al. (1999) obtained deep ($B \sim 27\,\mathrm{mag}$ and $R \sim 26\,\mathrm{mag}$) images from the Keck telescope. Only one object (star C) was found within the $2''$ High Resolution Imager (HRI) circle (we believe that the uncertainty of the HRI position was underestimated; see § 3.2.2). Optical spectroscopic

---

[†] A version of this chapter was published in *The Astrophysical Journal Letters*, vol. 588, L33–L36.

Table 3.1. Summary of Optical Observations

Telescope	Instrument	Date (UT)	Exposure (s)	Band
Keck II	LRIS	1998-Aug-24	1800	R
HST	STIS	2001-Jul-21	2700	50CCD
HST	STIS	2001-Jul-21	5360	F28X50LP

observations carried out at the Canada-France-Hawaii Telescope (CFHT) showed that star C was a distant late-type M dwarf.

However, the soft spectrum and the stable X-ray emission are better accounted for by a model in which RX J1605.3+3249 is an isolated neutron star. If so, the optical counterpart would be below (or perhaps just at) the limit of the Keck observations. As a part of our investigation of nearby neutron stars with *HST* we undertook deep observations of this field. In this Letter we report the discovery of a faint blue optical star which we identify with the optical counterpart of RX J1605.3+3249. Our discovery confirms that RX J1605.3+3249 is a nearby neutron star.

3.2 Observations & Data Reduction

3.2.1 Hubble Space Telescope Observations

We observed RX J1605.3+3249 with the Space Telescope Imaging Spectrograph (STIS) aboard *HST* in two modes: unfiltered CCD (50CCD aperture) and a long-pass filter that transmitted photons longward of ≈ 5500 Å; see Table 3.1. For each mode, the individual images were drizzled (Fruchter & Hook 2002) onto a single image with a pixel scale of 0.5. Thus final images had $0\farcs0254$ pixels.

3.2.2 Keck Observations

For astrometric purposes we obtained imaging data from the Low-Resolution Imaging Spectrometer (LRIS; Oke et al. 1995) on the Keck II telescope; see Table 3.1. These images were reduced in a standard manner using tasks in MIDAS: bias subtraction, flat-fielding, and stacking of the exposures. We show the LRIS image in Figure 3.1.

After correcting the stellar positions measured in a 30-second LRIS image for geometric distortions,[1] we fit for plate scale, zero point, and rotation using 20 unsaturated stars from the latest version of the Guide Star Catalog (GSC-2.2)[2], obtaining rms residuals of $0\farcs09$ in each coordinate (in what follows, astrometric uncertainties refer to rms values in each coordinate unless otherwise specified). We then determined the astrometric solution (plate scale, zero point, and rotation) of the full 30-minute LRIS image by using 24 stars common to that and the 30-second image, getting rms residuals of $0\farcs02$. Finally, we used 21 stars on the deep LRIS image to determine the plate scale, zero point, and rotation of the drizzled STIS 50CCD image (shown in Fig. 3.2), getting rms residuals of $0\farcs04$. The final uncertainty to which our STIS coordinates are on the ICRS is dominated by the $0\farcs3$ uncertainty of the GSC-2.2.[3]

---

[1] See `http://alamoana.keck.hawaii.edu/inst/lris/coordinates.html`.

[2] See `http://www-gsss.stsci.edu/support/data_access.htm`.

[3] See `http://www-gsss.stsci.edu/gsc/gsc2/calibrations/astrometry/astrometry.htm#method`.

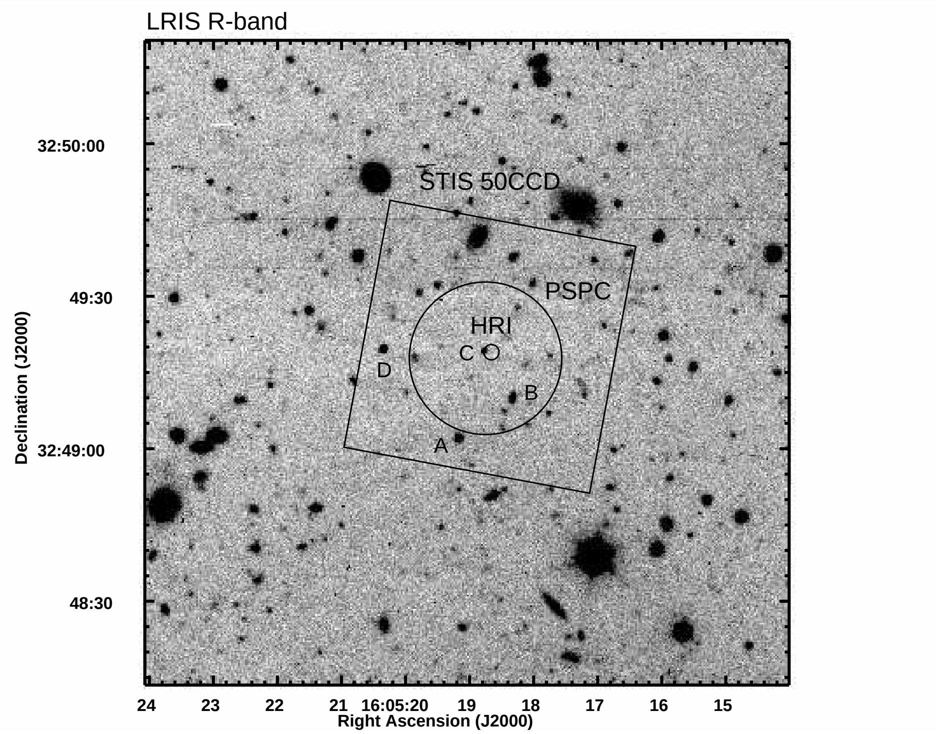

Figure 3.1 LRIS R-band image of the field around RX J1605.3+3249. The field of view of the STIS 50CCD observation is indicated by the box. The 15″-radius (90% confidence) PSPC and 1.″5-radius (90% confidence) updated HRI error circles are also indicated. Sources A, B, C, and D from Motch et al. (1999) are labeled.

We inspected all point sources on the STIS images that were within the PSPC error circle and found a very blue source. As can be seen from Figure 3.3 this is the bluest source in the PSPC error circle. The source, hereafter "X," is located at (J2000) $\alpha = 16^{\rm h}05^{\rm m}18\overset{\rm s}{.}52$ $\delta = +32^\circ 49' 18\overset{''}{.}0$, with uncertainties of about $0\overset{''}{.}3$, and lies $2\overset{''}{.}5$ from the HRI position from Motch et al. (1999), outside the nominal 90% error circle.

However, we have found a problem in comparing positions referenced to the USNO-A2.0 (Monet 1998), like the HRI position, and those referenced to the GSC-2.2/ICRS (our optical data). In this field, there appears to be a systematic shift between the GSC-2.2 and the USNO-A2.0 of $\langle \delta_{\rm USNO} - \delta_{\rm GSC} \rangle = 0\overset{''}{.}65$ (the shift in right ascension is a negligible $0\overset{''}{.}02$). If we correct the HRI position to the GSC-2.2 reference frame, we find the new position to be (J2000) $\alpha = 16^{\rm h}05^{\rm m}18\overset{\rm s}{.}66$ $\delta = +32^\circ 49' 19\overset{''}{.}0$. With this position, the error circle appears to be located properly with respect to star C, comparing with Fig. 4 of Motch et al. (1999).

Even with the updated position, X is slightly outside the 90% HRI error circle.[4] We have two possible explanations for this. First, RX J1605.3+3249 may have nonnegligible proper motion, such as that seen for RX J1856.5−3754 (Walter 2001). In this case the offset between the HRI position (epoch 1998.3) and the STIS image (2001.6) could be real. However, the LRIS data are not of sufficient quality to detect X with any confidence, so we will have to wait for additional data. Second, we note that the quoted uncertainty of the HRI position may be underestimated: Motch et al. (1999) used 6 reference sources for the boresight corrections and claim an uncertainty of $0\overset{''}{.}64$ with no contribution from systematic effects. In comparison, Hasinger et al. (1998) use 32 sources and get typical HRI uncertainties of 1.0″ that include a $0\overset{''}{.}5$ systematic error to achieve good X-ray-to-optical matches.

---

[4] X is within the error circle of the position obtained from a preliminary analysis of *XMM* data; van Kerkwijk et al., in preparation.

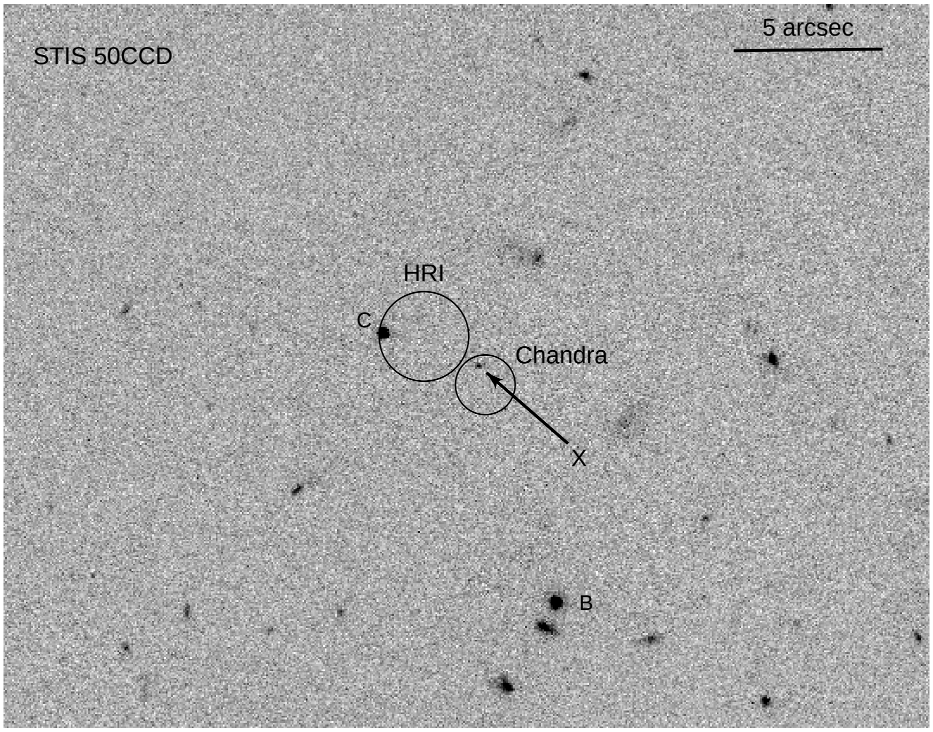

Figure 3.2 STIS/50CCD image of RX J1605.3+3249. The image has north up and east to the left. A 5″ scale bar is in the upper right. The updated 90% confidence error circles from *ROSAT*/HRI (1.″5 radius) and *Chandra* (1.″0 radius) are plotted. The likely counterpart to RX J1605.3+3249 is indicated by the X, and sources B and C from Motch et al. (1999) are labeled (source B is not just extended to the south-east, as noted by Motch et al. 1999, but is in fact composed of separate sources). The PSPC error circle (Fig. 3.1) is larger than this image.

In either case, the blue color of source X is similar to those of the counterparts of other isolated neutron stars (e.g., RX J1856.5−3754 and RX J1605.3+3249; Walter & Matthews 1997; van Kerkwijk & Kulkarni 2001b; Motch & Haberl 1998; Kulkarni & van Kerkwijk 1998). Thus we consider it likely that X is the counterpart of RX J1605.3+3249.

3.2.3 X-ray

While our identification based on color and position is plausible, the uncertainty in the *ROSAT* HRI position prevents us from being sure about the association (pulsations or a common proper motion would be definitive measurements). Fortunately, the availability of archival data from the *Chandra X-ray Observatory* offered us to opportunity to decrease the chance coincidence probability by a factor of 10. The *Chandra* observation (ObsID 2791) had a duration of 20 ks, and RX J1605.3+3249 was at the aim-point of the ACIS-I CCD array. Using standard processing steps[5] we corrected for a systematic astrometric error of $\Delta\alpha = -0.\!\!''35$ and $\Delta\delta = -0.\!\!''10$. As a cross-check, we compared the positions of other X-ray sources to GSC-2.2 stars (which, since we used the GSC-2.2 as the reference for the optical astrometry, ensures that they are on the same system as our *HST* data) and found that the coordinates match to better than 0.5 arcsecond.

We then measured the centroid of RX J1605.3+3249 (with a count rate of $\approx 0.15\ \mathrm{s}^{-1}$, RX J1605.3+3249

---

[5] `http://asc.harvard.edu/cal/ASPECT/fix_offset/fix_offset.cgi`.

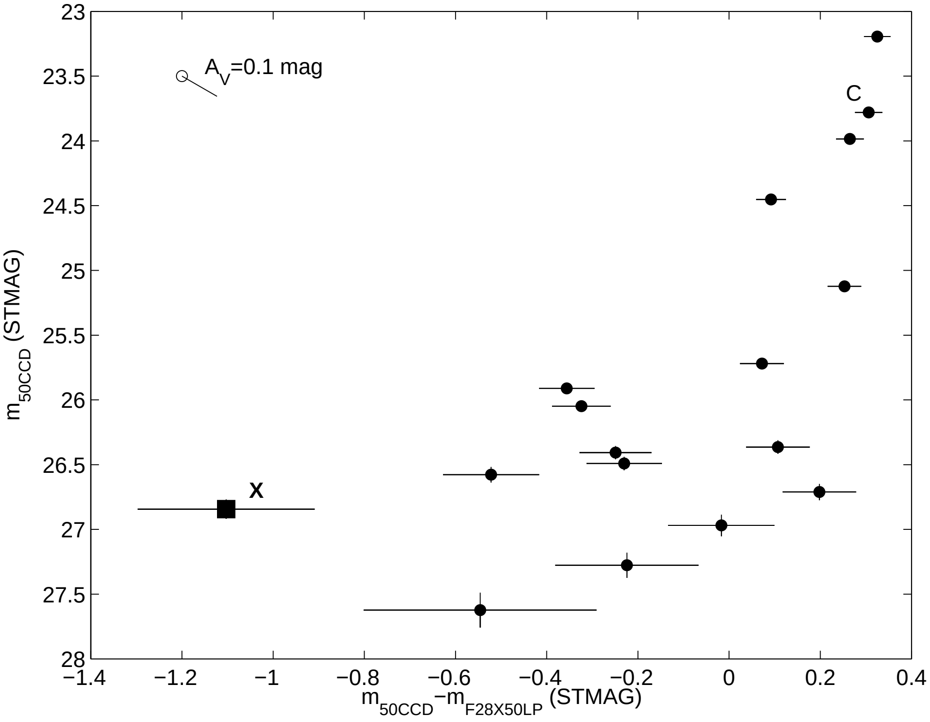

Figure 3.3 Color-magnitude diagram of point-like source from the STIS data. 50CCD magnitude is plotted against 50CCD − F28X50LP color. Source X is indicated and plotted as a square. Source C is also indicated. The sources have been corrected to "infinite" aperture using the correction most appropriate for RX J1605.3+3249 (§ 3.3). A reddening vector is plotted for $A_V = 0.1$ mag.

is somewhat affected by photon pileup, but this should not affect the centroid) to be (J2000) $\alpha = 16^{\rm h}05^{\rm m}18^{\rm s}\!.50$, $\delta = +32°49'17''\!.4$. We estimate a final 90% confidence radius of the X-ray position with respect to the STIS image of $\approx 1''\!.0$. As can be seen in Fig. 3.2, source X is well within this radius, lending credence to our identification.

3.3 Analysis & Discussion

We rely on the spectral fits to the *ROSAT* PSPC data presented in Motch et al. (1999): $kT = 92$ eV, $N_H = 1.1 \times 10^{20}$ cm^{-2}, and $R_\infty = 3.3 d_{300}$, where $d = 300 d_{300}$ pc is the distance and the normalization assumes 0.9 counts s^{-1} in the PSPC. The absorption column density implies an extinction of $A_V = 0.06$ mag, (Predehl & Schmitt 1995)—while this value is uncertain, it is low enough to not make a large difference. The total Galactic hydrogen column density is 2.4×10^{20} cm^{-2} (determined by COLDEN;[6] Dickey & Lockman 1990) so that the maximum extinction is 0.13 mag. This agrees with the extinction estimated from infrared dust emission (Schlegel, Finkbeiner, & Davis 1998), and confirms that the total extinction to RX J1605.3+3249 is low.

Within a $0''\!.25$-radius aperture, we measure magnitudes of $m_{\rm 50CCD} = 27.03 \pm 0.07$ mag and $m_{\rm F28X50LP} = 28.16 \pm 0.18$ mag for source X in the STMAG system. To correct the photometry to a nominal infinite aperture, we follow Kaplan, Kulkarni, & van Kerkwijk (2002a) and Kaplan et al. (2003b). As X is bluer than all of the stars in the image, we used the bluest of the available aperture corrections: 0.183 mag at $0''\!.25$

---

[6] See `http://asc.harvard.edu/toolkit/colden.jsp`.

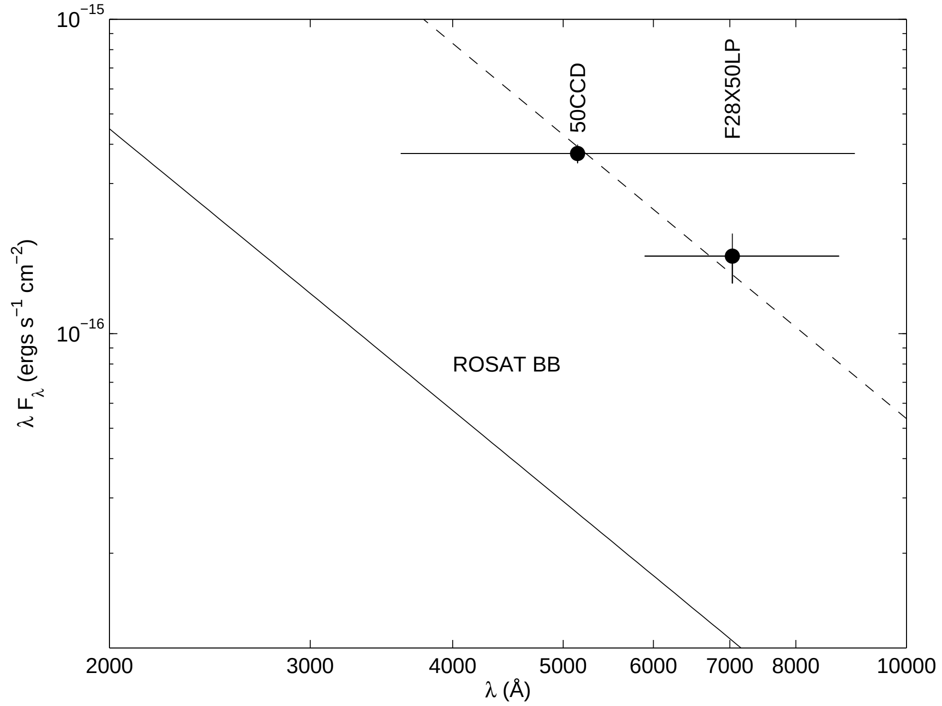

Figure 3.4 Spectral energy distribution for source X corrected for absorption with $A_V = 0.06$ mag. The STIS data are plotted as points. The extrapolation of the *ROSAT* blackbody (Motch et al. 1999) is the solid line (labeled "ROSAT BB"), and a Rayleigh-Jeans fit to the STIS data is the dashed line. The horizontal error-bars show the bandpasses of the filters.

radius for 50CCD and 0.214 mag at $0\farcs25$ radius for F28X50LP (T. Brown 2002, private communication). This then gives corrected magnitudes of $m_{\rm 50CCD} = 26.84 \pm 0.07$ mag and $m_{\rm F28X50LP} = 27.95 \pm 0.18$ mag, where we have incorporated a 0.02 mag uncertainty from the aperture corrections.

Since the STIS bandpasses are so wide we must use the shapes of the bandpasses to convert the measured magnitudes into fluxes. Following van Kerkwijk & Kulkarni (2001b), we find effective wavelengths $\langle\lambda\rangle$ of 5148 Å and 7137 Å and effective extinctions $\langle A_\lambda/A_V\rangle$ of 1.56 and 0.79 for 50CCD and F28X50LP, respectively. With these wavelengths, we can now apply the standard STMAG conversion of $F_\lambda(\langle\lambda\rangle) = 10^{-(m+21.1)/2.5}$ ergs s^{-1} cm^{-2} Å^{-1}.

We plot the spectral energy distribution of source X in Figure 3.4, assuming a blackbody spectrum in the X-ray regime.[7] As one can see, the optical photometry appears to follow a power-law with spectral index $\alpha \approx 2$ ($F_\nu \propto \nu^\alpha$), appropriate for a Rayleigh-Jeans tail and similar to that of other isolated neutron stars (van Kerkwijk & Kulkarni 2001b; Kaplan et al. 2003b). We also plot in Figure 3.4 the extrapolation of the best-fit *ROSAT* PSPC blackbody. The Rayleigh-Jeans fit to the STIS data has a normalization that is a factor of 14 ± 2 above the extrapolation of the blackbody. Other power-law indices are possible, as found for RX J0720.4−3125 (Kaplan et al. 2003b), but we do not believe that the current data warrant a full fit. The unabsorbed bolometric X-ray-to-optical flux ratio is $\log(f_X/f_{\rm opt}) = 4.4$ (assuming that the X-ray spectrum is well described by a blackbody).

The blueness of source X and its X-ray-to-optical flux ratio, taken together with the X-ray spectrum of RX J1605.3+3249, virtually guarantee that X is the optical counterpart of RX J1605.3+3249 and

---

[7] This blackbody is likely a simplification of a more realistic atmosphere model, but as yet such models have been unsuccessful in fitting sources like RX J1856.5−3754 and RX J0720.4−3125.

Table 3.2. Summary of Optically Detected Isolated Neutron Stars

Source	Period (s)	$kT^{\rm a}$ (eV)	$m_V{}^{\rm b}$ (mag)	$\log f_X/f_V{}^{\rm c}$	Optical[d] Excess	References
RX J1856.5−3754	⋯	61	25.8	4.4	6	1,2,3,4
RX J0720.4−3125	8.39	81	26.8	4.6	6	5,6
RX J1308.6+2127	10.31	91	28.7	5.0	5	7,8,9,10
RX J1605.3+3249	⋯	92	27.1	4.4	14	11,12

[a] Temperature of the best-fitting blackbody.

[b] V-band Vega magnitude, either measured or interpolated.

[c] Absorption-corrected bolometric X-ray-to-optical flux ratio, assuming that the X-ray emission is a blackbody. The V-band flux is computed according to $f_V = 10^{-(V+11.76)/2.5}$ ergs s^{-1} cm^{-2}, following Bessell, Castelli, & Plez (1998).

[d] The ratio of the observed V-band flux to the extrapolated X-ray blackbody flux at 5500 Å.

References. — 1: Ransom, Gaensler, & Slane (2002); 2: Burwitz et al. (2003); 3: Drake et al. (2002); 4: van Kerkwijk & Kulkarni (2001b); 5: Haberl et al. (1997); 6: Kaplan et al. (2003b); 7: Schwope et al. (1999); 8: Hambaryan et al. (2002); 9: Kaplan et al. (2002a); 10: Haberl (2003); 11: Motch et al. (1999); 12: this work.

that RX J1605.3+3249 is an isolated neutron star. It then joins 3 other sources (RX J1856.5−3754, RX J0720.4−3125, and possibly RX J1308.6+2127) that have soft X-ray blackbodies, blue optical counterparts, and no other emission; see Table 3.2. RX J1605.3+3249 stands out from the other sources in Table 3.2 by virtue of its relatively large optical excess: the optical flux is a factor of 14 above the extrapolated X-ray flux, where for the other sources the ratio is closer to 6 (this is despite the fact that the X-ray-to-optical flux ratio for RX J1605.3+3249 is within the range of the other sources). This can also be seen from the *ROSAT* data in Schwope et al. (1999), where RX J1605.3+3249 has a factor of 2 smaller count rate than RX J0720.4−3125 despite being hotter and having a comparable optical magnitude. There are two possibilities to explain the large excess of RX J1605.3+3249: either its X-ray emission is suppressed relative to the optical, or the optical emission is enhanced.

The first scenario implies that the blackbody radius ($3.3 d_{300}$ km, where the distance of ~ 300 pc is predicted based on the optical flux; see Kaplan, van Kerkwijk, & Anderson 2002c) is significantly smaller than those of the other sources (typically 6 km). If the blackbody radius can be interpreted as the radius of a hot polar cap, perhaps RX J1605.3+3249 has a different magnetic field configuration leading to a smaller cap size, or RX J1605.3+3249 is in an orientation where only half of the cap is visible (although this is difficult when relativistic beaming is taken into account; Psaltis, Özel, & DeDeo 2000).

The second scenario could occur if there were a significant contribution to the optical emission from nonthermal emission. Nonthermal emission could arise if there were a substantial spin-down luminosity, $\dot{E}$ (such as that seen for PSR B0656+14; Koptsevich et al. 2001). In this case, the high optical excess could indicate a large $\dot{E}$ for RX J1605.3+3249. While we cannot constrain the nonthermal emission from the current photometry, it may be difficult to reproduce the thermal-like spectrum observed in Figure 3.4 and to invoke significant nonthermal flux. One could appeal to light-element atmospheres for RX J1605.3+3249, as they have high optical excesses over blackbodies (Pavlov et al. 1996). However, these excesses are far too high (factors of 50–100, instead of 14) to fit our photometry, allowing us to reject such models.

Future observations, such as higher-precision X-ray spectroscopy from *Chandra* and *XMM* (being analyzed), additional optical photometry, and improved X-ray timing (in order to determine P and eventually $\dot{E}$ and the magnetic field B), should help to settle these issues. We are also searching for an Hα nebula around RX J1605.3+3249 (e.g., van Kerkwijk & Kulkarni 2001a). A single definitive measurement would be the distance, which would determine the areas of the X-ray and optical emission regions, but a parallax measurement with *HST* would require a significant investment of observing time.

We thank an anonymous referee for helpful comments. D. L. K. is supported by the Fannie and John Hertz Foundation and S. R. K. by NSF and NASA. Data presented herein were based on observations made with the NASA/ESA Hubble Space Telescope, obtained at the Space Telescope Science Institute, which is operated by the Association of Universities for Research in Astronomy, Inc., under NASA contract NAS 5-26555. Data presented herein were also obtained at the W. M. Keck Observatory, which is operated as a scientific partnership among the California Institute of Technology, the University of California, and the National Aeronautics and Space Administration. The Guide Star Catalog-II is a joint project of the Space Telescope Science Institute and the Osservatorio Astronomico di Torino. MIDAS is developed and maintained by the European Southern Observatory.

Chapter 4

X-ray Timing of the Enigmatic Neutron Star RX J0720.4−3125[†]

D. L. KAPLAN[a], S. R. KULKARNI[a], M. H. VAN KERWIJK[b‡], & H. L. MARSHALL[c]

[a]Department of Astronomy, 105-24 California Institute of Technology, Pasadena, CA 91125, USA

[a]Sterrenkundig Instituut, Universiteit Utrecht, Postbus 80000, 3508 TA Utrecht, The Netherlands

[c]Center for Space Research, Massachusetts Institute of Technology, Cambridge, MA 02139, USA

Abstract

RX J0720.4−3125 is the third brightest neutron star in the soft X-ray sky and has been a source of mystery since its discovery, as its long 8-s period separates it from the population of typical radio pulsars. Three models were proposed for this source: a neutron star accreting from the interstellar medium, an off-beam radio pulsar, or an old, cooling magnetar. Using data from *Chandra*, *ROSAT*, and *BeppoSAX* we are able to place an upper limit to the period derivative, $|\dot{P}| < 3.6 \times 10^{-13}$ s s^{-1} (3-σ). While our upper limit on $\dot{P}$ allows for the accretion model, this model is increasingly untenable for another similar but better studied neutron star, RX J1856.5−3754, and we therefore consider the accretion model unlikely for RX J0720.4−3125. We constrain the initial magnetic field of RX J0720.4−3125 to be $\lesssim 10^{14}$ G based on cooling models, suggesting that it is not and never was a magnetar, but is instead middle-aged neutron star. We propose that it is either a long-period high-magnetic field pulsar with $\dot{P} \sim 10^{-13}$ s s^{-1} similar to PSR J1814−1744, or a neutron star born with an initial period of ≈ 8.3 s and $\dot{P} \sim 10^{-15}$ s s^{-1}. The proximity of RX J0720.4−3125 is strongly suggestive of a large population of such objects; if so, radio pulsar surveys must have missed many of these sources.

4.1 Introduction

RX J0720.4−3125 was discovered by Haberl et al. (1997) as a soft ($kT \sim 80$ eV), bright X-ray source in the *ROSAT* All-Sky Survey. Given its very low hydrogen column density ($N_H \sim 1 \times 10^{20}$ cm^{-2}), nearly sinusoidal 8.39-second pulsations, relatively constant X-ray flux, and very faint ($B = 26.6$ mag), blue optical counterpart (Kulkarni & van Kerkwijk 1998; Motch & Haberl 1998), it was classified as a nearby, isolated neutron star.

[†] A version of this chapter was published in *The Astrophysical Journal Letters*, vol. 570, L79–L83.

[‡] Current address: Department of Astronomy and Astrophysics, University of Toronto, 60 St. George Street, Toronto, ON M5S 3H8, Canada.

Table 4.1. Summary of Observations

Date	MJD (day)	Exp. (ks)	Span (ks)	Counts	BG Counts[a]	Facility	Instrument/ Mode[b]	Period[c] (s)	TOA – MJD 50000[d] (TDB day)
1993-Sep-27	49257.2	3.2	12.0	5800	22.8	*ROSAT*	PSPC	8.3914(4)	−742.745297(3)
1996-Nov-03	50390.9	33.7	65.7	12662	79.0	*ROSAT*	HRI	8.39113(6)	391.300750(2)
1997-Mar-16	50523.1	18.1	99.4	407	15.4	*BeppoSAX*	LECS	8.39103(9)	523.705635(4)
1998-Apr-20	50923.2	8.1	460.3	3074	17.1	*ROSAT*	HRI	8.391114(14)	925.688213(5)
2000-Feb-01	51575.3	5.4	305.5	929	1.3	*CXO*	HRC-S+LETG 0	8.39111(2)[e]	1577.039569(2)
				671	127.0	*CXO*	HRC-S+LETG ±1	⋯	⋯
2000-Feb-02	51576.1	26.3	⋯	4584	5.2	*CXO*	HRC-S+LETG 0	⋯	⋯
				3027	454.0	*CXO*	HRC-S+LETG ±1	⋯	⋯
2000-Feb-04	51578.7	6.1	⋯	1119	1.2	*CXO*	HRC-S+LETG 0	⋯	⋯
				687	119.5	*CXO*	HRC-S+LETG ±1	⋯	⋯
2001-Dec-04	52247.7	15.0	168.6	31746	229.8	*CXO*	ACIS-S3/CC	8.391119(12)[e]	2248.6768200(8)
2001-Dec-05	52248.2	10.6	⋯	22825	155.8	*CXO*	ACIS-S3/CC	⋯	⋯
2001-Dec-06	52249.6	4.1	⋯	8786	61.4	*CXO*	ACIS-S3/CC	⋯	⋯

[a] Background counts scaled to the source extraction area. [b] HRC-S+LETG 0 indicates order 0; HRC-S+LETG ±1 indicates orders ±1. [c] Values in parentheses are 1-σ errors in the last decimal digit. [d] TOA is defined as the maximum of the folded light curve nearest the middle of the observation, as determined from the best-fit sine wave. The ACIS/CC times were corrected for spacecraft motion following Zavlin et al. (2000). [e] All pointings for each of the *Chandra* HRC-S and *Chandra* ACIS datasets were processed together.

As one of the closest ($d \sim 300$ pc; Kaplan, van Kerkwijk, & Anderson 2002c) neutron stars, RX J0720.4−3125 occupies a central position in our study of these objects. However, the long period is puzzling, and has led to three models: an old, weakly magnetized neutron star accreting matter from the interstellar medium (Wang 1997; Konenkov & Popov 1997); a middle-aged pulsar with $\sim 10^{12}$ G magnetic field whose radio beams are directed away from the Earth (Kulkarni & van Kerkwijk 1998); or an old magnetar (neutron star with magnetic field $> 10^{14}$ G; Duncan & Thompson 1992) that is kept warm by the decay of its strong magnetic field (Heyl & Hernquist 1998b; Heyl & Kulkarni 1998). These models predict different period derivatives: $\dot{P} < 5 \times 10^{-15}$ s s^{-1}, $\dot{P} \sim 10^{-15}$–10^{-13} s s^{-1}, and $\dot{P} \gtrsim$ few $\times 10^{-13}$ s s^{-1}, respectively.

Motivated thus, we undertook timing observations of RX J0720.4−3125 using the *Chandra X-ray Observatory* (*CXO*), supplemented with analysis of archival data from *ROSAT* and *BeppoSAX*.

After submission of this paper, we became aware of the work of Zane et al. (2002) reporting a timing analysis of RX J0720.4−3125. A "Notes added in manuscript" section regarding that analysis can be found at the end of the manuscript.

4.2 Observations

The primary data consist of two sets of observations obtained from *Chandra*: one using the HRC in the spectroscopic mode (HRC-S) with the Low Energy Transmission Grating (LETG), and one using ACIS in the continuous clocking (CC) mode. The primary and archival datasets are summarized in Table 4.1.

We processed the HRC-S data using the standard pipeline[1] and extracted 0th order events from a circle with radius 10 pixels ($1\farcs3$). For the ±1st orders, we extracted events from a region 0.0006° wide in the

---

[1] `http://asc.harvard.edu/ciao/threads/spectra_letghrcs/`

cross-dispersion direction (the `tg_d` coordinate) and from 0.08° to 0.35° along the dispersion direction (the `tg_r` coordinate). We extracted events from the ACIS data within $\pm 1''$ of the source. We then used the `axBary` program to barycenter the events in both these datasets.

The best fit position for RX J0720.4−3125, found by averaging the $0^{\rm th}$ order data from the three HRC-S datasets, is (J2000) $\alpha = 07^{\rm h}20^{\rm m}24\overset{\rm s}{.}96$, $\delta = -31^\circ 25' 49\overset{''}{.}6$, with rms uncertainty of $\approx 0\overset{''}{.}6$ in each coordinate due to *CXO* aspect uncertainties. This is consistent ($1\overset{''}{.}4$ away) with the optical position (Kulkarni & van Kerkwijk 1998). The X-ray source appears unresolved and its profile is consistent with that of a point source (half-power radius of $\approx 0\overset{''}{.}5$).

For the *ROSAT* HRI data, we extracted the events within a circle of radius 45 pixels ($22\overset{''}{.}5$) centered on the source. We used a circle of radius 200 pixels ($100''$) for the PSPC data. These events were barycentered using the `ftools` programs `abc` and `bct` and corrected to Barycentric Dynamical Time (TDB) according to Cox (2000, p. 14).

We extracted the *BeppoSAX* LECS events within a circle with radius of 25 pixels ($200''$) centered on the source and restricted to those with pulse-invariant (PI) amplitudes that were less than 90 (energies < 0.95 keV), in order to maximize the signal-to-noise. Finally, we barycentered the events with the `SAXDAS` tool `baryconv`.

4.3 Timing Analysis

For each dataset, we computed Z_1^2 power spectra around the known 8.39-second period. Specifically, we explored the period range from 8.376 s to 8.405 s in steps of 7 μs (oversampling by factors of 20–800 relative the nominal step-size of $P_0^2/\Delta T$, where $P_0 = 8.39$ s is the approximate period and ΔT is the span of the dataset from Table 4.1). As can be seen from Figure 4.1 all but the *Chandra* HRC-S and *ROSAT* HRI-2 datasets yielded unambiguous period estimates. For the HRC-S and HRI-2 sets the period estimates are ambiguous because the large gaps in the observations result in strong side-lobes. In Figure 4.2, we display the best-fit periods for the unambiguous determinations as well as possible periods for the HRC-S and HRI-2 datasets.

As can be seen from Figure 4.2, the ambiguity of the HRC-S and HRI-2 datasets can be resolved provided we assume (reasonably) that the period evolves smoothly with time. Our choice of period (for HRC-S and HRI-2) and the best fit periods (for the other datasets) are shown in Table 4.1. The errors on the periods were determined using the analytical expression from Ransom (2001). While that expression was derived for FFT power spectra, Z_1^2 power spectra have the same statistics (both are exponentially distributed) so the same relations should apply (we have verified this with numerical simulations). We also show in Table 4.1 times-of-arrival (TOAs) for each of the datasets.

The data in Table 4.1 are consistent with there being no measurable $\dot{P}$: fitting for a linear spin-down gives $P = 8.391115(8)$ s at MJD 51633 and $\dot{P} = (1 \pm 12) \times 10^{-14}$ s s^{-1}, with $\chi^2 = 1.54$ for 4 degrees of freedom (DOF). If, instead, we fit only for a constant period, we find $P = 8.391115(8)$ s, with $\chi^2 = 1.64$ for 5 DOF. Therefore we can constrain the secular period derivative to be $|\dot{P}| < 3.6 \times 10^{-13}$ s s^{-1} (3-σ).

The folded light curve is largely sinusoidal, with an rms pulsed-fraction (the rms of the light curve divided by the mean) of 8% for both *Chandra* datasets. However, this pulsed-fraction is energy-dependent: the fraction rises with decreasing energy (see Figure 4.3), in agreement with the *XMM* analysis (Paerels et al. 2001).

4.4 Discussion

Our upper limit of $|\dot{P}| < 3.6 \times 10^{-13}$ s s^{-1} is sufficiently high that we cannot meaningfully constrain the accretion model, for which we expect $\dot{P} < 5 \times 10^{-15}$ s s^{-1} (the limit is the case where all of the required

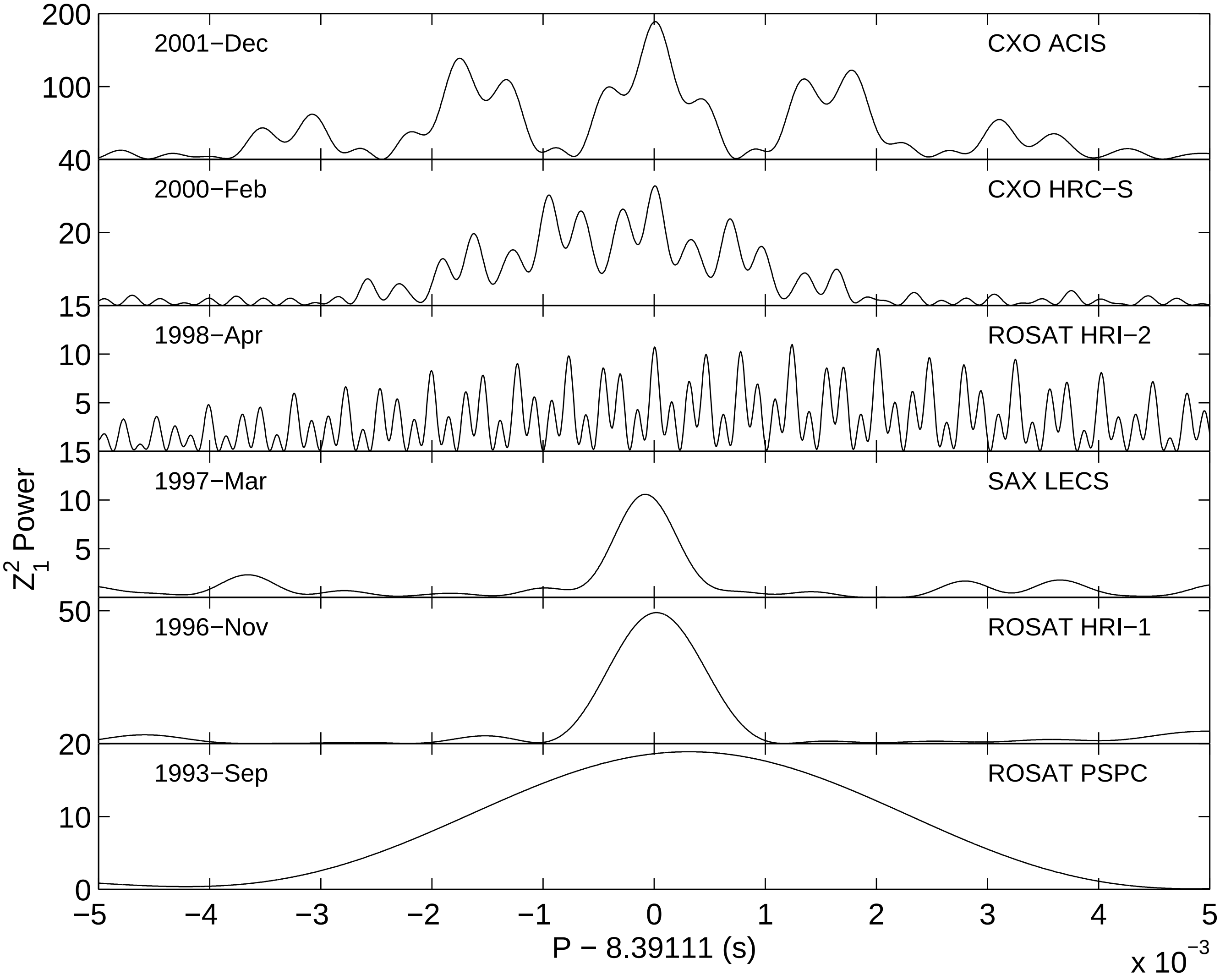

Figure 4.1 Z_1^2 periodograms for the datasets listed in Table 4.1. For each dataset, the Z_1^2 power is normalized so as to have unit mean (when no signal is present). Given that the statistics of Z_1^2 are exponential it follows that the variance is also unity. Note the different vertical scales which reflect the differing significance levels of the detections.

$\dot{M}$ of $\sim 10^{12}$ g s^{-1} couples to the neutron star at the corotation radius, giving maximum torque per unit mass). We note that the accretion model is no longer viable for another similar but better studied isolated neutron star, RX J1856.5−3754 (van Kerkwijk & Kulkarni 2001a). Regardless, the accretion model is best confronted by measuring the proper motion and distance, and looking for evidence of sufficiently dense ambient gas (deep Keck Hα imaging and *HST* astrometric observations are in progress).

However, we can constrain the pulsar and magnetar models. We can draw four inferences common to both models. First, the spin-down luminosity, $\dot{E} = I\dot{\omega}\omega < 2.4 \times 10^{31}$ ergs s^{-1}; here, $\omega = 2\pi/P$. Second, in the framework of a simple (vacuum magnetic dipole radiation) pulsar model, the physical age is roughly approximated (provided the current spin period is much larger than that at birth and that the magnetic field does not decay significantly) by the so-called characteristic age: $\tau_c \equiv P/(2\dot{P}) > 4 \times 10^5$ yr. Third, the strength of the dipole field is $B = 3.2 \times 10^{19} (P\dot{P})^{1/2} < 6 \times 10^{13}$ G. Fourth, we assume that the X-ray emission (well described by a blackbody; Haberl et al. 1997; Paerels et al. 2001) is cooling flux from the surface. The bolometric cooling luminosity is $L_{\rm cool} \approx 2 \times 10^{32} d_{300}^2$ ergs s^{-1} (Haberl et al. 1997), using the distance estimate of $300 d_{300}$ pc derived by scaling from RX J1856.5−3754 (Kaplan et al. 2002c).

Knowledge of $L_{\rm cool}$ enables us to estimate the cooling age, $t_{\rm cool}$, of RX J0720.4−3125. Magnetic fields, especially intense B fields such as those proposed for magnetars, can profoundly influence the cooling of neutron stars. To this end, we use the curves of L vs. t from Heyl & Kulkarni (1998) and find $t_{\rm cool} \approx (5-10) \times 10^5$ yr, assuming a 50% uncertainty in the distance and with only a slight dependence on B. This age is consistent with the characteristic age derived above.

In the magnetar model (we assume that the B-field decay is dominated by the slower irrotational mode; see Heyl & Kulkarni 1998) the expected B field at about 10^6 yr is, $\approx 2 \times 10^{14}$ G, well above the upper limit obtained from our $\dot{P}$ limit. Models that are consistent with both $L_{\rm cool}$ and our limit on $\dot{P}$ (and thus an upper limit on the current value of B) are those with initial $B \lesssim 10^{14}$ G. Based on this, we conclude that RX J1605.3+3249 is not a magnetar, motivating us to consider the pulsar model.

Earlier, Kulkarni & van Kerkwijk (1998) did not accept the radio pulsar model because in 1998 there were no radio pulsars with such long periods. However, over the past four years we have come to appreciate the existence of pulsars with $B > 10^{13}$ G (Camilo et al. 2000; see also Figure 4.4). In particular, the parameters of RX J0720.4−3125 are not too dissimilar to those of PSR J1814−1744, which has $P \approx 4$ s and $\dot{P} \approx 7.4 \times 10^{-13}$ s s^{-1}. Thus, the past objections against the radio pulsar model are no longer tenable, and RX J0720.4−3125 seems fully compatible with being an off-beam high-B pulsar. If that is the case, then we expect $\dot{P} \sim 10^{-13}$ s s^{-1}, a value that we should be able to measure in the near future.

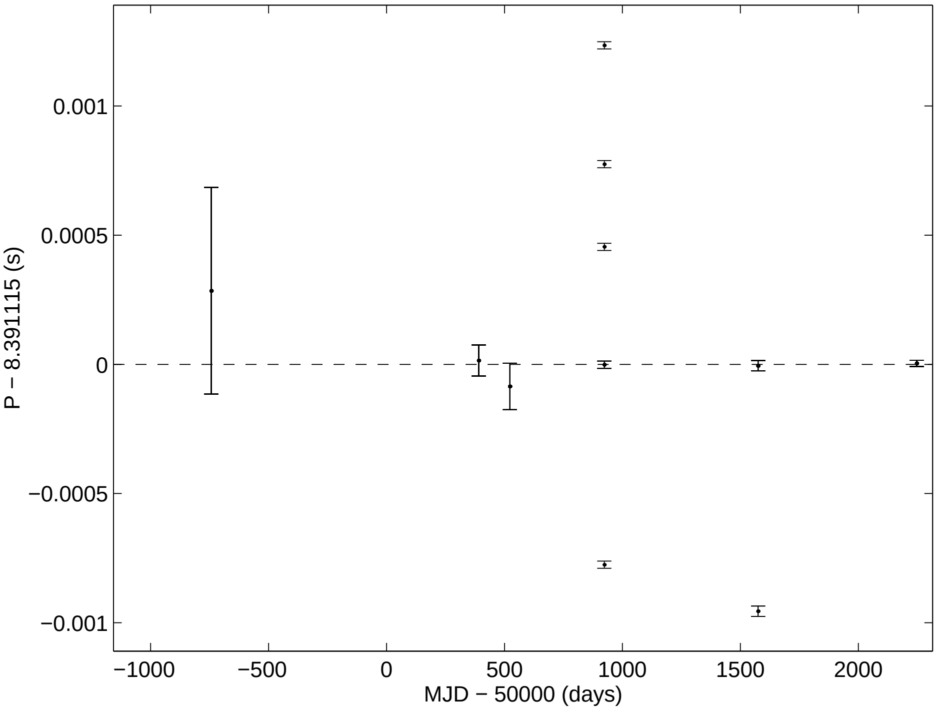

Figure 4.2 Period measurements for RX J0720.4−3125, using the data from Figure 4.1. As explained in the main text the *Chandra* HRC-S and *ROSAT* HRI-2 measurements are ambiguous owing to large gaps in the data. Probable periods are displayed. The best-fit constant period model is shown by the dashed line: $P = 8.391115(8)$ s.

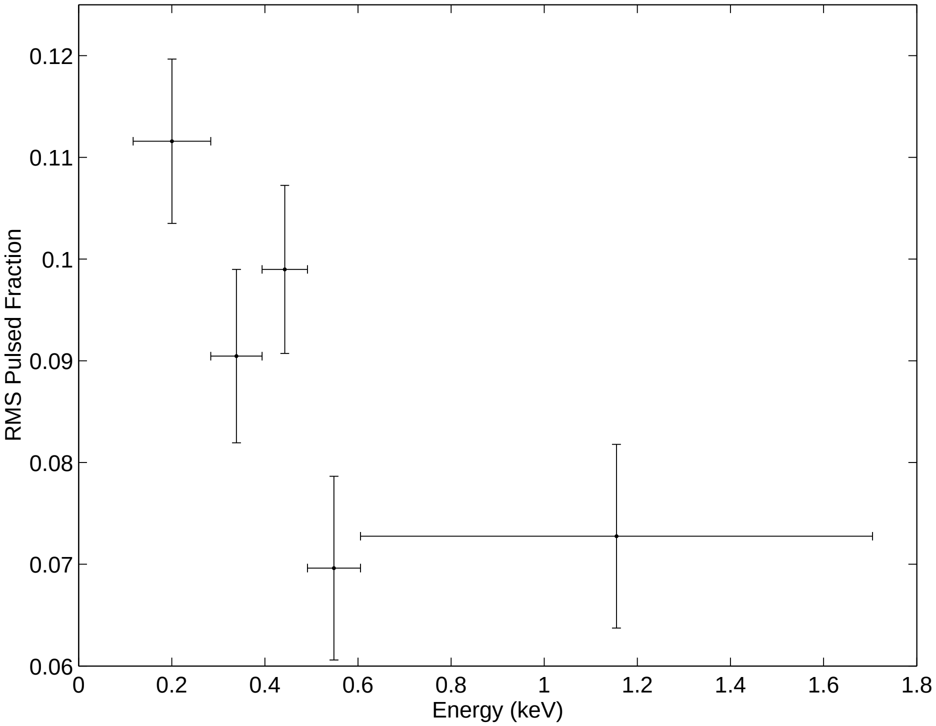

Figure 4.3 RMS pulsed-fraction (see § 4.3 for discussion) for different energy bins, from the *Chandra* ACIS data. The overall pulsed fraction is 8.1 ± 0.4%. Each bin was chosen to have the same number of total counts.

A separate possibility is that RX J0720.4−3125 is an off-beam pulsar with age compatible with $t_{\rm cool}$, but with a conventional ($\sim 10^{12}$ G) magnetic field and $\dot{P} \sim 10^{-15}$ s s^{-1} (and therefore $\tau_c \sim 10^8$ yr). RX J0720.4−3125 could then be similar to the 8.5-s, 2×10^{12}-G pulsar PSR J2144−3944 (Young, Manchester, & Johnston 1999; see Figure 4.4). With a braking index of 3, the age of a pulsar is $\tau = \tau_c \left(1 - (P_0/P)^2\right)$, where P_0 is the initial spin-period. If RX J0720.4−3125 does have $\tau \sim t_{\rm cool}$ and $B \sim 10^{12}$ G, we find and $P_0 \approx 8.3$ s, very close to P. Such as a pulsar would be an example of the "injection" hypothesis (Vivekanand & Narayan 1981), where pulsars are born with initial spin periods $P_0 \gg 10$ ms (as for the Crab). Such long initial periods are allowed and perhaps expected in some models of neutron-star formation (e.g., Spruit & Phinney 1998), where the precise initial period depends very sensitively on the details of the formation mechanism and may range over four orders of magnitude. While there are a few pulsars whose characteristic ages are factors of 10–100 times the ages derived from supernova remnant associations (Pavlov et al. 2002), this would be the first case for a source with $P_0 > 1$ s.

We make the following parenthetical observation: for most known pulsars the X-ray pulsed-fraction (largely) increases with photon energy (Perna, Heyl, & Hernquist 2001), whereas for RX J0720.4−3125 we see the opposite effect. However, for the pulsars (e.g., PSR B0656+14, PSR B1055−52), the X-ray luminosity has a strong, highly-pulsed, nonthermal component with $L_{X,\rm nonth} \sim 10^{-3}\dot{E}$ (Becker & Trümper 1997). Furthermore, in such objects heating of the polar caps by pulsar activity (probably dependent on $\dot{E}$) is likely significant. The interplay of these components with the viewing geometry can result in the large range of observed phenomena (e.g., Perna et al. 2001). For RX J0720.4−3125, though, with its small $\dot{E}$ there is little reason to expect a strong nonthermal contribution or a hot polar cap (although there must be some inhomogeneities to give the observed pulsations). We conjecture that the increase in the pulse fraction with decreasing photon energy is primarily due to the absence the additional components.

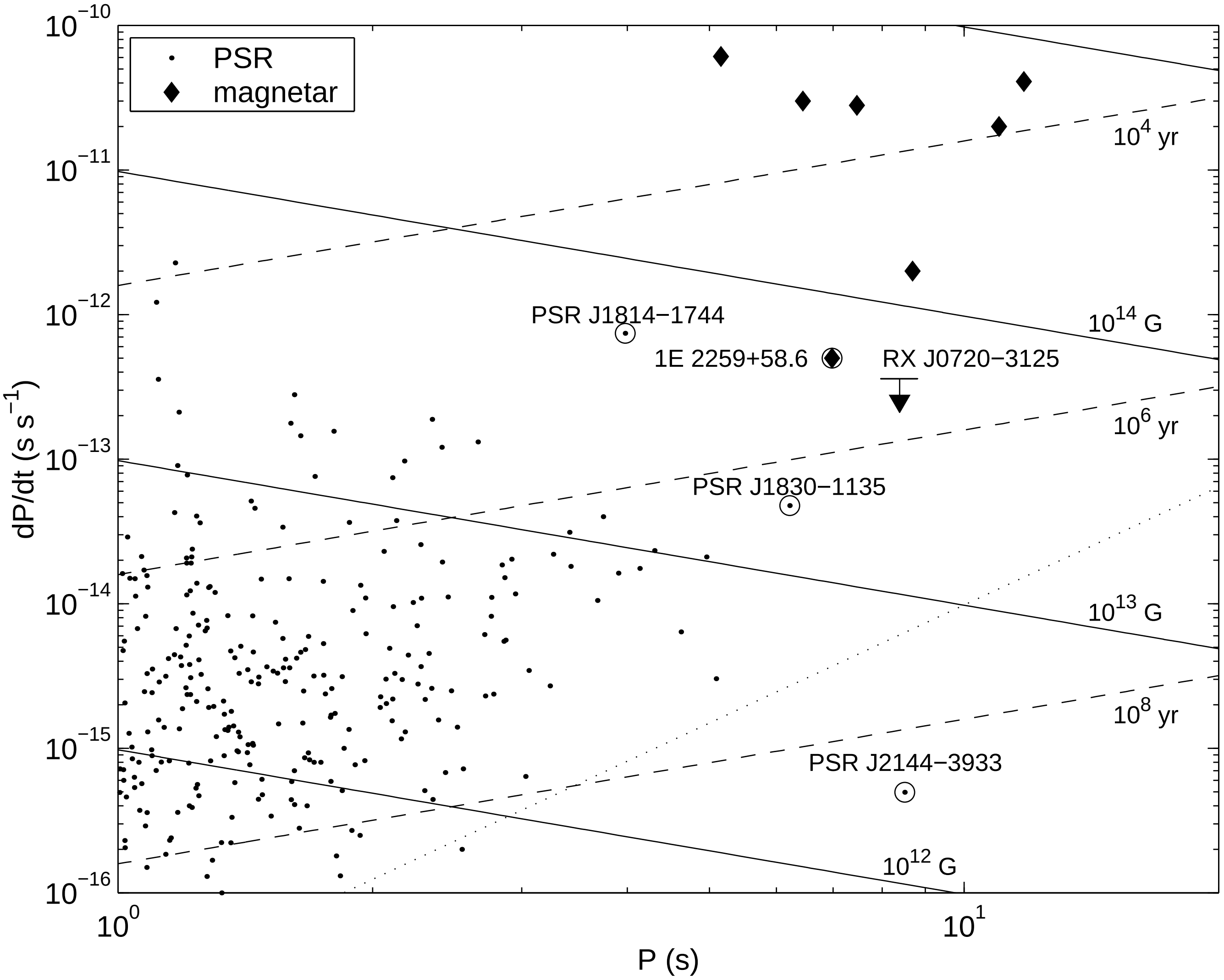

Figure 4.4 P-$\dot{P}$ diagram, showing only $P \geq 1$ s and $\dot{P} \geq 10^{-16}$ s s^{-1}. Radio pulsars are plotted as points, magnetars as diamonds. RX J0720.4−3125 is an upper limit. The magnetar 1E 2259+58.6 is circled, as are the high-B pulsars PSR J1830−1135 and PSR J1814−1744, and the long-period pulsar PSR J2144−3944 (Young et al. 1999). A version of the so-called "death line" is marked by the dotted line. The sloping solid lines are lines of constant dipole magnetic field $B_{\text{dipole}} \equiv 3.2 \times 10^{19}(P\dot{P})^{1/2}$ G, while the dashed lines are those of constant characteristic age $\tau_c \equiv P/(2\dot{P})$.

4.5 Conclusions

In this *Letter*, based on X-ray timing data and cooling models, we argue that the nearby soft X-ray source RX J0720.4−3125 is not a middle-aged magnetar but is likely a 10^6-yr off-beam pulsar. To accommodate its age and long period we speculate that it either has $B \gtrsim 10^{13}$ G or was born with $P_0 \approx 8.3$ s, a very surprising result as both source types are, at present, considered to be rare. We now consider the larger ramifications of our conclusions.

A volume-limited sample of neutron stars offers us an opportunity to sample the diversity of such sources. In this respect, soft X-ray surveys provide the best such samples since all neutron stars—normal radio pulsars, high-B pulsars, magnetars, and the mysterious Cas-A-like neutron stars—will cool through soft X-ray emission well into their middle ages. Indeed, this expectation is borne out by the local sample: pulsars such as PSR B0656+14, Geminga,[2] RX J0720.4−3125, a youngish magnetar (see below), and finally the very mysterious RX J1856.5−3754, of which we know nothing other than it is a cooling neutron star.[3]

The number of neutron stars belonging to a given class depends not only on the sensitivity of the X-ray survey but also on the product of the birth rate and the cooling age. Thus, for example, magnetars with their longer-lasting cooling radiation may dominate the local population despite a lower birthrate (Heyl & Kulkarni 1998). This bias and the long period led us to speculate that RX J0720.4−3125 was an old magnetar, a conclusion we have now refuted. In contrast, the soft thermal X-ray source RX J1308.6+2127, with $P = 5.2\,\mathrm{s}$ and $\dot{P} \sim 10^{-11}$ s s^{-1} (Hambaryan et al. 2002) appears to have a magnetar-strength field.

The proximity of RX J0720.4−3125 argues for a substantial Galactic population of similar sources, but very few such radio pulsars are known. The cause of this paucity is that radio surveys select against long-period pulsars, especially those with $B > 10^{13}$ G, in several ways. (1) The beaming factor is known to decrease with increasing period, reaching 3% at $P \sim 10$ s (Tauris & Manchester 1998). (2) As can be seen from Figure 4.4, the lifetime of a radio pulsar decreases with increasing B: a $B \sim 10^{12}$ G neutron star crosses the the radio death line at $\sim 10^8$ yr whereas a $B \sim 10^{13}$ G pulsar dies at $\sim 2 \times 10^7$ yr. The loss of throughput of a pulsar survey for a 5-second pulsar relative to a 1-second pulsar from these two effects alone is nearly one order of magnitude. (3) The true loss is even greater since long-period signals are frequently classified as interference (we note that population models do not constrain the population of long-period pulsars [Hartman et al. 1997], mainly due to reasons 1 and 2). Young high-B pulsars in supernova remnants would almost certainly create visible plerion nebulae due to their high $\dot{E}$'s, while long-period injected pulsars of similar ages would be invisible except for their cooling radiation (without assuming that the radio beams are directed toward the Earth). Thus, injected pulsars detectable only via X-ray emission may be present in many "hollow" supernova remnants (i.e., those without visible plerions). Radio pulsar searches better tuned to long periods and very deep radio and X-ray searches for young pulsars in supernova remnants may uncover the postulated class of long-period sources.

We thank M. Cropper and S. Zane for discussions on the TOAs and for alerting us to the different time systems used by different programs. We thank D. Frail and J. Heyl for useful discussions, and we thank an anonymous referee for constructive comments. We have used the NASA-maintained HEASARC web site for archival data retrieval and subsequent analysis. D.L.K. holds a fellowship from the Fannie and John Hertz Foundation, and his and S.R.K.'s research are supported by NSF and NASA. M.H.v.K. is supported by a fellowship from the Royal Netherlands Academy of Arts and Sciences.

Notes Added In Manuscript After we submitted our paper we became aware of a paper by Zane et al. (2002) reporting timing analysis of RX J0720.4−3125. Our period determinations of the archival data (PSPC, HRI-1, LECS, HRI-2, HRC-S) are in excellent agreement with those of Zane et al. Both papers also report new determinations, which are: *Chandra* ACIS-S3 (our paper) and XMMa (2000 May 13) and XMMb (2000 November 21; both from Zane et al.). We restricted our analysis to an incoherent combination of the various datasets, i.e., we looked for secular evolution of the period determined from each observation separately. We did not attempt to phase connect the datasets. Zane et al. do present a coherent analysis, using the archival and *XMM* data. However, in our opinion such an analysis is premature and not robust. First, it is premature, because the *XMM* derived periods of known pulsars have fractional errors $|\Delta P/P|$ ranging from 1.9×10^{-7} to 1.2×10^{-5} (as reported by the *XMM* calibration team; Kuster et al. 2002). This error alone may result in systematic uncertainties as high as $\dot{P}$ of 6×10^{-12} over the 6-month duration of the *XMM* datasets and $5 \times 10^{-13}\,\mathrm{s\ s}^{-1}$ over the entire span of the observations. Second, it is not robust,

---

[2] Presumably a standard pulsar that is not beamed toward us.

[3] It is further worth noting that the sample of soft X-ray neutron stars has at least three long-period objects (Haberl, Pietsch, & Motch 1999).

as phase connection without any ambiguity requires that the datasets be separated by time intervals less than “coherence” timescale, $\sim P^2/\sigma_P$ (where σ_P is the uncertainty in the measurement of P) and none of the datasets (including the *XMM* datasets) satisfy this condition. We note that neither of the two primary solutions from Zane et al. fits the TOAs in Table 4.1.

Chapter 5

The Nearby Neutron Star RX J0720.4−3125 from Radio to X-rays[†]

D. L. Kaplan[a], M. H. van Kerkwijk[b], H. L. Marshall[c], B. A. Jacoby[a], S. R. Kulkarni[a] &
D. A. Frail[d]

[a]Department of Astronomy, 105-24 California[b] Institute of Technology, Pasadena, CA 91125, USA

Dept. of Astronomy & Astrophysics, 60 St George St., Toronto, ON, M5S 3H8, Canada

[c]Center for Space Research, Massachusetts Institute of Technology, Cambridge, MA 02139, USA

[d]National Radio Astronomy Observatory, P.O. Box O, Socorro, NM 87801, USA

Abstract

We present radio, optical, ultraviolet, and X-ray observations of the isolated, thermally emitting neutron star RX J0720.4−3125 using the Parkes radio telescope, the Very Large Array, the *Hubble Space Telescope*, and the *Chandra X-ray Observatory.* From these data we show that the optical/UV spectrum of RX J0720.4−3125 is not well fit by a Rayleigh-Jeans tail as previously thought, but is instead best fit by either a single nonthermal power-law or a combination of a Rayleigh-Jeans tail and a nonthermal power-law. Taken together with the X-ray spectrum, we find the best model for RX J0720.4−3125 to be two blackbodies plus a power-law, with the cool blackbody implying a radius of 11–13 km at an assumed distance of 300 pc. This is similar to many middle aged (10^{5-6} yr) radio pulsars such as PSR B0656+14, evidence supporting the hypothesis that RX J0720.4−3125 is likely to be an off-beam radio pulsar. The radio data limit the flux at 1.4 GHz to be < 0.24 mJy, or a luminosity limit of $4\pi d^2 F < 3\times10^{25} d_{300}^2$ ergs s^{-1}, and we see no sign of extended nebulosity, consistent with expectations for a pulsar like RX J0720.4−3125.

5.1 Introduction

Thermally emitting neutron stars have been the targets of many observations recently, as these sources can potentially reveal the equation of state (EOS) of neutron stars, and thereby explore nuclear physics in realms inaccessible from laboratories (Lattimer & Prakash 2000). To obtain the EOS from the spectrum seems simple: determine the effective angular size from spectral fits, multiply by the distance (obtained from other means), and one has the apparent radius. This radius can be converted into the physical

---

[†] A version of this chapter was published in *The Astrophysical Journal*, vol. 590, 1008–1019.

radius through use of mass. The radius is the crucial quantity in differentiating between EOS, as most EOS predict a distinctive but small range of radii for a large range of masses. However, in order to use a neutron star to determine the EOS, one needs to (1) be certain that the radiation is from the surface, and (2) have a thorough understanding of this emission. Radio pulsars and accreting binaries are unsuitable since nonthermal magnetospheric emission or emission from the accreting material far exceeds the surface emission.

Therefore the identification of the nearest neutron stars by *ROSAT* was a major advance in the field (see reviews by Motch 2001 and Treves et al. 2000). Most of these sources do not have significant nonthermal emission, so they are prime targets for studies leading to the EOS. The closest of these sources, RX J1856.5−3754, has been the subject of much inquiry lately for just this purpose (e.g., Walter & Lattimer 2002; Drake et al. 2002; Braje & Romani 2002).

RX J0720.4−3125 was discovered by Haberl et al. (1997) as a soft ($kT \sim 80$ eV), bright X-ray source in the *ROSAT* All-Sky Survey—the second brightest neutron star that is not a radio pulsar. Given its very low hydrogen column density ($N_H \sim 1 \times 10^{20}$ cm^{-2}), nearly sinusoidal 8.39-second pulsations, relatively constant X-ray flux, and very faint ($B = 26.6$ mag), blue optical counterpart (Kulkarni & van Kerkwijk 1998; Motch & Haberl 1998), it was classified as a nearby, isolated, thermally emitting neutron star. It is perhaps the second closest source (next to RX J1856.5−3754) that does not show significant nonthermal emission. While originally thought to be an accreting source or possible an old magnetar, recent timing measurements limit the original magnetic field to be smaller than 10^{14} G, eliminating the magnetar hypothesis. However, the discoveries of radio pulsars with periods longer than 4 s (Camilo et al. 2000; Young, Manchester, & Johnston 1999) have led to the suggestion that RX J0720.4−3125 is instead an off-beam radio pulsar, likely with a magnetic field at the high end of the radio-pulsar range ($B \sim 10^{13}$ G; Kaplan et al. 2002b; Zane et al. 2002).

The spectrum emerging from a thermally emitting neutron star depends significantly on the composition of the surface (e.g., Romani 1987). In the past, three models have generally been considered. The first, a blackbody, is simple but not physically motivated. Next, light element (H or He, possibly due to accretion from the ISM) atmosphere have few features, all in the (extreme) ultraviolet, and peak, for a given temperature, at a substantially higher energy than a blackbody. Finally, heavy element (Fe, Ni) atmospheres peak at a similar location to blackbodies but have many spectral features at a variety of wavelengths.

None of these models can reproduce the X-ray and optical data for RX J0720.4−3125 and RX J1856.5−3754 (Pons et al. 2002b; Walter & Lattimer 2002; Drake et al. 2002; Paerels et al. 2001). The X-ray data are well fit by blackbodies, but these blackbodies underpredict the optical flux. The H/He models also match the general shape, but they overpredict the optical flux and the implied radii are larger than is possible for a neutron star. The Fe models have too many lines and edges to match the X-ray spectra. Consequently, the current generation of single-component models have been unsuccessful in fitting both the X-ray and optical fluxes while having radii consistent with those of neutron stars (Pons et al. 2002b; Kaplan, van Kerkwijk, & Anderson 2002c). We see, though, how both X-ray and optical data are required to fully constrain the models.

Motivated thus, we present observations of RX J0720.4−3125 from radio to X-ray wavelengths aimed at determining its spectral energy distribution and from that its underlying properties (composition, magnetic field, and geometry). In Section 5.2 we present new optical/UV data from the *Hubble Space Telescope*, and undertake detailed modeling of the optical/UV spectrum. In Section 5.3 we present spectroscopic data from the *Chandra X-ray Observatory*, and in Section 5.4 we present searches for radio sources (both persistent and pulsating) with the Very Large Array and the Parkes radio telescope. Finally, in Section 5.5 we discuss the spectrum of RX J0720.4−3125, and present our conclusions in Section 5.6. In the following, all radii refer to the radiation radius as observed at infinity, R_∞ ($R_\infty = R_{\rm phys}/\sqrt{1 - 2GM/R_{\rm phys}c^2}$, where

Table 5.1. Summary of STIS Observations

Detector/Filter	Date (UT)	Exposure (s)	$\langle\lambda\rangle$[a] (Å)	$\langle A_\lambda/A_V\rangle$[a] (mag)	Ap. Corr.[b] (mag)	ΔZ_{mag}[c] (mag)	Magnitude[d] (mag)
			Calculated for $\alpha_\nu = 2.00$ and $A_0 = 0.13$ mag.[e]				
CCD/50CCD	2001-Jul-16	5342	5148	1.56	0.102	⋯	26.68 ± 0.10
NUV MAMA/25Qtz	2001-Aug-05	5500	2286	2.58	0.276	0.029	23.82 ± 0.14
FUV MAMA/25SrF$_2$	2002-Jan-28	4800	1447	2.80	0.340	0.087	21.97 ± 0.11
FUV MAMA/25MAMA	2002-Feb-13	3850	1360	2.97	0.353	0.078	21.6 ± 0.2
			Calculated for $\alpha_\nu = 1.40$ and $A_0 = 0.10$ mag.[f]				
CCD/50CCD	⋯	⋯	5367	1.41	0.102	⋯	26.68 ± 0.10
NUV MAMA/25Qtz	⋯	⋯	2310	2.56	0.270	0.029	23.83 ± 0.14
FUV MAMA/25SrF$_2$	⋯	⋯	1450	2.79	0.339	0.088	21.96 ± 0.11
FUV MAMA/25MAMA	⋯	⋯	1365	2.95	0.352	0.079	21.7 ± 0.2

[a] Effective wavelength and normalized extinction; see Appendix A of van Kerkwijk & Kulkarni (2001b).

[b] Aperture correction from a radius of $0\farcs5$ to infinity. See § 5.2 for details.

[c] Change in the zero-point magnitude due to degradation of the MAMA detectors.

[d] Magnitude in the STMAG system, with $m_{\mathrm{ST}} = -21.1 - 2.5 \log_{10} F_\lambda$, corrected to infinite aperture.

[e] Appropriate for the RJ fit in Table 5.4.

[f] Appropriate for all fits except the RJ fit in Table 5.4.

Note. — All filter curves were taken from the `synphot` database. $\lambda_0 = 4500$ Å.

R_{phys} is the physical radius).

5.2 Optical and UV Data

5.2.1 Observations and Analysis

We observed RX J0720.4−3125 with the Space Telescope Imaging Spectrometer (STIS) aboard the *Hubble Space Telescope* (*HST*) four times, covering wavelengths from 125 nm to 900 nm; the observations are summarized in Table 5.1.

5.2.1.1 Optical Data

The optical data (50CCD mode) consist of eight unfiltered CCD observations taken in a four-point dither pattern. We assembled the images using the drizzle algorithm (Fruchter & Hook 2002) giving a plate scale of 25.3 mas pixel^{-1}. We show the stacked image in Figure 5.1.

We performed standard aperture photometry on the stacked STIS image using `IRAF`'s `daophot` package. The sky level was estimated using an annulus from $0\farcs75$–$1\farcs00$. The source flux was measured within an aperture of radius $0\farcs5$. While there were no aperture corrections strictly appropriate for a source with the color of RX J0720.4−3125 ($B - V \approx -0.3$ mag), we used the bluest of the color-dependent aperture corrections available (T. Brown 2002, personal communication) to correct the flux to an infinite aperture. We estimate that the aperture correction introduces an uncertainty of < 0.02 mag, as blue sources like

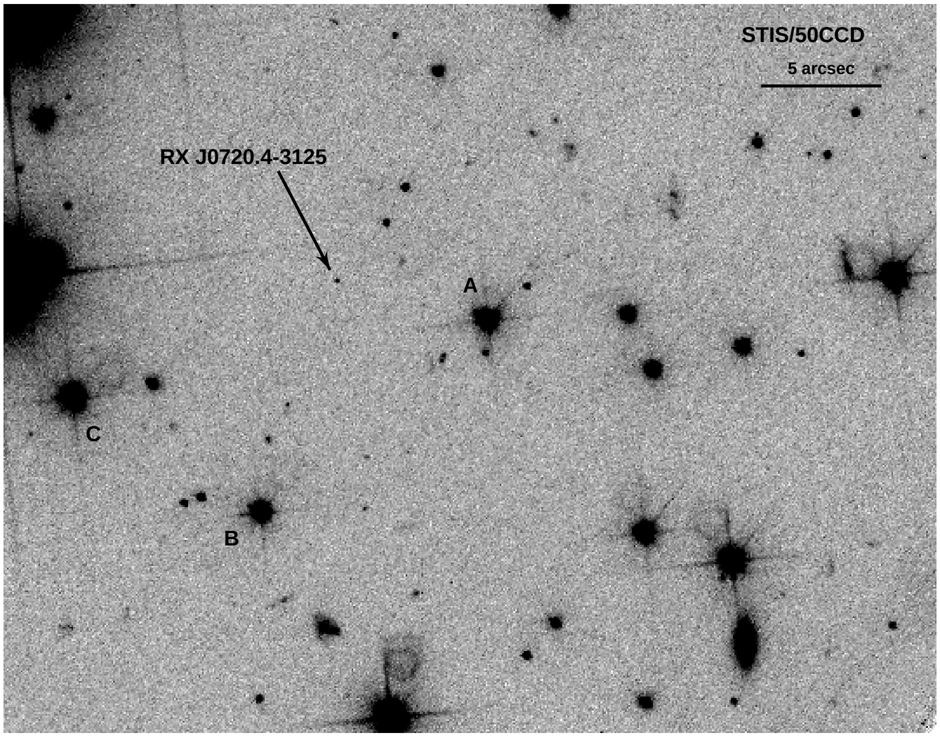

Figure 5.1 STIS optical image of RX J0720.4−3125. North is up, east to the left. The scale bar in the upper right indicates 5″. RX J0720.4−3125 is indicated by the arrow, and sources A, B, and C from Haberl et al. (1997) are also marked.

RX J0720.4−3125 have less scattered light than redder sources and therefore the aperture corrections are better determined (see Kaplan et al. 2002a). Given the very wide 50CCD bandpass (FWHM $\approx$ 441 nm) a single zero-point flux is not appropriate for all source spectra. Therefore, as a first order estimate, we calculated the zero-point flux at the mean wavelength of the filter (given in Table 5.1), assuming an input spectrum with $F_\lambda \propto \lambda^{-4}$ and $A_V \approx 0.1$ mag, appropriate for RX J0720.4−3125 (Kulkarni & van Kerkwijk 1998).

For astrometric purposes we used 10-second and 60-minute R-band images taken with the Low-Resolution Imaging Spectrograph (Oke et al. 1995) on the 10-meter Keck I telescope (the observations are described in Kulkarni & van Kerkwijk 1998). We determined the centroids of 231 stars from the Guide Star Catalog version 2.2 (GSC-2.2) on the 10-second image, rejecting 50 objects that were overexposed or appeared to be incorrectly identified. The pixel coordinates were corrected for instrumental distortion using a cubic radial distortion function,[1] and we then fit for the zero-point position, rotation, and plate scale of the image. The rms was $0\farcs12$ in each coordinate. We then fit the 70 nonsaturated stars from the 10-second image to the 60-minute composite image, again correcting for instrumental distortion. This fit had rms of $0\farcs024$ in each coordinate. Finally, we performed a fit using 25 stars from the 60-minute image to determine the zero point, scale, and rotation of the STIS image (which had been corrected for distortion during the drizzle process), giving an rms of $0\farcs025$ in each coordinate. Overall, the STIS image is tied to the frame of the GSC-2.2 with uncertainty of $0\farcs01$ in each coordinate, or tied to the International Coordinate Reference Frame (ICRF) with uncertainty of about $0\farcs2$ in each coordinate. The final position for RX J0720.4−3125 is (J2000, epoch MJD 52106) $\alpha = 07^{\rm h}20^{\rm m}24\fs961$, $\delta = -31^\circ25'50\farcs21$. This supersedes

---

[1] `http://alamoana.keck.hawaii.edu/inst/lris/coordinates.html`

Table 5.2. Source and Background Counts for STIS UV Data

Detector/Filter	Counts	
	Source	Background
NUV MAMA/25Qtz	3534 ± 59	2788 ± 15
FUV MAMA/25SrF$_2$	611 ± 25	128 ± 3
FUV MAMA/25MAMA	14502 ± 120	13788 ± 58

Note. — No aperture corrections have been applied. Background counts are normalized to the same area as the source counts.

the position of Kulkarni & van Kerkwijk (1998), as the significance of the new detection is far higher and the position is directly tied to the ICRF. The *HST* position is consistent with the X-ray position which has uncertainties of $\approx 0\overset{''}{.}6$ in each coordinate (Kaplan et al. 2002b).

5.2.1.2 UV Data

For the UV MAMA data, we corrected the arrival times of the data to the Solar System barycenter using the `stsdas` task `odelaytime`. We then filtered the photon lists for the FUV data for periods of high background. These occurred at the beginning of each orbit as *HST* was going into the Earth's shadow. Using a background annulus from $3\overset{''}{.}0$–$3\overset{''}{.}5$, we estimated the median background level from a light-curve binned to 50 s and only used the data where the background level was within $\pm 3\,\sigma$ of the median. We found that the background was noticeably high only for the FUV MAMA/25SrF$_2$ data, where we have retained 4800 s of the original 5500 s.

We then performed aperture photometry on the raw photon data. The source flux was computed using a radius of $0\overset{''}{.}5$, where the signal-to-noise was relatively high and the aperture corrections were well defined. The raw source and background counts are given in Table 5.2. The STIS MAMAs have wide point-spread-functions (psfs), with substantial flux beyond $0\overset{''}{.}5$, and therefore aperture corrections are particularly important. We took the monochromatic aperture corrections for the MAMAs (T. Brown 2002, personal communication) convolved with the expected source spectrum and the filter throughputs to compute aperture corrections for each filter, which we give in Table 5.1. Another issue with the STIS MAMAs is that the sensitivity changes with time (Stys et al. 2002) at the level of a few percent per year. Using a wavelength-dependent fit to the sensitivity changes (D. Stys 2002, personal communication; R. Diaz-Miller 2002, personal communication; these corrections are now incorporated into the STIS pipeline), we computed weighted zero-point corrections for the NUV and FUV MAMA data that are listed in Table 5.1. These corrections were small, less than 0.1 mag. As with the optical data, the zero-point fluxes were calculated at the mean wavelengths of the filters.

The STIS MAMA data are time-tagged with 125 μs resolution, but we could not detect the 8.39-second periodicity present in the X-rays. We find 90% confidence upper limits on the Fourier power (normalized to have unity mean and rms) present at the X-ray period (given by Kaplan et al. 2002b) of 5.3 and 5.9, for the NUV and FUV/SrF$_2$ data sets, respectively. These translate into limits on the rms pulsed fraction of 0.16 and 0.19, respectively.

5.2.2 Spectral Fits

5.2.2.1 Power-law Fits

We already know from Kulkarni & van Kerkwijk (1998) that the optical spectrum of RX J0720.4−3125 is roughly approximated by the Rayleigh-Jeans portion of a blackbody curve: $F_\lambda \propto \lambda^{-4}$. We can now investigate this more quantitatively and over a wider range of wavelengths. Here we use the optical and UV data presented in this paper as well as the B and R photometry from Kulkarni & van Kerkwijk (1998); for the data from Kulkarni & van Kerkwijk (1998), we used the zero-point fluxes from Bessell, Castelli, & Plez (1998).

Our spectral fitting followed van Kerkwijk & Kulkarni (2001b). We fit the data with a sum of extincted power-law (PL) of the form

$$F_\lambda = F_0 \left(\frac{\lambda}{\lambda_0}\right)^{-(2+\alpha_\nu)} 10^{-A_0 A'_\lambda/2.5}, \tag{5.1}$$

where α_ν is the spectral index,[2] F_0 is the observed flux at the reference wavelength λ_0, A_0 is the extinction at λ_0, and A'_λ is the normalized extinction at wavelength λ ($A'_\lambda \equiv A_\lambda/A_0$). We use the reddening curve of Cardelli, Clayton, & Mathis (1989), with corrections to the optical and UV portions from O'Donnell (1994). We chose $\lambda_0 = 4500$ Å ($A_0 = 1.29 A_V$, or $A_0 \approx A_B$), as this is the mean wavelength of the data.

For the fit, we calculated likelihood values as we varied F_0, A_0, and α_ν. However, as the spectral shape changes (i.e., variations in A_0 and α_ν) the aperture corrections, reference wavelengths, extinctions, and zero-point corrections (from Table 5.1) also change (these changes are most significant for the STIS/50CCD data). Therefore, during the iterations of the fitting, we recomputed all of the spectrum-dependent quantities for each combination of A_0 and α_ν.

The results of the fitting for the two basic models—Rayleigh-Jeans[3] (RJ) and unconstrained power-law (PL) are given in Table 5.3. These fits give values of the extinction $A_0 \sim 0.5$ mag. This is much higher than expected from other observations. From the X-ray spectrum of RX J0720.4−3125, we know that the hydrogen column density is $N_H \approx 1.3 \times 10^{20}$ cm^{-2}, which implies $A_V \approx 0.07$ mag (Predehl & Schmitt 1995) or $A_0 \approx 0.09$ mag. Kulkarni & van Kerkwijk (1998) have placed an upper limit on the reddening of $E_{B-V} < 0.04$, as RX J0720.4−3125 is in the foreground of the open cluster Collinder 140, which implies $A_0 < 0.10$ (for the standard ratio of $R_V = 3.2$). We therefore expect small values of the extinction: $A_0 \lesssim 0.15$ mag, allowing for uncertainties in N_H, R_V, and the relation between N_H and A_V. From this we can reject the models in Table 5.3.

Therefore we constrained A_0 from the information above. To formally include this in our fit, we performed a maximum likelihood fit with the following prior distribution for A_0:

$$f_{A_0}(A_0) = \mathcal{N}_6(A_0 | 0.09\text{ mag}, 0.06\text{ mag}), \tag{5.2}$$

where $\mathcal{N}_n(x|\mu,\sigma)$ is a generalized Gaussian distribution of degree n (n is even) with the form:

$$\mathcal{N}_n(x|\mu,\sigma) \equiv \frac{n}{2\sqrt{2}\pi\sigma}\Gamma\left(\frac{n-1}{n}\right)\sin\left(\frac{\pi}{n}\right)\exp\left[-\left(\frac{(x-\mu)}{\sqrt{2}\sigma}\right)^n\right]. \tag{5.3}$$

For $n = 6$, this distribution essentially requires that A_0 be between 0 mag and 0.18 mag. We could have used a uniform prior with $A_0 = 0$–0.15 mag, but the sharp edges of this distribution can make for discontinuities in the resulting posterior distributions, so we opted for Equation 5.2, which is a smoothed version of the uniform distribution.

---

[2] From this definition we also have the more standard $F_\nu \propto \nu^{\alpha_\nu}$.

[3] For blackbodies of the temperatures considered here, the Rayleigh-Jeans approximation holds at the shortest UV wavelength used to better than 4%—considerably smaller than the measurement error.

Table 5.3. Fits to RX J0720.4−3125 Optical/UV Data with A_0 Unconstrained

Parameter	Type of Fit	
	PL	RJ
A_0 (mag)	0.47(15)	0.59(6)
α_ν[a]	1.9(2)	2
F_0 ($\times 10^{-19}$ ergs s^{-1} cm^{-2} Å^{-1})	2.5(6)	3.0(3)
B_0 (mag)[b]	26.0(2)	25.82(10)
χ^2	1.0	1.1
DOF	3	4
χ^2/DOF	0.3	0.3

[a] The spectral index such that $F_\lambda \propto \lambda^{-(2+\alpha_\nu)}$.

[b] B-band Vega-magnitude corresponding to F_0.

Note. — Numbers in parentheses are 68% confidence limits in the last digit(s). Values without confidence limits were held fixed for the fit. Values with subscript 0 are for $\lambda_0 = 4500$ Å.

We consider four power-law models for the fit. The first, given in the PL column in Table 5.4, is a single power-law fit to the optical/UV data alone. The second, given in the RJ column in Table 5.4, is a single power-law fit to the optical/UV data, but where the power-law index is that of a Rayleigh-Jeans tail ($\alpha_\nu = 2$). The third is a fit where there are two power-laws, given in the PL+RJ column in Table 5.4: one has an unconstrained index, and the other has $\alpha_\nu = 2$. Finally, the fourth fit, given in the PL+X-ray column in Table 5.4, has a Rayleigh-Jeans power-law present, but its normalization is set by the X-ray fit (§ 5.3; the uncertainties in the X-ray flux extrapolated to optical/UV wavelengths is $\approx 10\%$).

In Tables 5.3 and 5.4 we give χ^2 values for each fit. These values were computed from the data without taking into account the prior distributions used in Table 5.4. The best-fit values of the parameters were computed not by using the χ^2 values themselves buy through the marginalized likelihood functions that incorporated the prior. The χ^2 values are there only as a reference, to show that even with the prior distribution in place the fits are still good. One should not use the typical $\Delta\chi^2$ technique (Press et al. 1992, p. 697) for determining parameter uncertainties—while the PL models from Tables 5.3 and 5.4 have χ^2's that differ by 0.9, the PL model from Table 5.3 is excluded very significantly by the fit in Table 5.4, as shown by the small uncertainties in the parameters of Table 5.4. Instead the confidence limits given in Tables 5.3 and 5.4 are single-parameter 68% limits determined from the marginalized likelihood functions.

We find a good fit for the single unconstrained power-law, shown in Figure 5.2. This model has $\chi^2 = 1.9$ for 3 degrees of freedom (DOF). The Rayleigh-Jeans fit, though, is significantly worse, with $\chi^2 = 26.5$ for 4 degrees of freedom under the same prior assumptions. We can therefore reject $\alpha_\nu = 2$ with $> 98\%$ confidence. For the PL+RJ fit, the results are given in the PL+RJ column of Table 5.4. The fit, shown in Figure 5.3, is good, with $\chi^2 = 0.8$ for 2 DOF. For the final fit, PL+X-ray, we also find an acceptable value of $\chi^2 = 1.4$ for 3 DOF. We can conclude that all of the fits except the RJ fit are acceptable.

As mentioned above, the values of $\langle\lambda\rangle$, A'_λ, the aperture correction and the zero-point correction change depending on the spectral model. However, except for the RJ fit, all of the models have sufficiently

Table 5.4. Fits to RX J0720.4−3125 Optical/UV Data with A_0 Constrained

Parameter	Type of Fit			
	PL	RJ	PL+RJ	PL+X-ray
A_0 (mag)	0.10(6)	0.19(2)	0.10(4)	0.09(4)
α_ν [a]	1.40(4)	2	0.3(7)	1.14(12)
F_0 ($\times 10^{-19}$ ergs s^{-1} cm^{-2} Å^{-1})	1.50(12)	1.12(7)	0.8(2)	1.24(9)
B_0 (mag)[b]	26.58(8)	26.88(7)	27.4(2)	26.79(8)
$\alpha_{\nu,2}$ [a]	⋯	⋯	2	2
$F_{0,2}$ ($\times 10^{-19}$ ergs s^{-1} cm^{-2} Å^{-1})	⋯	⋯	0.6(2)	0.27
$B_{0,2}$ (mag)[b]	⋯	⋯	27.5(3)	28.5
χ^2 [c]	1.9	26.5	0.8	1.4
DOF	3	4	2	3
χ^2/DOF	0.6	6.6	0.4	0.5

[a] The spectral index such that $F_\lambda \propto \lambda^{-(2+\alpha_\nu)}$.

[b] B-band Vega-magnitude corresponding to F_0.

[c] The χ^2 values are raw values that do not take into account the prior distributions (e.g., Eqn. 5.2). They are there only as a guide, showing which models do and do not fit the data independent of the prior distributions.

Note. — Numbers in parentheses are 68% confidence limits in the last digit(s). Values without confidence limits were held fixed for the fit. Values with subscript 0 are for $\lambda_0 = 4500$ Å. A_0 was constrained by use of Equation 5.2.

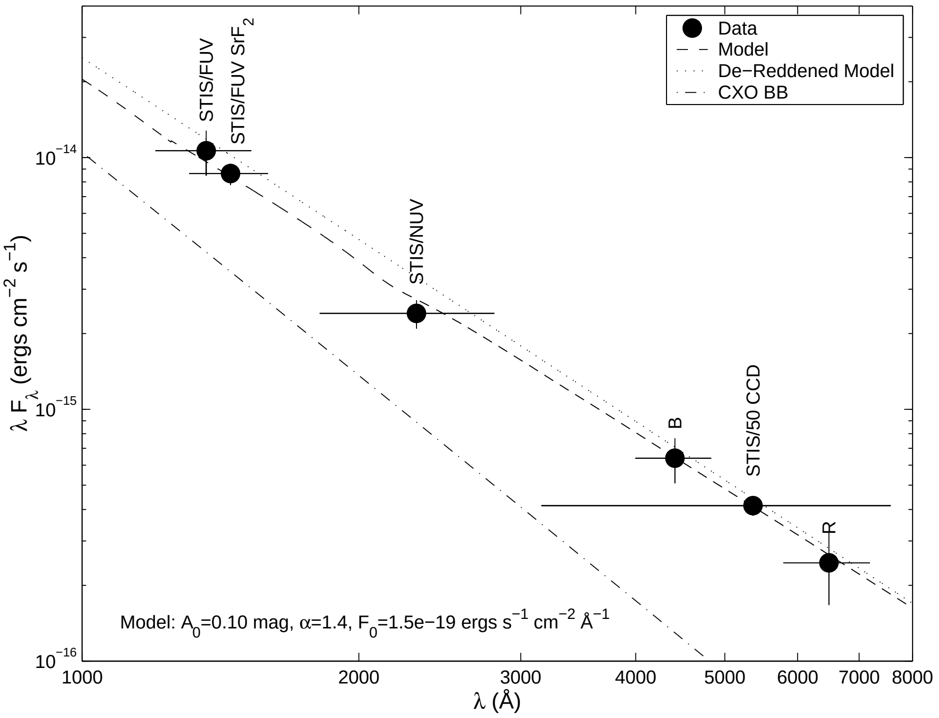

Figure 5.2 Optical/UV spectrum of RX J0720.4−3125, with data from Kulkarni & van Kerkwijk (1998) and this paper. The PL fit is shown, with: the best-fit model (dashed line), the best-fit model corrected for extinction (dotted line) and the extrapolation of the *Chandra* blackbody fit (dash-dotted line; "CXO BB"; see § 5.3). The different bands are labeled.

similar flux distributions, despite the different contributions from different components, that the values are essentially the same for these models. We give the values of these parameters for the best-fit values of α_ν and A_0 in Table 5.1; these will apply to the PL, PL+RJ, and PL+X-ray models. The only filter whose calibration changes significantly is the extremely broadband STIS/50CCD.

As seen in Figure 5.2, the PL fit has a shallower slope than the extrapolation of the *Chandra* blackbody spectrum. While an extrapolation of the optical/UV PL does not intersect the X-ray spectrum, it does come to within a factor of 1.2 (at 142 Å). By the lower energy end of the *Chandra* data (0.1 keV $\approx$ 125 Å), the optical/UV PL must have turned over as it is not seen in the X-rays. The power-law component of the PL+X-ray fit behaves similarly.

The best-fit Rayleigh-Jeans component of the PL+RJ model is a factor of 2.4(4) above the extrapolation of the X-ray blackbody (Fig. 5.3 and Tab. 5.4). The two components contribute equally at $\lambda = 4930$ Å: at shorter wavelengths the Rayleigh-Jeans component dominates, while at longer wavelengths the nonthermal component dominates. The nonthermal PL component is above the X-ray extrapolation in the optical regime, intersects it at 2680 Å, and the continues below it. Therefore, the nonthermal PL would not be seen in soft X-rays or in the radio (Fig. 5.4), although it may approach the X-ray spectrum at energies $\gtrsim$ 2 keV.

5.2.2.2 Disk Fits

We also considered fits to the optical/UV data that include a disk of accreting material, such as that proposed to account for the X-ray luminosity and periodicity of RX J0720.4−3125 (e.g., Wang 1997; Konenkov & Popov 1997; Alpar 2001). For the disk spectrum we used the model of Perna, Hernquist, & Narayan

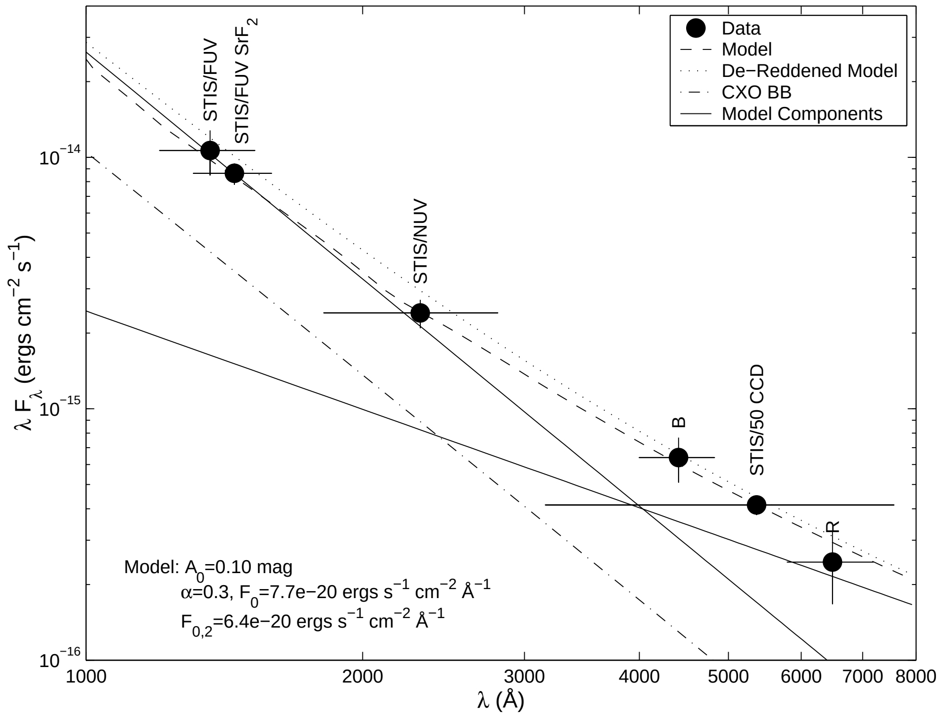

Figure 5.3 Optical/UV spectrum of RX J0720.4−3125, with data from Kulkarni & van Kerkwijk (1998) and this paper. The PL+RJ fit (unconstrained Rayleigh-Jeans tail plus a second PL) is shown: the best-fit model (dashed line), the best-fit model corrected for extinction (dotted line), the two components of the model (solid lines), and the extrapolation of the *Chandra* blackbody fit (dash-dotted line; "CXO BB"; see § 5.3). The different bands are labeled.

(2000). We found fits using a disk model to be unsatisfactory. As there are too many free parameters to do a formal fit (the inner and outer disk radii, the disk inclination, as well as two undetermined efficiency factors), we varied subsets of the parameters by hand. We first considered disks that extend in to the corotation radius and out to infinity. For most conceivable disk inclinations ($i \lesssim 85^\circ$) the disk alone is a factor of 10–20 above the optical data, and this is without any contribution to the optical emission from the neutron star surface. Toward the short-wavelength end of the disk, where the emission decreases below the level of our data and the contribution is primarily from the inner edge of the disk, the slope is entirely inconsistent with the optical/UV data: it goes approximately as $F_\lambda \propto \lambda^4$, while the excess flux in the optical (compared to a Rayleigh-Jeans tail) is like $F_\lambda \propto \lambda^{-2.3}$. We therefore consider this disk model to be very unlikely for RX J0720.4−3125.

There are disk models that can reproduce a spectrum roughly similar to that observed. This occurs when the inner radius is far inside the corotation radius and approaches the neutron star surface, while the outer radius move inward to $\sim 10^8$ cm. But while the spectral shapes are not inconsistent, the flux predicted by such disks is a factor of ~ 100 above the optical/UV data. Also, there is no natural reason for the disk to be truncated at such small radii (the optical data do not allow for any stellar companion). Therefore this disk model is also very unlikely for RX J0720.4−3125.

5.2.2.3 Variability

It is possible that the spectrum of RX J0720.4−3125 is a Rayleigh-Jeans tail in the optical, and that the deviations we see are temporal in nature: i.e., RX J0720.4−3125 could vary. However, we consider this

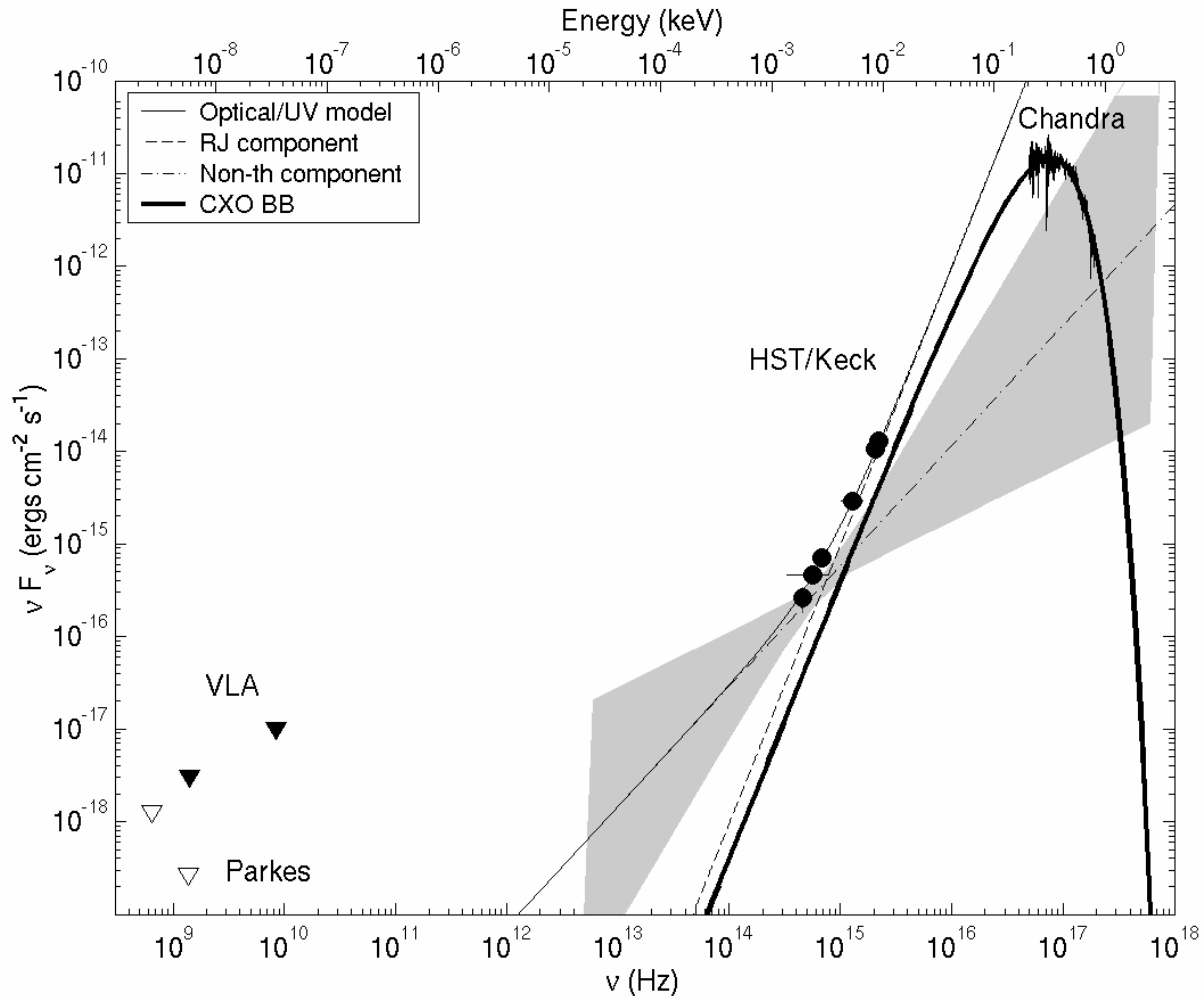

Figure 5.4 Broadband spectrum of RX J0720.4−3125, from radio to X-rays. The absorption-corrected optical/UV data (§ 5.2) are plotted as filled circles, the absorption-corrected X-ray data (§ 5.3) as points, the VLA upper limits (§ 5.4.1) as filled triangles, and the Parkes upper limits for pulse widths of 0.6–3% (§ 5.4.2) as the open triangles. The models are: X-ray blackbody (thick solid line), Rayleigh-Jeans component of the PL+RJ fit to the optical/UV data (dashed line), nonthermal component of the PL+RJ fit (dash-dotted line), and the overall PL+RJ fit to the optical/UV data (thin solid line). The $\pm 1\,\sigma$ uncertainties on the nonthermal PL are shown by the shaded region.

unlikely. First, the X-ray flux has been extremely constant over almost a decade of observation (Haberl et al. 1997; Paerels et al. 2001). Second, similar sources such as RX J1856.5−3754 and PSR B0656+14 have exhibited constant optical fluxes, again over several years of observations (van Kerkwijk & Kulkarni 2001b; Koptsevich et al. 2001).

Regardless, we can perform a simple test for variability. We have an ongoing series of *HST* observations that, while designed to measure the parallax and proper motion of RX J0720.4−3125, also provide a sensitive flux monitor. Only the first two epochs of data have been observed so far (at MJDs 52459 and 52532). The data are from 4950-s observations with the Advanced Camera for Surveys on *HST* using the High Resolution Camera (ACS/HRC) in the F475W filter. The photometric calibration of ACS is not complete, so we cannot directly compare the measured flux of RX J0720.4−3125 to the models presented

Table 5.5. Summary of *Chandra* HRC-S/LETG Observations

Date (UT)	Exposure (ks)	Counts	
		Order 0	Orders ±1
2000-Feb-01	5.4	929	671
2000-Feb-02	26.3	4584	3027
2000-Feb-04	6.1	1119	687

here (although the new data are roughly consistent), but we can look for variations in the flux of RX J0720.4−3125 and in that of the other sources in the field. We drizzled the data using a preliminary model of the ACS/HRC geometric distortion, and then performed aperture photometry on RX J0720.4−3125 and 11 other sources, ranging from much brighter than RX J0720.4−3125 to about as bright as RX J0720.4−3125. The field sources changed by 0.02 ± 0.04 mag from the first epoch to the second, while RX J0720.4−3125 changed by -0.10 ± 0.09 mag. This number is preliminary, but shows that the flux of RX J0720.4−3125 changed by at most 10% over two months. We will eventually have better-calibrated data spanning two years, which will allow us to make a much more rigorous test for variability.

5.3 X-ray Data

RX J0720.4−3125 was observed with the *Chandra X-ray Observatory*, using the High Resolution Camera spectroscopic detector (HRC-S) with the Low Energy Transmission Grating (LETG); the observations are summarized in Table 5.5. Here we describe the spectroscopic analysis of these data—timing analysis is described in Kaplan et al. (2002b) and Zane et al. (2002).

The spectral data were reduced from standard event lists using `IDL` using custom processing scripts as described in Marshall & Schulz (2002) and Marshall et al. (2002). Raw events were extracted from first and higher orders and calibrated with an updated model of the LETGS effective area[4] (EA), which was developed from observations of PKS 2155−304..

Integrating the observed fluxes over the 0.25–3.0 keV band gives an observed flux of $(9{\pm}2){\times}10^{-12}$ ergs cm^{-2} s^{-1} and an absorbed luminosity of $(9 \pm 2) \times 10^{31} d_{300}^2$ ergs s^{-1}, where $d = 300 d_{300}$ pc is the distance to RX J0720.4−3125 (Kaplan et al. 2002c). The data were rebinned adaptively to provide a signal-to-noise ratio (S/N) of 5 in each bin over the 0.10–2.0 keV range. The spectrum, shown in Figure 5.5, was first estimated using the first-order EA only. The contributions to the observed counts from high orders are estimated by folding a model for first-order through the high-order EA (important only below 0.2 keV).

Following previous analyses (Haberl et al. 1997; Paerels et al. 2001), we modeled the continuum by an absorbed blackbody; the fitted parameters are given in Table 5.6. We exclude the data below 0.15 keV from the fit where uncertainties in the high-order grating efficiencies can be important. This fit gives a temperature of 81.4(13) eV and a bolometric luminosity of $2.1 \times 10^{32} d_{300}^2$ ergs s^{-1}, consistent with the *ROSAT* and *XMM* analyses (Haberl et al. 1997; Paerels et al. 2001), given the uncertainties in modeling the effective areas below 0.2 keV and the higher order responses. The fit has a reduced $\chi^2 = 1.11$ (for 148 DOF), acceptable at the 90% level. Other models, such as those with nonthermal power-laws or a second blackbody, did not improve the fit.

---

[4] This effective area is available at
`http://cxc.harvard.edu/cal/Links/Letg/User/Hrc_QE/EA/correct_ea/letgs_NOGAP_EA_001031.mod`.

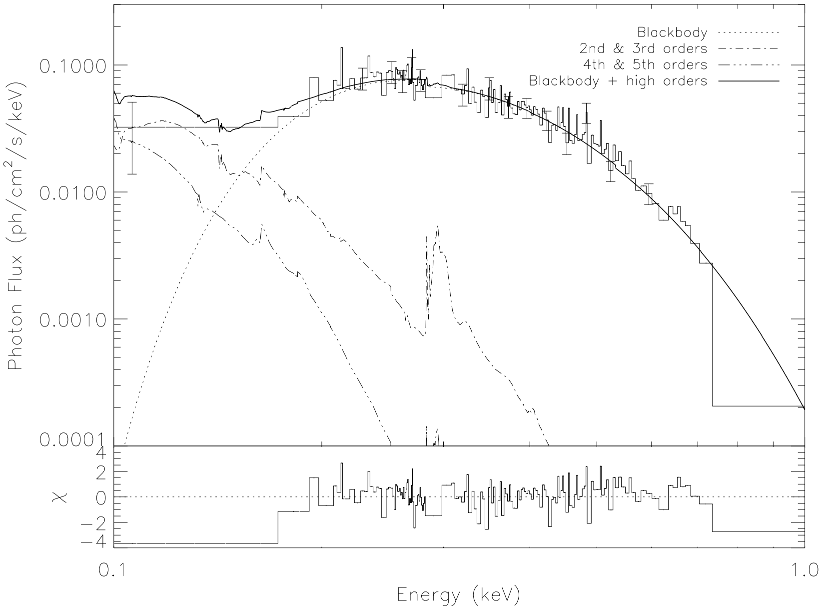

Figure 5.5 LETGS spectrum of RX J0720.4−3125. The bin sizes have been varied to provide good signals in each energy bin; the uncertainties are about 20% everywhere. Solid line: Model consisting of one blackbody component. High orders do not contribute significantly for $E > 0.20$ keV, while the data at low energies ($E < 0.15$ keV) are best modeled as the result of the sum of high orders.

Table 5.6. One and Two Blackbody Fit to the LETG Spectrum

Parameter	Value	
N_H ($\times 10^{20}$ cm^{-2})	1.32(14)	1.46(14)
$T_{\rm hot}$ ($\times 10^5$ K)	9.45(15)	9.47(15)
$R_{\rm hot}$ (km)	6.1(3)d_{300}	6.1(6)d_{300}
$T_{\rm cold}$ ($\times 10^5$ K)	···	3.72(10)
$R_{\rm cold}$ (km)	···	15(17)
χ^2	163.9	163.1
DOF	148	146
χ^2/DOF	1.11	1.12

Note. — Numbers in parentheses are 68% confidence limits in the last digit(s).

The best-fit model is plotted against the fitted data in Figure 5.5. The count spectrum (Fig. 5.6) was binned at 0.125 Å resolution in order to search for narrow spectral features against the continuum model. No significant emission or absorption features were found: in Figure 5.7 we give $3\,\sigma$ upper limits to the equivalent width of narrow-line features in our data. The *Chandra* data are generally consistent with the

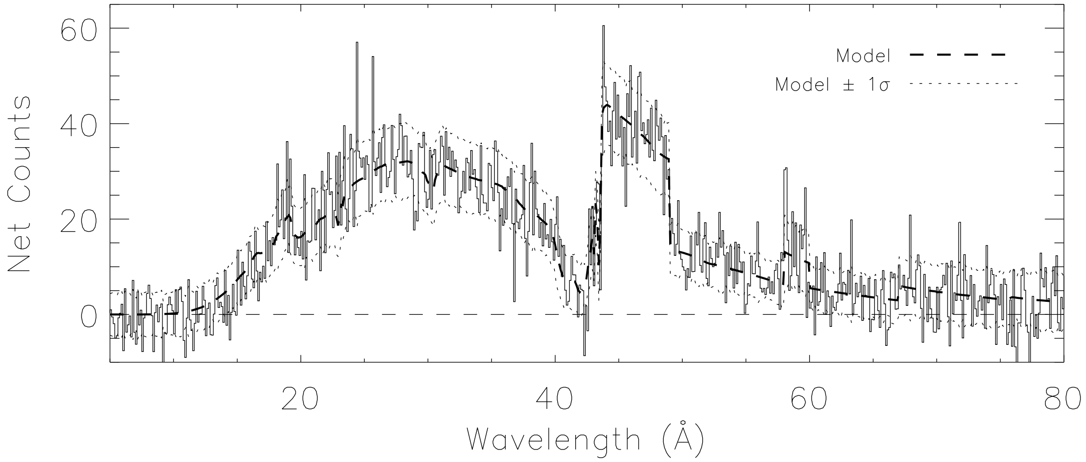

Figure 5.6 Count spectrum of RX J0720.4−3125 obtained with the LETGS. A binning of 0.125 Å was used to obtain sufficient signals per bin to search for narrow features. Heavy dashed line: Expected count spectrum from the single blackbody model shown in Fig. 5.5. Light dotted lines: $\pm 1\,\sigma$ uncertainties about the model. The residuals are consistent with statistical fluctuations about the model. The sharp edges in the model near the 50–70 Å range are the result of detector gaps.

XMM data (Paerels et al. 2001), although now the upper limit for the energy of any narrow features is somewhat lower, around 0.2 keV.

5.4 Radio Observations

5.4.1 Synthesis Imaging

We observed RX J0720.4−3125 with the Very Large Array (VLA) once at 8.4 GHz and twice at 1.4 GHz (summarized in Table 5.7) in the standard synthesis-imaging mode. All data sets were independently calibrated using `AIPS`, but the two 1.4 GHz observations were combined for imaging.

For the 1.4 GHz data, we performed imaging and self-calibration in `difmap`. We iteratively cleaned and self-calibrated (phase only) until the gain solution converged. Uniform weighting was used, yielding a synthesized beam with FWHM $\approx 34''$. An overall gain adjustment was added for one IF, effectively correcting for a nonzero spectral index across the two IF's. No additional amplitude self-calibration was necessary.

After cleaning, we found rms map noise to be 0.08 mJy, a factor of ~ 8 higher than the theoretical thermal noise but consistent with confusion (Condon et al. 1998). The final image (see Fig. 5.8) shows a 5.0 mJy point source next to the position of RX J0720.4−3125, but we believe that this source is unrelated. For reference, the radio source is at J2000 $\alpha = 07^{\rm h}20^{\rm m}28^{\rm s}28(2)$, $\delta = -31^\circ26'09\rlap{.}''9(3)$, $46''$ away from the nominal position of the source. No point-like or diffuse emission from RX J0720.4−3125 was found, which then gives $3\,\sigma$ upper limits to the flux of a point-source of 0.24 mJy and to that of an extended source of < 0.43 mJy arcmin^{-2}.

The imaging of the 8.4 GHz data proceeded similarly. Cleaning and phase self-calibration were done in `difmap`. Again, no source was found at the position of RX J0720.4−3125 (see Fig. 5.8), giving a $3\,\sigma$ flux limit of 0.12 mJy.

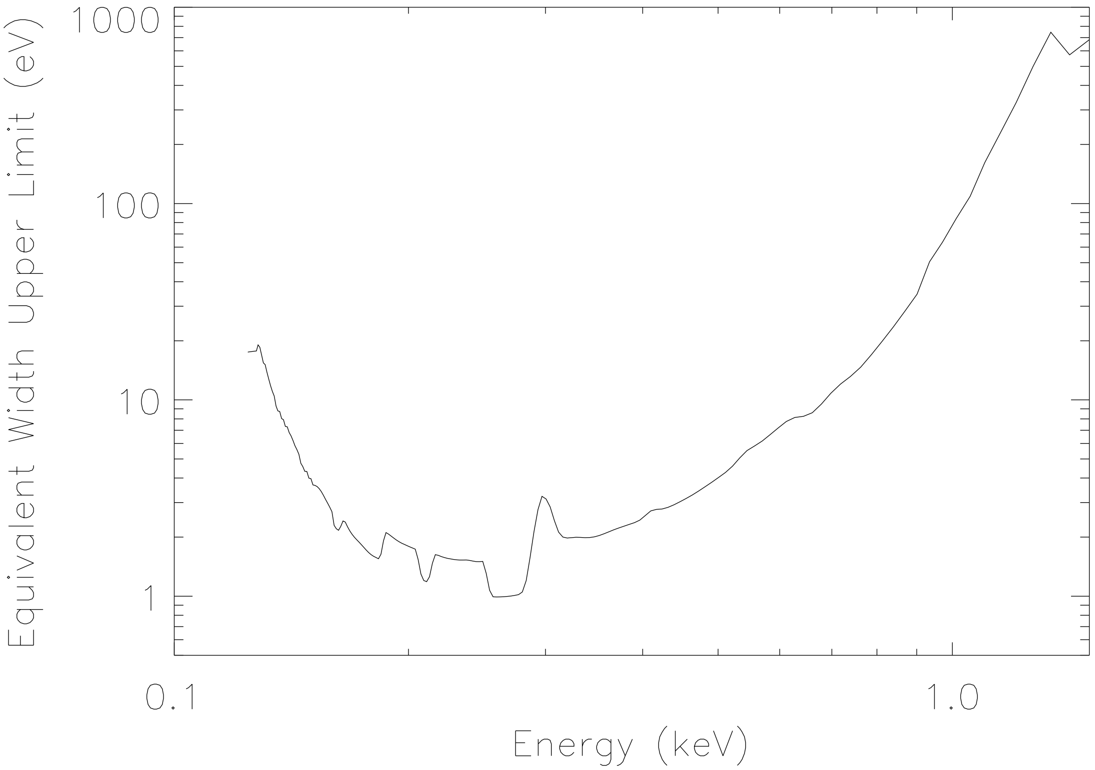

Figure 5.7 Estimates of the 3σ limits that can be placed on any emission lines whose FWHMs are comparable to the instrument resolution, as a function of energy. The computation uses the model fitted to the data (Fig. 5.5) and the effective areas. We assume that candidate features are only 2 bins (0.25 Å) wide. The curves are rather smooth, except for locations of chip gaps, so one may derive limits on broad features using these curves until the scale of the feature becomes comparable to that of the instrument calibration uncertainties. Limits on absorption features are identical when there are many counts but are systematically larger at the high and low ends of the spectrum, where there are fewer than 25 counts per bin.

5.4.2 Pulsation Searches

We observed RX J0720−3125 with the 64 m Parkes radio telescope on 11 January 2001 in an attempt to detect pulsed radio emission. The target position was observed for 10,800 s at center frequencies of 1374 MHz and 644 MHz. At the higher frequency we used the center beam of the Parkes multibeam receiver to feed a 3 MHz × 96-channel multibeam filterbank (see Lyne et al. 2000). At 644 MHz the front-end was the Parkes 50-cm receiver, and the back-end was a 0.125 MHz × 256-channel filterbank. Both observations employed a 1 ms sample period and one-bit digitization.

The interstellar dispersion toward RX J0720.4−3125 is unknown, but we can estimate it with the latest model of Galactic electron density (Cordes & Lazio 2002) which predicts a dispersion measure DM $= 4$ pc cm^{-3} at $d = 300$ pc or DM $= 30$ pc cm^{-3} at $d = 500$ pc. We therefore take DM $= 100$ pc cm^{-3} as a conservative upper limit to the DM (the search was highly insensitive to DM anyway, given the long period of RX J0720.4−3125). Both datasets were dedispersed with dispersion measures up to 100 pc cm^{-3} and searched for periodicities near the known X-ray period (Kaplan et al. 2002b; Zane et al. 2002) using

Table 5.7. Summary of VLA Observations

Date (UT)	Frequency (GHz)	Exposure (s)	Config.	Beam Size (arcsec)	RMS (μJy)
1998-Feb-07	8.4	6720	D→A[a]	$15'' \times 5''.8$	40
1999-Feb-18	1.4	4410	DnC	$36'' \times 32''$	80
1999-Apr-19[b]	1.4	7380	D	⋯	⋯

Note. — Observations all had 2 × 50 MHz bandwidths.

[a] Data were taken while switching from D configuration to A configuration.

[b] Processed with the 1999-Feb-18 observation.

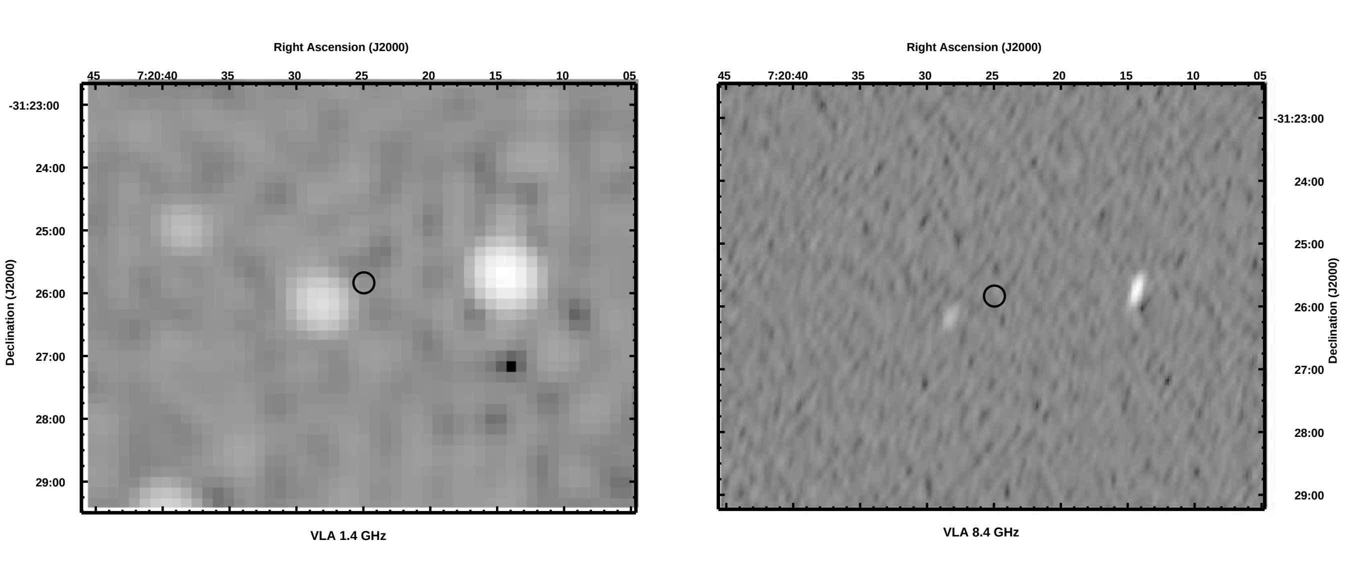

Figure 5.8 VLA maps of the field around RX J0720.4−3125. Left: 1.4 GHz map from the 1999 observations. Right: 8.4 GHz map. RX J0720.4−3125 is indicated with the circle at the center (the radius of the circle is $10''$).

standard folding and FFT-based techniques. No pulsar-like signals were detected.

Without a detection, we must estimate the limiting flux of a signal. While the search is insensitive to DM, the shape of the hypothetical pulse profile strongly affects the sensitivity. Assuming a pulse duty cycle of $w = 1\%$, our $8\,\sigma$ detection limits are 0.2 mJy at 644 MHz and 0.02 mJy at 1374 MHz, and they scale approximately as

$$S_{\rm min,\,644\,MHz} = 2.0\sqrt{\frac{w}{1-w}}\ {\rm mJy}$$

$$S_{\mathrm{min,\,1374\,MHz}} = 0.18\sqrt{\frac{w}{1-w}}\ \mathrm{mJy}. \tag{5.4}$$

For signals with high w (i.e., few harmonics) the 1.4 GHz sensitivity is comparable to that of the VLA observations (§ 5.4.1), where the large bandwidth of the multibeam system compensates for its smaller area and shorter integration. However, for very narrow signals (where many harmonics are summed) the periodicity search is a factor of ~ 7 deeper than the VLA observations.

5.5 Discussion

5.5.1 The Spectrum

We have shown in § 5.2 that the optical/UV spectrum of RX J0720.4−3125 does not follow a pure Rayleigh-Jeans tail. It is possible that the emission (minus the contribution of the Rayleigh-Jeans tail of the X-ray spectrum) is entirely nonthermal in origin (like the Crab pulsar, where the nonthermal emission entirely overwhelms any thermal component). However, the slope of the spectrum, $\alpha_\nu = 1.1$ is much steeper than that seen for other pulsars, whole spectral indices range from $\alpha_\nu = 0.11$ for the Crab (Sollerman et al. 2000) to $\alpha_\nu \sim -1$ for other sources (Zharikov et al. 2002, and references therein). In addition, the low spin-down power of RX J0720.4−3125 ($\dot{E} < 2.4 \times 10^{31}$ ergs s^{-1}; Kaplan et al. 2002b) compared to sources like the Crab or even middle-aged radio pulsars means that there is no reason to expect this much nonthermal emission from RX J0720.4−3125.

Of the six other isolated neutron stars with good optical/UV data, there are three (all $\lesssim 10^6$ yr old and within 500 pc) that show evidence for thermal optical emission: the pulsars PSR B0656+14 (Pavlov, Welty, & Córdova 1997) and Geminga (Martin, Halpern, & Schiminovich 1998),[5] and the nearby isolated neutron star RX J1856.5−3754 (van Kerkwijk & Kulkarni 2001b). [For the 10^4-yr Vela pulsar, the optical emission (Mignani & Caraveo 2001) is dominated by the nonthermal component, but the X-ray spectrum contains thermal and nonthermal contributions (Pavlov et al. 2001c).] Of these sources, RX J1856.5−3754 and PSR B0656+14 have thermal X-ray spectra too, like RX J0720.4−3125. We therefore believe that the optical/UV emission from RX J0720.4−3125 is mostly thermal in nature (i.e., $\alpha_\nu = 2$), with the deviation from a Rayleigh-Jeans tail arising either due to a multiplicative opacity or to an added component. We address each of these models separately.

5.5.1.1 One-Component Model with Absorption

It is possible that the emission from RX J0720.4−3125 is entirely thermal, but that the underlying Rayleigh-Jeans tail is modified by a frequency-dependent absorption to give the observed spectrum. An opacity $\kappa_\nu \propto \nu^{0.9}$ would give the correct result. However, this model is artificial, and is entirely contrary to what is seen with RX J1856.5−3754, PSR B0656+14, and the X-ray spectrum of RX J0720.4−3125 itself (§ 5.2.2.1). While we cannot reject this model based on our data alone, comparison with other sources makes it unlikely.

5.5.1.2 Two-Component Model

A simpler and more physically motivated model for the optical/UV spectrum of RX J0720.4−3125 is that the emission is composed of significant thermal emission plus a nonthermal PL (the PL+RJ model) similar to the spectra of PSR B0656+14 and Geminga. We have plotted brightness temperatures derived from model optical/UV spectra for these sources and RX J1856.5−3754 in Figure 5.9. The sources exhibit

---

[5] Martin et al. (1998) find the PL+RJ model acceptable for Geminga, although a single nonthermal PL is also allowed. In addition, they require an absorption feature in the spectrum.

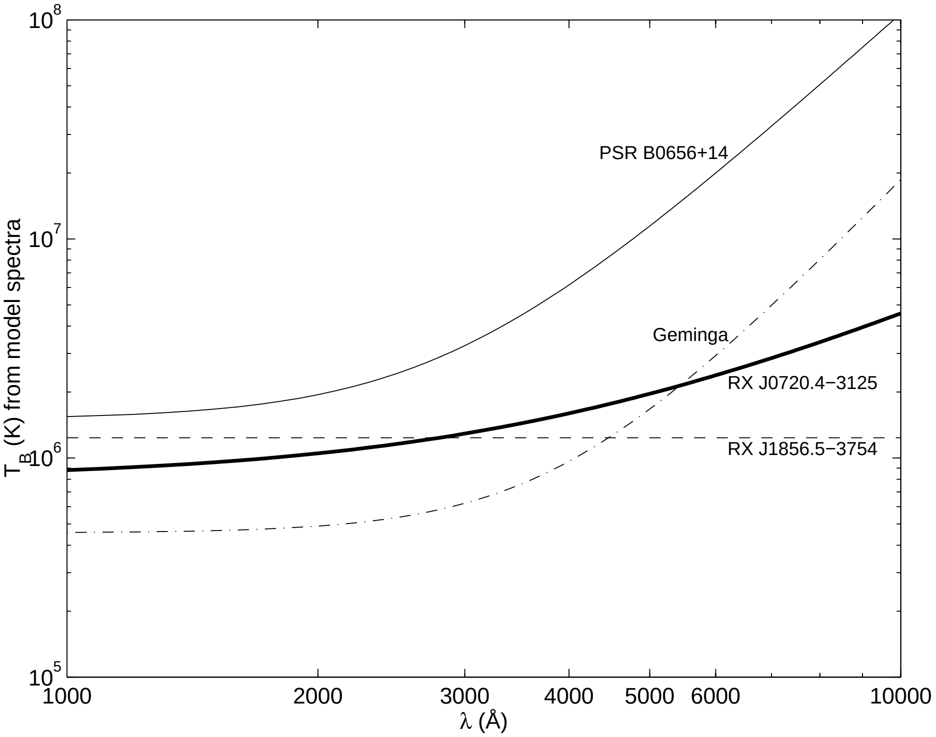

Figure 5.9 Brightness temperature T_B vs. wavelength for for RX J0720.4−3125 (solid line, this paper), RX J1856.5−3754 (dashed line, van Kerkwijk & Kulkarni 2001b), PSR B0656+14 (dotted line, Pavlov et al. 1997), and Geminga (dot-dashed line, Martin et al. 1998). The brightness temperature is defined as $T_B(\lambda) \equiv F_\nu(\lambda)\lambda^2\Omega/2k$, and the values were computed from model optical/UV spectra assuming a radius of 10 km and distances of 300 pc, 140 pc, 330 pc (Kaplan et al. 2002c; Walter & Lattimer 2002), and 160 pc (Caraveo et al. 1996), respectively. Deviations from a constant T_B indicate nonthermal emission.

some variety in their spectra, ranging from purely thermal (RX J1856.5−3754) to largely nonthermal (e.g., PSR B0656+14). While RX J0720.4−3125 shows less nonthermal emission than PSR B0656+14 or Geminga, it is otherwise unremarkable.

The (extinction corrected) B-band luminosity of RX J0720.4−3125 is $L_B = 6.5 \times 10^{27} d_{300}^2$ ergs s^{-1}. If we separate the nonthermal component, we find $L_{B,\mathrm{nonth}} = 3.2 \times 10^{27} d_{300}^2$ ergs s^{-1}. This compares well with the optical luminosities of similarly-aged pulsars given in Zharikov et al. (2002), which have $27 \lesssim \log L_B \lesssim 28$. As such, RX J0720.4−3125 fits in with the pulsar population despite its low rotational power ($\dot{E}$). We note, though, that all of the sources in Zharikov et al. (2002) with $\tau \gtrsim 10^5$ yr have very similar values of L_B, despite values of $\dot{E}$ that vary by about 3 orders of magnitude, and that the values of L_B show no apparent correlation with $\dot{E}$. So it appears that L_B is not simply related to $\dot{E}$, contrary to what is seen in the X-ray regime (Becker & Trümper 1997, see below). It may be, as suggested by Zharikov et al. (2002), that the efficiency of producing optical emission increases with time for $\tau \gtrsim 10^4$ yr so that L_B remains relatively constant despite variations in $\dot{E}$ (i.e., $L_B = \eta(t)\dot{E}$, where $d\eta(t)/dt > 0$ and $d\dot{E}/dt < 0$), or it may just be that the L_B is not directly coupled to $\dot{E}$. A final possibility is that the true distribution of L_B is closely tied to $\dot{E}$ but that we only see the brightest sources in this distribution due to observational bias: a source with $\log L_B = 26.5$ at 500 pc would have $B \approx 31$ mag, below modern detection limits. Similarly, the very well studied RX J1856.5−3754 at ≈ 140 pc, the limit to nonthermal emission is $\log L_B \lesssim 26.5$. Therefore, any other source with $\log L_B < 26.5$ could not be detected, and the true distribution of L_B may be poorly represented.

The slope of the nonthermal PL is $\alpha_\nu \approx 0.3$. This is consistent (within errors) with the slope of the optical PL for the Crab, and is not that far from the slope of the spectrum of PSR B0656+14 ($\alpha_\nu = -0.45 \pm 0.26$; Koptsevich et al. 2001). The nonthermal spectra of neutron stars have been observed to follow roughly the same slope for over ~ 5 orders of magnitude in energy (e.g., Koptsevich et al. 2001), suggesting a single underlying mechanism for the nonthermal optical and X-ray power-laws. Here, the nonthermal PL would contribute $\sim 1\%$ of the flux of the blackbody in the LETG band and would therefore be difficult to observe: $F(1\,\mathrm{keV}) = (5^{+25}_{-4}) \times 10^{-13}$ ergs s^{-1} cm^{-2}. At higher energies ($\gtrsim 2$ keV) the nonthermal PL could contribute substantial X-ray flux (although the PL is highly uncertain at these energies; see Figure 5.4), flux that was not detected in the *Chandra* or *XMM* data. The *XMM* EPIC-pn data roughly give a flux of 2×10^{-14} ergs s^{-1} cm^{-2} at 1.5 keV, consistent with a blackbody and barely consistent with the extrapolated optical/UV power-law. So, for RX J0720.4−3125 the nonthermal spectrum is not likely to bridge the X-ray and optical regimes.

Becker & Trümper (1997) have found a rough relation between the spin-down power and the nonthermal X-ray emission of pulsars: $L_{X,\mathrm{nonth}} \sim 10^{-3}\dot{E}$ (with $L_{X,\mathrm{nonth}}$ in the *ROSAT* band of 0.1–2.4 keV). Applying this to RX J0720.4−3125 we would expect $L_{X,\mathrm{nonth}} \lesssim 10^{28}$ ergs s^{-1}, or $F_{X,\mathrm{nonth}} \lesssim 10^{-15}$ ergs s^{-1} cm^{-2}. This is a factor of $> 10^4$ less than the observed thermal X-ray flux in the same band, and a factor of 10^2 less than the extrapolated nonthermal emission. However, there is considerable uncertainty in both the relation of Becker & Trümper (1997) (see, e.g., Possenti et al. 2002) and in the extrapolation of the nonthermal PL to the X-ray regime, so the difference between $F_{X,\mathrm{nonth}}$ predicted from the spin-down and that predicted from the optical/UV spectrum may not be significant.

The thermal component in the optical/UV band is, like that of RX J1856.5−3754, above a simple extrapolation of the X-ray spectrum (for RX J1856.5−3754 it exceeds the X-rays by a factor of ~ 16; van Kerkwijk & Kulkarni 2001b). This could just be a matter of temperature, though. For the sources PSR B0656+14 and PSR B1055−52, the X-ray spectrum is best-fit by a combination of a power-law and two blackbody components (Greiveldinger et al. 1996; Pavlov, Welty, & Córdova 1997; Koptsevich et al. 2001; Marshall & Schulz 2002; Pavlov, Zavlin, & Sanwal 2002), where the smaller hot portion (presumably the polar cap) contributes the majority of flux in the traditional X-ray band but the larger cool portion (along with the nonthermal emission) gives rise to the optical/UV flux (Pavlov et al. 2002). In both cases, the blackbody components are all hot enough ($\gtrsim 8 \times 10^5$ K) to appear in the X-ray band, and are therefore well modeled.

For RX J1856.5−3754, which is closer in temperature to RX J0720.4−3125, Braje & Romani (2002) again appealed to a multi-temperature surface, but here the second blackbody is not observed but only inferred (also see Walter & Lattimer 2002). It must be too cool for the X-ray band ($T_{\mathrm{cold}} \lesssim 5 \times 10^5$ K), while still hot enough to appear as a power-law in the optical/UV band. While not very well constrained, this model gave reasonable results for RX J1856.5−3754, including a weak constraint on the radius, and is therefore valuable. We now apply this model to RX J0720.4−3125.

We see from Table 5.6 that a second (unconstrained) blackbody component does not appreciably change the X-ray fit. However, we can use the goodness-of-fit (given by χ^2) to constrain the combinations of T_{cold} and R_{cold} that are allowed. The flux of a Rayleigh-Jeans tail goes as $F_\nu \propto R^2 T$. We know that the X-ray blackbody has $R_{\mathrm{hot}} = 6.1 d_{300}$ km and $T_{\mathrm{hot}} = 9.45 \times 10^5$ K, and since the thermal fit to the optical/UV data is a factor of 2.4 above the X-ray extrapolation, we find

$$T_{\mathrm{cold}} = 2.4 \times 10^5 \left(\frac{R_{\mathrm{cold},15}}{d_{300}} \right)^{-2} \ \mathrm{K}, \tag{5.5}$$

where the cold radius $R_{\mathrm{cold}} = 15 R_{\mathrm{cold},15}$ km has been taken to be the radius of the neutron star. Such a cool blackbody would not have been seen in the X-ray data (as shown by the large uncertainties on R_{cold} in Tab. 5.6), but we can constrain T_{cold} to be $\approx (3.5\text{–}5.0) \times 10^5$ K, or $R_{\mathrm{cold}} \approx (11\text{–}13) d_{300}$ km (at roughly 90%

confidence). This is similar to the temperature of the cold component found for RX J1856.5−3754 (Braje & Romani 2002)—not surprising since in both cases the cold component was forced to give a Rayleigh-Jeans tail in the optical while not giving significant contribution in the soft X-rays—and the size agrees well with estimates for the radius of a neutron star (Lattimer & Prakash 2000).

Cropper et al. (2001) model the phase-dependent hardness ratio of RX J0720.4−3125 in *XMM* data, and find that it is consistent with a polar-cap model for a large range of cap sizes with angular radii of 10–50°. This agrees quite well with our findings ($R_{\rm cold} = 15 d_{300}$ km corresponds to an angular radius of $\approx 25^\circ$).

Taken together, these observations show that a RJ+PL model for the optical/UV spectrum of RX J0720.4−3125 makes it entirely consistent with being an off-beam radio pulsar, one that likely has a cooler blackbody component in the extreme UV.

5.5.1.3 Constraints on the Magnetic Field

We find no significant absorption features in the pulse-averaged or pulse-phased spectra over the 0.15–0.80 keV band (§ 5.3). Thus, following Marshall & Schulz (2002) and Paerels et al. (2001), we can rule out electron and proton cyclotron resonance lines in this range. Paerels et al. (2001) already rule out the range $0.03 < B_{12} < 0.2$ and $50 < B_{12} < 200$, where $B_{12} = B/(10^{12}\ {\rm G})$. By extending the spectrum down to 0.15 keV, we extend the lower limits of the excluded ranges of magnetic fields to $B_{12} = 0.015$ and $B_{12} = 25$, though the lower limits could increase if the bulk of the emission comes from the equatorial zone, where the magnetic field is $\sim 50\%$ of the polar value, or if the absorbing plasma is far off the neutron surface. We can also use the lack of features in the spectrum to exclude hydrogen atmospheres for a range of magnetic field strengths. Again following Paerels et al. (2001), we can exclude the range $B_{12} > 15$. The excluded ranges of B agree with the finding that RX J0720.4−3125 is not a magnetar (Kaplan et al. 2002b), but otherwise the B is consistent with either of the models discussed in Kaplan et al. (2002b, see also § 5.5.2), namely that have $B_{12} \approx 1$–10.

5.5.2 Radio Luminosity

At a distance of $300 d_{300}$ pc, we limit the 1.4 GHz radio luminosity of RX J0720.4−3125 to $< 3 \times 10^{25} d_{300}^2$ ergs s^{-1} ($L_{\rm rad} \equiv 4\pi d^2 F$), or following the radio pulsar convention $L'_{\rm rad} < 0.02$ mJy kpc^2 ($L'_{\rm rad} \equiv F d^2$). This is significantly below what is expected of radio pulsars with parameters (P and $\dot{P}$) similar to those of RX J0720.4−3125. For instance, the two high-B radio pulsars discovered by Camilo et al. (2000) have $L_{\rm rad} \sim 5 \times 10^{26}$ ergs s^{-1}, while the 8-second 10^{12}-G pulsar PSR J2144−3944 has $L_{\rm rad} \sim 10^{30}$ ergs s^{-1} (Young et al. 1999). Similarly, the radio luminosity model of Arzoumanian, Chernoff, & Cordes (2002) predicts luminosities of 10^{27-28} ergs s^{-1}, depending on the value of $\dot{P}$. So we can see that RX J0720.4−3125, if it has any radio emission, must be beamed away from the Earth.

If RX J0720.4−3125 is like PSR J2144−3944, then we might expect a similarly narrow radio beam of $w \approx 0.6\%$, a beam width that agrees well with the extrapolation of Rankin (1993). RX J0720.4−3125 may however be more similar to the 10^{13} G radio pulsar PSR J1814−1744 (Camilo et al. 2000), which has a significantly wider beam ($w \approx 3\%$). In either case, we can expect that the radio beam subtends a small solid angle, making the lack of radio emission quite credible. For such beams, our upper limits to the radio luminosity *decrease*, as the limit from the Parkes data for a source with pulse width of $w = 0.6$–3% at 1.4 GHz is $L'_{\rm rad} \approx 0.002$ mJy kpc^2. Even the imaging (VLA) limit is quite faint, about a factor of 3 fainter than the limit for Geminga (Seiradakis 1992), and a factor of ~ 30 below that of PSR J0205+6449 in 3C 58 (Camilo et al. 2002d), but the implied limit for a narrow pulse width is far below that of all radio pulsars younger than 10^6 yr (Motch 2001).

With such small beams, the radio-quiet population of sources like RX J0720.4−3125 could potentially be very large, up to a hundred times the radio-loud population (assuming a sharp cutoff in the radio beam). While likely invisible to radio observations, such sources are of course bright X-ray emitters, and would be visible to $\sim$ 5 kpc in a 30 ks *XMM* observation. The total numbers of such sources (either radio-loud or -quiet) are small, making statistics uncertain, but there could be cooling radio-quiet neutron stars in as much as 1% of *XMM* observations. However, these sources would be all but impossible to confirm, as there would be few X-ray photons for spectral fitting or pulsation searches, and the optical/UV counterpart would be extremely faint.

5.6 Conclusions

We have shown, through a joint analysis of radio, optical, and X-ray data, that the spectrum of the isolated neutron star RX J0720.4−3125 cannot be fit by a single blackbody model. While statistically we cannot rule out a model with a single power-law in the optical/UV domain and an X-ray blackbody, from a more general perspective we believe that the best-fit model is one with three components: a hot ($\sim 9 \times 10^5$ K) blackbody on the polar cap, a cool ($\sim 4 \times 10^5$ K) blackbody over the whole surface, and a weak nonthermal power-law in the optical/UV. This is very similar to the spectra of middle aged radio pulsars such as PSR B0656+14 and PSR B1055−52, an observation that supports the identification of RX J0720.4−3125 with an off-beam radio pulsar.

RX J0720.4−3125 appears extremely similar to the very nearby RX J1856.5−3754, perhaps with orientation being the only difference between them (Braje & Romani 2002). We believe it likely that nonthermal emission and/or pulsations will be detected eventually for RX J1856.5−3754, as suggested by Braje & Romani (2002). Both sources seem to have spectra primarily composed of featureless blackbodies. If we can develop a full understanding of such spectra to properly relate the blackbody radii (such as that given here) to the true radii, these sources will be ideal targets for the determination of the equation-of-state.

In the near future, we will obtain *HST* astrometry allowing us to determine the distance and velocity of RX J0720.4−3125, as well as Hα imaging to search for bow-shock nebulae (e.g., van Kerkwijk & Kulkarni 2001a) that will place significant constraints on alternate models such as accretion. In the off-beam pulsar model, these data may limit the luminosity of any particle wind from RX J0720.4−3125, and will reduce uncertainty in the EOS by determining the conversion from solid angle to radius.

We thank the anonymous referee for valuable comments. D. L. K. is supported by the Fannie and John Hertz Foundation and S. R. K. by NSF and NASA. M. H. v. K. is supported by a fellowship from the Royal Netherlands Academy of Arts and Sciences. H. L. M. was supported under NASA contract SAO SV1-61010. DLK also thanks *Chandra* grant GO0-1024X for additional support. Data presented herein were based on observations made with the NASA/ESA Hubble Space Telescope, obtained at the Space Telescope Science Institute, which is operated by the Association of Universities for Research in Astronomy, Inc., under NASA contract NAS 5-26555. The National Radio Astronomy Observatory is a facility of the National Science Foundation operated under cooperative agreement by Associated Universities, Inc. Data presented herein were also obtained at the W. M. Keck Observatory, which is operated as a scientific partnership among the California Institute of Technology, the University of California, and the National Aeronautics and Space Administration. The Guide Star Catalog-II is a joint project of the Space Telescope Science Institute and the Osservatorio Astronomico di Torino.

Chapter 6

A Re-Analysis of the Parallax of Geminga

D. L. Kaplan

Abstract

We discuss analysis of archival *HST* observations of Geminga (PSR J0633+1746) that were used to determine a parallax of $\pi = 6.4 \pm 1.7$ mas. We find that using newer analysis techniques as well as additional data that the previous analysis was incorrect and grossly underestimated its errors. Instead of a 3.7-σ detection, we find that the parallax has not been detected ($\pi = 1 \pm 6$ mas).

6.1 Introduction

Since its discovery as a γ-ray source (Fichtel et al. 1975; Thompson et al. 1977), Geminga (PSR J0633+1746) has been an intriguing source. When X-ray (Bignami et al. 1983) and optical (Bignami et al. 1987, 1988; Halpern & Tytler 1988) counterparts were discovered the source attracted even more attention, and finally the identification of a 237 ms periodicity (Halpern & Holt 1992) led to its classification as a rotation-powered pulsar that has no detectable radio emission (McLaughlin et al. 1999). Whether it has no radio emission, or the radio beams simply do not intersect the Earth, is unknown.

6.2 A Parallax for Geminga?

Taking advantage of the angular resolution of the *Hubble Space Telescope* (*HST*), Caraveo et al. (1996, hereafter CMBT96) used three observations with the Wide-Field and Planetary Camera 2 (WFPC2) to measure a parallax for Geminga of $\pi = 6.4 \pm 1.7$ mas—an unprecedented feat at the time for a neutron star with no radio emission. However, characterization of the WFPC2 detectors for astrometry and the techniques used to analyze the data have both improved greatly since this date (Anderson & King 1999, 2000). We have re-analyzed the extant *HST* data and find the reported parallax to be unreproducible.[1] Below we describe the data and our reanalysis.

6.3 Observations

Geminga has been observed several times with *HST*. Specifically, there was on observation with the F555W filter in 1994 March, observations with the F555W and F675W filter in 1995 September, and observations

---

[1] This has been reproduced by several other groups (F. Walter et al. 2003, pers. comm.; G. Pavlov et al. 2003, pers. comm.).

with the F555W filter in 1994 September and 1995 March. A subset of these data (three of the F555W observations) were used by CBMT96 to measure its parallax.

6.4 New Analysis

We have re-analyzed the data presented in CBMT96 together with the additional data (including the F675W observation) and could not reproduce the previous analysis. In particular, we found that the positions were mismeasured and the errors at various stages of the analysis were seriously underestimated.

Below we detail the differences between our analysis (Using a more robust technique similar to that given in Kaplan et al. 2002c) and that presented in CBMT96. For comparison, we note that our measurement of the parallax of another neutron star (RX J1856.5−3754) from WFPC2 data (Kaplan et al. 2002c) has since been confirmed (Walter & Lattimer 2002), and that our measurement of the parallax of the Vela pulsar agrees with Caraveo et al. (2001) and Dodson et al. (2003).

6.4.1 Dither Pattern

The data were taken without any real dither pattern. This severely limits the astrometric accuracy due to the undersampling of the planetary camera (PC; see Anderson & King 2000), and also prevents any reliable estimations of the measurements uncertainties.

6.4.2 Centroiding

CBMT96 first smoothed the data and then fit for source positions using a Gaussian distribution. Anderson & King (2000) have shown that simple Gaussian techniques can improperly bias the positions of sources by as much as 0.2 pixels (10 mas). CBMT claim statistical uncertainties on source positions of 0.01–0.03 pixels for the field stars and 0.05-0.07 pixels for Geminga. Using the effective point-spread-function (ePSF) technique (Anderson & King 2000), we find uncertainties of 0.05–0.08 pixels for the field stars and 0.10–0.15 pixels for Geminga: a factor of 2 higher. These uncertainties agree roughly with the uncertainty relation as a function of source counts presented in Kaplan et al. (2002c), especially considering the poor spatial sampling afforded by the dither pattern. This difference of roughly a factor of two in position uncertainty accounts for a lot of the difference in the precision of our measurement compared to that of CBMT96.

6.4.3 Distortion Correction

CBMT96 used the geometric distortion model of Holtzman et al. (1995) to convert their measured pixel positions into relative celestial coordinates. We used the much more accurate model of Anderson & King (in preparation). We also accounted properly for the 34th-row error (Anderson & King 1999).

6.4.4 Frame Registration

Once one has the relative celestial coordinates of each object has been found in each epoch, one must convert those positions to a common reference grid. CBMT96 used a simple approach, assuming that the position angles of each observation were known exactly and given by the header values. They also assumed that the plate scales were constant across all of the observations. Fitting only for a position offset between epochs, they estimate the statistical uncertainty due to transformation errors to be 0.01 pixel or 0.5 mas.

However, Anderson & King (2000) have shown that there are differences in the plate scale and position angle of *HST* observations of can differ significantly from the nominal values (also see Kaplan et al. 2002c). We fit each epoch individually for position angle, plate scale, and position offset and found significant deviations of up to 0.05° in the position angle and up to 0.1% in the plate scale, which can produce offsets of up to 15 mas at the edges of the PC. We also allowed for the possibility that the field stars had nonnegligible proper motions themselves, an effect that can be significant (Kaplan et al. 2002c).

With the improved method, we find that the transformations are poorly determined. This is because there are at most 7 field stars on the PC that can be used to determine the transformations. Using these sources, we find that the transformation uncertainties add about a 10–20 mas uncertainty to the position of Geminga, significantly more than the centroiding uncertainty.

To see how well the transformation worked, CBMT96 compared the positions of the stars in each pair of observations (they were working with three observations and therefore had three pairs). They note that the average position displacements are ≈ 0.08 pixels (4 mas), much higher than their assumed transformation error of 0.5 mas. In Figure 6.1 we plot histograms of the position differences from CBMT96 and from our analysis. The differences from our analysis cluster near 0 and are consistent with the expected χ^2 distribution, while those from CBMT96 do not. Not only did they underestimate their position uncertainties (the mean of the absolute value of the displacement is $3\,\sigma$) but the shape of the distribution is incorrect.

6.4.5 Parallax Determination

Finally, with relative positions determined in every epoch, the remaining task is to fit for the proper motion and parallax. CBMT96 used a simplified model for the parallactic motion of Geminga. We performed a single fit for position, proper motion and parallax using all five available observations and using the precise parallactic ellipse for Geminga from the JPL DE200 ephemeris, and came up with $\pi = 1 \pm 6$ mas: a nondetection.

6.4.6 Additional Checks

To double-check our analysis, we jack-knifed the data, i.e., we repeated the analysis by removing individual data points (both entire epochs and single stars). No differences were found. We also performed Monte-Carlo simulations of our analysis, repeating it for data where the parallax and proper motion were known. For the position uncertainties that we obtained, we found the parallax to be unmeasurable ($\sigma_\pi \gtrsim \pi$). Even for the position uncertainties claimed by CBMT96, we found that they underestimated the error in the parallax, likely due to transformation uncertainties etc.

6.5 Conclusions

We have demonstrated through analysis of both the data from CBMT96 and additional data that the parallax of Geminga has not yet been measured and is not measurable from current data. This does not mean that the distance to Geminga must be drastically different from the value obtained by CBMT96: comparison with RX J1856.5$-$3754 and PSR B0656+14 (Brisken et al. 2003b) suggest that it is not. But at this point we must regard the true parallax as unknown. F. Walter has applied for and been granted new *HST* observations of Geminga that should give an accurate parallax and settle the issue.

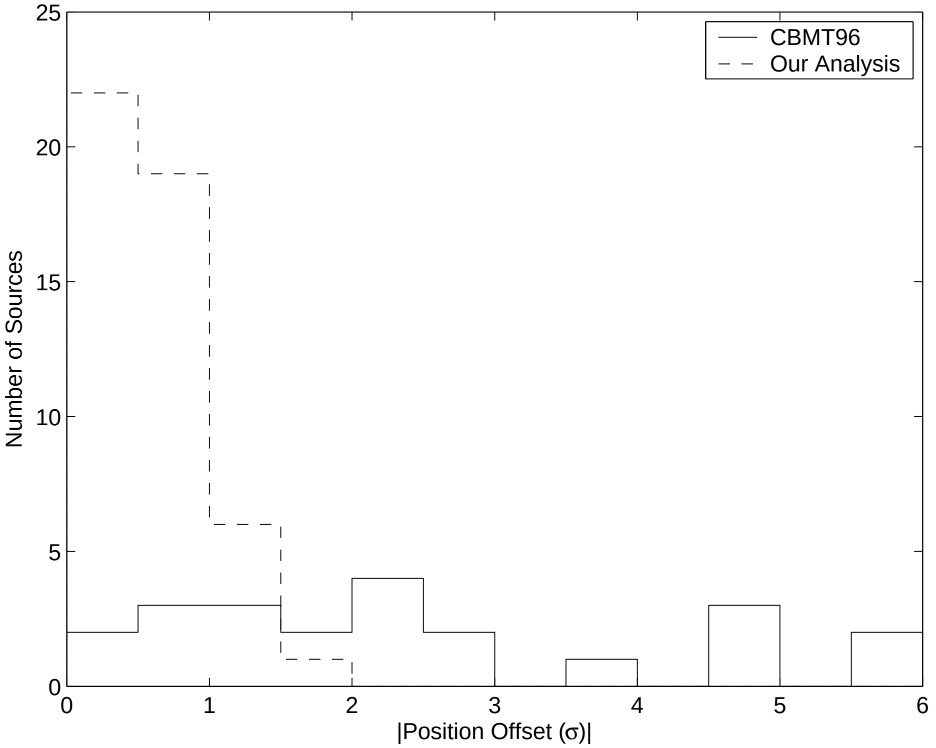

Figure 6.1 Difference in source positions between pairs of observations for field stars in units of σ. The solid line is from CBMT96 and the dashed line is from our analysis once the field stars have been corrected for their proper motions. The data from CBMT96 have much higher values that those from our analysis. Our position differences are very similar to the expected χ^2 distribution, while those from CBMT96 do not.

Chapter 7

The Nearby Isolated Neutron Stars

D. L. Kaplan

Abstract

We discuss the population of seven isolated neutron stars (INSs) discovered by *ROSAT*. We review the current observations across all wavelengths which lead us to conclude that the INSs are 10^6 yr cooling neutron stars with $> 10^{13}$ G magnetic fields—likely old versions of high-field radio pulsars. The large number of INSs within 500 pc implies a large total number of sources in the Galaxy, and suggests that the distribution of magnetic fields for neutron stars is roughly flat up to 10^{14} G. We also discuss the potential of the INSs for constraining fundamental physics, but conclude that such constraints are premature as no believable atmosphere models exist.

7.1 Introduction

7.1.1 Expectations

While over 1000 isolated neutron stars have now been discovered as radio pulsars, the total number in the Galaxy is much larger. Radio pulsars emit pulsations for $\sim 10^7$ yr and are visible due to radio beams that subtend 1–10% of the sky, so the total number of neutron stars just in the local region of the Galaxy (where radio pulsars are detectable) should be $\gtrsim 10^6$ (e.g., Lorimer 2003).

Are these objects truly invisible, or is there some chance of their being observed? For years astronomers have proposed that a large fraction of these objects would be visible through one of two mechanisms: accretion or cooling. The first mechanism could revive old, dead pulsars, while the second would primarily work for younger sources but would not depend on the presence of radio pulsations. Both mechanisms, however, make the neutron stars visible in the soft X-ray regime, not in the radio regime that had dominated the study of neutron stars.

Accretion takes advantage of the gravitational potential wells of neutron stars (with radii of ≈ 3 times their gravitational radii). First proposed by Ostriker et al. (1970), the idea was revived (Treves & Colpi 1991; Blaes & Madau 1993) when it was realized that the *ROSAT* satellite might be able to discover as many as 5000 of these sources. In this scenario, neutron stars moving through the interstellar medium (ISM) would accrete and material and shine due to the release of potential energy.

However, the estimates of these populations were very uncertain, as they depended critically on the (relatively unknown) velocity, spin, and magnetic field distributions of the sources as well as the distribution of the accreting matter. This is because the accretion rate scales as v^{-3} (in the nonmagnetized, spherical, Bondi-Hoyle limit, which is only approximate; Bondi & Hoyle 1944; Bondi 1952) and also depends critically on the strength and rotation rate of the magnetic field (e.g., Illarionov & Sunyaev 1975; Alpar 2001; Toropina et al. 2003; Perna et al. 2003).

Cooling takes advantage of the initially very hot ($\sim 10^{11}$ K) temperatures of newly-formed neutron stars to radiate primarily neutrinos but more importantly for observers X-rays as well for about 10^6 yr (e.g., Tsuruta & Cameron 1965; Tsuruta et al. 1972). After this point the neutron stars cools into the ultraviolet band, where interstellar absorption and the T^4 dependence of the flux render it invisible. While the basic formulation of neutron star cooling has been known for decades, the details are still elusive (e.g., Tsuruta et al. 2002; Yakovlev et al. 2002a; Yakovlev et al. 2003; Page et al. 2004), as uncertainties in the neutron star's structure, envelope, and magnetic field can all have significant effects.

These isolated neutron stars should have been identifiable based on the following criteria (Treves & Colpi 1991):

1. Largely thermal emission peaking in the soft X-ray or far-UV band, requiring small hydrogen column densities to remain visible
2. The absence of bright optical counterparts
3. Significant ($\gtrsim 0.1$ arcsec yr^{-1}) proper motions
4. Preferred locations in the Galactic plane

The first two criteria relate to the spectra of the neutron stars, and serve to rule out the active galaxies and stars that dominate X-ray surveys (Hertz & Grindlay 1988). The third criterion reflects the proximity of the sources (with maximum distances of ~ 1 kpc) and the large space velocities of known neutron stars (presumably due to supernova kicks). The final criterion comes from the Galactic nature of the sources, and is similar to the distribution of radio pulsars. As we shall see, while most of the original predictions were wrong, the first three criteria have been borne out observationally and the fourth may also be true.

The second criterion relates to many classes of neutron stars, not just the accreting/cooling sources discussed here. In fact, due to their small sizes and hot temperatures, neutron stars that are detectable in bands outside the radio regime generally have very high ratios of X-ray to optical flux. For thermal sources, this is approximately

$$\frac{L_{\rm X}}{L_{\rm opt}} \sim 10^{5.5+3\log(kT/100\ {\rm eV})} \tag{7.1}$$

(Treves et al. 2000; Rutledge et al. 2003). This compares to stars values of 10^{-3}–10^{-2} for stars (Katsova & Cherepashchuk 2000) and 0.1–10 for active galaxies (Brandt et al. 2001). Only white dwarfs and X-ray binaries (compact objects, like neutron stars) can come close, with ratios of 10–1000 (Hertz & Grindlay 1988). For a more general discussion of this, see Hulleman et al. (2000) or Kaplan et al. (2004).

7.1.2 The Legacy of *ROSAT*

Instead of the anticipated 5,000 objects, *ROSAT* discovered only half a dozen nearby cooling neutron stars (see reviews by Motch 2001; Haberl 2004; Tab. 7.1). Much of the difference can be ascribed to poor assumptions regarding the velocity distribution of pulsars (Colpi et al. 1998; Neuhäuser & Trümper 1999; Treves et al. 2000) and the effects of magnetic fields (Illarionov & Sunyaev 1975; Perna et al. 2003). However, they are all the more valuable because of their rarity.

The first such source to be discovered was RX J1856.5−3754. It was originally identified serendipitously as a soft, bright X-ray source with no obvious optical counterpart (Walter et al. 1996). Its location in front of the R CrA molecular cloud meant that it had to be nearby ($\lesssim 200$ pc)—otherwise the X-ray emission would have been absorbed. Confirmation of its nature came with the discovery of a very faint ($B \approx 25.8$ mag), blue optical counterpart (Walter & Matthews 1997).

Table 7.1. The Nearby Isolated Neutron Stars Detected By *ROSAT*

RX J	PSPC	kT	$E_{\rm abs}$[a]	P	B	Optical	$B_{\rm cyc}$[c]	$B_{\rm H}$[d]	d[e]
	(ct/s)	(eV)	(eV)	(s)	(mag)	Excess[b]	($\times 10^{13}$ G)		(pc)
1856.5−3754	3.64	60	···	···	25.8	6	···	···	175
0720.4−3125	1.64	85	271	8.39	26.5	6	5.6	1.6	290
1605.3+3249	0.90	95	450	···	26.9	9	9.4	14.3	370
0806.4−4123	0.38	96	460	11.37	> 25.5	···	9.6	15.8	> 190
1308.6+2127	0.29	90	< 300	10.31	28.5	6	6.2	2.5	740
2143.0+0654	0.18	92	···	··· [f]	$\gtrsim 22$	···	···	···	> 38
0420.0−5022	0.14	45	329	3.45	26.6	13	6.8	3.6	220

[a] Central energy of the best-fit Gaussian absorption feature.

[b] Extrapolation of X-ray blackbody into the optical band, divided by the optical flux.

[c] Magnetic field assuming that the absorption feature is due to the fundamental proton cyclotron line: $B_{\rm cyc} = 1.6 \times 10^{14} E_{\rm keV}(1+z)$ G. See Figure 7.7.

[d] Magnetic field assuming that the absorption feature is due to the bound-free transition of neutral hydrogen at an observed energy of $E \approx 0.31(\log(B/B_0))^2/(1+z)$ keV, where $B_0 = 2.35 \times 10^9$ G; (Potekhin 1998; Ho et al. 2003). See Figure 7.7.

[e] All distances are scaled from the distance and optical emission of RX J1856.5−3754: $d = 175\ {\rm pc}\sqrt{kT/60\ {\rm eV}}10^{(B-25.8)/5}$ (cf. Kaplan et al. 2002c).

[f] Has not been deeply searched for periodicities.

Note. — We assume a gravitational redshift $z = 0.3$.

References. — Walter et al. (1996); Walter & Matthews (1997); Haberl et al. (1997); Kulkarni & van Kerkwijk (1998); Zampieri et al. (2001); van Kerkwijk & Kulkarni (2001b); Kaplan et al. (2002c); Kaplan et al. (2002a); Ransom et al. (2002); Burwitz et al. (2003); Kaplan et al. (2003a); Kaplan et al. (2003b); Haberl et al. (2003a); van Kerkwijk et al. (2004); Haberl et al. (2003b); Haberl et al. (2004)

Since then, six other similar sources have been identified through the efforts of the group at MPE (Haberl et al. 1997, 1998; Schwope et al. 1999; Motch et al. 1999; Haberl et al. 1999; Zampieri et al. 2001). We summarize the properties of the sources in Table 7.1. Identification of additional sources that may still be present (Rutledge et al. 2003) in the *ROSAT* Bright Sources Catalog (containing ≈ 18000 sources with > 0.05 counts s^{-1} in the Position-Sensitive Proportional Counter, or PSPC; Voges et al. 1996) is extremely difficult given the poor positional accuracy of the PSPC (Fox 2004).

Right away with the discoveries of the first two sources (RX J1856.5−3754 and RX J0720.4−3125), astronomers had a puzzle: the first source did not pulsate at all, while the second pulsated with a period of 8.4 s. These were both far different from the known population of radio pulsars and led to a number of models being proposed for these sources, known as the isolated neutron stars (INSs):[1] accreting neutron stars with conventional magnetic fields spun down to long equilibrium spin periods (Konenkov & Popov 1997; Wang 1997; Alpar 2001); cooling middle-aged pulsars with $\sim 10^{12}$-G magnetic fields whose radio beams are directed away from the Earth (Kulkarni & van Kerkwijk 1998); cooling off-beam pulsars with high ($\sim 10^{13}$ G) magnetic fields (HBPSRs); or old magnetars (Duncan & Thompson 1992)—neutron stars with magnetic fields $> 10^{14}$ G—that are kept warm by the decay of their strong magnetic field (Heyl & Hernquist 1998b; Heyl & Kulkarni 1998).

In what follows we will discuss the observation of the INSs (§ 7.2). We will then apply these observations to the models discussed above, try to distinguish between them (§ 7.3), and place the INSs in the context of the greater pulsar population (§ 7.3.3). Finally, we will discuss how the INSs can be be used to constrain basic fundamental physics (§ 7.4).

7.2 Observations of Isolated Neutron Stars

7.2.1 X-ray Spectra

Like optical spectroscopy for stars, X-ray spectroscopy of neutron stars can be a powerful (if ambiguous) diagnostic of the surface conditions (e.g., Sanwal et al. 2002; Hailey & Mori 2002; Cottam et al. 2002). The first spectra of the INSs, determined from *ROSAT*, were featureless and consistent with blackbodies. The initial efforts with *Chandra* and *XMM* showed the same thing (Burwitz et al. 2001; Paerels et al. 2001). More recently, though, longer exposures, better calibration, and more careful analysis has shown that the spectra are more complex.

Observations of the INS have shown that their spectra are not smooth but instead have deviations consistent with Gaussian absorption lines having energies from ≈ 200–460 eV and equivalent widths from 30–150 eV (Haberl et al. 2003a,b, 2004; van Kerkwijk et al. 2004; see Table 7.1). These features are definitely associated with the neutron stars themselves and not with any intervening material as they have been observed to change as functions of pulse-phase. Additionally, for RX J0720.4−3125 the absorption has been observed to be variable (de Vries et al. 2004), growing significantly in strength toward the end of 2003. In Figure 7.1 we show *XMM* spectra of RX J1605.3+3249, RX J0720.4−3125, and RX J1308.6+2127 on the same scale. We can see that that the central energies and widths of the absorption vary significantly: for RX J1308.6+2127 we do not yet know what the central energy of the absorption is since it is below the observable band.

7.2.2 X-ray Timing

As with the radio pulsars, timing of the INSs should divulge a wealth of information about their ages, magnetic fields, and spin-down luminosities. However, timing of the INSs is far more difficult than that of

---

[1] They are also called the dim thermal neutron stars (DTNSs), radio-quiet neutron stars (RQNSs), X-ray dim isolated neutron stars (XDINs), and other variations.

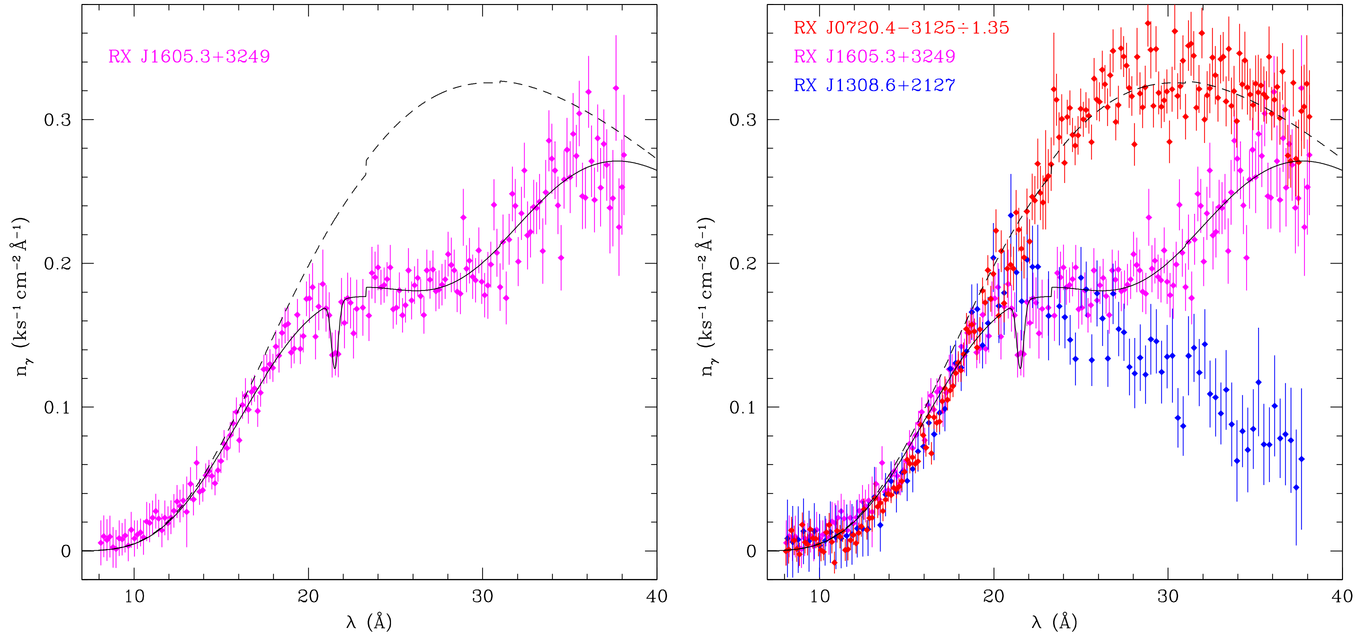

Figure 7.1 X-ray spectra of INSs. Left: *XMM*-EPIC spectrum of RX J1605.3+3249 (van Kerkwijk et al. 2004), showing the best-fit continuum model (dashed line) and the best-fit model including an broad absorption feature at 28 Å (450 eV). The narrow absorption at 570 eV may or may not be real. Right: *XMM*-EPIC spectra of RX J0720.4−3125 (divided by 1.35; top), RX J1605.3+3249 (middle), and RX J1308.6+2127 (bottom). The models are the same as those on the left. The data for RX J0720.4−3125 were taken from the period before the absorption feature became apparent (de Vries et al. 2004).

radio pulsars. The INSs have no detectable radio emission (Kaplan et al. 2002a; Johnston 2003; Kaplan et al. 2003b) so ground-based radio telescope cannot be used and X-ray satellites (where observing time is much harder to get) are required. Furthermore, the emission from the INSs is so soft that the X-ray satellite devoted to timing (the *Rossi X-ray Timing Explorer*, or *RXTE*) cannot observe them. Therefore one must use satellites like *Chandra* or *XMM*—missions not designed for timing and heavily requested for other operations.

Nonetheless, limited timing observations have been undertaken for two of the INSs. The effort to time RX J0720.4−3125 has been large. Both Kaplan et al. (2002b) and Zane et al. (2002) combined archival *Chandra* and *ROSAT* data, along with additional *Chandra* (Kaplan et al. 2002b) and *XMM* (Zane et al. 2002) data, to limit the secular spin-down to $|\dot{P}| < 3.6 \times 10^{-13}$ s s^{-1}. This was done using an incoherent analysis, comparing the periods derived from different observations but ignoring phase information. Zane et al. (2002) also attempted a coherent analysis, but this was plagued with uncertainties (both instrumental and fundamental) and was not constraining.[2]

Hambaryan et al. (2002) discovered 5.16-second pulsation in *Chandra* observations of RX J1308.6+2127, and used archival *ROSAT* data to constrain the spin-down to be $\dot{P} \approx 1.4 \times 10^{-11}$ s s^{-1}—a high value that implied a large dipole magnetic field of 3×10^{14} G. However, re-analysis (Haberl et al. 2003a) of the *Chandra* and *ROSAT* data together with newer *XMM* data make it clear that the source actually pulsates

---

[2] Cropper et al. (2004) claim to have updated both the incoherent and coherent timing analyses of RX J0720.4−3125, measuring $\dot{P} \approx 1.4 \times 10^{-13}$ s s^{-1} using the incoherent analysis. Despite objections to the applicability of the coherent analysis (we do not believe that their observations are spaced closely enough to yield reliable results; see Kaplan et al. 2002b), they did apply it, but found that a single timing solution did not fit the data. We are still examining the reliability of both of their analyses. In either case, both our and their conclusions for this object are largely unchanged over the situation in 2002.

at 10.31 s, or twice the original period. With the newer data $\dot{P}$ is no longer measured, but it is constrained to be $< 6 \times 10^{-12}$ s s^{-1}.

The current timing situation for the INSs, along with radio pulsars and magnetars, is summarized in Figure 7.2.

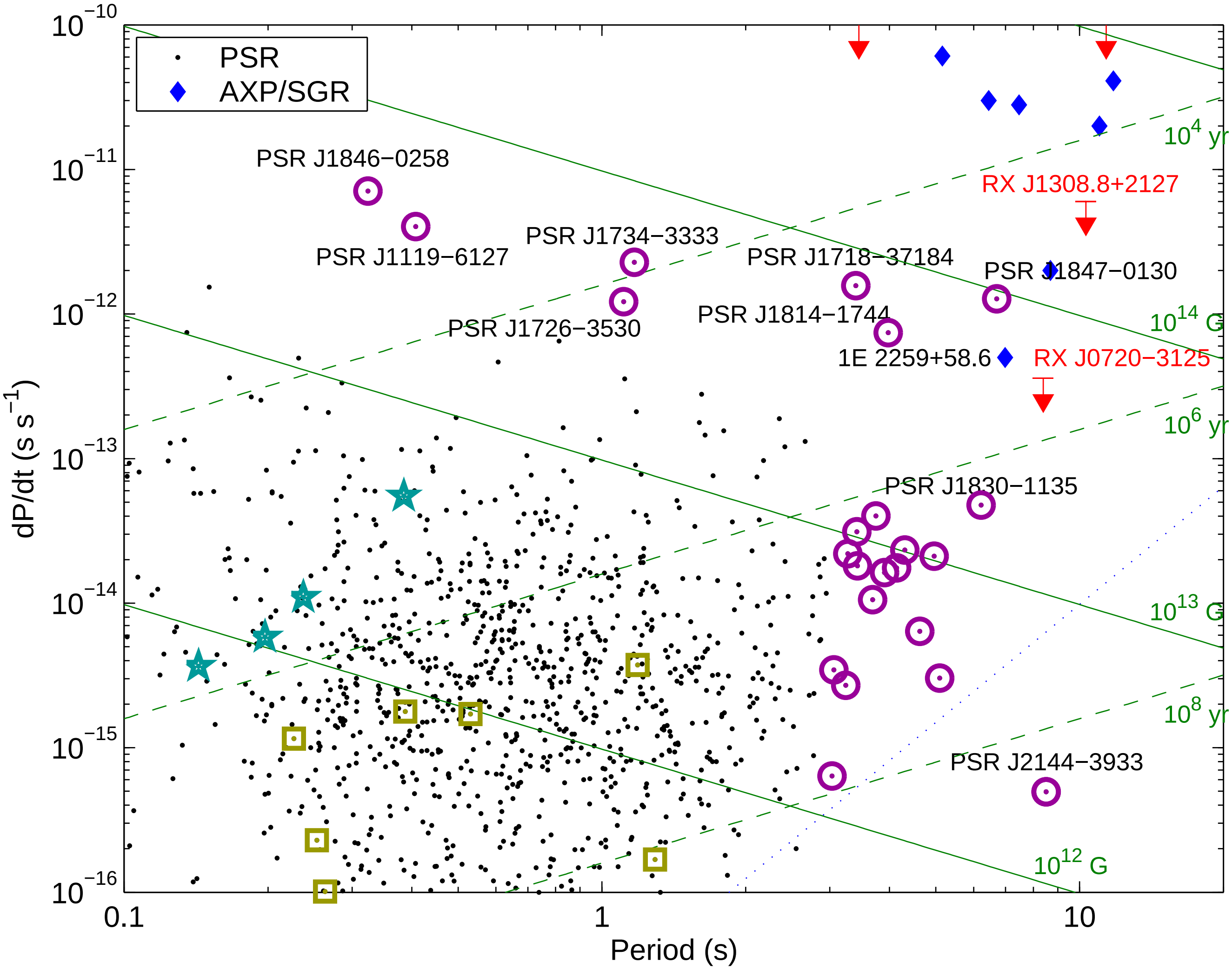

Figure 7.2 P-$\dot{P}$ diagram, showing only nonrecycled pulsars. Radio pulsars are plotted as points, magnetars (AXPs and SGRs) as diamonds. RX J1605.3+3249 and RX J1308.6+2127 are upper limits, and the periods of RX J0806.4−4123 and RX J0420.0−5022 are also indicated. The high-B/long-P pulsars from Table 7.3 are circled, the X-ray bright (PSPC > 0.05 s^{-1}) pulsars have stars, and the faint but nearby pulsars have squares. Selected sources are labeled. Also shown are a hypothetical pulsar "death line" (dotted line), lines of constant B-field strength (solid lines), and lines of constant age (dashed lines)—all estimated in the framework of the vacuum magnetic dipole model.

We have an ongoing effort to measure the spin-down of RX J0720.4−3125 through a coherent analysis using new *Chandra* data. Using two observations, each consisting of 25 ks of *Chandra* data spread into four exposures over two weeks, we should be able to measure the period to a precision of ~ 1 μs at each epoch. Phase-connection of these data should determine $\dot{P}$ to $\sim 10^{-14}$ s s^{-1}. We already have the first epoch of data, and do indeed find $\sigma_P = 1.7$ μs; the second epoch will be taken in August. Assuming the phase-connection is successful (i.e., that RX J0720.4−3125 is a stable rotator over that period), we will connect the data to a previous *Chandra* observation with the same instrumental configuration from 2001. This should determine $\dot{P}$ to better than 10^{-14} s s^{-1} and will provide a detailed assessment of the stability of its rotations (something called into doubt recently by observations of changing pulse profiles; de Vries et al. 2004) independent of instrumental issues. Then we can attempt a complete phase-connection of all of the data (*Chandra*, *XMM*, and *ROSAT*) going back to 1993, potentially determining $\dot{P}$ to 10^{-15} s s^{-1}.

7.2.3 Optical/UV Photometry & Spectroscopy

The classification of RX J1856.5−3754 (and later RX J0720.4−3125) as neutron stars was to some degree cemented by the discovery of their optical counterparts (Walter & Matthews 1997; Kulkarni & van Kerkwijk 1998; Motch & Haberl 1998). The extreme faintness (Tab. 7.1) and blueness of these sources left almost no doubt that RX J1856.5−3754 and RX J0720.4−3125 were neutron stars. The classifications of the sources identified later then followed from their similarity to the first two sources.

Since their identification, optical counterparts for two (or possibly three) more INSs have been identified (Kaplan et al. 2002a, 2003a; Haberl et al. 2004); see Figure 7.3. The characteristics of these optical sources are generally quite similar to those of the first two: they are very faint (X-ray-to-optical flux ratios in excess of 10^5) and very blue (in the case of RX J1605.3+3249, where some color information is known).

One of the most striking conclusions drawn from the optical counterparts was that the fluxes of the optical counterparts did not agree with extrapolations of the X-ray spectra, neither blackbody fits nor more sophisticated atmosphere fits (e.g., Pons et al. 2002b). The optical sources were all a factor of ~ 5 (the optical excess in Tab. 7.1) above the blackbody extrapolations (Fig. 7.4), with some variation. To account for this fact, one either needs a single atmosphere model that can reproduce all of the fluxes or an atmosphere with a temperature gradient over the surface (such as those assumed for PSR B0656+14 and PSR B1055−52; (Greiveldinger et al. 1996; Pavlov et al. 1997)).

The temperature-gradient models (Braje & Romani 2002; Kaplan et al. 2003b) are conceptually simple: there is a small, hot region (usually assumed to be the polar cap, where the magnetic field alters the conductivity and leads to a hotter surface) and a larger, cooler region (the rest of the star). The hot region gives rise to the X-rays, while the cool region emits the optical photons. This way the two regions of the spectrum can be decoupled. The cooler component is invisible in the X-ray band, and its properties (T, R) can only be constrained indirectly (we can measure TR^2 from the optical spectrum, assuming a Rayleigh-Jeans tail, and can set an upper limit on T from the fact that the peak of the cool component is not observed). This is in contrast to what is seen for radio pulsars (Koptsevich et al. 2001; Marshall & Schulz 2002; Pavlov et al. 2002), where both the hot and cold parts of the spectrum are visible in the X-ray band and the temperatures of each can be directly measured.

This model naturally leads to sinusoidal pulsations, since rotation would cause the small, hot region to move around and modulate the observed X-ray flux. However, since two of the INSs do not show pulsations (at amplitudes $> 2\%$; Ransom et al. 2002; van Kerkwijk et al. 2004) one must appeal to either favorable orientation (unlikely but possible; Braje & Romani 2002) or a more complex surface configuration to apply this model.

While simple single-temperature models do not give satisfactory fits, lately there have been two similar models proposed (Zane et al. 2003; Motch et al. 2003) that get around this fact. Motch et al. (2003) require a radial opacity gradient, with a hard, blackbody-like surface that radiates the X-rays. Above this is a thin layer of hydrogen that is optically thin at X-ray energies but not at optical. The optical photons then come from this layer, where the different opacity of hydrogen can explain their offset from the X-ray extrapolation. Turolla et al. (2004) instead have a bare, condensed heavy-element surface (typically iron), where the condensation suppresses low-energy emission relative to a blackbody and leads to the observed

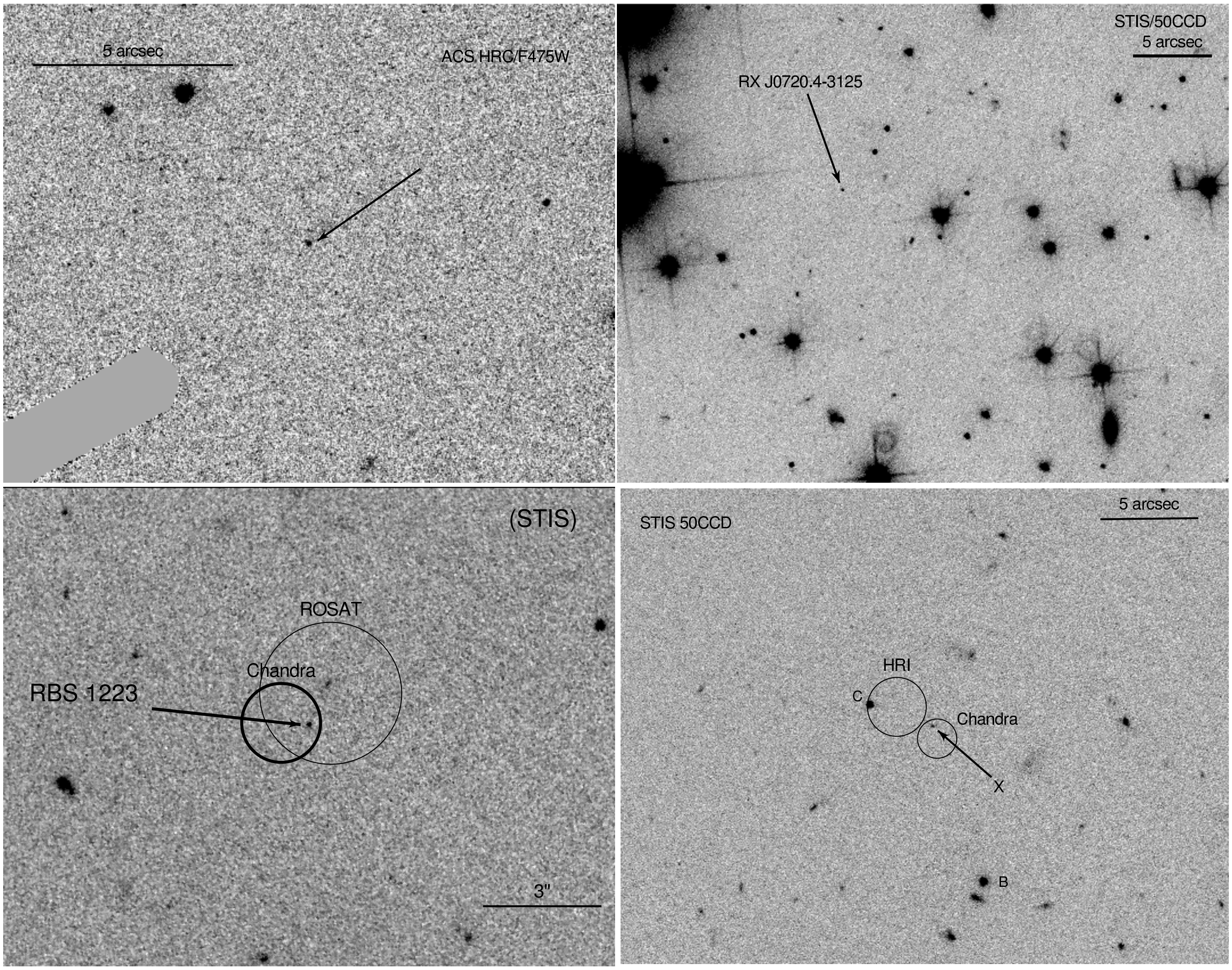

Figure 7.3 *HST* images of the optical counterparts of isolated neutron stars. Upper left: RX J1856.5−3754 (discovered by Walter & Matthews 1997 using *HST*); upper right: RX J0720.4−3125 (discovered by Kulkarni & van Kerkwijk 1998 using Keck); lower left: RX J1308.6+2127 (discovered by Kaplan et al. 2002a using *HST*); lower right: RX J1605.3+3249 (discovered by Kaplan et al. 2003a using *HST*).

spectral shape.

These models are attractive and do not lead directly to pulsations that would contradict observations, but they are not fully realistic. In particular, for the first model the amount of hydrogen must be fine-tuned so that it produces the observed optical flux and it does not yet include magnetic fields. Why all four (or five) of the seven INSs with optical counterparts would have similar optical excesses, with none having enough hydrogen to affect the X-rays, is not known. Similarly, the second model is only valid in a small region of T-B parameter space and it is not yet known how many (if any) of the INSs occupy this region.

The two sources with the first optical counterparts, RX J1856.5−3754 and RX J0720.4−3125, have also been subject to more detailed studies. van Kerkwijk & Kulkarni (2001b) took a dispersed spectrum of RX J1856.5−3754 with the VLT. They found that the optical emission was entirely consistent with a smooth power-law (modified only by interstellar absorption) whose index was that of a Rayleigh-Jeans (RJ) tail: $F_\lambda \propto \lambda^{-4}$.

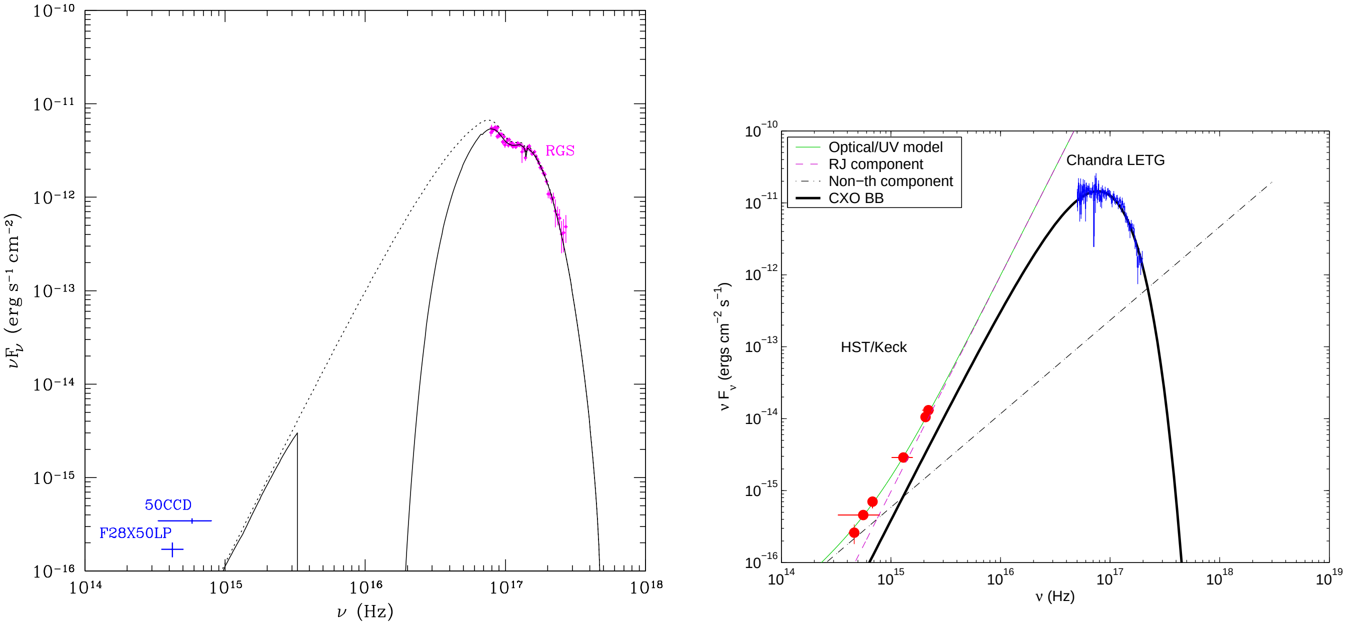

Figure 7.4 Spectral energy distribution of isolated neutron stars. Left: RX J1605.3+3249 (van Kerkwijk et al. 2004); right: RX J0720.4−3125 (Kaplan et al. 2003b). We see the optical excesses, and the possible extrapolation of the nonthermal emission of RX J0720.4−3125 into the X-ray regime.

In contrast, Kaplan et al. (2003b) found that the optical/UV emission of RX J0720.4−3125 was not consistent with a RJ tail. Using multi-band photometry they showed that the spectrum was consistent either with a single nonthermal power-law ($F_\lambda \propto \lambda^{3.40(4)}$) or with a combination of RJ and nonthermal power-laws (the nonthermal component having $F_\lambda \propto \lambda^{2.3(7)}$). This is similar to what is observed for Geminga (Martin et al. 1998) and PSR B0656+14 (Koptsevich et al. 2001) and may indicate that there is some pulsar-type activity occurring on RX J0720.4−3125.

7.2.4 Astrometry

Many of the objectives described in § 7.4 are predicated on accurate knowledge of the distances to the INSs. Perhaps the most basic way to measure distances is through geometric parallax—a technique that requires very high angular resolutions (milliarcsecond for the typical distances of the INSs). For radio pulsars, this is done with centimeter-wave interferometry using the developing technique of very-long baseline interferometry (VLBI) astrometry (Brisken et al. 2002; Chatterjee et al. 2004). For the INSs, though, since they have no radio emission (which also eliminates the timing parallaxes measured for radio pulsars; e.g., van Straten et al. 2001), this technique cannot by applied.

Optical observations, then, have the best angular resolution. The resolution of ground-based telescopes is better than (and in cases with adaptive optics or similar techniques can be much better than) that of X-ray telescopes ($\gtrsim 1''$), but is not sufficient. We are forced to rely on space-based telescopes.

The optical counterparts INSs are too faint for astrometric missions such as *Hipparcos* ($V \lesssim 12$ mag; ESA 1997), and are also beyond the range of observations with the Fine Guidance Sensor on the *Hubble Space Telescope* ($V \lesssim 17$ mag; Bradley et al. 1991; Benedict et al. 1999; Nelan et al. 2003). We are left then with data taken from instruments not designed for astrometry.

Efforts to date have concentrated on imaging instruments aboard *Hubble Space Telescope* (*HST*), primarily the Wide-Field and Planetary Camera 2 (WFPC2), although new projects using the Advanced Camera for Surveys (ACS) are under way. The first parallax measurement of a neutron star using *HST*

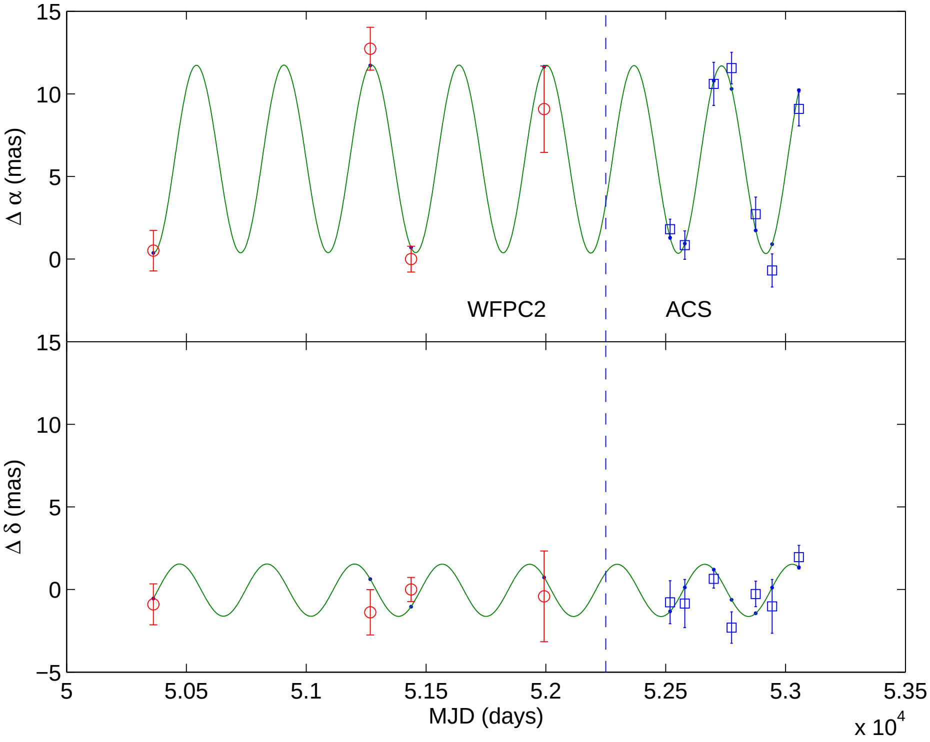

Figure 7.5 Motion of RX J1856.5−3754 with the best-fit proper motion subtracted, showing the parallax. The first four data points are from *HST*/WFPC2 (Kaplan et al. 2002c; Walter & Lattimer 2002), while the last seven are from new ACS data (Kaplan et al. 2004, in prep.). The circles/squares show the actual data, while the points are the parallactic curves at the same times as the observations. The error bars are 1-σ. The best-fit parallax (shown) is 5.7 ± 0.3 mas. Registration of the 11 epochs was done iteratively, fitting for the proper motions (but not parallaxes) of all of the stars, and gave a final $\chi^2 = 305.4/272 = 1.12$. Fitting just the parallax of RX J1856.5−3754 gave $\chi^2 = 2.3/3 = 0.8$.

was that of Geminga (Caraveo et al. 1996), followed by Vela (Caraveo et al. 2001) and RX J1856.5−3754 (Walter 2001).

The final measurement of $\pi = 16.5 \pm 2.3$ mas was puzzling, as it implied a tiny radius for RX J1856.5−3754 of ≈ 6 km (assuming a blackbody atmosphere)—far smaller than that expected with normal equations of state (Fig. 7.10). We re-analyzed the existing public *HST* data using newly available techniques (Anderson & King 1999, 2000) and found that the previous analysis had been wrong (Kaplan et al. 2002c): the parallax was instead $\pi = 7 \pm 2$ mas, and the inferred radii were substantially larger. Since then, Walter & Lattimer (2002) have re-analyzed the data (including an epoch not available for Kaplan et al. 2002c) and found $\pi = 9 \pm 1$ mas, a value consistent with Kaplan et al. (2002c).

Even more recently, we have begun a program to measure the parallax of RX J1856.5−3754 very accurately with *HST*, using 8 observations with the ACS spread over two years. We show a preliminary analysis of the data in Figure 7.5. We find now that $\pi = 5.6 \pm 0.6$ mas. This is inconsistent with the Walter & Lattimer (2002) result, but consistent with our previous result.

Along with RX J1856.5−3754 we are attempting to measure the parallax of RX J0720.4−3125 using a similar *HST*/ACS program. This is more difficult because RX J0720.4−3125 is a magnitude fainter than RX J1856.5−3754, and because we do not have the long time baseline afforded by the old WFPC2 data that can be used to subtract out the proper motion. The analysis is under way.

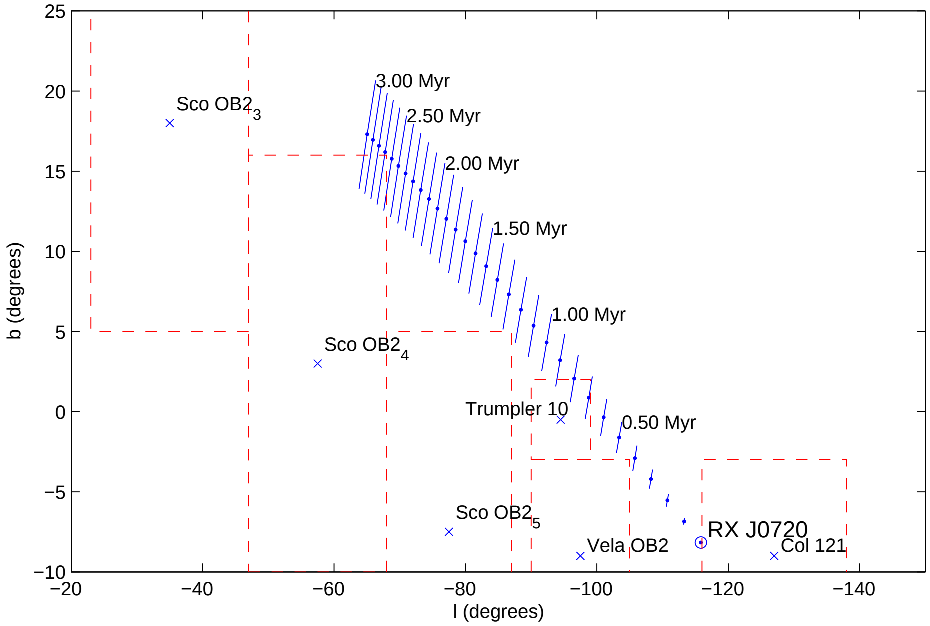

Figure 7.6 Proper motion of RX J0720.4−3125 as measured from new ACS data (Kaplan et al. 2004, in prep.), projected back in time to identify its likely origin in the Trumpler 10 OB association approximately 0.7 Myr ago.

Less important than the parallax but much easier to measure are proper motions. These have a number of uses. With estimates for distances (to turn the proper motions into velocities) they can be compared to the known distribution of velocities for radio pulsars (e.g., Arzoumanian et al. 2002) to compare the populations. They can also be used to assess accretion models (Kaplan et al. 2002c; Motch et al. 2003). Perhaps most interestingly, though, they can be used to trace the objects back to the OB star clusters or supernova remnants where they originated (e.g., Hoogerwerf et al. 2001; Walter 2001; Thorsett et al. 2003; Chatterjee et al. 2004; Vlemmings et al. 2004).

Walter (2001) did this for RX J1856.5−3754, and while the parallax from that analysis is incorrect, the proper motion is not and the association with the Upper Sco OB association (and consequent age of ≈ 0.5 Myr) is still plausible (Kaplan et al. 2002c; Walter & Lattimer 2002).

Motch et al. (2003) used ground-based data to measure a preliminary parallax for RX J0720.4−3125, and showed that it had a significant space velocity. However, their analysis was not sufficiently accurate to permit association with a birth site. We have done a preliminary analysis of the new ACS data and found that RX J0720.4−3125 likely comes from the Trumpler 10 OB association ≈ 0.7 Myr ago (Fig. 7.6).

7.2.5 Hα Nebulae

Radio pulsars have been known for years (Kulkarni & Hester 1988; Cordes et al. 1993; Bell et al. 1995) to produce bow-shock nebulae that emit primarily Hα photons (there are also radio and X-ray bow-shocks). For the pulsars, the scenario is that they move supersonically through the ISM. The bow-shock reflects the equilibrium between the ram-pressure of the pulsar's movement $\rho v_{\rm psr}^2$ and the pressure of the pulsar's relativistic wind $\dot{E}/4\pi R^2 c$, where ρ is the ambient density, $v_{\rm psr}$ is the pulsar's velocity through the medium, $\dot{E}$ is the pulsar's spin-down energy loss rate, and R is the stand-off radius (Wilkin 1996; Chatterjee & Cordes 2002). Therefore, one can relate $\dot{E}$ (known for pulsars) to ρ and $v_{\rm psr}$—constraining either the pulsar's motion or the ambient medium.

Unexpectedly, while studying the spectrum of RX J1856.5−3754, van Kerkwijk & Kulkarni (2001b) discovered extended Hα emission that was later discovered to arise from a full-fledged Hα bow-shock. This was unexpected because, while it was known that RX J1856.5−3754 was moving quickly (Walter 2001), there was no knowledge of $\dot{E}$.

Van Kerkwijk & Kulkarni (2001a) considered two models for RX J1856.5−3754: a traditional bow-shock produced by a relativistic wind or a moving ionization nebula (i.e., a moving Strömgren sphere) powered just by the known far-UV/X-ray emission of the neutron star. Quantitative consideration of the models, coupled with improved measurements of the distance and velocity of RX J1856.5−3754 (Kaplan et al. 2002c), have largely led to the dismissal of the second model. We are therefore left with the bow-shock model and the conclusion that RX J1856.5−3754 must have a substantial $\dot{E}$. Using the current best-fit value for the distance to RX J1856.5−3754, we find $\dot{E} \gtrsim 2 \times 10^{33}$ ergs s^{-1}.

We have unsuccessfully searched for Hα nebulae from other INSs (RX J0720.4−3125, RX J1308.6+2127, and RX J1605.3+3249). Because of the unconstrained velocities of these sources and the unknown variation in the ISM, our observations are not very constraining. However, we will continue to search for Hα bow-shocks because of their enormous utility.

7.3 What Are the INSs?

7.3.1 ISM Accretion

Models involving accretion from the ISM were favored for the INSs before their discovery, and even when *ROSAT* failed to discover the predicted number of sources some authors still preferred these models (e.g., Wang 1997). Now, however, they have largely been discounted. Perhaps the most constraints on this model come from observations of RX J1856.5−3754. Here the velocity inferred from its proper motion and parallax (Kaplan et al. 2002c) is high (≈ 220 km s^{-1}), which makes accretion ($\propto v^{-3}$) very improbable. Furthermore, models for the Hα nebula (van Kerkwijk & Kulkarni 2001a) lead to estimates for the ambient ISM density that essentially exclude accretion as a possibility.

Without accurate parallaxes for the other sources we cannot be as certain, but initial estimates (Motch et al. 2003; Fig. 7.6) for RX J0720.4−3125 also lead to velocities of > 100 km s^{-1} that largely rule out accretion. It is therefore highly unlikely that accretion is currently important for powering any of the INSs.[3]

This change, from predicting thousands of sources to observing zero, has been accommodated somewhat by more recent population models (Perna et al. 2003). These models include more accurate estimates for the velocity distribution of radio pulsars as well as more accurate prescriptions for accretion onto a magnetized object, and are consistent with the *ROSAT* nondetections.

7.3.2 Accretion from Fall-Back Disks

While quasi-spherical accretion from the ISM is ruled out, it is still possible that there is accretion from a fossil fall-back disk, i.e., a disk of material that fell back from the original supernova explosion and is slowly landing on the neutron star (Chatterjee et al. 2000; Alpar 2001). This model had been proposed largely to account for the soft γ-ray repeaters and anomalous X-ray pulsars (e.g., Marsden et al. 2001), but is also applicable to the INSs (Alpar 2001).

Accretion disks could contribute to the luminosities of the INSs in two ways. First, the gravitational energy of the accretion would be released, although this requires the accreted material to overcome the neutron star's centrifugal barrier and actually land on the star. Second, energy due to friction from an

---

[3] This does not mean that there is not/has not been any ISM accretion onto the INSs, just that this accretion is unlikely to affect the energetics or spin-down. Some accretion may still have occurred and altered the surface composition.

external torque can also be liberated (Alpar et al. 1984, 1985). These torques would of course produce changes to the spin rates of the INSs, on the order of

$$|\dot{\Omega}| \sim 10^{-12}\text{–}10^{-9}\ \mathrm{s}^{-2} \tag{7.2}$$

(Alpar 2001), or $|\dot{P}| = 10^{-11}\text{–}10^{-8}$ s s^{-1} for RX J0720.4$-$3125 (assuming a distance ~ 300 pc and that all of the observed luminosity comes from accretion-driven friction). We note that the timing observations of RX J0720.4$-$3125 rule out torques in this range.

If we allow that some of the luminosity comes from cooling or from accretion onto the surface, we can relax the requirements for $|\dot{\Omega}|$ into the observationally permissible range: $|\dot{\Omega}| < 3 \times 10^{-14}\ \mathrm{s}^{-2}$. This would mean that less than 1% of the observed luminosity comes from frictional heating.

If, instead, material is accreting onto the surface and producing significant X-rays, then the Alvén radius must be inside the co-rotation radius. This occurs when the rotation period is larger than the equilibrium period

$$P_{\mathrm{eq}} = 16.8\ \mathrm{s}\mu_{30}^{6/7}\dot{M}_{15}^{-3/7}m^{-5/7} \tag{7.3}$$

(Illarionov & Sunyaev 1975; Shapiro & Teukolsky 1983; Alpar 2001), where μ_{30} is the magnetic dipole moment in units of 10^{30} G cm^3, $\dot{M}_{15}$ is the mass accretion rate in units of 10^{15} g s^{-1}, and m is the mass of the neutron star in units of solar masses. For the INSs, with magnetic fields $\gtrsim 10^{13}$ G (§ 7.3.3.1), $\mu_{30} \sim 10$. Taking a characteristic period for the INSs of 10 s and assuming a mass of $1.4\,M_{\odot}$, we find $\dot{M}_{15} \sim 200$. This value is very large, and would require efficiencies of $< 10^{-6}$ (the conversion rate of gravitational energy to X-rays)—far below the conventional values of $\sim 10\%$. This is only possible if accretion occurs via an advection-dominated accretion flow (ADAF; Narayan et al. 1997). However, after transition to an ADAF, which can occur as early as 10^5 yr (Chatterjee et al. 2000), accretion becomes unimportant as most of the material is lost to winds.

We have demonstrated, then, that accretion from a disk cannot be important energetically, either because of frictional heating or direct accretion. It is still possible that there is a small disk around these sources that has no effect on the spin-down or X-ray flux. Such a disk would be primarily be visible through optical and infrared emission from the outer parts. To model this we use the work of Perna et al. (2000) and Perna & Hernquist (2000)—also see Kaplan et al. (2001b). The model includes the radiation of energy lost to viscous dissipation (Shakura & Sunyaev 1973) as well as re-radiation of X-rays from the central source (Vrtilek et al. 1990). This disk would extend in to the Alvén radius

$$R_{\mathrm{A}} = (\sqrt{2GM}\dot{M}B^{-2}R^{-6})^{-2/7} \approx 9.9 \times 10^8\ \mathrm{cm}\,\mu_{30}^{4/7}\dot{M}_{15}^{-2/7}m^{-1/7}, \tag{7.4}$$

where R and M are the stellar radius and mass, respectively, but could not reach the stellar surface. For an outer radius, we assume 10^{14} cm (Perna & Hernquist 2000), although the models are not very sensitive to this. Assuming average values for the inclination, we find that the current optical data for RX J0720.4$-$3125 (Kaplan et al. 2003b) exclude disks with $\dot{M}_{15} \gtrsim 0.01$. At this point, the optical emission is dominated by the viscous heating—the contribution of irradiation is small, which makes sense given the small X-ray luminosities of the INSs (Perna et al. 2000). If this accretion has occurred for the life of the source, then the total mass accreted is $< 10^{-7}M_{\odot}$ assuming a constant accretion rate—a negligible amount. Thus the possible values for $\dot{M}$ are so small as to be largely insignificant. The limit on $\dot{M}$ could be relaxed slightly if the magnetic field were higher (we assumed 3×10^{13} G), since this would increase R_{A} and the inner radius of the disk. For example, at $B = 8 \times 10^{13}$ G the limit becomes $\dot{M}_{15} \lesssim 0.03$, but this is at the extreme range of the probable values for the INSs and the conclusions regarding the importance of accretion remain the same.

Table 7.2. Pulsar Parameters Resulting from Different Models

Model	$\log_{10} B_{\rm dip}$ (G)	$\log_{10} \dot{P}$ (s s^{-1})	$\log_{10} \dot{E}$ (ergs s^{-1})
Magnetar	> 14	< 12	> 32
HBPSR .	13–14	12–14	30–32
Pulsar…	12–13	14–16	28–30

7.3.3 Pulsar Models & Demographics

The remaining models generally involve magnetized neutron stars. The main variation between them is the strength of the magnetic field: it is highest for the magnetar model, in the middle for the HBPSR, and lowest for the normal pulsar. Assuming the normal relation between B, P, and $\dot{P}$, different values of B then map directly to different values of $\dot{P}$ (and hence $\dot{E}$). See Table 7.2 for a summary of these models.

We first discuss what magnetic fields the INSs are likely to possess. Following that we will discuss more general issues of the population.

7.3.3.1 Magnetic Fields

To measure the magnetic fields of the INSs there are a number of different lines of evidence. Perhaps the most direct measurement would be spin-down, but this has not been conclusively measured for any source. For RX J0720.4−3125, which has the best limit, all that we can say is that $\dot{P} < 3.6 \times 10^{-13}$ ergs s^{-1}, which then limits the current dipole field to be $< 6 \times 10^{13}$ G.

We can get a constraint on the dipolar field of RX J1856.5−3754 if we accept the Hα bow-shock model and assume that age is $\approx 10^6$ yr. This gives $B_{\rm dip} \lesssim 1 \times 10^{13}$ G (van Kerkwijk & Kulkarni 2001a).

The most applicable but least reliable constraints come from interpretation of the absorption features in the X-ray spectra. Neutron star atmospheres are widely expected to be composed primarily of hydrogen (although this is by no means clear observationally; § 7.4.2.1), both due to accretion from the ISM and gravitational settling. At the temperatures of the INSs ($\sim 10^6$ K), hydrogen would be completely ionized and the spectrum would be smooth except for possible absorption due to the electron and proton cyclotron resonances.

However, in a hydrogen atmosphere in a very strong magnetic field, there could be other spectral features. This is because in a strong field, hydrogen atoms are squeezed into cylindrical shapes (e.g., Lai 2001), which leads to much increased binding energies (e.g., 0.541 keV for $B = 10^{14}$ G). Thus, in strong fields, even at temperatures of 10^6 K some neutral hydrogen will be present. This will lead to additional sources of energy-dependent opacity. Even molecular hydrogen may exist, as it becomes more strongly bound too (e.g., 0.311 keV at 10^{14} G).

In Fig. 7.7, we show, as a function of magnetic field strength, the electron and proton cyclotron energies, the atomic and molecular hydrogen binding energies, and the transitions energies from the ground state of atomic hydrogen to several excited states. The excited states can be of two kinds. The first are so-called "weakly-bound" states, which have wave functions with nodes along the magnetic field lines. As their name implies, these states are only loosely bound, and the energies relative to the ground state (short-dashed curves) are similar to the binding energy. The second type of excited states are called "tightly-bound"; these have no nodes along the field lines. For each of these, there is a critical field strength below which it

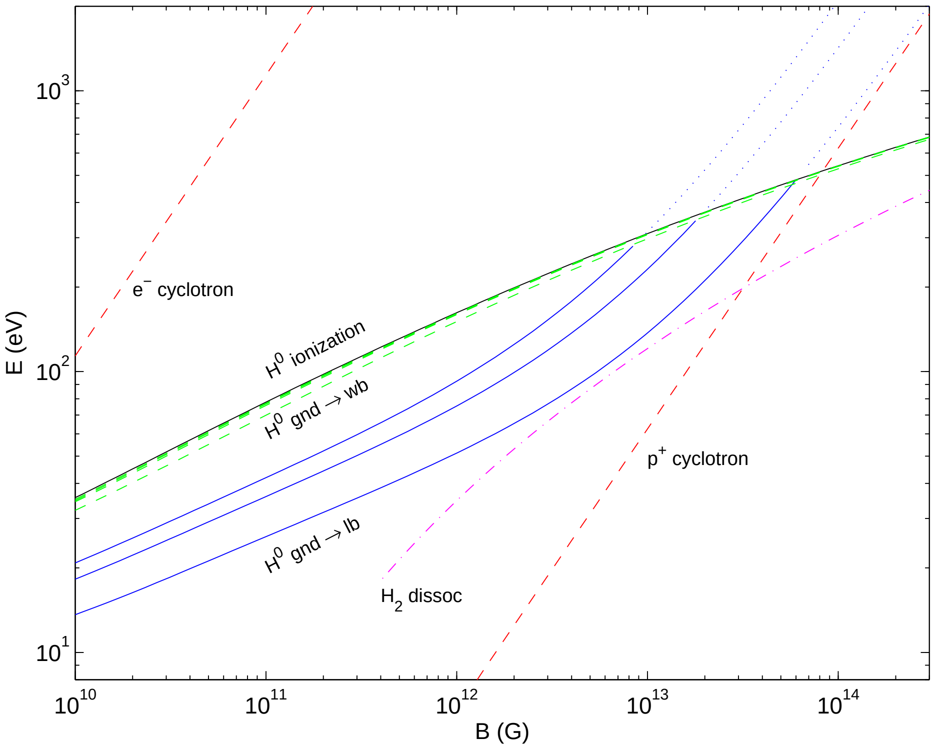

Figure 7.7 Rest-frame transition energies for hydrogen atmospheres, as a function of magnetic field strength. Shown are the electron and proton cyclotron lines, the atomic hydrogen binding energy, line transitions from the ground state to weakly-bound (wb) and tightly-bound (tb) states, and the dissociation energy of the H_2 molecule (Potekhin 1998; Lai 2001; Ho et al. 2003). The auto-ionizing (energies above the ionization energy) portion of the tightly-bound transitions are shown with the dotted extensions. For fields above $\sim 10^{14}$ G, features may be washed out due to the effects of vacuum resonance mode conversion (Lai & Ho 2003).

is bound (leading to transition energies less than the binding energy), and above which it is auto-ionizing (transition energies above the binding energy). In general, from model calculations (e.g., Zavlin & Pavlov 2002; Ho et al. 2003), it appears that it is the transitions to tightly-bound states that lead to the strongest absorption features. Transitions to not-too-strongly auto-ionizing states are likely still visible.

From Fig. 7.7 one sees that to have absorption features in the X-ray wavelength range, the magnetic field should be strong, above 10^{13} G. The range extends past the critical field $B_{\rm QED}$ ($B_{\rm QED} \equiv m_e^2 c^3/\hbar e = 4.4 \times 10^{13}$ G is the field strength at which the energy of the first Landau level exceeds the rest mass of the electron), at which nonlinear QED effects become important.

We can see, then, that there are a number of possible interpretations for the absorption features in the INS spectra (§ 7.2.1). If one could make a firm identification of the processes behind these features (i.e., which transition), one would then know the magnetic field strength. However, we do not know conclusively what the origin of the features is. Some authors (e.g., Haberl et al. 2004) believe them to be simply proton cyclotron lines, with the width coming from the fact that we see many lines of sight with slightly different magnetic field lines. Other authors (e.g., van Kerkwijk et al. 2004) prefer a model where the absorption comes from some transition(s) of neutral hydrogen[4] (Fig. 7.7).

---

[4] It is also possible that the absorption comes from other species, such as helium. While gravitational settling would lead to hydrogen atmospheres, effects such as diffusive nuclear burning (Chang & Bildsten 2003) could alter that. We do not

Even without this uncertainty, there are several other caveats to using the features to deduce magnetic field strengths.

First, the absorption is presumably taking place on the surface of the neutron star, and we therefore apply a correction of $(1+z)$ to the observed energy, where $z \equiv 2GM/Rc^2$ is the gravitational redshift. We assume the standard value $z \approx 0.3$ (cf. Cottam et al. 2002), and values of z for real equations of state do not vary too much from this value, but if the absorption were taking place higher in the magnetosphere then our correction would be wrong.

Second, we do not know to which multipolar component the observed magnetic field corresponds. The estimates above (spin-down, Hα) relate to the dipolar field—specifically the dipole field at the light-cylinder—but the absorption could come from higher-order moments on the neutron star surface.

Regardless of these details, the energies inferred from the absorption features imply magnetic fields of 10^{13}–10^{14} G (Tab. 7.1; also see Ho & Lai 2004). These magnetic fields agree roughly with the fields implied by dipole spin-down to periods of ≈ 10 s in $\approx 10^6$ yr, assuming that the initial period is much less than the current period.

One possible problem with this scenario is the recently observed variability in both the spectrum and pulse shape of RX J0720.4−3125 (de Vries et al. 2004). There are a number of models for these changes, none of them entirely satisfactory. Presumably the dipole field would not change significantly over the month-to-year timescale of the observations, so one could not appeal to changes in the field itself to lead to the variability. It is possible that there was some change in the global rotation of RX J0720.4−3125 (i.e., a glitch) that lead to both the variability and to some of the fitting difficulties of Cropper et al. (2004), but this would be more sudden than the observed changes. Free precession (Stairs et al. 2000) could perhaps account for the observations. This precession would be more visible in RX J0720.4−3125 than for radio pulsars (where it has only been observed in one of the >1000 pulsars) because the emission that we see comes from the surface of the star rather than far out in the magnetosphere, so small changes in the axes would be more visible. If this is the case then future observations should see a return to the former spectrum/pulse shape followed by roughly periodic variations. Finally, it could be local changes in the surface magnetic field configuration (perhaps similar to but more gradual than the field evolution seen for soft γ-ray repeaters; Woods et al. e.g., 2001) that drive the observed variability. These would naturally explain the changes in both the pulse shape and spectrum, as regions of different magnetic field strength pass over the magnetic poles from which we observe the pulses. The problem with this scenario is that it would prompt us to doubt the association of the field strengths inferred from the absorption features with the dipolar fields.

7.3.3.2 Magnetars

One of the original hypotheses for the INSs is that they are old magnetars. Magnetars are neutron stars with magnetic fields in excess of 10^{14} G (or even 10^{15} G) (Thompson & Duncan 1995). The evidence for this class comes from studies of soft γ-ray repeaters (SGRs; Hurley 2000), and the anomalous X-ray pulsars (AXPs; Mereghetti 2000). The intense bursts from the SGRs and the steady X-ray emission from AXPs are best accounted for by the magnetar model, in which the ultimate source of power is magnetism and not rotation or accretion.

The old magnetar theory was an elegant idea that would allow the INSs to be somewhat older than they are now (and thus requiring fewer of them in the Galaxy) by adding magnetic field decay to their sources of energy. Unfortunately, this idea has largely been discounted for RX J0720.4−3125 (Kaplan et al. 2002b; Zane et al. 2002). The reasoning for this is as follows.

---

consider other species in detail as the number of possible species and transitions is too high, especially since we have only one absorption feature per source (cf., Hailey & Mori 2002).

Magnetars generate energy through magnetic field decay. Using the cooling predictions of Heyl & Kulkarni (1998) that include decay via the irrotational mode, the observed luminosity of RX J0720.4−3125 implies an age of $\approx 10^6$ yr. At this age, the magnetic field of an object starting with a magnetar-strength field ($\sim 10^{15}$ G, such that it is important energetically) would be $\approx 2\times10^{14}$ G, which is well above the limit to the dipole field that we infer from timing observations. Models that are consistent with both the cooling luminosity and our limit on the magnetic field are those with initial $B < 10^{14}$ G, which are not magnetars. Therefore, despite its proximity to the SGRs and AXPs in Figure 7.2, it is not related evolutionarily. The other INSs do not have the data for such analyses, but their overwhelming similarity to RX J0720.4−3125 likely makes it unnecessary.

Having rejected accretion and magnetic fields as the dominant energy sources for the INS, we are left with traditional pulsars. In Table 7.3 we list 35 rotation-powered pulsars, each of which shares one or more characteristics of the INSs. We have identified these defining characteristics of the INSs as

1. PSPC > 0.05 ct s^{-1}
2. $d < 500$ pc
3. $P > 3$ s
4. $B > 3 \times 10^{13}$ G
5. $\tau < 10^6$ yr

Some of these criteria have exceptions—only four of the INSs are likely at $d < 500$ pc, three of the INSs do not have known periods, and magnetic field estimates are not uniformly available—but these are still largely true. We have identified the pulsars from Table 7.3 in Figure 7.2, and we also outline the different overlapping populations in Figure 7.8. Note that not all of these characteristics (for the pulsars) are entirely independent, since both B and τ are functions of P and $\dot{P}$, and of course X-ray flux should go as d^{-2} for a constant luminosity. There is a further degeneracy, since the X-ray luminosity is roughly proportional to $\dot{E}$ (Becker & Trümper 1997; Possenti et al. 2002) which is again a function of P and $\dot{P}$. Regardless, one can see right away that the INSs roughly double the number of X-ray bright neutron stars within 500 pc, and therefore constitute a significant fraction of the total population.

7.3.3.3 Rotation-Powered Pulsars

[We note that τ is only an accurate measure of pulsar age if: the initial period is much less than the current period, the braking index is 3, and no torque decay has occurred. None of these issues is settled observationally (Cordes & Chernoff 1998; Johnston & Galloway 1999; Kramer et al. 2003). However, the initial period problem should not affect sources older than a few thousand years, and most models that require some form of torque decay observationally (e.g., Phinney & Blandford 1981; Narayan 1987; Cordes & Chernoff 1998; Tauris & Kjær 2003) or theoretically (e.g., Ruderman et al. 1998; Tauris & Konar 2001) do so on time-scales $\gtrsim 10^6$ yr, so that τ should be reasonably accurate for sources between 10^4 and 10^6 yr like those considered here.]

There are no known radio pulsars that share all of the characteristics of the INSs. Some sources are close: Geminga and PSR B0656+14 have similar ages, distances, and X-ray fluxes, but their magnetic fields appear to be smaller. At the same time, their spin-down luminosities are higher ($\dot{E} < 2\times10^{32}$ ergs s^{-1} for RX J1308.6+2127, and $\dot{E} < 2\times10^{31}$ ergs s^{-1} for RX J0720.4−3125). We note that the limit on spin-down for RX J0720.4−3125 is somewhat consistent with the interpretation of the nonthermal optical emission as being due to $\dot{E}$ (like PSR B0656+14 and other pulsars), but this is by no means certain.

If the INSs had magnetic field strengths similar to typical radio pulsars, then one would have to ask why they have such long periods? It may be that the birth periods are longer than typically assumed

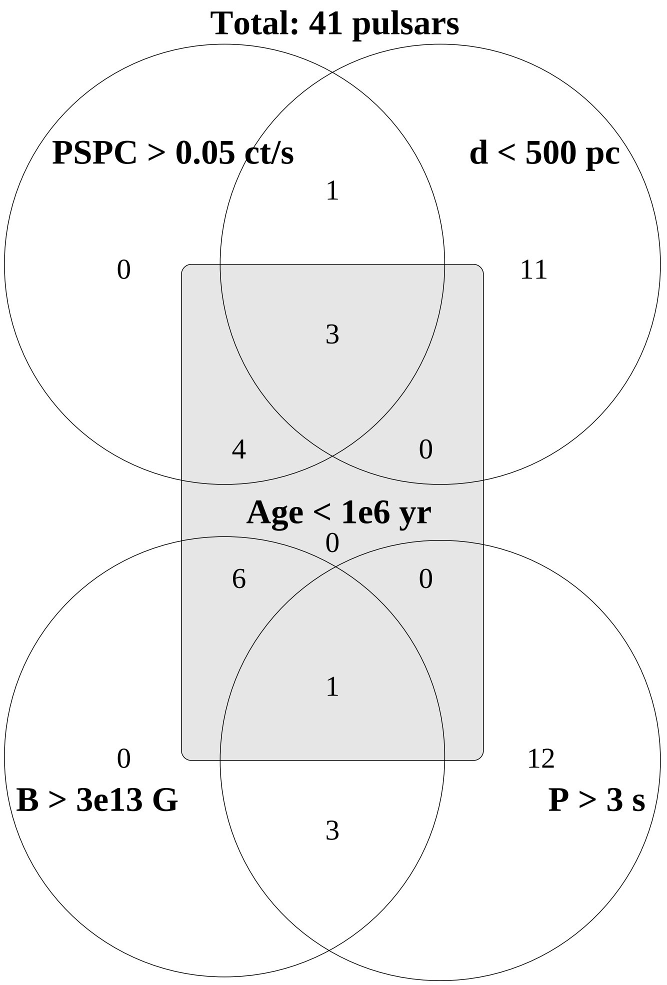

Figure 7.8 Venn diagram illustrating the characteristics of the pulsars in Table 7.3. The pulsars are separated by the following characteristics: PSPC > 0.05 s^{-1}, $d < 500$ pc, $\tau < 10^6$ yr, $B > 10^{13.5}$ G, and $P > 3$ s. The INSs, of course, would be in all the categories (except for the distance criterion, which RX J1308.6+2127 and possibly RX J0806.4−4123 and RX J2143.0+0654 would fail).

(10 ms), but while there is mounting evidence for birth periods of tens or even a hundred milliseconds (e.g., Kramer et al. 2003) there is no evidence[5] for initial periods of many seconds that would be required for the INSs.

Considering other fundamental properties such as P and B, the greatest similarity is to the radio pulsars with high magnetic fields, the HBPSRs. These sources have only been discovered recently and their population is probably not complete. However, the distribution of sources with respect to B_{dip} (Fig. 7.2) seems to lead to a continuous distribution leading to RX J0720.4−3125 (especially if one believes Cropper et al. 2004) and RX J1308.6+2127. The HBPSRs are younger than the INSs, but are much more distant and have higher values of $\dot{E}$/X-ray luminosity (for the two sources with detections). This last fact could possibly be explained just through the usual models for pulsar evolution: assuming a constant magnetic field, then $\dot{E}$ evolves as $B_{\mathrm{dip}}^{-2}t^{-2}$, so the difference of a factor of roughly 10^2 in age would correspond to 10^4 in $\dot{E}$. This would then give values consistent with the limits for the INSs. At the same time, as $\dot{E}$ dropped

---

[5] There were reports that indicated that the initial period for 1E 1207.4−5209 in the supernova remnant PKS 1209−51/52 had an initial period of 0.4 s (Pavlov et al. 2002), but this has since been refuted (Zavlin et al. 2004).

the dominant source of X-ray emission became the residual thermal emission that we see from the INSs instead of the power-law emission that we see from the HBPSRs (and from other active pulsars).

We therefore believe that the INSs represent a population of evolved HBPSRs. The HBPSRs are an emerging population so their total numbers are not known. Previous analyses of pulsar populations have usually not required pulsars beyond magnetic fields of 10^{13} G or so (e.g., Narayan 1987; Narayan & Ostriker 1990; Arzoumanian et al. 2002), but it now seems apparent that the true distribution extends further in significant numbers (a conclusion also becoming apparent just from recent pulsar surveys; Vranesevic et al. 2003).

There are no detections of radio emission (pulsed or continuous) for the INSs (Kaplan et al. 2002a; Johnston 2003; Kaplan et al. 2003b). The flux limits are reasonably low, and coupled with the small distances to the INSs the luminosity limits are orders of magnitude below the luminosities of the faintest known radio pulsars (such as PSR J0205+6449 in 3C 58; Camilo et al. 2002d). If the INSs are evolved HBPSRs then one might wonder why we see no radio emission from them (or from any other nearby, high-B source).

There are likely two reasons for this, one observational and one theoretical. Observationally the long-period pulsars/HBPSRs have very narrow radio beams (e.g., 3% for PSR J1847−0130 and 0.6% for PSR J2144−3944; McLaughlin et al. 2003; Young et al. 1999; see also Rankin 1993; Tauris & Manchester 1998) and therefore it would be easy for the beams from the nearby sources to miss the Earth; this has led to large uncertainties in the predicted number of long-period sources (e.g., Narayan 1987). Theoretically, the rapid evolution of the HBPSRs across the $P-\dot{P}$ plane (in the rotating-dipole model they move across the $P-\dot{P}$ plane in a time $\propto B_{\rm dip}^{-2}$) may drive them across the "death line" and terminate radio activity.[6]

The number of detected INSs, compared to the number of young pulsars in the same volume (observed radio pulsars may only make up 10% of the Galactic neutron star population of a given age; Lorimer 2003), implies a very large total number of similar sources in the Galaxy. From Figure 7.8 we see that there are three young pulsars and roughly four INSs within 500 pc. One of the pulsars is Geminga, which also does not have radio emission (presumably due to beaming; e.g., Romani & Yadigaroglu 1995). So only two of seven young neutron stars are visible as radio pulsars. This is perhaps not that surprising, giving the known beaming of pulsars, but what is surprising is the implied distribution of magnetic fields. It must be roughly flat from 10^{12} to 10^{14} G. This is a significant departure from previous models that only treated radio pulsars. However, more recent models (using more recently discovered pulsars) have found that $> 50\%$ of the radio pulsars may have $B > 10^{12.5}$ G (Vranesevic et al. 2003), and this is likely underestimated due to a simplified beaming model. The full distribution of magnetic fields for *all* sources, not just radio pulsars, may be even broader.

7.4 Isolated Neutron Stars: Laboratories for Extreme Physics

Now we will step back from the discussion of populations to consider the fundamental physics upon which the INSs impact. Independent of the puzzle of what the INSs are and of their place in neutron star demography, the INSs offer unique laboratories for the exploration of physics in extreme ranges, beyond that achievable on the Earth.

---

[6] The death line in Figure 7.2 is based on a simple model. It may be that the actual death line (if one truly exists) instead has a steeper slope that would separate the HBPSRs from the INSs. We note that the magnetars also do not have radio emission, but they have very different characteristics (and presumably evolutionary histories) than both the INSs and HBPSRs.

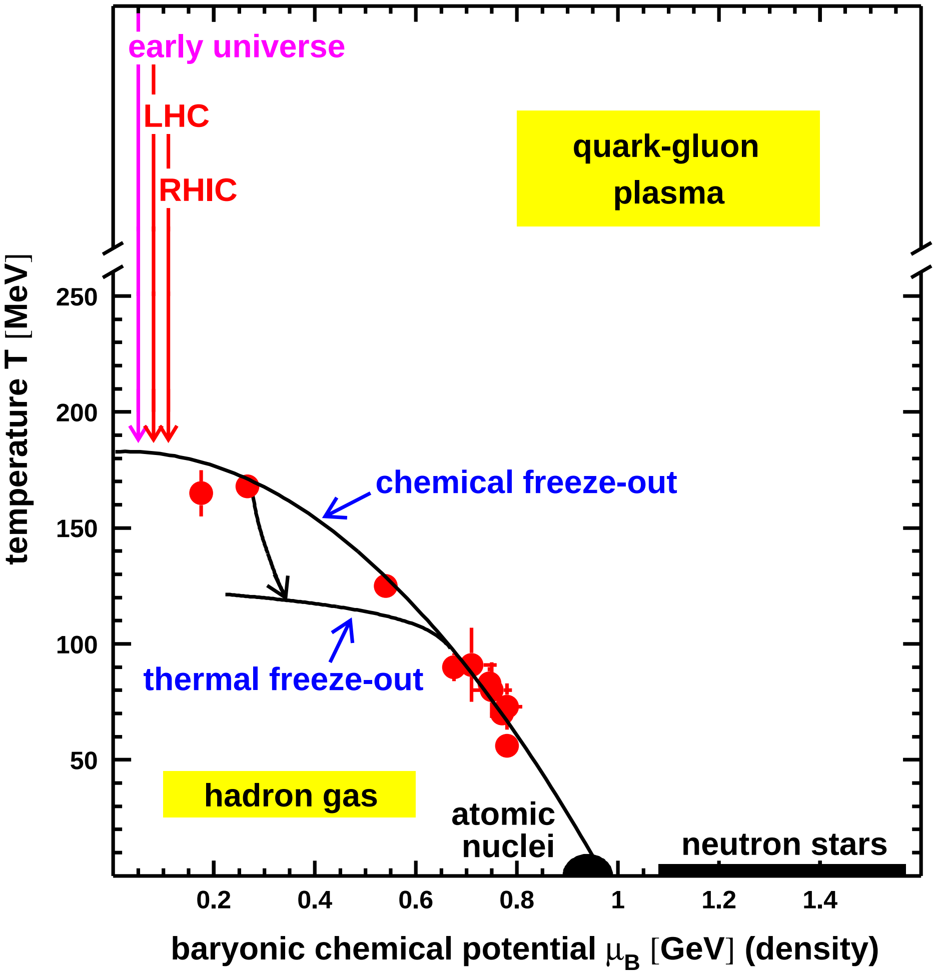

Figure 7.9 Conjectured QCD phase diagram, adapted from Rho (2000). This shows regions of temperature T and chemical potential μ_B (a proxy for density) where different states of matter dominate. Circles indicate data points, and the freeze-out lines show the transition between hadron gas and quark-gluon plasma. Atomic nuclei make the low-T, moderate-μ_B regime accessible and understood. The high-T, low-μ_B regime is where particle physics experiments (LHC, RHIC) and precision cosmology are converging. The low-T, high-μ_B regime only manifests as neutron stars, so that to constrain this area "there is need to resort to astrophysical observations. Neutron stars are the only laboratory available for this purpose…" (Rho 2000).

7.4.1 Neutron Stars as Probes of QCD

Over the last decade, astronomers and physicists have come to appreciate the importance of neutron stars as natural laboratories for quantum chromodynamics (QCD; Rho 2000). Essentially, the frontiers of QCD lie at high temperatures and at high densities, where the hadron to quark-gluon phase transition occurs (Figure 7.9). At high temperatures, accelerator experiments have led to excellent progress. In contrast, at high densities progress has been stymied both on the experimental and theoretical fronts: ion-ion collisions probe only mildly super-nuclear densities and we do not yet know how to handle many-body effects well enough.

Progress seems possible only using accurate measurements of neutron-star parameters, such as mass

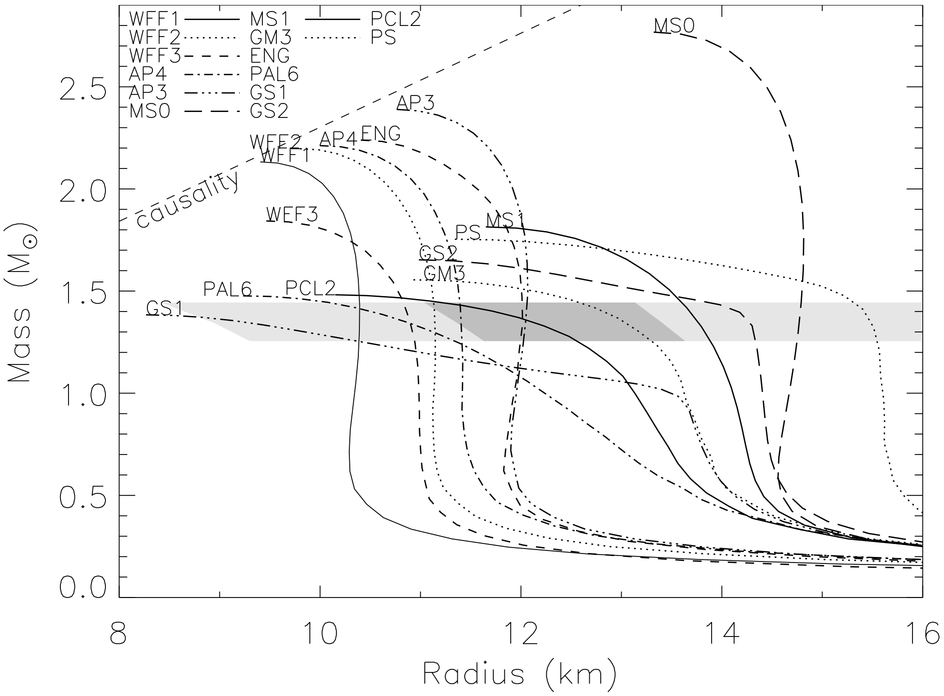

Figure 7.10 Neutron-star mass-radius relations for different equations of state (EOS). We have analyzed archival *HST* data and determined a parallax to RX J1856.5−3754 of 8 ± 2 mas and infer $R_\infty = 15^{+5}_{-3}$ km. The corresponding constraints on the radius $R_{\rm ns}$ are indicated by the lightly shaded area (for masses in the 95% confidence range of 1.26–1.45 $M_\odot$ inferred from radio pulsars; see Thorsett & Chakrabarty 1999). With the ongoing ACS measurements, we will be able to measure the parallax to ~ 0.5 mas. This would lead to a constraint on the radius like that shown by the more darkly shaded area, and would constitute the strongest constrain on EOS to date. Adapted from Lattimer & Prakash (2000).

and radius, which depend strongly on the equation of state (EOS; see Fig. 7.10). So far, however, susceptibility to systematic errors and/or modeling uncertainties have befuddled most such attempts (e.g., radius determinations from X-ray bursts, Lewin et al. 1993; innermost stable orbit from kHz QPOs, van der Klis 2000). The only accurate measurements are: the fastest spin period, 1.5 ms, which excludes the stiffest EOS (PSR B1937+214; Backer et al. 1982); and precise masses for binary radio pulsars, which until recently were all close to 1.4 $M_\odot$ and thus, as can be seen from Fig. 7.10, are not very restrictive (Thorsett & Chakrabarty 1999).

In the mass range of 1.26–1.45 $M_\odot$ in which neutron stars are typically found (95% confidence; Thorsett & Chakrabarty 1999), the radii depend strongly on the EOS, but, for most EOS, only weakly on mass (Fig. 7.10). Lattimer & Prakash (2000) have explored this issue thoroughly and show that a radius measurement accurate to 1 km would suffice for a useful constraint on the EOS.

7.4.2 Constraints on Cooling and Equation of State

Along with radius measurements that constrain the equation of state (§ 7.4.1 and Fig. 7.10), neutron star cooling is an extremely powerful probe of neutron star physics and interiors (e.g., Tsuruta et al. 2002; Yakovlev & Haensel 2003; Page et al. 2004). In some ways it is less sensitive that EOS studies to the complicated details of the neutron star atmospheres, since one does not necessarily need to disentangle the effective from the true temperatures.[7]

7.4.2.1 Surface Compositions

Knowledge of the surface composition is vital to interpreting the measured temperature (essentially $T_{\rm eff}$) for use in cooling or EOS measurements. The typical choices for the INSs are hydrogen, hydrogen/helium, mid-Z elements (O, Si, etc.), heavy elements (Fe, etc.), and metallic (i.e., blackbody). These all have different motivations: H and H/He should come from gravitational settling and ISM accretion, O/Si might come from supernova fall-back, Fe should come from the mass cut in the progenitor, and metallic surfaces could come from strange surface conditions (combinations of T and B).

The current evidence for the INSs is ambiguous. With only the smooth, Planckian spectra there were no good fits from proper model atmospheres—only the metallic models of Zane et al. (2003) and Motch et al. (2003) worked but as we discussed before they are simplifications and must be fine tuned.[8] More recently, the discovery of the broad absorption features has spurred more debate, with one side (Ho & Lai 2003) favoring magnetic hydrogen atmospheres where complex QED effects alter the observed spectrum and the other side (Haberl et al. 2004) preferring the metallic models. If one could identify more than one feature for a single source (e.g., Sanwal et al. 2002) or get some other direct constraint on the magnetic field one could resolve much of this debate, but this has not yet happened.

We will now discuss three observational areas that have the potential to give useful constraints on cooling and EOS studies. We will see, though, that the current uncertainties (both observational and theoretical) prevent us from making our own conclusions.

7.4.2.2 Accurate Distances

The most fundamental observational contribution to using neutron stars to constrain physics comes from accurate distances, such as those described in § 7.2.4. Distances play two basic but major roles: they relate flux and luminosity, and they relate the observed (angular) size to the actual (linear) size. RX J1856.5−3754 will soon have a parallax accurate to 5%, and RX J0720.4−3125 may have a parallax accurate to 20%. Beyond these the prospect for direct INS distances is dim. However, possession of two parallaxes, rather than just one for RX J1856.5−3754, will be a major improvement that may allow us to more rigorously evaluate models and determine if RX J1856.5−3754 is typical or if it is somehow pathological. This is especially true since RX J0720.4−3125 has a known period and will soon have a reliable spin-down, allowing incorporation of the magnetic field and viewing geometry (§ 7.2.3) into the models.

7.4.2.3 Accurate Ages

Next to distances (necessary to determine luminosities), which can to some degree be scaled from observations of other sources (Tab. 7.1; Kaplan et al. 2002c), accurate ages are perhaps the most difficult parameters one must establish before using sources to constrain models of neutron star cooling. For radio pulsars one can (to some degree) use their spin-down ages τ, but this involves many assumptions. Perhaps more accurate ages can be determined from observations of host supernova remnants (Kaplan et al. 2004) for those sources young and lucky enough to reside in remnants. But remnants only persist until 10^4–10^5 yr, while neutron stars can remain visible through cooling radiation until 10^6 yr.

---

[7] For studying cooling, one essentially plots temperature or luminosity versus age. While many authors prefer to plot temperature (perhaps because of the T^4 dependence of the luminosity and its consequent uncertainty), we feel that the temperature is too dependent on the assumptions about surface composition and radius, and that luminosities are more useful to compare to observations (Kaplan et al. 2004).

[8] In addition they do not account for the nonthermal optical emission of RX J0720.4−3125.

To estimate ages for sources with neither spin-down ages nor supernova remnants (i.e., the INSs), perhaps the most promising method is the use of proper motions to trace the sources back to their birth locations. This can be done both statistically (Brisken et al. 2003a) or for individual sources (Hoogerwerf et al. 2001), as discussed in Section 7.2.4.

Tracing back individual sources is by no means certain. A first estimate of the age can be determined just by considering scale-height arguments (Cordes & Chernoff 1998): pulsars presumably arise from OB stars that have a scale height of ≈ 50 pc (Reed 2000). Therefore, for sources that are young enough to not have been significantly perturbed by the Galactic potential ($\lesssim 10^7$ yr), one can estimate the age as just $|b/\mu_b|$, where b is the Galactic latitude and μ_b the proper motion along that axis. That assumes that the neutron stars are moving away from the plane of the Galaxy, but this is generally the case (Brisken et al. 2003a).

A more accurate (but not necessarily more reliable) age can be determined by tracing the motion of the neutron star back to a specific OB association. This then can also involve motion in the radial direction (not just projected onto the sky), as the distances of OB associations are often known (de Zeeuw et al. 1999). One must therefore match the distance estimate for the neutron star with that of the OB association, assuming a radial velocity.

After one finds an OB association, one must then ask if the association is probable, given the local density of associations. This can involve some *a priori* estimate of the age of the neutron star, since associations that would require wildly large or small ages can be excluded. So one essentially searches an annulus on the sky for OB associations at the right distance, and estimates the chance of a random encounter. For RX J0720.4−3125 (Fig. 7.6), we estimate the chance of a random association at $\approx 10\%$, so the association with Trumpler 10 is probable but not certain.

Only for RX J1856.5−3754 have the observations sufficiently constrained its age and distance to make it useful for cooling. RX J0720.4−3125 has a probable age, but without a distance it has limited utility. While we can infer a distance based on RX J1856.5−3754 (Tab. 7.1), this involves assumptions about the optical emission that are untested (for instance, we do not know the origin of the nonthermal power-law for RX J0720.4−3125 or what its effects on distance estimates are). With more knowledge about the optical emission of other sources (and possibly a parallax for RX J0720.4−3125), the distances of the other sources can estimated with more confidence.

7.4.2.4 Optical Observations

Optical photometry is potentially very powerful for constraining neutron star luminosities and radii. While X-ray observations probe the peak of the spectral energy distribution, this is not entirely advantageous. The X-ray emission from the INSs peaks near the bottom end of the *Chandra* and *XMM* bands, so one is not always confident that one measures the peak itself. Additionally, calibration at the soft end, uncertainties in the interstellar absorption, and the presence of low-energy absorption features can all contribute to the confusion. The flux of the peak goes as R^2T^4, and T must generally be inferred from the Wien tail of the Planck curve. So its uncertainties can magnified when estimating fluxes/luminosities. This is compared to optical emission that arises (presumably) from the Rayleigh-Jeans side whose flux goes like R^2T and is therefore less sensitive to uncertainties in T.

Without considering optical data, one would conclude that a blackbody spectrum works very well for RX J1856.5−3754 and would then infer a very small radius (e.g., Drake et al. 2002)—perhaps smaller than can be accommodated by typical equations-of-state (Fig. 7.10). However, the optical data force one to acknowledge the need for significantly more complicated compositions (§ 7.4.2.1) and larger radii (e.g., Pons et al. 2002b).

Once one has a model for the surface and its radiative transfer (including the effects of magnetic fields) one is then in a position to determine the true temperature and the radius. Many authors have attempted to do this for RX J1856.5−3754 (e.g., Pons et al. 2002b; Walter & Lattimer 2002; Drake et al. 2002; Burwitz et al. 2003; Zane et al. 2003), coming to a wide variety of conclusions. While this type of work is the ultimate goal of many of the observations discussed here, we believe that all current discussion is premature. There are currently no atmosphere models that fit all of the data (optical and X-ray) and include all relevant physics (especially magnetic fields). We therefore will refrain from making grand statements such as "all neutron star are quark-stars" and wait until the observations are better understood.

7.5 Conclusions

We have now seen that, despite identifying drastically fewer sources and not finding any sources powered by accretion, *ROSAT* has fundamentally fulfilled its promise in uncovering a new population of neutron stars. The identified sources satisfy four of the five criteria of Treves & Colpi (1991, see also § 7.1.1), and the failure for the fifth may just be due to statistics.

Overall, the observational picture of the INSs is not totally clear, but most observations suggest that the INSs are 10^6 yr cooling neutron stars with magnetic fields in excess of 10^{13} G. Models involving accretion, either from the ISM or from a fossil disk, are almost totally excluded for a number of sources.

The INSs are all quite nearby. There are more of them in a local volume than there are normal, 10^{12} G pulsars. The large number of INSs implies a large Galactic population of similar objects, and suggests that the distribution of neutron star magnetic fields is roughly flat up to 10^{14} G. They are likely related to, but somewhat older than, recently-discovered radio pulsars with $> 10^{13}$ G fields. The lack of radio emission from the INSs could be due to either beaming effects or the cessation of pulsar activity, as such high-field objects have short lifetimes.

Despite their perceived utility in constraining basic neutron star physics, most notably in the areas of cooling and equation-of-state, the INSs have so far not offered many reliable constraints. This is largely due to uncertainties in the surface composition and spectrum, although the limited availability of accurate distances and ages has also played a role.

We have improved upon the basic astronomical parameters that are needed for ultimately exploiting INSs: distance, age and strength of magnetic field field. In due course, we hope that the work reported here and increased understanding of X-ray spectra will help astronomers realize the unique diagnostics on dense matter that INSs can provide.

Table 7.3. Selected Rotation-Powered Pulsars

Source	PSPC[a] (ct/s)	kT (eV)	Γ[b]	P (msec)	$\log_{10} B_{\rm dip}$[c] (G)	$\log_{10} \dot{E}$[d] (ergs s^{-1})	$\log_{10} \tau$[e] (yr)	d (pc)
PSPC > 0.05 s^{-1}								
PSR J0437−4715	0.20	···	2.4	6	8.5	33.6	9.5	139
Crab	48.4	···	1.6	33	12.6	38.7	3.1	2000
PSR J0538+2817	0.06	182	···	143	11.9	34.7	5.8	1200[g]
Geminga	0.54	48	1.5	237	12.2	34.5	5.5	160[f]
PSR B0656+14	1.92	70+140	1.5	385	12.7	34.6	5.1	288
Vela	3.4	···	2.5	89	12.5	36.8	4.1	294
PSR B1055−52	0.35	70	1.5	197	12.0	34.5	5.7	700[g]
PSR B1951+32	0.07	···	1.6	40	11.7	36.6	5.0	2500
$d < 500$ pc and PSPC < 0.05 s^{-1}								
PSR J0030+0451	0.004	···	2	5	8.3	33.5	9.9	230[g]
PSR B0809+74	···	···	···	1292	11.7	30.5	8.1	433
PSR B0823+26	0.002	···	···	531	12.0	32.7	6.7	360
PSR B0950+08	0.005	···	···	253	11.4	32.7	7.2	262
PSR J1012+53	0.02	···	2.3	5	8.5	33.6	9.8	400[g]
PSR J1024−0719	0.001	···	2	5	8.1	32.9	10.4	380[g]
PSR B1133+16	···	···	···	1188	12.3	31.9	6.7	350
PSR B1451−68	···	···	···	263	11.2	32.3	7.6	460
PSR J1744−1134	0.001	···	2	4	8.2	33.6	10.0	357
PSR B1929+10	0.011	···	2.3	227	11.7	33.6	6.5	330
PSR J2124−3358	0.01	···	2	5	8.4	33.6	9.9	250[g]
$B > 10^{13.5}$ G								
PSR J1119−6127	0.001	···	2.2	407	13.7	36.4	3.2	8000[g]
PSR J1718−37184	···	···	···	3400	13.9	33.2	4.5	4000[g]
PSR J1726−3530	···	···	···	1110	13.6	34.5	4.2	10000[g]
PSR J1734−3333	···	···	···	1169	13.6	34.7	3.9	7000[g]
PSR J1814−1744	···	···	···	3956	13.7	32.7	4.9	10000[g]
PSR J1846−0258	0.04	···	2.2	324	13.7	36.9	2.9	19000
PSR J1847−0130	···	···	···	6707	14.0	32.2	4.9	8400[g]
$P > 3$ s and $B < 10^{13.5}$ G								
PSR B0320+39	···	···	···	3032	12.1	30.0	7.9	1000[g]
PSR B0525+21	···	···	···	3746	13.1	31.5	6.2	1600[g]
PSR J1148−6415	···	···	···	3241	12.5	30.5	7.3	5000[g]
PSR J1307−6318	···	···	···	4962	13.0	30.8	6.6	15000[g]
PSR J1414−6802	···	···	···	4630	12.7	30.4	7.1	7000[g]
PSR J1554−5512	···	···	···	3418	13.0	31.5	6.2	6500[g]
PSR J1617−4216	···	···	···	3428	12.9	31.2	6.5	3500[g]
PSR J1628−4828	···	···	···	4138	12.9	31.0	6.6	14000[g]
PSR J1653−4854	···	···	···	3060	12.5	30.7	7.1	6700[g]
PSR J1741−2019	···	···	···	3905	12.9	31.0	6.6	1700[g]

Table 7.3

Source	PSPC[a] (ct/s)	kT (eV)	Γ[b]	P (msec)	$\log_{10} B_{\rm dip}$[c] (G)	$\log_{10} \dot{E}$[d] (ergs s^{-1})	$\log_{10} \tau$[e] (yr)	d (pc)
PSR J1830−1135	⋯	⋯	⋯	6222	13.2	30.9	6.3	4000[g]
PSR B1845−19	⋯	⋯	⋯	4308	13.0	31.0	6.5	800[g]
PSR J1857−1027	⋯	⋯	⋯	3687	12.8	30.9	6.7	2900[g]
PSR J1951+1123	⋯	⋯	⋯	5094	12.6	30.0	7.4	2000[g]
PSR J2144−3944	⋯	⋯	⋯	8510	12.3	28.5	8.4	340[g]

[a] Count rate in the *ROSAT* PSPC, either measured directly or estimated from another X-ray measurement using W3PIMMS; `http://heasarc.gsfc.nasa.gov/Tools/w3pimms.html`.

[b] Power-law photon index, such that $N_E \propto E^{-\Gamma}$.

[c] Dipole magnetic field, assuming $B_{\rm dip} \equiv 3.2 \times 10^{19} \sqrt{P\dot{P}}$ G (Manchester & Taylor 1977).

[d] Spin-down energy loss rate $\dot{E} = 4\pi^2 I\dot{P}P^{-3}$, where we have assumed $I = 10^{45}$ g cm^2 (Manchester & Taylor 1977).

[e] Characteristic age $\tau \equiv P/2\dot{P}$ (Manchester & Taylor 1977).

[f] This parallax (Caraveo et al. 1996) could not be reproduced; better observations are under way.

[g] This distance is from the Galactic electron density model (Cordes & Lazio 2002) and not a parallax or other method.

Note. — The derived parameters (τ, $\dot{E}$, and $B_{\rm dip}$) for the millisecond pulsars have substantial uncertainties due to the Shklovskii effect.

References. — Becker & Trümper (1997); Becker & Trümper (1999); Toscano et al. (1999); Young et al. (1999); Gotthelf et al. (2000); Possenti et al. (2002); Gonzalez & Safi-Harb (2003); Hobbs & Manchester (2003); McLaughlin et al. (2003); McGowan et al. (2003); McLaughlin et al. (2003); Lyne et al. (2004); `http://www.astro.cornell.edu/%7Eshami/psrvlb/parallax.html`.

Part II

Neutron Stars in Supernova Remnants

Chapter 8

Neutron Stars in Supernova Remnants

D. L. Kaplan

8.1 Introduction

Young neutron stars are invaluable laboratories that impact on a number of diverse phenomena: stellar evolution, the physics of core collapse, neutron star cooling, and the diversity of neutron stars. The neutron stars that are found in supernova remnants (SNRs) are an even more valuable subset of the youngest ($\lesssim 10^4$ yr) neutron stars, as the SNRs can give age and distance estimates that are otherwise very difficult to obtain.

Here we summarize what is known about the formation and evolution of young neutron stars, concentrating on the applications to neutron stars associated with supernova remnants. First we discuss how massive stars evolve and explode, and what sorts of compact objects they leave behind with what frequency (§ 8.2). We then discuss the basic physics of neutron star cooling, as well as some possible modifications that can alter the assumed cooling rates (§ 8.3). We then move to observations, where in Section 8.4 we address the known neutron star/SNR associations, their discovery, and their basic properties. From this we see that a major gap exists in our knowledge of neutron star/SNR associations: the shell-type (or hollow) SNRs make up the majority of the population but are largely unconstrained with respect to associated neutron stars. We discuss this briefly in Section 8.5 and use this as an opportunity to introduce the work we have done on this topic which follows this chapter.

8.2 Outcomes of Stellar Evolution

The detailed evolution of massive stars as they approach the end of their lives is an extremely complicated problem with far too many effects to be modeled analytically. Astronomers have turned to computer simulations, but even these have significant computational and astrophysical uncertainties. On the astrophysical side, knowledge of the many presupernova parameters (composition, metallicity, rotation, convection, winds, magnetic fields, and possibly even a binary companion) can dramatically impact the resulting explosion (e.g., Heger et al. 2003). On the computational side, it has become clear recently that only with full treatments of three-dimensional effects and accurate neutrino transport can we have any hope of reliable results.

Nevertheless, one can estimate the probabilities of different global outcomes. By global outcome we mean whether the star will die and end up as a white dwarf without a supernova, a neutron star or a black hole after a supernova, a supernova that leaves no compact remnant, or a black hole without a supernova. We consider these results as discussed in recent reviews by Woosley et al. (2002) and Heger et al. (2003).

8.2.1 White Dwarfs

Below some mass limit, the star will end its life without a supernova and will leave a degenerate carbon-oxygen white dwarf (Weidemann 1987). This limit is likely in the range 7–8 $M_\odot$ (Weidemann 2000; Koester 2002). In the range 8 to $\approx 10\,M_\odot$, carbon burning and significant mass-loss occur in the proto-white dwarf and the result will be a O-Ne-Mg white dwarf. It is possible, though, that in a narrow range of masses below the upper threshold stars form O-Ne-Mg white dwarfs where the mass-loss is insufficient for them to maintain stability. Therefore they then explode off-center due to accelerated electron capture (e.g., Miyaji et al. 1980; Nomoto 1984, 1987). These supernovae probably leave neutron stars, but they may entirely destroy the stellar cores and leave nothing behind.

8.2.2 Neutron Stars

Above the threshold for white dwarf formation and below an unknown boundary ($M_{\mathrm{BH}} \approx 20 - 25\,M_\odot$; Ergma & van den Heuvel 1998; Fryer 1999 and references therein), stars are expected to undergo traditional Type II supernovae and end as neutron stars. As mentioned above, the detailed states (mass, rotation, velocity) of these neutron stars are currently unknown so precise prediction of the post-collapse properties is not possible, but the NSs should have masses of roughly 1.2–1.4 $M_\odot$ (after radiating away some fraction of their binding energies as neutrinos).

Neutron stars may also emerge from considerably more massive stars. Some authors (Woosley et al. 2002) suggest that there may be a range above 50 $M_\odot$ where neutron stars form due to extreme mass loss from the progenitor that strips away much of the original material. The supernovae in these cases would be Type Ib/c, since the hydrogen envelopes would have been ejected. On the other hand, Ergma & van den Heuvel (1998) cite evidence that the objects with progenitors $> 25\,M_\odot$ can have a mix of outcomes (neutron star or black hole), perhaps depending on one of the many complex parameters that are currently ignored or simplified (rotation, magnetic fields, asymmetries, etc.). In either case it is likely that some neutron stars can be formed by stars with initial masses $> M_{\mathrm{BH}}$, but most do not.

8.2.3 Black Holes

The conventional expectation is that above M_{BH} black holes will result from core collapse. These black holes can either form directly from collapse of the iron core, or can occur due to fallback of supernova ejecta onto a nascent neutron star. If the progenitor is near the neutron star boundary fallback or other delayed formation scenarios are more likely, but if the progenitor is more massive and has less than solar metallicity then the direct and immediate formation of the black hole could prevent any supernova. Overall, direct collapse is more likely for low metallicities, while fallback should occur for solar metallicities and above.

8.2.4 No Remnant

For the most massive stars ($\gtrsim 100\,M_\odot$) and low metallicities, pair-instability supernovae will likely occur. Here electron-positron pair creation absorbs energy that could have raised the temperature (and stabilized the collapse), leading to runaway collapse and then explosion. The explosion occurs with extreme violence and can entirely disrupt the core, leaving nothing behind.

8.2.5 Population Rates

With some prescription for outcomes, including a mapping of progenitor mass and metallicity to compact remnant type (e.g., Heger et al. 2003), one can then determine the rates for the formations of different compact objects by multiplying this mapping with an initial mass function (IMF). While this has many

Table 8.1. Summary of Outcomes for Massive Stars of Solar Metallicity

Initial Mass ($M_\odot$)	Compact Object	SN Type	Fraction[a]
< 8	C/O WD	⋯	94%
8–10	O/Ne/Mg WD	⋯	1.5%
≈ 10	NS	e^- capture	$< 0.5\%$
10–25	NS	IIp	3.2%
25–34	BH	weak(?) IIL/b	0.5%
34–50	BH	weak Ib/c	0.4%
> 50	NS	Ib/c	0.4%

[a] Fraction of stars with initial masses $\geq 1\,M_\odot$, assuming a Salpeter (1955) initial mass function.

Note. — All mass boundaries are approximate. From Woosley et al. (2002) and Heger et al. (2003).

uncertainties, Heger et al. (2003) do it and find that for solar metallicity one expects roughly 15% of massive stars ($\gtrsim 10\,M_\odot$) to leave black holes and 85% to leave neutron stars. For lower metallicities the fractions of black holes and remnant-less pair-instability SNe increase, while for higher metallicities the neutron star fraction increases up to unity (as extreme mass-loss prevents black-hole formation). We have summarized this in Table 8.1. We note that the values in Table 8.1 are very rough.

The supernova remnants (SNRs) that form around the compact objects to some degree track the compact object type. Neutron stars typically form from traditional Type II SNe, while black holes result from either weak Type II SNe or Type Ib/c SNe (either strong or weak). Weak Type II SNe occur primarily at low metallicities (below solar) and at masses just above the black hole transition where nickel falls back onto the compact remnant, lessening the optical emission, reducing the explosion energy, and creating a black hole through fallback. Weak Type Ib/c SNe can occur at higher metallicities and also produce black holes through fallback. The Type II vs. Type Ib/c distinction (based on the presence of hydrogen in the stellar envelope) is not too important for supernova remnants (except for the youngest remnants where detailed compositional studies are possible), but the difference between the strong and weak SNe may significantly affect the SNRs. The weak SNe are almost always associated with black hole formation, and so the observed population of SNRs may be slightly deficient in those containing black holes.

[The above discussion applies only to single stars, or to stars with distant companions that do not alter their evolution. For binary systems the situation is more complicated, especially with regards to mass-loss, and no detailed population estimates are available.]

8.2.6 Type Ia SNe

Type Ia SNe are believed to result from carbon detonation/deflagration of a white dwarf that has been pushed beyond its mass limit through accretion from a companion star or merger with another white dwarf. The resulting explosion completely disrupts the star, synthesizing nearly a solar mass of ^{56}Ni which ultimately decays to Fe. No compact core is left behind. The SNRs from such events thus form a subsample in which we do not expect to find an associated neutron star. The mean rate for Type Ia SNe is about 20–25% of that for core-collapse supernovae (Cappellaro et al. 1999) based on observations of extragalactic samples.

The fraction of detected supernova remnants in this Galaxy that are the results of Ia SNe is unknown. Simplistically it would be the same 20–25% of core-collapse remnants. However, there are a number of effects that could alter this number in either direction. First, since Type Ia SNe come from evolved low-mass stars, they have much wider spatial distributions than do core-collapse SNe, especially with respect to the height above the Galactic plane. The ambient density would then be lower on average, and the SNR could fade more rapidly. However, the sample of Galactic SNRs is by no means complete, and since Type Ia SNRs would occur at higher Galactic latitude where there is less confusion, these SNRs may be over-represented in the Galactic sample.

8.3 Neutron Star Cooling

The basic formulation of neutron star cooling has existed for decades (e.g., Tsuruta & Cameron 1965; Tsuruta et al. 1972). The newly born neutron stars are extremely hot (core temperatures $> 10^{11}$ K), but they cool very rapidly through neutrino emission to core temperatures of 10^9 K in about a day (Shapiro & Teukolsky 1983). At this point the cooling slows, although it is still dominated by neutrinos up to about 10^6 yr (10^8 K), when photons take over. During this period the surface temperature is roughly a factor of 100 less than the internal temperature. After the onset of photon cooling the neutron star cools very rapidly once again, and the internal temperature drops below 10^6 K (Baym & Pethick 1979).

The main reaction in this cooling is expected to be the modified URCA (MURCA; Chiu & Salpeter 1964) reaction:

$$\begin{aligned} \mathrm{nN} &\rightarrow \mathrm{pNe}\bar{\nu} \\ \mathrm{pNe} &\rightarrow \mathrm{nN}\nu, \end{aligned} \tag{8.1}$$

where n is a neutron and N is a bystanding nucleon (n or p). It is a modification of the direct URCA (DURCA) process (which is MURCA without the extra nucleon), and it dominates when the temperature is too low for DURCA to conserve both energy and momentum—the extra nucleon absorbs excess momentum. Compared to DURCA (which dominates in the first few days), MURCA is much slower, with emissivities a factor of 10^6 smaller (Yakovlev et al. 2003). Therefore the cooling should slow dramatically at the onset of MURCA.

DURCA can operate later for more massive neutron stars[1] (with higher internal densities and temperatures), so these more massive stars are expected to be significantly cooler than their lower-mass counterparts (Lattimer et al. 1991). This cooling is binary in effect: if the star is massive enough to support DURCA throughout its lifetime then the star cools to invisibility within tens of years, otherwise it will persist with surface temperatures of 10^5–10^6 K up to 10^6 yr.

Given the uncertainty in the interior structure of neutron stars, other reactions are possible. These generally involve the presence of exotic particles in the neutron-star cores, such as pions, kaons, or quark matter. These particles all have processes that look like DURCA (with pions replacing the neutrons, for example) and proceed much more quickly than MURCA since they involve fewer particles. The emissivities do not exceed those of DURCA, though (Yakovlev et al. 2003).

Besides the effects of exotic matter, other effects can alter neutron star cooling. Most important is

---

[1] DURCA may also operate somewhat in neutron star mantles, where the periodic lattice of nuclei can allow momentum conservation (Gusakov et al. 2004); if verified, this could accelerate cooling in lower-mass neutron stars.

the presence or absence of neutron and proton superfluidity in the interior. Superfluidity suppresses the MURCA reaction by making bystander nucleons unavailable and hence slows cooling. It also acts to broaden the MURCA/DURCA transition by introducing a region with intermediate cooling (Yakovlev et al. 2003). In this model, then, there are low-mass ($< 1.4\,M_{\odot}$) neutron stars that cool very slowly, high-mass ($\gtrsim 1.6\,M_{\odot}$) neutron stars that cool very quickly (using DURCA), and intermediate-mass neutron stars with cooling that depends sensitively on mass. This has led some authors to suggest that cooling observations can potentially be used to estimate neutron star masses in the absence of binary companions (Kaminker et al. 2001; Kaplan et al. 2004).

Recently, some authors (Page et al. 2004) have proposed another fundamental reaction that can cool superfluid neutron stars faster than MURCA. In their scenario, the continued breaking and formation of Cooper pairs in the superfluid at temperatures near the gap energies (~ 1 MeV) can add to the neutrino emissivities and may dominate the cooling, although the additional emissivity is not as dramatic as that between MURCA and DURCA.

Finally, the composition and magnetic field of the neutron star envelope (below the atmosphere but above the core) where strong temperature gradients exist can modify the cooling due to different opacities (Page et al. 2004). For instance, light elements (H, He, C, or O) can speed up cooling, since they have lower opacities and therefore advance the onset of photon cooling.

8.4 Observed Neutron Stars in SNRs

There are currently ≈ 38 associations between SNRs and neutron stars of various sorts (Table 8.2; also see Kaspi & Helfand 2002). Below we discuss how these associations have been identified by radio and X-ray observations.

Table 8.2. X-ray Properties of Neutron Stars in SNRs

Source	SNR	D (kpc)	$\log_{10} L_X$[a] (ergs s^{-1})	X-ray PWN?	Age[b] (kyr)	Refs	Notes
SAX J1747−2809	G000.9+0.1	10	36	Yes	1-7	1	
PSR B1757−24	G005.4−1.2	5	33.0	Yes[c]	> 39	2,3	
PSR J1811−1925	G011.2−0.3	5	33.7	Yes	1.6	4,5,6	
AX J1841−045	G027.4+0.0	7	35.3	No	2	7,8	AXP
AX J1845−0258	G029.6+0.1	15	35.1	No	< 8	9	AXP
PSR J1846−0258	G029.7−0.3	19	35.4	Yes	1–2	10	
CXO J185238.6+004020	G033.6+0.1	10	33.6	No	9	11	
PSR B1853+01	G034.7−0.4	2.5	31.2	Yes	20	12	
SS 433	G039.7−2.0	5	35	···	5–40	13	binary?
PSR J1930+1852	G054.1+0.3	5	33.3	Yes	2	14	
PSR B1951+32	G069.0+2.7	2	32.9	Yes	64	15	
1E 2259+586	G109.1−1.0	3	35.1	No	1-10	16	AXP
CXO J232327.8+584842	G111.7−2.1	3.4	34	No	0.3	17	
PSR B2334+61	G114.3+0.3	3.5	31.7	··· [d]	41	18	
RX J0007.0+7302	G119.5+10.2	1.4	31.2	Yes	13	19	
PSR J0205+6449	G130.7+3.1	3.2	32.2	Yes	0.8	20,21	
PSR J0538+2817	G180.0−1.7	1.2	32.9	Yes	30	22,23	
PSR B0531+21	G184.6−5.8	2.0	35.8	Yes	1.0	24	
CXO J061705.3+222127	G189.1+3.0	1.5	31.3	Yes	30	25	
PSR B0656+14	G203.0+12.0	0.3	31.1	No	100	26,27,28	
RX J0822−4300	G260.4−3.4	2.2	33.5	No	3.7	29,30	
SAX J0852.0−4615	G266.2−1.2	1	32.2	No	3	31	
PSR B0833−45	G263.9−3.3	0.3	32.5	Yes[c]	11	32	
PSR J1016−5857	G284.3−1.8	3	32.5	··· [d]	10	33	
AX J1111−6040	G291.0−0.1	3.5	···	Yes	···	34,35	

Table 8.2

Source	SNR	D (kpc)	$\log_{10} L_X$[a] (ergs s^{-1})	X-ray PWN?	Age[b] (kyr)	Refs	Notes
PSR J1124−5916	G292.0+1.8	6.2	33.0	Yes	2	36,37	
PSR J1119−6127	G292.2−0.5	6	32.5	Yes	2	38	
1E 1207.4−5209	G296.5+10.0	2.1	33.1	No	7	39,40	$P = 424$ ms
PSR B1338−62	G308.8−0.1	9	32.8	⋯ [d]	12	41	
PSR B1509−58	G320.4−1.2	5.2	34.1	Yes	6–20	42,43	
1E 161348−5055	G332.4−0.4	3.3	32.1–33.9	No	2	44	
PSR B1643−43	G341.2+0.9	7	⋯	⋯	33		
PSR B1706−44	G343.1−2.3	2.5	32.6	Yes[c]	18	45	
1WGA J1713.4−3949	G347.3−0.5	6	34.2	No	10	46	
PSR B1727−33	G354.1+0.1	5	< 32.6	⋯ [d]	15	24	
In LMC							
SGR 0526−66	N49	49.3	35.9	No	5–16	47	SGR
PSR J0537−6910	N157B	49.4	38.3	Yes	5	48,49	
PSR B0540−69	0540−69.3	49.4	36.3	Yes	1.5	49,50	

References. — 1: Gaensler et al. (2001a); 2: Kaspi et al. (2001); 3: Gaensler & Frail (2000); 4: Torii et al. (1997); 5: Roberts et al. (2003); 6: Stephenson & Green (2002); 7: Gotthelf et al. (1999b); 8: Morii et al. (2003); 9: Vasisht et al. (2000); 10: Helfand et al. (2003); 11: Seward et al. (2003); 12: Petre et al. (2002); 13: Kotani et al. (1996); 14: Camilo et al. (2002a); 15: Migliazzo et al. (2002); 16: Patel et al. (2001); 17: Mereghetti et al. (2002b); 18: Becker et al. (1996); 19: Slane et al. (2004); 20: Slane et al. (2002); 21: Stephenson (1971); 22: Romani & Ng (2003); 23: Kramer et al. (2003); 24: Becker & Trümper (1997); 25: Olbert et al. (2001); 26: Marshall & Schulz (2002); 27: Brisken et al. (2003b); 28: Greiveldinger et al. (1996); 29: Zavlin et al. (1999); 30: Pavlov et al. (2002); 31: Kargaltsev et al. (2002); 32: Pavlov et al. (2001c); 33: Camilo et al. (2001); 34: Moffett et al. (2002); 35: Harrus et al. (1998); 36: Hughes et al. (2003b); 37: Gaensler & Wallace (2003); 38: Gonzalez & Safi-Harb (2003); 39: Sanwal et al. (2002); 40: Zavlin et al. (2004); 41: Gaensler et al. (2003); 42: Greiveldinger et al. (1995); 43: Gaensler et al. (2002); 44: Gotthelf et al. (1999a); 45: Gotthelf et al. (2002); 46: Lazendic et al. (2003); 47: Kulkarni et al. (2003); 48: Wang et al. (2001); 49: Gotthelf (2003); 50: Gotthelf & Wang (2000). In addition, general pulsar data have been taken from Hobbs & Manchester (2003) and associations from Kaspi & Helfand (2002). See Kaplan et al. (2004).

[a] Luminosity for only the point-source in the 0.5–2.0 keV band. Upper limits to the luminosity are given for a power-law with $\Gamma = 2.2$.

[b] The best estimate of the age of the SNR if known, otherwise the pulsar spin-down age $P/2\dot{P}$.

[c] The X-ray PWNe here are significantly fainter compared to the pulsars than for other sources (Kaspi et al. 2001; Gotthelf et al. 2002).

[d] The current X-ray data do not sufficiently constrain the existence of a nebula.

Note. — All sources named PSR… are radio pulsars; the others show only high-energy emission.

8.4.1 Radio Observations

The vast majority of neutron stars are rotation-powered pulsars that have been discovered by radio searches. While young neutron stars also often have X-ray emission (§ 8.4.2), the availability and efficiency of radio observations have led to the identification of over 1000 neutron stars, compared to less than 50 for X-ray observations.

Aside from the occasional pulsar discovered serendipitously in the field of another source (e.g., Lorimer & Xilouris 2000), most pulsars were discovered through large-scale surveys that cover significant fractions of the sky. There have also been other surveys targeted toward areas thought to contain neutron stars, such as SNRs and globular clusters. As globular clusters contain only old neutron stars we will not consider those searches.

In the 1990s there were three efforts to use targeted radio searches of SNRs to discover pulsars: Gorham et al. (1996), Kaspi et al. (1996), and Lorimer et al. (1998) observed a total of 88 SNRs (mostly shell-type, although some were composite or filled; see Green 2001) with the Arecibo, Parkes and Jodrell Bank telescopes, respectively, at frequencies from 400–1500 MHz. The surveys used multiple pointings to cover large remnants (in 77 of the cases), and had 600-MHz limiting fluxes of ≈ 1 mJy. While the two later surveys discovered a few new field pulsars, none of the surveys discovered any new pulsar-SNR associations.

More recently, F. Camilo has undertaken a search for pulsars in compact pulsar wind nebulae (PWNe; Camilo 2003) and has been quite successful with five new associations (Halpern et al. 2001; Camilo et al. 2002b,c,d,a) out of 20 PWNe searched. These searches have certain advantages over the ones discussed above. First, the existence of the PWNe means that an energetic (and usually young) pulsar is present. Second, the compact sizes (a few arcminutes) of the PWNe compared to larger SNRs (several degrees) means that the searches make more efficient use of observing time. However, the major difference from the previous searches and distinguishes these new detections from the previously known population is depth of the searches and the faintness of the detected pulsars. The searches in the 1990s had flux limits of ≈ 1 mJy at 600 MHz; with an average spectral index of -1.8 (Maron et al. 2000) and an average distance of 5 kpc, this translates to a 1400-MHz "pseudo-luminosity"[2] limit of $S_{1400\,\mathrm{MHz}}d^2 \gtrsim 30$ mJy kpc^2. The new pulsars found by Camilo (2003) have luminosities over an order of magnitude fainter, around 1 mJy kpc^2, contradicting the common assumption that younger pulsars are more luminous. Thus there could be undiscovered low-luminosity pulsars in many of the larger SNRs searched previously.

One can also find pulsar-SNR associations through all-sky surveys such as the Parkes Multi-beam Survey (Manchester et al. 2001) and counterparts at other telescopes. This generation of surveys has flux limits reasonably comparable with the limits of the directed surveys of the last decade. But while they have detected over 600 new radio pulsars, only one of these is in an SNR (Camilo et al. 2000). This inefficiency could partly be due to the incompleteness of the known SNR sample, as the SNR in the one association was discovered after the pulsar (Crawford et al. 2001), but there are still a large number of known SNRs without pulsars in them (Camilo 2003; Kaplan et al. 2004) and many of the young pulsars discovered recently have been searched unsuccessfully for associated SNRs. There are other selection effects, such as the wide luminosity distribution discussed above and the increasingly broad distributions of pulse period and magnetic field (e.g., Camilo et al. 2000; McLaughlin et al. 2003) that make discoveries more difficult—Camilo (2003) notes that two of the six pulsar-SNR associations discovered recently by undirected searches have moderate luminosities of ~ 20 mJy kpc^2 but have unique spin parameters—but compensating for these effects and searching the many large remnants that remain is currently unfeasible.

8.4.1.1 Pulsar Beaming

Pulsar beaming may be one of the most significant selection effects that limit the population of neutron stars detectable by radio surveys. Pulsars emit nonthermal radio waves in one or more narrow cones. While they are rough, most estimates for the "beaming fraction" (i.e., the fraction of the sky over which a pulsar is visible) are around 10% (e.g., Tauris & Manchester 1998), with lower values for longer periods. X-ray emission, on the other hand, is observed to be much less beamed. Given this, then at some level one would not expect to find radio emission from a significant fraction of pulsars, although there might be X-ray emission (this may be the case with the population of thermally emitting neutron stars discovered by *ROSAT*; Haberl 2004).

These assumptions about beaming are roughly borne out by the results of Camilo (2003) in his searches for radio emission from PWNe. As mentioned above, the existence of a PWN means that an energetic

---

[2] The luminosities quoted are not real luminosities, since the actual shape of the pulsar beam is not known.

pulsar is present, whether or not it is beamed toward the Earth. Therefore, the fraction of PWNe with detections should be similar to the beaming fraction for young sources (which may be somewhat higher than the average; Tauris & Manchester 1998), taking into account sensitivity limits. Camilo (2003) reports detections of sources in five of 20 PWNe down to similar luminosity levels, suggesting a beaming fraction of $\sim 25\%$. This is higher than 10% but not drastically so, especially considering the small numbers. There remain a number of PWNe that have no detectable radio pulsars despite deep searches, although some of these do have X-ray point sources (e.g., IC 443). It remains to be seen, though, at what radio luminosity level the pulsar population stops. It was thought before the work of Camilo (2003) that many of the PWNe that he searched were mis-beamed (e.g., 3C 58), but this is obviously not the case.

8.4.2 X-ray Observations

X-ray observations are a powerful way to detect and characterize young neutron stars such as those found in SNRs. This is because all young neutron stars emit cooling radiation (§ 8.3), many also emit significant nonthermal radiation (Becker & Trümper 1997), and the X-ray emission (especially the thermal part) is observed to be much less beamed than radio emission. Therefore a wider variety of young neutron stars can be detected in a more uniform manner than possible with radio observations.

We have assembled X-ray data on all neutron stars that we believe are associated with SNRs in Table 8.2. There are a number of sources whose associations with SNRs are questionable, but we believe that the current evidence is reasonably strong for all of the sources that we included. This table expands upon the list from Kaplan et al. (2004) as it includes sources at distances > 5 kpc or with unreliable distances.

There are a total of 38 sources in Table 8.2, three of which are in the Large Magellanic Cloud. In Table 8.3 we separate these sources by class and also by whether they were included in Kaplan et al. (2004) or not. These classes are normal rotation-powered pulsar; pulsar wind nebula (PWN) which presumably has an as-yet undetected pulsar embedded in it; magnetar (Duncan & Thompson 1992): a source with a dipole field $\gtrsim 10^{14}$ G that is observed as an anomalous X-ray pulsar (AXP; Mereghetti 2000) or soft γ-ray repeater (SGR; Hurley 2000); compact central object (CCO; Pavlov et al. 2002; Pavlov et al. 2003): an X-ray source without a counterpart at other wavelengths that lacks pulsations and has a generally thermal spectrum; and other, comprising SS 433 (possibly a binary system), 1E 1207.4−5209, which is similar to the CCOs but shows 0.4-s pulsations and has a number of absorption features in its spectrum (Zavlin et al. 2000; Sanwal et al. 2002), and 1E 161348−5055, which is like the CCOs but shows variability (Gotthelf et al. 1999a).

Some of these distinctions are observational, such as the difference between the pulsars and the PWNe, but other (pulsar vs. magnetar vs. CCO) are intrinsic to the sources. Tables 8.2 and 8.3 serve to illustrate the observed diversity of young neutron stars: the sources span several orders of magnitude in spin-period, magnetic field, spin-down energy loss ($\dot{E}$), X-ray spectrum, and X-ray luminosity (see also Kaplan et al. 2004). This is also shown in Figure 8.1, where we plot the observed X-ray luminosity as a function of age. The magnetars and CCOs have reasonably tight ranges in luminosity, while the pulsars and PWNe have a larger span (this reflects their wide range in $\dot{E}$; Becker & Trümper 1997; Possenti et al. 2002).

The pulsars (and PWNe) dominate the observed population of neutron stars in SNRs, which may be somewhat remarkable given the narrow beaming of radio pulsars (although this beaming is not too narrow for young sources). There may be some undiscovered AXPs or SGRs in the Galaxy, but there are not likely to be too many of them given the small local density and their high luminosities (especially those of the SGRs during outburst). The really incomplete population is that of the CCOs, which we will address below.

Table 8.3 Classifications of Central Sources from Table 8.2

Class	$N_{<5\,\mathrm{kpc}}$[a]	N_{tot}
Pulsar[b]	12	22
PWN[c]	2	4
Magnetar[d]	0	4
CCO[e]	2	5
Other[f]	3	3
Total	19	38

[a] Sources with reliable distances that are ≤ 5 kpc, as compiled by Kaplan et al. (2004). Some of the other sources may be within 5 kpc but the distances are too uncertain.

[b] Rotation-powered pulsar with detected pulsations.

[c] PWNe presumably powered by rotation-powered pulsars but where the pulsations have not yet been detected (e.g., CXO J061705.3+222127 in IC 443).

[d] AXPs and SGRs.

[e] Compact central object: an X-ray source lacking counterparts at other wavelengths with a thermal spectrum and no pulsations (e.g., CXO J232327.8+584842 in Cas A).

[f] Includes: 1E 1207.4−5209, SS 433, and 1E 161348−5055.

8.5 The Hollow SNR Problem

As discussed above, SNRs with central PWNe almost certainly have energetic pulsars, many of which are detectable as radio pulsars (Camilo 2003) despite failed searches in the past. There are still, though, over 200 SNRs in the recent catalog (Green 2001) that are shell-type or hollow (see Vasisht & Gotthelf 1997), and that have no known central source. These SNRs have been a puzzle for many years (e.g., Helfand & Becker 1984). As discussed above, a small number of SNRs may be the result of Type Ia SNe or have central black holes (invisible in the absence of accretion), but neither of these should comprise more than 10 or 20% of the total SNR population.

While central sources in a number of hollow SNRs had been discovered over the years with *Einstein* and *ROSAT* (e.g., Tuohy & Garmire 1980; Helfand & Becker 1984), the discovery of the central source in Cas A with *Chandra* (Tananbaum 1999) reflected how this field had been re-energized with the launches of *Chandra* and *XMM*. For the first time, high angular and spatial resolution coupled with large collecting areas would make possible detailed studies of neutron stars in the X-rays.

Observations of the central source in Cas A have been puzzling. No pulsations have been detected (Murray et al. 2002a) and there is no counterpart at radio (McLaughlin et al. 2001) or optical/IR wavelengths (Kaplan et al. 2001a; Fesen et al. 2002). The X-ray spectrum is not particularly constraining: it can be fit with a steep power-law (photon index ~ 3), a thermal bremsstrahlung model, a blackbody with $kT \sim 0.7$ keV, or some combination (Mereghetti et al. 2002b). This spectrum rules normal pulsar models and while it is consistent with AXPs, AXPs are typically a factor of 100 brighter. A neutron star or a black hole accreting matter (from an isolated disk) is plausible (Pavlov et al. 2000; Chakrabarty et al. 2001), but our optical/IR data severely constrain the presence of any disk. In fact, observations of the other CCOs have generally failed to come to any real conclusions; only 1E 1207.4−5209 (previously lumped in with the

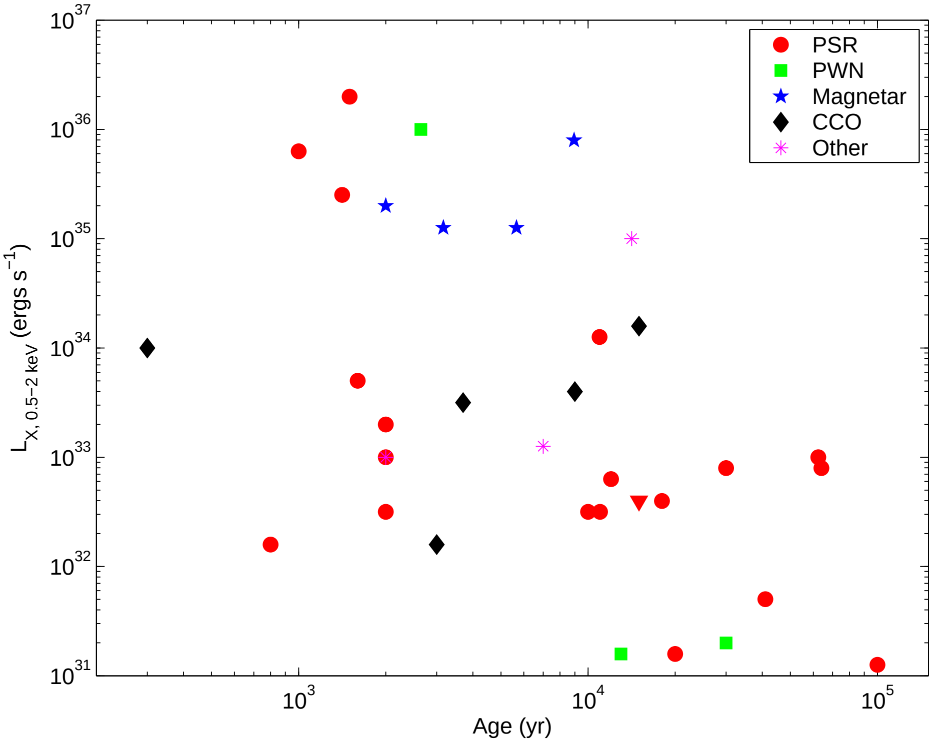

Figure 8.1 X-ray luminosity (0.5–2.0 keV) versus age for the neutron stars in SNRs from Table 8.2. Rotation-powered pulsars are circles, sources embedded in PWNe but no pulsations are squares, magnetars are stars, CCOs are diamonds, and the remaining sources are asterisks (see Table 8.3). The luminosities are only those of the point sources: the pulsars and PWN sources also have nebulae whose luminosities are typically a factor of 10 above those of the embedded sources. Also see Kaplan et al. (2004).

CCOs, but now differentiated due to its period and nontrivial spectrum) has had any progress.

8.5.1 A Comprehensive Search for Central Neutron Stars in Nearby SNRs

The continuing puzzle of Cas A and the large number of hollow SNRs present a problem that to date has not been confronted systematically. Much of the reason for this is the difficulty (discussed above) in finding new associations using either radio or X-ray observations. The advents of *Chandra* and *XMM* have changed this somewhat, but we are still forced to distinguish between neutron stars and the many foreground/background X-ray sources that are seen in the Galactic plane. Fortunately, we can filter out the neutron stars by virtue of the their high X-ray-to-optical flux ratio (Fig. 8.2) as demonstrated by our work on Cas A. Comparing deep optical/IR and X-ray observations is then a powerful way to discriminate between neutron stars and foreground/background sources like active stars and galaxies.

Moving beyond Cas A, we constructed a volume-limited sample of SNRs within 5 kpc that have reliable distances. There are 45 such sources, three of which are likely due to Type Ia SNe, and 19 of which have central neutron stars. This leaves 23 hollow SNRs. Thus more than half of the SNRs in our sample have no indication for any neutron star, while only $\lesssim 30\%$ of them should not have a neutron star based on our current understanding of core collapse.

To quantify this deficiency we have begun a survey for neutron stars in these SNRs using X-ray observations from *Chandra*, *XMM*, and *ROSAT* (via the *ROSAT* All-Sky Survey) and deep optical/IR observations. Our X-ray limits are designed to detect virtually all known young neutron stars: we go to

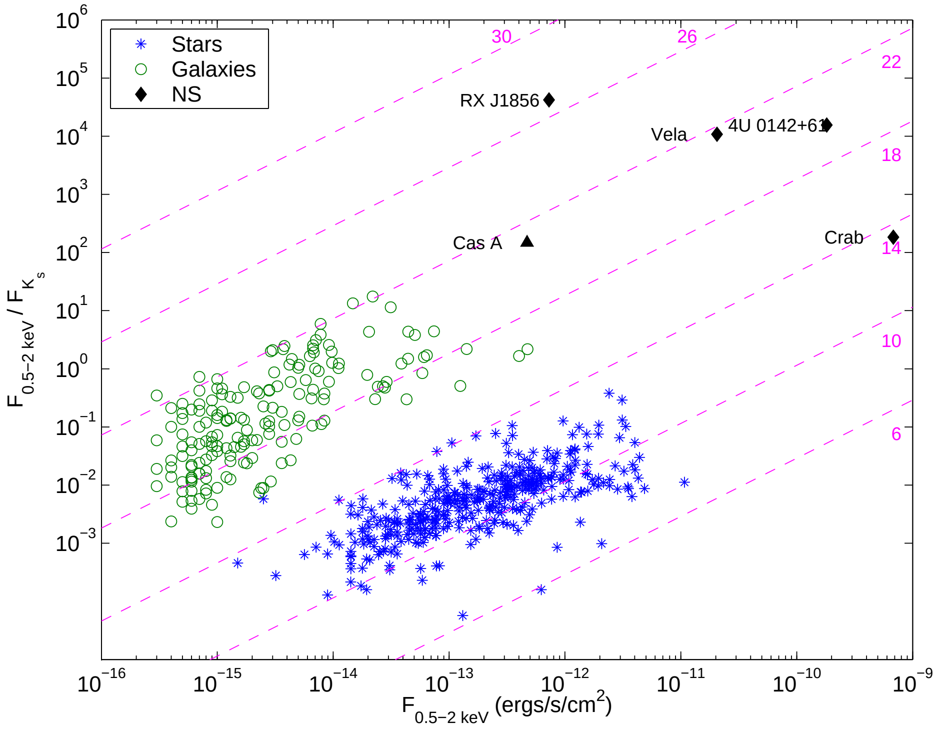

Figure 8.2 X-ray-to-IR flux ratio vs. X-ray flux for sources from the CDF/Orion studies (Brandt et al. 2001; Feigelson et al. 2002) and selected neutron stars. Stars from CDF/Orion are blue asterisks and galaxies are green circles. Selected neutron stars are black diamonds/limits, and are labeled. The diagonal lines represent constant magnitude, and are labeled by that magnitude.

luminosities 10^{31}–10^{32} ergs s^{-1} that are comparable to or below all of the sources in Figure 8.1. In the next chapters we describe the design and implementation of our survey, as well as the initial results.

Chapter 9

Search for an Near-IR Counterpart to the Cas A X-ray Point Source[†]

D. L. Kaplan[a], S. R. Kulkarni[a], & S. S. Murray[b]

[a]Department of Astronomy, 105-24 California Institute of Technology, Pasadena, California 91125, USA

[b]Harvard-Smithsonian Center for Astrophysics, MS-4, 60 Garden Street, Cambridge, Massachusetts 02138, USA

Abstract

We report deep near-infrared and optical observations of the X-ray point source in the Cassiopeia A supernova remnant, CXO J232327.9+584842. We have identified a $J = 21.4 \pm 0.3$ mag and $K_s = 20.5 \pm 0.3$ mag source within the 1-σ error circle, but we believe this source is a foreground Pop II star with $T_{\rm eff} = 2600$–2800 K at a distance of ≈ 2 kpc, which could not be the X-ray point source. We do not detect any sources in this direction at the distance of Cas A, and therefore place 3-σ limits of $R \gtrsim 25$ mag, F675W $\gtrsim 27.3$ mag, $J \gtrsim 22.5$ mag and $K_s \gtrsim 21.2$ mag (and roughly $H \gtrsim 20$ mag) on emission from the X-ray point source, corresponding to $M_R \gtrsim 8.2$ mag, $M_{\rm F675W} \gtrsim 10.7$ mag, $M_J \gtrsim 8.5$ mag, $M_H \gtrsim 6.5$ mag, and $M_{K_s} \gtrsim 8.0$ mag, assuming a distance of 3.4 kpc and an extinction $A_V = 5$ mag.

9.1 Introduction

Cassiopeia A (Cas A) is the youngest Galactic supernova remnant (SNR) with an age of ~ 320 yr, as according to Ashworth (1980) it is associated with the explosion observed by Flamsteed (1725) in 1680. Hughes et al. (2000) have found that the elemental abundances in Cas A are consistent with those expected from the remnant of a massive star, possibly a Wolf-Rayet star (Fesen et al. 1987), and therefore Cas A is considered to have been a Type II supernova. One therefore expects a compact central remnant, such a neutron star or black hole, based on the initial mass function of Type II supernovae (e.g., de Donder & Vanbeveren 1998). From the first-light images of the *Chandra X-ray Observatory* (CXO), Tananbaum (1999) reported detection of a compact source located at the apparent center of Cas A. The detection of this source, CXO J232327.9+584842 (hereafter the X-ray point source or XPS), was later confirmed in archival *ROSAT* (Aschenbach 1999) and *Einstein* (Pavlov & Zavlin 1999) data.

The XPS is located within 5″ of the expansion center of Cas A (van den Bergh & Kamper 1983), and given the space density of AGNs the chance of finding one within this distance of the center is quite small. We convert the count rates from Chakrabarty et al. (2001) to the 0.5–2.4 keV band, and get an

---

[†] A version of this chapter was published in *The Astrophysical Journal*, vol. 558, 270–275.

absorbed flux of $\approx 4 \times 10^{-13}$ ergs s^{-1} cm^{-2}. Comparing this with the AGN $\log N$-$\log S$ relation from Georgantopoulos et al. (1996), we would expect ~ 0.4 AGN deg^{-2}, or $\sim 2 \times 10^{-6}$ AGNs of this flux at the center of Cas A. It is thus extremely improbable that the XPS is an AGN, a fact further confirmed by its relatively steep spectrum (Chakrabarty et al. 2001).

Therefore, it is generally believed that the XPS is associated with the remnant of the Cas A progenitor (Chakrabarty et al. 2001). The X-ray spectrum of the XPS, as determined by Pavlov et al. (2000) and Chakrabarty et al. (2001), can be fitted by a power-law with a photon index ~ 3. Other acceptable fits include thermal bremsstrahlung ($kT^{\infty} \approx 1.7$ keV), blackbody ($kT^{\infty} \approx 0.5$ keV, $R^{\infty} \approx 0.5$ km), or neutron star atmospheres ($kT^{\infty} \approx 0.4$ keV, $R^{\infty} \approx 0.8$ km for the model of Heyl & Hernquist 1998a; $kT^{\infty} \approx 0.27$ keV, $R^{\infty} \approx 2$ km for the model of Zavlin et al. 1996).

The nature of the XPS is unclear. However, we have an idea as to what it is not. The spectral index of the XPS is significantly steeper than those typical for young X-ray pulsars, its luminosity is $\gtrsim 10^2$ times less than those of young X-ray pulsars, and there is no evidence for a synchrotron nebula (McLaughlin et al. 2001). The spectrum is similar to that of an anomalous X-ray pulsar (AXP; see Mereghetti 2000), but the X-ray luminosity is at least several (if not 10–100) times fainter than that typical for AXPs. The XPS is cooler but much more luminous than isolated neutron stars (Motch 2001).

Furthermore, there have not been any detections of optical (van den Bergh & Pritchet 1986; Ryan et al. 2001) or radio (McLaughlin et al. 2001, and references therein) emission from the XPS, nor have X-ray pulsations been detected (Chakrabarty et al. 2001), though the current limits are not very constraining. Therefore, the XPS is almost certainly not a young pulsar similar to the Crab. Theories as to its identity range from a cooling neutron star emitting from polar caps to an accreting black hole (Umeda et al. 2000; Pavlov et al. 2000).

From measures of line ratios in the Cas A remnant, Searle (1971) finds the extinction to be $A_V = 4.3$ mag in the direction of one filament. Later radio studies found significant variations of A_V on scales of $\sim 1'$, and overall values ranging from 4–5 mag for the north and northeastern rim and $\gtrsim 5$–6 mag for the rest of the SNR (Troland et al. 1985). Similarly, Hurford & Fesen (1996) find extinction values of 4.6–5.4 mag across the northern portion (assuming $R_V = 3.1$). We will therefore adopt a middle value of $A_V \approx 5$ mag. We assume that Cas A and the XPS are at a distance of $3.4^{+0.3}_{-0.1}$ kpc (Reed et al. 1995), which we parameterize as $D = 3.4 d_{3.4}$ kpc.

In this letter we report on optical/near-IR searches for a counterpart to the XPS. We believe that given the unknown nature of XPS, searches at all wavelengths are warranted and even upper limits may constrain the nature of this enigmatic source. The paper is organized as follows: in Section 9.2 we detail our observations and reduction techniques. Section 9.3 contains a description of the results, while Section 9.4 presents an analysis of these results. Finally, a discussion and conclusions are in Section 9.5.

9.2 Observations

9.2.1 Cas-A Central Point Source Position

The SNR Cas A was observed several times with the CXO. After the initial detection in the first-light images (Tananbaum 1999), a long HRC-I observation was obtained on 1999 December 20, and a third observation with the HRC-S in imaging mode was taken on 2000 October 5. A discussion of the results from this observation is in preparation (Murray et al. 2001); here we provide only the source location information. Table 9.1 gives the point source locations and estimated uncertainties (including estimates of systematic errors). We estimate that the overall positional uncertainty for all of these observations is $1\farcs0$ (1-σ).

Table 9.1. Cas A X-ray Observation Summary

OBSID	Date	CXO Instrument	Exposure (ks)	RA[a] (J2000)	Dec[a] (J2000)
214	1999 Aug 20	ACIS S3	6	$23^{\mathrm{h}}23^{\mathrm{m}}27^{\mathrm{s}}.94$	$+58^\circ48'42''.4$
1505	1999 Dec 20	HRC-I	50	$23^{\mathrm{h}}23^{\mathrm{m}}27^{\mathrm{s}}.88$	$+58^\circ48'42''.1$
1857	2000 Oct 05	HRC-S	50	$23^{\mathrm{h}}23^{\mathrm{m}}27^{\mathrm{s}}.75$	$+58^\circ48'43''.8$
Average				$23^{\mathrm{h}}23^{\mathrm{m}}27^{\mathrm{s}}.857$	$+58^\circ48'42''.77$
Uncertainty[b]				$0^{\mathrm{s}}.097$	$0''.91$

[a] The individual source positions were calculated as centroids of the event distributions taken within a $1''.0$ radius circle about the location and iterated until the centroid location shifted by less than $0''.1$.

[a] Uncertainties are 1-σ.

Table 9.2. Cas A Optical/Near-IR Observation Summary

Date	Telescope / Instrument	Observer	Band	Exposure (s)	Conditions
2000 Jan 22	HST/WFPC2	R. Fesen	F675W	4000	⋯
2000 Jun 27	Keck I/NIRC	S. Kulkarni	J	1600	slight cirrus
			K_s	2364	
2000 Jul 04	P200/COSMIC	P. Mao	R	1010	photometric
2000 Jul 05	P200/COSMIC	P. Mao	R	1000	high cirrus
2000 Jul 24	P60/P60CCD	D. Kaplan	R	150	photometric
			I	150	
2000 Sep 06	P200/PFIRCAM	D. Kaplan /	J	1680	photometric
		J. Cordes	H	1680	
			K_s	1120	

9.2.2 Optical and Near-IR Observations

The observations were carried out primarily with the Near Infrared Camera (NIRC; Matthews & Soifer 1994) mounted on the 10 meter Keck I telescope, augmented with archival HST/WFPC2 images. We also took auxiliary optical and infrared calibration images with the COSMIC imager on the Palomar 5-meter telescope (P200), the PFIRCAM (Jarrett et al. 1994) infrared imager on the P200, and the P60CCD optical imager on the Palomar 1.5-meter telescope (P60). A summary of the instruments, filters, exposures, and conditions is listed in Table 9.2.

The optical data were reduced with the standard `IRAF ccdred` package. The images were bias subtracted, flat-fielded, registered, and co-added. The infrared data were reduced with custom `IRAF` software. The images were dark subtracted, flat-fielded, and corrected for bad pixels and cosmic rays. We then made object masks, which were used in a second round of flat-fielding to remove holes from the flats. The data were then registered, shifted, and co-added. The HST images were processed using the standard drizzling procedure (Fruchter & Mutchler 1998).

The data from the P60CCD were used as the astrometric reference. We matched 36 nonsaturated stars to those from the USNO-A2.0 catalog (Monet 1998). Using the task `ccmap` we computed a transformation solution, giving $0\farcs2$ residuals (all astrometric residuals are 1-σ for each coordinate unless otherwise indicated). We then used this solution to fit stars on the COSMIC images. Using 37 stars, we again obtained $0\farcs2$ residuals.

We then used 15 stars on the COSMIC images to fit the HST image, getting $0\farcs07$ residuals. This solution was then used for the infrared images, fitting 10 stars on the NIRC images with $0\farcs05$ residuals. This gives $0\farcs4$ position uncertainties relative to the ICRS, assuming the uncertainties intrinsic to the USNO-A2.0 are $0\farcs3$ (for each axis; Monet 1998) We then transfered this solution to the PFIRCAM images ($0\farcs3$ residuals), but as this is only a photometric reference the absolute position is not important.

For the optical photometry, we used V, R, and I observations of the standard fields[1] Landolt 110, NGC 7790, and PG 1657 (Landolt 1992; Stetson 2000) carried out with the P60CCD. We fit the observations over the whole night using airmass corrections and first-order color terms, and measured the R zero-point magnitude. We then examined 25 stars on the Cas A images common to both the P60CCD and COSMIC images, and from this determined the zero point for the photometric night. From these data we also determined the limiting magnitude to be $R \sim 25$ mag.

For the infrared photometry, we used 3 observations of the faint UKIRT standard stars FS 29 and FS 31 (Casali & Hawarden 1992) taken with the PFIRCAM. These observations were used to determine J, H, and K_s zero points (we assumed the K_s magnitudes were the same as the K magnitudes, as the correction is typically $\lesssim 0.01$ mag: much smaller than our uncertainties; Persson et al. 1998). From these images we then found 5 stars common to the PFIRCAM and NIRC images, and determined zero-point magnitudes for NIRC.

9.3 Results

We searched for a counterpart to the X-ray point source, at position $\alpha(J2000) = 23^{\rm h}23^{\rm m}27\fs857$, $\delta(J2000) = +58^\circ48'42\farcs77$, with $1\farcs0$ uncertainty (Table 9.1). See Figure 9.1 for the separate optical/IR images. There was no source on COSMIC images, giving $R \gtrsim 25$ mag (3-σ limit) for any possible counterpart (this agrees with the previous limit of $R \gtrsim 24.8$ mag and $I \gtrsim 23.5$ mag; van den Bergh & Pritchet 1986). On the NIRC, PFIRCAM, and HST images there was a source $1\farcs7$ away from the X-ray position, at $\alpha(J2000) = 23^{\rm h}23^{\rm m}27\fs78$, $\delta(J2000) = +58^\circ48'41\farcs2$ ($\pm0\farcs4$ in each coordinate). Given the astrometric uncertainties, the overall position uncertainty is $1\farcs1$ in each axis, so this source is 1.5-σ away from the nominal position. We label this source A, and consider it as a potential candidate counterpart or companion to the X-ray source. The magnitudes of source A are F675W $= 26.7 \pm 0.2$ mag, $J = 21.4 \pm 0.3$ mag, $H \approx 20.5 \pm 0.8$ mag, and $K_s = 20.5 \pm 0.3$ mag. There are no other sources within the $2\farcs3$ radius 90% confidence circle.

9.4 Analysis

Using the reddening and zero-point calibration data from Bessell et al. (1998), we plot the spectral energy distribution (SED) for source A in Figure 9.2. This incorporates both the detections and limits.

---

[1] `http://cadcwww.dao.nrc.ca/cadcbin/wdb/astrocat/stetson/query/`

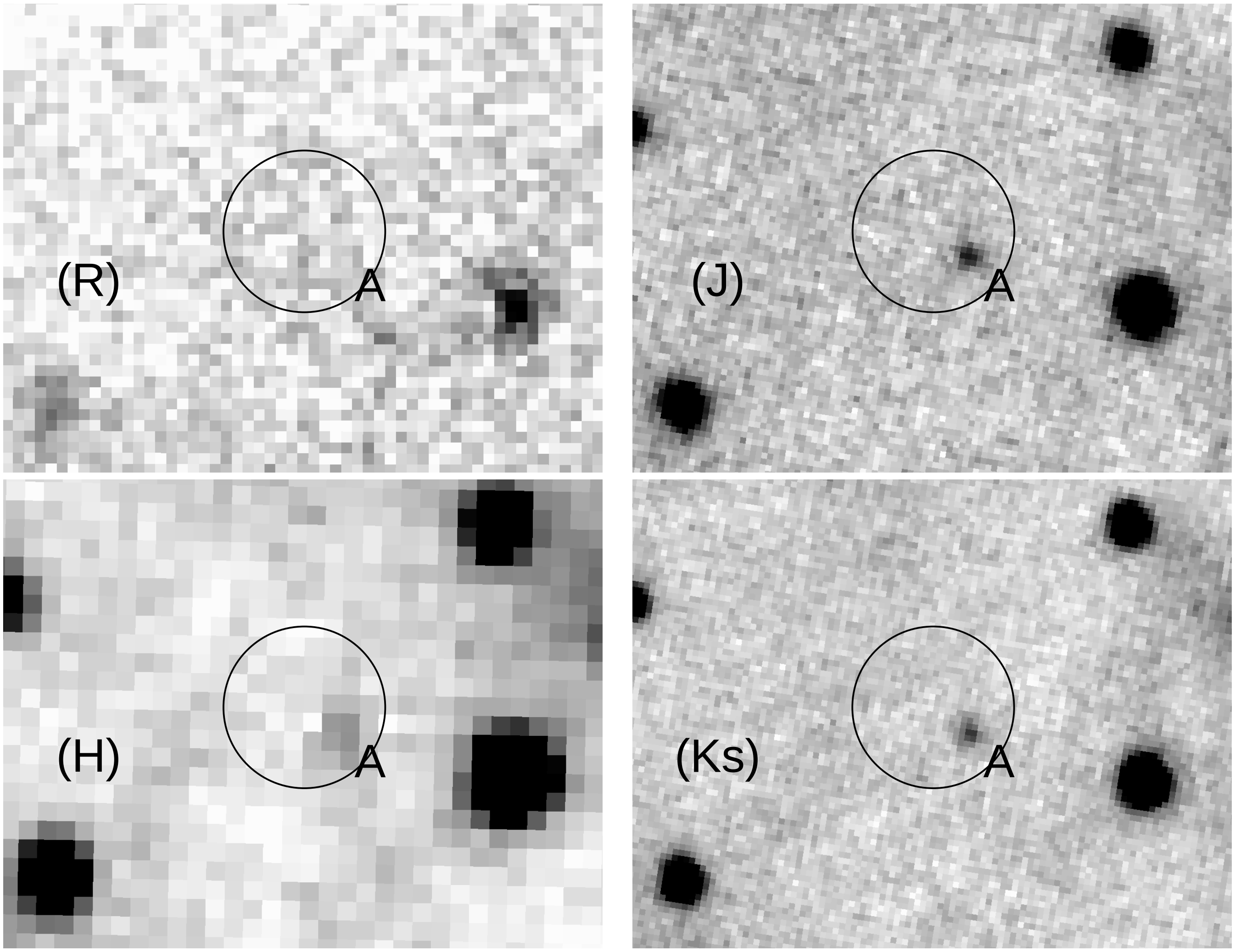

Figure 9.1 Images of the region around the XPS. They are: R-band (COSMIC; upper left); J-band (NIRC; upper right); H-band (PFIRCAM; lower left); K_s-band (NIRC; lower right). A $2\rlap{.}''3$ radius circle (90% confidence) is drawn around the position of the XPS, and candidate source A is indicated. North is up, and east is to the left. The images are $\approx 15''$ on each side.

To determine if source A could be a star, we compared model stellar colors from Bessell et al. (1998) with our data. We fitted for three parameters: the visual extinction A_V, the distance in kpc $D_{\rm kpc}$, and the stellar model (which includes the effective temperature $T_{\rm eff}$, the surface gravity g, and the metallicity [Fe/H]). We assumed that the star would be a zero-age main-sequence star such that $\log(R/R_\odot) = 0.7\log(M/M_\odot) - 0.1$ (Habets & Heintze 1981), and used the bolometric corrections and reddening from Bessell et al. (1998) to find the expected magnitudes. To account for the upper limits in our fitting, we minimized a modified χ^2 statistic, such that

$$\chi^2 = \sum_i^{\rm Detect} \left(\frac{m_i - m_{i,\rm mod}}{\sigma_i}\right)^2 + \sum_i^{\rm non-Detect} \begin{cases} 0 & \text{if } m_{i,\rm mod} \geq m_i; \\ \left(\frac{m_{i,\rm mod} - m_i}{\sigma_i}\right)^2 & \text{otherwise.} \end{cases} \tag{9.1}$$

Here, i runs over the different filters, m_i is the observed magnitude or limit for that filter, $m_{i,\rm mod}$ is the model magnitude, and σ_i is the uncertainty. The model uses standard Vega-based magnitudes,

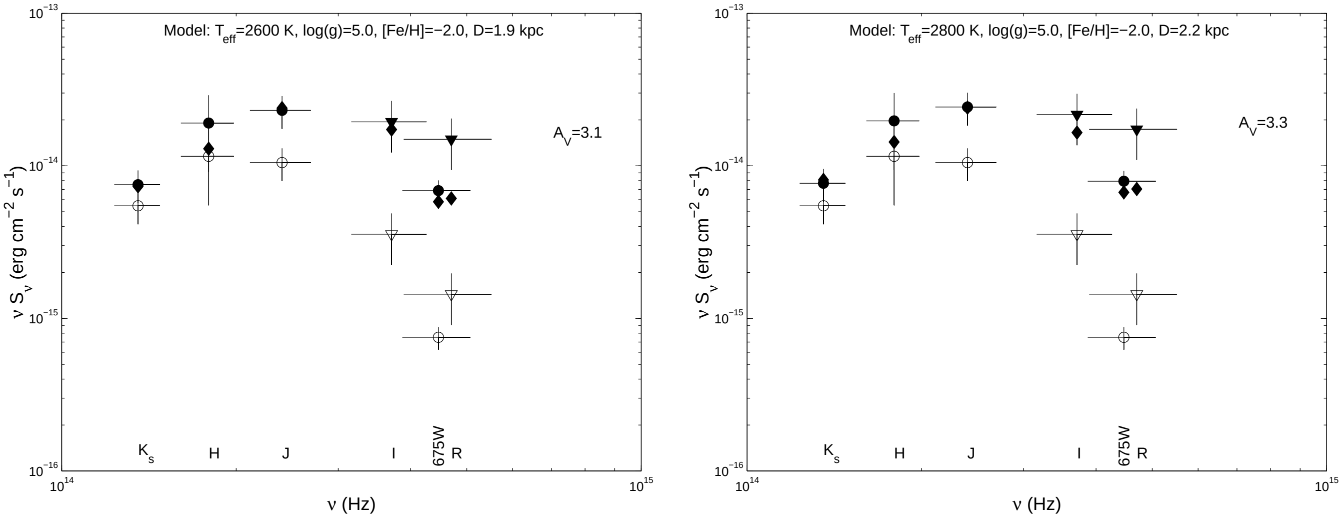

Figure 9.2 Spectral energy distribution for source A, a foreground star from the Cas A X-ray error circle, and best-fit data for two different stellar models: $T_{\rm eff}$ = 2600 K (left); $T_{\rm eff}$ = 2800 K (right). The open symbols are the observed data, the filled circles and limits those corrected for reddening, and the diamonds the model values. The model parameters, from Bessell et al. (1998), are listed on the figures.

where the HST data do not. Therefore we converted the HST magnitude to the Vega-based system using $R-\mathrm{F675W} = -1.05$ mag, appropriate for sources of this color.[2] We do not incorporate model uncertainties into this statistic. Minimizing this χ^2 seeks the best model that comes close in magnitude to the detections while remaining fainter than the nondetections. A full-fledged Bayesian analysis (e.g., Gregory & Loredo 1992; Cordes & Chernoff 1997) would be more accurate, but we only wish to demonstrate the plausibility of model fits, not assign specific probabilities to different models.

Given the number of variables, this fit is somewhat unconstrained. We restrict the extinction and distance to reasonable values ($0.5 \lesssim A_V \lesssim 8$ mag, $0.5 \lesssim D_{\rm kpc} \lesssim 5$), and fit for $\log(g) = 5.0$ (appropriate for late M stars; Habets & Heintze 1981). In addition, we require that A_V roughly scale with D, excluding models that are very distant but have almost no extinction. We find that our detections and limits are entirely consistent with a cool (M6–8), Pop II, main-sequence star, which is between the Earth and Cas A. Good fits are obtained for stars with $T_{\rm eff}$ = 2600–2800 K, [Fe/H]= −2.0, $D_{\rm kpc}$ = 1.8–2.0 kpc, and A_V = 3.1–3.2 mag (see Figure 9.2 for examples). We do not give the χ^2 value or formal confidence regions, as the χ^2 in Equation 9.1 is somewhat contrived and the models for stars this cool are not well determined (Bessell et al. 1998), but Figure 9.2 demonstrates the plausibility of the fits. That there is a star within $1\farcs7$ of the XPS is quite believable: the theoretical star-count models of Nakajima et al. (2000) give 1.5×10^6 stars deg^{-2} of the appropriate colors with $J \leq 22.5$ mag, leading to a false coincidence rate of 1.0. The best-fit star has $R = 0.2 R_\odot$, $M = 0.1 M_\odot$, and $L = 0.004 L_\odot$. Slightly deeper I band observations should be able to verify the classification of source A.

As one might expect, there is a significant anti-correlation in the fits between values of $D_{\rm kpc}$ and A_V, with ±0.25 kpc and ±0.5 mag variations giving reasonable fits, but the fits for the range of likely extinctions for Cas A (4–6 mag) at 3.4 kpc are definitely poor.

Assuming that source A is a late-type star, we examine whether it could be associated with the XPS, implying that both are in the foreground and that the XPS is not associated with Cas A. From Katsova & Cherepashchuk (2000), we see that for a star with $B - V \geq 1.8$ (from the model for source A), the

---

[2] http://www.stsci.edu/instruments/wfpc2/Wfpc2_phot/wfpc2_cookbook.html

X-ray luminosity is $L_{\mathrm{X,star}}(0.1\text{–}2.4\ \mathrm{keV}) \lesssim 10^{28}$ ergs s^{-1} (also James et al. 2000; Marino et al. 2000), giving unabsorbed (denoted by superscript U) X-ray-to-infrared flux ratios of $f_{\mathrm{X}}^{\mathrm{U}}/(\nu_J f_{\nu,J}^{\mathrm{U}}) = 6 \times 10^{-4}$ and $f_{\mathrm{X}}^{\mathrm{U}}/(\nu_{K_s} f_{\nu,K_s}^{\mathrm{U}}) = 2 \times 10^{-3}$ for such a star. Converting the flux of the XPS to the ROSAT passband (using W3PIMMS,[3]) it has ratios of $f_{\mathrm{X}}^{\mathrm{U}}/(\nu_J f_{\nu,J}^{\mathrm{U}}) = 34$, $f_{\mathrm{X}}^{\mathrm{U}}/(\nu_{K_s} f_{\nu,K_s}^{\mathrm{U}}) = 111$, which are drastically different. In addition, Pavlov et al. (2000) and Chakrabarty et al. (2001) did not observe any variability from the XPS, unlike late-type stars that can vary by factors of $\sim 10^2$ on small time scales (Marino et al. 2000). Source A therefore could not emit the X-rays observed from the XPS.

We conclude that the XPS was not detected, and add F675W $\gtrsim 27.3$ mag, $J \gtrsim 22.5$ mag and $K_s \gtrsim 21.2$ mag (3-σ), along with a rough limit of $H \gtrsim 20$ mag, to the previously mentioned limits.

9.5 Discussion & Conclusions

Based on a synthesis of CXO, *ROSAT*, and *Einstein* data, Pavlov et al. (2000) fit the X-ray spectrum of the XPS. The absorbed flux is 8.2×10^{-13} ergs $\mathrm{cm}^{-2}\ \mathrm{s}^{-1}$ in the 0.3–6.0 keV range (Pavlov et al. 2000). Power-law and pure blackbody models give good fits to the absorption-corrected data, and are plotted as representative X-ray spectra in Figure 9.3. These results are similar to those from Chakrabarty et al. (2001). Pavlov et al. (2000) prefer the results of a H/He polar-cap model with a cooler Fe surface, but all we wish to illustrate is that blackbody models are consistent with the optical limits, while power-law models require a break between the X-ray and optical bands.

In Figure 9.3 we also plot the expected optical magnitudes of representative X-ray sources (an AXP and a tight X-ray binary) for comparison. These magnitudes are derived by taking the X-ray-to-optical flux ratios for these objects and scaling them to the X-ray flux of the XPS. We can likely reject sources like 4U 1626−67 (Chakrabarty 1998) from consideration, but the extrapolation of the AXP 4U 0142+61 (Hulleman et al. 2000) is consistent with the current limits.

Giving the presumed distance and reddening, our limits translate to $M_R \gtrsim 8.2$ mag, $M_{\mathrm{F675W}} \gtrsim 10.7$ mag, $M_J \gtrsim 8.5$ mag, $M_H \gtrsim 6.5$ mag, and $M_{K_s} \gtrsim 8.0$ mag. We find the observed X-ray-to-infrared flux ratios to be $f_{\mathrm{X}}/(\nu_{\mathrm{F675W}} f_{\nu,\mathrm{F675W}}) \gtrsim 2872$, $f_{\mathrm{X}}/(\nu_J f_{\nu,J}) \gtrsim 212$, $f_{\mathrm{X}}/(\nu_{K_s} f_{\nu,K_s}) \gtrsim 280$ (the X-ray flux is in the 0.3–6.0 keV band). If we correct for interstellar absorption, we find unabsorbed ratios of $f_{\mathrm{X}}^{\mathrm{U}}/(\nu_{\mathrm{F675W}} f_{\nu,\mathrm{F675W}}^{\mathrm{U}}) \gtrsim 231$, $f_{\mathrm{X}}^{\mathrm{U}}/(\nu_J f_{\nu,J}^{\mathrm{U}}) \gtrsim 166$ and $f_{\mathrm{X}}^{\mathrm{U}}/(\nu_{K_s} f_{\nu,K_s}^{\mathrm{U}}) \gtrsim 467$, using the X-ray flux from Chakrabarty et al. (2001). These flux ratios, larger than those inferred previously, tighten constraints on the identity of the XPS (e.g., Umeda et al. 2000; Pavlov et al. 2000).

We would like to thank T. Nakajima for supplying star-count models, and J. Cordes for sharing observing time. DLK is supported by the Fannie and John Hertz Foundation and SRK by NSF and NASA. DLK thanks the ITP at Santa Barbara, where part of the work presented here was done, for hospitality. The ITP is supported by the National Science Foundation under Grant No. PHY99-07949. Data presented herein were obtained at the W.M. Keck Observatory, which is operated as a scientific partnership among the California Institute of Technology, the University of California and the National Aeronautics and Space Administration. The Observatory was made possible by the generous financial support of the W.M. Keck Foundation. Data are also based on observations with the NASA/ESA Hubble Space Telescope, obtained from the data Archive at the Space Telescope Science Institute, which is operated by the Association of Universities for Research in Astronomy, Inc. under NASA contract No. NAS5-26555

---

[3] `http://heasarc.gsfc.nasa.gov/Tools/w3pimms.html`

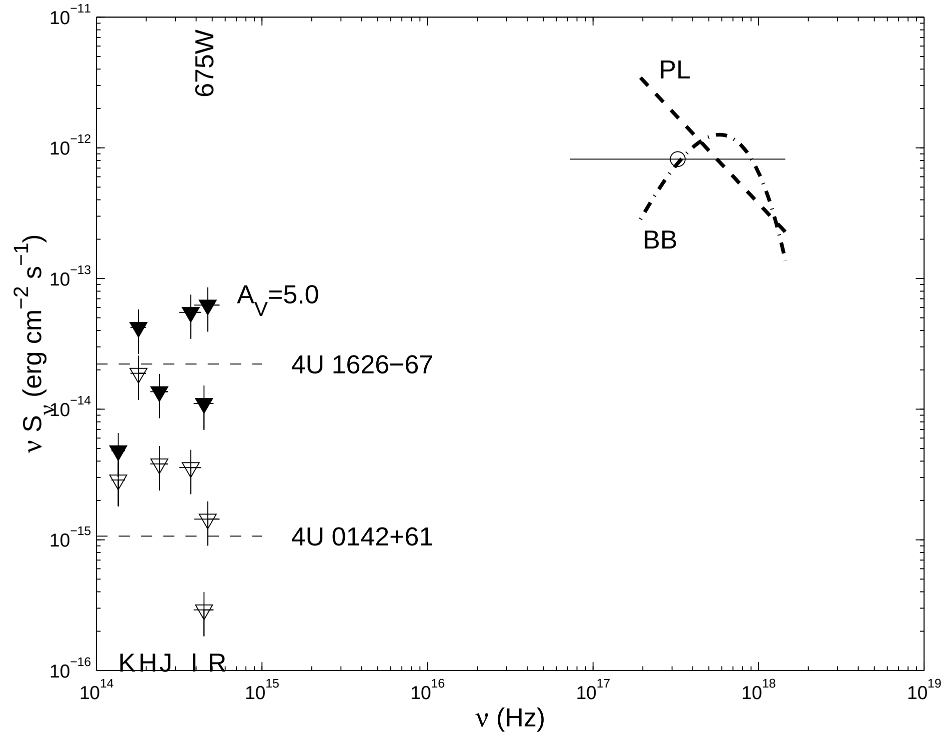

Figure 9.3 Spectral energy distribution for the XPS. This incorporates optical limits (this work) and X-ray data (Pavlov et al. 2000). The open triangles are the measured values, while the filled triangles are those corrected with $A_V = 5.0$ mag. The open circle is the measured CXO flux, while the thick lines are model spectra corrected for absorption: power-law (PL; dashed) and blackbody (BB; dash-dotted). The thin dashed lines are derived from the unabsorbed X-ray-to-R-band ratios of the AXP 4U 0142+61 (Hulleman et al. 2000, with $A_V = 4.4$ mag) and the very close X-ray binary 4U 1626−67 (Chakrabarty 1998, with $A_V = 0.2$ mag), assuming a 0.5–10 keV luminosity of 10^{34} ergs s^{-1} for the XPS. We do not plot the more complicated atmosphere models from Pavlov et al. (2000) or Chakrabarty et al. (2001).

Chapter 10

An X-ray Search for Compact Central Sources in Supernova Remnants I: SNRs G093.3+6.9, G315.4−2.3, G084.2+0.8, & G127.1+0.5[†]

D. L. Kaplan[a], D. A. Frail[b], B. M. Gaensler[c], E. V. Gotthelf[d], S. R. Kulkarni[a],
P. O. Slane[c], & A. Nechita[e]

[a]Department of Astronomy, 105-24 California Institute of Technology, Pasadena, CA 91125

[b]National Radio Astronomy Observatory, P.O. Box O, Socorro, NM 87801

[c]Harvard-Smithsonian Center for Astrophysics, 60 Garden Street, MS-6, Cambridge, MA 02138

[d]Columbia Astrophysics Laboratory, Columbia University, 550 West 120th Street, New York, NY 10027

[e]Harvard College, Cambridge, MA 02138

Abstract

Most astronomers now accept that stars more massive than about $9\,M_\odot$ explode as supernovae and leave stellar remnants, either neutron stars or black holes, with neutron stars being more prevalent. Recent modeling of the explosions suggests a significant diversity in the key natal properties—rotation rate, velocity, and magnetic field strength—of the resulting neutron stars that account for the association of active radio pulsars, pulsar wind nebulae, and magnetars with supernova remnants (SNRs). The discovery of a central X-ray source in Cas A, the youngest known Galactic SNR, dramatized the expected diversity. However, less than half of the SNRs within 5 kpc have identified central sources, and only three are identified as the remnants of Type Ia SNe. Here, we report a systematic effort to search for compact central sources in the remaining 23 SNRs of this distance limited sample. Our search was inspired, on empirical considerations, by the enigmatic faint X-ray source in Cas A; motivated, on theoretical grounds, by the expectation that young neutron stars emit cooling X-ray emission; and made possible by the superb angular resolution offered by the *Chandra* X-ray mission and the sensitivity of the *XMM-Newton* mission.

In this first paper we report *Chandra* observations of four SNRs (G093.3+6.9, G315.4−2.3, G084.2+0.8, and G127.1+0.5). We have undertaken a systematic optical/IR identification program of the X-ray sources detected in the field of each SNR. Foreground (flare stars, active stars) and background (active galactic nuclei) sources have identifiable IR/optical counterparts. In contrast, the counterparts of neutron stars (or

---

[†] A version of this chapter will be published in *The Astrophysical Journal Supplement*, vol. 153.

black holes) are expected to be very faint. We are able to account for all the well-detected X-ray sources and thus able to state with some confidence that there are no associated central sources down to a level of one tenth of that of the Cas A central source, $L_X \lesssim 10^{31}$ ergs s^{-1}. We compare our limits with cooling curves for neutron stars and find that any putative neutron stars in these SNRs must be cooling faster than expected for traditional $1.35\,M_\odot$ neutron stars and that any putative pulsar must have low spin-down luminosities $\dot{E} \lesssim 10^{34}$ ergs s^{-1}. However, our limits are unable to constrain the presence or absence of more unusual options, such as relatively more massive neutron stars with $M \gtrsim 1.45\,M_\odot$, neutron stars with exotic interiors, or quiescent black holes. In subsequent papers, we will report on the X-ray and optical/IR observations of the remaining members of the 5-kpc sample.

10.1 Introduction

Understanding the deaths of massive stars is one of the frontiers of modern astrophysics. Considerable observational evidence substantiates the idea that stars below $M_w \sim 8\,M_\odot$ end their lives as white dwarfs (Weidemann 1987), while the detection of neutrinos from SN 1987A dramatically illustrated that more massive stars undergo core collapse (Hirata et al. 1987). The outcome of core collapse can either be a neutron star or a black hole (Woosley, Heger, & Weaver 2002). However, there are great uncertainties in the mapping between initial mass of the star and the end product, and even more uncertainties in the natal properties of the stellar remnant. It is these uncertainties that give observers opportunities to make new discoveries and theorists to predict or “postdict” these discoveries.

The first issue—the state of the star prior to collapse—is very dependent on the mass loss history of stars (Heger et al. 2003), a phenomenon that is poorly understood and can easily be modified by the presence of a binary companion. For solar metallicity (the situation relevant to this paper), stars with between $M_l \sim 9\,M_\odot$ and $M_u \sim 25\,M_\odot$ are expected to form a neutron star (Heger et al. 2003), while stars above M_u are expected to form a black hole either by fall-back of material which transmutes the neutron star to a black hole or by direct collapse. As an aside we note that progenitors with masses between M_w and M_l may form an O-Ne-Mg white dwarf that may collapse to neutron stars or simply explode (Miyaji et al. 1980; Nomoto 1984, 1987).

The second issue—the natal properties of the stellar remnant—apparently involves delicate physics but has strong observational ramifications. The gravitational binding energy of a neutron star is 10^{53} ergs, of which only 1% appears to be coupled to the ejecta (which ultimately powers the SNR). Even more minuscule fractions go into rotational energy, kinetic energy (bulk motion) and magnetic fields. It is now generally agreed that three-dimensional effects in the explosion determine the natal properties (Burrows 2000; Kifonidis et al. 2003).

So far the discussion has assumed that the only gross parameter of interest is the mass of the star. However, it is likely that rotation of the progenitor can also profoundly affect the outcome.

These two issues are now propelling two different areas of inquiry. The relationship between the progenitor properties (mass, rotation) and the gross outcome of core collapse (neutron star or black hole) is observationally being determined by systematic studies of supernovae and GRBs and their interconnection. The second area is in understanding the natal properties of neutron stars, which is the main focus of the paper.

The discovery of pulsars in the Vela SNR (Large, Vaughan, & Mills 1968) and the Crab Nebula (Staelin & Reifenstein 1968) made concrete the suggestion that core collapse results in neutron stars (Baade & Zwicky 1934), some of which manifest themselves as radio pulsars. Young pulsars, in addition to pulsing in the radio, can and usually do power synchrotron nebulae (Weiler & Panagia 1978) that are indirect markers of pulsars. These synchrotron nebulae are commonly called pulsar wind nebulae, or PWNe. Over the following two decades, the notion that neutron stars resemble the Crab pulsar guided the search for central objects as well as intensive radio mapping of SNRs. As a result of these efforts, the term "composite" SNR (PWN + shell) was added to the SNR lexicon (see Milne et al. 1979).

However, over the last 5 years there have been three developments that have severely revised our picture of young neutron stars. First, astronomers have come to accept of tremendous diversity in the natal properties of young neutron stars. Anomalous X-ray pulsars (AXPs), soft γ-ray repeaters (SGRs), nearby thermal and radio-quiet neutron stars, and long-period radio pulsars with high inferred magnetic fields (HBPSR) are now routinely found in astronomical literature. These new classes of neutron stars have primarily come from high-energy (X-ray and γ-ray) observations. Second, there is appreciation that the radio luminosities of PWNe are poorly dependent on the spin-down luminosity of their central pulsars. For example, energetic pulsars may have faint PWNe (e.g., PSR J1119−6127; Gonzalez & Safi-Harb 2003), and very sensitive imaging of the regions around identified central sources has frequently yielded only upper limits to the surface brightness of putative PWNe (e.g., Gaensler, Bock, & Stappers 2000). Third, seven nearby cooling NSs have been identified (Haberl 2003) through *ROSAT* observations. Many of these neutron stars do not appear to be evolved versions of standard radio pulsars; e.g., RX J0720.4−3125 has a period longer than almost any known radio pulsar but has a typical B-field strength (Kaplan et al. 2002b; Zane et al. 2002).

While this diversity is clearly demonstrated observationally, theory and simulation cannot yet constrain the fundamental birth properties of neutron stars (e.g., Burrows et al. 2003). Models still have difficulties achieving explosions, much less following the activity in the post-collapse object in any detail.

Three years ago we began a program of observationally investigating the stellar remnants in a volume-limited census of Galactic supernova remnants. The approach we took was inspired by the first light picture of *Chandra*, the discovery of a central X-ray source in the well-studied and youngest known supernova remnant in our Galaxy, Cassiopeia A (Tananbaum 1999). The nature of the object continues to be debated (Pavlov et al. 2000; Chakrabarty et al. 2001; Murray et al. 2002a). However, one conclusion is crystal clear: the X-ray source is not a standard radio pulsar (unbeamed or otherwise).

The basis of our effort is that observationally, all central sources in SNRs known to date, regardless of the band of their initial identification (γ-ray, X-ray, or radio) appear to possess detectable X-ray emission. Theoretically, we expect thermal X-ray emission from young neutron stars. Thus, on both counts the search for central sources in young remnants is very well motivated. However, a follow-up program is essential since many other foreground sources such as flare stars, young stars, and accreting sources and background sources such as active galactic nuclei (AGNs) dominate the source counts (Hertz & Grindlay 1988; Mushotzky et al. 2000). Fortunately, the subarcsecond spatial resolution of *Chandra* allow efficient filtering of such contaminating objects.

To this end, we have identified a sample of SNRs within 5 kpc of the Sun that do not have known radio pulsars or PWNe and have not been associated with Type Ia explosions (Table 10.1. We successfully proposed for a "large" *Chandra* effort in AO-3 to image nine SNRs. This initial allocation has been supplemented with additional time in AO-4 of *Chandra* and AO-2 of *XMM.* Followup of the X-ray sources has been undertaken with a plethora of ground-based telescopes in the optical and near-IR bands (Palomar 60 inch, Palomar 200 inch, Las Campanas 40 inch, ESO 3.5 m, Magellan 6.5 m and Keck 10 m). Here, we report the first analysis of four SNRs for which the followup is now complete. The analysis for the remaining remnants will be reported in future papers.

The organization of the paper is as follows. In § 10.2 we summarize the empirical X-ray properties of the known sample of young neutron stars. Such a summary is essential since the guiding principle of our effort is to place our search for central objects against the framework of existing classes of sources. Specifically, we are not entirely guided by the relatively poorly understood cooling of neutron stars. Our search has been designed to find objects as faint as one tenth of the central X-ray source in Cassiopeia A. In § 10.3.1 we present a complete sample of cataloged SNRs within 5 kpc. Of these, 18 have an identified central source or are known to be a composite remnant, while three are thought to be the results of

Type Ia SNe. The remaining 23 seemingly "hollow" SNRs form our primary sample. By "hollow," we refer to SNRs that have distinct shells but no obvious indication of central neutron stars—see Vasisht & Gotthelf (1997). Section 10.4 has a general overview of our observations and analysis techniques: in § 10.4.1–10.4.4 we present a summary of the details of our *Chandra* observations and data reduction, and a likewise global description of the extensive multi-wavelength followup is given in § 10.4.5. We follow this by detailed descriptions of each of the first four SNRs, its observations, and identification of counterparts to its X-ray sources in §§ 10.5.1, 10.5.2, 10.5.3, and 10.5.4 for SNRs G093.3+6.9, G315.4−2.3, G084.2+0.8, and G127.1+0.5, respectively. It must be appreciated that complete identification of all X-ray sources is essential, given the small sample size. We hope that our detailed cataloging will be of help to efforts such as *ChaMPlane* (Grindlay et al. 2003). Finally, in § 10.6 we discuss what limits our data can place on the existence of central sources in the four SNRs, and we conclude in § 10.7.

Table 10.1. SNRs Within 5 kpc

SNR G	Other Name	Dist. (kpc)	Distance Method	Size[a] (arcmin)	Type[b]	Central Source/ Ia	X-ray?[d]	Sample[e]	Refs[f]
004.5+6.8	Kepler[g]	4.5	Optical expansion/H I	3	S	Ia?[c]	···	···	1
005.4−1.2	Duck	5	H I absorption	35	C?	pulsar?	yes	···	2,3
006.4−0.1	W 28[g]	3.0	OH masers	42	S	···	···	···	4
011.2−0.3		5	H I absorption	4	C	pulsar	yes	···	5
013.3−1.3		2.4	CO absorption	70	S	···	···	*XMM*-AO2	
034.7−0.4	W44	2.5	H I absorption	35	C	pulsar	yes	···	6,7,8
039.7−2.0	W50	5	VLBI	120	?	SS 433	yes	···	9,10
053.6−2.2	3C 400.2	2.8	H I association	33	S	···	···	*CXO*-AO3	
054.4−0.3	HC 40	3.3	CO association	40	S	···	···	*CXO*-AO3	
065.3+5.7		0.8	Optical velocity	310	S	···	···	*CXO*-AO4	
069.0+2.7	CTB 80	2	H I absorption	80	?	pulsar	yes	···	11,12
074.0−8.5	Cygnus Loop	0.44	Optical proper motion	230	S	X-ray source?	···	*CXO*-AO4	13
078.2+2.1	γ Cygni	1.2	OH/CO association	60	S	···	···	*XMM*-AO2	14
084.2−0.8		4.5	H I/CO association	20	S	···	···	*CXO*-AO3	
089.0+4.7	HB 21	0.8	OB association	120	S	···	···	···	
093.3+6.9	DA 530	3.5	H I absorption/X-ray fitting	27	S	···	···	*CXO*-AO3	
111.7−2.1	Cas A	3.4	Optical expansion	5	S	CCO	yes	···	15
114.3+0.3		3.5	H I association	90	S	pulsar	yes	···	16,17,18
116.5+1.1		4	H I association	80	S	···	···	···	
116.9+0.2	CTB 1	3.1	Optical lines	34	S	···	···	*CXO*-AO3	
119.5+10.2	CTA 1	1.4	H I association	90	S	γ-/X-ray neutron star	···	···	19,20,21
120.1+1.4	Tycho	2.4	Proper motion/shock vel.	8	S	Ia	···	···	22
127.1+0.5	R5	1.3	Assoc. with NGC 559	45	S	···	···	*CXO*-AO3	
130.7+3.1	3C 58	3.2	H I absorption	9	F	pulsar	yes	···	23,24
132.7+1.3	HB 3	2.2	Interactions with ISM	80	S	···	···	*XMM*-AO2	
156.2+5.7		1.3	NEI fits	110	S	···	···	*CXO*-AO4	
160.8+2.6	HB9	< 4	H I optical vel.	140	S	···	···	*CXO*-AO4	
166.0+4.3	VRO 42.05.01	4.5	H I association	55	S	···	···	*CXO*-AO3	
166.2+2.5		4	H I interaction	90	S	···	···	···	
180.0−1.7	S147	1.2	pulsar dispersion measure	180	S	pulsar	yes	···	25,26,27

Table 10.1

SNR G	Other Name	Dist. (kpc)	Distance Method	Size[a] (arcmin)	Type[b]	Central Source/ Ia	X-ray?[d]	Sample[e]	Refs[f]
184.6−5.8	Crab	2	proper motion/radial vel.	7	F	pulsar	yes	···	28
189.1+3.0	IC 443	1.5	Opt. vel./assoc. with S249	45	S	neutron star	yes	···	29
203.0+12.0	Monogem Ring	0.3	O VI absorption/modeling	1500	S	pulsar	yes	···	30
205.5+0.5	Monoceros	1.2	Optical velocity	220	S	···	···	*CXO*-AO4	
260.4−3.4	Puppis A	2.2	H I association	60	S	CCO	yes	···	31,32
263.9−3.3	Vela	0.3	pulsar parallax	255	C	pulsar	yes	···	33
296.5+10.0	PKS 1209−51/52	2.1	H I association	90	S	CCO/X-ray pulsar	yes	···	34,35
309.8+0.0		3.6	H I absorption	25	S	···	···	*CXO*-AO3	
315.4−2.3	RCW 86	2.8	Optical lines	42	S	···	···	*CXO*-AO3	36
327.4+0.4	Kes 27	4.3	H I absorption/interact.	30	S	···	···	···	
327.6+14.6	SN 1006	2.2	Spectra/proper motion	30	S	Ia	···	···	37,38
330.0+15.0	Lupus Loop	0.8	H I	180	S	···	···	*CXO*-AO4	
332.4−0.4	RCW 103	3.3	H I absorption	10	S	CCO	yes	···	39
343.1−2.3		2.5	H I absorption	32	C	pulsar	yes	···	40,41
354.1+0.1		5	recombination lines	15	C	pulsar?	no	···	42,43

[a] Major axis.

[b] Types are: S (shell), C (composite), and F (filled, or PWN), as determined by Green (2001). A question mark indicates that the type is poorly determined.

[c] Indicates whether a central source is known, or whether the SNR is thought to be of type Ia. If a central source is known and it falls into one of the classes from § 10.2, it is labeled accordingly.

[d] Indicates whether the central source has been detected in X-rays. See Table 10.2.

[e] Refers to X-ray samples of shell SNRs described in § 10.4.1.

[f] References deal only with the central source or Ia classification. General SNR properties were taken from Green (2001) and references therein.

[g] Has already been observed with *Chandra*.

References. — 1: Kinugasa & Tsunemi (1999); 2: Frail & Kulkarni (1991); 3: Manchester et al. (1991); 4: Yusef-Zadeh et al. (2000); 5: Torii et al. (1997); 6: Wolszczan, Cordes, & Dewey (1991); 7: Harrus et al. (1997); 8: Petre et al. (2002); 9: Clark, Green, & Caswell (1975); 10: Watson et al. (1983); 11: Kulkarni et al. (1988); 12: Migliazzo et al. (2002); 13: Miyata et al. (1998b); 14: Brazier et al. (1996); 15: Tananbaum (1999); 16: Kulkarni et al. (1993); 17: Becker, Brazier, & Trümper (1996); 18: Fürst, Reich, & Seiradakis (1993); 19: Seward, Schmidt, & Slane (1995); 20: Slane et al. (1997); 21: Slane et al. (2004); 22: Baade (1945); 23: Murray et al. (2002b); 24: Camilo et al. (2002d); 25: Anderson et al. (1996); 26: Romani & Ng (2003); 27: Kramer et al. (2003); 28: Comella et al. (1969); 29: Olbert et al. (2001); 30: Thorsett et al. (2003); 31: Pavlov, Zavlin, & Trümper (1999); 32: Zavlin, Trümper, & Pavlov (1999); 33: Large et al. (1968); 34: Helfand & Becker (1984); 35: Zavlin et al. (2000); 36: Vink et al. (2000); 37: Fesen et al. (1988); 38: Allen et al. (2001); 39: Gotthelf, Petre, & Hwang (1997); 40: McAdam, Osborne, & Parkinson (1993); 41: Becker, Brazier, & Trümper (1995); 42: Frail et al. (1994); 43: Becker & Trümper (1997).

10.2 X-ray Properties of Young Neutron Stars

The first manifestations of neutron stars associated with SNRs were traditional rotation-powered pulsars (such as those in the Crab and Vela SNRs). With the advent of high-energy missions a number of new classes were discovered. These include soft gamma repeaters (SGRs; for a review see Hurley 2000), anomalous X-ray pulsars (AXPs; for a review see Mereghetti et al. 2002a), and compact central objects (CCOs; for a review see Pavlov et al. 2002). Finally, recent radio surveys have uncovered central Crab-like pulsars with field strengths beyond 10^{13} G—the so-called high-B pulsars (HBPSRs; Camilo et al. 2000; Gotthelf et al. 2000). SGRs and AXPs have been suggested to be magnetars (Duncan & Thompson 1992; Thompson & Duncan 1995): neutron stars with extremely strong field strengths, $B \gtrsim 10^{15}$ G. CCO is the generic name for a heterogeneous group of X-ray sources emitting largely unpulsed soft (thermal) emission and lacking detectable radio emission. Another possibly related class are the isolated neutron stars (INSs; Haberl 2003), also called radio-quiet neutron stars (RQNSs) or dim thermal neutron stars (DTNSs). Below we summarize the general properties of each of these classes in turn.

10.2.1 Radio Pulsars

Radio pulsars observed in the X-rays often have two-component spectra. Here, the thermal component tends to be softer ($\lesssim 0.3$ keV) and the power-law component harder ($\Gamma = 1.5$–2.5) than those of AXPs; see Becker & Trümper (1997), Possenti et al. (2002), and Tables 10.2 and 10.3. A rough relation was originally discovered by Seward & Wang (1988) between the X-ray luminosity and the rotational energy loss rate $\dot{E}$: $L_{\mathrm{X},0.1-2.4\,\mathrm{keV}} \approx 10^{-3}\dot{E}$ (Becker & Trümper 1997). While this relation has been updated for specific classes of neutron stars and different energy bands (e.g., Possenti et al. 2002) and has considerable scatter, it still holds on average . The observed X-ray luminosities of radio pulsars then vary between 10^{31} and 10^{37} ergs s^{-1}, depending on their values of $\dot{E}$ (and through that, their values of P and $\dot{P}$).

While only millisecond pulsars and "old" ($> 10^6$ yr) pulsars from the sample of Possenti et al. (2002) have values of $\dot{E}$ less than 10^{34} ergs s^{-1}, there have been three young pulsars discovered recently that are more extreme. These are the HBPSRs PSR J1814−1744 ($P = 4.0$ s and $\dot{E} = 4.7 \times 10^{32}$ ergs s^{-1}; Camilo et al. 2000), PSR J1847−0130 ($P = 6.7$ s and $\dot{E} = 1.7 \times 10^{32}$ ergs s^{-1}; McLaughlin et al. 2003), and PSR J1718-37184 ($P = 3.4$ s and $\dot{E} = 1.6 \times 10^{33}$ ergs s^{-1}; McLaughlin et al. 2003). The first two do not have detected X-ray emission (Pivovaroff, Kaspi, & Camilo 2000, McLaughlin et al. 2003), while the third does have a very faint ($L_{2-10\,\mathrm{keV}} \approx 9 \times 10^{29}$ ergs s^{-1}) X-ray counterpart [the energetic ($\dot{E} \gtrsim 10^{36}$ ergs s^{-1}) HBPSRs have brighter X-ray counterparts (Gaensler et al. 2002; Gonzalez & Safi-Harb 2003, Helfand, Collins, & Gotthelf 2003)], consistent with their values of $\dot{E}$.

10.2.2 Pulsar Wind Nebulae

Pulsar wind nebulae (PWNe) are bright, centrally condensed nebulae with nonthermal (power-law) X-ray and radio spectra often associated with young, energetic pulsars and SNRs (here we refer only to "bubble" PWNe, as differentiated by the bow-shock PWNe produced by the motion of the pulsars through the ambient medium; for reviews, see Chevalier 1998 or Gaensler 2003). The photon indices range from 1.3 to 2.3 (Gotthelf 2003), similar to those of pulsars, but they are roughly ~ 10 times as luminous for a given $\dot{E}$ (Gotthelf 2004) and the sizes range from a few arcseconds to several arcminutes. PWNe, both X-ray and radio, offer a great advantage over bare radio pulsars for inferring the existence of neutron stars: they are unbeamed. This fact has historically been used in a number of cases to infer the existence of energetic pulsars where the pulsar had not been seen itself, such as 3C 58 (Becker, Helfand, & Szymkowiak 1982, Frail & Moffett 1993), N157B (Wang & Gotthelf 1998), and Kes 75 (Becker & Helfand 1984).

The evolution of a PWN (see van der Swaluw, Downes, & Keegan 2003 for a recent review) begins as it expands supersonically through the shocked ejecta of the SNR. Here the radius of the PWN is $\propto \dot{E}^{1/5}t^{6/5}$

Table 10.2. X-ray Properties of Central Sources from Table 10.1

Source	SNR G	kT_∞^{BB} (keV)	Γ	$\log_{10} L_X$[a] (ergs s^{-1})	X-ray PWN?	Age[b] (kyr)	Refs
PSR B1757−24	005.4−1.2	···	1.6	33.0	Yes[e]	> 39	1,2
PSR J1811−1925	011.2−0.3	···	1.7	33.7	Yes	1.6	3,4,5
PSR B1853+01	034.7−0.4	···	1.3	31.2	Yes	20	6
SS 433[c]	039.7−2.0	···	0.7	35	···	5–40	7
PSR B1951+32	069.0+2.7	···	1.6	32.9	Yes	64	8
CXO J232327.8+584842	111.7−2.1	0.7	3.0	33.5/34.7[h]	No	0.3	9
PSR B2334+61	114.3+0.3	···	2.0[d]	31.7	··· [g]	41	10
RX J0007.0+7302	119.5+10.2	0.14	1.5	31.2	Yes	13	11
PSR J0205+6449	130.7+3.1	···	1.7	32.2	Yes	0.8	12,13
PSR J0538+2817	180.0−1.7	0.16	···	32.9	Yes	30	14,15
PSR B0531+21	184.6−5.8	···	1.6	35.8	Yes	1.0	16
CXO J061705.3+222127	189.1+3.0	0.7	···	31.3	Yes	30	17
PSR B0656+14	203.0+12.0	0.07+0.14	1.5	31.1	No	100	18,19,20
RX J0822−4300	260.4−3.4	0.4	···	33.5	No	3.7	21,22
PSR B0833−45	263.9−3.3	···	2.5	32.5	Yes	11	23
1E 1207.4−5209	296.5+10.0	0.26	···	33.1	No	7	24
1E 161348−5055[c]	332.4−0.4	0.6	···	32.1–33.9	No	2	25
PSR B1706−44	343.1−2.3	0.14	2.0	32.6	Yes[e]	18	26
PSR B1727−33	354.1+0.1	···	···	$< 32.6/< 32.5$	··· [g]	15	16

References. — 1: Kaspi et al. (2001); 2: Gaensler & Frail (2000); 3: Torii et al. (1997); 4: Roberts et al. (2003); 5: Stephenson & Green (2002); 6: Petre et al. (2002); 7: Kotani et al. (1996); 8: Migliazzo et al. (2002); 9: Mereghetti, Tiengo, & Israel (2002b); 10: Becker et al. (1996); 11: Slane et al. (2004); 12: Slane et al. (2002); 13: Stephenson (1971); 14: Romani & Ng (2003); 15: Kramer et al. (2003); 16: Becker & Trümper (1997); 17: Olbert et al. (2001); 18: Marshall & Schulz (2002); 19: Brisken et al. (2003b); 20: Greiveldinger et al. (1996); 21: Zavlin et al. (1999); 22: Pavlov et al. (2002); 23: Pavlov et al. (2001c); 24: Sanwal et al. (2002); 25: Gotthelf, Petre, & Vasisht (1999a); 26: Gotthelf, Halpern, & Dodson (2002). In addition, general pulsar data have been taken from Hobbs & Manchester (2003).

[a] Luminosity for only the point-source in the 0.5–2.0 keV band, assuming the distance from Table 10.1. Upper limits to the luminosity are given for a blackbody with $kT_\infty = 0.25$ keV and for a power-law with $\Gamma = 2.2$.

[b] The best estimate of the age of the SNR if known, otherwise the pulsar spin-down age $P/2\dot{P}$.

[c] Possibly not an isolated neutron star.

[d] Assumed.

[e] The X-ray PWNe here are significantly fainter compared to the pulsars than for other sources (Kaspi et al. 2001; Gotthelf et al. 2002).

[g] The current X-ray data do not sufficiently constrain the existence of a nebula.

[h] The current X-ray data do not constrain the spectrum: either a blackbody or power-law model is possible.

Table 10.3. Properties of Rotation-Powered Pulsars Associated with SNRs

PSR	SNR	P (ms)	$\tau^{\rm a}$ (kyr)	$\log_{10}\dot{E}$ (ergs s^{-1})	D (kpc)	$\log_{10} L_X{}^{\rm b}$ (ergs s^{-1})	Refs.
J0205+6449	G130.7+3.1	66	5.4	37.4	3.2	32.2	
J0537−6910	N157B$^{\rm c}$	16	5.0	38.7	49.4	38.3	1,2
J0538+2817	G180.0−1.7	143	620	34.7	1.8	32.9	
B0531+21	G184.6−5.8	33	1.2	38.7	2.0	35.8	
B0540−69	0540−69.3$^{\rm c}$	50	1.7	38.2	49.4	36.3	2,3
B0833−45	G263.9−3.3	89	11	36.8	0.3	32.5	
J1016−5857	G284.3−1.8	107	21	36.5	3	32.5	4
J1119−6127	G292.2−0.5	408	1.6	36.4	6	32.5	5
J1124−5916	G292.0+1.8	135	2.9	37.1	> 6	33.0	6,7
B1338−62	G308.8−0.1	193	12	36.1	9	32.8	8
B1509−58	G320.4−1.2	151	1.6	37.3	5.2	34.1	9,10
B1643−43	G341.2+0.9	232	33	35.5	7	...	
B1706−44	G343.1−2.3	102	18	36.5	2.5	32.6	
B1727−33	G354.1+0.1	139	26	36.1	5	<32.6	
B1757−24	G005.4−1.2	125	16	36.4	5	33.0	
J1811−1925	G011.2−0.3	65	23	36.8	5	33.7	
J1846−0258	G029.7−0.3	324	0.72	36.9	19	35.4	11
B1853+01	G034.7−0.4	267	20	35.6	2.5	31.2	
J1930+1852	G054.1+0.3	136	2.9	37.1	5	33.3	12
B1951+32	G069.0+2.7	40	110	36.6	2	35	
J2229+6114	G106.6+2.9	52	11	37.3	3	32.8	13,14
B2334+61	G114.3+0.3	495	41	34.8	3.5	31.7	

Note. — Pulsar-SNR associations are largely drawn from Kaspi & Helfand (2002).

[a] Characteristic age $\tau \equiv P/2\dot{P}$.

[b] X-ray luminosity in the 0.5–2.0 keV band. Upper limits to the luminosity are given for a power-law with $\Gamma = 2.2$.

[c] In the Large Magellanic Cloud.

References. — 1: Wang et al. (2001); 2: Gotthelf (2003); 3: Gotthelf & Wang (2000); 4: Camilo et al. (2001); 5: Gonzalez & Safi-Harb (2003); 6: Hughes et al. (2001); 7: Gaensler & Wallace (2003); 8: Gaensler, Kaspi, & Manchester (2003); 9: Greiveldinger et al. (1995); 10: Gaensler et al. (2002); 11: Helfand et al. (2003); 12: Camilo et al. (2002a); 13: Kothes, Uyaniker, & Pineault (2001); 14: Halpern et al. (2001) . Also see references from Tabs. 10.1 and 10.2.

(assuming that the total luminosity of the neutron star is $\propto \dot{E}$; van der Swaluw et al. 2001; van der Swaluw 2003), so it depends only weakly on $\dot{E}$ but more strongly on the remnant age. Eventually, however, the reverse shock of the SNR crashes back on the PWN at a time $t_{\rm col} \sim 10^4$ yr (van der Swaluw et al. 2003, although this depends on the ejecta mass). After this occurs , the spherical portion of the PWN continues to expand subsonically with its radius $\propto t^{11/15}$ (van der Swaluw et al. 2001), while at the same time the pulsar moves away from the center of the SNR and begins to form a bow-shock nebula (when its motion through the SNR ejecta becomes supersonic at ages of $\gtrsim 3000$ yr; van der Swaluw et al. 2003). The passage of the reverse shock should reheat and energize the PWN, causing it to brighten.

10.2.3 AXPs & SGRs

In the X-ray band, traditional AXPs are characterized by a two-component spectrum: a power-law with index 3–4, and a soft blackbody with temperature 0.3–0.7 keV (Mereghetti et al. 2002a). While the distances are quite uncertain, especially to those not in SNRs, the luminosities are relatively constant and greater than 10^{34} ergs s^{-1} (in the 1–10 keV band; Mereghetti et al. 2002a), substantially greater than their spin-down energy loss rates. These sources are characterized by slow spin periods (6–12 s) with substantial period derivatives that indicate the presence of very strong magnetic fields ($B > 10^{14}$ G).

There are two objects, however, that may indicate AXPs can have substantial X-ray variability. First, AX J184453$-$025640 (Vasisht et al. 2000) is a 7 s X-ray pulsar that varied by a factor of $\gtrsim 10$ in flux but whose properties are otherwise found to be fully consistent with an AXP. More recently, the AXP-candidate XTE J1810$-$197 was discovered in *RXTE* data (Ibrahim et al. 2003); *Chandra* and *XMM* data confirm the pulsations present in the *RXTE* data and allow for comparison with archival *Einstein*, *ROSAT*, and *ASCA* data where it is a factor of ≈ 100 fainter (Gotthelf et al. 2004). In the bright (current) state, XTE J1810$-$197 has an absorbed X-ray flux (0.5–10 keV) of $\approx 4 \times 10^{-11}$ ergs cm^{-2} s^{-1}, while *ROSAT* data from 1993 have a flux of $\approx 5 \times 10^{-13}$ ergs cm^{-2} s^{-1}. Converting the fluxes to luminosities is uncertain because of the largely unconstrained distance, but Gotthelf et al. (2004) determine an upper limit of 5 kpc. With this, the current luminosity in the 0.5–2 keV range is $\lesssim 3 \times 10^{35}$ ergs s^{-1}, similar to other AXPs, but the "quiescent" luminosity is $\sim 10^{33}$ ergs s^{-1}. While less certain, AX J184453$-$025640 shows a roughly similar range of luminosities.

SGRs have roughly similar quiescent luminosities (Hurley 2000), although their spectra are somewhat harder. However, none of the SGRs is firmly associated with an SNR (Gaensler et al. 2001b). There is now mounting observational evidence that SGRs and AXPs are related objects (Gavriil, Kaspi, & Woods 2002, Kulkarni et al. 2003; Kaspi et al. 2003), confirming the hypothesis of Thompson & Duncan (1996). In what follows, we do not treat the SGRs as separate objects since their quiescent X-ray properties are sufficiently similar to those of AXPs.

10.2.4 Cooling Radio-Quiet Neutron Stars/Compact Central Objects

Regardless of emission at other wavelengths, young neutron stars should have thermal X-ray emission from their surfaces as they cool. Indeed, it is likely that *ROSAT* has detected a number of nearby, $\sim 10^6$ yr (too old to be in SNRs) neutron stars (Treves et al. 2000; Haberl 2003) with no detectable radio emission (Kaplan, Kulkarni, & van Kerkwijk 2003a, Kaplan et al. 2003b; Johnston 2003)—hence the name RQNS. The *ROSAT* sources have temperatures of $\lesssim 100$ eV. This thermal emission is almost certain to be present at some level, regardless of whatever other processes are occurring (radio emission, accretion, etc.), but the exact level of emission depends on the mass of the neutron star and on the presence or absence of exotic particles (pions, kaons, hyperons, free quarks, etc.) and/or processes (i.e., direct URCA cooling) in the core (Kaminker, Yakovlev, & Gnedin 2002, Tsuruta et al. 2002).

A number of superficially similar sources known as CCOs have been discovered in SNRs, such as the sources in Cas A and Puppis A. The temperatures of CCOs should be higher than those of the field RQNSs by a factor of 5 or so, depending on cooling physics (e.g., Page 1998). For some of these sources, it is likely that there is little if any radio emission owing to the low values of $\dot{E}$ (Kaplan et al. 2002b), but for others the lack of such emission may just be beaming effect (i.e., as with Geminga), implying beaming fractions of $\sim 50\%$ (Brazier & Johnston 1999). The radii of the blackbody fits to the CCOs in Table 10.2 are typically less than the 10–15 km expected for a neutron star (presumably since a blackbody, while providing an adequate spectral fit, does not actually represent the emission of the surface)—values of $R_\infty \approx 1$–3 km are common.

10.3 Survey Design

10.3.1 A Volume-Limited Sample of Shell SNRs

The success of this effort hinges upon defining an objectively constructed sample so that strong conclusions can be drawn not only from detections but also nondetections. Bearing this in mind, we identified all of the SNRs[1] that are at a distance of less than 5 kpc as determined from a reliable distance determination (e.g., derived from the kinematic velocity of associated line emission or a parallax, rather than from N_H or the $\Sigma - D$ relation). This sample is comprised of the 45 SNRs listed in Table 10.1. This is not an entirely complete sample, as illustrated by the void in the third quadrant in Figure 10.1 and the relative paucity of distant SNRs toward the Galactic center, but the criteria for inclusion in the sample (detected SNR with a robust distance) should not be correlated with the properties of the central objects. We estimate that we cover $\sim 15\%$ of the Galactic molecular gas, and hence sites of massive star formation, with our distance criteria (based on Dame 1993). For the X-ray observations we eliminated all SNRs that were of Type Ia or those that are already associated with a NS and/or central synchrotron nebula[2]—i.e., we only include those that are type S in Table 10.1.

The shell remnants are the major remaining sample in which the neutron star population has not been systematically assessed. For the SNRs with PWNe, some estimate as to the neutron star's properties can be made even if the source itself has not been detected, but the shell remnants permit no such estimation. Therefore, these shell-type SNRs are the subject of our survey. Below we first discuss the status of neutron star velocities, an issue that affects our survey design. We then continue to describe the survey itself.

10.3.2 Neutron Star Velocities

Radio pulsars have high space velocities, among the highest in the Galaxy, as measured from timing, scintillation, and interferometry. Various authors (e.g., Hansen & Phinney 1997; Lorimer et al. 1997; Cordes & Chernoff 1998; Arzoumanian et al. 2002) have modeled the distribution slightly differently, but they all agree that a substantial number of pulsars move with speeds greater than 300 km s^{-1}, while $\approx 90\%$ have speeds less than 700 km s^{-1}.

The space velocities of neutron stars can also be inferred from their offsets from the centers of associated supernova remnants. Such an approach demands reliable estimates for the distance and age of the system under consideration. It also assumes that the geometric center of an SNR is easily identifiable, and that this center corresponds to the site of the supernova. With these caveats in mind, such an analysis potentially provides a direct measurement of the neutron star velocity distribution, free from the many selection effects associated with proper motion studies.

---

[1] Drawn from the Galactic SNR Catalog (Green 2000). Since we constructed the table, the catalog has been updated (Green 2001), and it is this list and more recent references that we use to determine the properties of the SNRs.

[2] We assume that sources like IC 443, which has a synchrotron nebula but where pulsations have not yet been detected, still do have central neutron stars.

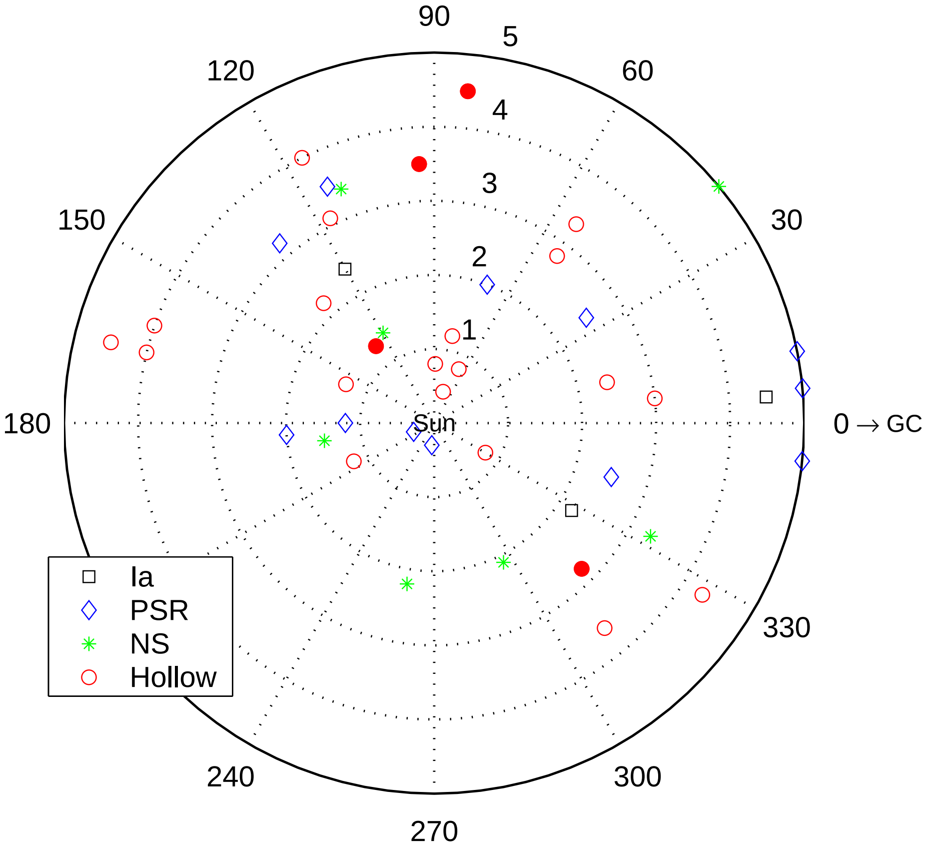

Figure 10.1 Galactic distribution of SNRs from Table 10.1. Galactic longitude l (degrees) is plotted against distance (kpc), with the Sun at the origin and the Galactic center to the right. Black squares are the Ia SNRs, blue diamonds are associated with radio pulsars, green asterisks are associated with other types of neutron stars (RQNS, etc.), and the red circles are the hollow SNRs. The four filled circles are the SNRs from this paper with detailed analyses.

Frail, Goss, & Whiteoak (1994) carried out a detailed study of the offsets of radio pulsars from the centers of SNRs. From a sample of 15 pulsar/SNR associations, Frail et al. (1994) concluded that young radio pulsars are born with projected space velocities ranging between 50 and 1000 km s^{-1}, with a mean of $\sim$500 km s^{-1}. While at that time this distribution represented a somewhat more rapidly moving population than that which had been inferred from proper motion studies, it agrees well with the more recent determinations discussed above.

However, the preceding discussion assumes that pulsars were born near the centers of what are now SNRs. Some authors dispute that this is always the case (Gvaramadze 2002), suggesting that if the SN progenitors have large space velocities they could evacuate a bubble with their winds, move toward the edges of those bubbles, and then explode (in a so-called off-center cavity explosion). This would make the origins of neutron stars closer to the edges of SNRs. While an interesting possibility for a few sources, the large number of associations where the neutron star is close to the center of the SNR mean that this hypothesis cannot work for the majority of sources.

It is not yet known whether other populations of neutron star have different velocity distributions from that seen for radio pulsars. The location of several SGRs on or beyond the perimeters of SNRs originally led to the suggestion that SGRs had very high space velocities, $v_{\perp} \sim 1000-2000$ km s^{-1}, as might result from the anisotropic neutrino emission associated with the formation of such highly-magnetized objects (e.g., Duncan & Thompson 1992). However, it has since been argued that many of these SGR/SNR associations are spurious (Lorimer & Xilouris 2000; Gaensler et al. 2001b), in which case these inferred velocities are not valid. On the other hand, several AXPs have convincing associations with young SNRs. In all these cases, the AXP lies close to the geometric center of its SNR, implying projected space velocities for this population $\lesssim$ 500 km s^{-1} (Gaensler, Gotthelf, & Vasisht 1999, Gaensler et al. 2001b), consistent with the velocities of radio pulsars. The emerging and still enigmatic class of central compact objects (CCOs) are also centrally located in young SNRs (see Pavlov et al. 2002 for a review), and most likely also have relatively low space velocities.

What little is known about the velocities of older neutron stars that are not radio pulsars roughly agrees with the situation for radio pulsars: the velocities are high, $\gtrsim$ 100 km s^{-1}. Specifically, the velocities of the INSs RX J1856.5$-$3754 and RX J0720.4$-$3125 are both $\approx$ 200 km s^{-1} (Kaplan, van Kerkwijk, & Anderson 2002c, Motch, Zavlin, & Haberl 2003).

10.4 Observations and Data Analysis

In this section we give an overview of the analysis procedure that we used for the different SNRs. We start by describing the splitting of the SNRs into observationally-based subsamples, of which the *Chandra* ACIS subsample is the major component discussed here (§ 10.4.1). We then describe the analysis of the *Chandra* data that were used to identify potential compact objects (§ 10.4.2). Finally, we describe the motivation for and basic analysis of the optical and infrared followup observations that were used to reject contaminating foreground and background X-ray sources (§ 10.4.5). Following this section, we present the actual detailed analyses of the four SNRs in this paper (§ 10.5).

10.4.1 *Chandra* ACIS Survey

We defined three subsamples among the 23 SNRs that had no central sources from Table 10.1. The subsamples were defined largely by size so that the X-ray observations have a good chance of identifying the central compact source. Our primary subsample was designed for the *Chandra* ACIS-I detector, with its 16$'$ field of view. We parameterize as follows: a neutron star has a typical transverse velocity of $100v_{100}$ km s^{-1}, distance d in kpc, and an age of $10^4 t_4$ yr. To ensure that a NS lies within 8$'$ of its SNRs geometric center (and so will fall on the ACIS-I array; see Figs. 10.2–10.5 for illustrations of the ACIS field

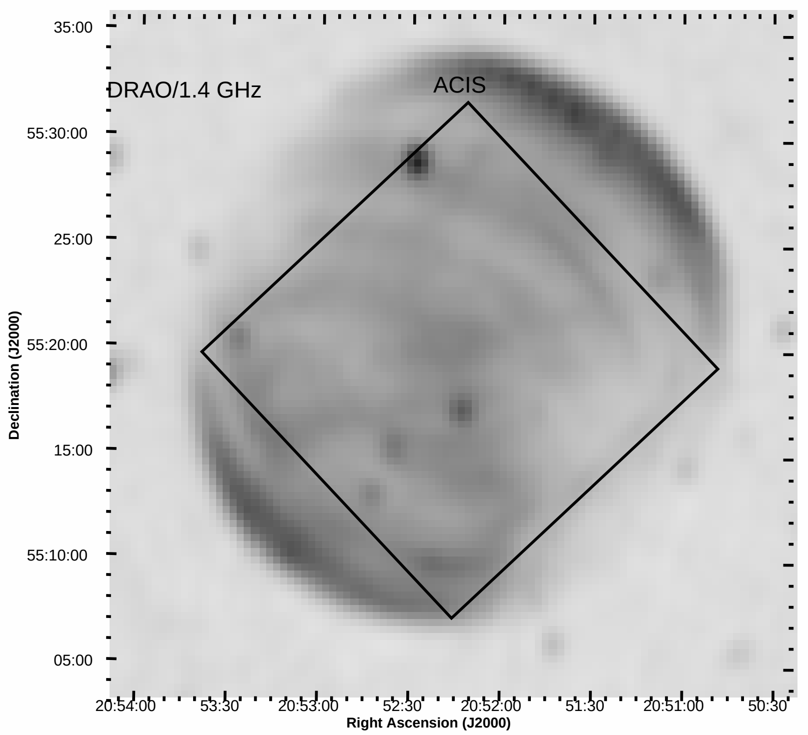

Figure 10.2 DRAO 1.4 GHz radio image of SNR G093.3+6.9 (Landecker et al. 1999), showing the placement of the ACIS-I detector.

of view), we require $t_4 \leq 2.27d/v_{100}$. For a Sedov-phase remnant, we have $t_4 = 7 \times 10^{-3}\theta d T_7^{-1/2}$, where θ arcmin is the SNR diameter and $10^7\,T_7$ K is the shock temperature. Our limit is thus $\theta \leq 324 T_7^{1/2} v_{100}^{-1}$. We expect $T_7 \approx 1$ for a broad range of SNR ages; given the somewhat weak dependence on T we adopt $T_7 = 1$ in this calculation. A conservative constraint on pulsar velocities is $v_{100} \leq 7$. This then yields the condition $\theta \lesssim 46'$. There are 14 SNRs that meet this criterion, of which three (Cas A, IC 443, and Kepler) have already been observed by *Chandra*. This then leaves 11 SNRs for further *Chandra* observations, although SNR G327.4+0.4 only recently had a distance determination and was not included in the original *Chandra* sample. We therefore proposed for ACIS-I observations of the 10 remaining SNRs (identified by *CXO*-AO3 in Tab. 10.1), and were awarded observations of nine (the tenth, G006.4−0.1, was awarded to J. Rho in another AO-3 proposal).

We then constructed a sample of the larger SNRs for *XMM*, and one of the largest SNRs using the literature and the *ROSAT* All-Sky Survey Bright Source Catalog (BSC) (Voges et al. 1996), coupled with *Chandra* snap-shot images. These samples are identified by *XMM*-AO2 and *CXO*-AO4 in Table 10.1 (our *XMM* proposal was for seven SNRs, of which we were only allocated time for the three that are identified as "*XMM*-AO2'). We defer detailed discussion of these samples to later papers.

To determine exposure times for these sources, we examined the types of neutron stars found in the SNRs from Table 10.1 (see also Chakrabarty et al. 2001 and § 10.2). These neutron stars are listed in Table 10.2. We see two groups among them: those with nonthermal spectra (characterized by a power-law with photon index $\Gamma \sim 1.6$) and those with thermal spectra (characterized by a blackbody with temperature $kT_\infty \approx 0.5$ keV). Among the shell-type SNRs in Table 10.1, the thermal sources predominate, and these also produce the lowest X-ray count rates. Therefore, we computed exposure times for a thermal source with $kT_\infty = 0.25$ keV (toward the low-end of those in Tab. 10.2) and a bolometric luminosity

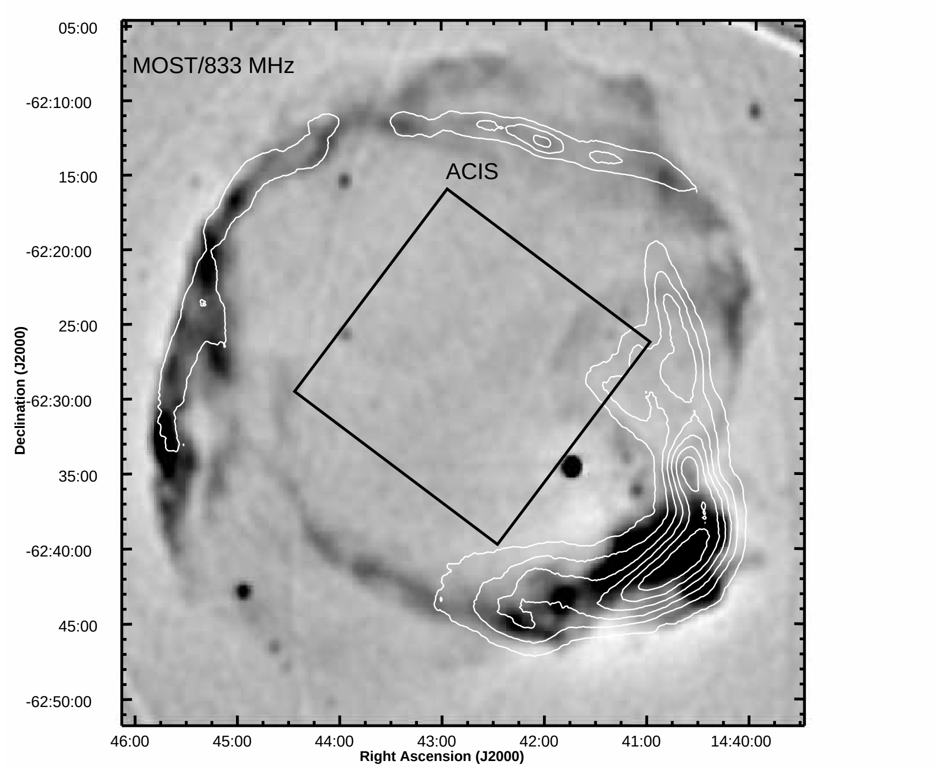

Figure 10.3 MOST (Whiteoak & Green 1996) 833 MHz radio image of SNR G315.4−2.3, showing the placement of the ACIS-I detector. The bright region toward the south-west is the nebula RCW 86 (Rodgers, Campbell, & Whiteoak 1960). The contours are from *ROSAT* PSPC data (sequence RP500078).

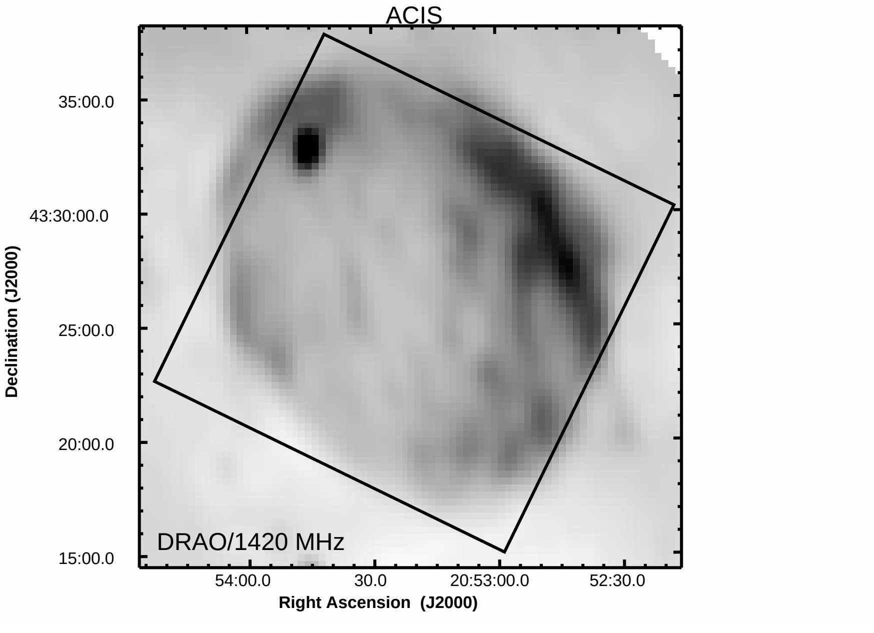

Figure 10.4 DRAO 1.4 GHz radio image of SNR G084.2−0.8 (Taylor et al. 2003), showing the placement of the ACIS-I detector.

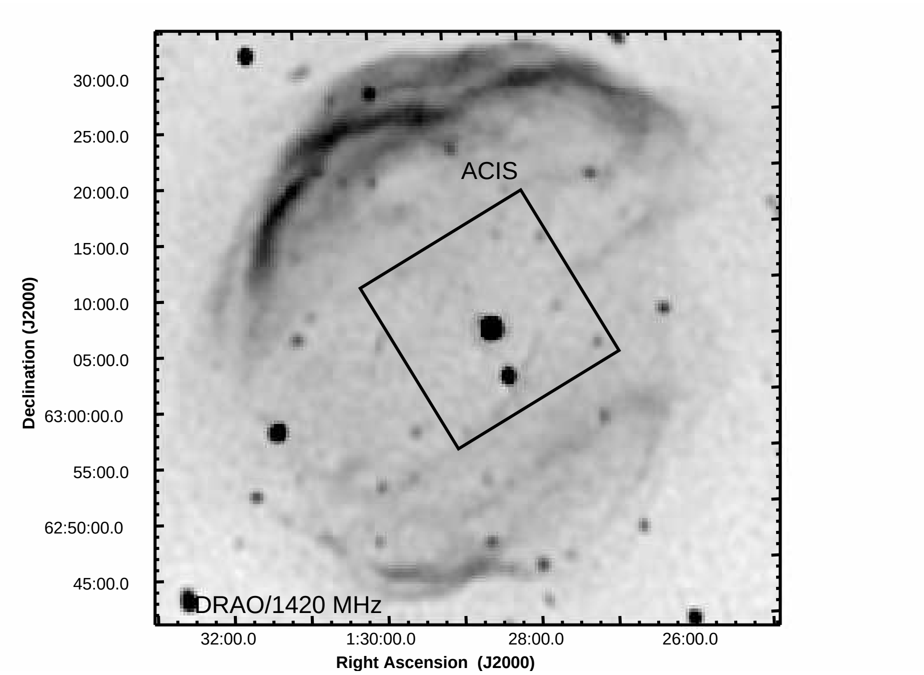

Figure 10.5 DRAO 1.4 GHz radio image of SNR G127.1+0.5, showing the placement of the ACIS-I detector.

$L_{\rm bol} = 10^{32}$ ergs s^{-1}, a factor of ~ 10 lower than those of most of the thermal sources. For the column densities $N_{\rm H}$ we used the best available estimates from the literature. For these shell SNRs, there is very little contribution from the SNR itself in the interior, especially with the resolution of *Chandra*, so this was not an issue, although we calculate the expected background contribution, using surface-brightnesses compiled from the literature. The exposure times are those that should detect a source with a prototypical spectrum but a factor of 10 less luminous than normal with a significance of at least $5\,\sigma$ above the background.

10.4.2 X-ray Point-Source Detection

To analyze the data, we first reprocessed the raw (level 1) event data to take advantage of updates in the *Chandra* calibration since the data were first taken. Specifically, the reprocessing included a correction for charge transfer inefficiency (CTI; Townsley et al. 2002),[3] and we removed the ±0.5 pixel randomization added to the events. We did not include any correction for the degradation of the quantum efficiency (QE) of the ACIS detectors,[4] as at no point did we do a complete spectral analysis that would have used the available correction techniques.[5] These corrections are minor ($\approx 10\%$ yr^{-1}) and are beyond our level of accuracy. We selected only events that have the "standard" *ASCA* grades (0, 2, 3, 4, and 6). After generating a new level 2 event file, we corrected the data for *Chandra* aspect errors[6]: for example, the change for SNR G093.3+6.9 was $-0\farcs13$ in right ascension and $0\farcs32$ in declination. Smoothed images of the data are shown in Figure 10.6–10.9.

Starting from this level 2 event file, we processed the data and extracted sources much as was done in the *Chandra* Deep Field (CDF; Brandt et al. 2001) and the 82 ks observation of the Orion Nebula

---

[3] Following `http://asc.harvard.edu/ciao/threads/acisapplycti/`.

[4] See `http://cxc.harvard.edu/cal/Acis/Cal_prods/qeDeg/`.

[5] See `http://cxc.harvard.edu/ciao/threads/apply_acisabs/`.

[6] Following `http://asc.harvard.edu/cal/ASPECT/fix_offset/fix_offset.cgi`.

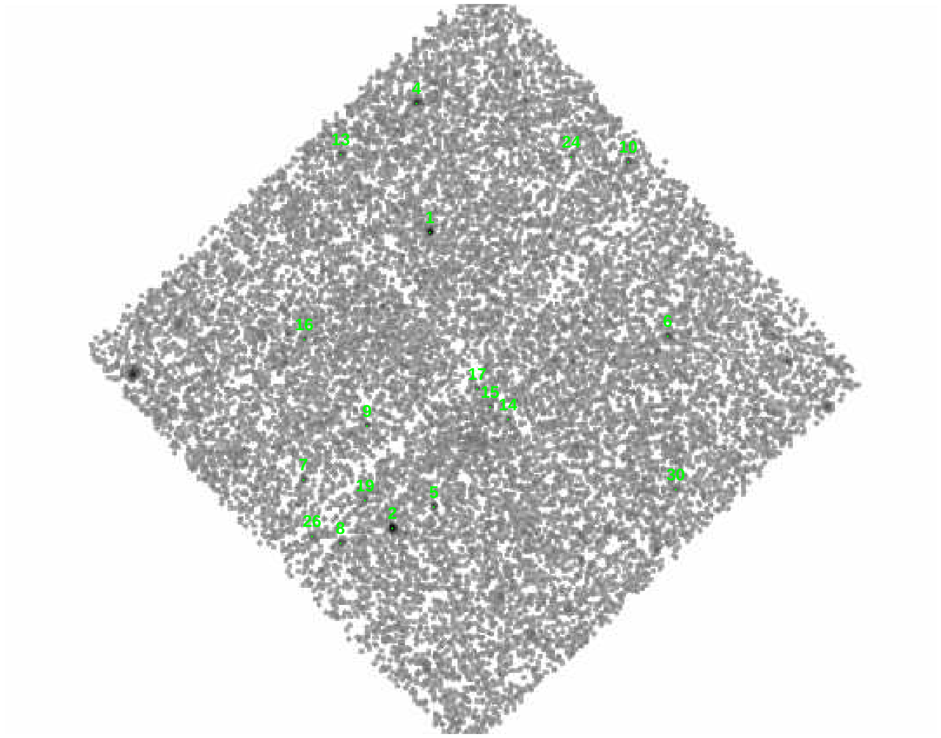

Figure 10.6 Smoothed ACIS-I image (0.3–8.0 keV) of SNR G093.3+6.9. North is up, and east is to the left. The brightness is scaled proportional to the logarithm of the counts in $2''$ bins, smoothed with a Gaussian filter. The sources from Table 10.4 are labeled.

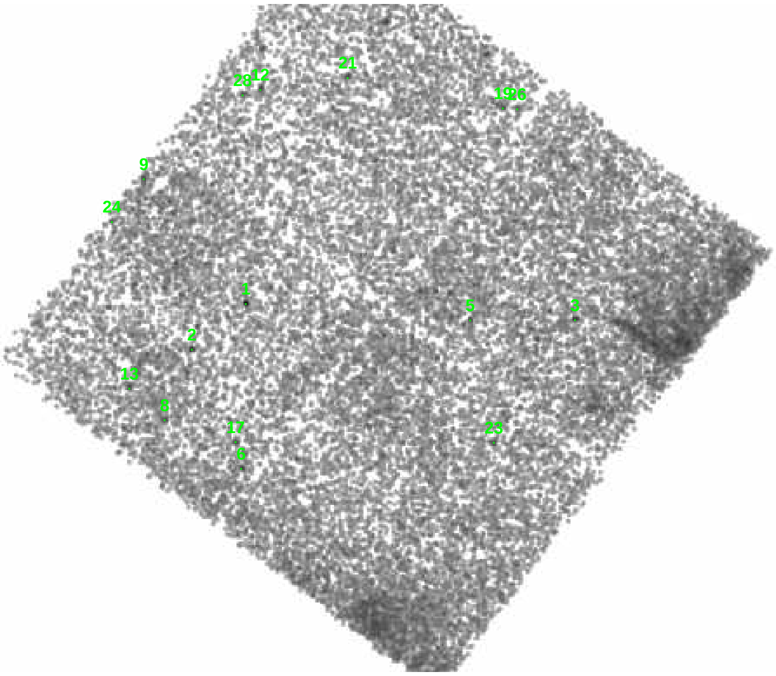

Figure 10.7 Smoothed ACIS-I image (0.3–8.0 keV) of SNR G315.4−2.3. North is up, and east is to the left. The brightness is scaled proportional to the logarithm of the counts in 2″ bins, smoothed with a Gaussian filter. The sources from Table 10.5 are labeled. The diffuse emission to the west and south-west is the RCW 86 complex.

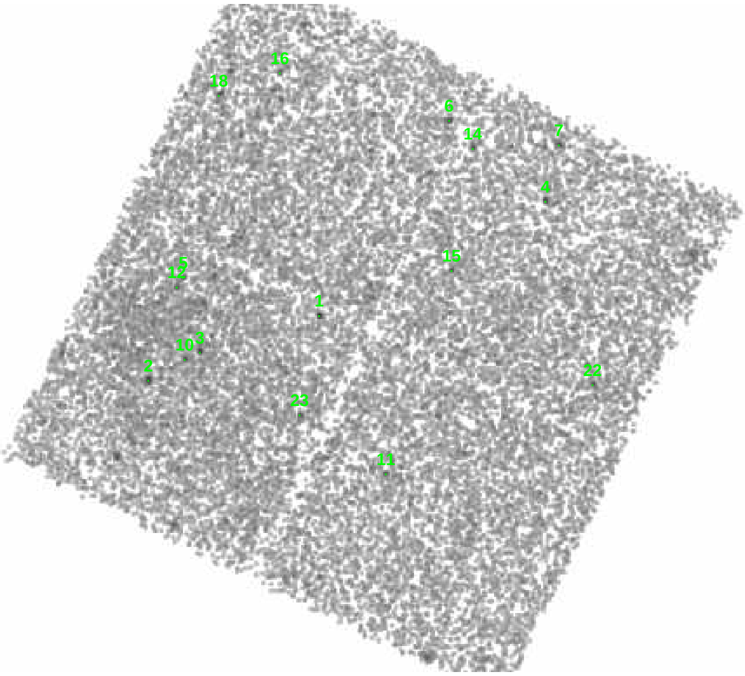

Figure 10.8 Smoothed ACIS-I image (0.3–8.0 keV) of SNR G084.2−0.8. North is up, and east is to the left. The brightness is scaled proportional to the logarithm of the counts in 2″ bins, smoothed with a Gaussian filter. The sources from Table 10.6 are labeled.

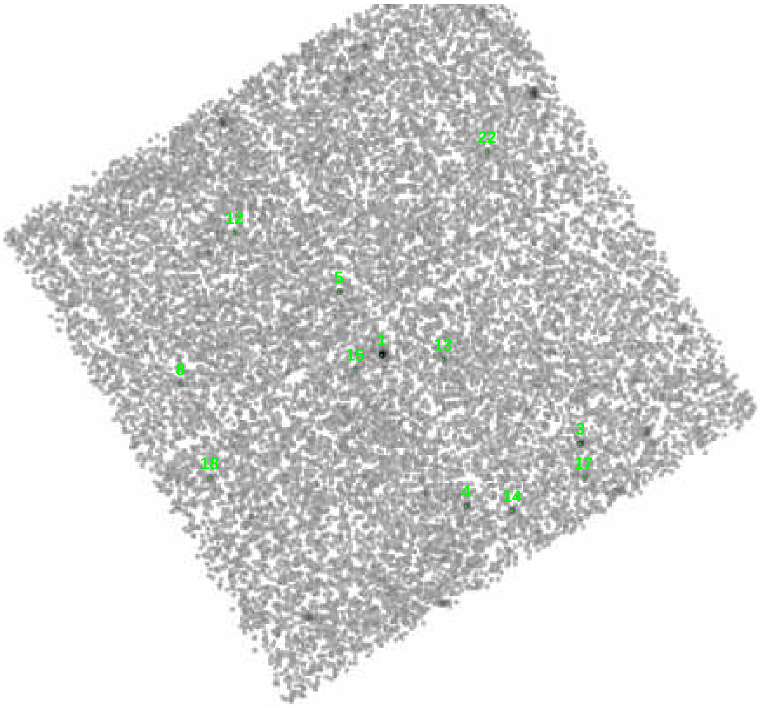

Figure 10.9 Smoothed ACIS-I image (0.3–8.0 keV) of SNR G127.1+0.5. North is up, and east is to the left. The brightness is scaled proportional to the logarithm of the counts in 2″ bins, smoothed with a Gaussian filter. The sources from Table 10.7 are labeled.

(Feigelson et al. 2002). First we separated the level 2 events by energy into three bands: 0.3–2.0 keV (L), 2.0–8.0 keV (H), and 0.3–8.0 keV (A). These bands are slightly modified from those of the CDF and Orion, as our potential sources are softer. We then separated the data by CCD, using only the four ACIS-I CCDs. This then gave 12 separate event files (3 bands × 4 CCDs).

For each of these event files, we generated instrument and exposure maps, following standard CIAO threads.[7] Creating an exposure map requires a source model: for this model, we assumed a blackbody with a temperature of $kT_\infty = 0.25$ keV (similar to that of the Cas A central point source) and a column density appropriate for each SNR (§§ 10.5.1–10.5.4).

Then, for each of the event files (now with exposure maps), we ran `wavdetect` (Freeman et al. 2002), using wavelet scales of $1, \sqrt{2}, 2, \sqrt{8}, \ldots, 16$ pixels and a nominal energy of 1.5 keV. The significance threshold was 10^{-6}.

We then merged the `wavdetect` source files for further analysis. First we merged by CCD, creating a source list for each band. Then, to merge the data from different bands (which are spatially coincident), we considered sources identical if the positions (as determined by `wavdetect`) differed by less than $2\farcs5$, for sources at off-axis angles of less than $6'$, or differed by less than $4''$, for sources at off-axis angles of $\geq 6'$. While these are large tolerances given the typical astrometric uncertainty of `wavdetect` ($0\farcs6$ for on-axis sources, approaching $1\farcs5$ for off-axis sources), the source density is so low (~ 0.2 arcmin^{-2} for this observation) that the number of false matches is negligible. Even so, only five sources had match-radii of more than $1\farcs5$, and most were less than $0\farcs5$. After manually examining the list of sources, we then removed those that appeared spurious. We then limited the source list to those sources with ≥ 10 counts. This limit allows us to have enough photons that the position is well determined (critical when trying to identify counterparts) and that an estimate can be made of the hardness ratio. Given that our exposure times were calculated such that a low-luminosity neutron star would be detected with more than 25 counts, the 10 count limit is conservative. The final merged source list contains 12–18 sources, depending on the SNR. The sources are all consistent with being point sources.

For each source, we then performed additional aperture photometry. This allowed us to (1) use knowledge of the psf size in determination of the source counts and (2) obtain source counts for sources that were detected in only one or two bands. The radii of the photometric apertures were determined from the analytic fit to the 95% encircled energy radius given in Feigelson et al. (2002). We measured the number of counts in these apertures for each band and subtracted the number of counts in a background annulus extending from 2 to 3 times the 95% encircled energy radius to determine the net number of counts. To aid in comparison with the CDF/Orion data sets, we also extracted photons in the more standard 0.5–2.0 keV band. The final source data are presented in Tables 10.4–10.7. We plot the L-band counts versus the H-band counts for the detected sources in Figures 10.10–10.13.

10.4.2.1 Nomenclature

Herein, for convenience, we label the *Chandra*-detected X-ray sources by their field identification—for example, SNR G093.3+6.9:5 refers to the fifth source in the SNR G093.3+6.9 field. This is not meant to imply that all of these sources are associated with the SNRs—the vast majority are not. These are meant to be internal designations only and do not replace the official IAU names of the form CXOU JHHMMSS.s±DDMMSS, where HHMMSS.s represents the right ascension and ±DDMMSS represents the declination. When detailing the source identifications (Tabs. 10.4–10.7) we give both the internal and official names, but in the rest of this paper we use only the internal names. When initially identifying X-ray sources we numbered then consecutively, but the numbers in Tables 10.4–10.7 are no longer consecutive as we have removed sources at radii greater than $8'$ and with fewer than 10 counts (§ 10.4.2).

---

[7] `http://asc.harvard.edu/ciao/threads/expmap_acis_single/`.

Table 10.4. X-ray Sources in SNR G093.3+6.9

ID[a]	CXOU J[b]	α (J2000)	δ	r_{90}[c] ($''$)	ΔR[d] ($'$)	Counts$_{\rm L}$	Counts$_{\rm H}$	Counts$_{\rm A}$	Counts (0.5 − 2.0 keV)	HR$_{\rm L,H}$[e]
1	205222.8+552343	20:52:22.89	+55:23:43.7	0.5	3.5	310(20)	47(7)	360(20)	290(20)	−0.73(0.04)
2	205230.9+551437	20:52:30.98	+55:14:37.5	0.6	6.4	270(20)	127(12)	390(20)	260(20)	−0.35(0.05)
4	205225.8+552741	20:52:25.82	+55:27:41.6	1.3	7.4	47(7)	48(7)	93.9(10.2)	44(7)	0.01(0.11)
5	205222.0+551516	20:52:22.01	+55:15:16.9	0.8	5.3	20(5)	13(4)	33(6)	19(4)	−0.20(0.18)
6	205231.3+552031	20:51:31.37	+55:20:31.6	1.4	6.1	14(4)	18(4)	32(6)	13(4)	0.13(0.19)
7	205250.2+551606	20:52:50.20	+55:16:06.6	1.5	6.8	23(5)	2.2(1.8)	25(5)	22(5)	−0.83(0.14)
8	205242.1+551409	20:52:42.19	+55:14:09.8	1.6	7.5	17(4)	8.0(3.2)	25(5)	16(4)	−0.36(0.21)
9	205226.4+551746	20:52:36.48	+55:17:46.0	0.7	4.2	11(3)	7.1(2.8)	18(4)	11(3)	−0.19(0.24)
10	205139.8+552553	20:51:39.85	+55:25:53.4	1.7	7.3	11(4)	11(3)	22(5)	9.3(3.5)	−0.02(0.23)
13	205242.2+552607	20:52:42.26	+55:26:07.1	1.8	6.9	9.3(3.3)	13(4)	22(5)	9.5(3.3)	0.16(0.23)
14	205205.9+551758	20:52:05.96	+55:17:58.5	0.7	2.8	2.1(1.5)	9.2(3.2)	11(3)	2.1(1.5)	0.63(0.24)
15	205209.8+551821	20:52:09.87	+55:18:21.2	0.8	2.2	7.4(2.8)	4.0(2.1)	11(3)	7.4(2.8)	−0.30(0.30)
16	205250.0+552025	20:52:50.09	+55:20:25.6	1.1	5.1	10(3)	1.4(1.5)	12(4)	10(3)	−0.77(0.24)
17	205212.6+551854	20:52:12.65	+55:18:54.4	0.6	1.6	3.2(1.8)	6.3(2.6)	10(3)	3.2(1.8)	0.33(0.31)
19	205236.8+551528	20:52:36.89	+55:15:28.8	1.4	6.0	4.3(2.4)	8.4(3.0)	12(4)	3.2(2.1)	0.33(0.29)
24	205152.2+552602	20:51:52.23	+55:26:02.7	1.8	6.4	7.7(3.0)	4.5(2.4)	12(4)	7.1(2.8)	−0.26(0.30)
26	205248.3+551422	20:52:48.32	+55:14:22.3	3.1	7.8	5.9(2.8)	5.3(2.6)	12(4)	5.9(2.8)	−0.05(0.34)
30	205129.7+551548	20:51:29.72	+55:15:48.5	3.0	7.9	5.1(2.6)	9.0(3.3)	14(4)	4.0(2.4)	0.28(0.29)

[a] Internal identifier of the form SNR G093.3+6.9:N.

[b] Official IAU name.

[c] Approximate 90% confidence radius.

[d] Angle from the center of the SNR.

[e] Hardness ratio, computed according to $(C_{\rm H} - C_{\rm L})/(C_{\rm H} + C_{\rm L})$, where C is the number of counts in a band.

Note. — Quantities in parentheses are 1-σ uncertainties. Here and in Tables 10.5–10.7, Counts$_A$ = Counts$_L$ + Counts$_H$, but the three columns have been rounded separately.

Table 10.5. X-ray Sources in SNR G315.4−2.3

ID[a]	CXOU J[b]	α (J2000)	δ (J2000)	r_{90}[c] (″)	ΔR[d] (′)	Counts$_{\mathrm{L}}$	Counts$_{\mathrm{H}}$	Counts$_{\mathrm{A}}$	Counts (0.5 − 2.0 keV)	HR$_{\mathrm{L,H}}$[e]
1	144319.3−622804	14:43:19.31	−62:28:04.2	0.7	3.4	20(5)	25(5)	45(7)	19(4)	0.11(0.15)
2	144333.7−622928	14:43:33.74	−62:29:28.2	1.1	5.2	20(5)	1.6(1.5)	22(5)	20(5)	−0.85(0.13)
3	144151.5−622833	14:41:51.59	−62:28:33.5	2.0	6.8	11(4)	10(3)	22(5)	12(4)	−0.05(0.23)
5	144219.5−622834	14:42:19.54	−62:28:34.5	1.1	3.5	2.9(1.8)	8.4(3)	11(3)	2.9(1.8)	0.49(0.28)
6	144320.6−623308	14:43:20.63	−62:33:08.6	2.0	6.0	12(4)	−0.5(0.2)	11(4)	12(4)	−1.09(0.04)
8	144341.0−623138	14:43:41.05	−62:31:38.3	1.9	6.8	13(4)	2.4(1.8)	16(4)	14(4)	−0.69(0.21)
9	144346.3−622413	14:43:46.37	−62:24:13.1	3.4	7.7	16(5)	2.2(1.8)	16(5)	14(4)	−0.77(0.19)
12	144315.3−622128	14:43:15.36	−62:21:28.8	1.6	7.5	8.0(3.2)	6.1(2.8)	14(4)	7.2(3)	−0.13(0.30)
13	144350.4−623040	14:43:50.45	−62:30:40.0	2.2	7.4	12(4)	3.2(2.1)	15(4)	12(4)	−0.57(0.25)
17	144322.1−623219	14:43:22.12	−62:32:19.3	1.7	5.4	4.3(2.4)	10(3)	15(4)	4.3(2.4)	0.41(0.27)
19	144210.9−622202	14:42:10.94	−62:22:02.8	2.7	7.7	10(4)	3.5(2.1)	14(4)	8.8(3.3)	−0.50(0.26)
21	144252.1−622107	14:42:52.16	−62:21:07.1	2.4	7.2	10(4)	5.8(2.6)	17(4)	9.8(3.5)	−0.28(0.26)
23	144213.1−623220	14:42:13.16	−62:32:20.4	1.5	5.8	9.2(3.2)	3.7(2.1)	12(4)	9.0(3.2)	−0.43(0.27)
26	144207.1−622204	14:42:07.16	−62:22:04.3	3.8	8.0	7.5(3.2)	4.0(2.4)	12(4)	8.0(3.2)	−0.30(0.33)
28	144320.0−622138	14:43:20.06	−62:21:38.7	1.9	7.5	11(4)	0.6(1.5)	12(4)	11(4)	−0.90(0.24)

[a] Internal identifier of the form SNR G315.4−2.3:N.

[b] Official IAU name.

[c] Approximate 90% confidence radius.

[d] Angle from the center of the SNR.

[e] Hardness ratio, computed according to $(C_{\mathrm{H}} - C_{\mathrm{L}})/(C_{\mathrm{H}} + C_{\mathrm{L}})$, where C is the number of counts in a band.

Note. — Quantities in parentheses are 1-σ uncertainties.

Table 10.6. X-ray Sources in SNR G084.2−0.8

ID[a]	CXOU J[b]	α (J2000)	δ (J2000)	r_{90}[c] (″)	ΔR[d] (′)	$\mathrm{Counts_L}$	$\mathrm{Counts_H}$	$\mathrm{Counts_A}$	Counts (0.5 − 2.0 keV)	$\mathrm{HR_{L,H}}$[e]
1	205328.9+432659	20:53:28.96	+43:26:59.1	0.5	1.3	40(6)	−0.3(0.1)	40(6)	38(6)	−1.01(0.01)
2	205357.9+432459	20:53:57.92	+43:24:59.3	1.3	6.9	5.9(2.8)	37(6)	44(7)	7.2(3)	0.73(0.12)
3	205349.1+432551	20:53:49.18	+43:25:51.2	0.9	5.1	11(3)	22(5)	33(6)	11(3)	0.33(0.17)
4	205250.5+433030	20:52:50.55	+43:30:30.0	1.2	6.5	27(5)	4.5(2.4)	31(6)	27(5)	−0.71(0.14)
5	205352.0+422809	20:53:52.03	+43:28:09.7	1.2	5.5	6.1(2.6)	14(4)	20(5)	5.8(2.6)	0.40(0.21)
6	205306.9+423259	20:53:06.89	+43:32:59.7	1.2	6.3	−0.5(0.2)	27(6)	26(6)	−0.5(0.2)	1.04(0.02)
7	205248.2+433214	20:52:48.25	+43:32:14.0	2.0	7.9	4.3(2.4)	23(5)	26(6)	4.0(2.4)	0.69(0.16)
10	205351.7+432537	20:53:51.76	+43:25:37.9	1.4	5.7	1.7(1.8)	14(4)	16(4)	1.7(1.8)	0.79(0.21)
11	205317.6+432206	20:53:17.66	+43:22:06.8	1.2	5.2	0.3(1.1)	13(4)	13(4)	0.3(1.1)	0.95(0.16)
12	205353.1+432751	20:53:53.13	+43:27:51.5	1.1	5.7	8.7(3.2)	4.0(2.4)	13(4)	8.7(3.2)	−0.37(0.30)
14	205302.8+433207	20:53:02.87	+43:32:07.6	1.5	5.9	12(4)	2.4(1.8)	13(4)	12(4)	−0.67(0.23)
15	205306.5+432822	20:53:06.50	+43:28:22.2	0.6	3.0	4.2(2.1)	11(3)	16(4)	4.2(2.1)	0.46(0.23)
16	205335.6+433427	20:53:35.66	+43:34:27.6	1.9	7.6	14(4)	0.4(1.9)	12(4)	9.3(3.5)	−0.94(0.26)
18	205346.0+433345	20:53:46.04	+43:33:45.7	2.4	7.8	−0.4(1.5)	20(5)	20(5)	−0.1(1.5)	1.04(0.16)
22	205242.6+432451	20:52:42.61	+43:24:51.0	1.2	7.6	9.9(3.7)	4.9(2.8)	15(5)	8.3(3.3)	−0.34(0.30)
23	205332.2+432355	20:53:32.27	+43:23:55.7	0.7	3.9	−0.3(0.1)	17(4)	17(4)	−0.3(0.1)	1.03(0.02)

[a] Internal identifier of the form SNR G084.2−0.8:N.

[b] Official IAU name.

[c] Approximate 90% confidence radius.

[d] Angle from the center of the SNR.

[e] Hardness ratio, computed according to $(C_\mathrm{H} - C_\mathrm{L})/(C_\mathrm{H} + C_\mathrm{L})$, where C is the number of counts in a band.

Note. — Quantities in parentheses are 1-σ uncertainties.

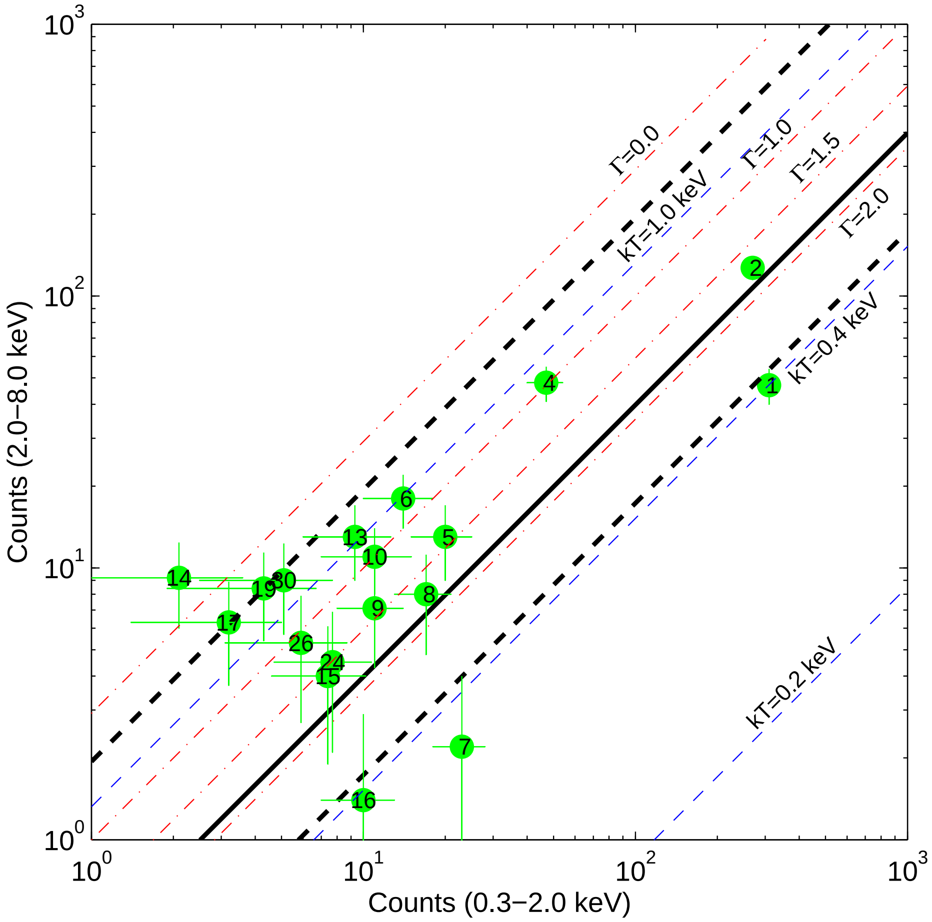

Figure 10.10 L-band count vs. H-band counts for SNR G093.3+6.9. The sources from Table 10.4 are shown in green and are numbered. Model spectra (computed using `PIMMS`) with $N_{\rm H} = 2 \times 10^{21}$ cm^{-2} are plotted as diagonal lines: power-law models as red dash-dotted lines (Γ is as indicated) and blackbody models as blue dashed lines (kT_∞ is as indicated). The solid thick black line represents the median spectrum from the CDF/Orion studies, with the dashed thick black lines showing the 25- and 75-percentile spectra.

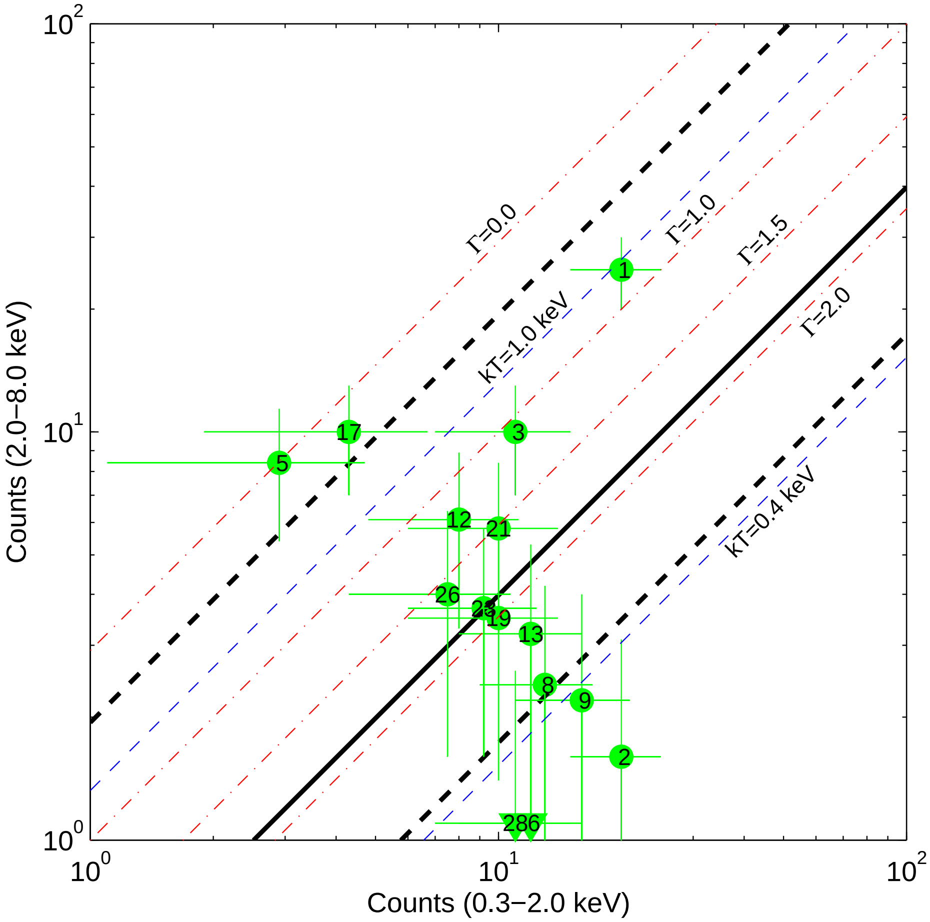

Figure 10.11 L-band count vs. H-band counts for SNR G315.4−2.3. The sources from Table 10.5 are shown in green and are numbered. Model spectra (computed using `PIMMS`) with $N_{\mathrm{H}} = 2 \times 10^{21}$ cm^{-2} are plotted as diagonal lines: power-law models as red dash-dotted lines (Γ is as indicated) and blackbody models as blue dashed lines (kT_∞ is as indicated). The solid thick black line represents the median spectrum from the CDF/Orion studies, with the dashed thick black lines showing the 25- and 75-percentile spectra.

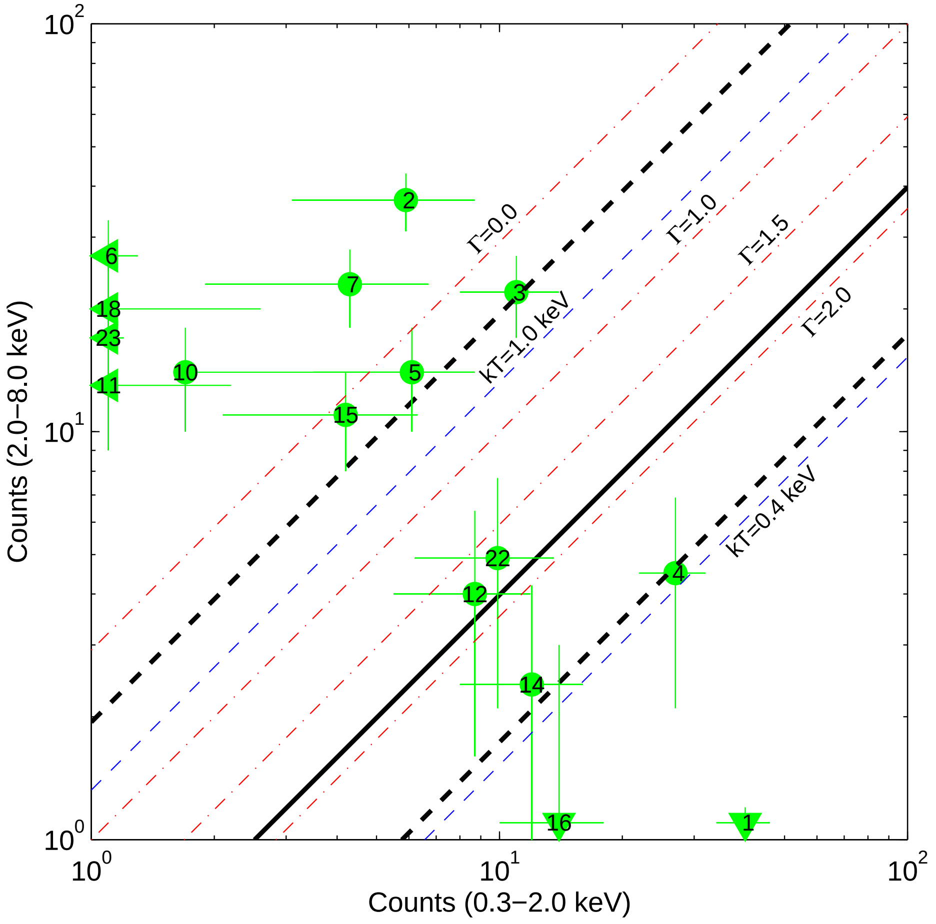

Figure 10.12 L-band count vs. H-band counts for SNR G084.2−0.8. The sources from Table 10.6 are shown in green and are numbered. Model spectra (computed using `PIMMS`) with $N_{\mathrm{H}} = 2 \times 10^{21}$ cm^{-2} are plotted as diagonal lines: power-law models as red dash-dotted lines (Γ is as indicated) and blackbody models as blue dashed lines (kT_∞ is as indicated). The solid thick black line represents the median spectrum from the CDF/Orion studies, with the dashed thick black lines showing the 25- and 75-percentile spectra.

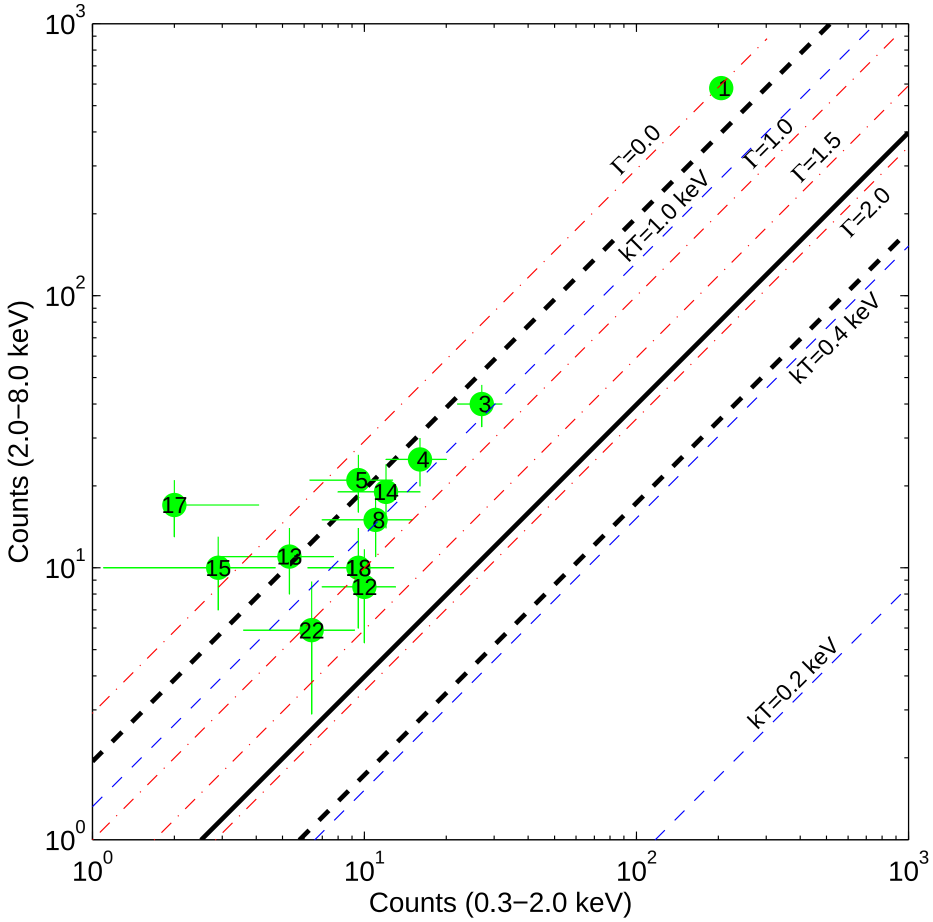

Figure 10.13 L-band count vs. H-band counts for SNR G127.1+0.5. The sources from Table 10.7 are shown in green and are numbered. Model spectra (computed using `PIMMS`) with $N_{\rm H} = 2 \times 10^{21}$ cm^{-2} are plotted as diagonal lines: power-law models as red dash-dotted lines (Γ is as indicated) and blackbody models as blue dashed lines (kT_∞ is as indicated). The solid thick black line represents the median spectrum from the CDF/Orion studies, with the dashed thick black lines showing the 25- and 75-percentile spectra.

Table 10.7. X-ray Sources in SNR G127.1+0.5

ID[a]	CXOU J[b]	α (J2000)	δ	r_{90}[c] ($''$)	ΔR[d] ($'$)	$\mathrm{Counts_L}$	$\mathrm{Counts_H}$	$\mathrm{Counts_A}$	$\mathrm{Counts_{0.5-2.0\ keV}}$	$\mathrm{HR_{L,H}}$[e]
1	012830.6+630629	01:28:30.64	+63:06:29.9	0.4	0.2	205(15)	580(20)	780(30)	182(14)	0.48(0.03)
3	012736.6+630345	01:27:36.60	+63:03:45.5	1.3	6.9	27(5)	40(7)	68(9)	25(5)	0.19(0.13)
4	012807.7+630150	01:28:07.72	+63:01:50.5	1.3	5.5	16(4)	25(5)	41(7)	17(4)	0.21(0.16)
5	012842.3+630825	01:28:42.31	+63:08:25.6	0.6	2.2	9.5(3.2)	21(5)	32(6)	8.4(3)	0.38(0.17)
8	012925.4+630535	01:29:25.43	+63:05:35.3	1.7	6.1	11(4)	15(4)	26(5)	9.3(3.3)	0.17(0.21)
12	012910.8+631014	01:29:10.86	+63:10:14.8	1.6	5.7	10(3)	8.5(3.2)	20(5)	11(3)	−0.10(0.25)
13	012813.9+630621	01:28:13.91	+63:06:21.1	0.9	2.1	5.3(2.4)	11(3)	17(4)	6.3(2.6)	0.33(0.24)
14	012755.2+630141	01:27:55.23	+63:01:41.6	1.5	6.4	12(4)	19(5)	33(6)	7.9(3)	0.23(0.18)
15	012837.8+630602	01:28:37.83	+63:06:02.8	0.8	0.8	2.9(1.8)	10(3)	13(4)	2.9(1.8)	0.56(0.24)
17	012735.7+630241	01:27:35.75	+63:02:41.6	1.7	7.4	2.0(2.1)	17(4)	19(5)	0.1(1.5)	0.79(0.21)
18	012917.4+630242	01:29:17.42	+63:02:42.3	2.1	6.4	9.5(3.3)	10(4)	20(5)	7.7(3)	0.03(0.25)
22	012801.8+631244	01:28:01.83	+63:12:44.5	2.0	7.1	6.4(2.8)	5.9(3)	12(4)	5.3(2.6)	−0.04(0.33)

[a] Internal identifier of the form SNR G127.1+0.5:N.

[b] Official IAU name.

[c] Approximate 90% confidence radius.

[d] Angle from the center of the SNR.

[e] Hardness ratio, computed according to $(C_\mathrm{H} - C_\mathrm{L})/(C_\mathrm{H} + C_\mathrm{L})$, where C is the number of counts in a band.

Note. — Quantities in parentheses are 1-σ uncertainties.

10.4.3 X-ray Extended-Source Detection

No extended sources were detected during the `wavdetect` runs, with a maximum wavelet scale of 16 pixels or $8''$. We also manually examined the X-ray images for sources with larger sizes and did not find any (there is some extended emission in SNR G315.4−2.3 toward the south and west, but that is almost certainly due to diffuse thermal emission from the SNR/RCW 86 complex as it has the same general spectrum; see Fig. 10.3).

To quantify the limits on extended emission, we determine the average background counts in a region free from sources. These counts are presented in Table 10.8, where we also find the $3\,\sigma$ limits to extended emission.

10.4.4 X-ray Timing

The majority of the detected sources have too few photons for meaningful analyses of their variability. We can perform some analysis, however, with the brightest sources (we set a limit of 100 counts for a light curve, which eliminated all of the sources in SNRs G315.4−2.3 and G084.2+0.8). In Figure 10.14 we show X-ray light curves for the two sources in SNR G093.3+6.9 with more than 100 counts, SNR G093.3+6.9:1 and SNR G093.3+6.9:2. The light curve for SNR G093.3+6.9:2 is quite constant, but that for SNR G093.3+6.9:1 has a significant flare lasting ≈ 1.5 hr. Searches for periodic variation, however, showed nothing. With the 3.2-second sampling of ACIS-I we were unable to search for rapid variability, but the low count rates made that impossible anyway. We took the barycentered arrival-time data for SNR G093.3+6.9:1 and SNR G093.3+6.9:2 and performed FFTs with the data binned into 4-second intervals. No significant peaks in the periodogram were found over the frequency range 0.01–0.12 Hz.

Table 10.8. Limits to Extended X-ray Emission in SNRs G093.3+6.9, G315.4−2.3, G084.2+0.8, & G127.1+0.5

SNR	BG Counts ($\times 10^{-2}$ arcsec^{-2})	Count Limits ($\times 10^{-2}$)	L Limits ($\times \theta^2 10^{28}$ ergs s^{-1})	$L(\theta = 1')$ Limits ($\times 10^{32}$ ergs s^{-1})
G093.3+6.9	1.75(1)	$6\theta^2 + 70\theta$	8	3
G315.4−2.3	2.10(2)	$7\theta^2 + 70\theta$	10	4
G084.2+0.8	2.34(2)	$6\theta^2 + 70\theta$	10	4
G127.1+0.5	2.03(2)	$7\theta^2 + 80\theta$	1	0.3

Note. — θ is the radius of the extended region in arcseconds. The limits assume uniform weighting over θ, and are at the $3\,\sigma$ level. The counts are in the 0.3–8.0 keV range. The luminosity limits assume a power-law with $\Gamma = 1.5$.

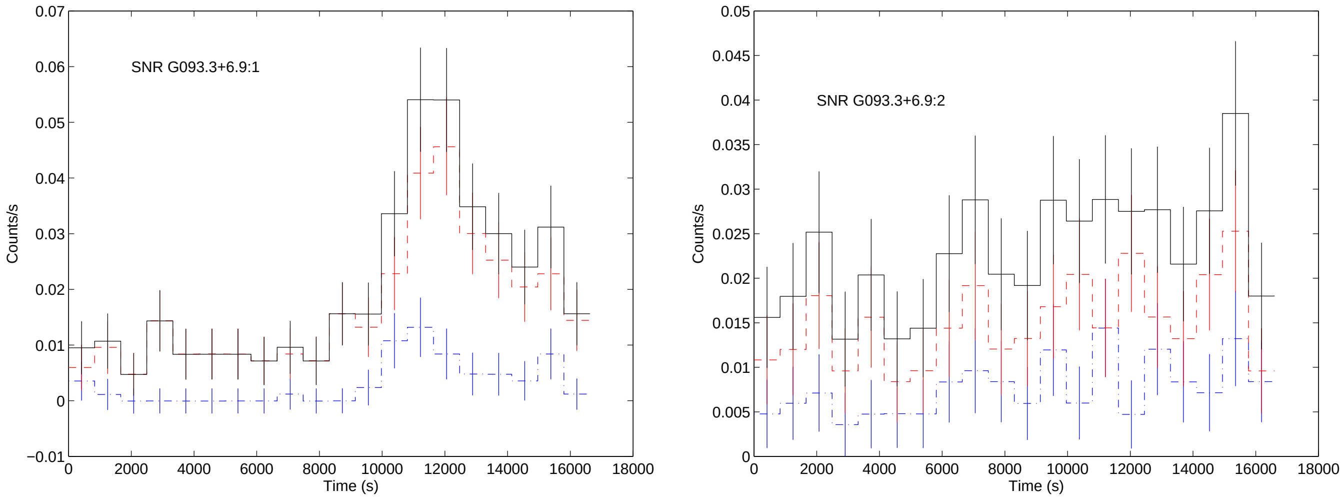

Figure 10.14 Background-subtracted X-ray light curves of sources in SNR G093.3+6.9 with > 100 counts. Left: SNR G093.3+6.9:1; right: SNR G093.3+6.9:2. The dashed red line is 0.3–2.0 keV (L-band), the dot-dashed blue line is 2.0–8.0 keV (H-band) and the solid black line is 0.3–8.0 keV (A-band). A flare lasting ≈ 6000 s and with an amplitude change of ≈ 500% is present in the light curve of SNR G093.3+6.9:1.

In Figure 10.15 we show the X-ray light curve for the only source in SNR G127.1+0.5 that has more than 100 counts: SNR G127.1+0.5:1. The light curve is consistent with a constant flux.

10.4.5 Multi-wavelength Followup & Counterpart Identification

10.4.5.1 Motivation

After identifying X-ray sources with *Chandra* (or *XMM*), the question is then to determine which, if any, are the compact remnants of the SNRs. We have used source-count statistics (Brandt et al. 2001; Mushotzky et al. 2000; Feigelson et al. 2002) to estimate the number of foreground/background sources given the $N_{\rm H}$ and diffuse SNR background toward each target—we expect to detect 10–50 field sources toward each SNR in the *CXO*-AO3 sample. Most of these sources will be detected with few counts (10–

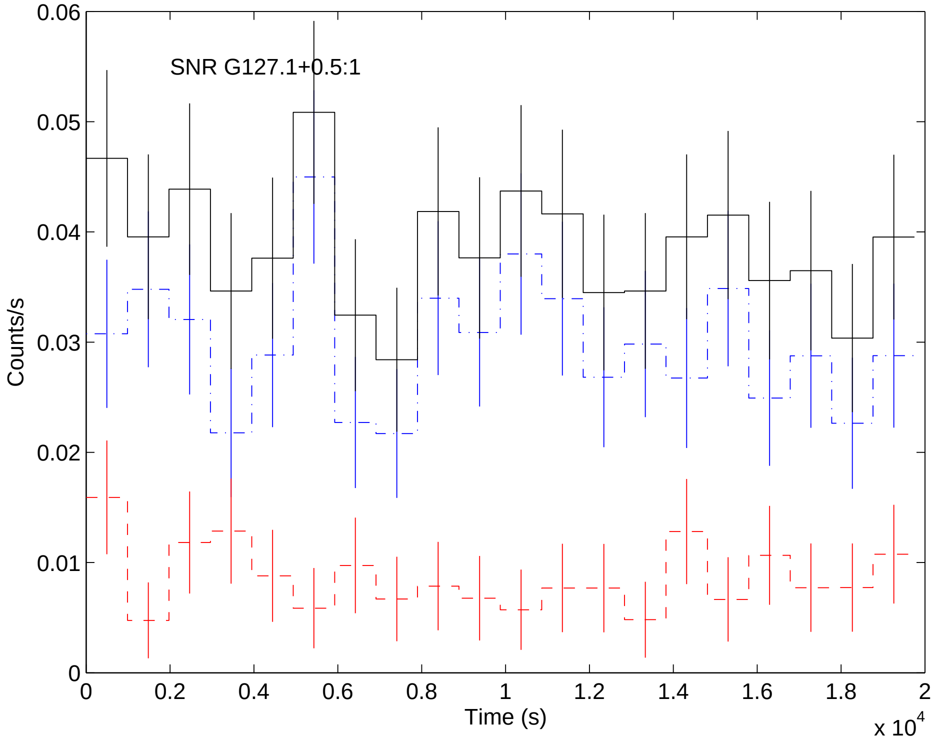

Figure 10.15 Background-subtracted X-ray light curve of SNR G127.1+0.5:1. The dashed red line is 0.3–2.0 keV (L-band), the dot-dashed blue line is 2.0–8.0 keV (H-band) and the solid black line is 0.3–8.0 keV (A-band).

30), and will therefore not be suitable for X-ray spectroscopy that could, of itself, determine which are neutron stars. Because of their small X-ray count rates, weeding out interlopers requires multi-wavelength observations.

Isolated neutron stars have high X-ray to optical flux ratios (Hulleman, van Kerkwijk, & Kulkarni 2000)—deep optical/IR imaging is therefore an efficient way to identify background sources. We thus follow our X-ray observations with successively deeper optical and IR observations, identifying progressively fainter counterparts as we go.

Interloper sources, on the other hand, typically have much brighter optical/IR counterparts (Hertz & Grindlay 1988; Grindlay et al. 2003). In the Galactic plane, the majority of sources are either nearby bright stars or active late-type stars. Other possible sources are RS CVn binaries, X-ray binaries, or cataclysmic variables. The extragalactic sources are usually AGNs or star-forming galaxies, although some nearby spiral galaxies are also detectable (e.g., Barger et al. 2003). Stars with spectral types A–M can have some detectable X-ray emission (largely dependent on rotation and magnetic fields) that appears as a hot (5–7×10^6 K) plasma (Katsova & Cherepashchuk 2000). X-ray binaries usually have harder spectra characterized by power laws with indices $\Gamma \approx 1.5$–2 (Grindlay et al. 2003). Stars are unresolved optical/IR sources, but for nearby binaries the X-ray emission may not lie exactly coincident with the optical/IR emission (if, for example, the optical emission is from the stars but the X-ray emission is from interacting coronae between the stars) and the binary members may be merged to give the appearance of an extended sources. The extragalactic sources also have hard spectra with power-law indices $\Gamma \approx 1.5$–2 (Bauer et al. 2002) and are optically fainter ($R \gtrsim 18$). While the nuclei of these galaxies are unresolved, the closer galaxies can have resolved optical/IR emission.

There are a small number of galaxies that have somewhat extreme X-ray-to-optical flux ratios. In a sample of 503 X-ray sources over 448 arcmin^2, Koekemoer et al. (2004) have identified a few sources with X-ray-to-optical (850 nm) flux ratios exceeding 100, including seven sources without 850 nm detections. While the identities are unclear, they suggest that these galaxies have such faint optical counterparts through a combination of intrinsic reddening and high redshift. However, these galaxies should not significantly impact our sample. We might expect 1–3 of these sources in each of our *Chandra* images, but even without optical detections we should be able to identify these as galaxies in the near-infrared, as all but one of the sources were detected at K_s band (where we have our deepest observations) and the X-ray spectra are harder than those of most neutron stars (also see Gandhi et al. 2004). In addition, these galaxies appear to just be the tail end of the X-ray-to-optical flux ratio distribution, with most neutron stars being significantly higher.

10.4.5.2 Execution

Therefore, after the detection of the X-ray sources we obtained progressively deeper optical and IR data of the SNR fields. Starting with small telescopes (Palomar 60 inch, Las Campanas 40 inch) we moved to larger telescopes (Palomar 200 inch, NTT, Magellan, and finally Keck) as we identified counterparts to more and more of the X-ray sources (see below). The details of the optical/IR observations are in Tables 10.9–10.12.

We began by registering all of the data for an SNR (we also included 2MASS J- and K_s-band images) to the same frame and then searched for optical/IR counterparts to the X-ray sources using `SExtractor` (Bertin & Arnouts 1996). We considered a source as a potential counterpart if it was within the 90% confidence radius of the X-ray source combined with a $0\farcs2$ uncertainty for the optical astrometry. We also inspected all X-ray sources to see if there was an optical source at the edge of the error circle, if there were multiple sources, etc. We then determined the positions and magnitudes of all of the detected sources, which we list in Table 10.13–10.16. The positions in Tables 10.13–10.16 are the averages of the positions for all images where the source was detected, except for sources that were saturated in several bands but

Table 10.9. Optical/IR Observations of SNR G093.3+6.9

Telescope	Instrument	Band(s)	Date (UT)	Seeing (arcsec)	Exposure (s)	Sources[a]
P60	P60CCD	$BVRI$	2001-Jul-23	1.9–2.5	300	−4
P200	LFC	$g'r'$	2002-Jan-18	1.9	600	−13
Keck I	LRIS	g	2002-Jun-15	0.9	2300	5,14,15,17
		R		0.9	2000	5,14,15,17
		g		0.9	1380	2,5,7,8,9,16,19,26
		R		1.0	1200	2,5,7,9,16,19,26
Keck I	NIRC	K_s	2002-Jun-02	0.5	250	5,6,9,14,15,17
P60	P60IR	K_s	2002-Jul-26	2.0	900	4,10,13,19
Keck II	ESI	R	2002-Sep-03	0.8	540	4
		I		0.8	900	4
		I		0.8	2520	8,26
		R		0.7	660	10,24
		I		0.6	600	10
		R		0.7	960	13
Keck I	NIRC	K_s	2002-Nov-16	0.5	2950	19
P200	WIRC	K_s	2003-Jul-24	0.8	1080	−6,−10,−16

[a] Indicates which sources from Table 10.4 were on which images. Negative numbers indicate that all sources but the negated one(s) were on the image.

Note. — The telescopes/instruments used were P60CCD: the CCD camera on the Palomar 60-inch; P60IR: the Infrared camera on the Palomar 60-inch (Murphy et al. 1995); LFC: the Large Format Camera on the Palomar 200-inch; LRIS: the Low-Resolution Imaging Spectrometer on the 10 m Keck I telescope (Oke et al. 1995); NIRC: the Near-Infrared Camera on the 10 m Keck I telescope (Matthews & Soifer 1994); ESI: the Echellette Spectrograph and Imager on the 10 m Keck II telescope (Sheinis et al. 2002); WIRC: the Wide-field Infrared Camera on the Palomar 200-inch.

which had unambiguous 2MASS detections, where we used the 2MASS position alone. For sources that had multiple detections in the same band but by different instruments (e.g., C40 and EMMI R-band), we used the detection that had the highest S/N without being saturated. We show postage-stamp images of the optical/IR counterparts to the X-ray sources in Figures 10.16–10.18 (for SNR G093.3+6.9), Figures 10.19–10.21 (for SNR G315.4−2.3), Figures 10.22–10.24 (for SNR G084.2−0.8), and Figures 10.25–10.26 (for SNR G127.1+0.5). The instrument(s)/band(s) chosen for each source are those that best illustrate the detection.

To determine limiting magnitudes, we simulated Gaussian stars with the same FWHM as the average seeing for the image. We placed the stars randomly in regions that were not too crowded, similar to the regions where the X-ray sources actually were, and determined the $3\,\sigma$ limiting flux by performing photometry (again using `SExtractor`) on the stars.

We define optical/IR fluxes using the zero-point calibrations of Bessell, Castelli, & Plez (1998), where $F(m) = F_0 10^{-m/2.5}$ and $F_0 = (2.0\times10^{-5}, 1.4\times10^{-5}, 9.0\times10^{-6}, 8.7\times10^{-7})$ ergs s^{-1} cm^{-2} for (V,R,I,K_s), respectively. We also use the reddening coefficients of Bessell et al. (1998), such that $A_\lambda/A_V = (1.0, 0.82, 0.62, 0.11)$ again for (V,R,I,K_s), respectively.

Table 10.10. Optical/IR Observations of SNR G315.4−2.3

Telescope	Instrument	Band(s)	Date (UT)	Seeing (arcsec)	Exposure (s)	Sources[a]
C40	C40CCD	$BVRI$	2002-Apr-18	1.3	3600	−3
		BR	2002-Apr-20	1.5	3600	−21
NTT	EMMI	VRI	2002-Jun-14	0.8	1130	1,5,17,23
Magellan II	MagIC	BR	2003-Apr-03	0.8	1800	1
		R	2003-Apr-03	0.8	3000	12,28
		R	2003-Apr-03	0.8	3000	6,17
		I	2003-Apr-04	0.7	1500	1
		I	2003-Apr-04	0.6	900	6,17
Magellan II	PANIC	K_s	2003-Apr-18	0.8	2160	1
		K_s	2003-Apr-18	0.9	2160	12,28
		K_s	2003-Apr-18	1.0	2160	6,17
		K_s	2003-Apr-20	0.6	2160	1
		K_s	2003-Apr-20	0.5	2160	12,28
		K_s	2003-Jun-07	0.4	900	5[b]

[a] Indicates which sources from Table 10.5 were on which images. Negative numbers indicate that all sources but the negated one(s) were on the image.

[b] Observed by M. van Kerkwijk.

Note. — The telescopes/instruments used were C40CCD: the direct-imaging CCD camera on the Las Campanas 40-inch; EMMI: the ESO Multi-Mode Instrument (red imaging arm only) on the 3.5 m New Technology Telescope (NTT) at La Silla; MagIC: Raymond and Beverly Sackler Magellan Instant Camera on the 6.5 m Clay (Magellan II) telescope; PANIC: Persson's Auxiliary Nasmyth Infrared Camera on the 6.5 m Clay (Magellan II) telescope.

Table 10.11. Optical/IR Observations of SNR G084.2−0.8

Telescope	Instrument	Band(s)	Date (UT)	Seeing (arcsec)	Exposure (s)	Sources[a]
P200	LFC	r'	2002-Oct-07	1.5	2730	all
P200	WIRC	J	2002-Nov-01	1.2	4500	all
		K_s	2002-Nov-01	0.9	2640	all
Keck I	NIRC	K_s	2003-Aug-11	0.5	450	2,6,10,11,14,18,23

[a] Indicates which sources from Table 10.6 were on which images. Negative numbers indicate that all sources but the negated one(s) were on the image.

Note. — The telescopes/instruments used follow from Table 10.9.

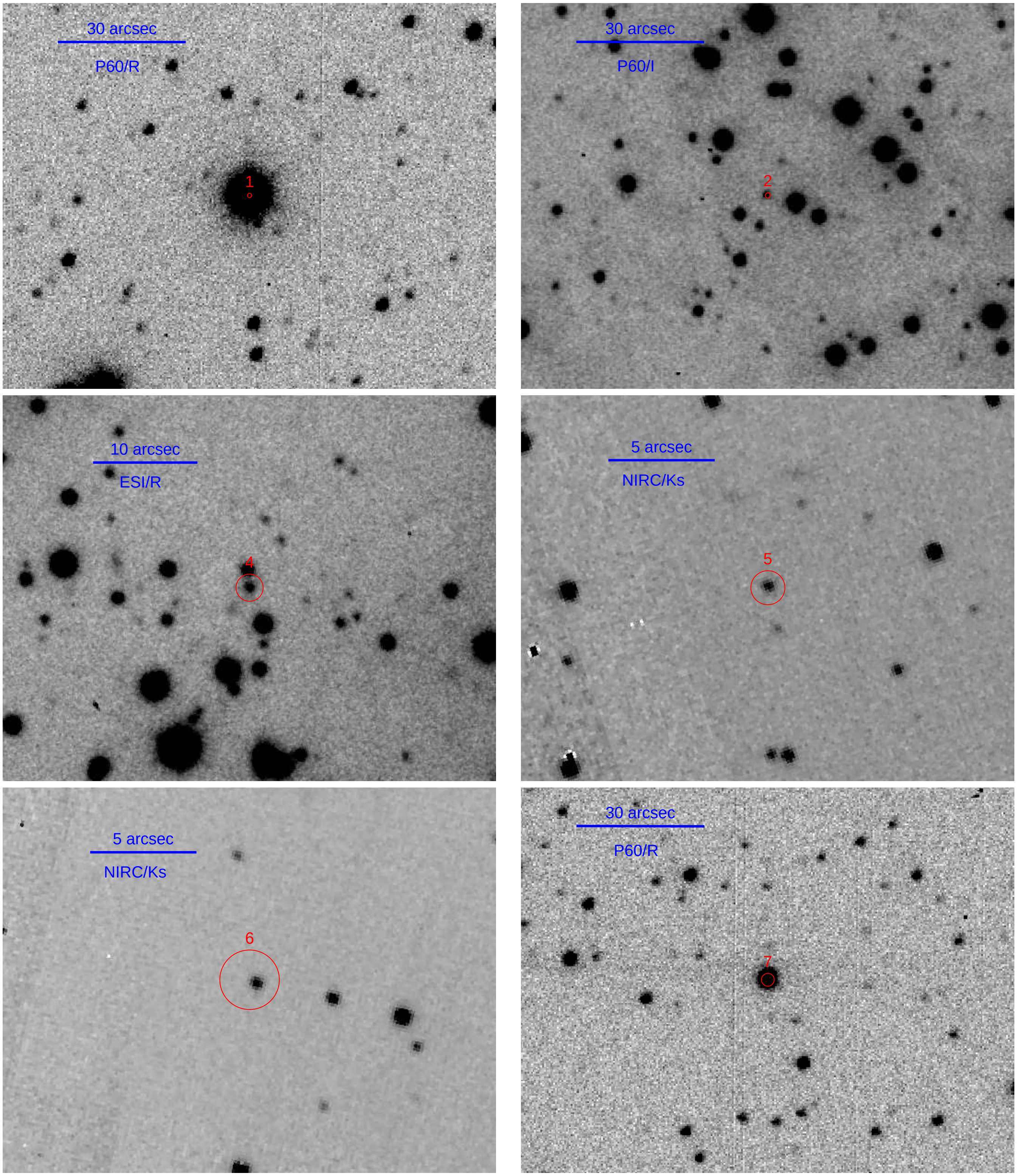

Figure 10.16 Optical/IR images of counterparts to X-ray sources in SNR G093.3+6.9. North is up, east is to the left, and a scale bar is in the upper left corner.

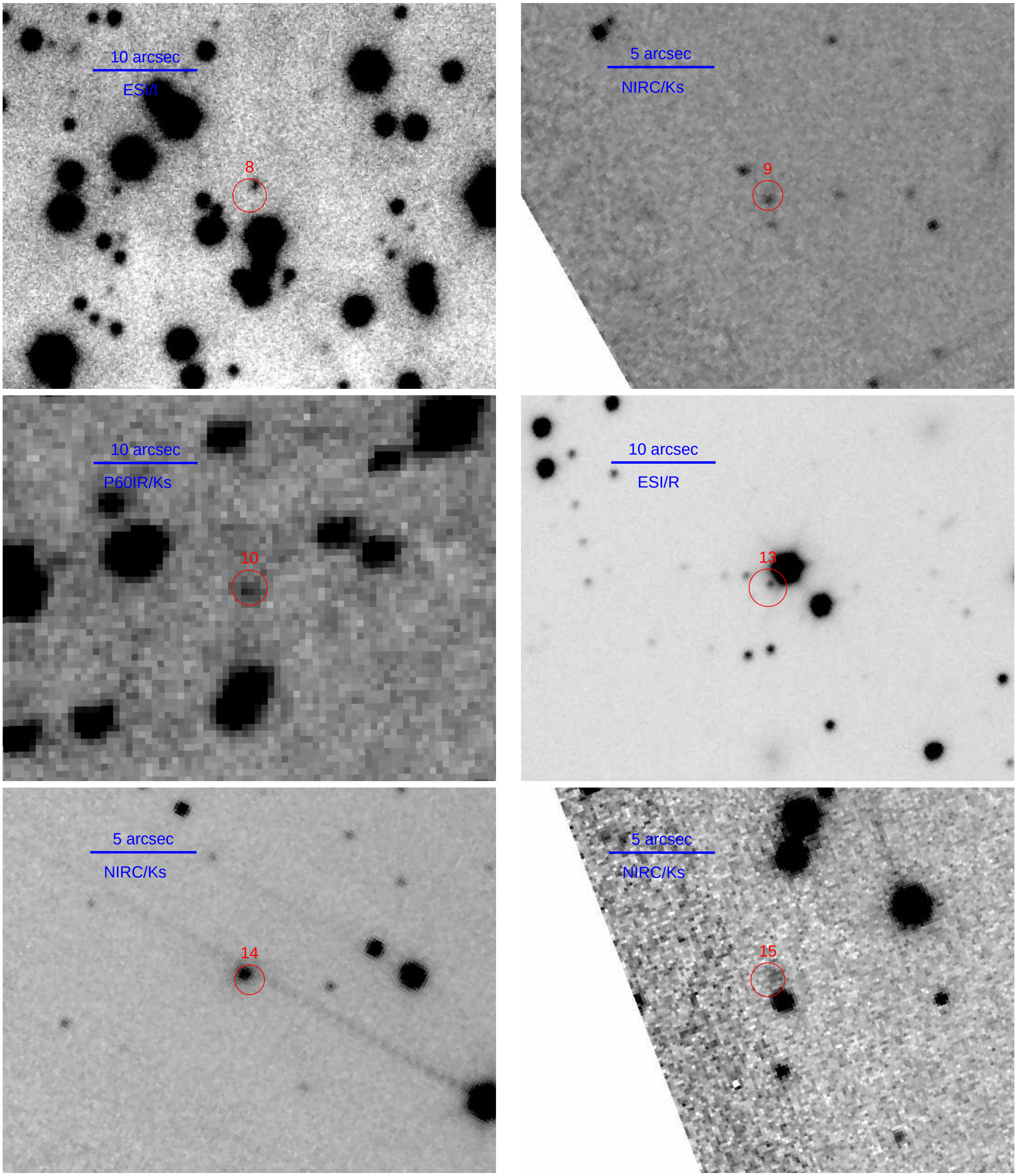

Figure 10.17 Optical/IR images of counterparts to X-ray sources in SNR G093.3+6.9 (cont.). North is up, east is to the left, and a scale bar is in the upper left corner.

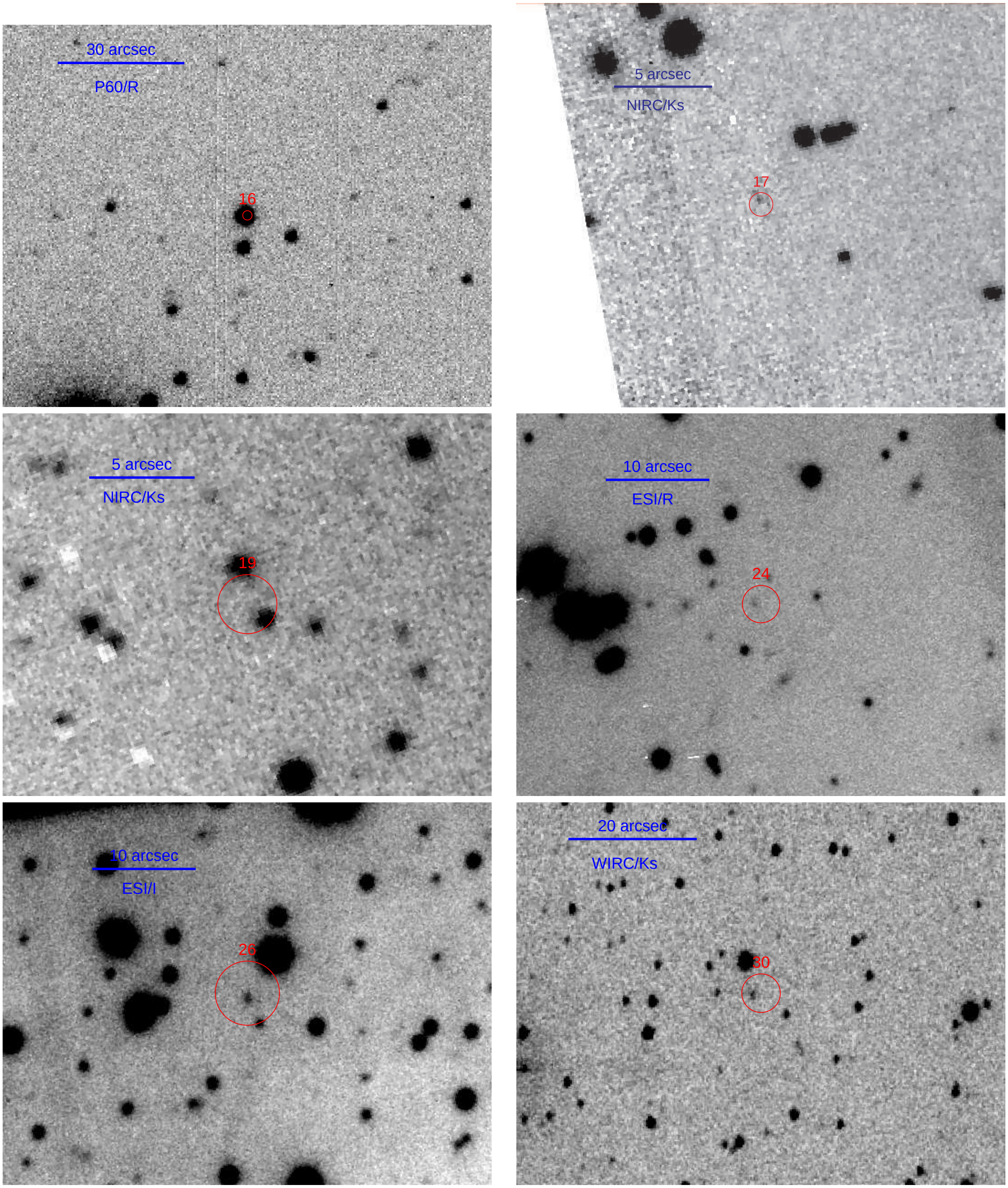

Figure 10.18 Optical/IR images of counterparts to X-ray sources in SNR G093.3+6.9 (cont.). North is up, east is to the left, and a scale bar is in the upper left corner.

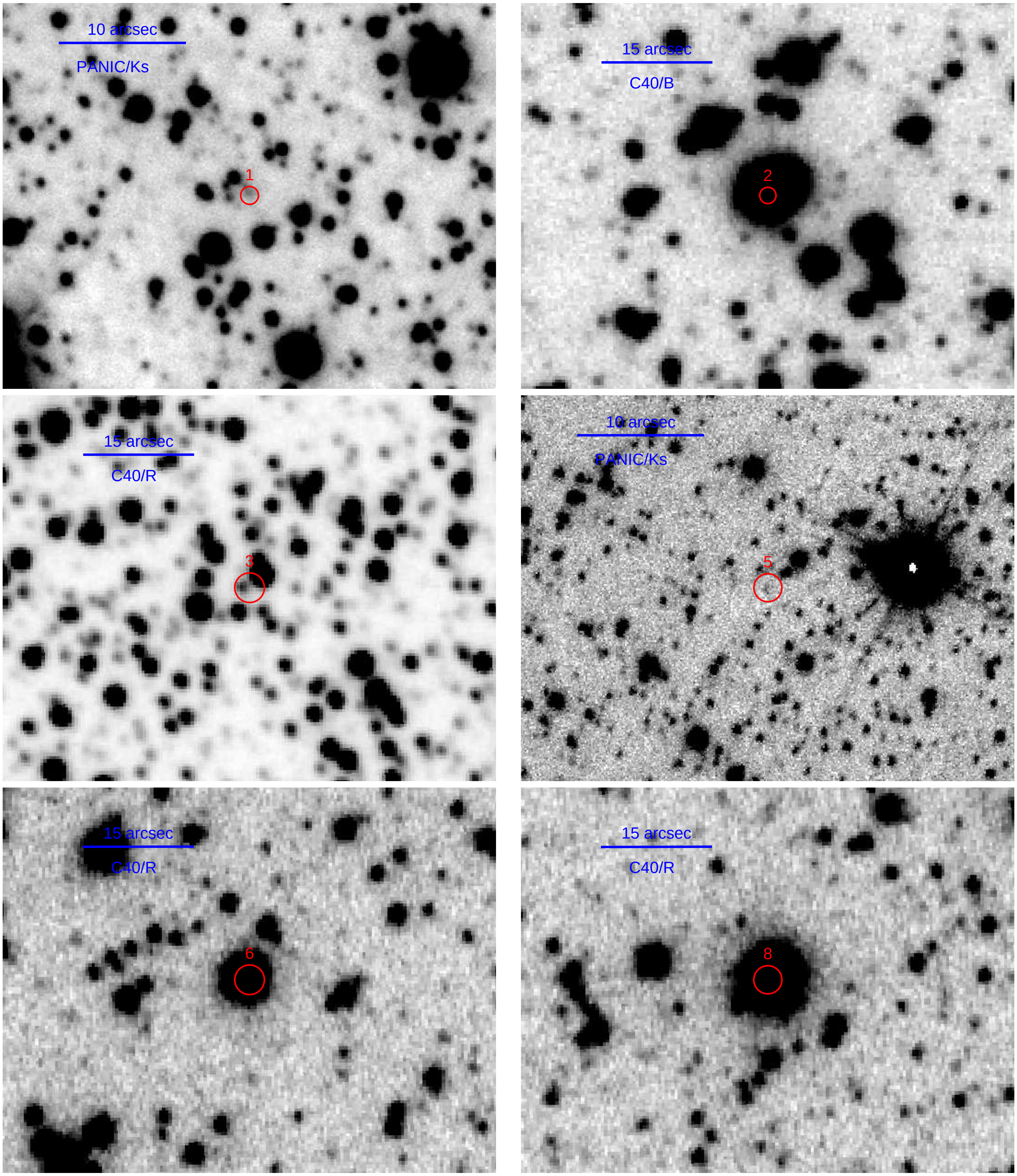

Figure 10.19 Optical/IR images of counterparts to X-ray sources in SNR G315.4−2.3. North is up, east is to the left, and a scale bar is in the upper left corner.

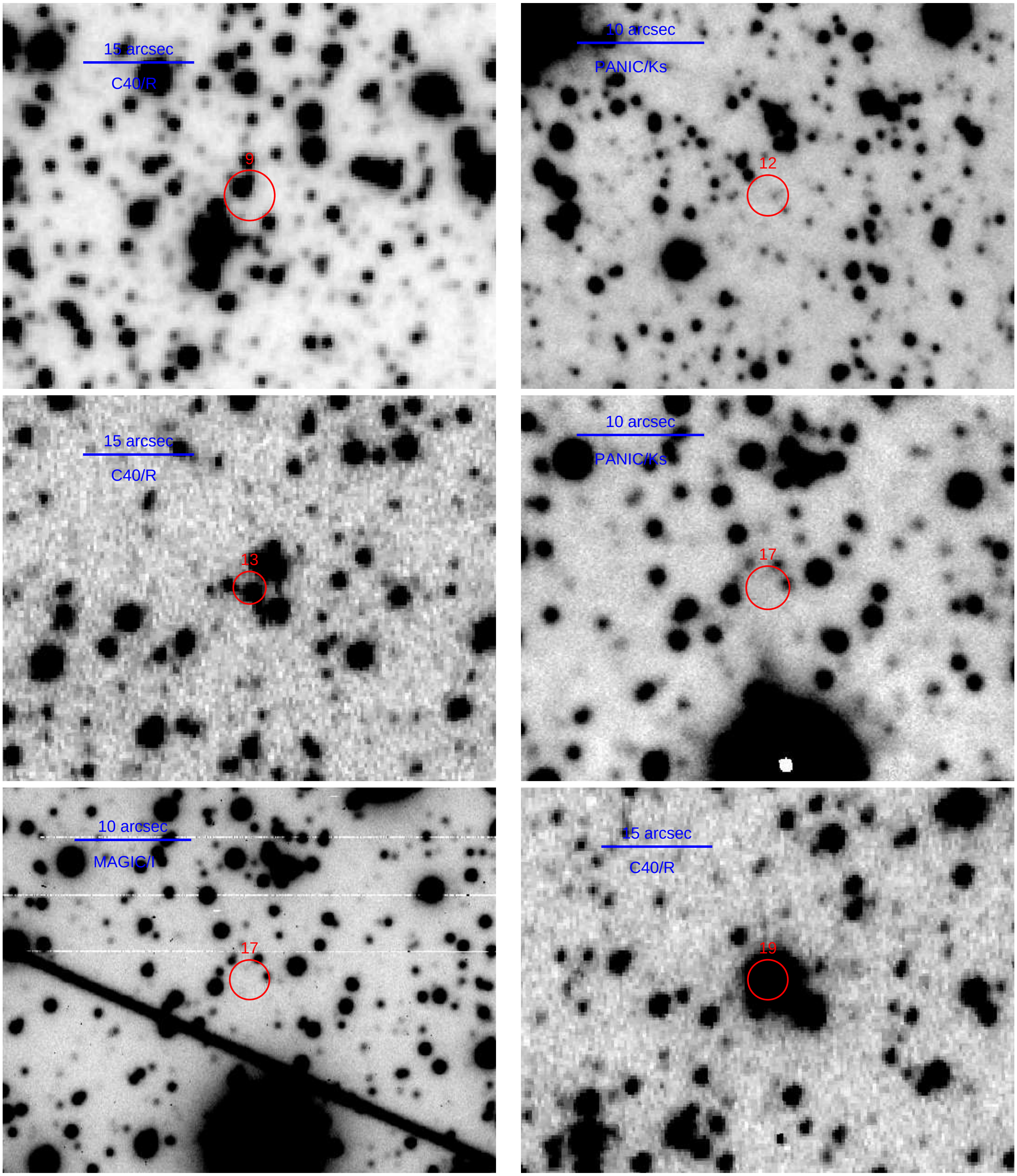

Figure 10.20 Optical/IR images of counterparts to X-ray sources in SNR G315.4−2.3 (cont.). North is up, east is to the left, and a scale bar is in the upper left corner.

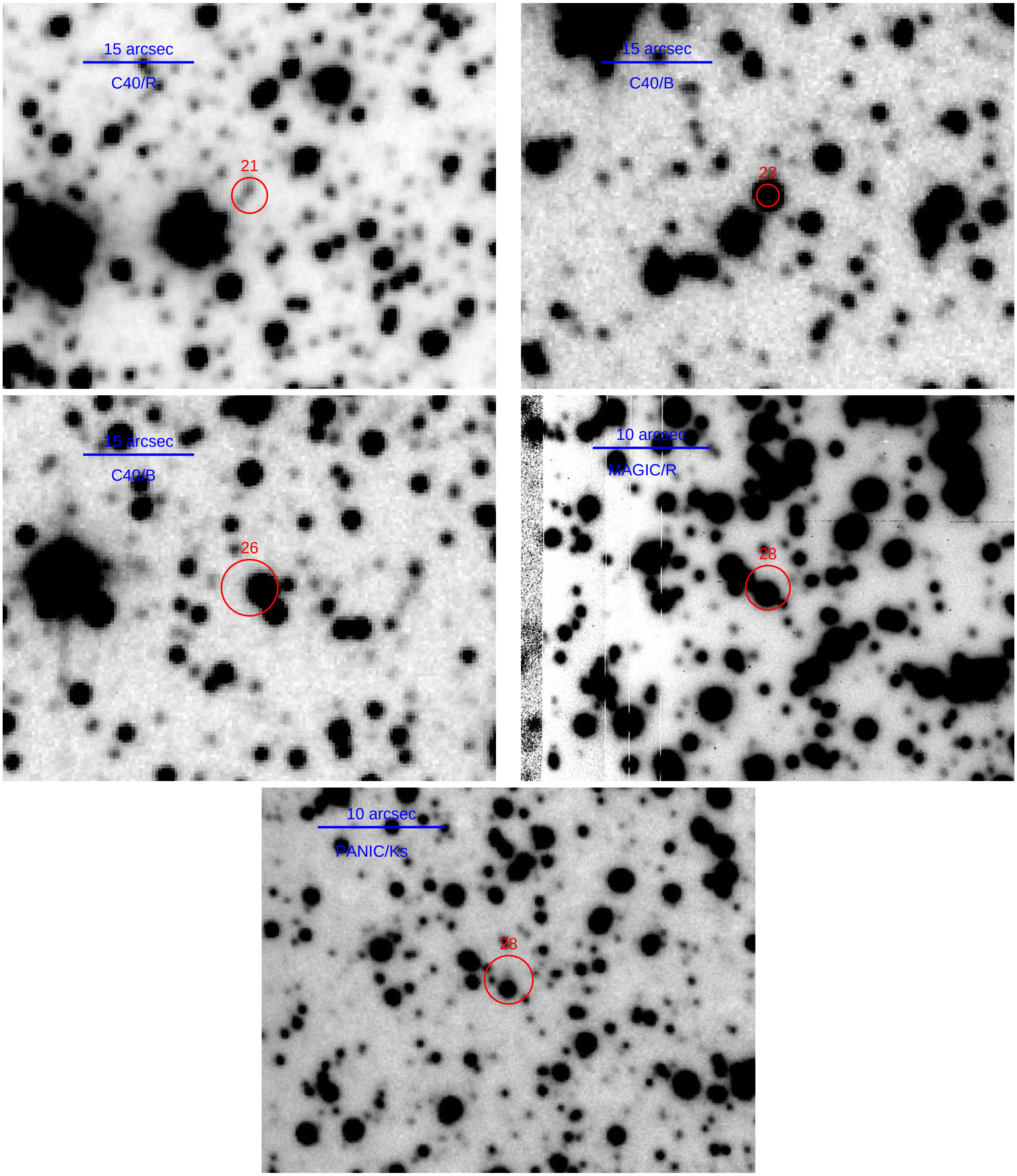

Figure 10.21 Optical/IR images of counterparts to X-ray sources in SNR G315.4−2.3 (cont.). North is up, east is to the left, and a scale bar is in the upper left corner.

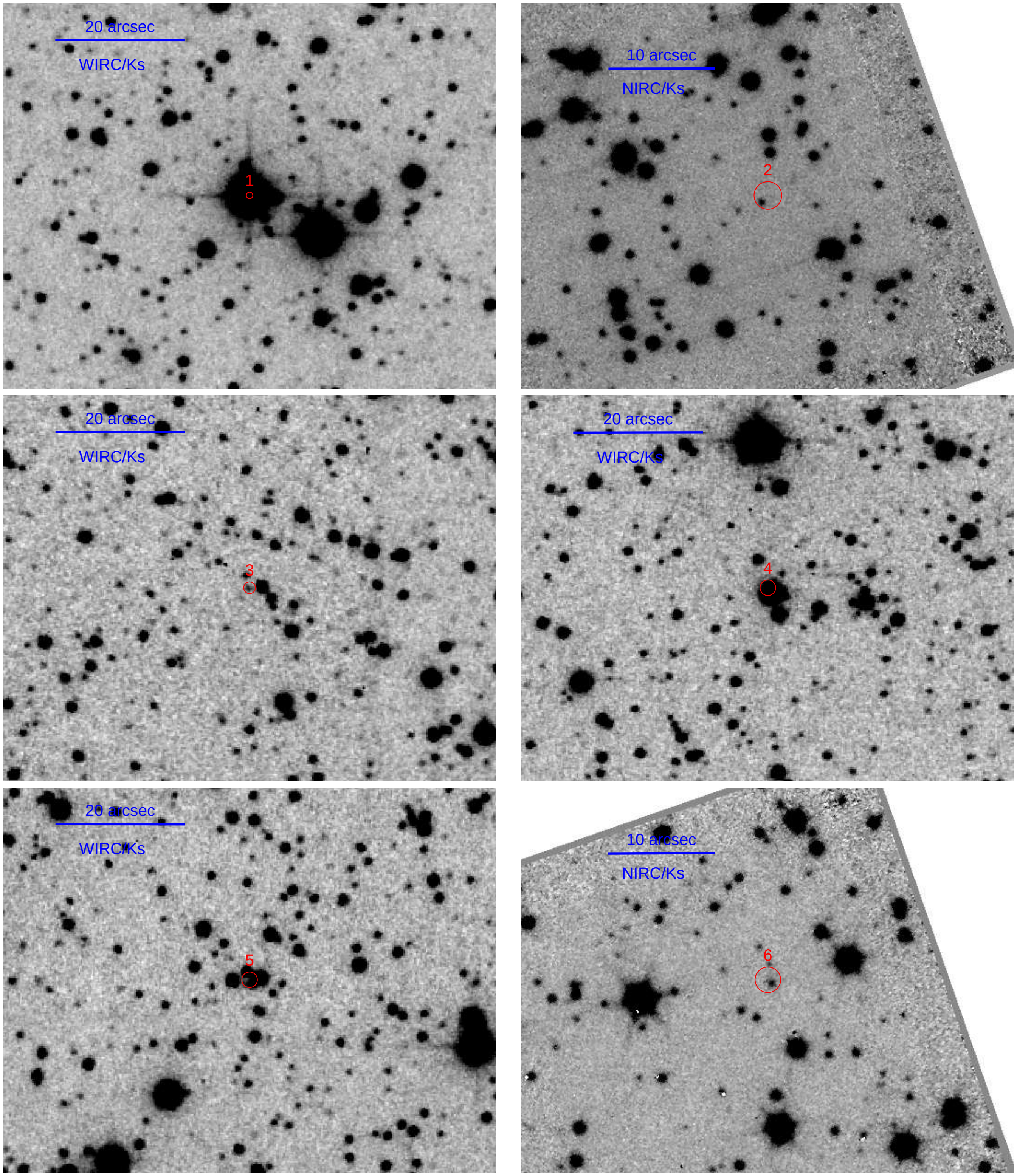

Figure 10.22 Optical/IR images of counterparts to X-ray sources in SNR G084.2−0.8. North is up, east is to the left, and a scale bar is in the upper left corner.

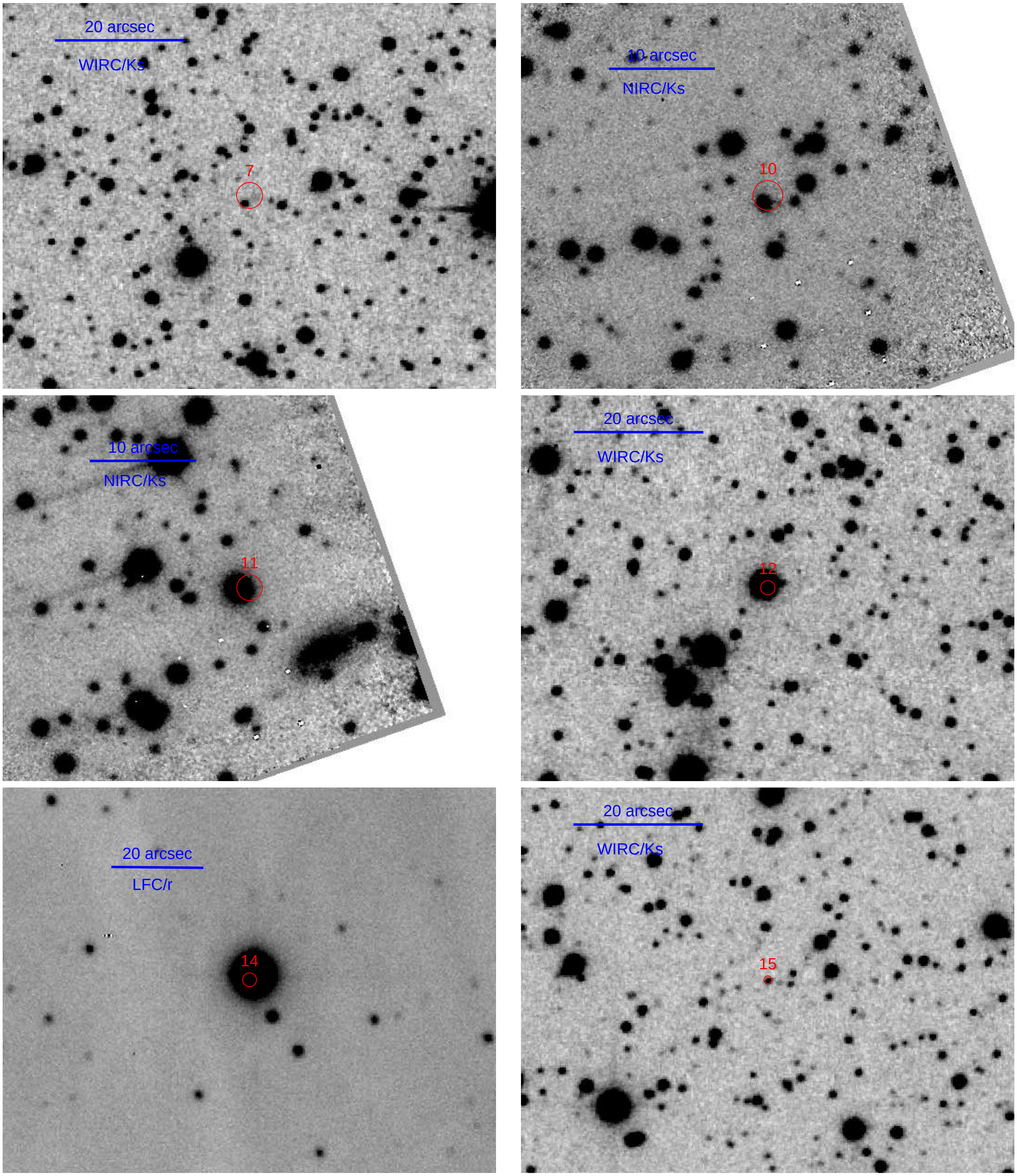

Figure 10.23 Optical/IR images of counterparts to X-ray sources in SNR G084.2−0.8 (cont.). North is up, east is to the left, and a scale bar is in the upper left corner.

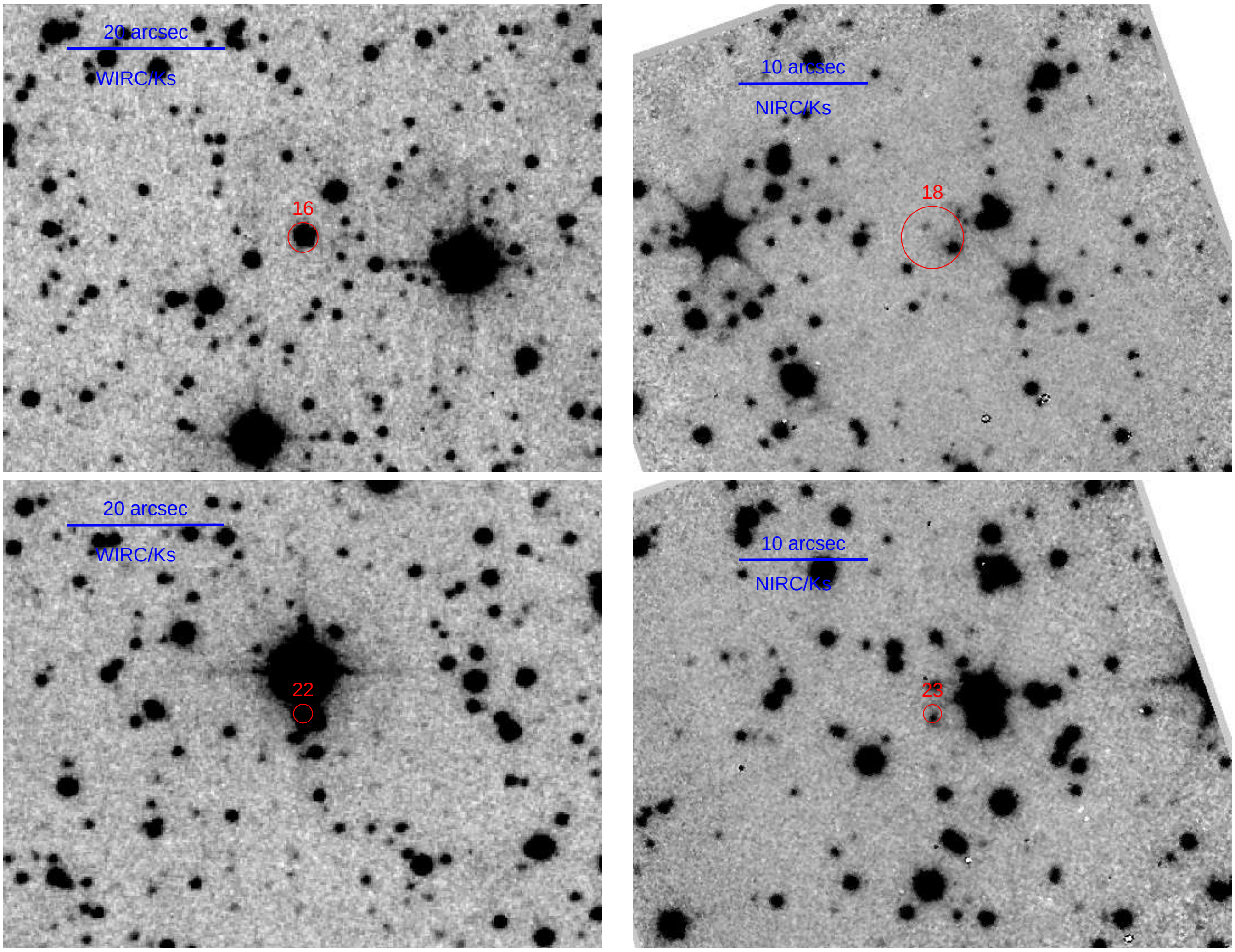

Figure 10.24 Optical/IR images of counterparts to X-ray sources in SNR G084.2−0.8 (cont.). North is up, east is to the left, and a scale bar is in the upper left corner.

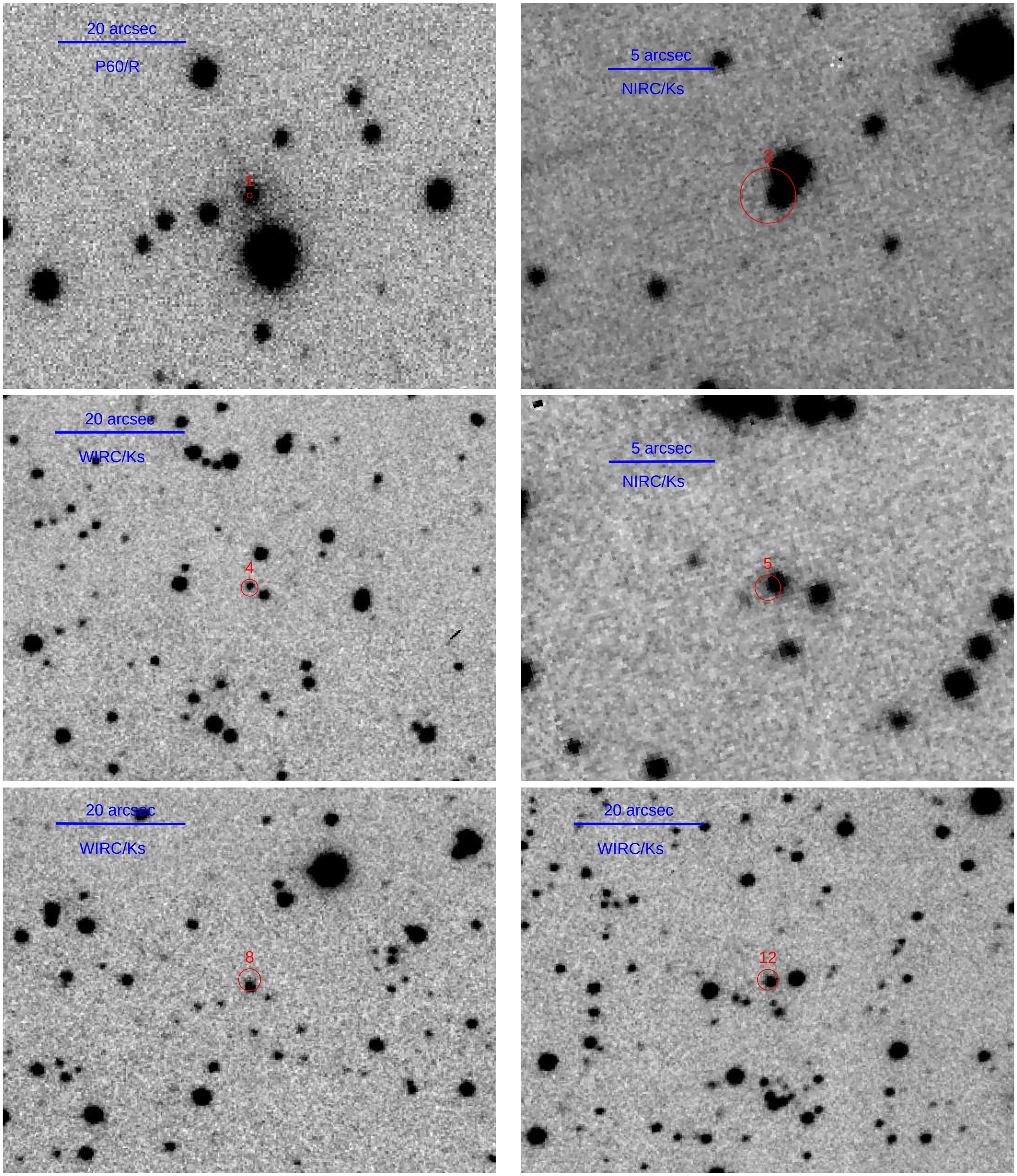

Figure 10.25 Optical/IR images of counterparts to X-ray sources in SNR G127.1+0.5. North is up, east is to the left, and a scale bar is in the upper left corner.

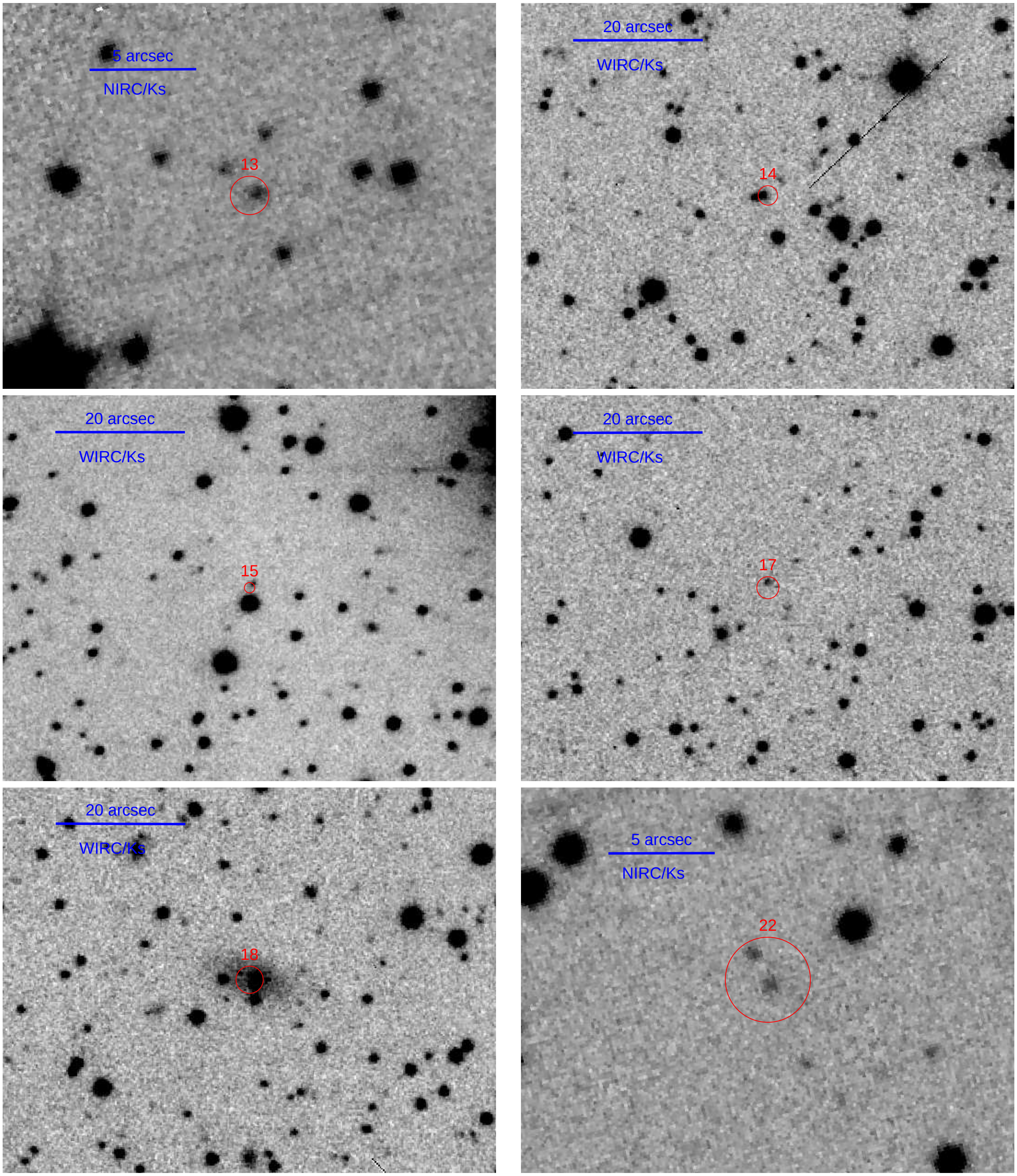

Figure 10.26 Optical/IR images of counterparts to X-ray sources in SNR G127.1+0.5 (cont.). North is up, east is to the left, and a scale bar is in the upper left corner.

Table 10.12. Optical/IR Observations of SNR G127.1+0.5

Telescope	Instrument	Band(s)	Date (UT)	Seeing (arcsec)	Exposure (s)	Sources[a]
P60	P60CCD	R	2001-Jul-23	1.9	3900	−22
		I	2001-Jul-23	1.5	300	−22
P200	LFC	r'	2002-Oct-07	1.9	2700	all
P200	WIRC	J	2002-Oct-28	0.9	4050	all
		K_s	2002-Oct-28	0.8	2700	all
Keck I	NIRC	K_s	2003-Aug-11	0.6	900	3,5,13,22

[a] Indicates which sources from Table 10.7 were on which images. Negative numbers indicate that all sources but the negated one(s) were on the image.

Note. — The telescopes/instruments used follow from Table 10.9.

10.4.5.3 Counterpart Evaluation

It is certainly possible that there will be an unrelated optical/IR source in the error circle of an X-ray source (e.g., Kaplan, Kulkarni, & Murray 2001a), especially if the X-ray sources are off-axis and/or have few counts, and therefore have large position uncertainties. There is no entirely accurate way to prevent this from happening and leading to the false association of what is actually a neutron star with another source, which would cause us to reject the neutron star from our sample.

However, there are ways that we can guard against this and incorporate our uncertainties into our limits. If enough is known about the optical/IR source (e.g., colors), it is possible to determine what the source is (Kaplan et al. 2001a) and thereby assign some likelihood to its association with an X-ray source. This is not always possible for the sources in our sample as the information is often limited to optical/IR detections in one or two bands (Tabs. 10.13– 10.16). Similarly, for the few sources with enough X-ray counts a determination can be made based on the X-ray spectrum (or just hardness) and light curve (Fig. 10.14). For the majority of the sources, however, we must examine them relative to the sources in other samples, specifically the CDF and Orion samples (many of the stars in the Orion sample are younger than the general Galactic population, but they do cover a wide range of stellar masses). For this reason we plot the optical/IR-to-X-ray flux ratio against X-ray flux in Figures 10.27–10.30 (we compute the X-ray flux from the observed count rate by using conversion factors determined from W3PIMMS for a blackbody with $kT_\infty = 0.25$ keV and $N_{\rm H}$ appropriate for each SNR; a change to a power-law with photon index of 1.5 raises the implied fluxes by a factor of ≈ 2). Sources that fall in the loci defined by the other samples are likely to be of similar type. This is of course not a definitive assignment, but it should work most of the time. For instance, if we had associated Star A from Kaplan et al. (2001a) with the X-ray flux from CXO J232327.8+584842 (the central source in Cas A), it would appear in Figure 10.27 with the same X-ray flux as the compact source in Cas A and < 1 mag brighter than the limit we have plotted. In other words, it would be far outside the Orion/CDF loci. This argument, that Star A could not be the source of the X-rays from CXO J232327.8+584842 just on the basis of its X-ray-to-optical flux ratio, was made by Kaplan et al. (2001a), who then followed it up by a detailed analysis of multiband photometry of Star A (see also Fesen et al. 2002).

This will not work so well for the sources here, as the X-ray fluxes are significantly less than that of CXO J232327.8+584842 and consequently the location in Figure 10.27 for a random optical/IR counterpart

Table 10.13. Optical/IR Matches to X-ray Sources in SNR G093.3+6.9

ID[a]	α[b]	δ[b]	Δr[c]	B	V	R	I	g/g'[d]	r'	J	K_s	$N(< K_s)$[e]
	(J2000)		(arcsec)					(mag)				
1	20:52:22.90	+55:23:43.7	0.1	13.34(7)	13.16(3)	12.76(3)	12.535(10)	sat	sat	11.172(9)	10.859(11)	< 0.01
2	20:52:31.01	+55:14:37.6	0.3	>23.5	>22.5	20.74(5)	19.52(4)	22.61(10)	21.05(6)	>15.8	15.52(1)	< 0.01
4	20:52:25.83	+55:27:41.7	0.1	···	···	23.30(11)	21.60(10)	>24.0	>23.5	>15.8	17.46(17)	< 0.01
5	20:52:22.01	+55:15:16.9	0.1	>23.5	>22.5	>25.0	>20.7	>26.5	>23.5	>15.8	20.1(4)	< 0.01
6	20:51:31.33	+55:20:31.4	0.4	>23.5	>22.5	>22.3	>20.7	>24.0	>23.5	>15.8	16.1(4)	< 0.01
7	20:52:50.22	+55:16:06.7	0.2	17.67(7)	16.23(3)	15.18(3)	13.857(10)	sat	sat	12.363(16)	11.475(16)	< 0.01
8	20:52:42.13	+55:14:10.7	1.1	>23.5	>22.5	>22.3	23.43(13)	>26.1	>23.5	>15.8	18.9(1)	0.06
9	20:52:36.48	+55:17:45.8	0.2	>23.5	>22.5	>25.1	>20.7	>26.1	>25.1	>15.8	22.3(4)	< 0.01
10	20:51:39.85	+55:25:53.1	0.3	>23.5	>22.5	22.99(11)	21.36(10)	>24.0	>23.5	>15.8	17.45(11)	< 0.01
13	20:52:42.23	+55:26:07.4	0.4	···	···	22.5(5)	···	···	···	>15.8	17.44(6)	< 0.01
14	20:52:05.98	+55:17:58.6	0.2	>23.5	>22.5	22.72(6)	>20.7	>26.3	>23.5	>15.8	17.04(5)	< 0.01
15	20:52:09.83	+55:18:21.4	0.4	>23.5	>22.5	>22.3	>20.7	>26.3	>25.2	>15.8	20.2(4)	0.01
16	20:52:50.16	+55:20:25.3	0.7	17.63(7)	16.22(3)	15.49(3)	14.732(10)	sat	sat	13.61(3)	13.02(3)	< 0.01
17	20:52:12.66	+55:18:54.6	0.2	>23.5	>22.5	>25.2	>20.7	>26.3	>23.5	>15.8	21.1(4)	< 0.01
19	20:52:36.79	+55:15:28.1	1.1	>23.5	>22.5	24.99(14)	>20.7	>26.1	>23.5	>15.8	19.9(4)	0.09
”	20:52:36.92	+55:15:30.5	1.8	>23.5	>22.5	>22.3	>20.7	>26.1	>23.5	>15.8	19.5(4)	0.22
24	20:51:52.31	+55:26:02.8	0.7	>23.5	>22.5	25.2(2)	>20.7	>24.0	>23.5	>15.8	19.1(1)	0.03
26	20:52:48.31	+55:14:21.8	0.5	>23.5	>22.5	>22.3	23.00(11)	>26.1	>23.5	>15.8	17.98(7)	0.01
30	20:51:29.88	+55:15:48.2	1.4	>23.5	>22.5	>22.3	>20.7	>24.0	>23.5	>15.8	18.1(1)	0.07

[a] Source number from Table 10.4.

[b] Position of optical/IR source, averaged over all the bands in which there were detections.

[c] Position difference between the X-ray and optical/IR source.

[d] For brevity, we give both g-band (from LRIS) and g'-band (from LFC) data in the same column. The limits of 24.0-mag are g-band, while the limits of 26.1/26.3-mag are g'-band.

[e] The chance of finding a star within Δr of the X-ray source given the K_s magnitude, using the star-count model of Nakajima et al. (2000).

Table 10.14. Optical/IR Matches to X-ray Sources in SNR G315.4−2.3

ID[a]	α[b]	δ[b]	Δr[c]	B	V	R	I	J	K_s	$N(< K_s)$[d]
	(J2000)		(arcsec)				(mag)			
1	14:43:19.33	−62:28:04.1	0.2	> 22.3	> 24.5	> 23.9	> 22.5	> 15.8	19.60(8)	0.04
2	14:43:33.73	−62:29:27.7	0.5	14.52(2)	13.23(4)	12.41(8)	11.5(1)	10.62(2)	9.84(2)	< 0.01
3	14:41:51.73	−62:28:33.4	1.0	> 22.8	⋯	19.88(6)	⋯	> 15.8	> 14.6	⋯
5	14:42:19.56	−62:28:34.6	0.2	> 22.3	> 24.5	> 23.9	> 22.5	> 15.8	20.5(4)	0.05
6	14:43:20.72	−62:33:08.4	0.7	14.49(2)	13.73(4)	13.27(8)	12.63(10)	12.23(2)	11.77(3)	< 0.01
8	14:43:40.99	−62:31:38.3	0.4	sat	12.39(4)	11.92(8)	11.35(10)	10.88(2)	10.50(2)	< 0.01
9	14:43:46.51	−62:24:12.1	1.4	20.11(3)	18.58(3)	17.35(4)	16.12(7)	14.50(6)	13.40(5)	0.02
12	14:43:15.26	−62:21:28.7	0.7	> 22.3	> 21.8	> 25.5	> 19.7	> 15.8	19.44(10)	0.38
13	14:43:50.38	−62:30:40.8	0.9	19.71(3)	17.79(5)	17.04(8)	15.55(10)	14.33(5)	13.31(5)	0.01
17	14:43:21.90	−62:32:19.0	1.5	> 22.3	> 21.8	> 25.6	20.73(5)	> 15.8	17.71(6)	0.43
19	14:42:10.79	−62:22:02.9	1.1	13.63(2)	13.10(2)	12.92(4)	12.29(7)	11.52(2)	11.19(3)	< 0.01
21	14:42:52.36	−62:21:08.1	1.7	> 22.3	> 21.8	20.76(2)	> 19.7	> 15.8	> 14.6	⋯
”	14:42:52.19	−62:21:06.5	0.7	> 22.3	> 21.8	19.69(8)	> 19.7	> 15.8	> 14.6	⋯
23	14:42:13.11	−62:32:20.6	0.2	17.83(2)	16.18(4)	15.00(8)	13.76(10)	12.46(3)	11.42(3)	< 0.01
26	14:42:06.91	−62:22:04.7	1.8	17.18(2)	16.26(2)	15.53(4)	14.87(7)	14.02(4)	13.37(6)	0.03
28	14:43:20.25	−62:21:38.7	1.3	> 22.3	> 21.8	23.14(6)	> 19.7	> 15.8	18.44(6)	0.62
”	14:43:19.88	−62:21:40.2	2.0	> 22.3	> 21.8	22.23(6)	> 19.7	> 15.8	18.38(6)	1.41
”	14:43:20.07	−62:21:39.4	0.7	> 22.3	> 21.8	18.66(5)	> 19.7	> 15.8	16.12(5)	0.02

[a] Source number from Table 10.5.

[b] Position of optical/IR source, averaged over all the bands in which there were detections.

[c] Position difference between the X-ray and optical/IR source.

[d] The chance of finding a star within Δr of the X-ray source given the K_s magnitude, using the star-count model of Nakajima et al. (2000).

Table 10.15. Optical/IR Matches to X-ray Sources in SNR G084.2−0.8

ID[a]	α[b]	δ[b]	Δr[c]	r'	J	K	$N(< K_s)$[d]
	(J2000)		(arcsec)		(mag)		
1	20:53:28.97	+43:26:58.7	0.4	sat	10.36(2)	10.11(2)	< 0.01
2	20:53:57.97	+43:24:58.6	0.9	>23.2	>20.8	19.68(6)	0.41
3	20:53:49.20	+43:25:51.1	0.2	>23.2	>20.8	18.32(7)	< 0.01
4	20:52:50.51	+43:30:29.3	0.8	15.08(7)	12.99(2)	12.25(3)	< 0.01
5	20:53:52.06	+43:28:10.8	1.2	> 23.2	17.44(4)	15.97(2)	0.05
”	20:53:51.87	+43:28:09.9	1.7	18.83(7)	15.45(2)	14.39(1)	0.03
”	20:53:51.99	+43:28:08.9	0.8	>23.2	>20.8	17.95(5)	0.10
6	20:53:06.86	+43:32:59.3	0.5	>23.2	>20.8	19.45(6)	0.11
7	20:52:48.32	+43:32:12.7	1.5	>23.2	20.67(13)	17.64(3)	0.27
10	20:53:51.79	+43:25:37.1	0.9	>23.2	20.69(15)	17.10(4)	0.06
”	20:53:51.65	+43:25:37.2	1.3	>23.2	>20.8	21.0(2)	1.53
11	20:53:17.76	+43:22:06.6	1.1	>23.2	18.43(4)	15.332(10)	0.03
12	20:53:53.17	+43:27:52.0	0.7	sat	13.39(3)	11.88(2)	< 0.01
14	20:53:02.75	+43:32:08.5	1.5	sat	11.97(2)	11.61(2)	< 0.01
15	20:53:06.49	+43:28:21.9	0.3	>23.2	>20.8	18.37(5)	0.02
16	20:53:35.61	+43:34:27.5	0.6	18.22(7)	14.84(4)	14.01(7)	< 0.01
18	20:53:46.08	+43:33:46.4	0.9	>23.2	>20.8	20.91(14)	0.71
”	20:53:45.89	+43:33:44.8	1.8	>23.2	>20.8	18.08(3)	0.56
22	20:52:42.55	+43:24:50.5	0.8	19.40(7)	14.73(7)	13.26(5)	< 0.01
23	20:53:32.25	+43:23:55.2	0.5	>23.2	>20.8	18.23(4)	0.05

[a] Source number from Table 10.6.

[b] Position of optical/IR source, averaged over all the bands in which there were detections.

[c] Position difference between the X-ray and optical/IR source.

[d] The chance of finding a star within Δr of the X-ray source given the K_s magnitude, using the star-count model of Nakajima et al. (2000).

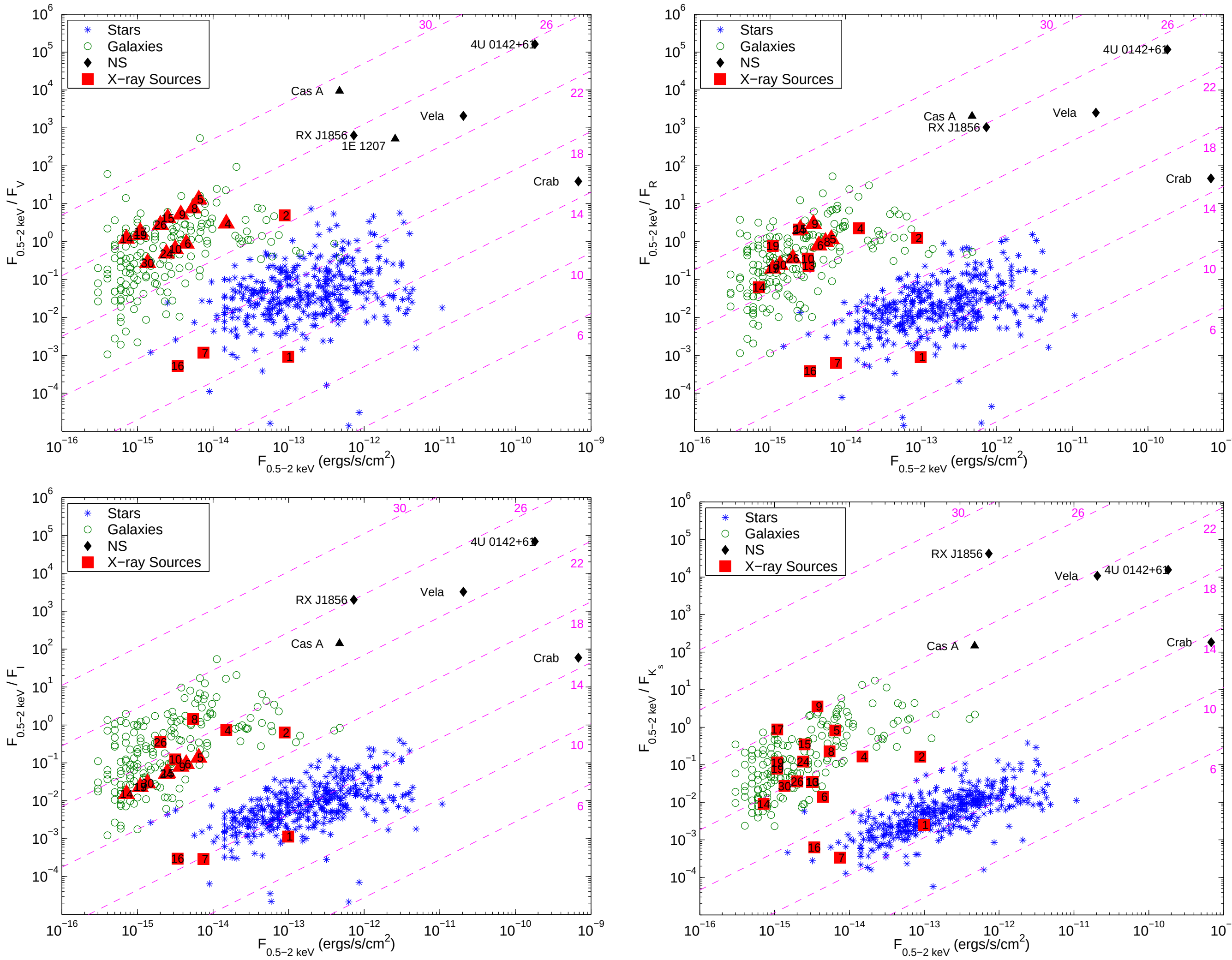

Figure 10.27 X-ray-to-optical/IR flux ratio vs. X-ray flux for sources in SNR G093.3+6.9 (Tabs. 10.4 and 10.13) with sources from the CDF/Orion studies and selected neutron stars. Upper left: V-band; upper right: R-band; lower left: I-band; lower right: K_s-band. Stars from CDF/Orion are blue asterisks, galaxies are green circles. Selected neutron stars are black diamonds/limits, and are labeled. The unidentified X-ray sources in SNR G093.3+6.9 are the red squares/limits and are also labeled (in the case of multiple possible counterparts, the source is plotted multiple times). The diagonal lines represent constant magnitude, and are labeled by that magnitude. For the sources in SNR G093.3+6.9 the counts were converted to a flux by $F_{0.5-2.0\ \mathrm{keV}} = \mathrm{counts}_{0.5-2.0\ \mathrm{keV}} \times 3.4 \times 10^{-16}$ ergs s^{-1} cm^{-1}, appropriate for a blackbody with $kT_\infty = 0.25$ keV and $N_\mathrm{H} = 2 \times 10^{21}$ cm^{-2}. As seen in Table 10.18, the X-ray fluxes change can be a factor of ≈ 2 higher for a power-law spectrum.

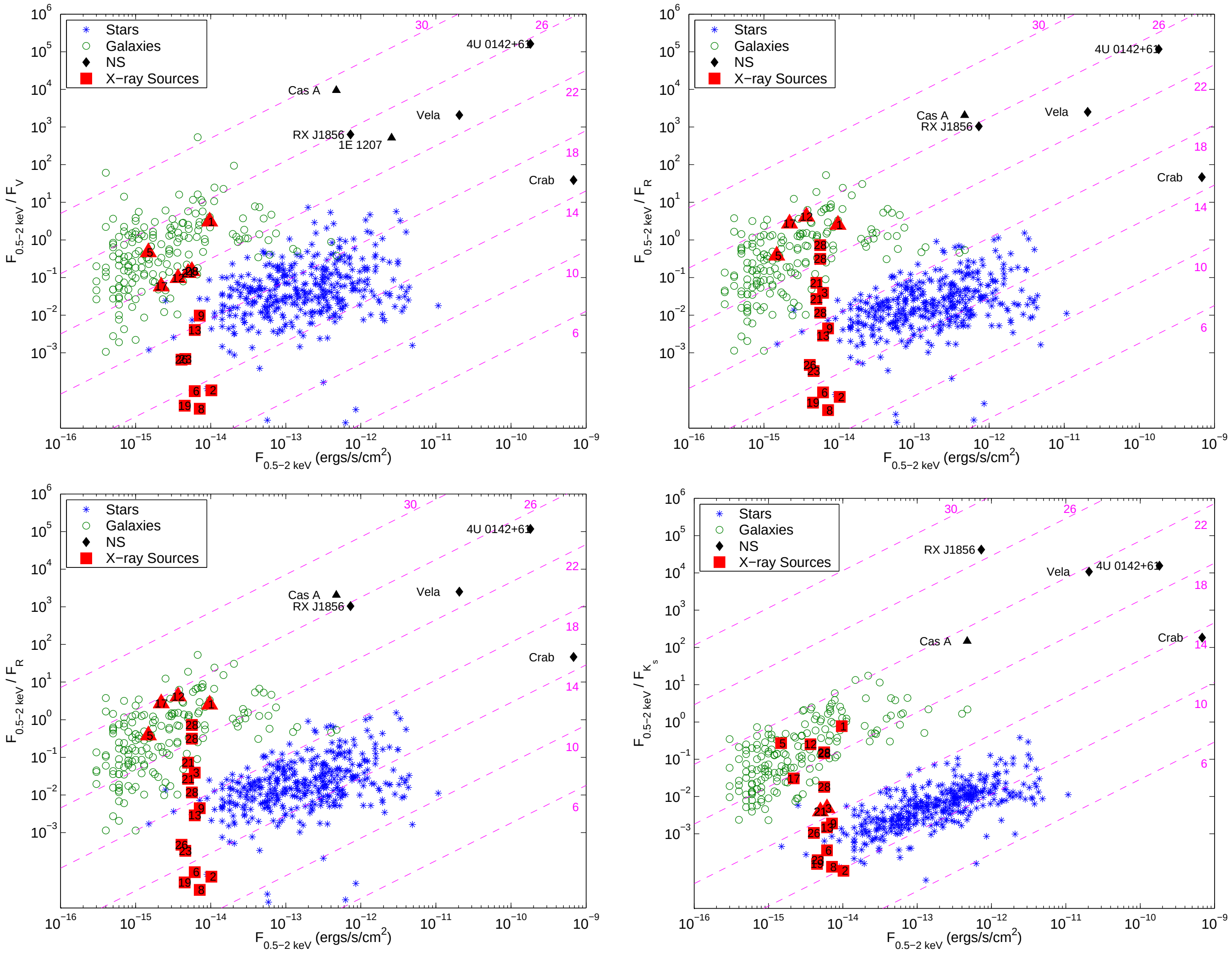

Figure 10.28 X-ray-to-optical/IR flux ratio vs. X-ray flux for sources in SNR G315.4−2.3 (Tabs. 10.5 and 10.14) with sources from the CDF/Orion studies and selected neutron stars, following Figure 10.27. Upper left: V-band; upper right: R-band; lower left: I-band; lower right: K_s-band. For the sources in SNR G315.4−2.3 the counts were converted to a flux by $F_{0.5-2.0\ \mathrm{keV}} = \mathrm{counts}_{0.5-2.0\ \mathrm{keV}} \times 5.1 \times 10^{-16}$ ergs s^{-1} cm^{-1}, appropriate for a blackbody with $kT_\infty = 0.25$ keV and $N_\mathrm{H} = 2 \times 10^{21}$ cm^{-2}.

Table 10.16. Optical/IR Matches to X-ray Sources in SNR G127.1+0.5

ID[a]	α[b]	δ[b]	Δr[c]	R	I	r'	J	K_s	$N(<K_s)$[d]
	(J2000)		(arcsec)			(mag)			
1	01:28:30.58	+63:06:29.7	0.4	16.59(4)	sat	17.76(5)	13.96(12)	12.09(8)	<0.01
3	01:27:36.51	+63:03:45.5	0.6	>23.0	>21.3	>24.5	blended	17.82(3)	0.03
4	01:28:07.70	+63:01:50.6	0.2	22.18(9)	20.69(10)	22.64(7)	19.45(6)	17.74(4)	<0.01
5	01:28:42.25	+63:08:25.8	0.4	>23.0	>21.3	>24.5	>21.1	18.80(4)	0.02
8	01:29:25.42	+63:05:34.2	1.1	21.80(8)	20.48(8)	22.43(6)	18.39(2)	16.86(3)	0.04
12	01:29:10.80	+63:10:14.4	0.6	>23.0	>21.3	>24.5	18.91(5)	16.60(3)	0.01
13	01:28:13.86	+63:06:21.2	0.3	>23.0	>21.3	>24.5	>21.1	19.85(8)	0.02
14	01:27:55.35	+63:01:41.5	0.8	>23.0	>21.3	>24.5	20.32(7)	17.08(3)	0.03
15	01:28:37.77	+63:06:03.3	0.7	>23.0	>21.3	>24.5	blended	18.53(8)	0.06
17	01:27:35.74	+63:02:42.4	0.8	>23.0	>21.3	>24.5	>21.1	18.17(8)	0.06
18	01:29:17.27	+63:02:42.3	1.0	>23.0	>21.3	>24.5	16.717(14)	14.774(15)	0.01
22	01:28:01.81	+63:12:44.2	0.3	>23.0	>21.3	>24.5	>21.1	20.34(13)	0.03
"	01:28:01.93	+63:12:45.7	1.4	>23.0	>21.3	>24.5	>21.1	20.81(15)	0.75

[a] Source number from Table 10.7.

[b] Position of optical/IR source, averaged over all the bands in which there were detections.

[c] Position difference between the X-ray and optical/IR source.

[d] The chance of finding a star within Δr of the X-ray source given the K_s magnitude, using the star-count model of Nakajima et al. (2000).

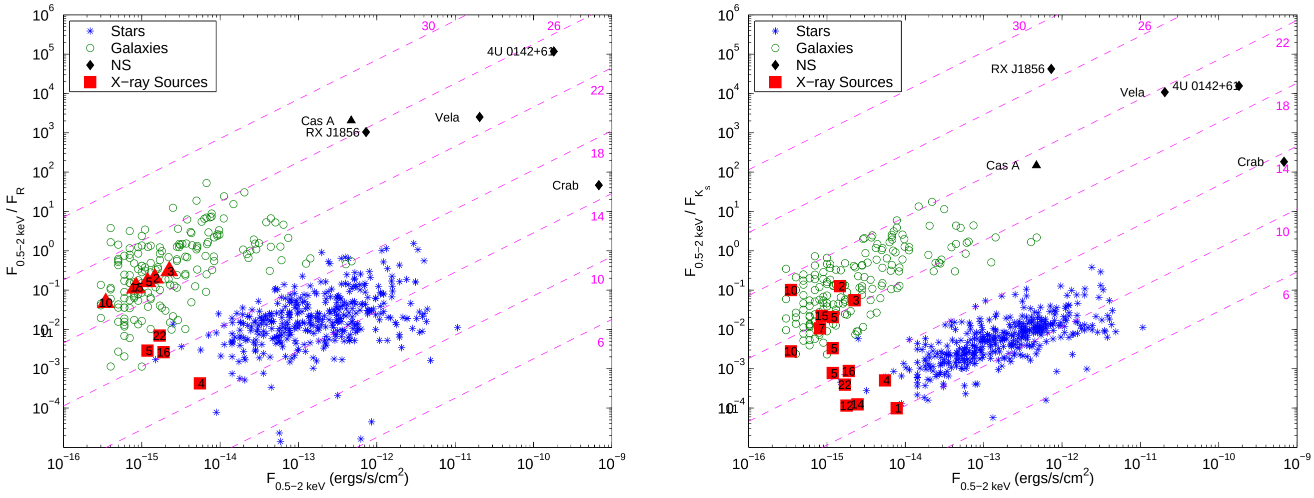

Figure 10.29 X-ray-to-optical/IR flux ratio vs. X-ray flux for sources in SNR G084.2−0.8 (Tabs. 10.6 and 10.15) with sources from the CDF/Orion studies and selected neutron stars, following Figure 10.27. Left: R-band; right: K_s-band. For the sources in SNR G093.3+6.9 the counts were converted to a flux by $F_{0.5-2.0\ \mathrm{keV}} = \mathrm{counts}_{0.5-2.0\ \mathrm{keV}} \times 2.0 \times 10^{-16}$ ergs s^{-1} cm^{-1}, appropriate for a blackbody with $kT_\infty = 0.25$ keV and $N_\mathrm{H} = 2 \times 10^{21}$ cm^{-2}.

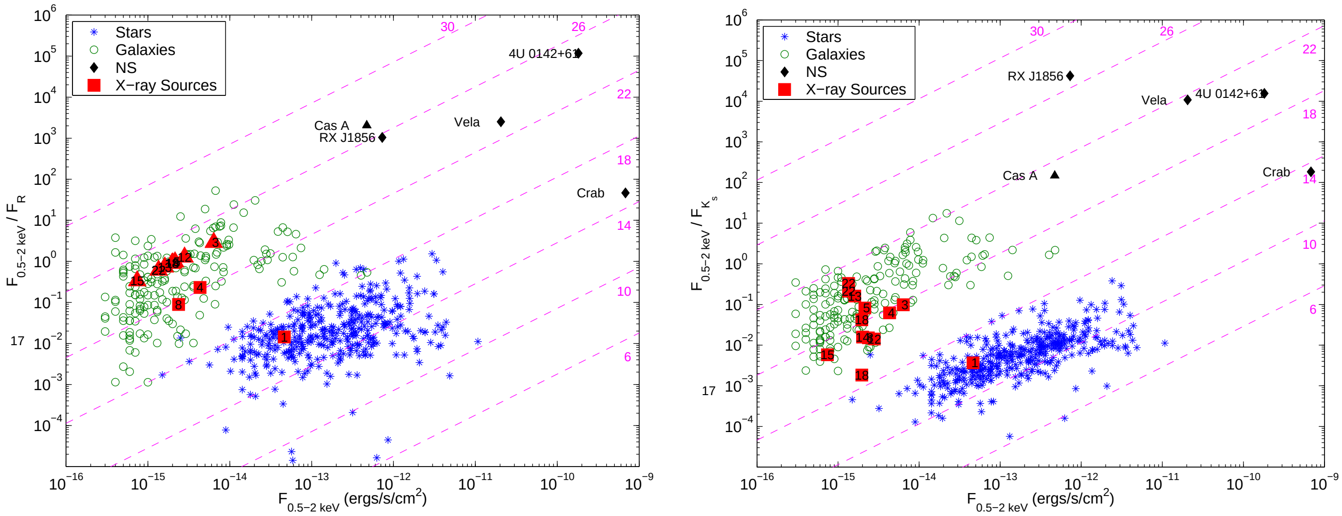

Figure 10.30 X-ray-to-optical/IR flux ratio vs. X-ray flux for sources in SNR G127.1+0.5 (Tabs. 10.7 and 10.16) with sources from the CDF/Orion studies and selected neutron stars, following Figure 10.27. Left: R-band; right: K_s-band. For the sources in SNR G127.1+0.5 the counts were converted to a flux by $F_{0.5-2.0\ \mathrm{keV}} = \mathrm{counts}_{0.5-2.0\ \mathrm{keV}} \times 2.6 \times 10^{-16}$ ergs s^{-1} cm^{-1}, appropriate for a blackbody with $kT_\infty = 0.25$ keV and $N_\mathrm{H} = 2 \times 10^{21}$ cm^{-2}.

would be closer to the Orion/CDF loci.

To determine the probabilities of random false associations, we have used the IR star-counts as modeled by Nakajima et al. (2000) and galaxy-counts observed by Cimatti et al. (2002). We plot in Figure 10.31 the number of sources brighter than a given K_s magnitude per square arcsecond for all four SNRs (because of their lower Galactic latitudes, the numbers for SNR G315.4−2.3 and SNR G084.2−0.8 are a factor of 5–15 higher than those for SNR G093.3+6.9, and SNR G127.1+0.5 is in between). We chose to plot the counts in the K_s band as these are least affected by extinction. In Tables 10.13–10.16 we also give, for sources with K_s detections, the expected number of random stars[8] brighter than the detected source within Δr (the distance between the K_s source and the X-ray source). For most cases, especially the bright 2MASS stars, these numbers are very low (< 0.01), but for a few of the fainter sources the numbers can become significant ($\gtrsim 0.5$). For those cases with roughly even chances of random associations we also examine (in §§ 10.5.1.3, 10.5.2.3, 10.5.3.3, and 10.5.4.3) other factors like the source spectrum and optical/IR colors, where available. In Figures 10.32–10.34 we show plots of expected stellar color versus magnitude for different distances and extinctions. Using these plots can help us determine the approximate type of the stellar counterparts in Tables 10.13–10.16, as demonstrated in Sections 10.5.1.3, 10.5.2.3, 10.5.3.3, and 10.5.4.3. These plots are not exact, however: they assume $A_V \propto D$ and they are only for main-sequence stars. When possible, the $J - K_s$ color should be used instead of other combinations as it is least susceptible to reddening effects ($E(J - K_s) = 0.18$, compared to $E(R - K_s) = 0.71$), but it is less sensitive to stellar type than other combinations.

In Figures 10.35 and 10.36 we examine the X-ray-to-optical offset. We see that even for sources with large offsets, the values are reasonably consistent with the expected distribution. Compare with Figure 1 of Barger et al. (2003).

We can see some general trends from the discussions for the different SNRs (SS 10.5.1.3, 10.5.2.3, 10.5.3.3, and 10.5.4.3) and from Figures 10.27–10.30. Namely, SNR G093.3+6.9 and SNR G127.1+0.5

---

[8] As seen in Figure 10.31, the chance of random associations with a galaxy is quite small compared to the chance of association with a star, and is usually negligible.

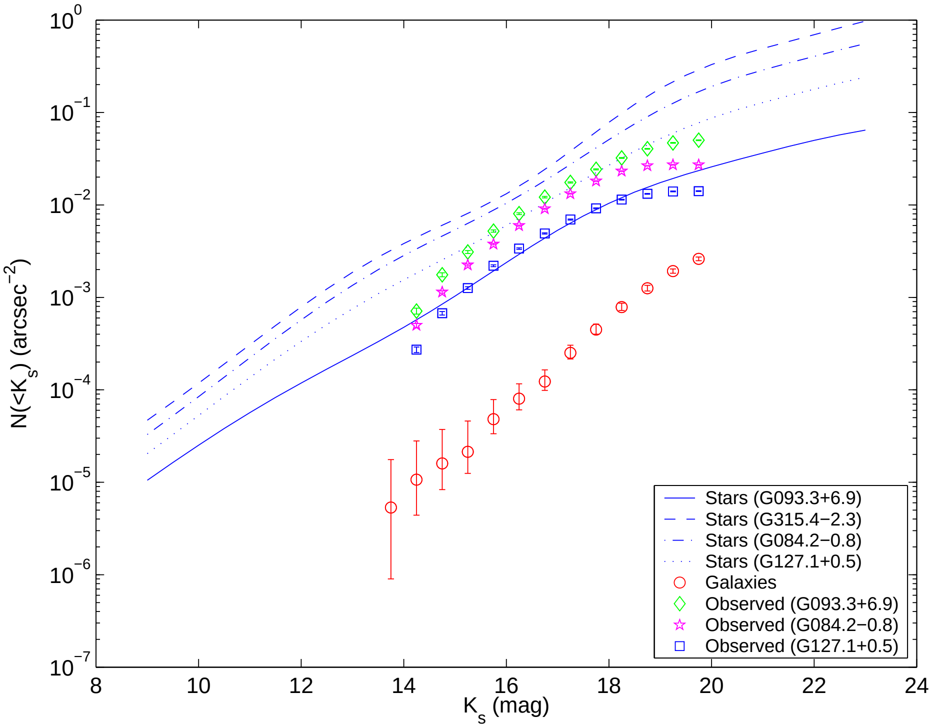

Figure 10.31 Number density of IR sources. The number per square arcsecond brighter than a given K_s magnitude is plotted against K_s magnitude. The data for stars are from the model of Nakajima et al. (2000), and are plotted for SNR G093.3+6.9 (solid line), SNR G315.4−2.3 (dashed line), SNR G084.2−0.8 (dash-dotted line), and SNR G127.1+0.5 (dotted line). For galaxies (circles) the counts are from the K-20 project (Cimatti et al. 2002). The observed data for SNR G093.3+6.9, SNR G084.2−0.8, and SNR G127.1+0.5 are from the WIRC observations, and are likely not complete for $K_s \gtrsim 19$. The predicted star counts are within a factor of 3 of the observed counts.

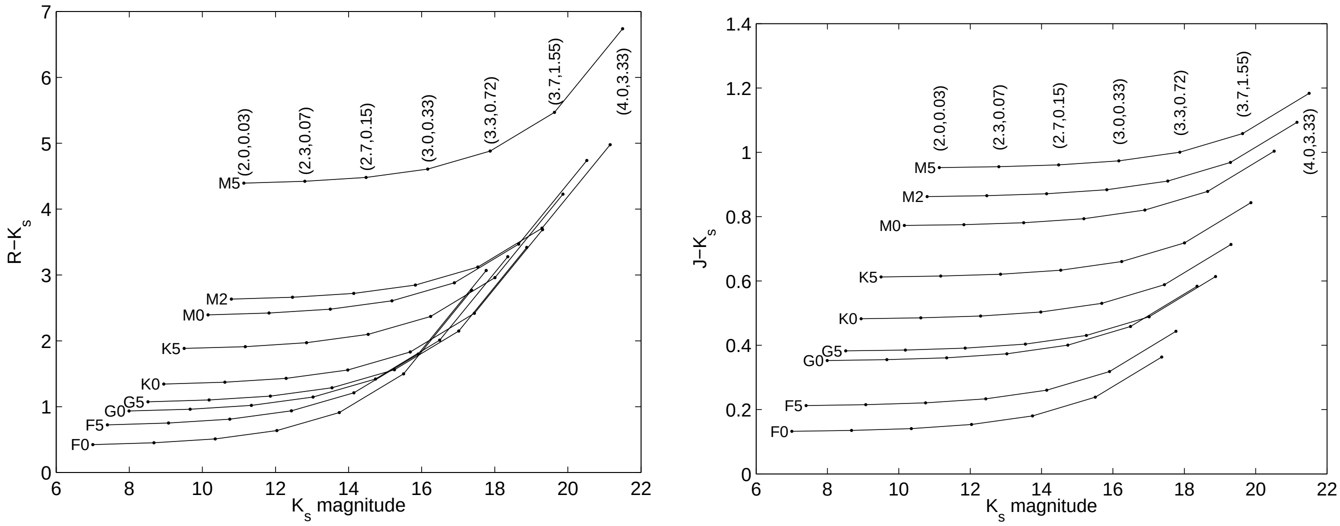

Figure 10.32 Stellar color vs. magnitude for main-sequence stars, from Cox (2000, pp. 151 & 388): we have assumed that $A_V \propto d$, normalized to $A_V = 1$ mag at $d = 3$ kpc (roughly appropriate for SNR G093.3+6.9 and SNR G315.4−2.3). Left: $R - K_s$ color vs. K_s magnitude. Right: $J - K_s$ color vs. K_s magnitude. Shown are tracks for luminosity class V stellar types F0, F5, G0, G5, K0, K5, M0, M2, and M5 (as labeled). Points along the tracks are labeled by $(\log_{10}(d/\text{pc}), A_V)$, and the tracks progress from (2.0,0.03) to (4.0,3.3). The maximum values of A_V expected along the lines of sight to SNR G093.3+6.9 and SNR G315.4−2.3 are 2 mag and 5 mag, respectively (Predehl & Schmitt 1995). The majority of the stars from Nakajima et al. (2000) are of spectral type M0–M3.

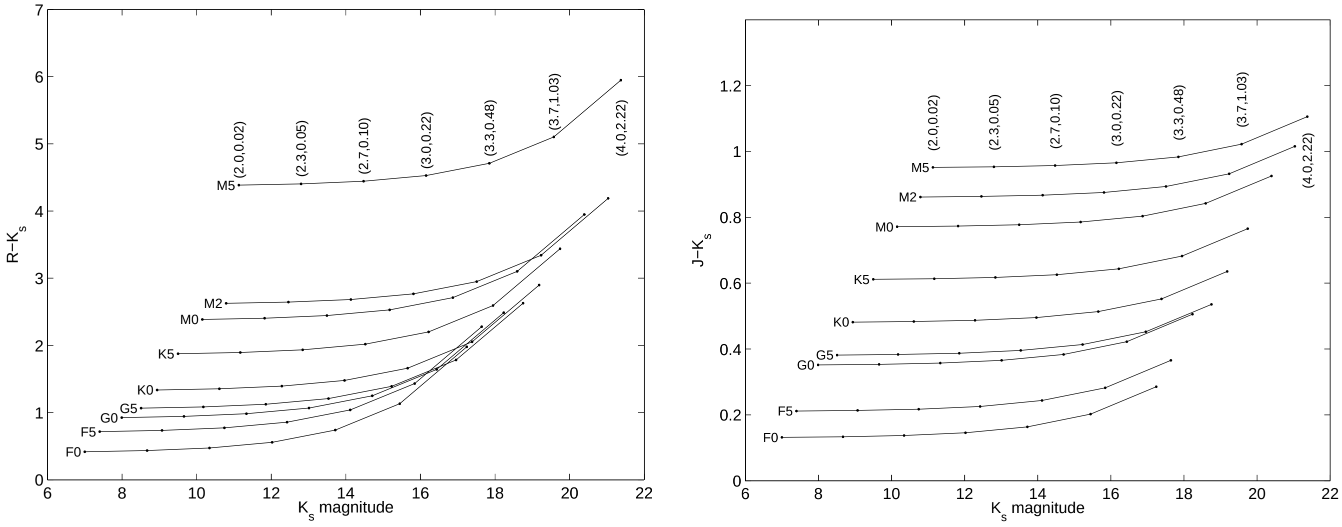

Figure 10.33 Stellar color vs. magnitude for main-sequence stars, from Cox (2000, pp. 151 & 388): we have assumed that $A_V \propto d$, normalized to $A_V = 1$ mag at $d = 4.5$ kpc (roughly appropriate for SNR G084.2−0.8). Otherwise the figures are the same as Figure 10.32. The maximum value of A_V expected along the line of sight to SNR G084.2−0.8 is 5 mag (Predehl & Schmitt 1995).

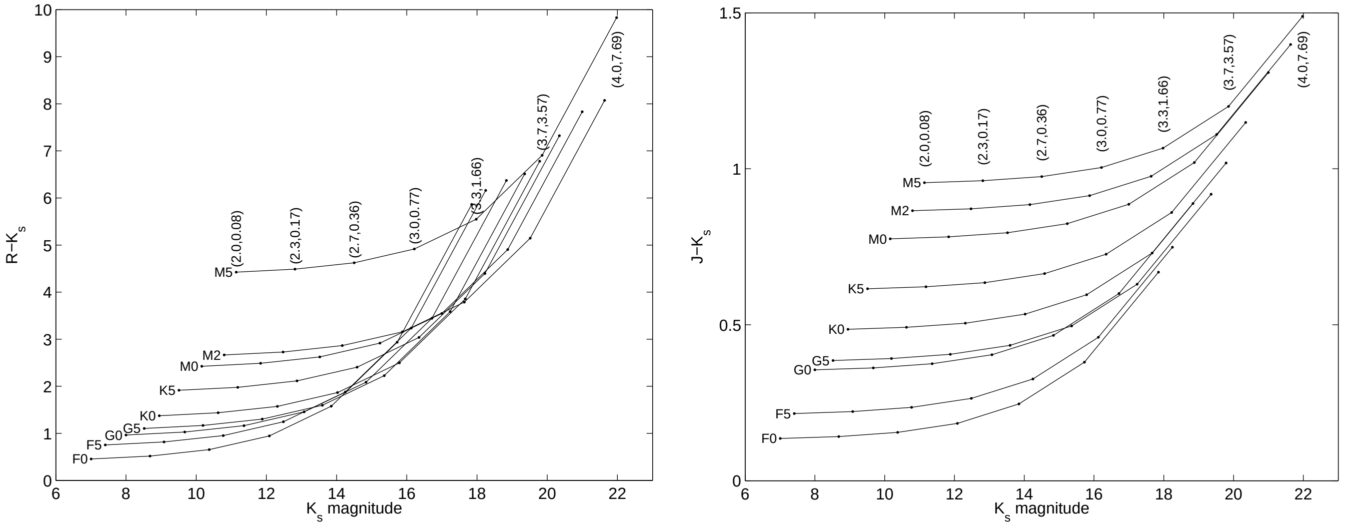

Figure 10.34 Stellar color vs. magnitude for main-sequence stars, from Cox (2000, pp. 151 & 388): we have assumed that $A_V \propto d$, normalized to $A_V = 1$ mag at $d = 1.3$ kpc (roughly appropriate for SNR G127.1+0.5). Otherwise the figures are the same as Figure 10.32. The maximum value of A_V expected along the line of sight to SNR G127.1+0.5 is 5 mag (Predehl & Schmitt 1995).

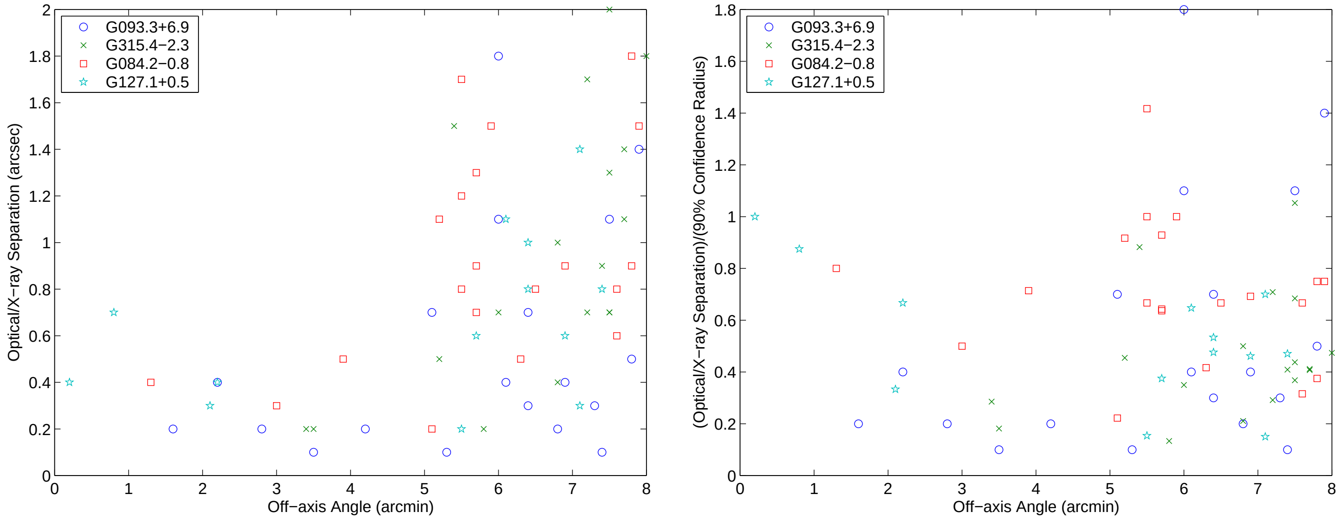

Figure 10.35 Distribution of offset between X-ray sources and their proposed optical/IR counterparts as a function of off-axis angle. Left: offset (in arcsec) vs. off-axis angle (in arcmin). Right: offset normalized to the 90% radius (from Tabs. 10.4–10.7) vs. off-axis angle (in arcmin). Sources from SNR G093.3+6.9 are circles, those from SNR G315.4−2.3 are x's, those from SNR G084.2−0.8 are squares, and those from SNR G127.1+0.5 are stars.

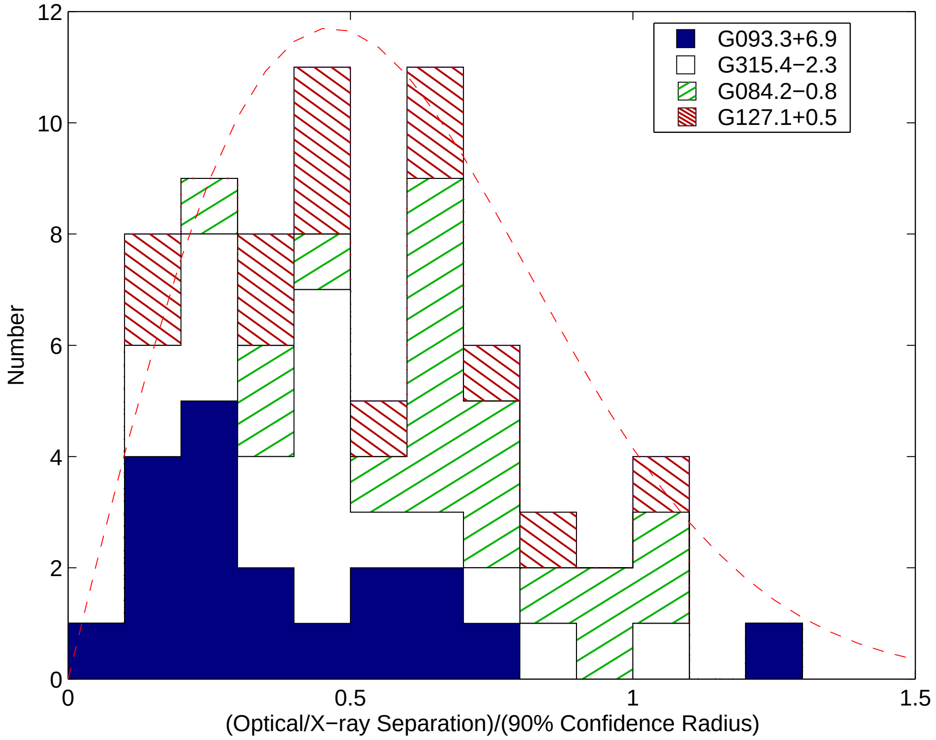

Figure 10.36 Histogram of the offsets between X-ray sources and their proposed optical/IR counterparts normalized to the 90% radius (from Tabs. 10.4– 10.7). Sources from SNR G093.3+6.9 are solid blue, those from SNR G315.4−2.3 are in white, those from SNR G084.2−0.8 are the green hatched region, and those from SNR G127.1+0.5 are the maroon hatched region. The red dashed line is the expected distribution ($f(r) \propto r\exp(-r^2)$).

Table 10.17. Classifications of X-ray Sources in SNRs G093.3+6.9, G315.4−2.3, G084.2+0.8, & G127.1+0.5

SNR	Stars	Galaxies	Uncertain[a]
G093.3+6.9	3	15	0
G315.4−2.3	8	4	3: 17, 21, 28
G084.2−0.8	6	8	2: 5, 10
G127.1+0.5	0	9	3: 12, 18, 22
Total	17	36	8

Note. — Classifications follow the discussion in §§ 10.5.1.3, 10.5.2.3, 10.5.3.3, and 10.5.4.3.

[a] Uncertain sources are those for which the classification as a star or galaxy was unclear. This encompasses both sources that definitely have counterparts but where the type is uncertain and sources where the counterpart itself is uncertain. The uncertain sources for each SNR are listed.

have the highest fractions of probable galaxies, with SNR G084.2−0.8 intermediate, and SNR G315.4−2.3 the lowest (summarized in Tab. 10.17). This is largely due to the differing Galactic latitudes and longitudes of the four SNRs, and it is also seen somewhat in Figure 10.31. SNR G315.4−2.3, at a relatively low $|b|$ and well in quadrant IV, is along the line of sight of many stars and the short exposure time of the observation helps to keep the number of background galaxies down. SNR G084.2−0.8 is at a lower $|b|$, but it's position near $l = 90°$ and at the edge of a spiral arm (Feldt & Green 1993) lowers the number of stars, while the longer exposure identified more galaxies (many of whom are heavily reddened). The total $N_{\rm H}$ along this line of sight helps to delineate galaxies and stars even without optical counterparts, as can be seen from Figure 10.12. Finally, SNR G093.3+6.9 is at a relatively high $|b|$ and also does not look toward the inner Galaxy, and SNR G127.1+0.5 is decidedly toward the outer Galaxy, so the X-ray sources are predominantly background galaxies.

10.5 Results

Here we discuss the results of applying the techniques in § 10.4 to the first four SNRs from our *Chandra* sample: SNRs G093.3+6.9, G315.4−2.3, G084.2+0.8, and G127.1+0.5. For each SNR, we first discuss its general properties, then details of the X-ray analysis, optical observations and analysis, and finally identification of counterparts.

10.5.1 SNR G093.3+6.9

The radio source SNR G093.3+6.9 (also known as DA 530) was first identified as an SNR by Roger & Costain (1976), whose radio observations showed a shell 27′ in diameter with bright rims and high polarization (Haslam, Salter, & Pauls 1980)—see Figure 10.2. The kinematic distance based on H I emission gives a distance of 2.5 ± 0.4 kpc, but allowing for noncircular motion relaxes the distance limits and constrains the distance to be 1.0–3.5 kpc.

While infrared and optical emission have been only marginally detected, SNR G093.3+6.9 has been detected by *ROSAT* (Landecker et al. 1999). Based on fits to the X-ray spectrum, Landecker et al. (1999) prefer a distance of 3.5 kpc. In X-rays, it appears superficially similar to SN 1006, which has been suggested to be the remnant of a Type Ia SN (Fesen et al. 1988, Allen, Petre, & Gotthelf 2001). Taken together with the high Galactic latitude of 7°, some authors believe that SNR G093.3+6.9 is also the young (≈ 5000 yr) remnant from a Type Ia SN (e.g., Landecker et al. 1999), but there are some problems with this, as none of the X-ray spectral models give fully consistent results and they imply that the SNR may have occurred in a especially low-density bubble such as might exist around a massive star (i.e., the progenitor of a Type II SN).

Most of the X-ray fits in Landecker et al. (1999) assumed a hydrogen column density of $N_{\rm H} = 2.1 \times 10^{21}$ cm^{-2}, which is consistent with the value inferred from the H I data. This is the nominal value that we adopt for this source below. However, some of the fits required larger values of $N_{\rm H}$, up to 6×10^{21} cm^{-2}, while the total Galactic column density[9] in this direction is only 4×10^{21} cm^{-2}.

Lorimer, Lyne, & Camilo (1998) searched SNR G093.3+6.9 unsuccessfully for a radio pulsar down to a limit of 0.8 mJy at 606 MHz, implying a luminosity limit of $Sd^2 < 9.8$ mJy kpc^2. Extrapolating to a frequency of 1400 MHz using an average spectral index of -1.8 (Maron et al. 2000), this is still a factor of almost 10 brighter than the luminosities of the emerging class of faint radio pulsars such as PSR J0205+6449 in 3C 58 (Camilo et al. 2002d). Landecker et al. (1999) identified six point sources in the *ROSAT* PSPC data, three of which are inside the remnant (see § 10.5.1.1), but they conclude that none of these is likely the compact remnant of the explosion as they are all relatively hard (however, neutron stars such as the Crab can also have hard spectra).

10.5.1.1 X-ray Observations

We observed SNR G093.3+6.9 with the *Chandra X-ray Observatory* (Weisskopf et al. 2000) on 2001 December 17. Based on examination of the *ROSAT*/PSPC data, we determined the center of the remnant[10] to be at J2000 position $20^{\rm h}52^{\rm m}14^{\rm s}$, $+55°20'30''$, about $1.5'$ away from the nominal position from Green (2001). The aim point was on the ACIS-I imaging array, and the final exposure time was 16.4 ks. See Figure 10.2 for the placement of the ACIS-I detector relative to the SNR. A smoothed image of the data is shown in Figure 10.6 with the X-ray sources that we identified (Tab. 10.4) labeled.

The analysis of the *Chandra* data proceeded according to Section 10.4.2. In Figure 10.10 we plot the H-band counts versus the L-band counts for the sources in Table 10.4. We also plot the lines for sources with power laws having $\Gamma = 0$, 1.0, 1.5, and 2.0 and blackbody models having $kT_\infty = 0.2$, 0.4, and 1.0 keV, all with $N_{\rm H} = 2 \times 10^{21}$ cm^{-2}, and the median and 25-/75-percentiles of count ratios ($C_{\rm H}/C_{\rm L}$) for the sources from the CDF and Orion. Most of the sources are consistent with power laws having indices from 0.0 to 2.0, such as one would expect for energetic pulsars like the Crab or for AGNs. A few sources (SNR G093.3+6.9:1, SNR G093.3+6.9:7, and SNR G093.3+6.9:16) are softer, with implied temperatures (for blackbody models) of $kT_\infty \approx 0.4$ keV.

Three of the sources were also detected by Landecker et al. (1999) in *ROSAT* data. Source SNR G093.3+6.9:1 is source 6 from Landecker et al. (1999), SNR G093.3+6.9:2 is source 5 from Landecker et al. (1999), and SNR G093.3+6.9:7 is source 4 from Landecker et al. (1999). While it is difficult to compare directly because of the small numbers of counts involved, the count rates and hardness ratios are roughly

---

[9] Determined using Colden, `http://asc.harvard.edu/toolkit/colden.jsp`.

[10] The geometric centers of SNRs were identified by eye, with the understanding that the actual site of the SNR is not always at the geometric center (e.g., Gvaramadze 2002).

comparable between those that we observed here and those predicted by converting the *ROSAT* count rates to *Chandra* using `W3PIMMS`[11]

10.5.1.2 Optical/IR Observations

We observed the field of SNR G093.3+6.9 a number of times with a number of instruments, as described in Table 10.9. The aim of the observations was to identify counterparts to the X-ray sources in Table 10.4 with progressively deeper exposures (§ 10.4.5). Data reduction for the optical data used standard `IRAF` routines to subtract the bias, flat-field, and then combine separate exposures. For the LFC and LRIS-B data, where significant focal-plane distortion prevented simple addition of data and where there are multiple CCDs, we used the `IRAF MSCRED` package to flatten each image with custom distortion maps prior to addition. For the infrared data, we subtracted dark frames, then produced a sky frame for subtraction by taking a sliding box-car window of 4 exposures on either side of a reference exposure. We then added the exposures together, identified all the stars, and produced masks for the stars that were used to improve the sky frames in a second round of sky subtraction.

We determined *BVRI* photometric zero points for the P60CCD data using observations of the Stetson fields[12] PG1657 and NGC 6823 (Stetson 2000). We then determined zero points for the other optical data referenced to the P60CCD observations, employing appropriate transformations (Jorgensen 1994; Smith et al. 2002).

We determined a K_s zero point for the P60IR data using observations of the standard stars SJ 9101, SJ 9166, SJ 9177, and SJ 9188 (Persson et al. 1998). For the NIRC observations, we determined zero points using 1–4 2MASS (Skrutskie et al. 1997) stars in each field (the K_s magnitudes include a 0.3 mag systematic uncertainty arising from zero point calibration). For the WIRC observations, we determined zero points using 400 unsaturated 2MASS stars.

We performed absolute astrometry on the R-band P60CCD data, the LFC data, the LRIS data, and the WIRC data. After applying distortion corrections to the LFC and LRIS data (we did not use any distortion for the P60CCD data or WIRC), we solved for plate scale, rotation, and central position relative to stars from version 2.2 of the Guide Star Catalog (GSC-2.2[13]) for all but WIRC and relative to 2MASS stars for WIRC, getting residuals in each coordinate of $0\farcs22$ (427 stars), $0\farcs08$ (135 stars), $0\farcs13$ (613 stars), and $0\farcs10$ (530 stars) for P60CCD, LRIS, LFC, and WIRC, respectively. For the remaining data (ESI, P60IR, and NIRC) we used nonsaturated stars from the other observations to boot-strap the astrometry, getting typical residuals of $< 0\farcs05$ in each coordinate.

10.5.1.3 Notes on Individual Sources

SNR G093.3+6.9:1 This source is almost certainly an active star: the infrared colors are indicative of class G0 or so, the source falls on the locus of stars in Figure 10.27, and the variability (Fig. 10.14) is typical of that seen for stars (Marino, Micela, & Peres 2000). The X-ray luminosity expected of such a star, 10^{29-31} ergs s^{-1} (Katsova & Cherepashchuk 2000) implies that it is ~ 500 pc away, consistent with its K_s magnitude (Fig. 10.32).

SNR G093.3+6.9:2 This is likely a galaxy, given its position in Figure 10.27 and its constant X-ray flux (Fig. 10.14).

SNR G093.3+6.9:4 This is likely a galaxy, given its position in Figure 10.27.

---

[11] See `http://heasarc.gsfc.nasa.gov/Tools/w3pimms.html`.

[12] `http://cadcwww.dao.nrc.ca/cadcbin/wdbi.cgi/astrocat/stetson/query`

[13] `http://www-gsss.stsci.edu/support/data_access.htm`

SNR G093.3+6.9:5 This is likely a galaxy, given its position in Figure 10.27.

SNR G093.3+6.9:6 The IR counterpart places it midway between the stars and galaxies in Figure 10.27. It could be a spurious counterpart, but there are other sources in its vicinity in Figure 10.27. Based on its hard spectrum and extremely red $R - K_s$ colors, it is likely a galaxy.

SNR G093.3+6.9:7 While redder than SNR G093.3+6.9:1, it is otherwise similar, suggesting that this is very likely also an active star of type M2 or so.

SNR G093.3+6.9:8 The optical counterpart is near the edge of the error circle, but it is far off-axis and therefore this is not unexpected. This source is otherwise consistent with being a galaxy.

SNR G093.3+6.9:9 This source has the most extreme X-ray-to-IR flux ratio of the sources in Table 10.13, but it most likely is not the associated neutron star. The optical counterpart has a very small ($0\farcs2$) offset from the X-ray source, suggesting that while it may be 2 mag fainter than other counterparts it is still likely to be a real association. It is still reasonably consistent with the CDF locus and it is somewhat red ($R - K_s > 3$), contrary to known neutron stars (Kaplan et al. 2003b) but similar to that of other galaxy candidates like SNR G093.3+6.9:10. Also, the X-ray spectrum is moderately hard, consistent with the power-law expected from an AGN. Without an optical counterpart, it might be a candidate for a low-luminosity Crab-like pulsar (L_X would be $\approx 2 \times 10^{31}$ ergs s^{-1}), but with the counterpart it is very likely an AGN.

SNR G093.3+6.9:10 This is likely a galaxy, given its position in Figure 10.27.

SNR G093.3+6.9:13 This is likely a galaxy, given its position in Figure 10.27.

SNR G093.3+6.9:14 This is likely a galaxy, given its position in Figure 10.27 and hard spectrum.

SNR G093.3+6.9:15 This is likely a galaxy, given its position in Figure 10.27. It may be extended, indicating a low redshift (Fig. 10.17).

SNR G093.3+6.9:16 While redder than SNR G093.3+6.9:1, it is otherwise similar, suggesting that this is very likely also an active star of type K5.

SNR G093.3+6.9:17 This is likely a galaxy, given its hard spectrum and position in Figure 10.27. The IR source may also be extended (Fig. 10.18).

SNR G093.3+6.9:19 There are multiple IR sources listed in Table 10.13, one just in the error circle and one outside (see Fig. 10.18). The true counterpart is likely the one in the circle (the first source in Tab. 10.13), which is likely a galaxy, given its position in Figure 10.27 and its colors.

SNR G093.3+6.9:24 This is likely a galaxy, given its position in Figure 10.27.

SNR G093.3+6.9:26 This is likely a galaxy, given its position in Figure 10.27.

SNR G093.3+6.9:30 This is likely a galaxy, given its hard spectrum and position in Figure 10.27, similar to SNR G093.3+6.9:19. The X-ray hardness ratio is, while harder than most galaxies, not unheard of in that context (Bauer et al. 2002).

10.5.2 SNR G315.4−2.3

SNR G315.4−2.3 (RCW 86, or MSH 14−63) is a large (45′), nonthermal Galactic radio shell (Fig. 10.3) identified as an SNR by Hill (1967) and considered as the remnant of the historic supernova explosion SN 185 (Clark & Stephenson 1977).

The identification of SNR G315.4−2.3 with the historic supernova explosion of AD 185 is a matter of some controversy.[14] Geometric considerations would require a distance to the remnant of less than 1 kpc (Strom 1994), while the kinematic distance of the remnant is found to be 2.8 ± 0.4 kpc (Rosado et al. 1996). The latter distance suggests a physical connection with an OB association (Westerlund 1969), an interpretation that is supported by the light elemental abundance, which favors a Type II supernova and by the measured interstellar column density. However, some recent modeling of X-ray data suggest a distance as close as 1.2 kpc and abundances more typical of a Type Ia explosion (Bocchino et al. 2000), more in line with that expected if SNR G315.4−2.3 were the remnant of SN 185, although these interpretations are by no means secure (Rho et al. 2002). In what follows, we assume the 2.8 kpc distance; if the SNR were closer (and younger), then our luminosity limits would be lower and even more constraining if SNR G315.4−2.3 is the result of a core-collapse event.

In addition to radio emission, SNR G315.4−2.3 shows thin Balmer-dominated filaments (Long & Blair 1990; Smith 1997) and X-ray emission (Pisarski, Helfand, & Kahn 1984; Vink, Kaastra, & Bleeker 1997) that have the same general morphology. There is X-ray spectral variation over the remnant, but the hydrogen column density is likely $\approx (2-3) \times 10^{21}$ cm^{-2} (Vink et al. 1997) (the total Galactic column density from Colden in this direction is 9×10^{21} cm^{-2}). The age of SNR G315.4−2.3 is somewhat uncertain, as it has features of both young (a few thousand years) and old ($> 10^4$ yr) remnants (Dickel, Strom, & Milne 2001). On average, probably the best estimate for its age is 4000 yr, although ages up to 10^4 yr are not impossible (Rosado et al. 1996; Petruk 1999; Bocchino et al. 2000; Borkowski et al. 2001).

Kaspi et al. (1996) searched SNR G315.4−2.3 unsuccessfully for a radio pulsar down to a limit of 1.3 mJy at 436 MHz and 0.2 mJy at 1520 MHz, both implying a 1400-MHz luminosity limit of $Sd^2 < 1.5$ mJy kpc^2. This is quite faint—a factor of three fainter than PSR J0205+6449.

Based on *ROSAT* and *Einstein* data, Vink et al. (2000) identified an X-ray point source inside SNR G315.4−2.3 that they conclude is likely an active star. Unfortunately, this source is outside our X-ray observations so we cannot confirm or deny their conclusion. Similarly, Gvaramadze & Vikhlinin (2003) used *Chandra* data of the bright south-west region to search for point sources, motivated by their hypothesis that SNR G315.4−2.3 was a significantly off-center cavity SN. They find one source at the edge of the remnant (Fig. 10.3) without an optical counterpart, although the only limit they cite is from the Digital Sky Survey ($m_{\rm lim} \sim 21$), and they conclude based on this and the source's X-ray spectrum that it may be a neutron star (we have examined 2MASS and see no clear counterpart to this source there, implying limits of $J > 15.8$ and $K_s > 14.6$). However, these optical/IR limits are far from constraining (§ 10.5.2.2) and it is quite possible that, while not an active star like the other source they identify, this source is an active galaxy. In any case, all of these sources are quite far out from the nominal center of the remnant. If the explosion occurred near what we define as the center of the SNR, none of the sources in Vink et al. (2000) or Gvaramadze & Vikhlinin (2003) could be the compact remnant without transverse velocities in excess of 1500 km s^{-1}—not an unheard of velocity (§ 10.6.1.1), but certainly large.

10.5.2.1 X-ray Observations

We observed SNR G315.4−2.3 with *Chandra* on 2002 December 02. We determined the center of the remnant to be at (J2000) $14^{\rm h}42^{\rm m}50^{\rm s}$, $-62^\circ28'20''$. The aim point was on the ACIS-I imaging array, and

---

[14] While some recent reviews of the Chinese record even question the association of SN 185 with a supernova explosion event (Chin & Huang 1994; Schaefer 1995; Smith 1997), this is not universally accepted (Stephenson & Green 2002).

the final exposure time was 10.0 ks. See Figure 10.3 for the placement of the ACIS-I detector relative to the SNR. A smoothed image of the data is shown in Figure 10.7 with the X-ray sources that we identified (Tab. 10.5) labeled.

The analysis of the *Chandra* data proceeded according to Section 10.4.2. In Figure 10.11 we plot the H-band counts versus the L-band counts for the sources in Table 10.5. Most of the sources are consistent with power-laws having indices from 0.0–2.0, but the sources are slightly softer than those in SNR G093.3+6.9. A few sources (SNR G315.4−2.3:2, SNR G315.4−2.3:6, SNR G315.4−2.3:8, SNR G315.4−2.3:9, SNR G315.4−2.3:26, and SNR G315.4−2.3:28) are soft, with implied temperatures (for blackbody models) of $kT_\infty \leq 0.4$ keV.

10.5.2.2 Optical/IR Observations

For SNR G315.4−2.3 we also observed the field with a variety of instruments, listed in Table 10.10. The reduction proceeded as in § 10.5.1.2.

We determined $BVRI$ zero points for the C40 data using observations of the Stetson fields[15] E4 and L107 (Stetson 2000). We then determined zero points for the other optical data referenced to the C40 observations, employing appropriate transformations (Jorgensen 1994; Smith et al. 2002). We determined a K_s zero point for the PANIC data with ≈ 20 2MASS stars in each field.

Astrometry was performed relative to 2MASS.[16] For the C40 and EMMI data, where there is some optical distortion, we computed solutions (plate scale, rotation, and central position) locally around each X-ray source, limiting the fields to $\pm 1'$. These solutions typically used 45 stars and had residuals of $0\farcs09$ in each coordinate. For the MagIC and PANIC images, we computed solutions for the entire image, using ≈ 80 stars and giving residuals of $0\farcs05$ in each coordinate.

10.5.2.3 Notes on Individual Sources

SNR G315.4−2.3:1 This is likely a galaxy, given its position in Figure 10.28 and its hard spectrum (Fig. 10.11). However, we only detect the counterpart in a single band and it is quite faint, so it is possible that the counterpart is a coincidence.

SNR G315.4−2.3:2 This is likely a star, given its position in Figure 10.28 and its soft spectrum (Fig. 10.11). Based on its IR colors and magnitude, this may be a K2III giant star.

SNR G315.4−2.3:3 The optical counterpart places it midway between the stars and galaxies in Figure 10.28. It could be a spurious counterpart, but there are other sources in its vicinity in Figure 10.28. Based on its hard spectrum, it is likely a galaxy.

SNR G315.4−2.3:5 This is likely a galaxy, given its position in Figure 10.28 and its hard spectrum (Fig. 10.11).

SNR G315.4−2.3:6 This is likely a star, given its position in Figure 10.28 and its very soft spectrum (Fig. 10.11). Based on its IR colors, it is likely type K0 or so.

SNR G315.4−2.3:8 This is likely a star, given its position in Figure 10.28 and its soft spectrum (Fig. 10.11). Based on its IR colors, it is likely type G5 or so.

---

[15] `http://cadcwww.dao.nrc.ca/cadcbin/wdbi.cgi/astrocat/stetson/query`

[16] The 2MASS data for this field were released before those for SNR G093.3+6.9, SNR G084.2−0.8, and SNR G127.1+0.5, where we used the GSC-2.2 for some of the astrometry. We have compared the results of 2MASS and GSC-2.2 astrometry and found them indistinguishable.

SNR G315.4−2.3:9 This is likely a star, given its position in Figure 10.28 and its soft spectrum (Fig. 10.11). Based on its IR colors, it is likely type M7 or so.

SNR G315.4−2.3:12 This is likely a galaxy, given its position in Figure 10.28 and its hard spectrum (Fig. 10.11). While the chance of a random star in the error circle is non negligible, only the reddest stars have $R-K_s>6$ (Fig. 10.32) and these stars make up only a small fraction of those in this line of sight (Nakajima et al. 2000).

SNR G315.4−2.3:13 This is likely a star, given its position in Figure 10.28. Based on its IR colors, it is likely type M6 or so.

SNR G315.4−2.3:17 The optical/IR source is on the edge of the X-ray error circle in Figure 10.20 (to the west of center). There is also a faint smudge that is below the detection threshold and may be an extension of the source just to the north of the error circle. If the source to the west is the counterpart, the offset is large but not entirely unreasonable (Fig. 10.36; see also Barger et al. 2003). The source would then be a galaxy, given its position in Figure 10.28, hard spectrum (Fig. 10.11), and red colors ($R-K_s>8$; see Thompson et al. 1999). It is also possible that the northern source is the correct counterpart, in which case the source would also likely be a galaxy. A third possibility is that the X-ray and optical/IR emission are not entirely spatially coincident, such as would be the case for a nearby interacting binary star or a low-redshift galaxy. This might explain the X-ray-to-optical offset. It is unlikely that this source is a neutron star, as its spectrum is quite hard—harder than that expected of a Crab-like pulsar.

SNR G315.4−2.3:19 This is likely a star, given its position in Figure 10.28. Based on its IR colors, it is likely type F7 or so.

SNR G315.4−2.3:21 There are two optical sources in the X-ray error circle (Fig. 10.21), or perhaps one extended source. Separately, each source is near the star/galaxy boundary in Figure 10.28, and the X-ray spectrum is intermediate, so no quick classification is possible. This may be an interacting binary (CV, X-ray binary, etc.), sources that would not have been in the Orion sample but are present in the general Galactic/extragalactic populations (Hertz & Grindlay 1988; Grindlay et al. 2003).

SNR G315.4−2.3:23 This is likely a star, given its position in Figure 10.28. Based on its IR colors, it is likely type M5 or so.

SNR G315.4−2.3:26 This is likely a star, given its position in Figure 10.28. Based on its IR colors, it is likely type K5 or so.

SNR G315.4−2.3:28 There are three possible counterparts in Figure 10.21. The brightest is the closest to the center of the error circle and would be consistent with being a star, and it may be extended to the north, possibly indicating a binary companion. The source to the east of the circle's center is more consistent with a galaxy. Finally, the source to the south-west of the circle's center, on the edge of the circle, is also more consistent with a galaxy. Given the soft X-ray spectrum of this source, the bright stellar companion is likely the correct one. It is also possible that there is no companion (the random probability for a star is somewhat high, even for the closest source), in which case it would be a candidate neutron star, but a definitive answer will have to await additional X-ray observations (assessing the spectrum and variability and improving the position).

10.5.3 SNR G084.2−0.8

SNR G084.2−0.8 was identified as a Galactic SNR by Matthews et al. (1977), who observed a well-defined nonthermal radio shell (Fig. 10.4) with diameters of about $20' \times 14'$. Feldt & Green (1993) identified CO and H I emission interacting with SNR G084.2−0.8, giving the remnant a kinematic distance of 4.5 kpc and a size of 28 pc × 22 pc. It has not been detected in X-rays so there are no spectral fits to determine its age or temperature. The hydrogen column density to SNR G084.2−0.8 is $N_{\rm H} \approx 2 \times 10^{21}$ (again using Colden) and integrating the appropriate velocity range), while the total hydrogen through the Galaxy is $N_{\rm H} \approx 1 \times 10^{22}$. Assuming a Sedov-phase remnant, we find (see § 10.4.1) $t_4 \approx 0.6T_7^{-1/2}$, and since $T_7 \approx 1$ holds for most SNRs, we can say that $t_4 \approx 0.3$–1.0 (with $T_7 = 0.3$–3).

Lorimer et al. (1998) searched SNR G084.2−0.8 unsuccessfully for a radio pulsar down to a limit of 1.1 mJy at 606 MHz, implying a luminosity limit of $Sd^2 < 44$ mJy kpc^2. Extrapolating to a frequency of 1400 MHz using an average spectral index of −1.8, this is a factor of almost > 50 brighter than the luminosity of PSR J0205+6449.

10.5.3.1 X-ray Observations

We observed SNR G084.2−0.8 with *Chandra* on 2002 November 24. We determined the center of the remnant to be at (J2000) $20^{\rm h}53^{\rm m}21^{\rm s}$, $+43^\circ26'55''$. The aim point was on the ACIS-I imaging array, and the final exposure time was 24.6 ks. See Figure 10.4 for the placement of the ACIS-I detector relative to the SNR. A smoothed image of the data is shown in Figure 10.8 with the X-ray sources that we identified (Tab. 10.6) labeled.

The analysis of the *Chandra* data proceeded according to Section 10.4.2. In Figure 10.12 we plot the H-band counts versus the L-band counts for the sources in Table 10.6. About half of the sources are consistent with power-laws having indices from 0.0–2.0, but a number of the sources are significantly harder. These are likely distant AGNs that have had their soft photons heavily absorbed by Galactic gas—a source with $\Gamma = 0.5$ and $N_{\rm H} = 2 \times 10^{22}$ cm^{-2} would have $\mathrm{HR}_{\rm L,H} = 0.8$, similar to the hardest sources. A few sources (SNR G084.2−0.8:1, SNR G084.2−0.8:4, SNR G084.2−0.8:14, SNR G084.2−0.8:16) are soft, with implied temperatures (for blackbody models) of $kT_\infty \leq 0.4$ keV.

10.5.3.2 Optical/IR Observations

We observed the field of SNR G084.2−0.8 a number of times with a number of instruments, as described in Table 10.11. The reduction proceeded as in § 10.5.1.2.

We determined the photometric zero points for the LFC data by bootstrapping from VRI Palomar 60 inch observations of the Stetson fields[17] L98, NGC 7654, and PG 0231 (Stetson 2000) and by employing appropriate transformations (Jorgensen 1994; Smith et al. 2002) to LFC observations of these fields. For the WIRC observations, we determined zero points using 1700 unsaturated 2MASS (Skrutskie et al. 1997) stars. For the NIRC observations, we determined zero points using about 60 stars from the WIRC image.

We performed absolute astrometry on the LFC data and the WIRC data. After applying distortion corrections to the LFC data (we did not use any distortion correction for WIRC), we solved for plate scale, rotation, and central position relative to stars from version 2.2 of the Guide Star Catalog (GSC-2.2[18]) for all but WIRC and relative to 2MASS stars for WIRC, getting residuals in each coordinate of $0\farcs13$ (600 stars), and $0\farcs19$ (2500 stars) for LFC and WIRC respectively. For the NIRC data we used nonsaturated stars from the WIRC to boot-strap the astrometry, getting typical residuals of $< 0\farcs06$ in each coordinate with about 60 stars.

---

[17] `http://cadcwww.dao.nrc.ca/cadcbin/wdbi.cgi/astrocat/stetson/query`

[18] `http://www-gsss.stsci.edu/support/data_access.htm`

10.5.3.3 Notes on Individual Sources

SNR G084.2−0.8:1 This source is almost certainly an active star: the infrared colors are indicative of class F6 or so, the X-ray spectrum is quite soft, and the source falls on the locus of stars in Figure 10.29.

SNR G084.2−0.8:2 This is likely a galaxy, given its position in Figure 10.29 and its hard X-ray spectrum.

SNR G084.2−0.8:3 This is likely a galaxy, given its position in Figure 10.29 and its hard X-ray spectrum.

SNR G084.2−0.8:4 This source is probably an active star: the infrared colors are indicative of class M0 or so, the X-ray spectrum is quite soft, and the source falls on the locus of stars in Figure 10.29. There is an offset between the X-ray and IR positions, but this is consistent with the X-ray positional uncertainty and the number of chance stars of this brightness is quite low.

SNR G084.2−0.8:5 This is probably a galaxy, given its position in Figure 10.29 and its hard X-ray spectrum. However, the multiple possible IR counterparts make a clear identification impossible.

SNR G084.2−0.8:6 This is likely a galaxy, given its very hard X-ray spectrum. It does not appear in Figure 10.29 as there are no L-band counts, but its K_s magnitude is similar to that of other galaxies such as SNR G084.2−0.8:2.

SNR G084.2−0.8:7 This is likely a galaxy, given its position in Figure 10.29 and its hard X-ray spectrum.

SNR G084.2−0.8:10 This is likely a galaxy, given its position in Figure 10.29 and its hard X-ray spectrum. However, the multiple possible IR counterparts make a clear identification impossible.

SNR G084.2−0.8:11 This source may be an active star, given how bright its IR counterpart is (it is possible, but not likely, that the counterpart is due to chance). However, the X-ray spectrum is quite hard, and the IR colors are far redder than those typical for stars (an M7 star would have $J - K_s \approx 1.3$, which would require $A_V \approx 10$ mag to get to the observed value of $J - K_s$). Therefore, this source is likely an active galaxy, where intrinsic $J - K_s \gtrsim 2$ is not that unusual (e.g., Franx et al. 2003) and a larger foreground $N_{\rm H}$ is expected.

SNR G084.2−0.8:12 This source is probably an active star: the infrared colors are redder than typical for a main-sequence star of its magnitude, but it could be a distant M5 giant. In addition, the X-ray spectrum is quite soft, and the source falls on the locus of stars in Figure 10.29.

SNR G084.2−0.8:14 This source is almost certainly an active star: the infrared colors are indicative of class G0, the X-ray spectrum is quite soft, and the source falls on the locus of stars in Figure 10.29.

SNR G084.2−0.8:15 This is likely a galaxy, given its position in Figure 10.29 and its hard X-ray spectrum.

SNR G084.2−0.8:16 This source is probably an active star: the infrared colors are indicative of class M1 (or possible a K giant), the X-ray spectrum is quite soft, and the source falls on the locus of stars in Figure 10.29.

SNR G084.2−0.8:18 This may be a galaxy, given its hard X-ray spectrum and the faint IR counterparts. However, the error circle is large, and the IR counterparts could be spurious. Even so, it would still probably be extragalactic in origin as the X-ray source is too hard to be Galactic. For a power-law source with $\Gamma = 0.7$ (very hard for a neutron star, but plausible for an AGN) we would need $N_{\rm H} \gtrsim 5 \times 10^{22}\ {\rm cm}^{-2}$ to give the observed hardness ratio. This value is significantly higher than the column density expected to SNR G084.2−0.8, and is in fact even somewhat higher than the Galactic column density in this direction (although the AGN spectrum could have $\Gamma < 0.7$).

SNR G084.2−0.8:22 This source is probably an active star: the infrared colors are redder than typical for a main-sequence star of its magnitude, but it could be a distant M5 giant. In addition, the X-ray spectrum is quite soft, and the source falls on the locus of stars in Figure 10.29.

SNR G084.2−0.8:23 This is probably a galaxy, given its hard X-ray spectrum and the faint IR counterparts.

10.5.4 SNR G127.1+0.5

SNR G127.1+0.5 (R5) is a 45′ diameter radio shell (Fig. 10.5), also known as R5, which was identified as an SNR by Caswell (1977). It is remarkable in that it has a bright (396 mJy at 1.4 GHz), flat-spectrum radio point source (G127.11+0.54) near the center (Caswell 1977, Joncas, Roger, & Dewdney 1989), but optical observations (Kirshner & Chevalier 1978, Spinrad, Stauffer, & Harlan 1979) and H I absorption measurements (Pauls et al. 1982; Goss & van Gorkom 1984) instead favor an identification with a massive elliptical galaxy at ≈ 100 Mpc distance, similar to M87.

The distance is likely 1.2–1.3 kpc, if it is in fact associated with the open cluster NGC 559 (Pauls 1977). It has not been detected in X-rays, so there are no spectral fits to determine its age or temperature. The hydrogen column density to SNR G127.1+0.5 is $N_{\rm H} \approx 2 \times 10^{21}$ (again using Colden) and integrating the appropriate velocity range, while the total hydrogen through the Galaxy is $N_{\rm H} \approx 1 \times 10^{22}$. Again assuming a Sedov-phase remnant, we find (see § 10.4.1) $t_4 \approx 0.6 T_7^{-1/2}$, or $t_4 \approx 0.2$–0.8 (with $T_7 = 0.3$–3).

Lorimer et al. (1998) searched SNR G127.1+0.5 unsuccessfully for a radio pulsar down to a limit of 0.8 mJy at 606 MHz, implying a luminosity limit of $Sd^2 < 1.4$ mJy kpc^2. Extrapolating to a frequency of 1400 MHz using an average spectral index of −1.5, this is a factor of almost > 500 brighter than the luminosity of PSR J0205+6449.

10.5.4.1 X-ray Observations

We observed SNR G127.1+0.5 with *Chandra* on 2002 September 14. We determined the center of the remnant to be at (J2000) $01^{\rm h}28^{\rm m}32^{\rm s}$, $+63°06'34''$. The aim point was on the ACIS-I imaging array, and the final exposure time was 19.5 ks. See Figure 10.5 for the placement of the ACIS-I detector relative to the SNR. A smoothed image of the data is shown in Figure 10.9 with the X-ray sources that we identified (Tab. 10.7) labeled.

The analysis of the *Chandra* data proceeded according to Section 10.4.2. In Figure 10.13 we plot the H-band counts vs. the L-band counts for the sources in Table 10.7. Virtually all of the sources are consistent with power-laws having indices from 0.0–2.0. It may be that we have underestimated the $N_{\rm H}$ to SNR G127.1+0.5, which would put the distribution of hardness ratios closer to what is seen in the other SNRs, but this does not affect our analysis of the sources.

10.5.4.2 Optical/IR Observations

We observed the field of SNR G127.1+0.5 a number of times with a number of instruments, as described in Table 10.12. The reduction proceeded as in § 10.5.1.2.

We determined the photometric zero points for the LFC data from VRI Palomar 60-inch observations of the Stetson fields[19] L98, NGC 7654, and PG 0231 (Stetson 2000) and by employing appropriate transformations (Jorgensen 1994; Smith et al. 2002) to LFC observations of the SNR. For the WIRC observations,

---

[19] `http://cadcwww.dao.nrc.ca/cadcbin/wdbi.cgi/astrocat/stetson/query`

we determined zero points using 900 unsaturated 2MASS (Skrutskie et al. 1997) stars. For the NIRC observations, we determined zero points using about 20–30 stars from the WIRC image.

We performed absolute astrometry on the LFC data and the WIRC data. After applying distortion corrections to the LFC data, we solved for plate scale, rotation, and central position relative to stars from version 2.2 of the Guide Star Catalog (GSC-2.2[20]) for LFC and relative to 2MASS stars for WIRC, getting residuals in each coordinate of $0\farcs12$ (1200 stars), and $0\farcs22$ (1100 stars) for LFC and WIRC respectively. For the NIRC data we used non saturated stars from the WIRC to boot-strap the astrometry, getting typical residuals of $< 0\farcs07$ in each coordinate with about 20 stars.

10.5.4.3 Notes on Individual Sources

SNR G127.1+0.5:1 This source is coincident with the nonthermal radio source G127.11+0.54 and with its optical counterpart (Kirshner & Chevalier 1978; Spinrad et al. 1979). The X-ray spectrum is quite hard, fitting with the identification as an active galaxy. Interestingly, this is the only source for SNR G127.1+0.5 to be in the stellar locus in Figure 10.30, when we know it to be extragalactic. The optical counterpart is somewhat brighter than those of most galaxies relative to the X-ray flux (similar to SNR G084.2−0.8:11). This could be due to the extended stellar emission seen from this source, or due to the orientation of the optical jets.

SNR G127.1+0.5:3 This is probably a galaxy, given its hard X-ray spectrum and the faint IR counterpart.

SNR G127.1+0.5:4 This is probably a galaxy, given its hard X-ray spectrum and the faint IR counterpart.

SNR G127.1+0.5:5 This is probably a galaxy, given its hard X-ray spectrum and the faint IR counterpart.

SNR G127.1+0.5:8 This is probably a galaxy, given its hard X-ray spectrum and the faint IR counterpart.

SNR G127.1+0.5:12 This source is among the softest of the sources in SNR G127.1+0.5 and its position in Figure 10.30 is intermediate between the stars and galaxies, so it could be an active star. However, the spectrum is not actually all that soft, and it is more likely to be a galaxy, given its faint, red IR counterpart.

SNR G127.1+0.5:13 This is probably a galaxy, given its hard X-ray spectrum and the faint IR counterpart.

SNR G127.1+0.5:14 This is probably a galaxy, given its hard X-ray spectrum and the faint IR counterpart.

SNR G127.1+0.5:15 This is probably a galaxy, given its hard X-ray spectrum and the faint IR counterpart.

SNR G127.1+0.5:17 This is probably a galaxy, given its hard X-ray spectrum and the faint IR counterpart.

SNR G127.1+0.5:18 This source is among the softest of the sources in SNR G127.1+0.5 and its position in Figure 10.30 is intermediate between the stars and galaxies, so it could be an active star. Like

---

[20] `http://www-gsss.stsci.edu/support/data_access.htm`

SNR G127.1+0.5:12, however, the spectrum is still reasonably hard. The source could be a galaxy, given its X-ray spectrum and the faint, red IR counterpart. If it were a star, it would have to be a distant M giant in order to produce the observed $J-K_s$ value. It could also be a chance coincidence, given how crowded the region is in Figure 10.26.

SNR G127.1+0.5:22 This could be a galaxy, given its hard X-ray spectrum and the faint IR counterparts. The second counterpart in Table 10.7 is almost certainly a star, as suggested by the last column of Table 10.7. The first source may also be spurious, but the chances of a real association are reasonable.

10.6 Limits on Central Sources

In Sections 10.5.1.3, 10.5.2.3, 10.5.3.3, and 10.5.4.3, we showed that almost all of the X-ray sources from Tables 10.4–10.7 can be identified either with foreground or background sources. Therefore, there does not appear to be any detected neutron star in SNRs G093.3+6.9, G315.4−2.3, G084.2+0.8, or G127.1+0.5. There are a small number of cases in which either the association or the type of source (star vs. galaxy; see Tab. 10.17) is uncertain, either because of an optical/IR detection in only one band and/or a detection at a somewhat large distance from the X-ray source, but there are certainly no sources that scream out "I am a neutron star." If we accept this, we can then draw two limits to the flux of any compact central source: a conservative limit (Limit I), and a loose limit (Limit II). The conservative limit will be the flux of the brightest source for which the optical/IR counterpart is at all in doubt. For SNR G093.3+6.9, this would be source SNR G093.3+6.9:8: this counterpart is faint, has unknown colors, is somewhat far from the X-ray source, and is somewhat soft. For SNR G315.4−2.3, this would be source SNR G315.4−2.3:1: again this is faint, has unknown colors, and is in a crowded region. For SNR G084.2−0.8, the limiting source would be SNR G084.2−0.8:5: the multiple IR counterparts make a firm association impossible, and the spectrum is not so hard as to eliminate the possibility of a Crab-like pulsar. Finally, for SNR G127.1+0.5, the limiting source is SNR G127.1+0.5:18, where the crowding and uncertain classification make a firm association impossible, and again the spectrum is not so hard as to eliminate the possibility of a Crab-like pulsar. Here we have played devil's advocate, and questioned all of the associations in Section 10.5 as much as possible. We in fact believe that the associations are reasonably secure, but we cannot be certain. The looser limits in each case come from the faintest sources in Tables 10.4–10.7, and we assume that all of the associations in Tables 10.13–10.16 are correct. We present the limits, along with approximate fluxes and luminosities for three different source models, in Table 10.18. In Figure 10.37, we plot the blackbody limits along with the luminosities of the sources in Table 10.2. The limits for SNR G127.1+0.5 are significantly below those of the other SNRs as it had never been observed in the X-rays before, so we did not know what the level of the diffuse background would be and therefore selected an exposure time that would guarantee sufficient counts from a source above even the most pessimistic background.

Below we discuss the implications of not detecting any sources in the contexts of different models for what the sources could be (§ 10.2). We also include discussions of limitations imposed by our observing strategy, specifically the limited field of view and the gaps in the ACIS-I detector.

10.6.1 Instrumental Limitations

10.6.1.1 Field of View

While we did not detect any bright X-ray sources that were obviously compact objects, it may be that this was because the sources had extremely high velocities that carried them beyond the ACIS-I field of view. This would imply $v_\perp > 1600$ km s^{-1} for both SNR G093.3+6.9 and SNR G315.4−2.3, $v_\perp > 1700$ km s^{-1}

Table 10.18. Limits on Central Sources in SNRs G093.3+6.9, G315.4−2.3, G084.2+0.8, & G127.1+0.5

Model	Limit I			Limit II		
	Counts[a]	F_{X}[ab]	L_{X}[ac]	Counts[a]	F_{X}[ab]	L_{X}[ac]
SNR G093.3+6.9:						
BB ($kT_\infty = 0.25$ keV)	25	9.1	2.6	11	4.0	1.1
PL ($\Gamma = 1.5$)	”	20.7	3.7	”	9.1	1.6
PL ($\Gamma = 3.5$)	”	13.1	7.3	”	5.8	3.2
SNR G315.4−2.3:						
BB ($kT_\infty = 0.25$ keV)	45	24.7	4.5	11	6.0	1.1
PL ($\Gamma = 1.5$)	”	55.8	6.4	”	13.6	1.6
PL ($\Gamma = 3.5$)	”	35.3	12.4	”	8.6	3.0
SNR G084.2−0.8:						
BB ($kT_\infty = 0.25$ keV)	20	4.3	2.0	12	2.5	1.2
PL ($\Gamma = 1.5$)	”	9.9	2.9	”	5.9	1.7
PL ($\Gamma = 3.5$)	”	6.3	5.7	”	3.8	3.4
SNR G127.1+0.5:						
BB ($kT_\infty = 0.25$ keV)	20	5.4	0.1	12	3.2	0.1
PL ($\Gamma = 1.5$)	”	12.5	0.3	”	7.4	0.1
PL ($\Gamma = 3.5$)	”	7.9	0.2	”	4.8	0.1

[a] In the 0.3–8.0 keV band.

[b] X-ray flux $\times 10^{-15}$ ergs s^{-1} cm^{-2}.

[c] X-ray luminosity $\times 10^{31}$ ergs s^{-1}, corrected for absorption according to §§ 10.5.1–10.5.4, and using the distances in Table 10.1.

Note. — Fluxes and luminosities were computed using W3PIMMS. See § 10.6 for definition of limit types.

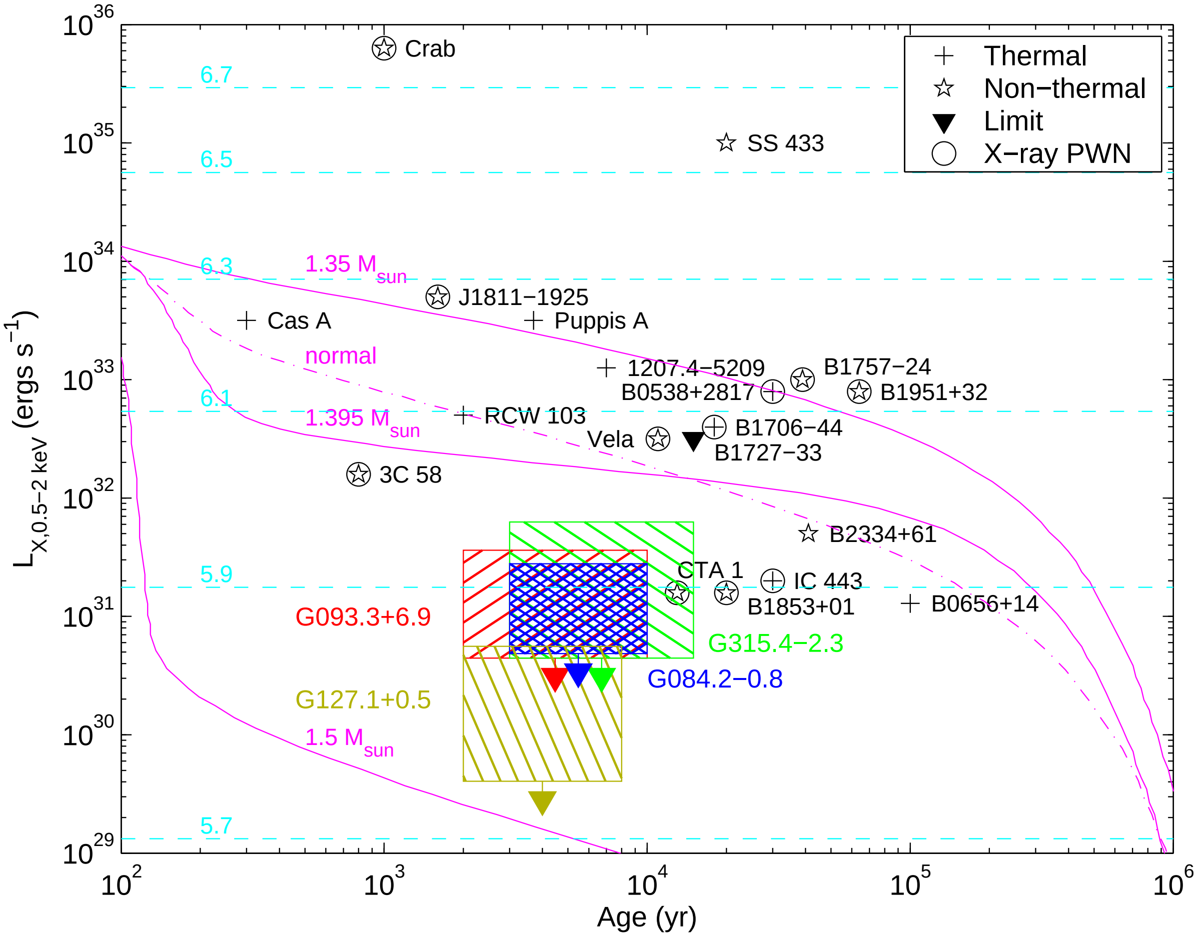

Figure 10.37 X-ray luminosities (0.5–2 keV) as a function of age for neutron stars in SNRs from Table 10.2. Sources whose emission is primarily thermal are indicated with plus symbols, those whose emission is primarily nonthermal are indicated with stars, and those with only limits are indicated with triangles. The sources that have X-ray PWNe, which are typically >10 times the X-ray luminosity of the neutron stars themselves, are circled. We also plot the limits to blackbody emission from sources in SNRs G093.3+6.9 (red hatched region), G315.4−2.3 (green hatched region), G084.2+0.8 (blue cross-hatched region), and G127.1+0.5 (gold hatched region). A 30% uncertainty in the distance has been added to the range of luminosities given in Table 10.18 (i.e., we have taken the Type I limits with a 30% larger distance and the Type II limits with a 30% smaller distance, to give the widest probable range of luminosities), and the likely range of ages is also shown. The cooling curves are the 1p proton superfluid models from Yakovlev et al. (2003) (solid lines, with mass as labeled) and the normal (i.e., nonsuperfluid) $M = 1.35\,M_\odot$ model (dot-dashed line), assuming blackbody spectra and $R_\infty = 10$ km. These curves are meant to be illustrative of general cooling trends, and should not be interpreted as detailed predictions. The horizontal lines show the luminosity produced by blackbodies with $R_\infty = 10$ km and $\log T_\infty$ (K) as indicated. Faster cooling than the curves is possible, due either to the presence of exotic particles in the NS core or to the full onset of direct URCA cooling for a heavier NS (e.g., Yakovlev et al. 2002b).

for SNR G084.2−0.8, and $v_\perp > 700$ km s^{-1} for SNR G127.1+0.5 (all assuming centered explosions). The value of $v_\perp = 1600$ km s^{-1} is higher than the velocities of 99% of the radio pulsar population, while $v_\perp = 700$ km s^{-1} is higher than 90% of the population (Arzoumanian et al. 2002). For one source, this might be acceptable, but for two or more sources the chances become too low ($\sim 10^{-7}$ for all four sources), requiring another explanation.

Gvaramadze & Vikhlinin (2003) believe that SNR G315.4−2.3 was the result of an off-center explosion in a cavity created by the SN's moving progenitor, and they have similar hypotheses about other SNRs (e.g., Bock & Gvaramadze 2002).

10.6.1.2 Chip Gaps

The ACIS-I detector has gaps between the four CCDs where the sensitivity falls to zero. During normal observations some compensation is made for this by the dithering of the spacecraft. For our observations, we ended up with approximately 5% of the area having an effective exposure that was ≈ 50% of the nominal exposure. The `wavdetect` program used exposure maps to account for this effect when detecting sources, so that sources located in the chip gaps can have fewer detected counts but end up with the same significance as a source in the middle of the chips, so we should not be missing sources as a result of the chip gaps. But there is a 5% chance of having a source in the gap region that is not detected for which the flux/luminosity limits should be a factor of 2 higher than those stated in Table 10.18.

10.6.2 AXPs

The properties of AXPs in Section 10.2.3 allow us to state that there are no such sources in the central $8'$ of SNRs G093.3+6.9, G315.4−2.3, G084.2+0.8, or G127.1+0.5: the luminosity limits for $\Gamma = 3.5$ in Table 10.18 are at most 10^{32} ergs s^{-1}, or two orders of magnitude below those of most AXPs and a factor of 10 less than the "quiescent" states of the possibly variable AXPs. This discrepancy cannot be solved by a slight change in distance or absorption and is therefore quite firm.

10.6.3 Cooling Radio-Quiet Neutron Stars

Using the standard cooling curve (modified URCA only) in Figure 10.37, we would estimate luminosities of $(2\text{–}5)\times10^{32}$ ergs s^{-1} for any compact sources. Obviously, our limits are below those values. Our limits are also below the luminosities of most of the sources in Table 10.2: only PSR B2334+61, CXO J061705.3+222127, PSR B1853+01, and RX J0007.0+7302 are comparable (while PSR B1853+01 is dominated by nonthermal X-ray emission, any cooling radiation would have to be below this level). However, most of these objects are older ($\gtrsim$ 30 kyr) than the SNRs considered here ($\lesssim$ 10 kyr), and three of these sources have substantial X-ray (and radio) PWNe that would make them detectable in the absence of point-source emission.

With our limits in Table 10.18, any thermal emission from sources in SNRs G093.3+6.9, G315.4−2.3, G084.2+0.8, or G127.1+0.5 would have to have $T_\infty \lesssim 8 \times 10^5$ K (or $kT_\infty \lesssim 70$ eV, for $R_\infty \approx 10$ km): see Figure 10.37. Even for radii of 3 km (§ 10.2.4), the limits on kT_∞ are ≈ 100 eV. These are lower than expected from standard cooling curves (Page 1998; Slane, Helfand, & Murray 2002; Kaminker et al. 2002; Yakovlev et al. 2002b) and would require some exotic physics (pion cooling, direct URCA cooling, etc.) that may be related to a more massive neutron star (Yakovlev et al. 2003).

10.6.4 Radio Pulsars

If we compare the luminosity limits for the $\Gamma = 2.0$ model for SNRs G093.3+6.9, G315.4−2.3, G084.2+0.8, and G127.1+0.5 with the luminosities of known radio pulsars (Tab. 10.3), we see that our limits are below most but not all of luminosities of pulsars found in SNRs. Translating our limits to limits on $\dot{E}$

(roughly, $L_{\mathrm{X},0.1-2.4\,\mathrm{keV}} \approx 0.5 L_{\mathrm{X},0.3-8\,\mathrm{keV}}$ and using $L_{\mathrm{X},0.1-2.4\,\mathrm{keV}} \sim 10^{-3}\dot{E}$; Becker & Trümper 1997) we find $\dot{E} \lesssim 3 \times 10^{34}$ ergs s^{-1} (for the type I limit) or $\dot{E} \lesssim 8 \times 10^{33}$ ergs s^{-1} (for the type II limit) for SNR G093.3+6.9, SNR G315.4−2.3, and SNR G084.2−0.8, and $\dot{E} \lesssim 2 \times 10^{33}$ ergs s^{-1} (for the type I limit) or $\dot{E} \lesssim 3 \times 10^{32}$ ergs s^{-1} (for the type II limit) for SNR G127.1+0.5. Comparing with the values of $\dot{E}$ given in Section 10.2.1, these limits are below those of traditional pulsars but are compatible with the values for the low-$\dot{E}$ HBPSRs. Our limits on L_X are consistent with the one low-$\dot{E}$ HBPSR that has detected X-ray emission—PSR J1718−37184 (McLaughlin et al. 2003)—but its age and distance are poorly known and its luminosity of $\sim 10^{30}$ ergs s^{-1} is roughly what is expected from standard cooling curves for a source with $\tau \approx 30$ kyr in contrast to the sources discussed here (§ 10.6.3).

Since we cannot constrain the existence of a low-$\dot{E}$ pulsar in any of these four SNRs, we can ask what its period might be. To do so we must assume that initial period is much less than the current period so that the characteristic age $\tau \equiv P/2\dot{P}$ is similar to the actual age and that the braking index has the constant value $n = 3$. We know that this is not always the case (e.g., Murray et al. 2002b; Migliazzo et al. 2002; Lyne 2004), but it is the best guess that one can make. Under this assumption one finds $P \sim 1.4 \times 10^{23} \sqrt{I_{45}} (\tau \dot{E})^{-0.5}$ s and $B \sim 3.2 \times 10^{42} \sqrt{I_{45}} (\tau^2 \dot{E})^{-0.5}$ G, where $I = 10^{45} I_{45}$ g cm^2 is the moment of inertia. With $\tau \approx 4000$–6000 yr, we find $P \gtrsim 3$ s for SNR G093.3+6.9, SNR G315.4−2.3, and SNR G084.2−0.8, and $P \gtrsim 9$ s for SNR G127.1+0.5. These periods are larger than those of most but not all radio pulsars (Young, Manchester, & Johnston 1999; Camilo et al. 2000; McLaughlin et al. 2003) and may be high enough to take any source in SNR G093.3+6.9 or SNR G315.4−2.3 beyond the radio "death line." The implied dipole magnetic fields are also high, $\gtrsim 2 \times 10^{14}$ G for SNR G093.3+6.9, SNR G315.4−2.3, and SNR G084.2−0.8 and $\gtrsim 5 \times 10^{15}$ G for SNR G127.1+0.5, similar to PSR J1814−1744 and PSR J1847−0130. This may be indicative of a growing population of such objects: young, nonenergetic long-period pulsars. The lack of detected pulsed radio emission in any of these four SNRs (Lorimer et al. 1998; Kaspi et al. 1996) may be intrinsic (i.e., there is no radio emission), it may be an orientation effect, or it may just be that the SNRs have not been searched deeply enough over enough of an area, as there is now a growing number of radio pulsars with luminosities (defined here as $F_{\mathrm{radio}} d^2$) below 1 mJy kpc^2 (e.g., Camilo et al. 2002d,a), far lower than typical for radio pulsars.

10.6.4.1 Pulsar Wind Nebulae

Any PWNe in the SNRs discussed here are $\gtrsim 3000$ yr old and may have already interacted with the reverse shocks (§ 10.2.2), so their sizes and brightnesses would be hard to predict. We therefore examine limits on PWNe for a range of sizes (as in § 10.4.3). We also scale to a fiducial size of 1 pc $\approx 1'$—we did not detect any sources with those sizes in our images except for the known thermal emission from RCW 86.

To quantify this, we take the limits on extended sources from Section 10.4.3 and Table 10.8. We convert the count limits to luminosity limits using a photon index of $\Gamma = 1.5$, getting the limits in Table 10.8. These limits are below the luminosities of virtually all young PWNe detected in X-rays (Possenti et al. 2002), but are consistent with some older sources such as the Vela PWN, CTB 80, and W44 (Pavlov et al. 2001a). However, these PWNe all have significant nonthermal radio emission, emission that is not present in SNR G093.3+6.9, SNR G315.4−2.3, SNR G084.2−0.8, or SNR G127.1+0.5 since they are all shell-type SNRs.

10.6.5 Binary Systems

As many as 50% of massive stars originate in binary systems, which presumably give rise to X-ray binaries and eventually millisecond pulsars. One might expect that we could see a binary system in which the more massive star has gone supernova but the less massive has not evolved. In this case, we would see X-ray emission that appears to be (but is not physically) associated with an optically detected star that might be hard to distinguish from the active stars that make up the majority of Galactic X-ray sources (if the star did evolve and the companion were close enough, it would donate matter to the compact object and would appear as an X-ray binary and would have different properties).

However, after only one supernova the binary system would have a small space velocity, < 100 km s^{-1} (Pfahl, Rappaport, & Podsiadlowski 2002a, Pfahl et al. 2002b). It would therefore be restricted to a smaller region than the full search, which accommodates velocities up to 1500 km s^{-1} (§ 10.6.1.1). A velocity of 100 km s^{-1} is an angular offset of $\approx 30''$ (for an average distance of 3 kpc and age of 5 kyr)—much smaller than the ACIS-I field of view.

As seen in Tables 10.4–10.7, we have found only one source within a radius of $30''$ of the center: SNR G127.1+0.5:1, which is known to be extragalactic. In fact, none of the stellar sources (as determined in §§ 10.5.1.3, 10.5.2.3, 10.5.3.3, and 10.5.4.3) appear to be at distances beyond 1 kpc (comparing with Fig. 10.32). This is likely a selection effect of our X-ray flux limits: for stellar luminosities of 10^{29}–10^{31} ergs s^{-1}, our flux limits translate into distance limits of ~ 1 kpc.

If none of the stellar sources could be companions to a neutron star, we must ask if any of the sources identified as galaxies could in fact be stars, and their identifications as galaxies could be coincidence. As seen from Figures 10.32–10.34, a main-sequence star at the distances of SNRs G093.3+6.9, G315.4−2.3, G084.2+0.8, or G127.1+0.5 would have $K_s \approx 15$–19, depending on stellar type (giant stars at these distance would mostly be too bright, with $K \lesssim 10$). All of the "galaxies" in Sections 10.5.1.3, 10.5.2.3, 10.5.3.3, and 10.5.4.3 have $K > 17$ except SNR G084.2−0.8:11 (and this is too red to be at the distance/reddening of SNR G084.2−0.8), so if they were main-sequence stars they would be type K5 or later. However, even if one of these sources is a companion to a neutron star, the Type I limits still apply, and any neutron star would be under-luminous (§ 10.6.3).

10.6.6 Accreting Black Holes

If the SNe produced black holes (BHs) and not neutron stars, the black holes themselves would be invisible. X-ray emission would only be detected if there were material accreting into the BHs. Models for such emission are not very well understood. Thermal emission might be expected to come from the inner portion of the accretion disk itself, with an area of several times πR_S^2 (Chakrabarty et al. 2001), where R_S is the Schwarzschild radius of the BH. For a $10\,M_\odot$ BH (with $R_S = 15$ km), the area would be $\gtrsim 1000$ km^2, or much larger than the limits on thermal emission (§ 10.6.3) for temperatures $\gtrsim 100$ eV. It is also possible that the X-ray emission arises from Compton scattering in an optically thin corona over a thin disk or via optically thin bremsstrahlung emission from a hot advection-dominated accretion flow (ADAF, as in the model of Narayan, Barret, & McClintock 1997), but these models are not well enough developed to provide useful constraints.

10.6.7 Type Ia Supernovae

Type Ia SNe are believe to result from carbon detonation/deflagration of a white dwarf that has been pushed beyond its mass limit through accretion from a companion star. The resulting explosion completely disrupts the star, synthesizing nearly a solar mass of ^{56}Ni, which ultimately decays to Fe. No compact core is left behind. The SNRs from such events thus form a subsample in which we do not expect to find an associated neutron star. The mean rate for Type Ia SNe is $\sim 20\%-25\%$ of that for core-collapse supernovae (Cappellaro, Evans, & Turatto 1999), so we expect less than 20% of the observable SNRs to be the result of such explosions.

The ejecta produced in Type Ia events differs considerably than that from core-collapse SNe. The former are rich in Fe and Si while SNRs from core-collapse events are richer in O and Ne. For young SNRs, the X-ray spectra can be used to identify those of Type Ia origin (e.g., Hughes et al. 1995, 2003a;

Lewis et al. 2003). Once the X-ray emission is dominated by swept-up circumstellar or interstellar matter, such discrimination is much more difficult. SNRs originating from core collapse are often found near the molecular clouds in which the progenitors formed, while those from Type Ia events are from stars with sufficiently long lifetimes that they can have traveled far from their birthplaces. Thus, for SNRs located in the near vicinity of active star-forming regions one can reasonably assume that they originated from massive stars. However, the absence of nearby star formation or dense molecular material is not necessarily a direct indicator of a Type Ia progenitor. There are three Galactic SNRs that are commonly thought of as the products of Ia events—Tycho, SN 1006, and perhaps Kepler (Baade 1945; Fesen et al. 1988; Allen et al. 2001)—all reasonably young "historic" remnants (Stephenson & Green 2002).

If any of the SNRs discussed here were known to be the result of a Type Ia explosion (as suggested by some authors for both SNR G093.3+6.9 and SNR G315.4−2.3), then we would not expect to see a compact remnant. Observing a known Ia remnant would then be a good test case for our methodology: as we have not found any candidate compact remnant, it demonstrates that our method is not inclined to find false positives. However, while knowing that an SNR is from a Type Ia explosion precludes the existence of compact objects, the lack of compact objects does not require an SNR to be from a Type Ia. Therefore, we cannot conclude that SNR G093.3+6.9 or SNR G315.4−2.3 is the result of a Type Ia explosion.

10.7 Conclusions

There are 45 known SNRs that are reliably within 5 kpc of the Sun. Most of these SNRs are expected to contain central neutron stars: $\lesssim 20\%$ are expected to result from Type Ia SNe and thus not contain a central compact source, while $\sim 20\%$ (dependent on the stellar initial mass function, the limiting mass for black holes, and binary evolution; Heger et al. 2003) are expected to host a central black hole that may not be easily identified as such. Thanks to the persistent efforts by astronomers over the past four decades, central sources have been detected in the X-ray and/or radio bands in 18 of these SNRs, and three have been identified as probable Type Ia SNe. In some cases, only a centrally located PWN is detected, but in those cases (i.e., IC 443) it is reasonably assumed that the PWN is powered by a central compact source.

We have begun a program of searching for compact sources in the remaining 23 SNRs. The program has been motivated by the discovery of a point-like X-ray source at the very center of the youngest known Galactic SNR, Cas A. The program has two observational components: imaging with *Chandra* or *XMM* in the X-ray band followed by ground-based optical/IR followup. The latter is essential because of the high incidence of interlopers (foreground stars and background galaxies). Such a comprehensive program is possible thanks to the astrometric accuracy of the X-ray missions combined with high sensitivity.

In this paper we report on *Chandra* ACIS-I observations of four shell remnants (G093.3+6.9, G315.4−2.3, G084.2+0.8, G127.1+0.5). We undertook optical and IR observations of every X-ray source detected with more than 10 counts. For all detections, we found, within astrometric errors, a counterpart in one or more bands. These counterparts were consistent with either foreground (stars) or background (galaxies) sources. In particular, the X-ray flux and/or the X-ray to optical (IR) ratio of the detected X-ray sources were not as extreme as all known classes of neutron stars: accreting neutron stars, radio pulsars, AXPs and SGRs.

In § 10.6 we discuss reasons why standard neutron stars were not found in these SNRs: they could have fallen in the gap between the chips, they could have escaped our field of view owing to very high velocities, they could be undetectable black holes, or they could not exist owing to the SNRs being the results of Type Ia explosions. All of these scenarios are unlikely for a single source, and even more so for all four but are technically possible. If, on the other hand, these scenarios do not apply, then four remnants contain neutron stars that are fainter than our X-ray detection limit (typically, $L_X \lesssim 10^{31}$ ergs s^{-1} in the 0.5–10 keV band).

We now consider this last (and most interesting) possibility. In the absence of other forms of energy generation (accretion, rotation power, magnetic field decay) the minimum X-ray flux one expects is set by the cooling of the neutron star. From Section 10.6.3 and Figure 10.37 we immediately see that the central neutron stars in these four remnants must be cooler than those present for example in the similarly-aged Puppis A, PKS 1205−51/52 and RCW 103.

Our knowledge of the physics of cooling is by no means firm. There is considerable debate among theorists as to which of the multitude of physical processes can significantly affect the cooling output and as to which of the physical parameters (mass, rotation rate, magnetic field) controls these processes (Yakovlev et al. 2002a). Nonetheless, there is agreement that more massive neutron stars (with their larger mean densities) cool more rapidly than those with smaller mass; this expectation is illustrated in Figure 10.37. Thus, our upper limits can be made consistent with the cooling possibility provided the central neutron stars in these four SNRs are more massive than known cooling neutron stars. Indeed, the known examples of radio-quiet objects could well result from a strong selection effect, namely the earlier X-ray observations by *Einstein* and *ROSAT* detected the warmer cooling neutron stars (ignoring the neutron stars detected because of nonthermal emission). The existing data may already hint at a parameter affecting cooling, as exemplified by PSR J0205+6449 (Slane et al. 2002) and the Vela pulsar (Pavlov et al. 2001c), but also possibly by PSR B1853+01 (Petre, Kuntz, & Shelton 2002) and RX J0007.0+7302 (Slane et al. 2004).

Of course, we also do not see rotation-powered pulsars such as the majority of the objects in Table 10.2. Recent observations are finding pulsars with lower radio luminosities and values of $\dot{E}$ than ever before, and our limits would only be consistent with these newer sources. One might then ask why we see neither a standard cooling neutron star nor a standard active pulsar, assuming that there is no intrinsic correlation between these properties. It is possible that there truly are no neutron stars in these SNRs, allowing one to speculate wildly about what actually is there.

In subsequent papers we plan to report the X-ray observations and ground-based follow-up of the remaining 19 SNRs. If no central sources are identified then the hypothesis proposed here, namely that there is a parameter that determines cooling of neutron star will be strengthened. The simplest (and most reasonable) suggestion is that this second parameter is the mass of neutron stars, so that cooling observations could be used to "weigh" isolated neutron stars (as discussed by Kaminker, Haensel, & Yakovlev 2001). This hypothesis is at odds with the strong clustering of binary neutron star masses (Thorsett & Chakrabarty 1999). We note, however, that mass determination is only possible for neutron stars in compact binary systems where significant interaction with the companion may have taken place. Thus it is possible that neutron stars resulting from single stars are systematically more massive than those which evolve in compact binary systems (and have gained mass through accretion).

D. L. K. is supported by a fellowship from the Fannie and John Hertz Foundation. B. M. G., P. O. S., and A. N. acknowledge support from NASA contract NAS8-39073 and grant G02-3090. E. V. G. is supported by NASA LTSA grant NAG5-7935, and B. M. G. is supported by NASA LTSA grant NAG5-13032. S. R. K. is supported by grants from NSF and NASA. Support for this work was provided by the National Aeronautics and Space Administration through Chandra award NAS8-39073 issued by the *Chandra X-Ray Observatory* Center, which is operated by the Smithsonian Astrophysical Observatory for and on behalf of NASA under contract NAS8-39073. The NRAO is a facility of the National Science Foundation operated under cooperative agreement by Associated Universities, Inc. We have made extensive use of the SIMBAD database, and we are grateful to the astronomers at the Centre de Données Astronomiques de Strasbourg for maintaining this database. We would like to thank an anonymous referee for helpful comments, D. Fox for assistance with the X-ray analysis, E. Persson for assistance with the PANIC observing, M. van Kerkwijk for assistance with ESO and Magellan observing, and P. McCarthy for assistance with Las Campanas observing. We would like to thank T. Landecker and DRAO for supplying the radio image of SNR G093.3+6.9. The Dominion Radio Astrophysical Observatory (DRAO) is operated as a national facility by the National Research Council of Canada. The Canadian Galactic Plane Survey is a Canadian project with international partners and is supported by a grant from the Natural Sciences and Engineering Research Council of Canada. Data presented herein were collected at the European Southern Observatory, Chile (program ESO 69.D-0072). Data presented herein were also obtained at the W. M. Keck Observatory, which is operated as a scientific partnership among the California Institute of Technology, the University of California, and the National Aeronautics and Space Administration. The Guide Star Catalog-II is a joint project of the Space Telescope Science Institute and the Osservatorio Astronomico di Torino.

Chapter 11

An X-ray Search for Compact Central Sources in Supernova Remnants II: Large Diameter SNRs

D. L. Kaplan[a], D. A. Frail[b], B. M. Gaensler[c], E. V. Gotthelf[d], S. R. Kulkarni[a],
and
P. O. Slane[c]

[a]Department of Astronomy, 105-24 California Institute of Technology, Pasadena, CA 91125

[b]National Radio Astronomy Observatory, P.O. Box O, Socorro, NM 87801

[c]Harvard-Smithsonian Center for Astrophysics, 60 Garden Street, MS-6, Cambridge, MA 02138

[d]Columbia Astrophysics Laboratory, Columbia University, 550 West 120th Street, New York, NY 10027

Abstract

We present the second in a series of papers searching for X-ray emission from new neutron stars in supernova remnants (SNRs). This paper deals with the largest six SNRs, where neither *Chandra* nor *XMM* could cover the SNR in a single pointing. These SNRs are nearby, though, with typical distances of < 1 kpc. We therefore used the *ROSAT* Bright Source Catalog to identify X-ray point sources in and near the SNRs. Out of 50 *ROSAT* sources, plus four sources from the literature, we were able to identify optical/IR counterparts to 41 immediately from SIMBAD and sky surveys.

We obtained *Chandra* snap-shot images of the remaining 13 sources. Of these, 10 were point sources with readily identified counterparts; of the others two were extended (one of which is likely extragalactic) and one was not detected in the *Chandra* observation but is likely a flare star. One of the extended sources may be a pulsar wind nebula, but if so it is probably not associated with the nearby SNR. We are then left with no possible neutron stars in these six SNRs down to luminosity limits of $\sim 10^{32}$ ergs s^{-1}. These limits are generally less than the luminosities of typical neutron stars of the same ages, but are compatible with some lower-luminosity sources such as those in CTA 1 and IC 443.

11.1 Introduction

Kaplan et al. (2004, hereafter Paper I) describe the construction and initial results of a survey designed to address our lack of understanding of stellar death and neutron star cooling by defining a volume-limited ($d < 5$ kpc) sample of supernova remnants (SNRs), examining the neutron stars that they contain, and attempting to detect or significantly constrain neutron stars in the remaining remnants with X-ray observations. Paper I divided the 23 SNRs within 5 kpc that have no known neutron star into three subsamples: the primary one where the SNR diameter is $< 45'$ such that *Chandra* will observe a significant fraction with its ACIS-I detector, one with $45' < \theta < 90'$ for which *XMM* is suitable, and one with $\theta > 90'$. Here we discuss the analysis of these largest SNRs.

The organization of the paper is as follows. First, in § 11.2 we give brief summaries of the six SNRs discussed here. Then, in § 11.3 we describe our identification of candidate X-ray sources in and around the SNRs. In § 11.4 we detail the initial identification of optical/IR counterparts to the X-ray sources using available sky surveys: as discussed in Paper I, optical/IR observations are a powerful way to reject X-ray sources that are not neutron stars (see also e.g., Rutledge et al. 2003). With the sky surveys we were able to identify most of the X-ray sources with high confidence: those for which we were not certain were selected for additional *Chandra* observations and optical/IR observations (§ 11.5). Finally, we conclude in § 11.6.

11.2 Supernova Remnants

11.2.1 SNR G065.3+5.7

SNR G065.3+5.7 was identified as an SNR by Gull et al. (1977) by its filamentary line emission. It has a diameter of $310' \times 240'$. According to Mavromatakis et al. (2002), the age is 20–25 kyr, and the distance is ≈ 0.8 kpc (derived from the velocity of optical emission lines). Mavromatakis et al. (2002) show data from pointed *ROSAT* observations (Lu & Aschenbach 2002) but do not discuss any point sources that they might have found. They do mention, though, that the *ROSAT* data detect diffuse emission from much of the interior at $> 2.5 \times 10^{-4}$ cts s^{-1} pixel^{-1}, with $45''$ pixels. The inner $10'$ were searched for radio pulsars by Gorham et al. (1996), but given the size of SNR G065.3+5.7 the lack of detection was not very constraining.

11.2.2 SNR G074.0−8.5

SNR G074.0−8.5, also known as the Cygnus Loop, is a $230' \times 160'$ radio and X-ray shell. The distance, estimated from measurements of the shock velocity and proper motion is 0.44 kpc (Blair et al. 1999) and the age is 8 kyr (Levenson et al. 2002). *ASCA* observations detected ≈ 8.8 count s^{-1} in the interior over a $22'$ field, and led Miyata et al. (1998a) to conclude that SNR G074.0−8.5 was likely the result of a Type II supernova.

Miyata et al. (1998b) also searched SNR G074.0−8.5 for promising X-ray point sources, and identified two: AX J2049.6+2939 and AX J2050.0+2941, the second of which they later concluded was an AGN based on its long-term X-ray variability and radio counterpart (Miyata et al. 2001). They were unable to classify AX J2049.6+2939, and since it is potentially a neutron star, we observed it in addition to the *ROSAT* sources described below.

The inner $10'$ were searched for radio pulsars by Gorham et al. (1996), but as with SNR G065.3+5.7 the lack of detection was not very constraining. The inner $30'$ were also searched by Biggs & Lyne (1996) for pulsars down to a 400-MHz flux of 3 mJy.

11.2.3 SNR G156.2+5.7

SNR G156.2+5.7 was discovered in the *ROSAT* All-Sky Survey by Pfeffermann et al. (1991). It has a faint $110'$ shell in both X-rays and radio, and nonequilibrium fits to the X-ray data place it at a distance of ≈ 1.3 kpc with an age of 15 kyr (Yamauchi et al. 1999). Lorimer et al. (1998) searched SNR G156.2+5.7

for radio pulsars, tiling seven pointings of the 76-m Lovell telescope at Jodrell Bank, each of which covered $\approx 0.5°$. The search did not find any pulsars, down to a flux limit of 0.7 mJy at 606 MHz.

11.2.4 SNR G160.9+2.6

SNR G160.9+2.6, also known as HB 9, is a $140' \times 120'$ radio shell with bright X-rays in the interior. Leahy & Aschenbach (1995) use X-ray fitting to estimate a distance of 1.5 kpc and an age of 8–20 kyr. This distance is consistent with the upper limit of 4 kpc derived from other measurements (Lozinskaya 1981; Leahy & Roger 1991).

The inner $30'$ were also searched by Biggs & Lyne (1996) for pulsars down to a 610-MHz flux of 15 mJy. Damashek et al. (1978) discovered an old radio pulsar (PSR B0458+46) in the interior of the SNR, although the association between the pulsar and the SNR is generally considered to be false due to the factor of $\gtrsim 30$ discrepancy in the ages of the pulsar and the SNR (e.g., Kaspi 1996).

11.2.5 SNR G205.5+0.5

SNR G205.5+0.5, also known as the Monoceros nebula, is a $220'$ radio shell. The velocity of the optical emission puts the SNR at a distance of 0.8 kpc (Lozinskaya 1981), although distances up to 1.6 kpc are preferred by low-frequency radio data (Odegard 1986). The age is likely ~ 30 kyr, as inferred from fits to X-ray data (Leahy et al. 1986). Leahy et al. (1986) also identified several point sources with *Einstein* in the interior of SNR G205.5+0.5 that they considered as possible counterparts. We therefore also observed sources 1, 3, and 6 from Leahy et al. (1986), known as EX J062723+053739, EX J063053+061113, and EX J063646+051757, respectively.

11.2.6 SNR G330.0+15.0

SNR G330.0+15.0, or the Lupus Loop, is a low surface brightness radio shell approximately $180'$ in diameter. The distance is likely ~ 500 pc based on H I, and fits to the X-ray data imply an age of 10–20 kyr for this distance (Leahy et al. 1991).

11.3 The Sample

Chandra or *XMM* imaging of the entire fields of the large-diameter SNRs listed in Table 11.1 is impractical because of their sizes. Their proximity ($d \lesssim 1$ kpc), though, means that we do not need the high sensitivities of *Chandra* or *XMM*. We therefore used the *ROSAT* All-Sky Survey Bright Source Catalog (RASS BSC; Voges et al. 1996) for our source selection. This was a survey of the entire sky with the Position-Sensitive Proportional Counter (PSPC) aboard *ROSAT*. The positional accuracy of the PSPC is typically are $10''$, and its limit of 0.05 count s^{-1} in the PSPC is roughly comparable depth to our *Chandra* observations in Paper I: $(1–10)\times 10^{31}$ ergs s^{-1} (Tab. 11.1). The brightness and softness of the X-ray sources compared to those in Paper I means that very often stars from the Digital Sky Survey (DSS; Lasker et al. 1990) or the Two Micron All Sky Survey (2MASS; Skrutskie et al. 1997) are identified as counterparts.

We selected the BSC sources within twice the nominal radii of the SNRs in Table 11.1 (as defined by their positions and sizes given by Green 2000) that had ≥ 0.05 count s^{-1} and were listed as unextended (a value of 0 in the `ext` column of the BSC catalog). Searching outside the remnants allowed us to find neutron stars that have overtaken the SNR shocks—not an uncommon occurrence (van der Swaluw et al. 2003) in SNRs of the ages considered here (10–30 kyr). The sources are listed in Table 11.2. For the sake of comparison between sources, we plot the distribution of hardness ratios in Figure 11.1.

Table 11.1. Large SNRs

SNR	Other Name	Size (arcmin)	D (kpc)	Distance Method	$N_{\mathrm{H}}/10^{21}$ (cm^{-2})[a]	$L_{\mathrm{X}}/10^{31}$ (ergs s^{-1})[b]
G065.3+5.7		310 × 240	0.8	optical velocity	1.4	6.7
G074.0−8.5	Cygnus Loop	230 × 160	0.44	optical proper motion	0.8	1.7
G156.2+5.7		110	1.3	NEI fits	3.5	29
G160.9+2.6	HB9	140 × 120	1.5	H I, optical velocity	1	21
G205.5+0.5	Monoceros	220	1.2	optical velocity	0.8	13
G330.0+15.0	Lupus Loop	180	0.8	H I	0.5	5.1

[a] Hydrogen column density to SNR. Derived from previous observations (if available), otherwise determined from measured H I absorption or using `COLDEN` integrated over velocity range appropriate for SNR distance.

[b] Unabsorbed X-ray luminosity (0.3–8.0 keV) of a 0.05 s^{-1} *ROSAT* PSPC source at the distance and absorption of the SNR, assuming a blackbody spectrum with $kT = 0.25$ keV.

Table 11.2. *ROSAT* Point Sources and Stellar Counterparts

N	1RXS J	PSPC (count/s)	ΔR^{b} (arcmin)	σr^{c} (arcsec)	RA[a] (J2000)	DEC[a] (J2000)	Star	2MASS J	δr^{d} (arcsec)	V (mag)	K_s (mag)
SNR G065.5+5.7:											
1	193445.6+303100	0.066	45.1	11	$19^{h}34^{m}45^{s}.23$	$+30^{\circ}30'58^{s}.9$	HD 184738	19344524+3030590	5.0	10.41	8.108
2	193840.0+303035	0.083	82.7	9	$19^{h}38^{m}40^{s}.10$	$+30^{\circ}30'28^{s}.0$	V* EM Cyg	19384012+3030284	7.1	12.6	11.150
3	193922.4+300921	0.054	101.8	12	$19^{h}39^{m}22^{s}.61$	$+30^{\circ}09'12^{s}.0$	HD 185734	19392261+3009119	9.9	4.685	2.499
4	194337.2+322523	0.256	155.8	8	$19^{h}43^{m}36^{s}.80$	$+32^{\circ}25'20^{s}.7$	BDS 9566 B	19433674+3225206	5.6	9.9	8.082
”	”	”	”	”	$19^{h}43^{m}37^{s}.90$	$+32^{\circ}25'12^{s}.7$	HD 331149	19433790+3225124	13.6	10.7	7.179
5	193458.1+335301	0.051	165.0	14	$19^{h}34^{m}58^{s}.10$	$+33^{\circ}53'01^{s}.5$	···	···	···	···	···
6	192722.3+280934	0.110	194.4	15	$19^{h}27^{m}21^{s}.91$	$+28^{\circ}09'42^{s}.8$	USNO 1181−0406270	19272197+2809452	9.8	11.620[e]	8.426
7	194401.5+284456	0.138	202.7	8	$19^{h}44^{m}01^{s}.37$	$+28^{\circ}45'09^{s}.9$	GSC 02151−03394	19440138+2845099	14.0	···	8.691
8	194902.9+295258	0.357	219.9	7	$19^{h}49^{m}02^{s}.99$	$+29^{\circ}52'58^{s}.3$	HD 187460	19490298+2952582	1.2	8.32	5.734
9	193228.6+345318	0.091	223.4	9	$19^{h}32^{m}28^{s}.59$	$+34^{\circ}53'18^{s}.5$	···	···	···	···	···
10	191449.0+315131	0.057	237.0	14	$19^{h}14^{m}50^{s}.21$	$+31^{\circ}51'37^{s}.3$	HD 180314	19145022+3151371	16.5	6.618	4.312
11	193856.2+351407	0.290	255.7	8	$19^{h}38^{m}55^{s}.77$	$+35^{\circ}14'13^{s}.0$	HD 185696	19385576+3514132	8.0	8.29	6.858
12	193936.8+263718	0.074	285.6	8	$19^{h}39^{m}36^{s}.67$	$+26^{\circ}37'16^{s}.1$	AG+26 2090	19393666+2637169	3.0	11.1	7.345
13	193113.0+360730	0.153	298.4	7	$19^{h}31^{m}12^{s}.57$	$+36^{\circ}07'30^{s}.0$	G 125−15	19311257+3607300	13.1	···	8.839
14	191151.1+285012	0.052	305.3	11	$19^{h}11^{m}50^{s}.81$	$+28^{\circ}50'07^{s}.6$	USNO 1188−0330651	19115080+2850075	5.7	12.510[e]	8.898
SNR G074.0−8.5:											
1	205042.9+284643	0.111	113.3	12	$20^{h}50^{m}42^{s}.90$	$+28^{\circ}46'43^{s}.5$	···	···	···	···	···
2	204457.4+291613	0.104	114.4	10	$20^{h}44^{m}58^{s}.09$	$+29^{\circ}16'21^{s}.3$	HD 335070	20445809+2916211	11.9	10.8	8.746
3	205812.8+292037	0.129	122.3	8	$20^{h}58^{m}12^{s}.82$	$+29^{\circ}20'28^{s}.6$	USNO 1193−0519643	20581282+2920282	8.9	15.980[e]	14.258
”	”	”	”	”	$20^{h}58^{m}12^{s}.80$	$+29^{\circ}20'37^{s}.5$	···	20581257+2920454	8.5	···	13.405
4	205208.5+270546	0.225	214.7	8	$20^{h}52^{m}07^{s}.68$	$+27^{\circ}05'49^{s}.1$	HD 198809	20520768+2705491	11.4	4.576	2.722
SNR G156.2+5.7:											
1	050639.1+513607	0.051	75.3	20	$05^{h}06^{m}40^{s}.63$	$+51^{\circ}35'51^{s}.8$	HD 32537	05064067+5135519	20.8	4.980	4.124
SNR G160.9+2.6:											
1	045707.4+452751	0.061	82.5	9	$04^{h}57^{m}07^{s}.40$	$+45^{\circ}27'51^{s}.0$	···	···	···	···	···
2	050339.8+451715	0.061	87.2	11	$05^{h}03^{m}39^{s}.80$	$+45^{\circ}17'15^{s}.0$	···	···	···	···	···
3	045222.2+455619	0.052	99.0	10	$04^{h}52^{m}21^{s}.51$	$+45^{\circ}56'23^{s}.7$	HD 30736	04522151+4556236	8.6	6.695	5.407
SNR G205.5+0.5:											
1	064108.3+052250	0.086	74.3	11	$06^{h}41^{m}08^{s}.07$	$+05^{\circ}22'52^{s}.1$	USNO 0155−01104−1	06410807+0522522	4.0	10.780[e]	8.905
”	”	”	”	”	$06^{h}41^{m}07^{s}.96$	$+05^{\circ}22'43^{s}.8$	···	06410796+0522438	8.0	···	12.121
2	064136.2+080218	0.054	100.1	11	$06^{h}41^{m}35^{s}.94$	$+08^{\circ}02'05^{s}.6$	HD 262113	06413601+0802055	13.0	10.3	8.712
3	064109.3+044733	0.076	107.4	17	$06^{h}41^{m}09^{s}.61$	$+04^{\circ}47'35^{s}.8$	USNO 0947−0100759	06410953+0447354	5.4	17.650[e]	15.084
”	”	”	”	”	$06^{h}41^{m}09^{s}.82$	$+04^{\circ}47'35^{s}.1$	USNO 0947−0100763	06410988+0447350	8.1	15.840 [e]	14.636
”	”	”	”	”	$06^{h}41^{m}09^{s}.00$	$+04^{\circ}47'23^{s}.9$	···	06410900+0447239	10.1	···	12.182
”	”	”	”	”	$06^{h}41^{m}09^{s}.27$	$+04^{\circ}47'18^{s}.7$	USNO 0155−02167−1	06410924+0447187	14.3	11.100[e]	8.688
4	064641.1+082152	0.092	160.1	10	$06^{h}46^{m}40^{s}.73$	$+08^{\circ}21'47^{s}.3$	HD 49015	06464073+0821471	7.6	7.5	6.080
5	062740.3+073103	0.082	179.5	8	$06^{h}27^{m}40^{s}.30$	$+07^{\circ}31'03^{s}.0$	···	···	···	···	···
6	062937.2+082930	0.088	183.9	9	$06^{h}29^{m}36^{s}.89$	$+08^{\circ}29'32^{s}.8$	HD 45759	06293689+0829327	5.1	7.62	6.306
7	063715.7+032005	0.109	191.7	10	$06^{h}37^{m}15^{s}.22$	$+03^{\circ}20'08^{s}.0$	USNO 0150−00332−1	06371522+0320081	7.6	10.640[e]	9.323
”	”	”	”	”	$06^{h}37^{m}15^{s}.85$	$+03^{\circ}20'04^{s}.3$	···	06371585+0320043	2.5	···	14.508
”	”	”	”	”	$06^{h}37^{m}15^{s}.55$	$+03^{\circ}20'02^{s}.6$	···	06371555+0320026	3.7	···	11.813

Table 11.2

N	1RXS J	PSPC (count/s)	$\Delta R^{\rm b}$ (arcmin)	$\sigma r^{\rm c}$ (arcsec)	RA[a] (J2000)	DEC[a] (J2000)	Star	2MASS J	$\delta r^{\rm d}$ (arcsec)	V (mag)	K_s (mag)
8	062554.8+065543	0.106	196.7	11	$06^h25^m55^s.24$	$+06^\circ55'38^s.8$	USNO 0145−01717−1	06255524+0655386	7.8	9.660[e]	8.019
SNR G330.0+15.0:											
1	150818.8−401730	0.077	26.1	10	$15^h08^m18^s.80$	$-40^\circ17'30^s.0$	···	···	···	···	···
2	151059.6−392655	0.082	35.0	12	$15^h10^m59^s.06$	$-39^\circ26'58^s.5$	USNO 0505−0350285	15105908−3926590	7.2	0.000[e]	15.066
”	”	”	”	”	$15^h10^m58^s.25$	$-39^\circ26'50^s.2$	USNO 7826−00179−1	15105821−3926499	16.4	10.600[e]	8.374
”	”	”	”	”	$15^h10^m59^s.72$	$-39^\circ26'56^s.9$	USNO 0505−0350290	···	2.4	0.000[e]	···
3	150814.0−403445	0.069	40.3	16	$15^h08^m12^s.12$	$-40^\circ35'02^s.1$	HD 133880	15081213−4035022	27.1	5.762	5.934
4	150428.9−392423	0.051	72.7	11	$15^h04^m28^s.65$	$-39^\circ24'26^s.1$	CD-38 9913	15042865−3924261	3.9	10.7	8.293
5	150526.4−385709	0.073	81.8	8	$15^h05^m26^s.01$	$-38^\circ57'000^s.8$	RX J1505.4−3857	15052586−3857031	9.4	12.55	9.124
6	150139.6−403815	0.125	103.2	14	$15^h01^m39^s.60$	$-40^\circ38'15^s.5$	···	···	···	···	···
7	151849.8−405108	0.107	113.6	17	$15^h18^m52^s.82$	$-40^\circ50'52^s.8$	V* LX Lup	15185282−4050528	38.4	11.01	8.547
8	145951.7−401158	0.085	117.1	11	$14^h59^m52^s.44$	$-40^\circ11'59^s.5$	HD 132349	14595244−4011594	8.6	9.90	8.401
9	151659.2−382648	0.065	123.0	16	$15^h16^m59^s.35$	$-38^\circ26'51^s.4$	HD 135549	15165935−3826514	3.4	6.876	5.789
10	152046.2−405405	0.074	135.1	10	$15^h20^m46^s.97$	$-40^\circ53'52^s.7$	HD 136206	15204697−4053526	15.1	7.83	6.518
11	145837.5−391507	0.084	138.2	10	$14^h58^m37^s.56$	$-39^\circ15'02^s.7$	USNO 0507−0344267	14583744−3915033	4.9	11.850[e]	8.648
12	152211.8−395958	0.080	140.1	11	$15^h22^m11^s.75$	$-39^\circ59'49^s.6$	V* LZ Lup	15221162−3959509	8.4	12.02	9.100
13	145721.8−401401	0.099	145.9	9	$14^h57^m22^s.07$	$-40^\circ13'58^s.6$	···	14572207−4013586	4.2	···	13.333
14	151806.7−380423	0.115	148.5	12	$15^h18^m07^s.15$	$-38^\circ04'23^s.8$	···	15180715−3804238	5.3	···	10.600
”	”	”	”	”	$15^h18^m07^s.61$	$-38^\circ04'23^s.6$	USNO 7822−00433−1	15180762−3804237	10.7	10.650[e]	7.999
15	151446.3−422020	0.054	150.7	13	$15^h14^m47^s.48$	$-42^\circ20'14^s.9$	RX J1514.8−4220	15144748−4220149	14.2	···	9.011
16	152012.2−382159	0.153	152.8	8	$15^h20^m12^s.53$	$-38^\circ21'57^s.9$	CD-37 10147C	15201253−3821579	4.2	···	8.454
17	151942.8−375255	0.061	169.1	10	$15^h19^m42^s.80$	$-37^\circ52'55^s.0$	···	···	···	···	···
18	152445.4−394238	0.105	170.4	11	$15^h24^m45^s.01$	$-39^\circ42'37^s.0$	HD 136933	15244501−3942367	4.7	5.367	5.495
19	145613.6−385121	0.176	172.5	8	$14^h56^m14^s.04$	$-38^\circ51'20^s.1$	HD 131675	14561404−3851200	5.2	9.15	7.323
20	145744.3−414140	0.051	173.7	15	$14^h57^m44^s.90$	$-41^\circ41'38^s.8$	USNO 0483−0366208	14574495−4141394	6.9	11.790[e]	9.351
”	”	”	”	”	$14^h57^m44^s.14$	$-41^\circ41'40^s.8$	···	14574414−4141408	1.8	···	14.698

[a] This is the position of the optical counterpart if known, otherwise it is the X-ray position.

[b] Separation between the X-ray source and the SNR center.

[c] X-ray position uncertainty.

[d] Separation between the X-ray and optical sources.

[e] No V magnitude was available from SIMBAD, so this is the $R2$ magnitude from USNO-B1.0.

Note. — Stellar identifications were made only on the basis of the *ROSAT* data and SIMBAD. See also Table 11.3.

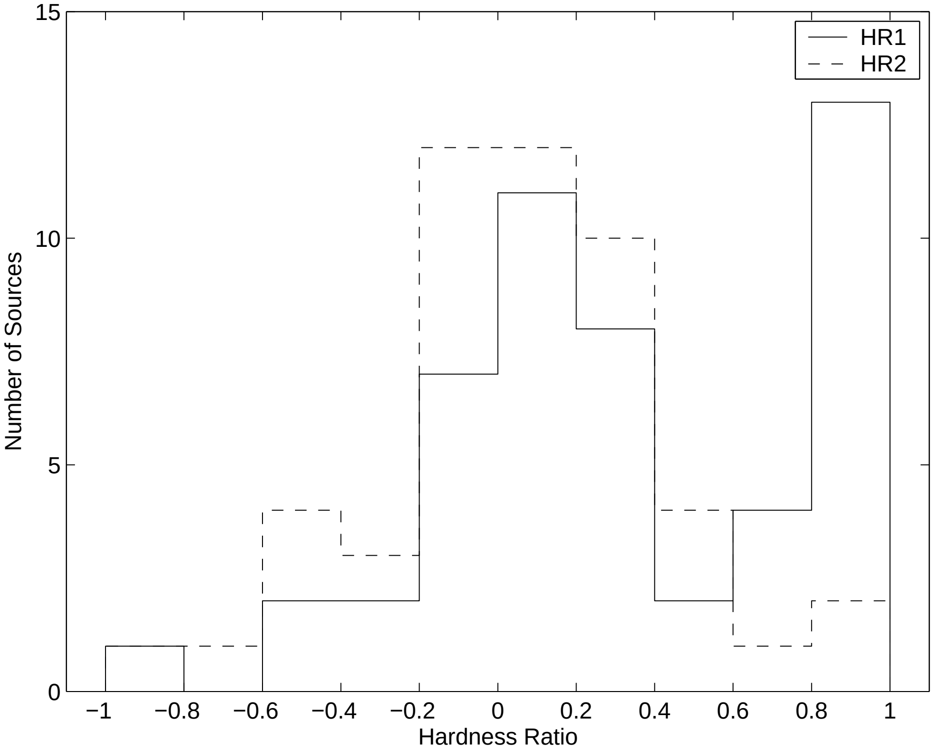

Figure 11.1 Hardness ratios of BSC sources from Table 11.2. HR1 is the solid line, while HR2 is the dashed line.

11.3.1 Extended Sources

In our analysis, we rejected those BSC sources that were identified as extended. This was for several reasons: we eliminated peaks in diffuse background emission that may have been identified as discreet sources, we eliminated large extended objects such as galaxy clusters and background SNRs, and we eliminated confused point sources. Practically, point-sources offer much better astrometry and are better suited to counterpart identification.

However, in some sense our selection was less than ideal. We would have eliminated any bright PWNe, although these might have been identified by previous searches. Also, source confusion makes our resulting luminosity limits less constraining than they might otherwise be. Given the relatively low space density of BSC sources (Fig. 11.2) this should not be a major effect, but it should still be noted. In contrast, our *Chandra* observations do not suffer from any confusion limitations.

One might ask if the diffuse emission from the SNRs themselves will limit the depth of the BSC in the SNR interiors. We have found in general that this is not the case. Figure 11.2 shows the density of BSC sources (both point-like and of all sizes) within different radii from the SNR centers. While the inner reaches of the SNRs have few sources and therefore poor statistics, in no case is there a statistically significant deficit of point sources inside the SNR. There might be a slight deficit inside SNR G156.2+5.7 or SNR G160.9+2.6, but these are also the smallest of the SNRs and therefore have the fewest total sources. Similarly, in Figure 11.3 we show the average background count rates determined when extracting the sources plotted in Figure 11.2, with the same binning. Two of the SNRs (G065.3+5.7 and G074.0−8.5) do show background increases in the interiors, two do not (G205.5+0.5 and G330.0+15.0), and two are uncertain due to few counts (G156.2+5.7 and G160.9+2.6), but even an increase of a factor of three above the mean background rate ($\approx 10^{-3}$ counts s^{-1} $arcmin^{-2}$) would give only ≈ 0.005 counts s^{-1} within the

90% confidence radius of a PSPC source (at 0.3 keV[1]) which is a factor of 10 less than the minimum source count rate for the BSC. Therefore the diffuse SNR emission should not have significantly affected the BSC source detection, and it is unlikely that there were any point sources that were missed.

11.4 Counterpart Identification

Once we had assembled the list of X-ray sources, we then examined the publicly available surveys (DSS, 2MASS,[2] and the NRAO VLA Sky Survey[3] or NVSS; Condon et al. 1998), as well as examination of SIMBAD and the relevant literature. Forty one out of 50 sources in Table 11.2 were cross-identified with reasonable confidence; additional notes and a summary of the identifications are listed in Table 11.3. The separations between the nominal X-ray and optical positions were consistent with the predicted X-ray position uncertainties (Fig. 11.4).

---

[1] `http://heasarc.gsfc.nasa.gov/docs/heasarc/caldb/docs/rosat/cal_ros_92_001/cal_ros_92_001.html.`

[2] When we were doing the initial source selection, the final 2MASS data had not been released, so there were cases where we made decisions based only on DSS data.

[3] For all SNRs but SNR G330.0+15.0, which is below the $\delta = -40^\circ$ limit of the NVSS.

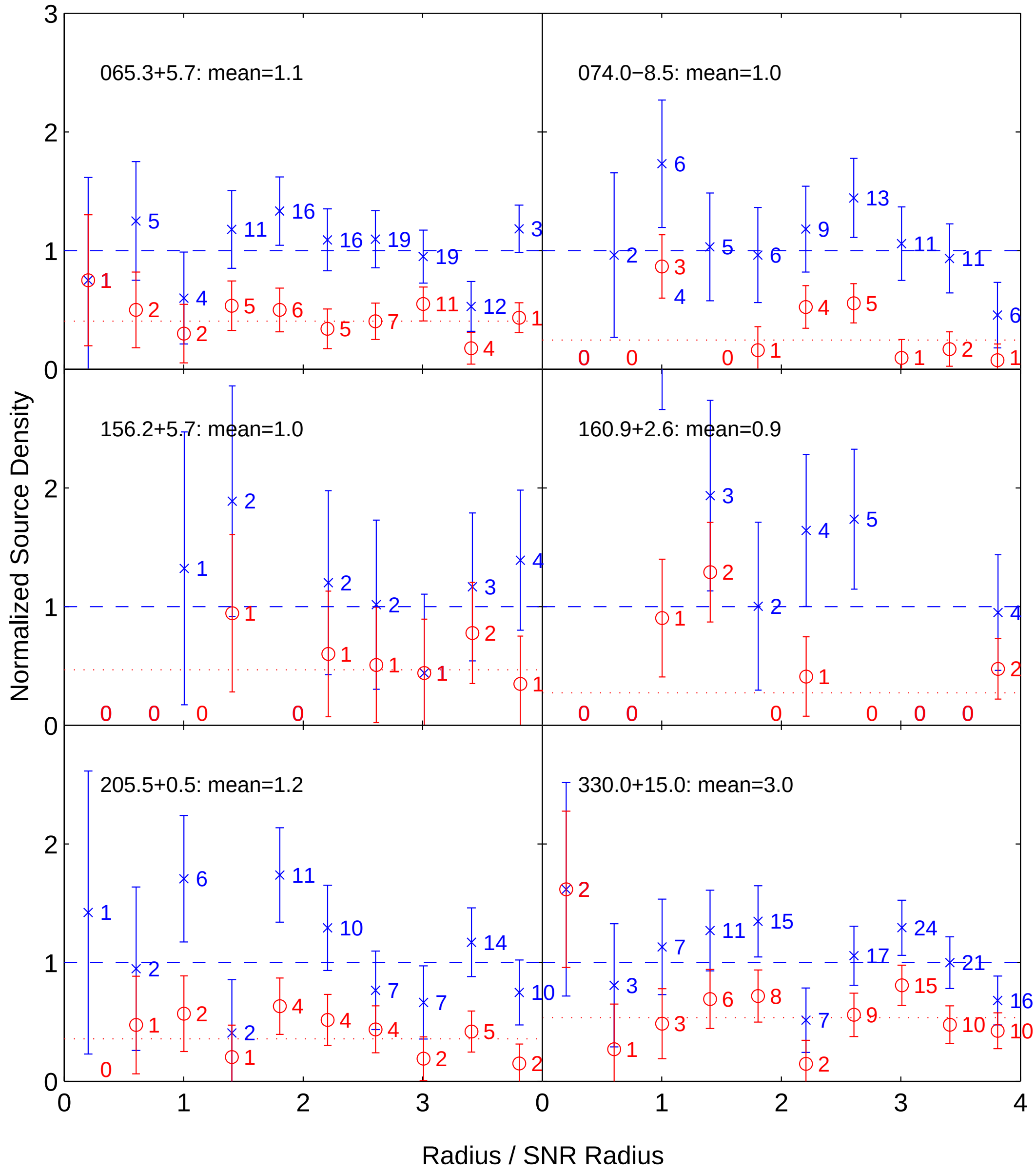

Figure 11.2 Normalized density of BSC sources in each of the SNRs from Table 11.1. The number of sources per square arcminute divided by the mean density is plotted against radius (in units of the SNR radius). All sources are shown as the blue x's, while only the unresolved sources are shown as the red circles. The means of the different source densities are shown as the blue dashed and red dotted lines, respectively. The means of the total source densities (in units of 10^{-4} arcmin^{-2}) are given next to the SNR names. At the position of each bin is printed the number of sources contributing to that bin. For bins with no sources plotted, these deficits are in all cases consistent with the small number counts (i.e., we expect $\lesssim 1$ source in each of those bins) except for the eighth and ninth bins of SNR G160.9+2.6, where zero sources are detected but 3.3 and 3.8 sources are expected, respectively. However, even in these bins there is no significant deficit of point sources.

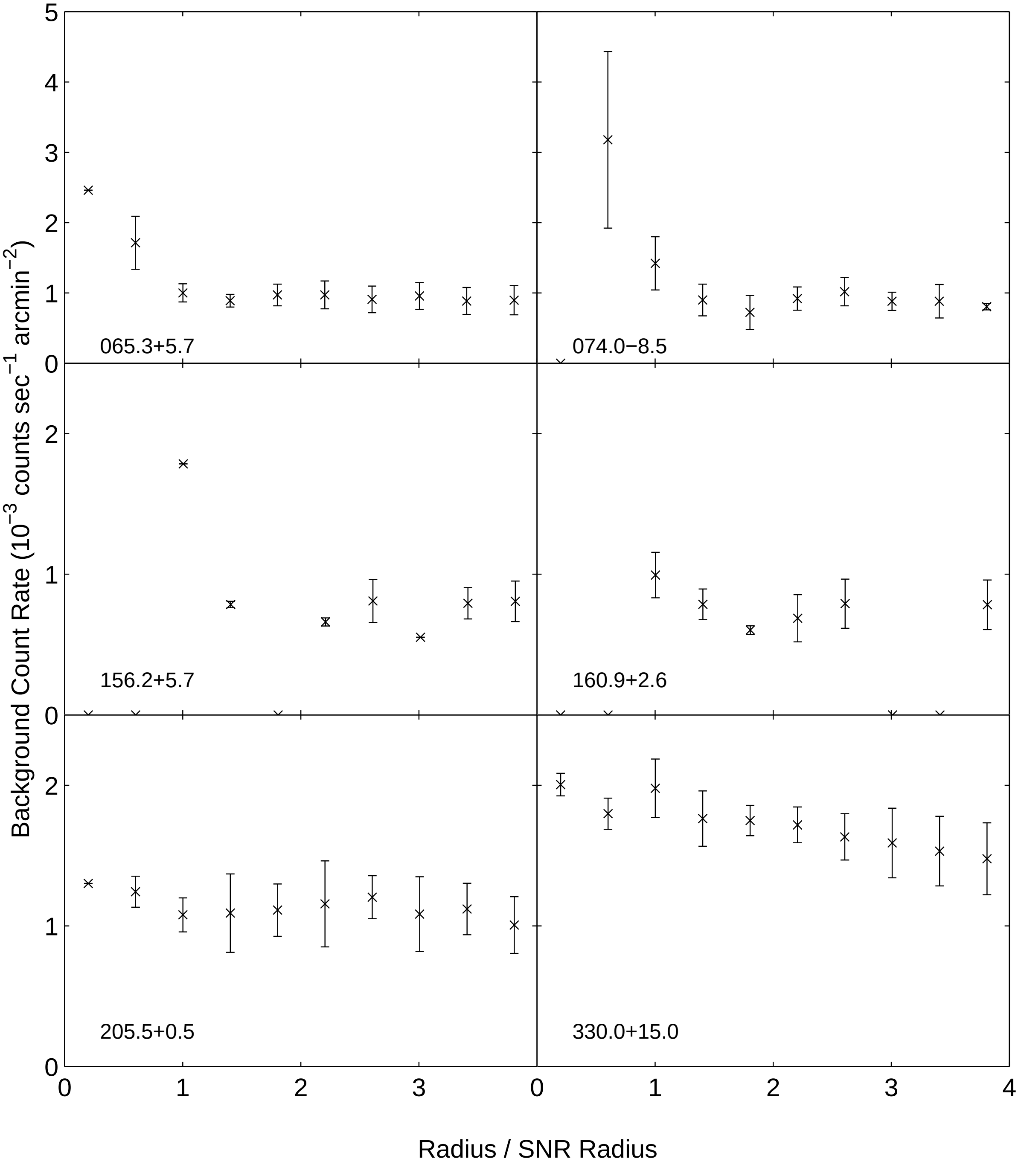

Figure 11.3 Background count rate vs. radius for the BSC sources in each of the SNRs from Table 11.1. The average background count rate (10^{-3} counts s^{-1} arcmin^{-2}) in each of 10 radial bins between 0 and 4 times the SNR radius is shown, along with uncertainties showing the standard deviation in each bin. SNRs G065.3+5.7 and G074.0−8.5 do show a factor of 2–3 increase in background rate inside the SNRs. For SNRs G156.2+5.7 and G160.9+2.6, the situation is not as clear because there are very few sources inside (see Fig. 11.2). For SNRs G205.5+0.5 and G330.0+15.0, there do not appear to be a significant rises toward the interiors.

Table 11.3. Identification of *ROSAT* Sources

1RXS J	Star(s)[a]	Optical Figure(s)[b]	*CXO*?[c]	Additional Notes[d]
SNR G065.3+5.7:				
193445.6+303100	HD 184738	11.5	N	Planetary nebula, associated with 235.2 mJy NVSS source at $19^{h}34^{m}45^{s}20$ $+30^{\circ}30'58''.8$ (Condon & Kaplan 1998)
193840.0+303035	V* EM Cyg	11.5	N	Dwarf nova; X-ray emission confirmed by SIMBAD
193922.4+300921	HD 185734	11.5	N	Spectroscopic binary; type G8III
194337.2+322523	BDS 9566 B/ HD 331149	11.5	N	Binary system, late-type
193458.1+335301	···	11.5,11.24	Y	Extended *Chandra* source
192722.3+280934	USNO 1181−0406270	11.5	N	
194401.5+284456	GSC 02151−03394	11.6	N	Late-type
194902.9+295258	HD 187460	11.6	N	Pulsating variable star of type K2II-III
193228.6+345318	2MASS J19322722+3453	11.6,11.18	Y	35.4 mJy NVSS counterpart at $19^{h}32^{m}27^{s}20$, $+34^{\circ}53'14''.8$; flare star (Fuhrmeister & Schmitt 2003)
191449.0+315131	HD 180314	11.6	N	Late-type
193856.2+351407	HD 185696	11.6	N	Double star system; late-type
193936.8+263718	AG+26 2090	11.6	N	Late-type
193113.0+360730	G 125−15	11.7	N	
191151.1+285012	USNO 1188−0330651	11.7	N	
SNR G074.0−8.5:				
205042.9+284643	···	11.8	Y	Flare star?
204457.4+291613	HD 335070	11.8	N	Late-type
205812.8+292037	USNO 1193−0519643/ 2MASS J20581257+2920454	11.8	N	Association may be questionable
205208.5+270546	HD 198809	11.8	N	Variable type G7III star
SNR G156.2+5.7:				
050639.1+513607	HD 32537	11.9	N	Variable star of the γ-Dor type
SNR G160.9+2.6:				
045707.4+452751	2MASS J04570832+4527	11.10,11.18	Y	
050339.8+451715	2MASS J05033958+4516	11.10,11.18	Y	Associated with the 34.3 mJy NVSS source at $05^{h}03^{m}39^{s}59$, $+45^{\circ}16'58''.9$; flare star?
045222.2+455619	HD 30736	11.10	N	Late-type
SNR G205.5+0.5:				
064108.3+052250	USNO 0155−01104−1/ 2MASS J06410796+0522438	11.11	N	Binary system?
064136.2+080218	HD 262113	11.11	N	Late-type
064109.3+044733	USNO 0947−0100759/ USNO 0947−0100763/ 2MASS J06410900+0447239/ USNO 0155−02167−1	11.11	N	Multiple-star system
064641.1+082152	HD 49015	11.11	N	Variable star of the γ-Dor type
062740.3+073103	2MASS J06274012+0731006	11.11,11.18	Y	
062937.2+082930	HD 45759	11.11	N	Late-type
063715.7+032005	USNO 0150−00332−1/ 2MASS J06371585+0320043/ 2MASS J06371555+0320026	11.12	N	Multiple-star system?
062554.8+065543	USNO 0145−01717−1	11.12	N	

Table 11.3

1RXS J	Star(s)[a]	Optical Figure(s)[b]	*CXO*?[c]	Additional Notes[d]
151849.8−405108	V* LX Lup	11.14	N	T Tauri star
145951.7−401158	HD 132349	11.14	N	Late-type
151659.2−382648	HD 135549	11.14	N	Late-type
152046.2−405405	HD 136206	11.14	N	Late-type
145837.5−391507	USNO 0507−0344267	11.14	N	
152211.8−395958	V* LZ Lup	11.14	N	T Tauri star
145721.8−401401	2MASS J14572207−4013586	11.15	N	Extended on the DSS/2MASS images (2MASX J14572207−4013588); likely a galaxy
151806.7−380423	USNO 7822−00433−1/ 2MASS J15180762−3804237	11.15	N	Multiple-star system?
151446.3−422020	RX J1514.8−4220	11.15	N	
152012.2−382159	CD−37 10147C	11.15	N	Multiple-star system?
151942.8−375255	···	11.15,11.20	Y	Star detected in Magellan data
152445.4−394238	HD 136933	11.15	N	Double star; type A0sp...
145613.6−385121	HD 131675	11.16	N	Late-type
145744.3−414140	USNO 0483−0366208/ 2MASS J14574414−4141408	11.16	N	Multiple-star system?

[a] Name(s) of likely stellar companion(s). In contrast to Table 11.2, this also includes identifications made from *Chandra* followup observations.

[b] Figure(s) where optical/IR counterparts are identified.

[c] Indicates if source was selected for *Chandra* followup; see § 11.5.1.

[d] Classifications are from SIMBAD unless otherwise noted. "Late-type" means that the star is of type mid-F or later, and hence is likely to have intrinsic X-ray emission (e.g., Stelzer et al. 2003).

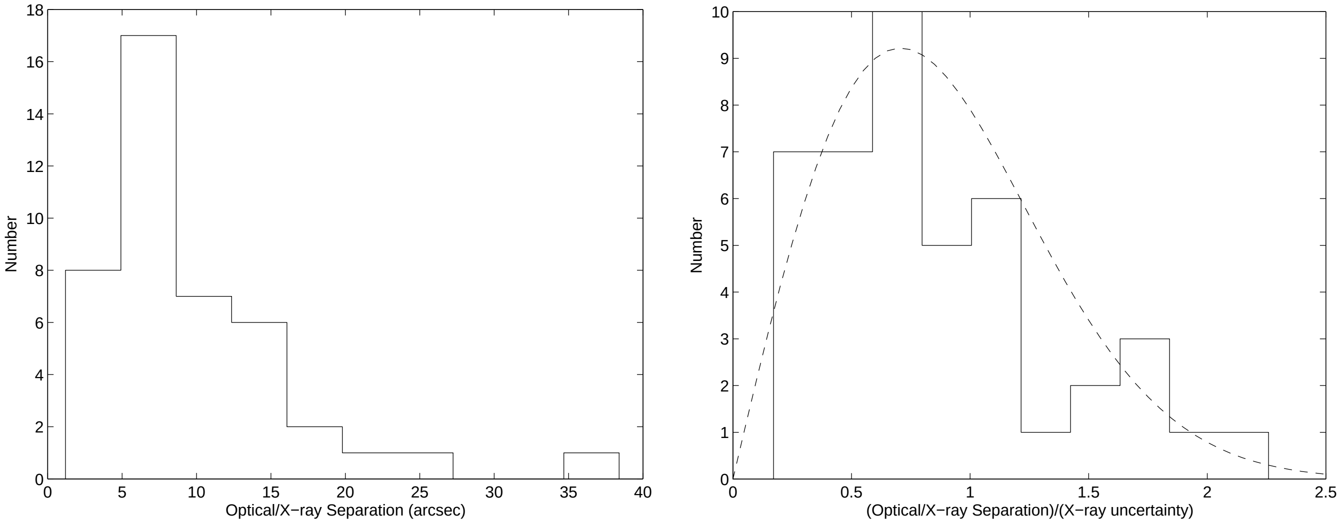

Figure 11.4 Distribution of the separation between the *ROSAT* positions and the positions of their optical counterparts. Left: absolute separation in arcsec; right: separation normalized to the X-ray position uncertainty, with the expected distribution ($f_r \propto r\exp(-r^2)$) also plotted.

There are a number of cases where there were multiple stars within the X-ray error circles, some of which were known to be physically associated (as noted in SIMBAD). In these cases we list multiple possible counterparts in Table 11.2. The true source of the X-ray emission may be any one of the stars, or may in fact come from the interactions between them.

The identifications were made primarily on the basis of position coincidence with bright stars, but in many cases additional evidence lends credence to our identifications. For example, many of the stars are so bright ($V < 5$ mag) that the chances of a false association are negligible or are of types known to have X-ray emission (e.g., T Tauri stars). We show 2MASS images of the X-ray sources with the optical counterparts indicated in Figures 11.5–11.16. Given the uncertainties in spectrum and foreground column density, most of the X-ray sources are consistent with being stars (Fig. 11.17).

11.5 *Chandra* Observations

The nine BSC sources that had no obvious optical counterparts, plus the four sources from §§ 11.2.2 and 11.2.5, were selected for *Chandra* followup observations. Here, as in Paper I, we selected the exposure times (3–6 ks) based on the known column densities to the SNRs (Tab. 11.1) and a blackbody spectrum with $kT = 0.25$ keV. The positions are known to sufficient accuracy to allow use of the ACIS-S3 CCD. In order to avoid photon pileup we used the 1/2- or 1/4-subarray modes (which also provide improved timing information), depending on the position uncertainties. A log of these observations is in Table 11.4.

In most of the cases, the *Chandra* observations revealed nothing extraordinary. In the case of the BSC sources, the *Chandra* data typically showed that the BSC position was significantly off and/or the counterpart was faint (Figs. 11.18 and 11.19). The additional sources from the literature were all coincident with stellar sources, once we had *Chandra* positions. Of the 13 sources with *Chandra* followup, nine had point-like *Chandra* sources with obvious IR counterparts (§ 11.5.1). Of the other four sources: two show extended X-ray emission with *Chandra*, one has no obvious 2MASS counterpart, and one source did not appear in the *Chandra* observation. We discuss these sources in some detail in Section 11.5.1.

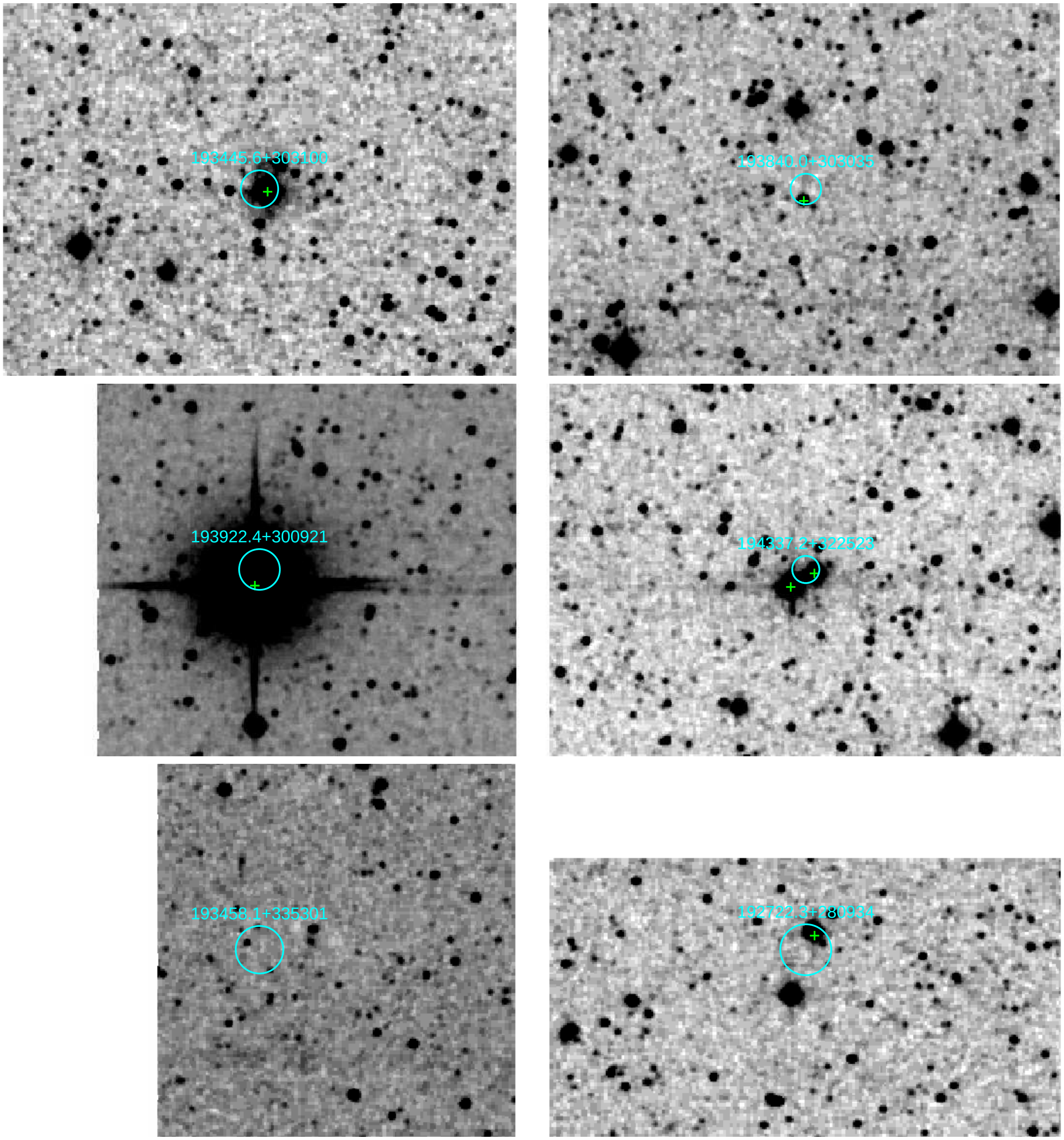

Figure 11.5 2MASS K_s-band images of the sources in SNR G065.3+5.7 from Table 11.2. The images are $5'$ to a side, with north up and east to the left. The X-ray position uncertainties are indicated by the circles, and the proposed optical counterparts are shown by the crosses.

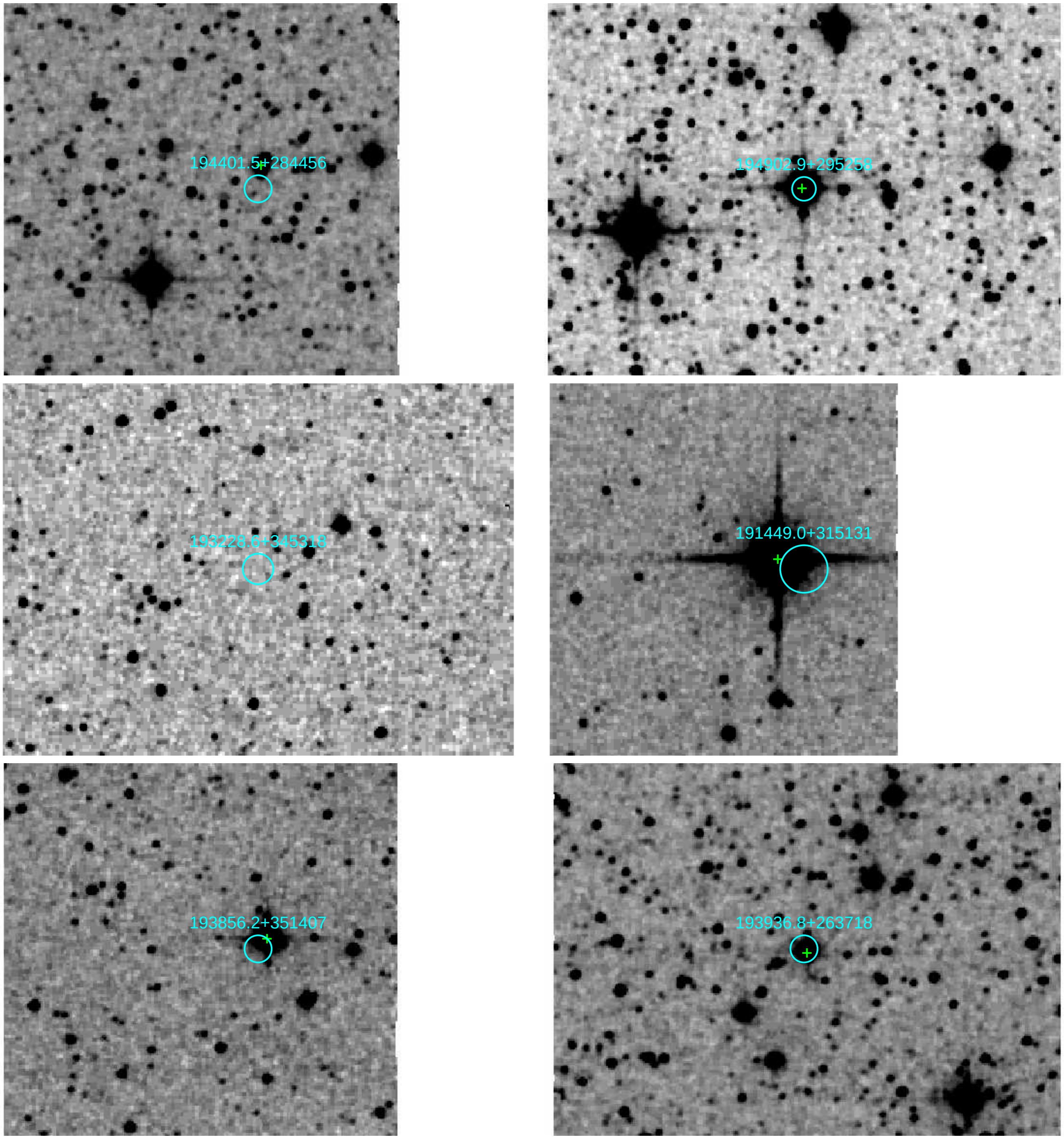

Figure 11.6 2MASS K_s-band images of the sources in SNR G065.3+5.7 from Table 11.2. The images are $5'$ to a side, with north up and east to the left. The X-ray position uncertainties are indicated by the circles, and the proposed optical counterparts are shown by the crosses.

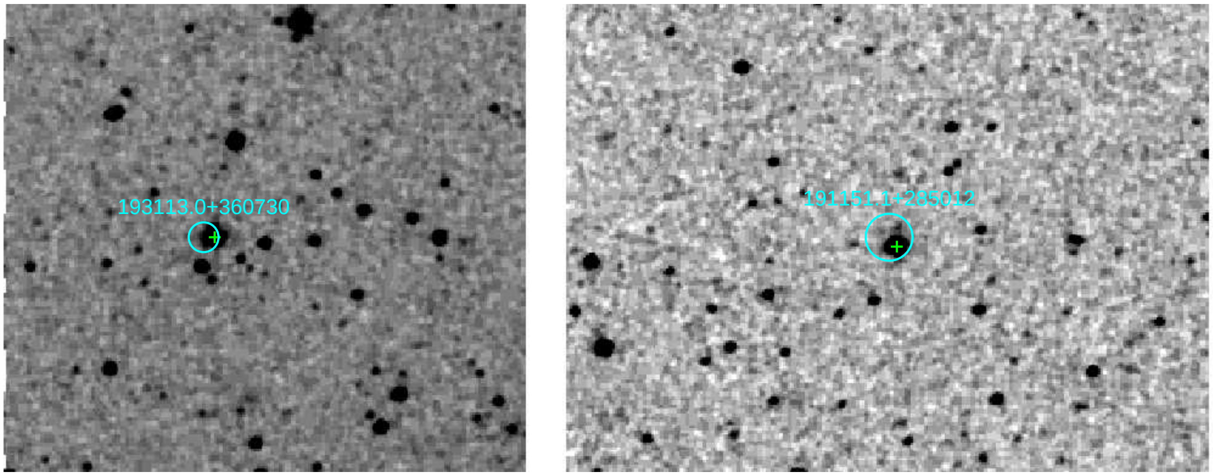

Figure 11.7 2MASS K_s-band images of the sources in SNR G065.3+5.7 from Table 11.2. The images are 5′ to a side, with north up and east to the left. The X-ray position uncertainties are indicated by the circles, and the proposed optical counterparts are shown by the crosses.

Table 11.4. Log of *Chandra* Observations

Source	Date	Exp. (ks)	Subarray Mode
SNR G065.3+5.7:			
1RXS J193228.6+345318	2002-Dec-08	3.7	1/4
1RXS J193458.1+335301	2003-Jan-26	3.5	1/4
SNR G074.0−8.5:			
AX J2049.6+2939	2003-Mar-19	3.2	1/2
1RXS J205042.9+284643	2003-Mar-19	3.9	1/4
SNR G160.9+2.6:			
1RXS J045707.4+452751	2003-Jan-04	5.2	1/4
SNR G205.5+0.5:			
1RXS J050339.8+451715	2003-Jan-08	5.4	1/4
1RXS J062740.3+073103	2003-Mar-11	3.4	1/4
EX J062723+053739	2002-Dec-07	3.5	1/2
EX J063053+061113	2003-Apr-22	3.6	1/2
EX J063646+051757	2003-Mar-11	3.8	1/2
SNR G330.0+15.0:			
1RXS J150139.6−403815	2003-Mar-18	2.9	1/4
1RXS J150818.8−401730	2003-Mar-18	3.7	1/4
1RXS J151942.8−375255	2003-Mar-10	2.9	1/4

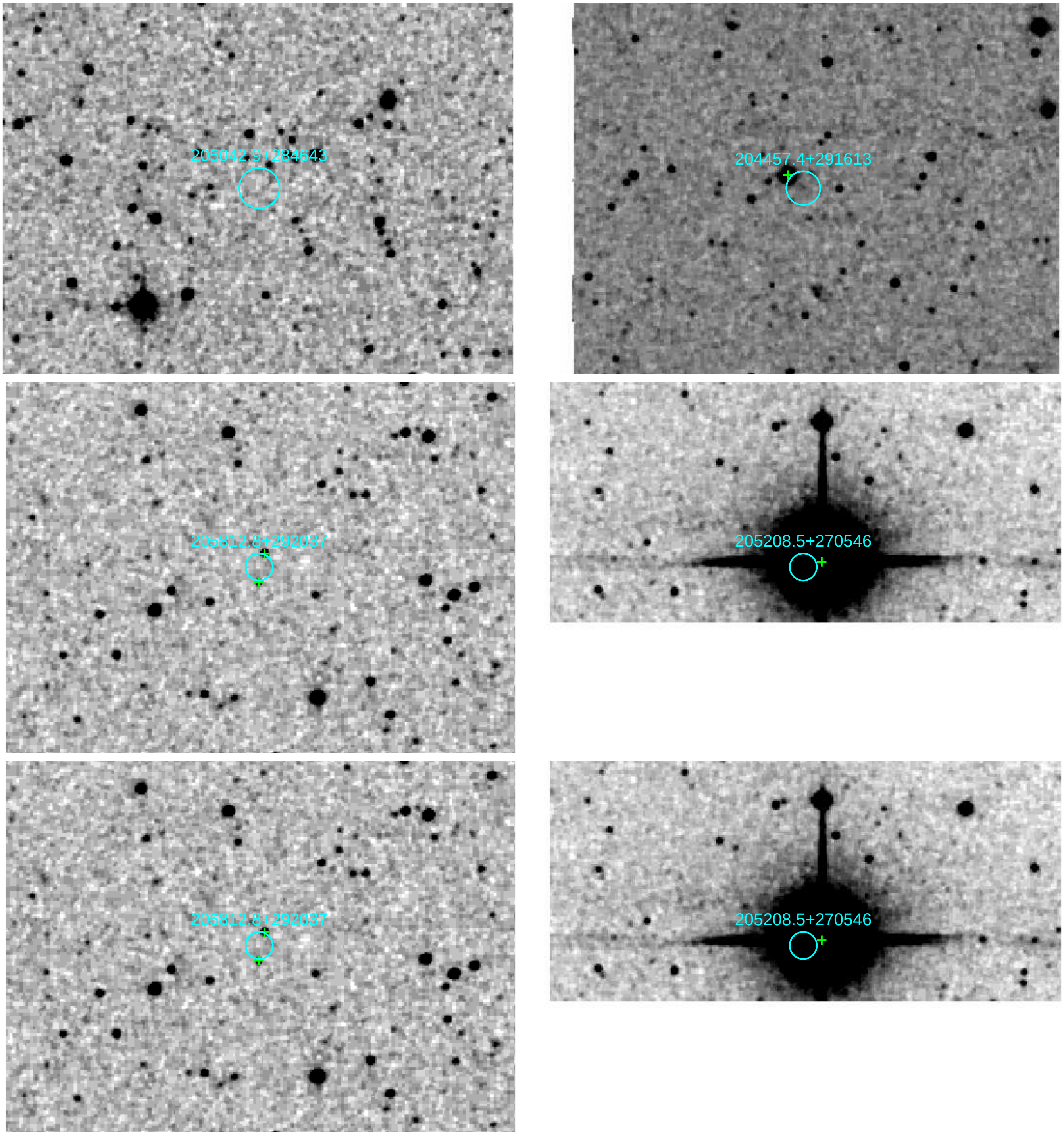

Figure 11.8 2MASS K_s-band images of the sources in SNR G074.0−8.5 from Table 11.2. The images are 5′ to a side, with north up and east to the left. The X-ray position uncertainties are indicated by the circles, and the proposed optical counterparts are shown by the crosses.

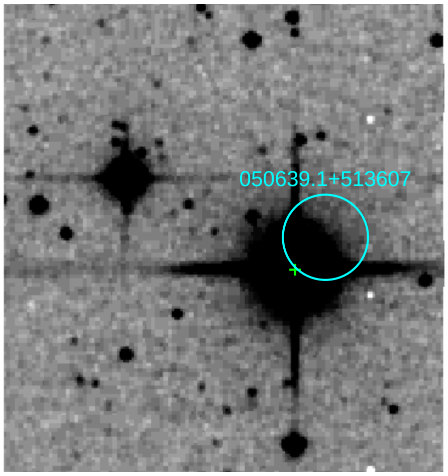

Figure 11.9 2MASS K_s-band image of the source in SNR G156.2+5.7 from Table 11.2. The images are 5′ to a side, with north up and east to the left. The X-ray position uncertainties are indicated by the circles, and the proposed optical counterparts are shown by the crosses.

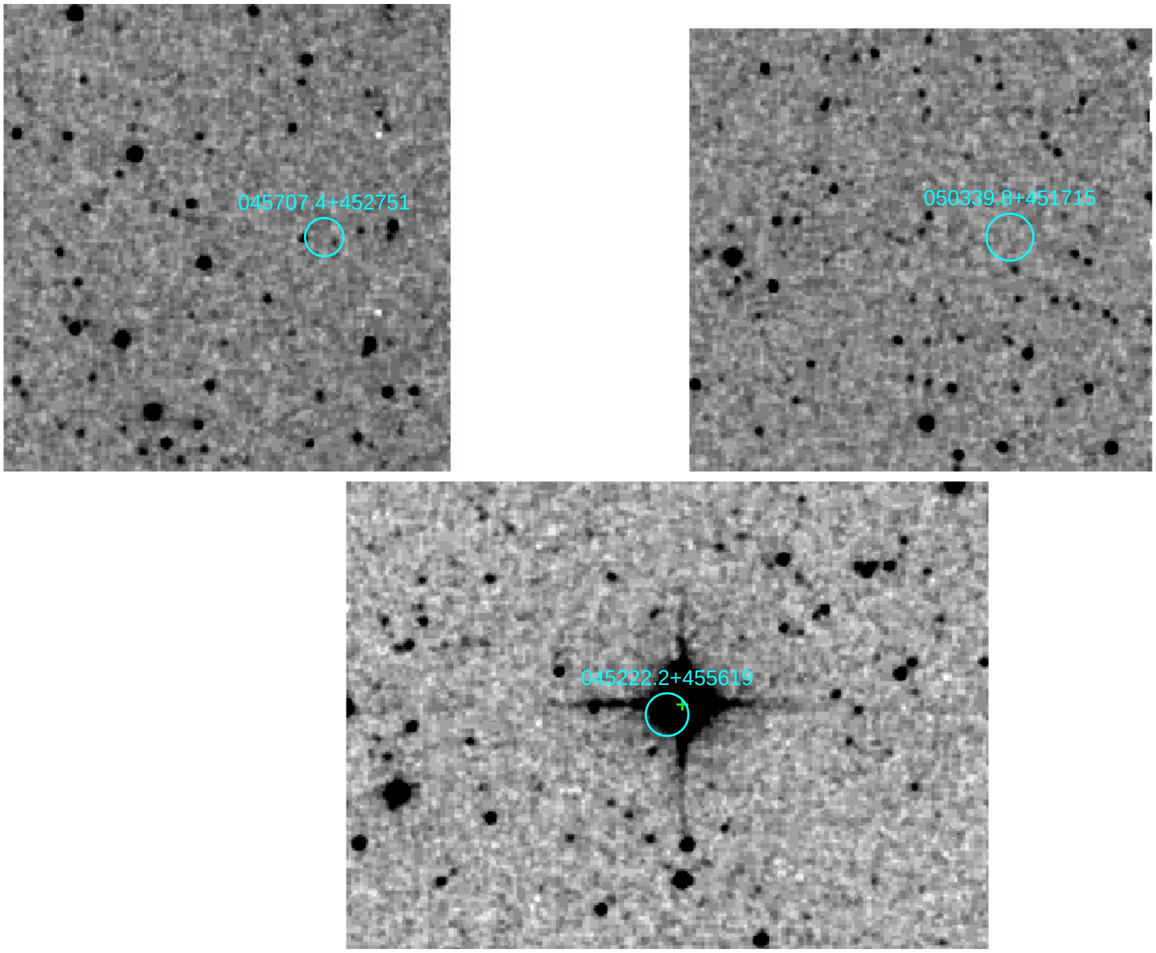

Figure 11.10 2MASS K_s-band images of the sources in SNR G160.9+2.6 from Table 11.2. The images are 5′ to a side, with north up and east to the left. The X-ray position uncertainties are indicated by the circles, and the proposed optical counterparts are shown by the crosses.

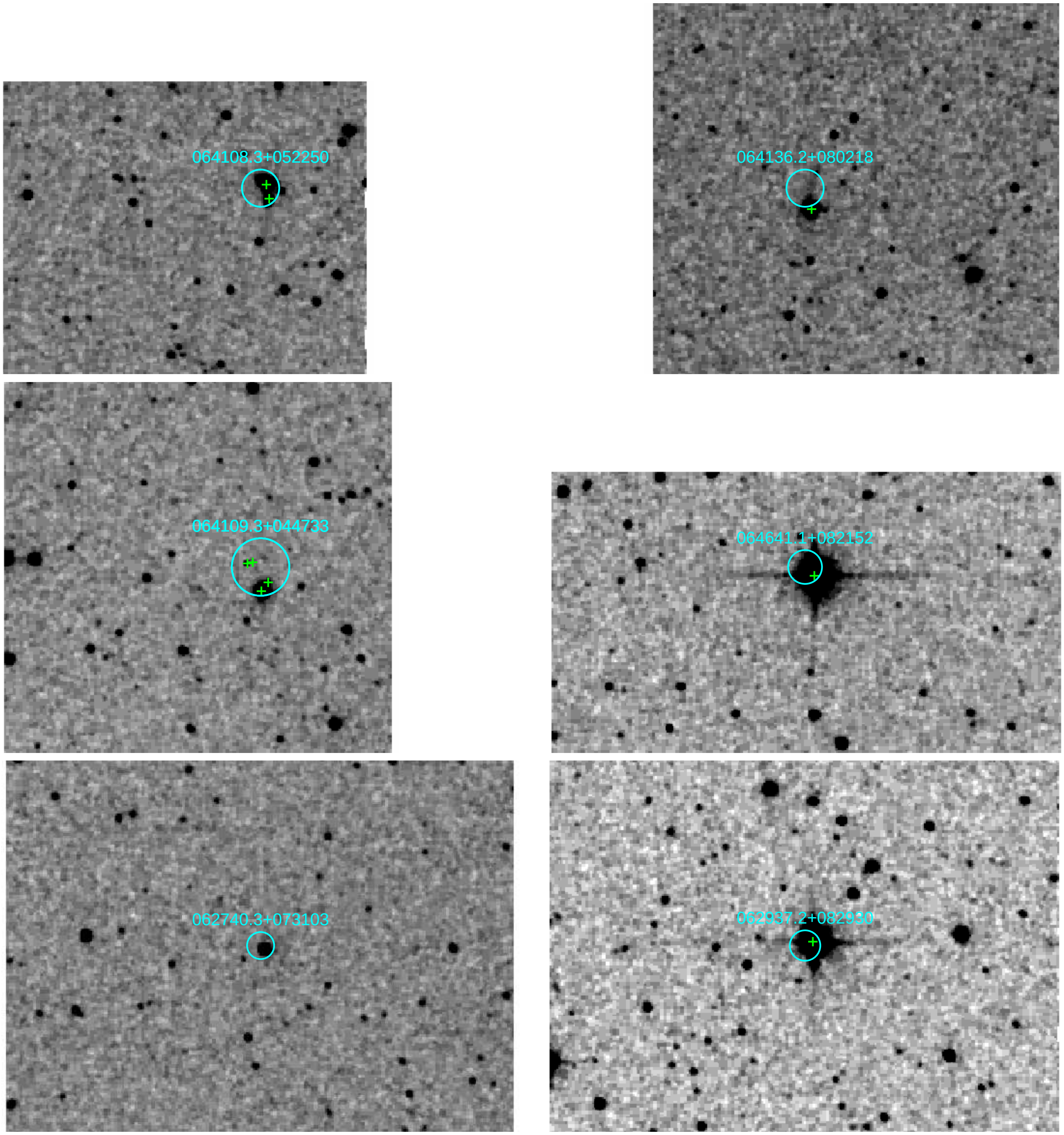

Figure 11.11 2MASS K_s-band images of the sources in SNR G205.5+0.5 from Table 11.2. The images are $5'$ to a side, with north up and east to the left. The X-ray position uncertainties are indicated by the circles, and the proposed optical counterparts are shown by the crosses.

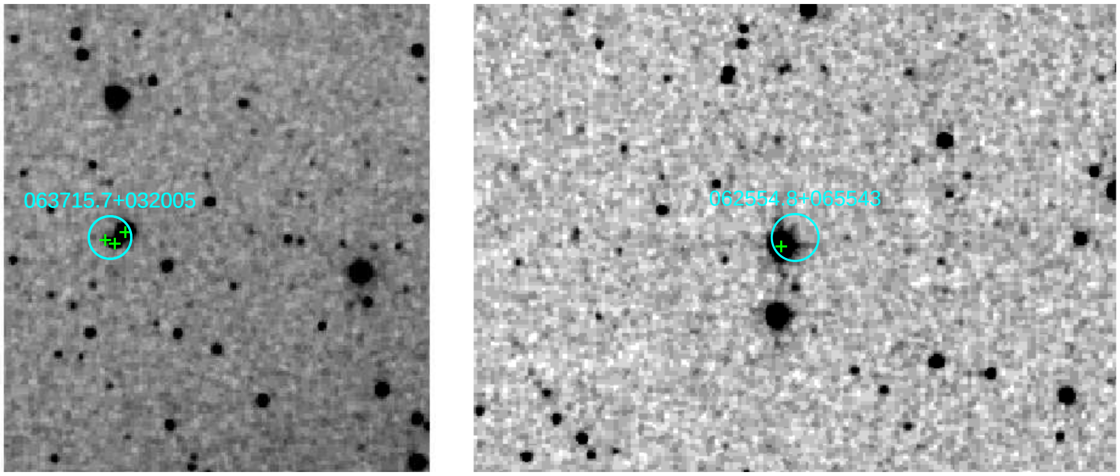

Figure 11.12 2MASS K_s-band images of the sources in SNR G205.5+0.5 from Table 11.2. The images are $5'$ to a side, with north up and east to the left. The X-ray position uncertainties are indicated by the circles, and the proposed optical counterparts are shown by the crosses.

11.5.1 Notes on *Chandra* Sources

In the cases where *Chandra* point-sources were detected, the counterpart identifications are essentially secure. This is due to the very small positional uncertainty of the *Chandra* positions ($< 1''$) coupled with the brightnesses of the counterparts (see Paper I). See Figures 11.18 and 11.19 for images of those sources with counterpart identifications.

1RXS J193458.1+335301 The *Chandra* source is extended. See § 11.5.3.1.

1RXS J193228.6+345318 The *Chandra* source is point-like, and is at $19^{\rm h}32^{\rm m}27^{\rm s}\!.25$, $+34^\circ53'14^{\rm s}\!.8$ ($17''$ away from the BSC position). It is coincident with the $K_s = 14.2$-mag source 2MASS J19322722+3453148, the $B = 16.8$-mag source USNO 1248-0333432, and with the NVSS source identified in Table 11.3. It was identified as a flare star by Fuhrmeister & Schmitt (2003) after our initial source selection.

1RXS J205042.9+284643 There is no *Chandra* source in the followup observation. See § 11.5.3.2.

AX J2049.6+2939 This ASCA source was identified as a possible neutron star by Miyata et al. (1998b) and Miyata et al. (2001). The *Chandra* source is point-like, and is at $20^{\rm h}49^{\rm m}35^{\rm s}\!.41$, $+29^\circ38'50''\!.9$. It is coincident with the $K_s = 10.0$-mag source 2MASS J20493540+2938509.

1RXS J045707.4+452751 The *Chandra* source is point-like, and is at $04^{\rm h}57^{\rm m}08^{\rm s}\!.31$, $+45^\circ27'49''\!.8$ ($10''$ away from the BSC position). It is coincident with the $K_s = 14.5$-mag source 2MASS J04570832+4527499.

1RXS J050339.8+451715 The *Chandra* source is point-like, and is at $05^{\rm h}03^{\rm m}39^{\rm s}\!.59$, $+45^\circ16'59''\!.5$ ($15''$ away from the BSC position). It is coincident with the $K_s = 15.0$-mag source 2MASS J05033958+4516594 and with the NVSS source identified in Table 11.3. There is no USNO counterpart.

1RXS J062740.3+073103 The *Chandra* source is point-like, and is at $06^{\rm h}27^{\rm m}40^{\rm s}\!.12$, $+07^\circ31'00''\!.3$ ($4''$ from the BSC position). It is coincident with the $K_s = 10.1$-mag source 2MASS J06274012+0731006.

EX J062723+053739 The *Chandra* source is point-like, and is at $06^{\rm h}30^{\rm m}05^{\rm s}\!.29$, $+05^\circ45'40''\!.8$. It is coincident with the $K_s = 10.0$-mag source 2MASS J06300529+0545407.

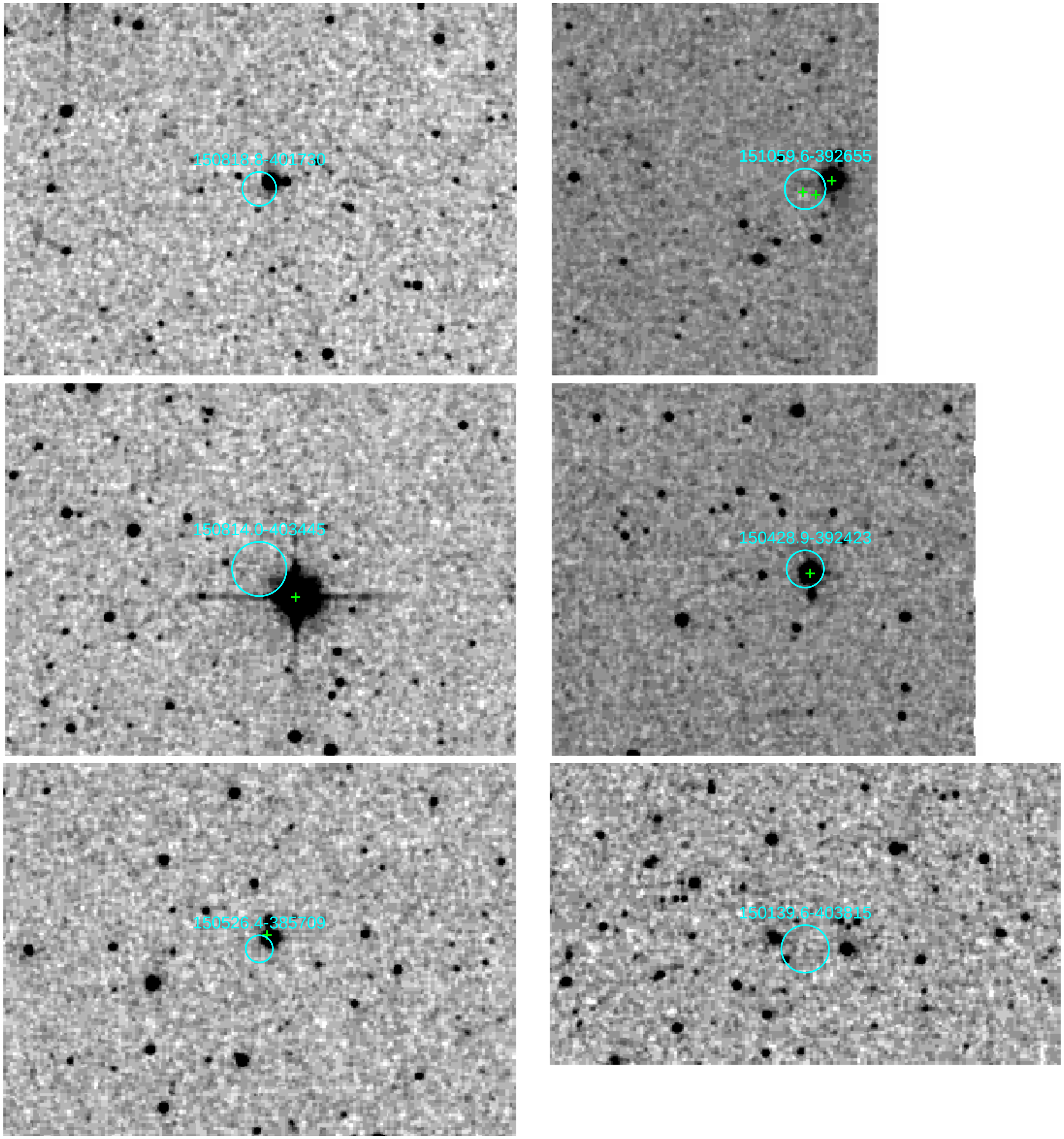

Figure 11.13 2MASS K_s-band images of the sources in SNR G330.0+15.0 from Table 11.2. The images are $5'$ to a side, with north up and east to the left. The X-ray position uncertainties are indicated by the circles, and the proposed optical counterparts are shown by the crosses.

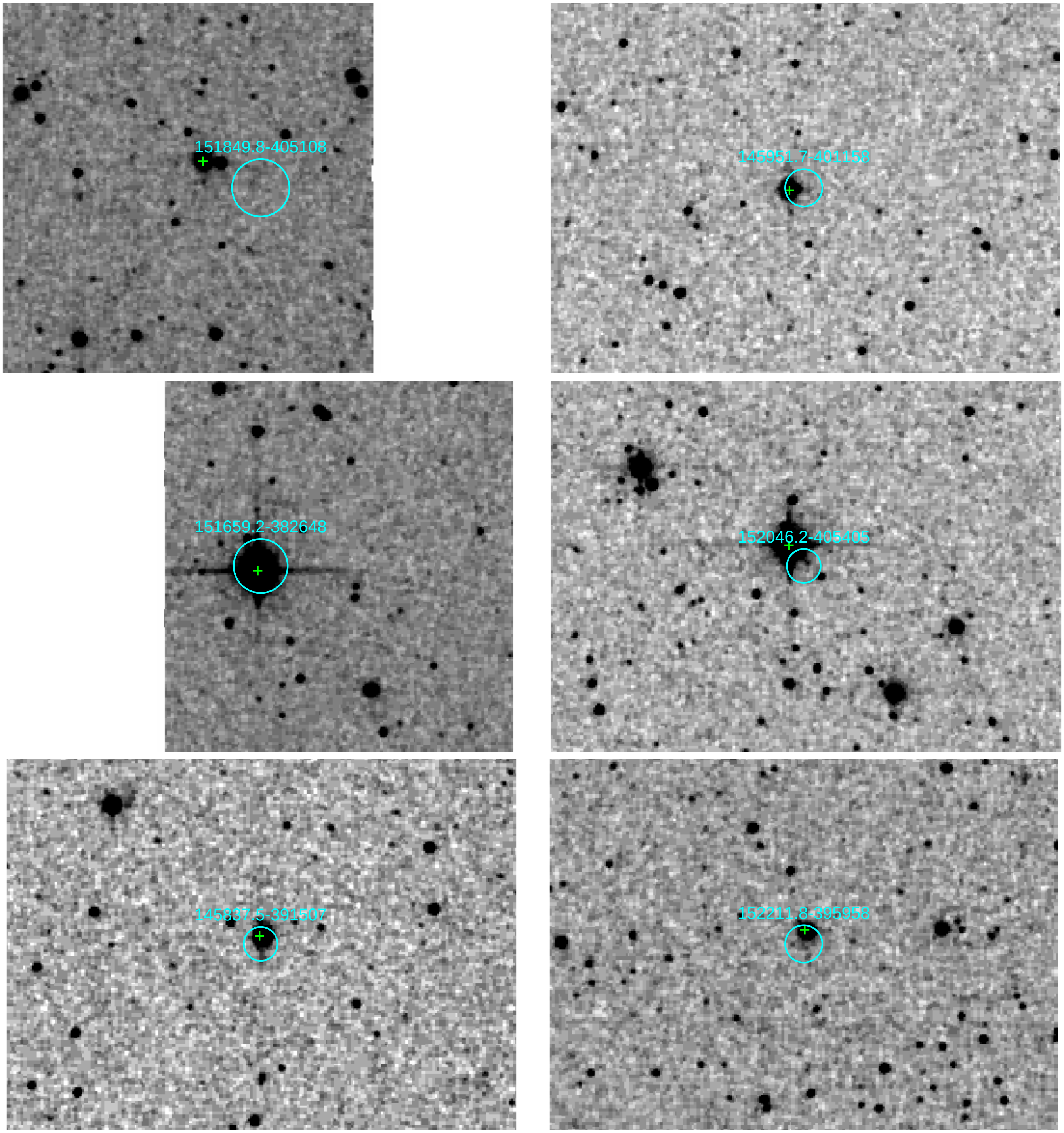

Figure 11.14 2MASS K_s-band images of the sources in SNR G330.0+15.0 from Table 11.2. The images are 5′ to a side, with north up and east to the left. The X-ray position uncertainties are indicated by the circles, and the proposed optical counterparts are shown by the crosses.

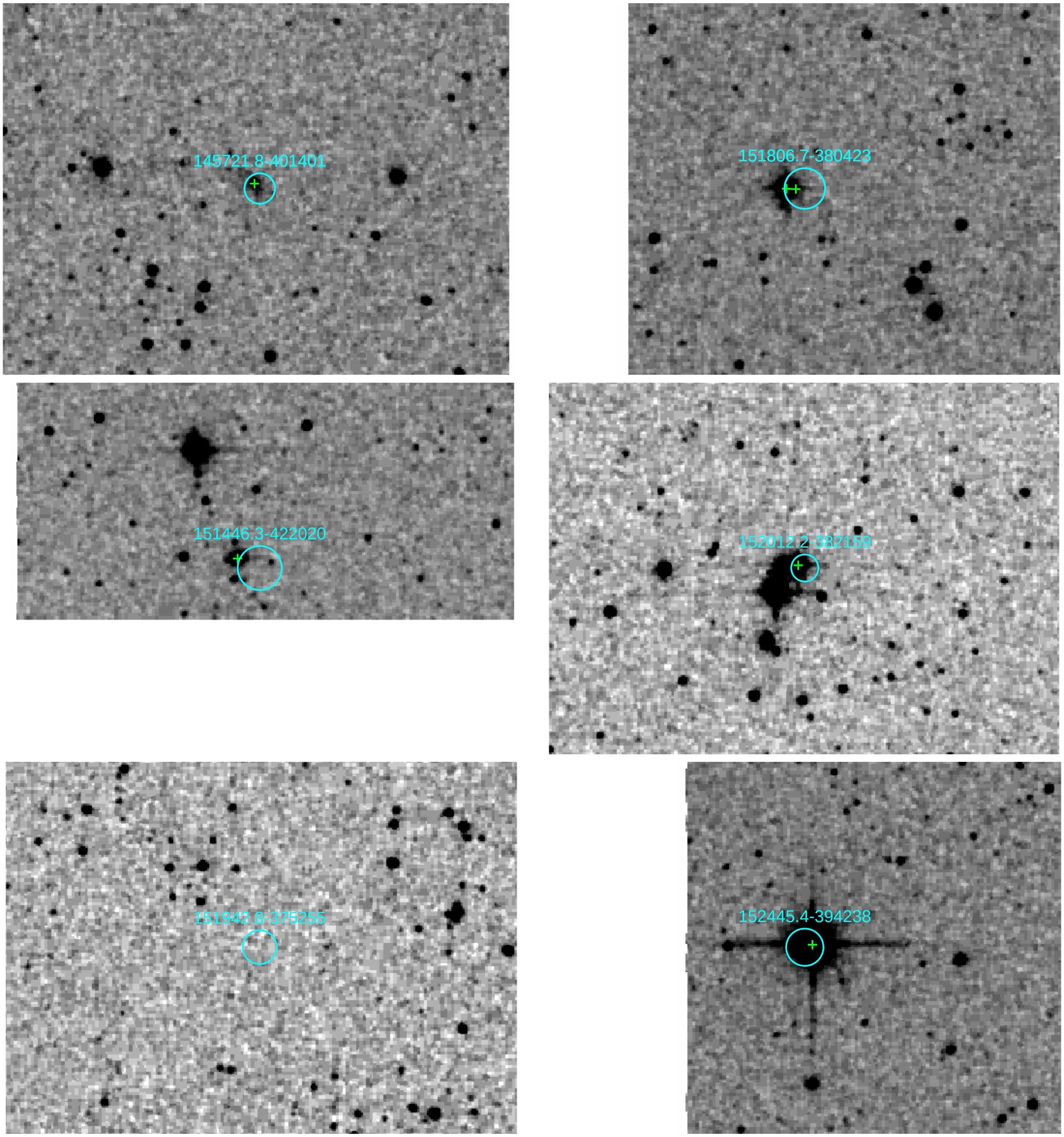

Figure 11.15 2MASS K_s-band images of the sources in SNR G330.0+15.0 from Table 11.2. The images are 5′ to a side, with north up and east to the left. The X-ray position uncertainties are indicated by the circles, and the proposed optical counterparts are shown by the crosses.

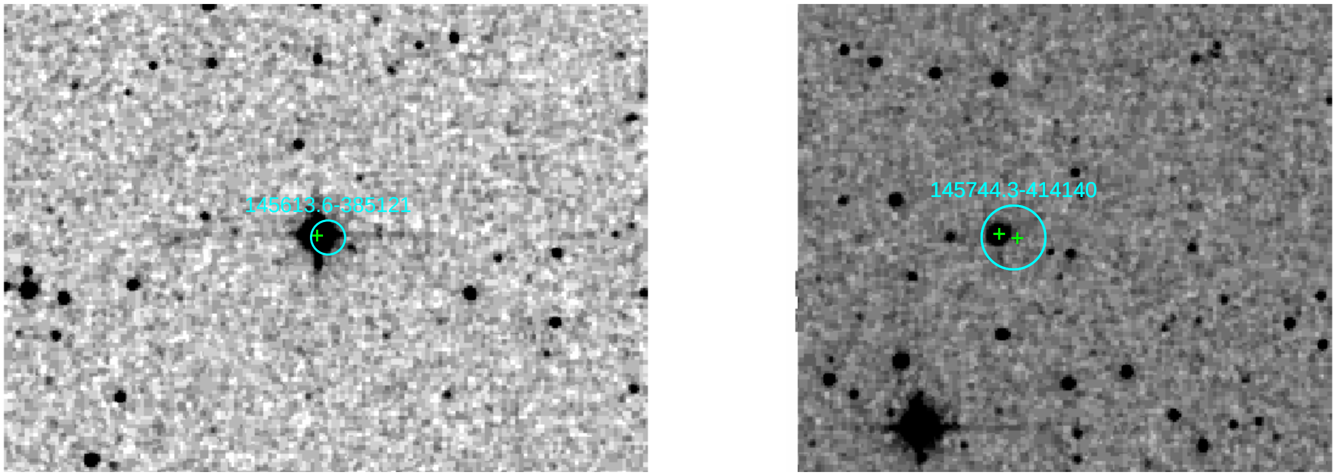

Figure 11.16 2MASS K_s-band images of the sources in SNR G330.0+15.0 from Table 11.2. The images are $5'$ to a side, with north up and east to the left. The X-ray position uncertainties are indicated by the circles, and the proposed optical counterparts are shown by the crosses.

EX J063053+061113 The *Chandra* source is point-like, and is at $06^{\rm h}33^{\rm m}33^{\rm s}.22$, $+06^\circ08'39''.5$. It is coincident with the $K_s = 13.4$-mag source 2MASS J06333322+0608396.

EX J063646+051757 The *Chandra* source is point-like, and is at $06^{\rm h}39^{\rm m}25^{\rm s}.67$, $+05^\circ14'30''.1$. It is coincident with the $K_s = 11.6$-mag source 2MASS J06392566+0514301.

1RXS J150818.8−401730 The *Chandra* source is point-like, and is at $15^{\rm h}08^{\rm m}18^{\rm s}.17$, $-40^\circ17'26''.0$ ($8''$ away from the BSC position). It is coincident with the $K_s = 9.3$-mag source 2MASS J15081819−4017261.

1RXS J150139.6−403815 The *Chandra* source is extended. See § 11.5.3.4.

1RXS J151942.8−375255 The *Chandra* source is point-like, and is at $15^{\rm h}19^{\rm m}42^{\rm s}.98$, $-37^\circ52'51''.4$ ($4''$ away from the BSC position). There is no 2MASS counterpart, but we do identify a counterpart on our Magellan MAGIC and PANIC observations (§ 11.5.2 and Fig. 11.20). The source has $R = 19.1$-mag and $K_s = 15.79$-mag.

11.5.2 Optical and Infrared Followup

We obtained optical and infrared followup observations of the three of the four sources where the *Chandra* followup did not immediately identify a counterpart (see § 11.5.1), namely 1RXS J193458.1+335301, 1RXS J150139.6−403815, and 1RXS J151942.8−375255. The log of the observations is given in Table 11.5. Reduction and calibration followed standard procedures.

The Magellan data were taken during the same observing runs as data presented in Paper I, and details can be found there. For the reduction of the remaining data, we used standard `IRAF` routines to subtract the bias, flat-field, and then combine separate exposures. Significant focal-plane distortion prevented simple addition of the LFC data, so we used the `IRAF MSCRED` package to flatten each image with custom distortion maps prior to addition. We then performed absolute astrometry, solving for plate scale, rotation, and central position relative to stars the 2MASS catalog, and getting residuals in each coordinate of $0''.13$ (2100 stars) and $0''.17$ (4000 stars) for P60CCD and LFC, respectively.

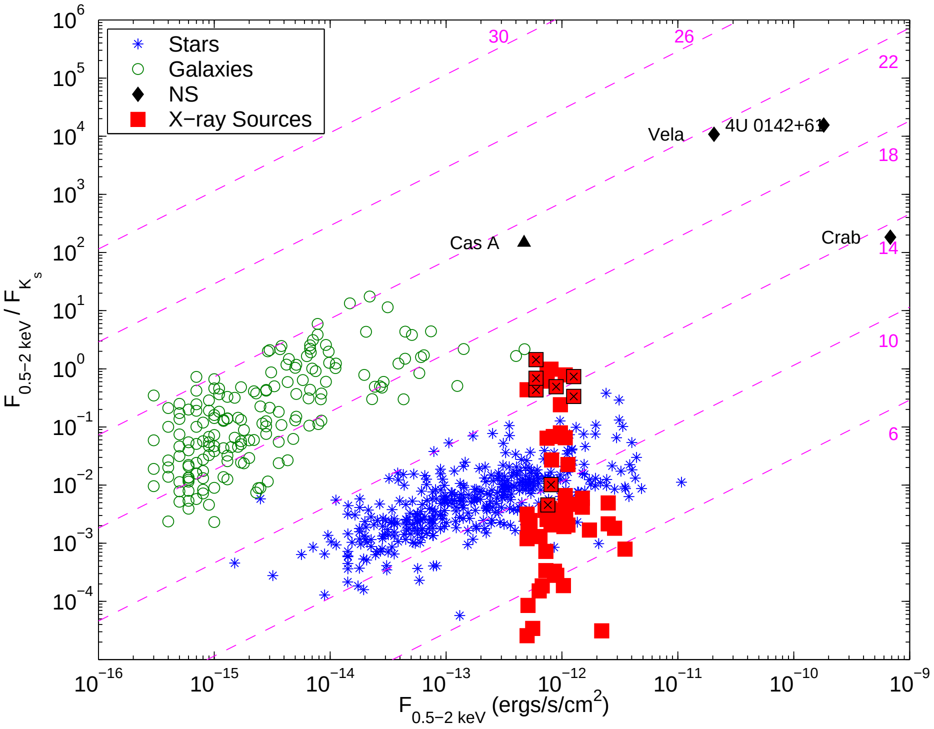

Figure 11.17 X-ray-to-K_s flux ratio vs. X-ray flux for sources from Table 11.2, with sources from the CDF/Orion studies and selected neutron stars. Stars from CDF/Orion are blue asterisks, galaxies are green circles. Selected neutron stars are black diamonds/limits, and are labeled. The X-ray sources from Table 11.2 (including detections from § 11.5.1) are the red squares (those with *Chandra* followup, plus 1RXS J205812.8+292037, have an "x" in their squares). The diagonal lines represent constant magnitude, and are labeled by that magnitude. For the X-ray sources from Table 11.2, the PSPC were converted to a flux by $F_{0.5-2.0\ \mathrm{keV}} = \mathrm{PSPC} \times 1 \times 10^{-11}$ ergs s^{-1} cm^{-2}, appropriate for a blackbody with $kT_\infty = 0.25$ keV and $N_\mathrm{H} = 5 \times 10^{20}$ cm^{-2}. The X-ray source are largely consistent with foreground stars, especially considering the possible range of temperatures and column densities, but a number may also be active galaxies such as those found in Rutledge et al. (2003).

11.5.3 Remaining Sources

We now find, that after investigating 50 BSC sources plus four sources from the literature, and obtaining *Chandra* followup of 13 of these sources, that there remain three X-ray sources that do not have very likely optical counterparts and are therefore worthy of extended discussion. As noted in § 11.5.1, these sources are: 1RXS J193458.1+335301, 1RXS J205042.9+284643, and 1RXS J150139.6−403815. The first and third have extended X-ray emission, while the second has no apparent *Chandra* counterpart. We also include here 1RXS J205812.8+292037, which has a probable but not definite association with optical/IR sources.

11.5.3.1 1RXS J193458.1+335301

The BSC lists 1RXS J193458.1+335301 as having 0.051(12) count s^{-1} in the PSPC, with hardness ratios of HR1 = 1.00(17) and HR2 = 0.10(23) (see Voges et al. 1996 for definitions of bands and hardness ratios). The *Chandra* source is clearly extended, as shown in Figure 11.21. There are no other X-ray sources nearby, indicating that the *Chandra* source is very likely 1RXS J193458.1+335301 despite the

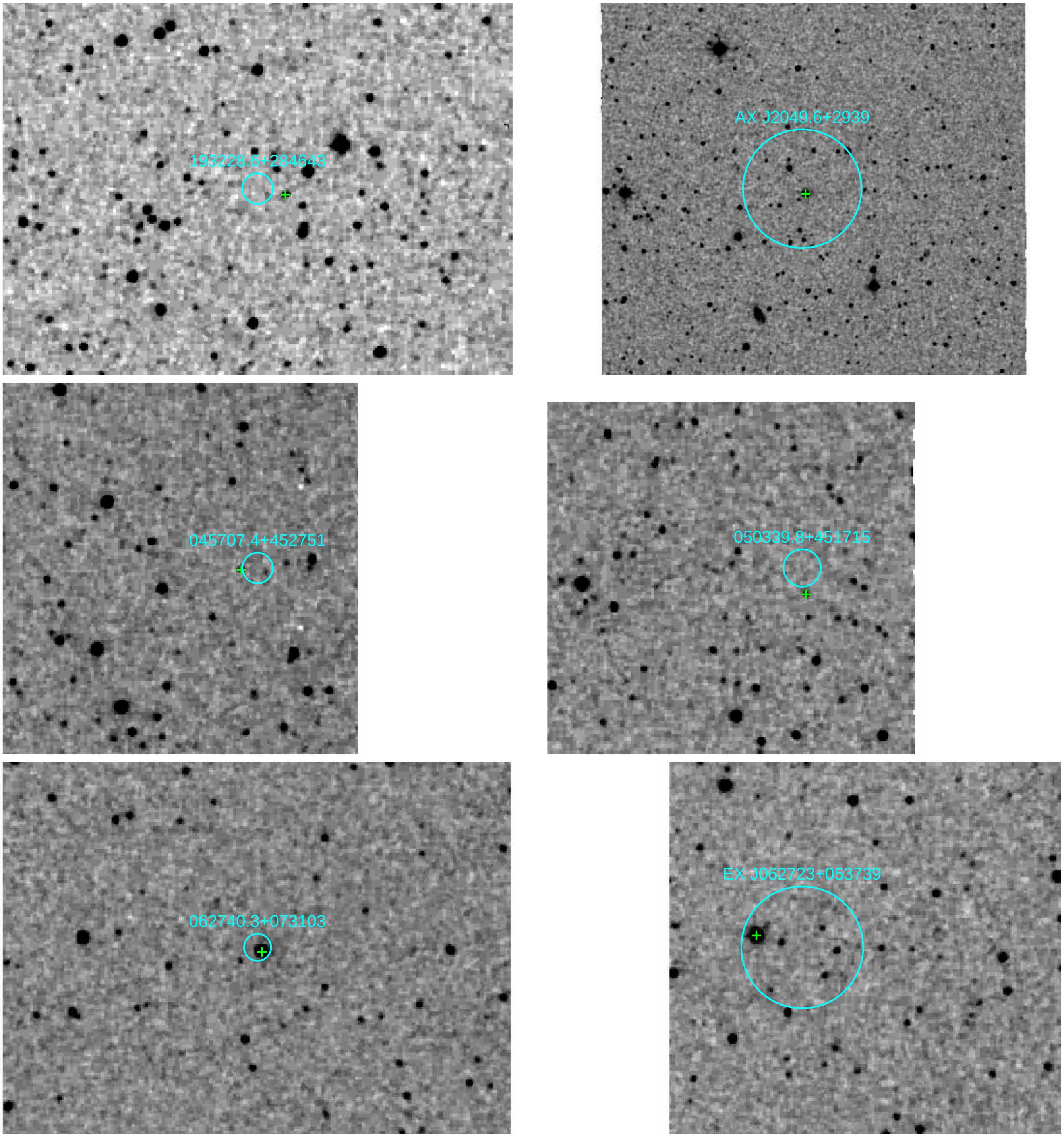

Figure 11.18 2MASS K_s-band images of the sources from Table 11.4 with point-like X-ray sources and secure counterpart identifications. The images are $5'$ to a side (except for that of AX J2049.6+2939, which is $10'$ to a side), with north up and east to the left. The BSC X-ray position uncertainties are indicated by the circles, and the *Chandra* positions and optical counterparts are shown by the crosses.

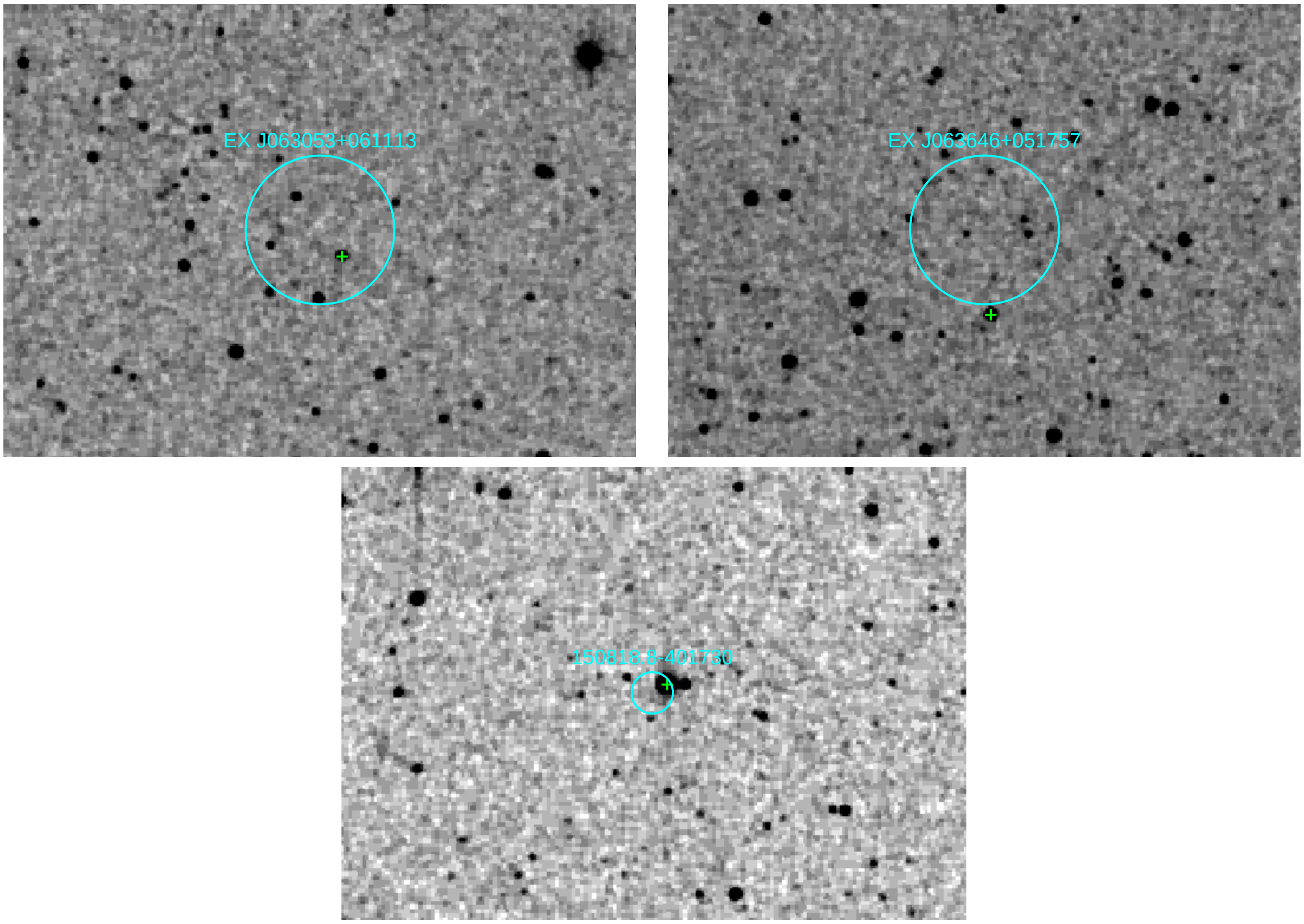

Figure 11.19 2MASS K_s-band images of the sources from Table 11.4 with point-like X-ray sources and secure counterpart identifications. The images are 5′ to a side, with north up and east to the left. The BSC X-ray position uncertainties are indicated by the circles, and the *Chandra* positions and optical counterparts are shown by the crosses.

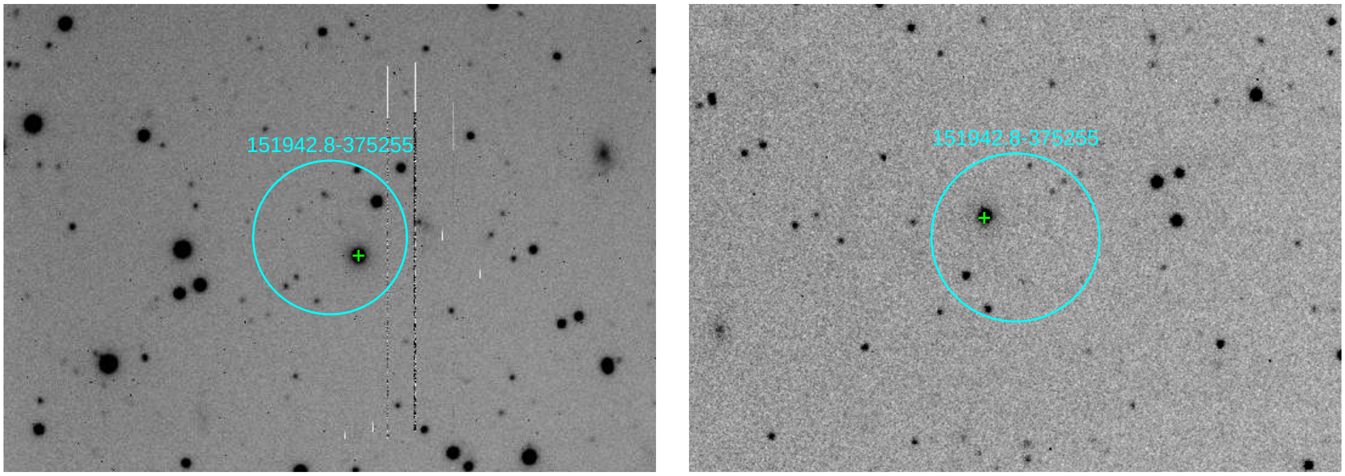

Figure 11.20 Magellan images of 1RXS J151942.8−375255. Left: MAGIC R-band; right: PANIC K_s-band. The images are $\approx 45''$ to a side, with north up and east to the left. The BSC X-ray position uncertainties are indicated by the circles, and the *Chandra* positions and optical counterparts are shown by the crosses.

Table 11.5. Log of Optical/IR Observations

Source	Date	Telescope	Instrument	Band(s)	Exp. (s)
1RXS J193458.1+335301	2003-Jul-03	P200	LFC	g'	300
1RXS J193458.1+335301	2003-Jul-24	P60	P60CCD	Hα/Offband	1200
1RXS J151942.8−375255	2003-Apr-08	Magellan II/Clay	MagIC	R	930
	2003-Apr-18	Magellan II/Clay	PANIC	K_s	200
1RXS J150139.6−403815[a]	2004-Feb-16	Magellan II/Clay	MagIC	R	60
				B	160

Note. — The telescopes/instruments used were LFC: the Large Format Camera on the Palomar 200-inch; P60CCD: the CCD camera on the Palomar 60-inch; MagIC: Raymond and Beverly Sackler Magellan Instant Camera on the 6.5 m Clay (Magellan II) telescope; and PANIC: Persson's Auxiliary Nasmyth Infrared Camera on the 6.5 m Clay (Magellan II) telescope.

[a] Observed by C. Rakowski.

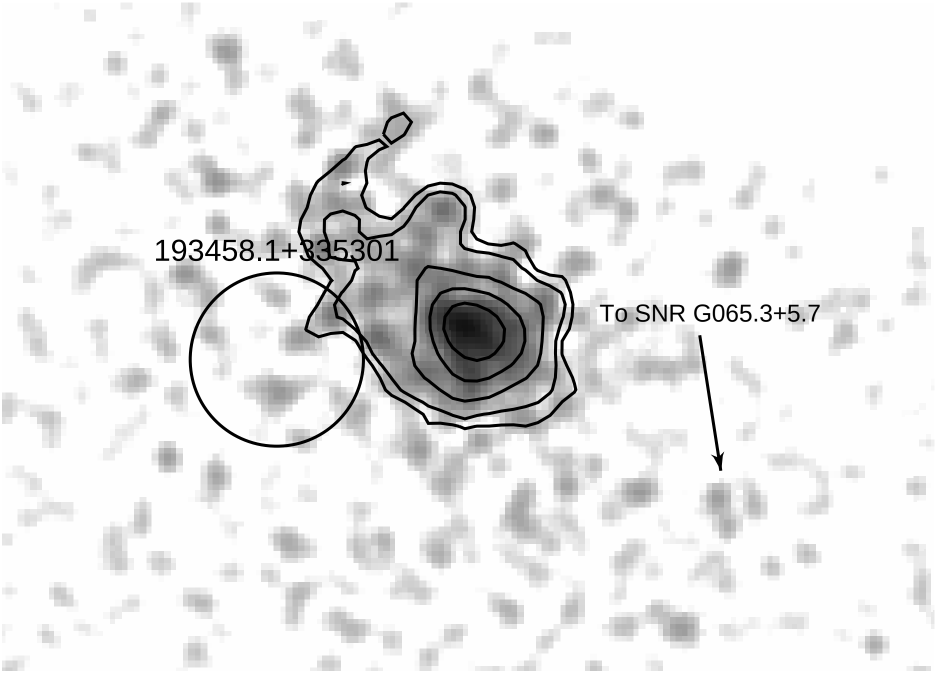

Figure 11.21 *Chandra* ACIS-S3 image of 1RXS J193458.1+335301. The BSC source and 1-σ (14″) uncertainty are shown by the circle. The data have been binned to 2″ resolution and smoothed with a Gaussian filter. The contours are in steps from 0.2–2.2 counts per bin, with spacing proportional to the square root of the counts. The arrow indicates the direction to the center of SNR G065.3+5.7. The image is $\approx 150''$ to a side, and has north up and east to the left.

$\approx 32''$ distance between the two. The peak of the *Chandra* emission is at $19^{\rm h}34^{\rm m}55\overset{\rm s}{.}61$, $+33^\circ53'06\overset{''}{.}0$. The overall source is large and somewhat asymmetric, with a maximum visible radius of $\approx 40''$ from the peak to the north-east and a minimum radius of $\approx 15''$ from the peak to the south-west, although there is some diffuse emission that extends further. Averaged over azimuth, the half-power radius is 11″, and 95% of the power is within 42″ (Fig. 11.22). Fitting the spatial profile to a β-model was successful, with $r_c = 3.5(1)''$, $\beta = 0.451(5)$, an amplitude of 0.64(3), and $\chi^2 = 9.6$ for 12 degrees of freedom.

We extracted photon events from a $45'' \times 22''$ region and created source and background response files using the `CIAO` task `acisspec`. We made use of the latest versions of `CIAO` and `CALDB` (3.0.2 and 2.26, respectively) in order to compensate for low-energy degradation of the ACIS detector.[4] We then fit the data in `sherpa`. The events were binned so that each bin had ≥ 25 counts.

While there are not very many counts (601 source counts, with 77.2 background counts), the data are well fit (Fig. 11.23) by an absorbed power-law model, with $N_{\rm H} = 3.0(6) \times 10^{21}$ cm^{-2}, $\Gamma = 2.4(2)$, and an amplitude of $4.6(8) \times 10^{-4}$ photons cm^{-2} s^{-1} keV^{-1} at 1 keV (giving $\chi^2 = 18.7$ for 16 degrees of freedom; all uncertainties are 1-σ). The observed flux from this model is 1.0×10^{-12} ergs cm^{-2} s^{-1} (0.3–8.0 keV), while the unabsorbed flux is 2.2×10^{-12} ergs cm^{-2} s^{-1}. Raymond & Smith (1977) plasma models do not fit, giving $\chi^2 = 70/16$.

The extended morphology and the hard spectrum of the source suggest several models: (1) a very hot nebula of Galactic origin, (2) a very hot nebula but of extra-galactic origin (gas from a cluster or an early-type galaxy; Fabbiano 1989; Brown & Bregman 1998), (3) the superposition of many bright LMXBs (with power-law spectra) in an early-type galaxy (Matsushita et al. 1994), or (4) a pulsar wind nebula

---

[4] `http://cxc.harvard.edu/ciao/threads/apply_acisabs/`.

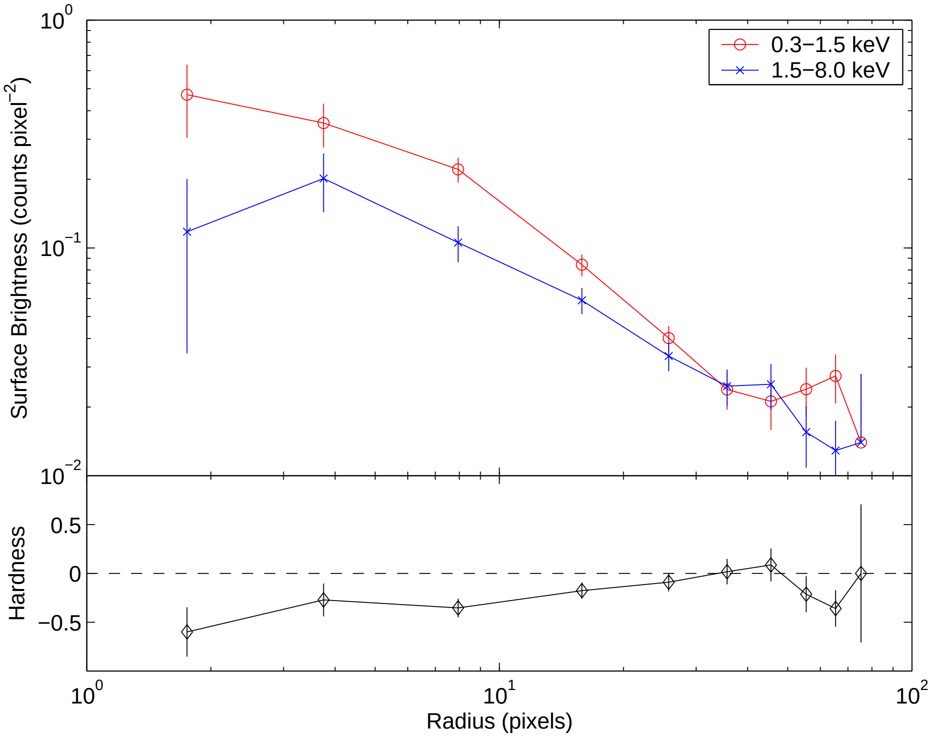

Figure 11.22 Top: radial profiles of the events for 1RXS J193458.1+335301 in two different energy bands. The background-subtracted surface brightness is plotted against radius for soft (0.3–1.5 keV) and hard (1.5–8.0 keV) bands. Bottom: hardness of the radial profile, defined as $(B_{\rm H} - B_{\rm S})/(B_{\rm H} + B_{\rm S})$, where $B_{\rm H}$ ($B_{\rm S}$) is the surface brightness in the 1.5–8.0 keV (0.3–1.5 keV) band. There appears to be an excess of hard photons toward the center.

radiating via synchrotron emission.

The lack of a bright optical or IR central source (to heat the nebula; see Fig. 11.24) appears to preclude possibility (1) leaving us the other three possibilities. We consider each in turn.

Extragalactic Nebula The X-ray emission is much more compact than is typical for galaxy groups or clusters (even clusters at $z \sim 0.5$–1 have $r_c \gg 10''$; Arnaud et al. 2002; Cotter et al. 2002), the spectrum is wrong (thermal plasma models do not fit), and the value of β is too small.

Early-type Galaxy The size is similar to what is often seen for early-type (E and S0) galaxies. In those galaxies the X-ray emission comes from a combination of hot gas (plasma with $kT \approx 0.5$–1.0 keV; Fabbiano 1989; Brown & Bregman 1998) and the superposition of many hard X-ray point sources (whose spectra are power-laws with $\Gamma \approx 1.7$)—reasonably compatible with the observed spectrum of 1RXS J193458.1+335301.

For these galaxies, the hard X-ray luminosity scales reasonably well with the integrated B or K band luminosities as $L_{\rm X}/L_B \approx 10^{30}$ ergs s$^{-1}L_{\odot,B}^{-1}$ or $L_{\rm X}/L_K \approx 10^{29}$ ergs s$^{-1}L_{\odot,K}^{-1}$, where the X-ray luminosity is in the 0.3–8.0 keV band and all luminosities are corrected for extinction (Kim & Fabbiano 2003); the scatter in this (from a sample of 14 galaxies) is a factor of 2–3 (there is more scatter in Brown & Bregman 1998, but their work concerns the soft emission more than the hard emission, and the scatter is still only a factor of ~ 10). We can convert the relations from Kim &

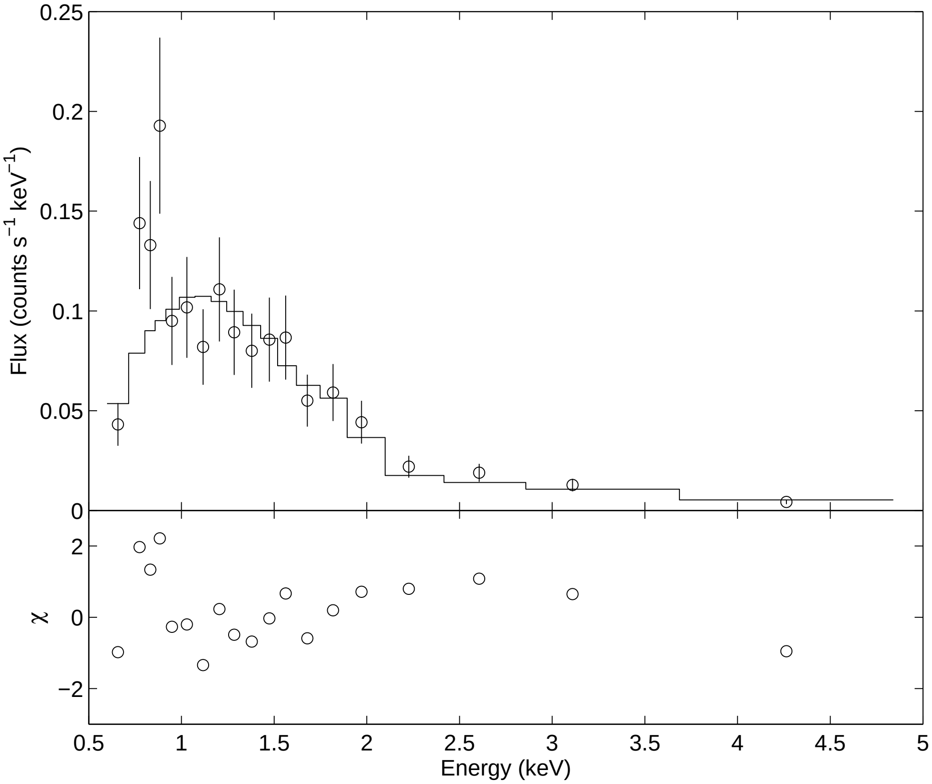

Figure 11.23 *Chandra* ACIS-S3 spectrum of 1RXS J193458.1+335301, with the best-fit power-law model. The residuals are plotted in the bottom panel.

Fabbiano (2003) into relations for fluxes and magnitudes (i.e., observables), giving

$$\begin{aligned}\frac{L_X}{L_B} &= 4\pi \times 10^{39} F_X 10^{(m_B - M_{\odot,B} - N_{H,21}/1.3)/2.5} \frac{\text{ergs s}^{-1}}{L_{\odot,B}} \\ \frac{L_X}{L_K} &= 4\pi \times 10^{39} F_X 10^{(m_K - M_{\odot,K} - N_{H,21}/16)/2.5} \frac{\text{ergs s}^{-1}}{L_{\odot,K}}, \qquad (11.1)\end{aligned}$$

where F_X is the absorption-corrected X-ray flux in the 0.3–8.0 keV band in units of ergs s^{-1} cm^{-2}, m_B (m_K) is the observed B-band (K-band) magnitude, $N_{H,21}$ is the Galactic column density along the line of sight in units of 10^{21} cm^{-2}, and $M_{\odot,B} = 5.47$ mag ($M_{\odot,K} = 3.33$ mag) is the B-band (K-band) absolute magnitude of the Sun.

The relation in Equation 11.1 implies that for $F_X = 10^{-12}$ ergs s^{-1} cm^{-2} and $N_{H,21} = 1$, $m_B \approx 12$ mag and $m_K \approx 5$ mag (this indeed matches what is seen for sources in Kim & Fabbiano 2003). Therefore, such sources should be readily visible on even shallow images. Examining 2MASS and Palomar (Fig. 11.24) images of 1RXS J193458.1+335301 we see that there are two optical/IR sources near the peak of the X-ray emission: the northern source (2MASS J19345557+3353136) is brighter but appears stellar (FWHM≈ $1\overset{''}{.}4$), while the southern source (2MASS J19345569+3353063) is fainter and may have some extended emission[5] to the north-east, although this is probably a superposition of point sources. Neither of these sources is a great candidate for the origin of the X-ray emission,

---

[5] There are no data from the 2MASS Extended Source Catalog (XSC) in this region owing to the presence of a bright ($V = 6.7$ mag) M star 90″ to the south.

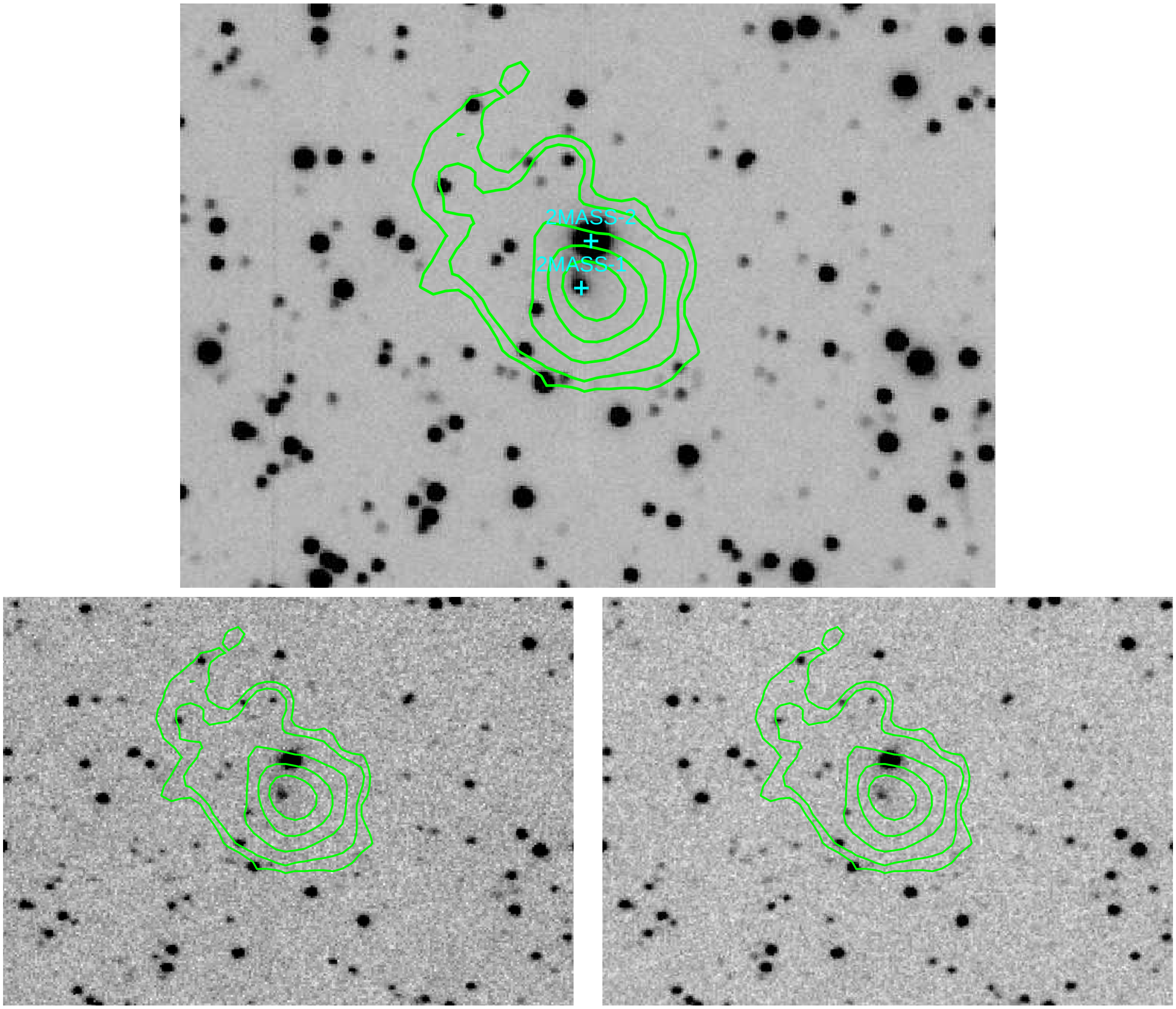

Figure 11.24 Top: Palomar 200-inch g'-band image of 1RXS J193458.1+335301. Bottom: Palomar 60-inch images of 1RXS J193458.1+335301, taken with Hα (left) and off-band (right, 6584 Å) filters. The images are $\approx 120''$ to a side, and have north up and east to the left. The contours are those from Figure 11.21 showing the extent of the X-ray emission. The two bright 2MASS sources identified near the peak of the X-ray emission are indicated with the crosses in the top image; the southern source is 2MASS J19345569+3353063 while the northern is 2MASS J19345557+3353136. We do not detect any diffuse Hα emission associated with 1RXS J193458.1+335301.

though, as they are too faint by several orders of magnitude ($K_s = 14.4$ mag and $K_s = 12.6$ mag for the northern and southern sources, respectively) and not extended enough. Therefore, while not impossible that 1RXS J193458.1+335301 is an early-type galaxy, we consider it unlikely. Deeper X-ray observations should be conclusive: if 1RXS J193458.1+335301 is a galaxy, it should resolve into discreet point sources. Optical spectroscopy would also be useful in determining the natures of the optical/IR sources.

There are some early-type galaxies with significant excesses of X-ray emission (Vikhlinin et al. 1999b), largely due to increases in the amounts of hot gas, that give roughly the same X-ray-to-optical ratio as would be necessary here. However, the optical/IR sources in Fig. 11.24 do not look like bright galaxies (unlike the galaxies from Vikhlinin et al. 1999b which are typically $> 20''$ in the optical) and the spectrum of 1RXS J193458.1+335301 is wrong: again, thermal plasma models do not fit. Also, the surface-brightness profile of 1RXS J193458.1+335301 is too tight, with $\beta = 0.45$ instead of $\beta > 0.6$. Therefore, while not impossible that 1RXS J193458.1+335301 is an early-type galaxy, we consider it unlikely.

PWN A pulsar wind nebula (i.e., a nebula excited by a pulsar or PWN; for reviews, see Chevalier 1998 or Gaensler 2003) is consistent with the size and spectrum of 1RXS J193458.1+335301. The source is generally harder toward the center, much as is expected for PWNe. There is no obvious Hα emission from 1RXS J193458.1+335301 in Figure 11.24 as there can be from PWNe (Hester et al. 1990; Caraveo et al. 1992; Hester 2000; Chatterjee & Cordes 2002), but this could just be due to the limited depth of the images.

1RXS J193458.1+335301 is outside SNR G065.3+5.7 and is asymmetric in the wrong direction, making an association between the two unlikely (the fitted value of $N_{\rm H}$ is just about at the maximum predicted for this line of sight by COLDEN[6] and is somewhat higher than the nominal value for SNR G065.3+5.7, suggesting that the source may be more distant and highly absorbed than SNR G065.3+5.7). However, this is not entirely unexpected, as there are a number of young, newly-discovered PWNe that have no definitively associated SNRs (e.g., Roberts et al. 2002).

11.5.3.2 1RXS J205042.9+284643

The BSC lists 1RXS J205042.9+284643 as having 0.11(2) count s^{-1} in the PSPC, with hardness ratios of $\mathrm{HR1} = -0.03(17)$ and $\mathrm{HR2} = -0.87(14)$. The *Chandra* observation of 1RXS J205042.9+284643 had a total exposure time of 3.7 ks, and which should give ≈ 1000 ACIS-S counts. However, as shown in Figure 11.25 there are no point detected sources anywhere within three times the nominal position uncertainty (a conservative limit, as seen in Fig. 11.4): the only significant source detected (using `wavdetect` on scales from 1–32 pixels; see Paper I) in the data-set is at $20^{\rm h}50^{\rm m}39\overset{\rm s}{.}01$, $+28^\circ45'43\overset{''}{.}6$ (with 12 ± 3 counts), which is $79''$ or 6-σ away from 1RXS J205042.9+284643. We can then set a limit of ≈ 3 counts to any point source. There are no obvious extended sources, but such limits are more difficult to quantify: overall, there are 1047 events in the 0.3–5.0 keV energy range over the whole $512'' \times 128''$ image, so the average background rate is 0.0160(5) arcsec^{-2}. Then, in a region $\theta \times \theta$ arcsec^2 in area, the 3-σ limits will be $3\sqrt{0.016\theta^2 + 3 \times 10^{-7}\theta^4}$ counts. There are no regions in the event list with such concentrations, so no extended sources are present.

One obvious explanation of the disappearance of 1RXS J205042.9+284643 is intrinsic variability. This is not atypical among the most common class of soft X-ray sources in the Galactic plane: active stars. Flares and other chromospheric/magnetospheric events often lead to dramatic changes in the fluxes of these sources. While other sources, such as X-ray binaries, active galaxies, and some anomalous X-ray pulsars, do exhibit variability, these sources have hard X-ray spectra generally inconsistent with the BSC emission. We therefore think it likely that 1RXS J205042.9+284643 is an active star, but of course this cannot be confirmed without additional data. It is also possible that the source is extended, and therefore too diffuse to have been detected by *Chandra*. The softness of the BSC emission make this unlikely, though, in contrast to the spectra of 1RXS J193458.1+335301 and 1RXS J150139.6−403815.

It is possible, but unlikely, that 1RXS J205042.9+284643 is a neutron star. Most of the neutron stars considered in Paper I have stable X-ray emission: only some of the AXPs vary significantly. However, as

---

[6] `http://asc.harvard.edu/toolkit/colden.jsp`.

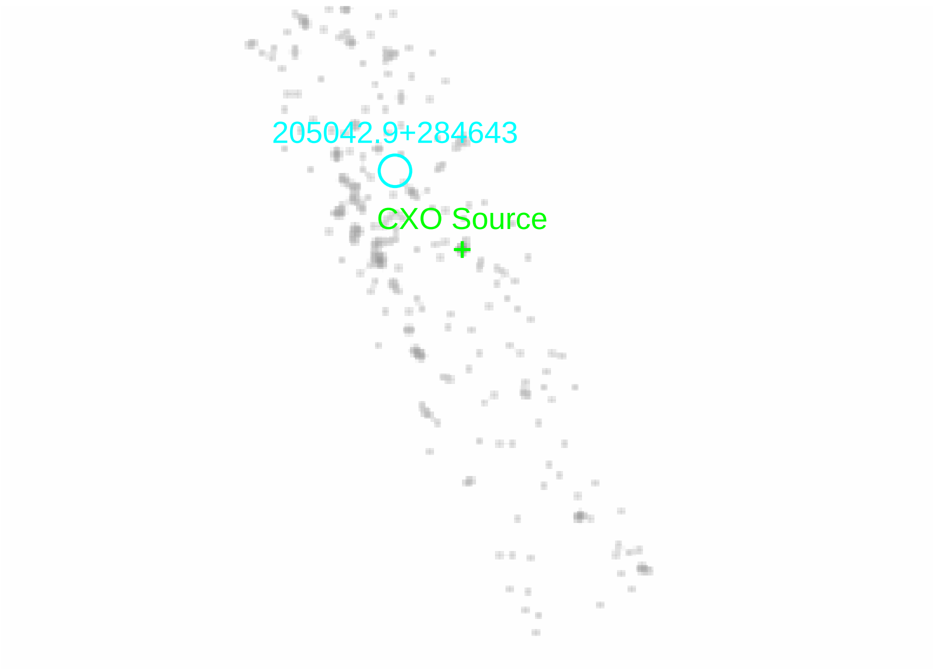

Figure 11.25 *Chandra* ACIS-S image of the field around 1RXS J205042.9+284643. The position of the *ROSAT* source is shown by the circle with a radius of 12″, which is the 1-σ position uncertainty. The only significant point source detected in the *Chandra* observation is shown by the cross, 79″ away from the *ROSAT* position. See § 11.5.3.2. The *Chandra* data show the logarithm of the 0.3–5.0 keV counts in 2″ bins, and have been additionally smoothed with a Gaussian kernel.

discussed above the spectrum of 1RXS J205042.9+284643 is unlike those of AXPs (typically a power-law with $\Gamma \sim 3$).

11.5.3.3 1RXS J205812.8+292037

The BSC lists 1RXS J205812.8+292037 as having 0.13(2) count s^{-1} in the PSPC, with hardness ratios of HR1 = 0.63(11) and HR2 = 0.27(13). This is moderately hard compared to the other sources in Fig. 11.1, but is not too extreme. In retrospect we should have chosen this source for follow-up *Chandra* observations since it does not have a definitive counterpart and its spectrum is consistent with nonthermal emission from neutron stars. We therefore discuss this source in more detail.

Within 10′ of 1RXS J205812.8+292037, there are 1627 2MASS sources, for an average density of $1.44(4) \times 10^{-3}$ arcsec^{-2}. Finding a source within 9″ (as in the case of 1RXS J205812.8+292037) has a chance probability of 37%, which is not small enough for a definite association.

1RXS J205812.8+292037 is similar, though, in both hardness and optical brightness to other sources like 1RXS J193228.6+345318, 1RXS J045707.4+452751, or 1RXS J151942.8−375255. These sources did not have certain associations based on *ROSAT* alone, but the *Chandra* data unambiguously relate them to optical sources that are somewhat fainter than the majority of the sources discussed here. This faintness, together with the hardness of the X-ray spectrum, likely reflects extragalactic origins of the sources: in Figure 11.17 these sources are largely those with the highest X-ray-to-IR flux ratios most similar to the extragalactic sample. Therefore, as with 1RXS J205042.9+284643 we do not believe that 1RXS J205812.8+292037 is a neutron star, but we cannot rule out this possibility.

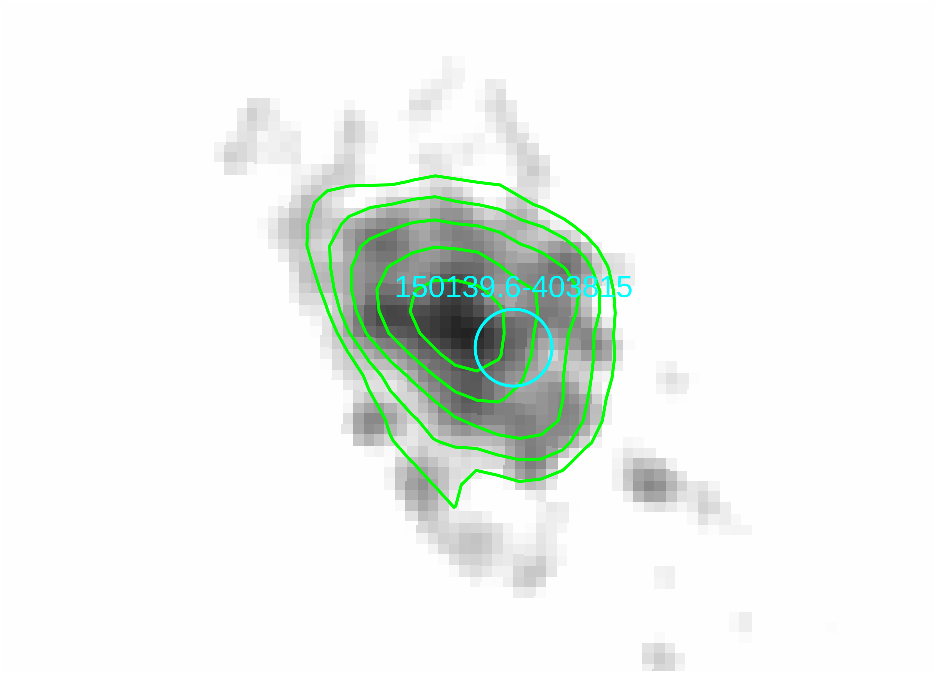

Figure 11.26 *Chandra* ACIS-S3 image of 1RXS J150139.6−403815. The BSC source and uncertainty are shown by the circle. The grayscale is proportional to the logarithm of the counts in 8-pixel bins, and has been additionally smooth with a Gaussian filter. The contours are in steps from 1.5–3.8 counts per bin, with spacing proportional to the square root of the counts. The image is ≈ 330″ to a side, and has north up and east to the left.

11.5.3.4 1RXS J150139.6−403815

The BSC lists 1RXS J150139.6−403815 as having 0.12(2) count s^{-1} in the PSPC, with hardness ratios of HR1 = 0.88(11) and HR2 = 0.14(20). The *Chandra* source is fainter than that of 1RXS J193458.1+335301, but nonetheless it appears extended, as shown in Figure 11.26. Again, we can be quite confident that *Chandra* source is 1RXS J150139.6−403815, since there are no other sources nearby. Since this source is more diffuse than 1RXS J193458.1+335301, the spatial measurements are not as precise, but the center is at approximately $15^{\mathrm{h}}01^{\mathrm{m}}41^{\mathrm{s}}1$, $-40°38'08''$. The source is ≈ 1′ in radius.

Similar to our analysis of 1RXS J193458.1+335301 (§ 11.5.3.1), we extracted photon events from a $112'' \times 22''$ region and created source and background response files using the `CIAO` task `acisspec`. We then fit the data in `sherpa`, where the events were binned so that each bin had ≥ 25 counts.

Again, there are not very many counts (1305 source counts, with 478.5 background counts), but the data are well fit (Fig. 11.27) by an absorbed power-law model, with $N_{\mathrm{H}} = 1.0(4) \times 10^{21}$ cm^{-2}, $\Gamma = 1.65(15)$, and an amplitude of $4.7(6) \times 10^{-4}$ photons cm^{-2} s^{-1} keV^{-1} at 1 keV (giving $\chi^2 = 21.6$ for 32 degrees of freedom). The observed flux from this model is 2.6×10^{-12} ergs cm^{-2} s^{-1} (0.3–8.0 keV), and the unabsorbed flux is 3.0×10^{-12} ergs cm^{-2} s^{-1}. The column density is higher than but consistent with both the column density of SNR G330.0+15.0 and the total expected along this line of sight (6×10^{20} cm^{-2}).

As with 1RXS J193458.1+335301, we considered different models for 1RXS J150139.6−403815. Figure 11.28 does not identify a single hot source, so a thermal Galactic nebula is unlikely. Based on 1RXS J193458.1+335301, our first idea is that 1RXS J150139.6−403815 is a PWN. The size is about right and the spectrum is typical for PWNe. However, as with 1RXS J193458.1+335301 there is a problem: 1RXS J150139.6−403815 is outside of SNR G156.2+5.7, and the largely symmetric morphology rules out

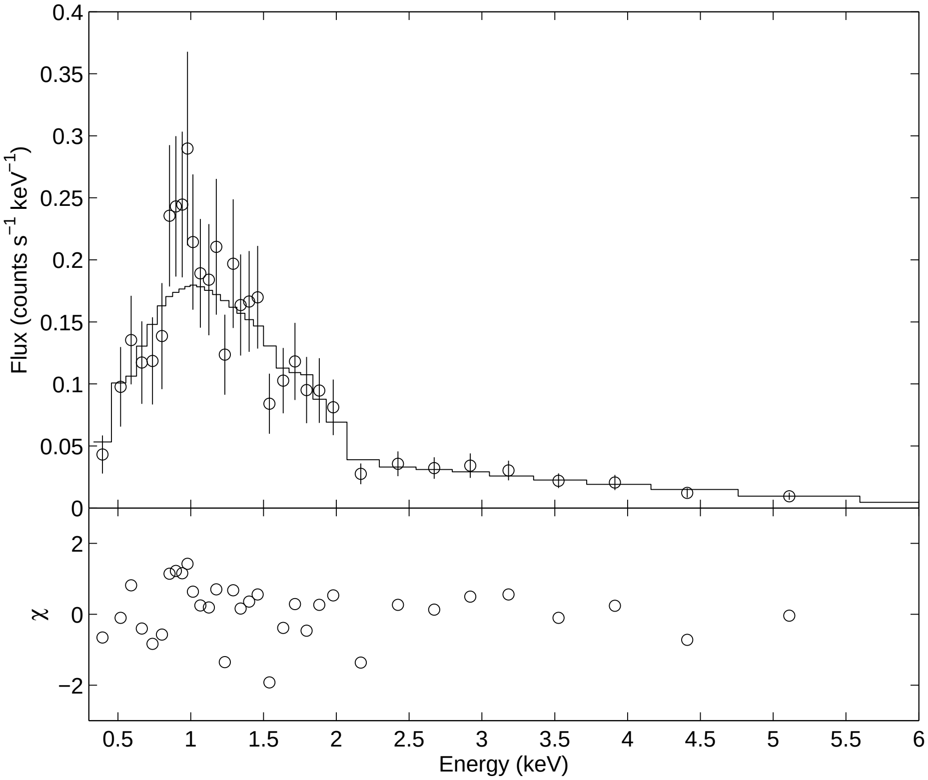

Figure 11.27 *Chandra* ACIS-S3 spectrum of 1RXS J150139.6−403815, with the best-fit power-law model. The residuals are plotted in the bottom panel.

a bow-shock type nebula that could preserve the association between 1RXS J150139.6−403815 and SNR G330.0+15.0 (Gaensler 2003).[7]

We then examined possible extragalactic classifications for 1RXS J150139.6−403815. 1RXS J150139.6−403815 is larger than 1RXS J193458.1+335301, and is more compatible with the sizes of typical galaxy clusters ($\gtrsim 30''$): a fit to a β model has $r_c = 32''$ and $\beta = 0.4$ The spectral data are reasonably well fit by a Raymond & Smith (1977) plasma model, having $N_{\rm H} = 5(2) \times 10^{20}$ cm^{-2}, $kT = 9^{+5}_{-2}$ keV, and a normalization[8] of $5.6(5) \times 10^{-3}$ cm (giving $\chi^2 = 22.0$ for 32 degrees of freedom), such as what one would expect for a cluster (White et al. 1997). With this model the observed flux is 2.7×10^{-12} ergs cm^{-2} s^{-1} (0.3–8.0 keV), and the unabsorbed flux is 2.9×10^{-12} ergs cm^{-2} s^{-1}.

Examining the 2MASS image we see an extended elliptical source, 2MASXJ15014110−4038093, near the center of the X-ray emission (Fig. 11.28). This source has a radius of $\approx 10''$ (20 mag arcsec^{-2} isophotal radius), a K_s magnitude of 12.7 mag within that radius, and $J - K_s = 1.2$ mag. Higher-resolution optical images of 1RXS J150139.6−403815 (Fig. 11.28) show that 2MASX J15014110−4038093 is partially decomposed into two sources: an extended source labeled A that is at the exact position of 2MASX J15014110−4038093 (within uncertainties), and a source labeled B $3''$ to the east. There is also another extended source labeled C $5''$ to the north-east, but this is a separate 2MASS source

---

[7] We searched the Sydney University Molongolo Sky Survey (SUMMS; Bock et al. 1999), and there is no extended or point-like emission present at the position of 1RXS J193458.1+335301; nor is there any sign of a new SNR around it. SUMSS is particularly sensitive to extended emission, and would almost certainly have identified any SNR around 1RXS J150139.6−403815.

[8] The normalization follows the `xspec` units of $10^{-14}\left(4\pi(D_A(1+z))^2\right)^{-1}\int dV\, n_e n_{\rm H}$, where D_A is the angular-size distance (in cm), n_e is the electron density (in cm^{-3}), and $n_{\rm H}$ is the hydrogen density (in cm^{-3}).

Table 11.6. Properties of Optical Sources in Figure 11.28

Source	$\alpha - 15^{\mathrm{h}}01^{\mathrm{m}}$	$-\delta - 40^{\circ}38'$	B		R	
	(s)	(arcsec)	FWHM[a]	Mag	FWHM[b]	Mag
	(J2000)		(arcsec)		(arcsec)	
A	41.12	09.4	3.2	12.1	3.6	9.5
B	41.30	09.3	0.8	12.1	0.8	11.1
C	41.46	06.7	1.3	12.9	3.6	11.2

Note. — The astrometry has absolute uncertainties of $\approx 0''.2$ in each coordinate owing to uncertainties in 2MASS. The photometry has systematic uncertainties of ≈ 0.5 mag owing to uncertain zero-point calibration.

[a] The seeing was $\approx 0''.77$.

[b] The seeing was $\approx 0''.66$.

(2MASS J15014145−4038068). We performed a rough photometric calibration using 80 stars from the USNO-B1.0 catalog[9] and then ran `SExtractor` (Bertin & Arnouts 1996) on the images: the results for sources A–C are given in Table 11.6. Source A is very clearly extended, although it is not as large as 2MASX J15014110−4038093 (the FWHM of the IR emission is $\approx 6''$). Source B is very likely unresolved (within uncertainties), and source C is extended. Source A is very red ($B - R \approx 2.6$ mag), consistent with the 2MASS data. We believe that the 2MASS source is primarily due to source A, given the position coincidence and the extreme redness of A compared to B or C. If this is the case, then A has $R - K_s \approx -3.2$ mag.

The IR colors of 2MASX J15014110−4038093 are similar to the brighter galaxies in known clusters (e.g., Kodama & Bower 2003). Therefore, 2MASX J15014110−4038093 could be the central galaxy of an unknown cluster. The X-ray temperature is reasonably high, implying a high luminosity ($\sim 10^{45}$ ergs s^{-1}; Mushotzky 2003), so this source cannot be part of a nearby, low-L group. However, the value of β is lower than those of most known clusters (Vikhlinin et al. 1999a), and is more similar to those of low-L systems (Mulchaey et al. 2003).

While 1RXS J150139.6−403815 is compatible with the sizes and spectra of early-type galaxies, and there is an extended optical/IR source near the peak of the X-ray emission, the scenario is not entirely consistent. The optical/IR source is, like those in 1RXS J193458.1+335301, about 7 magnitudes fainter than expected (the predicted magnitude following Eqn. 11.1 is $K_s \approx 5$ mag). This is far greater than the variation seem among galaxies. We do not believe that the difference can be due to an excess of soft emission in 1RXS J193458.1+335301 or 1RXS J150139.6−403815 (Eqn. 11.1 refers only to the contribution of hard point sources), as the spectra of 1RXS J193458.1+335301 and 1RXS J150139.6−403815 are hard and similar to the prototypical sources assumed in Kim & Fabbiano (2003), and when one fits primarily for the soft emission (as in Brown & Bregman 1998) one finds a similar relation to that of Kim & Fabbiano (2003). It is possible that 1RXS J150139.6−403815 is an overluminous elliptical galaxy, such as those discussed in Vikhlinin et al. (1999b), as the size, optical/X-ray flux ratio, and luminosity are similar

---

[9] This calibration agreed with the nominal calibration at `http://occult.mit.edu/instrumentation/magic/`.

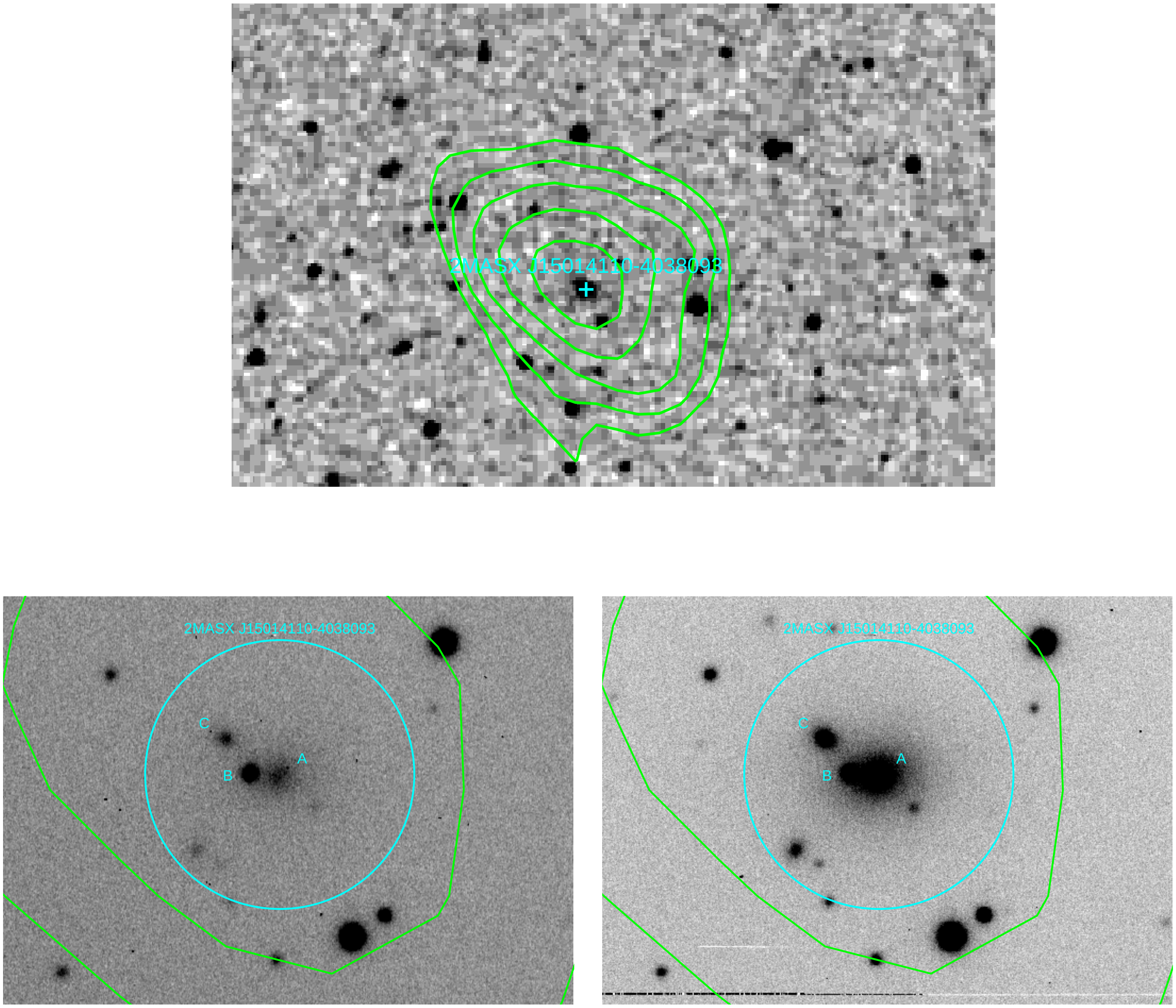

Figure 11.28 Top: 2MASS K_s-band image of 1RXS J150139.6−403815. The image is $5'$ to a side, with north up and east to the left. The contours from Figure 11.26 are plotted, and the source 2MASX J15014110−4038093 is indicated by the cross. Bottom: Magellan B (left) and R (right) images of 1RXS J150139.6−403815. The images are $40''$ to a side, with north up and east to the left. Again, the contours from Figure 11.26 are plotted, and the source 2MASX J15014110−4038093 is indicated by the circles ($10''$ radius).

to these sources ($L_{\rm X}/L_{\rm opt} \sim 10^{32}$ ergs $\mathrm{s}^{-1} L_\odot^{-1}$; $L_{\rm opt} \sim 10^{11} L_\odot$ assuming $z \sim 0.1$), but again there are difficulties: the temperature of 1RXS J150139.6−403815 is considerably higher than those of Vikhlinin et al. (1999b), and the value of β is too low.

We see that no scenario is entirely consistent for 1RXS J150139.6−403815. PWNe, isolated elliptical galaxies, and galaxy clusters all have problems. We believe it likely that 1RXS J150139.6−403815 does have an extragalactic origin, as 2MASX J15014110−4038093 looks like an elliptical galaxy and it is probably associated with the X-ray emission: there are 39 extended 2MASS sources within $20'$ of 1RXS

J150139.6−403815, giving a false-association rate of 0.005% for a source within $1\farcs3$. However, it is not clear exactly what 1RXS J150139.6−403815 is. As with 1RXS J193458.1+335301, deeper X-ray observations and optical spectroscopy (to definitively classify the optical counterpart and obtain a redshift) should be conclusive for 1RXS J150139.6−403815.

11.6 Discussion & Conclusions

We have fully investigated the population of *ROSAT* BSC point sources in six large-diameter SNRs. Our identifications of counterparts to 50 of the 54 sources are quite secure: in most cases the position coincidence between the X-ray and optical/IR sources has been augmented by identification of an abnormal stellar type (variable, T Tau, binary, etc.), by the extreme brightness (and hence rarity) of the optical source, or by a previous classification in the literature. This conclusion echoes that of Rutledge et al. (2003), who searched for older neutron stars using *ROSAT* and found only previously identified neutron stars, along with 17 sources that are definitely not neutron stars and 13 that are probably not (their classification is somewhat more skeptical than ours). Rutledge et al. (2003) go on to obtain optical spectra of many of their candidate counterparts, and these spectra certainly augment the believability of the associations, but we believe that they are not necessary.

The remaining sources, as discussed in Section 11.5.3, are more intriguing. However, none of them is likely to be a neutron star associated with one of the SNRs in Table 11.1. To begin with, all are outside their SNRs. While this is not impossible for older sources and fast neutron stars (e.g., Gaensler & Johnston 1995), it lessens the chance of association.

For 1RXS J193458.1+335301 and 1RXS J150139.6−403815 the X-ray morphologies rule out associations, since any PWNe outside the SNRs would have elongated bow-shock appearances, in contrast to what we see (of course, 1RXS J193458.1+335301 and/or 1RXS J150139.6−403815 could be extragalactic). 1RXS J205042.9+284643 and 1RXS J205812.8+292037, neither of which has a *Chandra* detection, are more uncertain. 1RXS J205042.9+284643 is very likely a flare star (§ 11.5.3.2). 1RXS J205812.8+292037 does not have a provisional classification but it is likely extragalactic in origin.

Given 1RXS J193458.1+335301, we might ask if we should have detected young field pulsars in our search. There are 63 young pulsars (those with characteristic ages $< 10^5$ yr, which might be expected to have significant X-ray emission) in the ATNF pulsar catalog (Hobbs & Manchester 2003) that are within the ≈ 1500 square degrees of the Parkes Multibeam Survey (Manchester et al. 2001). We searched a total of ≈ 57 square degrees so one might expect that we would have identified one or two young pulsars in our area. However, significant portions of our were at Galactic latitudes higher than the Parkes survey ($|b| < 5^\circ$), and the pulsar population falls off rapidly with latitude. Similarly, our search was designed for nearby, lightly-absorbed sources while the Parkes search found pulsars at typical distances of 5–10 kpc. Therefore, our detection of at most one field pulsar (1RXS J193458.1+335301) is not very constraining.

Since we have ruled out (to some degree of certainty) neutron stars in all six SNRs considered here, we can then follow Paper I and place the resulting X-ray luminosity limits on a cooling diagram. This is shown in Figure 11.29. To account for the uncertainties of 1RXS J205042.9+284643 and 1RXS J205812.8+292037, both in SNR G074.0−8.5, we have adjusted the luminosity of SNR G074.0−8.5 from Table 11.1 to correspond to 0.15 count s^{-1}—above the count rates of both of the uncertain sources and therefore a more secure limit. Further X-ray observations of 1RXS J205812.8+292037 would very likely detect counterparts (for 1RXS J205042.9+284643, it might have only been included in the BSC due to a flare, and therefore significantly deeper X-ray observations may be necessary). With secure counterparts, the limit for SNR G074.0−8.5 would decrease by a factor of 3.

The limits in Figure 11.29 are not as uniform or as constraining as those from Paper I. The lack of uniformity is due to the sample construction: the different distances and column densities of the SNRs make the BSC limit of 0.05 counts s^{-1} translate into different luminosities. So, SNRs G074.0−8.5, G330.0+15.0, and G065.3+5.7 all have reasonably tight limits (and those of SNR G074.0−8.5 could get better). SNRs G160.9+2.6 and G205.5+0.5 have loose limits primarily due to uncertain distances: we have used the upper limit of 4 kpc for SNR G160.9+2.6 and the full range of 0.8–1.6 kpc for SNR G205.5+0.5 in Figure 11.29. Finally, SNR G156.2+5.7 is more highly absorbed than the other SNRs.

While all of the limits are below the luminosities of sources like Cas A, Puppis A, and 1E 1207.4−5209 (and are therefore in concordance with our original survey design from Paper I), some are further below than others. The impacts of these limits on the cooling curves are somewhat lessened, though, as the SNRs are all older (10–30 kyr) than the sources in Paper I (3–10 kyr). Therefore they cooling curves have descended, and there are other neutron stars that have similar or even lower luminosities (CTA 1, IC 443, PSR B1853+01 compare with the SNRs that have tighter limits, while Vela, PSR B2334+61, PSR B1706−44, and PSR B1727−33 compare with remaining SNRs), although 5/7 of these sources have X-ray PWNe that increase their luminosities by a factor of ~ 10.

In one sense, though, the limits here are tighter than those of Paper I. By using the BSC to go to twice the SNR radii, we have virtually eliminated the possibility that there are high-velocity neutron stars in these SNRs (as discussed in § 11.3.1 confusion is most likely not a limiting factor in detecting X-ray sources). It is of course possible that the SN explosions were type Ia or produced black holes, but as discussed in Paper I these alternate scenarios are not very likely for more than one source.

Therefore, while not as tight as those of Paper I (or e.g., Slane et al. 2002), our limits are still useful. They are not below all detected neutron stars, so do not require appeals to exotic physics or cooling processes, but they conclusively demonstrate that there is a significant range in the observed cooling luminosities of neutron stars, even including experimental uncertainties. It is clear that the neutron stars of a single age must be able to produce a luminosities differing by a factor of > 10. Whether the unknown parameter that controls the cooling is one of the usual culprits (rotation, composition, magnetic field) or something entirely different is not known.

It is amusing that our conclusions mirror those of 20 years ago (Helfand 1981, 1984), despite the significant theoretical and observational advances over that time. While much of the data used to make these arguments in the past has been improved and/or changed, our work here still echoes Shapiro & Teukolsky (1983), who suggest: "… either that the neutron star cooled more rapidly than the standard calculations allow, or that no neutron star was left behind by the supernova explosion."

D. L. K. is supported by a fellowship from the Fannie and John Hertz Foundation. B. M. G. and P. O. S. acknowledge support from NASA Contract NAS8-39073 and Grant G02-3090. E. V. G. is supported by NASA LTSA grant NAG5-7935, and B. M. G. is supported by NASA LTSA grant NAG5-13032. S. R. K. is supported by grants from NSF and NASA. Support for this work was provided by the National Aeronautics and Space Administration through Chandra award G03-4088X issued by the *Chandra X-Ray Observatory* Center, which is operated by the Smithsonian Astrophysical Observatory for and on behalf of NASA under contract NAS8-39073. The NRAO is a facility of the National Science Foundation operated under cooperative agreement by Associated Universities, Inc. We have made extensive use of the SIMBAD database, and we are grateful to the astronomers at the Centre de Données Astronomiques de Strasbourg for maintaining this database. We would like to thank E. Persson for assistance with the PANIC observing.

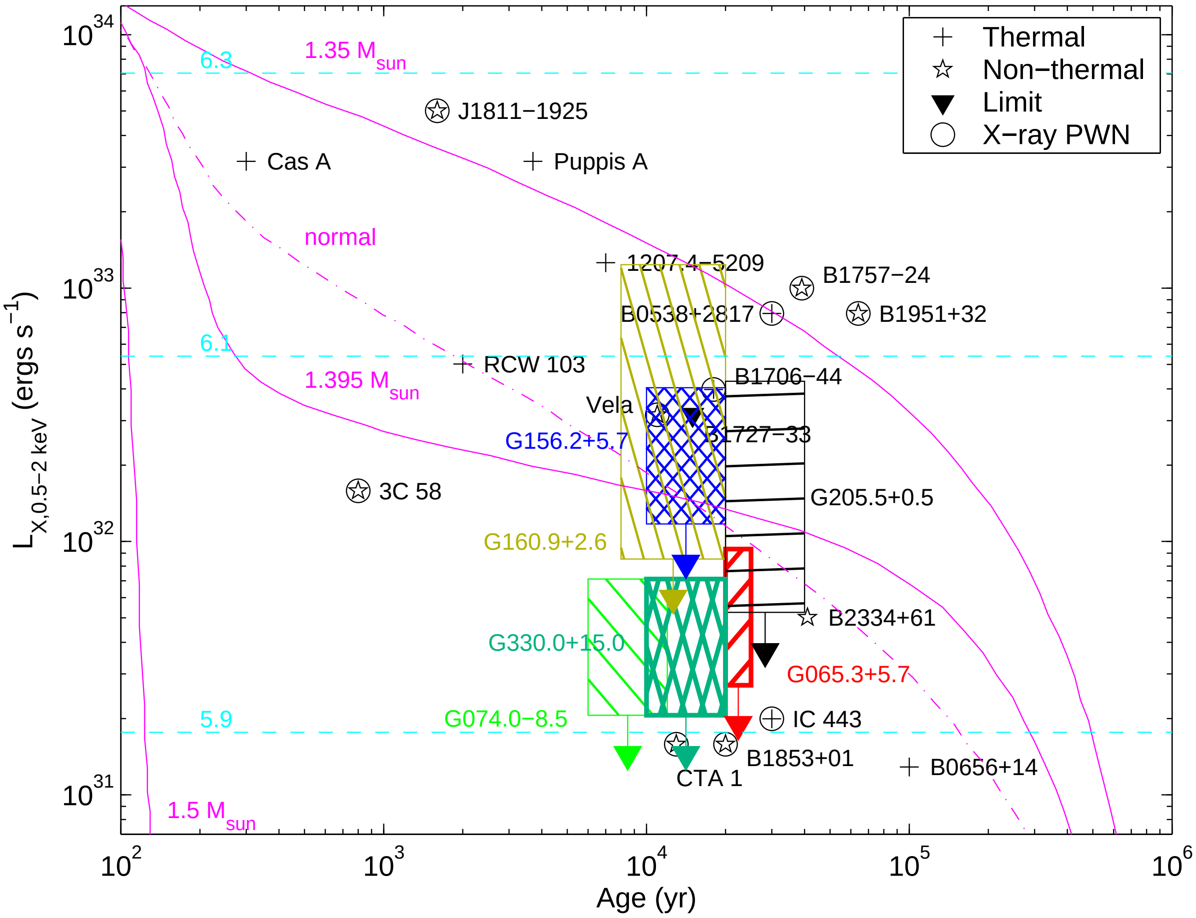

Figure 11.29 X-ray luminosities (0.5–2 keV) as a function of age for neutron stars in SNRs from Paper I and limits to blackbody emission from sources in SNRs G065.3+5.7 (red hatched region), G074.0−8.5 (green hatched region), G156.2+5.7 (blue cross-hatched region), G160.9+2.6 (gold hatched region), G205.5+0.5 (black hatched region), and G330.0+15.0 (dark green cross-hatched region). Sources whose emission is primarily thermal are indicated with plus symbols, those whose emission is primarily nonthermal are indicated with stars, and those with only limits are indicated with triangles. The sources that have X-ray PWNe, which are typically >10 times the X-ray luminosity of the neutron stars themselves, are circled. A 30% uncertainty in the distance has been added to the luminosities given in Table 11.1 and § 11.2 and the likely range of ages is also shown (for SNR G074.0−8.5, the luminosity has been increased to account for uncertain associations with 1RXS J205042.9+284643 and 1RXS J205812.8+292037). The cooling curves are the 1p proton superfluid models from Yakovlev et al. (2003) (solid lines, with mass as labeled) and the normal (i.e., nonsuperfluid) $M = 1.35\,M_\odot$ model (dot-dashed line), assuming blackbody spectra and $R_\infty = 10$ km. These curves are meant to be illustrative of general cooling trends, and should not be interpreted as detailed predictions. The horizontal lines show the luminosity produced by blackbodies with $R_\infty = 10$ km and $\log T_\infty$ (K) as indicated. Compare to Fig. 37 of Paper I.

Chapter 12

Optical and Infrared Observations of CCOs in Puppis A, Vela Jr., and RCW 103

D. L. Kaplan[a], B. M. Gaensler[b], & S. R. Kulkarni[a]

[a]Department of Astronomy, 105-24 California Institute of Technology, Pasadena, CA 91125

[b]Harvard-Smithsonian Center for Astrophysics, 60 Garden Street, MS-6, Cambridge, MA 02138

Abstract

We present deep optical and infrared observations of RX J0822−4300, SAX J0852.0−4615, and 1E 161348−5055: three members of the growing class of Compact Central Objects. These are enigmatic sources (presumably neutron stars) in the centers of supernova remnants that show no pulsations or signs of magnetospheric activity. We do not detect any likely counterparts to these sources. Our limits imply similar X-ray-to-optical/IR flux ratios as have been seen in the past for sources like CXO J232327.8+584842 in the Cas A remnant.

12.1 Introduction

In contrast to the vast majority of neutron stars that appear as radio pulsars, an increasing number of intriguing X-ray sources are being discovered in supernova remnants (SNRs). These sources are presumably compact objects (neutron stars or black holes), although exactly what the properties and emission mechanisms are is unclear. For lack of a better phrase they are collectively called Central Compact Objects or CCOs (see Pavlov et al. 2003 for a review).

Unlike radio pulsars, the CCOs lack radio emission, pulsations, and nonthermal X-ray emission. While they are found near the centers of SNRs, X-rays alone are not enough to definitively identify the sources as CCOs: they could also be active stars or galaxies. Identification of CCOs therefore relies on multi-wavelength observations, the most powerful of which combine deep optical/IR imaging with accurate X-ray positions from *Chandra* (e.g., Kaplan et al. 2001a; Kaplan et al. 2004). Stars and galaxies have much higher optical/IR fluxes relative to their X-ray fluxes than do the CCOs (or any known neutron stars), so finding an X-ray source without any optical or infrared counterpart is the best way to identify CCOs.

Here we discuss deep searches for optical and infrared emission from three CCOs: RX J0822−4300 in SNR G260.4−3.4 (Puppis A; Petre et al. 1982), SAX J0852.0−4615 in SNR G266.2−1.2 (Vela, Jr.; Aschenbach 1998), and 1E 161348−5055 in SNR G332.4−0.4 (RCW 103; Tuohy & Garmire 1980). These sources were all identified from the previous generation of X-ray observatories and had relatively inaccurate

Table 12.1. Optical and Infrared Observations of CCOs

Object	RA[a]	Dec	Date	Band[b]	Exp.	Seeing
	(J2000)		(UT)		(s)	(arcsec)
RX J0822−4300...	$08^{\rm h}21^{\rm m}57\overset{\rm s}{.}42$	$-43^\circ00'16\overset{''}{.}6$	2003-Apr-05	B	1800	0.7
				R	1230	0.7
			2003-Apr-19	K_s	2040	0.8
SAX J0852.0−4615	$08^{\rm h}52^{\rm m}01\overset{\rm s}{.}38$	$-46^\circ17'53\overset{''}{.}3$	2003-Apr-04	B	3600	0.7
				R	3960	0.7
			2003-Apr-18	K_s	2160	0.8
1E 161348−5055 ..	$16^{\rm h}17^{\rm m}36\overset{\rm s}{.}26$	$-51^\circ02'25\overset{''}{.}0$	2003-Apr-04	I	3060	0.4
			2003-Apr-18	K_s	1920	0.8

[a] The positions are from *Chandra* ACIS-S observations (this work) for RX J0822−4300, Pavlov et al. (2001b) for SAX J0852.0−4615, and Garmire et al. (2000) for 1E 161348−5055.

[b] The instruments used were MagIC: Raymond and Beverly Sackler Magellan Instant Camera for B- and R-band data; and PANIC: Persson's Auxiliary Nasmyth Infrared Camera for K_s-band data, both on the 6.5 m Clay (Magellan II) telescope.

positions, but now *Chandra* observations are available. Previous optical/IR observations did search for counterparts, but because of the limited positional accuracy and telescope size the data were not as constraining as recent data on other sources (Kaplan et al. 2001a; De Luca et al. 2004). We therefore searched for emission from these three CCOs using the 6.5 meter Magellan telescope, hoping to either detect emission (which would be very useful in constraining the emission mechanisms) or at least set the best possible limits.

12.2 Observations

We observed the fields of RX J0822−4300, SAX J0852.0−4615, and 1E 161348−5055 using the 6.5 meter Magellan II telescope at Las Campanas. A log of the observations is in Table 12.1.

Data reduction for the optical data used standard `IRAF` routines to subtract the bias, flat-field, and then combine separate exposures. For the infrared data, we subtracted dark frames, then produced a sky frame for subtraction by taking a sliding box-car window of 4 exposures on either side of a reference exposure. We then added the exposures together, identified all the stars, and produced masks for the stars that were used to improve the sky frames in a second round of sky subtraction.

We determined zero points for the Magellan data referenced to observations with the Las Campanas 40-inch (Kaplan et al. 2004), employing appropriate transformations (Jorgensen 1994; Smith et al. 2002). We determined a K_s zero point for the PANIC data with ≈ 20 2MASS stars in each field. Astrometry for the Magellan data was performed relative to 2MASS, using ≈ 80 stars and giving residuals of $0\overset{''}{.}05$ in each coordinate.

Limiting magnitudes for the cases not dominated by confusion were determined by inserting and detecting fake stars—the 3σ limit is then the point at which the scatter between the measured magnitudes and the input magnitude equals 0.3. All magnitudes are reported without systematic zero-point uncertainties, which may be up to 0.1 mag.

12.2.1 RX J0822−4300

For this source, there is not a high-quality (i.e., *Chandra*) position available in the literature. We therefore examined the publicly available *Chandra* data. We determined the source position from an 11 ks ACIS-S observation (ObsID 750), having corrected the data to account for aspect errors.[1] The position is given in Table 12.1.

There is no counterpart to the X-ray source in any of the optical/IR images in Figure 12.1 (the small objects in the B- and $R-$band images are cosmic rays). We find limiting magnitudes of 26.5 (B), 26.0 (R), and 20.6 (K_s).

12.2.2 SAX J0852.0−4615

We do not detect any infrared emission at the location of the X-ray source, as seen in Figure 12.2. In the R-band data, however, there is a diffuse extended source near the X-ray position. This source was identified as an Hα nebula by Pellizzoni et al. (2002), so its disappearance in the K_s-band is not surprising. We find limiting magnitudes to point-like emission of 23.7 (R) and 20.2 (K_s)—the R-band limit is high because of the increased background produced by the Hα emission.

Pellizzoni et al. (2002) argued for an association between SAX J0852.0−4615 and the Hα nebula, suggesting that it was either a bow-shock produced by the supersonic motion of SAX J0852.0−4615 through the surrounding medium or an ionization nebula. If true, this would give an extremely valuable constraint on SAX J0852.0−4615 (see van Kerkwijk & Kulkarni (2001a)).

In Figure 12.2, the nebula appears roughly as bright as other regions of diffuse Hα emission, but Pellizzoni et al. (2002) claim that its ratio of off-band to Hα flux is somewhat anomalous. Their images show a roughly circular nebula, while we resolve it somewhat and show that one side (the south-east) is brighter than the other, consistent with a bow-shock interpretation. Overall, though, the amount of Hα in the vicinity, due to the ionizing flux of the Wolf-Rayet star Wray 16-30 (located to the south-west of SAX J0852.0−4615 in Fig. 12.2) makes us skeptical, and we require additional confirmation (namely spectroscopy that could identify nebular lines common to H II regions but not Balmer-dominated shocks) of the association.

12.2.3 1E 161348−5055

This field (seen in Figure 12.3) is considerably more crowded than the other images. Neither the optical nor the infrared data show any point sources at the location of the X-ray source. The infrared image is somewhat confused, and there may be some diffuse emission at the X-ray location, but the I-band image (which has better seeing) shows that all of the sources are likely unresolved and located outside the error circle, and that the emission seen inside the circle in the K_s-band image is just noise.

Source A has $K_s = 18.16(4)$ mag and $I \gtrsim 24.7$. Source B has $I = 21.90(4)$ and $K_s = 15.71(1)$. Source C has $I = 20.68(1)$, and D has $I = 20.20(1)$. Source A is red, and is a possible counterpart to 1E 161348−5055 (Wang & Chakrabarty 2002; Z. Wang 2004, pers. comm.), but we believe it to be a reddened star instead: at least from our data, its colors are not that different from those of nearby sources and the X-ray-to-infrared flux ratio would be somewhat low compared to other neutron stars (Fig. 12.5), but we have not undertaken any detailed modeling and we note that 1E 161348−5055 shows substantial variability unlike the other CCOs (Gotthelf et al. 1997) and may in fact be entirely different. In what follows we treat 1E 161348−5055 as a nondetection, which implies a additional limit of 20 mag (K_s) , but this is only approximate given the confusion.

---

[1] See `http://cxc.harvard.edu/cal/ASPECT/fix_offset/fix_offset.cgi`.

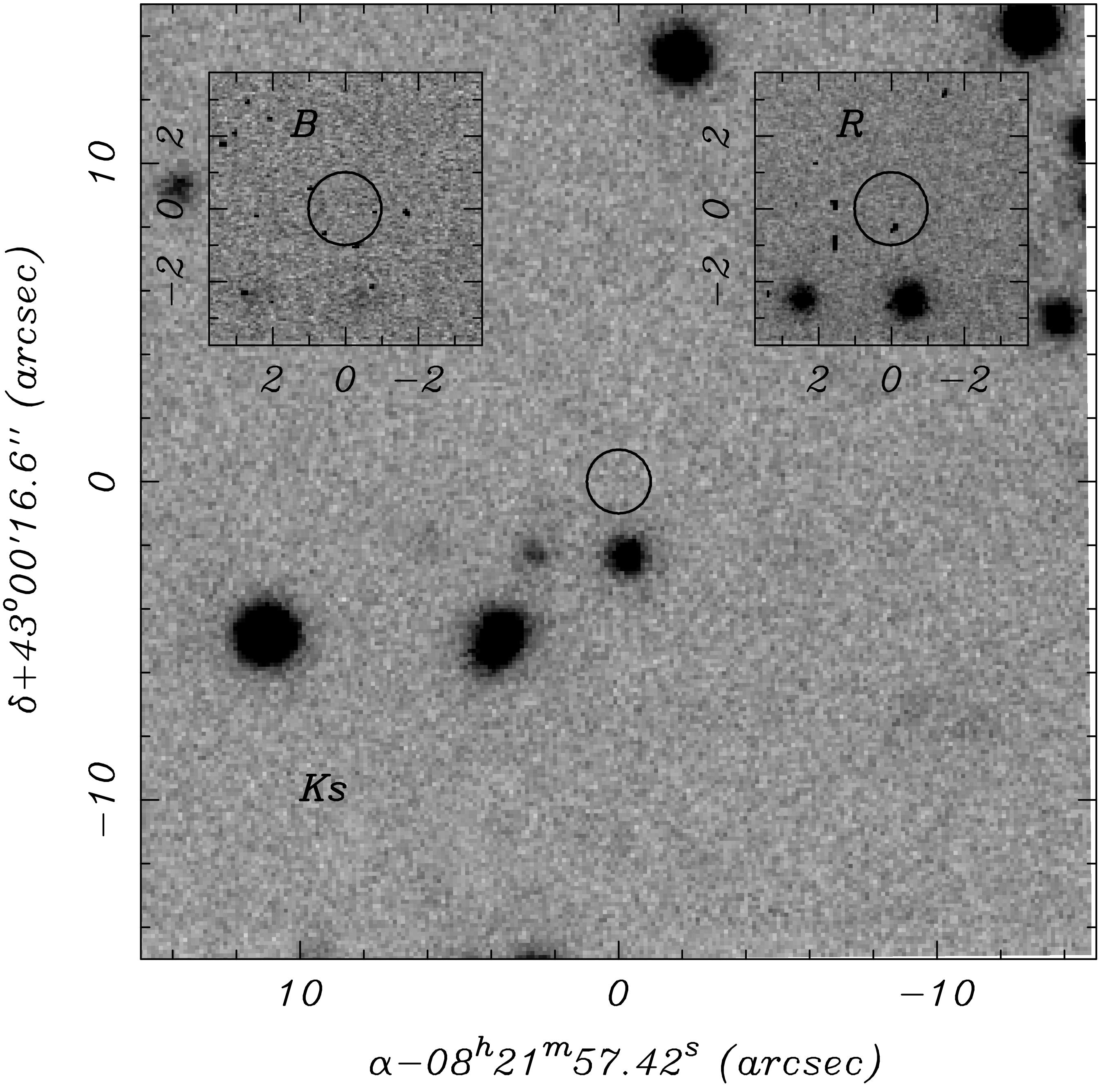

Figure 12.1 Optical and infrared images of RX J0822−4300. The large image is PANIC K_s-band, while the insets are MagIC B-band (left) and R-band (right). The error circle is $1''$ in radius. There are cosmic rays present in both the B- and R-band error circles, but there are no real sources.

12.3 Discussion & Conclusions

Assuming that we did not in fact detect any of the CCOs, we can plot the limits to the optical/IR emission along with the X-ray flux in Figure 12.5 (also see Kaplan et al. 2004). We see that, like the source in Cas A and unlike the vast majority of X-ray sources, the CCOs discussed here have very high X-ray-to-optical flux ratios ($\gtrsim 10^3$). This makes their identifications as compact objects essentially secure (although this

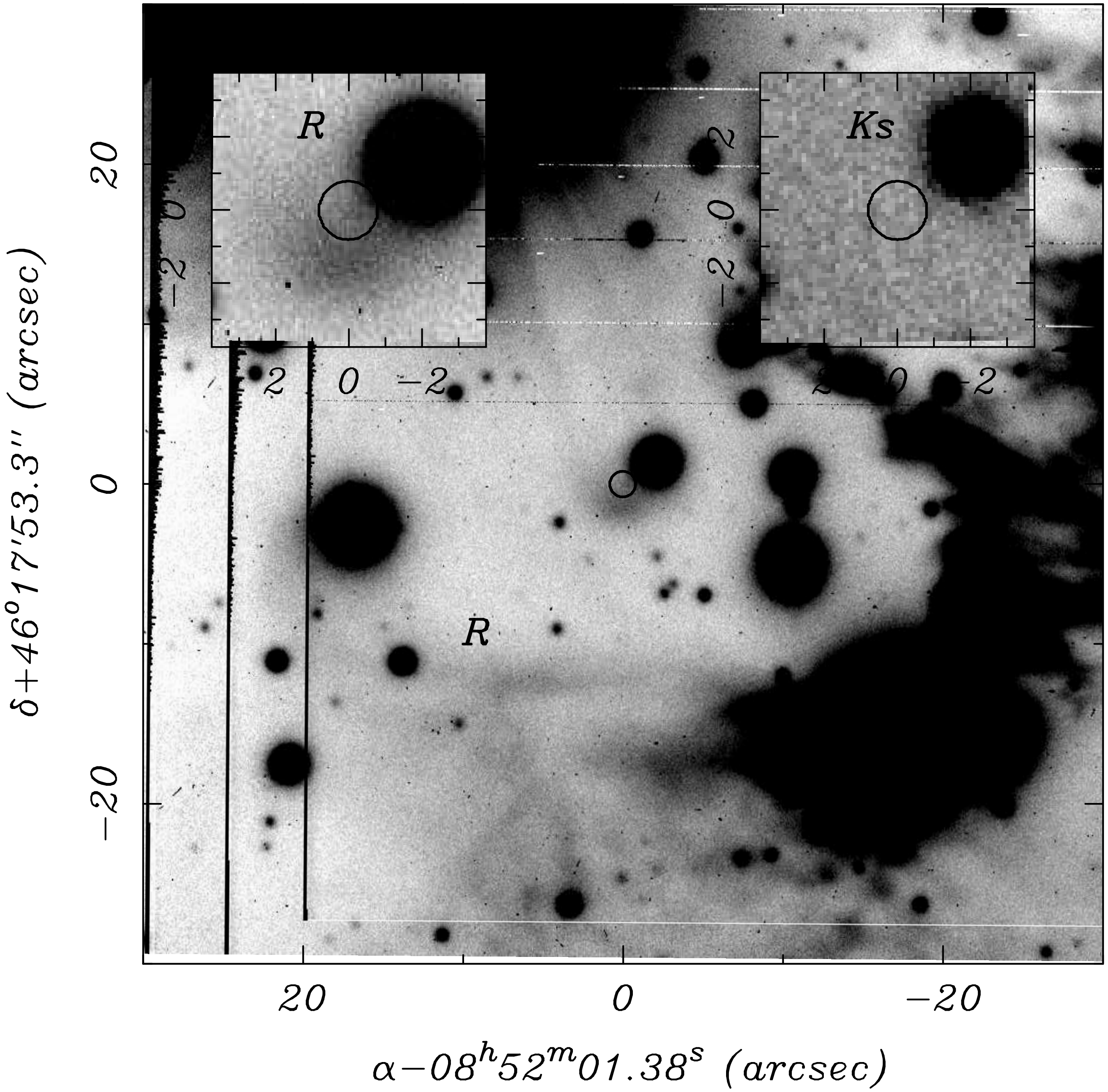

Figure 12.2 Optical and infrared images of SAX J0852.0−4615. The large image is MagIC *R*-band, while the insets are MagIC *R*-band (zoomed in; left) and PANIC K_s-band (right); the *B*-band image is too contaminated by the light from a bright nearby star. The error circle is 0.8″ in radius. The source to the north-west of the X-ray circle is star "Z" from Pavlov et al. (2001b). The horizontal and vertical stripes are artifacts from the combination of the separate exposures.

was not really in doubt), and allows us to reject most accretion models or binary companions as we did for the source in Cas A (Kaplan et al. 2001a). Hopefully, deeper observations in the future (such as those in progress now with *HST*) can detect the optical/IR counterparts to some of the CCOs. One things that

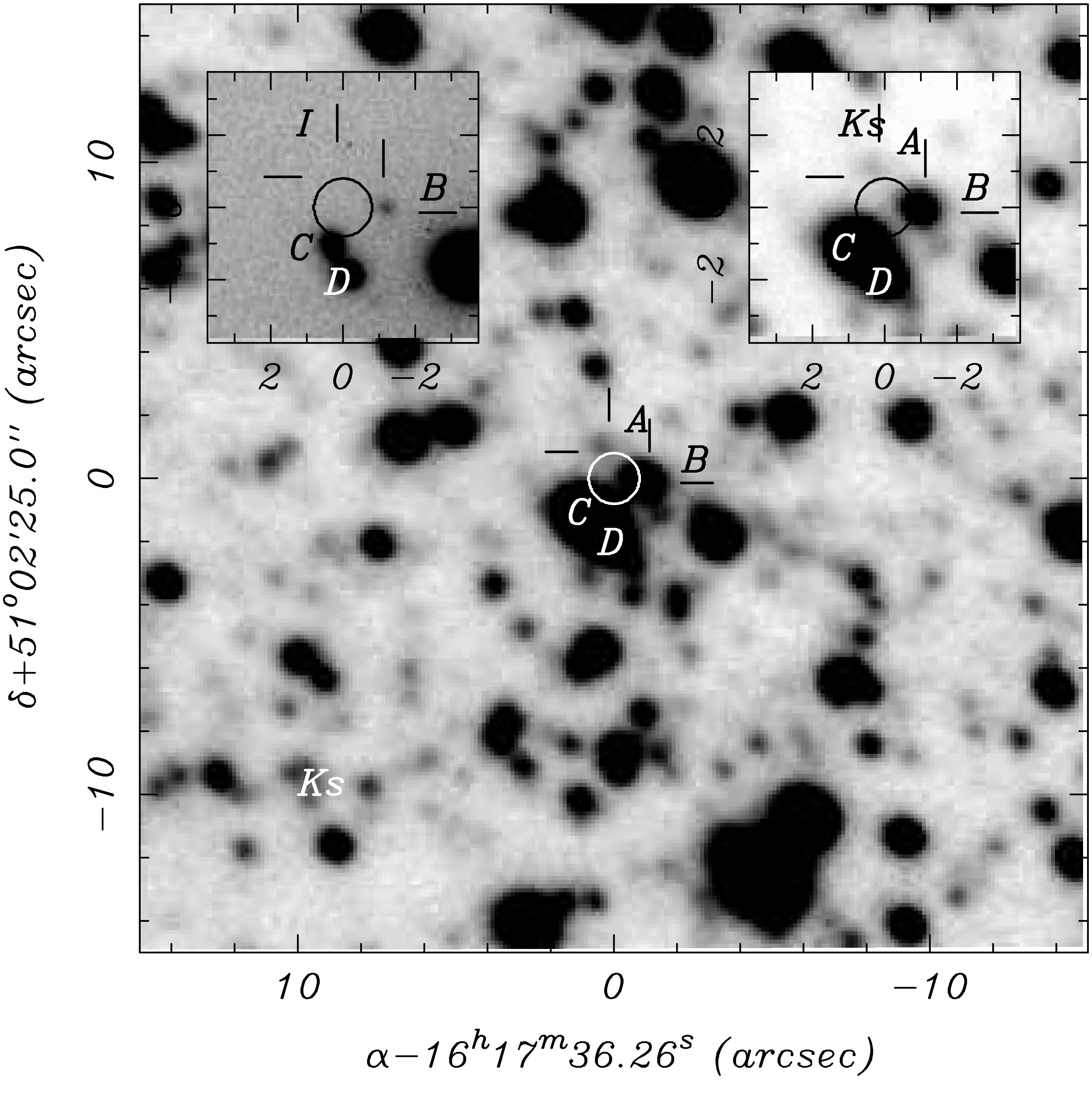

Figure 12.3 Optical and infrared images of 1E 161348−5055. The large image is PANIC K_s-band, while the insets are MagIC I-band (left) and PANIC K_s-band (right; with an adjusted color stretch). The error circle is 0.8″ in radius. We identify four sources near the X-ray position, labeled A–D (sources A and B are also indicated by the tick marks). Source A is not visible in the I-band image, while sources C and D are not deblended in the K_s image.

these data do show, though, is that the technique of finding new CCOs through the combination of X-ray and optical observations (Kaplan et al. 2004) should work.

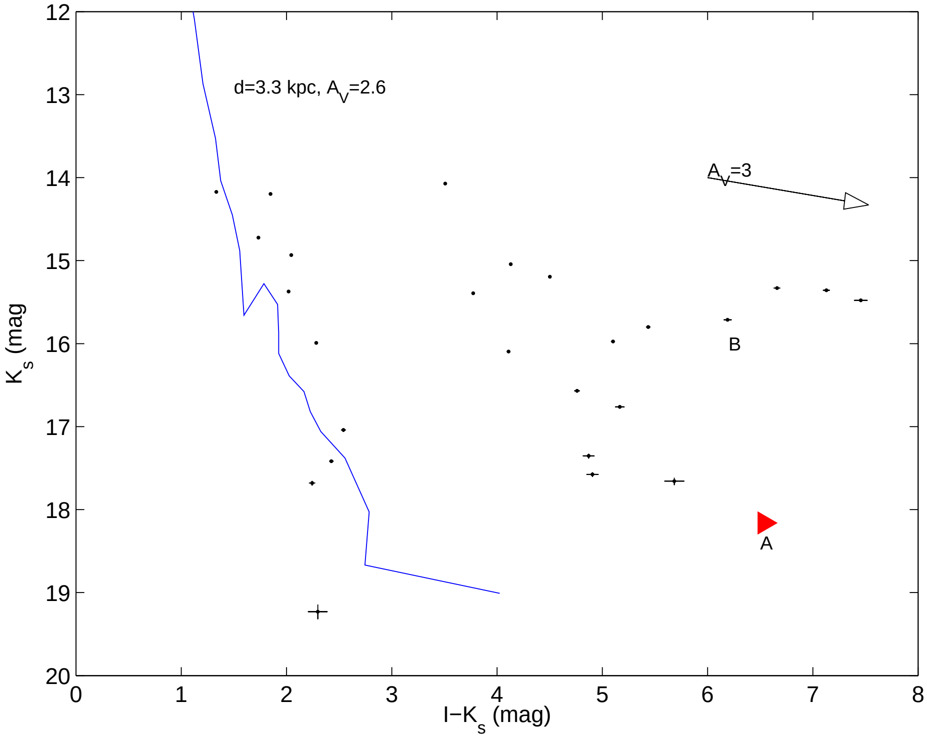

Figure 12.4 Color-magnitude diagram for sources within 20″ of 1E 161348−5055. Sources A and B are indicated (we do not plot sources C and D because they were too blended to obtain accurate K_s-band photometry). The line is a main sequence at a distance of 3.3 kpc and an extinction of $A_V = 2.6$ mag (following Wang & Chakrabarty 2002), based on Cox (2000, pp. 388 and 151). The arrow shows the reddening vector for $A_V = 3$ mag. While source A is red, it is not all that inconsistent with other sources and is likely a distant, highly-reddened giant star.

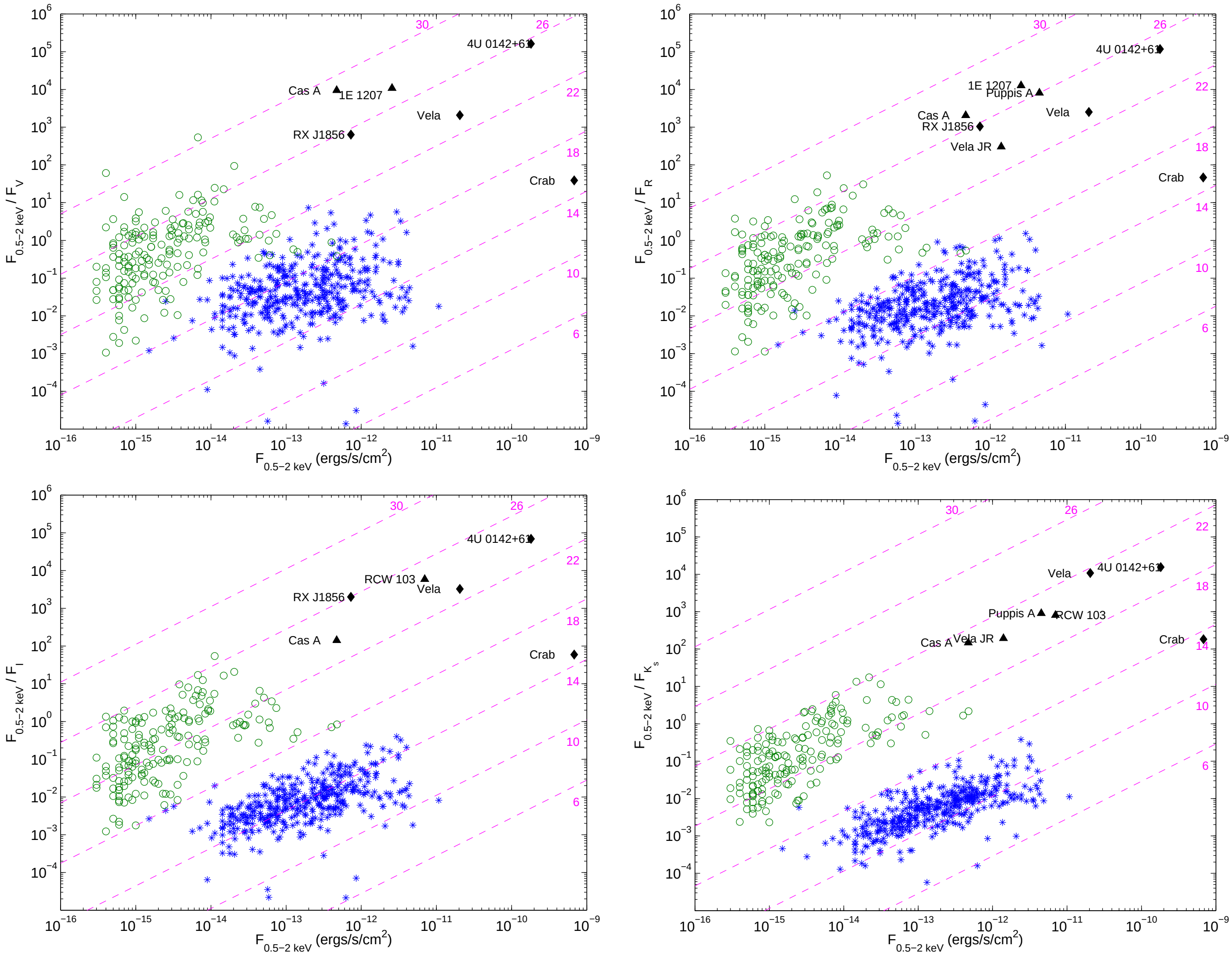

Figure 12.5 X-ray-to-optical/IR flux ratio vs. X-ray flux for sources from the CDF/Orion studies (Brandt et al. 2001; Feigelson et al. 2002) and selected neutron stars. Stars from CDF/Orion are asterisks and galaxies are circles. Selected neutron stars are diamonds/limits, and are labeled: the data include new limits from this work and De Luca et al. (2004). The diagonal lines represent constant magnitude, and are labeled by that magnitude. Data are not corrected for interstellar absorption. We note that the X-ray flux from 1E 161348−5055 in RCW 103 is variable by a factor of 10 or more.

Bibliography

Allen, G. E., Petre, R., & Gotthelf, E. V. 2001, ApJ, 558, 739

Alpar, M. A. 2001, ApJ, 554, 1245

Alpar, M. A., Nandkumar, R., & Pines, D. 1985, ApJ, 288, 191

Alpar, M. A., Pines, D., Anderson, P. W., & Shaham, J. 1984, ApJ, 276, 325

Anderson, J. & King, I. R. 1999, PASP, 111, 1095

—. 2000, PASP, 112, 1360

Anderson, S. B., Cadwell, B. J., Jacoby, B. A., Wolszczan, A., Foster, R. S., & Kramer, M. 1996, ApJ, 468, L55

Arnaud, M., Majerowicz, S., Lumb, D., Neumann, D. M., Aghanim, N., Blanchard, A., Boer, M., Burke, D. J., Collins, C. A., Giard, M., Nevalainen, J., Nichol, R. C., Romer, A. K., & Sadat, R. 2002, A&A, 390, 27

Arzoumanian, Z., Chernoff, D. F., & Cordes, J. M. 2002, ApJ, 568, 289

Aschenbach, B. 1998, Nature, 396, 141

—. 1999, IAUC, 7249, 1

Ashworth, W. B. 1980, Journal for the History of Astronomy, 11, 1

Baade, W. 1945, ApJ, 102, 309

Baade, W. & Zwicky, F. 1934, Proceedings of the National Academy of Science, 20, 254

Backer, D. C., Kulkarni, S. R., Heiles, C., Davis, M. M., & Goss, W. M. 1982, Nature, 300, 615

Barger, A. J., Cowie, L. L., Capak, P., Alexander, D. M., Bauer, F. E., Fernandez, E., Brandt, W. N., Garmire, G. P., & Hornschemeier, A. E. 2003, AJ, 126, 632

Bauer, F. E., Vignali, C., Alexander, D. M., Brandt, W. N., Garmire, G. P., Hornschemeier, A. E., Broos, P. S., Townsley, L. K., & Schneider, D. P. 2002, in New X-Ray Results from Clusters of Galaxies and Black Holes: 34th COSPAR Scientific Assembly, ed. E. Puchnarewicz & M. Ward, (astro-ph/0212389)

Baym, G. & Pethick, C. 1979, ARAA, 17, 415

Becker, R. H. & Helfand, D. J. 1984, ApJ, 283, 154

Becker, R. H., Helfand, D. J., & Szymkowiak, A. E. 1982, ApJ, 255, 557

Becker, W., Brazier, K. T. S., & Trümper, J. 1995, A&A, 298, 528

—. 1996, A&A, 306, 464

Becker, W. & Trümper, J. 1999, A&A, 341, 803

Becker, W. & Trümper, J. 1997, A&A, 326, 682

Bell, J. F., Bailes, M., Manchester, R. N., Weisberg, J. M., & Lyne, A. G. 1995, ApJ, 440, L81

Benedict, G. F., McArthur, B., Chappell, D. W., Nelan, E., Jefferys, W. H., van Altena, W., Lee, J., Cornell, D., Shelus, P. J., Hemenway, P. D., Franz, O. G., Wasserman, L. H., Duncombe, R. L., Story, D., Whipple, A. L., & Fredrick, L. W. 1999, AJ, 118, 1086

Bertin, E. & Arnouts, S. 1996, A&AS, 117, 393

Bessell, M. S., Castelli, F., & Plez, B. 1998, A&A, 333, 231

Biggs, J. D. & Lyne, A. G. 1996, MNRAS, 282, 691

Bignami, G. F., Caraveo, P. A., & Lamb, R. C. 1983, ApJ, 272, L9

Bignami, G. F., Caraveo, P. A., & Paul, J. A. 1988, A&A, 202, L1

Bignami, G. F., Caraveo, P. A., Paul, J. A., Salotti, L., & Vigroux, L. 1987, ApJ, 319, 358

Blaes, O. & Madau, P. 1993, ApJ, 403, 690

Blair, W. P., Sankrit, R., Raymond, J. C., & Long, K. S. 1999, AJ, 118, 942

Bocchino, F., Vink, J., Favata, F., Maggio, A., & Sciortino, S. 2000, A&A, 360, 671

Bock, D. C.-J. & Gvaramadze, V. V. 2002, A&A, 394, 533

Bock, D. C.-J., Large, M. I., & Sadler, E. M. 1999, AJ, 117, 1578

Bondi, H. 1952, MNRAS, 112, 195

Bondi, H. & Hoyle, F. 1944, MNRAS, 104, 273

Borkowski, K. J., Rho, J., Reynolds, S. P., & Dyer, K. K. 2001, ApJ, 550, 334

Bradley, A., Abramowicz-Reed, L., Story, D., Benedict, G., & Jefferys, W. 1991, PASP, 103, 317

Braje, T. M. & Romani, R. W. 2002, ApJ, 580, 1043

Brandt, W. N., Alexander, D. M., Hornschemeier, A. E., Garmire, G. P., Schneider, D. P., Barger, A. J., Bauer, F. E., Broos, P. S., Cowie, L. L., Townsley, L. K., Burrows, D. N., Chartas, G., Feigelson, E. D., Griffiths, R. E., Nousek, J. A., & Sargent, W. L. W. 2001, AJ, 122, 2810

Brazier, K. T. S. & Johnston, S. 1999, MNRAS, 305, 671

Brazier, K. T. S., Kanbach, G., Carraminana, A., Guichard, J., & Merck, M. 1996, MNRAS, 281, 1033

Brisken, W. F., Benson, J. M., Goss, W. M., & Thorsett, S. E. 2002, ApJ, 571, 906

Brisken, W. F., Fruchter, A. S., Goss, W. M., Herrnstein, R. M., & Thorsett, S. E. 2003a, AJ, 126, 3090

Brisken, W. F., Thorsett, S. E., Golden, A., & Goss, W. M. 2003b, ApJ, 593, L89

Brown, B. A. & Bregman, J. N. 1998, ApJ, 495, L75

Burrows, A. 2000, Nature, 403, 727

Burrows, A., Ott, C. D., & Meakin, C. 2003, in 3-D Signatures in Stellar Explosions, (astro-ph/0309684)

Burwitz, V., Haberl, F., Neuhäuser, R., Predehl, P., Trümper, J., & Zavlin, V. E. 2003, A&A, 399, 1109

Burwitz, V., Zavlin, V. E., Neuhäuser, R., Predehl, P., Trümper, J., & Brinkman, A. C. 2001, A&A, 379, L35

Camilo, F. 2003, in ASP Conf. Ser. 302: Radio Pulsars, ed. M. Bailes, D. J. Nice, & S. E. Thorsett (San Fransisco: ASP), 145, (astro-ph/0210620)

Camilo, F., Bell, J. F., Manchester, R. N., Lyne, A. G., Possenti, A., Kramer, M., Kaspi, V. M., Stairs, I. H., D'Amico, N., Hobbs, G., Gotthelf, E. V., & Gaensler, B. M. 2001, ApJ, 557, L51

Camilo, F., Kaspi, V. M., Lyne, A. G., Manchester, R. N., Bell, J. F., D'Amico, N., McKay, N. P. F., & Crawford, F. 2000, ApJ, 541, 367

Camilo, F., Lorimer, D. R., Bhat, N. D. R., Gotthelf, E. V., Halpern, J. P., Wang, Q. D., Lu, F. J., & Mirabal, N. 2002a, ApJ, 574, L71

Camilo, F., Manchester, R. N., Gaensler, B. M., & Lorimer, D. R. 2002b, ApJ, 579, L25

Camilo, F., Manchester, R. N., Gaensler, B. M., Lorimer, D. R., & Sarkissian, J. 2002c, ApJ, 567, L71

Camilo, F., Stairs, I. H., Lorimer, D. R., Backer, D. C., Ransom, S. M., Klein, B., Wielebinski, R., Kramer, M., McLaughlin, M. A., Arzoumanian, Z., & Müller, P. 2002d, ApJ, 571, L41

Cappellaro, E., Evans, R., & Turatto, M. 1999, A&A, 351, 459

Caraveo, P. A., Bignami, G. F., Mereghetti, S., & Mombelli, M. 1992, ApJ, 395, L103

Caraveo, P. A., Bignami, G. F., Mignani, R., & Taff, L. G. 1996, ApJ, 461, L91

Caraveo, P. A., De Luca, A., Mignani, R. P., & Bignami, G. F. 2001, ApJ, 561, 930

Cardelli, J. A., Clayton, G. C., & Mathis, J. S. 1989, ApJ, 345, 245

Casali, M. & Hawarden, T. G. 1992, UKIRT Newsletter, 4, 33

Caswell, J. L. 1977, MNRAS, 181, 789

Chakrabarty, D. 1998, ApJ, 492, 342

Chakrabarty, D., Pivovaroff, M. J., Hernquist, L. E., Heyl, J. S., & Narayan, R. 2001, ApJ, 548, 800

Chang, P. & Bildsten, L. 2003, ApJ, 585, 464

Chatterjee, P., Hernquist, L., & Narayan, R. 2000, ApJ, 534, 373

Chatterjee, S. & Cordes, J. M. 2002, ApJ, 575, 407

Chatterjee, S., Cordes, J. M., Vlemmings, W. H. T., Arzoumanian, Z., Goss, W. M., & Lazio, T. J. W. 2004, ApJ, 604, 339

Chevalier, R. A. 1998, Memorie della Societa Astronomica Italiana, 69, 977

Chin, Y. N. & Huang, Y. L. 1994, Nature, 371, 398

Chiu, H. & Salpeter, E. E. 1964, Physical Review Letters, 12, 413

Cimatti, A., Mignoli, M., Daddi, E., Pozzetti, L., Fontana, A., Saracco, P., Poli, F., Renzini, A., Zamorani, G., Broadhurst, T., Cristiani, S., D'Odorico, S., Giallongo, E., Gilmozzi, R., & Menci, N. 2002, A&A, 392, 395

Clark, D. H., Green, A. J., & Caswell, J. L. 1975, Australian Journal of Physics Astrophysical Supplement, 75

Clark, D. H. & Stephenson, F. R. 1977, The historical supernovae, 1st edn. (Oxford [Eng.]: Pergamon Press)

Colpi, M., Turolla, R., Zane, S., & Treves, A. 1998, ApJ, 501, 252

Comella, J. M., Craft, H. D., Lovelace, R. V. E., Sutton, J. M., & Tyler, G. L. 1969, Nature, 221, 453

Condon, J. J., Cotton, W. D., Greisen, E. W., Yin, Q. F., Perley, R. A., Taylor, G. B., & Broderick, J. J. 1998, AJ, 115, 1693

Condon, J. J. & Kaplan, D. L. 1998, ApJS, 117, 361

Cordes, J. M. & Chernoff, D. F. 1997, ApJ, 482, 971

—. 1998, ApJ, 505, 315

Cordes, J. M. & Lazio, T. J. W. 2002, astro-ph/0207156

Cordes, J. M., Romani, R. W., & Lundgren, S. C. 1993, Nature, 362, 133

Cottam, J., Paerels, F., & Mendez, M. 2002, Nature, 420, 51

Cotter, G., Buttery, H. J., Das, R., Jones, M. E., Grainge, K., Pooley, G. G., & Saunders, R. 2002, MNRAS, 334, 323

Cox, A. N. 2000, Allen's Astrophysical Quantities, 4th edn. (New York: AIP Press/Springer)

Crawford, F., Gaensler, B. M., Kaspi, V. M., Manchester, R. N., Camilo, F., Lyne, A. G., & Pivovaroff, M. J. 2001, ApJ, 554, 152

Cropper, M., Haberl, F., Zane, S., & Zavlin, V. 2004, MNRAS, in press, (astro-ph/0403380)

Cropper, M., Zane, S., Ramsay, G., Haberl, F., & Motch, C. 2001, A&A, 365, L302

Damashek, M., Taylor, J. H., & Hulse, R. A. 1978, ApJ, 225, L31

Dame, T. M. 1993, in AIP Conf. Proc. 278: Back to the Galaxy, 267–278

de Donder, E. & Vanbeveren, D. 1998, A&A, 333, 557

de Geus, E. J., de Zeeuw, P. T., & Lub, J. 1989, A&A, 216, 44

De Luca, A., Mereghetti, S., Caraveo, P. A., Moroni, M., Mignani, R. P., & Bignami, G. F. 2004, A&A, 418, 625

de Vries, C. P., Vink, J., Méndez, M., & Verbunt, F. 2004, A&A, 415, L31

de Zeeuw, P. T., Hoogerwerf, R., de Bruijne, J. H. J., Brown, A. G. A., & Blaauw, A. 1999, AJ, 117, 354

Deutsch, E. W. 1999, AJ, 118, 1882

Dickel, J. R., Strom, R. G., & Milne, D. K. 2001, ApJ, 546, 447

Dickey, J. M. & Lockman, F. J. 1990, ARAA, 28, 215

Dodson, R., Legge, D., Reynolds, J. E., & McCulloch, P. M. 2003, ApJ, 596, 1137

Drake, J. J., Marshall, H. L., Dreizler, S., Freeman, P. E., Fruscione, A., Juda, M., Kashyap, V., Nicastro, F., Pease, D. O., Wargelin, B. J., & Werner, K. 2002, ApJ, 572, 996

Duncan, R. C. & Thompson, C. 1992, ApJ, 392, L9

Ergma, E. & van den Heuvel, E. P. J. 1998, A&A, 331, L29

ESA. 1997, The Hipparcos and Tycho Catalogues (Noordwijk: ESA)

Fabbiano, G. 1989, ARAA, 27, 87

Feigelson, E. D., Broos, P., Gaffney, J. A., Garmire, G., Hillenbrand, L. A., Pravdo, S. H., Townsley, L., & Tsuboi, Y. 2002, ApJ, 574, 258

Feldt, C. & Green, D. A. 1993, A&A, 274, 421

Fesen, R. A., Becker, R. H., & Blair, W. P. 1987, ApJ, 313, 378

Fesen, R. A., Chevalier, R. A., Holt, S. S., & Tananbaum, H. 2002, in ASP Conf. Ser. 271: Neutron Stars in Supernova Remnants, ed. P. O. Slane & B. M. Gaensler (San Fransisco: ASP), 305

Fesen, R. A., Wu, C., Leventhal, M., & Hamilton, A. J. S. 1988, ApJ, 327, 164

Fichtel, C. E., Hartman, R. C., Kniffen, D. A., Thompson, D. J., Ogelman, H., Ozel, M. E., Tumer, T., & Bignami, G. F. 1975, ApJ, 198, 163

Flamsteed, J. 1725, HISTORIA Coelestis Britannicae, tribus Voluminibus contenta (1675-1689), (1689-1720), vol. 1, 2, 3 (London: H. Meere; in folio; DCC.f.9, DCC.f.10, DCC.f.11)

Fox, D. B. 2004, astro-ph/0403261

Frail, D. A., Goss, W. M., & Whiteoak, J. B. Z. 1994, ApJ, 437, 781

Frail, D. A. & Kulkarni, S. R. 1991, Nature, 352, 785

Frail, D. A. & Moffett, D. A. 1993, ApJ, 408, 637

Franx, M., Labbé, I., Rudnick, G., van Dokkum, P. G., Daddi, E., Förster Schreiber, N. M., Moorwood, A., Rix, H., Röttgering, H., van de Wel, A., van der Werf, P., & van Starkenburg, L. 2003, ApJ, 587, L79

Freeman, P. E., Kashyap, V., Rosner, R., & Lamb, D. Q. 2002, ApJS, 138, 185

Fruchter, A. & Mutchler, M. 1998, Space Telescope Science Institute Memo, 28 July

Fruchter, A. S. & Hook, R. N. 2002, PASP, 114, 144

Fryer, C. L. 1999, ApJ, 522, 413

Fuhrmeister, B. & Schmitt, J. H. M. M. 2003, A&A, 403, 247

Fürst, E., Reich, W., & Seiradakis, J. H. 1993, A&A, 276, 470

Gaensler, B. M. 2003, in Texas in Tuscany: XXI Symposium on Relativistic Astrophysics, ed. R. Bandiera, R. Maiolino, & F. Mannucci (Singapore: World Scientific), 297–304, (astro-ph/0303427)

Gaensler, B. M., Arons, J., Kaspi, V. M., Pivovaroff, M. J., Kawai, N., & Tamura, K. 2002, ApJ, 569, 878

Gaensler, B. M., Bock, D. C., & Stappers, B. W. 2000, ApJ, 537, L35

Gaensler, B. M. & Frail, D. A. 2000, Nature, 406, 158

Gaensler, B. M., Gotthelf, E. V., & Vasisht, G. 1999, ApJ, 526, L37

Gaensler, B. M. & Johnston, S. 1995, MNRAS, 277, 1243

Gaensler, B. M., Kaspi, V. M., & Manchester, R. N. 2003, in preparation

Gaensler, B. M., Pivovaroff, M. J., & Garmire, G. P. 2001a, ApJ, 556, L107

Gaensler, B. M., Slane, P. O., Gotthelf, E. V., & Vasisht, G. 2001b, ApJ, 559, 963

Gaensler, B. M. & Wallace, B. J. 2003, ApJ, 594, 326

Gandhi, P., Crawford, C. S., Fabian, A. C., & Johnstone, R. M. 2004, MNRAS, 348, 529

Garmire, G. P., Pavlov, G. G., Garmire, A. B., & Zavlin, V. E. 2000, IAUC, 7350, 2

Gavriil, F. P., Kaspi, V. M., & Woods, P. M. 2002, Nature, 419, 142

Georgantopoulos, I., Stewart, G. C., Shanks, T., Boyle, B. J., & Griffiths, R. E. 1996, MNRAS, 280, 276

Gonzalez, M. & Safi-Harb, S. 2003, ApJ, 591, L143

Gorham, P. W., Ray, P. S., Anderson, S. B., Kulkarni, S. R., & Prince, T. A. 1996, ApJ, 458, 257

Goss, W. M. & van Gorkom, J. H. 1984, Journal of Astrophysics and Astronomy, 5, 425

Gotthelf, E. V. 2003, ApJ, 591, 361

Gotthelf, E. V. 2004, in ASP Conf. Ser.: IAU Symposium 218: Young Neutron Stars and Their Environments, ed. F. Camilo & B. M. Gaensler (San Fransisco: ASP)

Gotthelf, E. V., Halpern, J. P., Buxton, M., & Bailyn, C. 2004, ApJ, 605, 368

Gotthelf, E. V., Halpern, J. P., & Dodson, R. 2002, ApJ, 567, L125

Gotthelf, E. V., Petre, R., & Hwang, U. 1997, ApJ, 487, L175
Gotthelf, E. V., Petre, R., & Vasisht, G. 1999a, ApJ, 514, L107
Gotthelf, E. V., Vasisht, G., Boylan-Kolchin, M., & Torii, K. 2000, ApJ, 542, L37
Gotthelf, E. V., Vasisht, G., & Dotani, T. 1999b, ApJ, 522, L49
Gotthelf, E. V. & Wang, Q. D. 2000, ApJ, 532, L117
Green, D. A. 2000, A Catalogue of Galactic Supernova Remnants (2000 August version), Mullard Radio Astronomy Observatory, Cavendish Laboratory, Cambridge, UK, (available on the World-Wide-Web at http://www.mrao.cam.ac.uk/surveys/snrs/)
—. 2001, A Catalogue of Galactic Supernova Remnants (2001 December version), Mullard Radio Astronomy Observatory, Cavendish Laboratory, Cambridge, UK, (available on the World-Wide-Web at http://www.mrao.cam.ac.uk/surveys/snrs/)
Gregory, P. C. & Loredo, T. J. 1992, ApJ, 398, 146
Greiveldinger, C., Camerini, U., Fry, W., Markwardt, C. B., Ögelman, H., Safi-Harb, S., Finley, J. P., Tsuruta, S., Shibata, S., Sugawara, T., Sano, S., & Tukahara, M. 1996, ApJ, 465, L35
Greiveldinger, C., Caucino, S., Massaglia, S., Oegelman, H., & Trussoni, E. 1995, ApJ, 454, 855
Grindlay, J., Zhao, P., Hong, J., Jenkins, J., Kim, D.-W., Schlegel, E., Drake, J., Kashyap, V., Edmonds, P., Cohn, H., Lugger, P., & Cool, A. 2003, Astronomische Nachrichten, 324, 57, (astro-ph/0211527)
Gull, T. R., Kirshner, R. P., & Parker, R. A. R. 1977, ApJ, 215, L69
Gusakov, M. E., Yakovlev, D. G., Haensel, P., & Gnedin, O. Y. 2004, A&A, submitted, (astro-ph/0404165)
Gvaramadze, V. V. 2002, in ASP Conf. Ser. 271: Neutron Stars in Supernova Remnants, ed. P. O. Slane & B. M. Gaensler (San Fransisco: ASP), 23
Gvaramadze, V. V. & Vikhlinin, A. A. 2003, A&A, 401, 625
Haberl, F. 2003, in High Energy Studies of Supernova Remnants and Neutron Stars: 34th COSPAR Scientific Assembly, ed. W. Becker & W. Hermsen, (astro-ph/0302540)
Haberl, F. 2004, in XMM-Newton EPIC Consortium meeting, Palermo, 2003 October 14-16, (astro-ph/0401075)
Haberl, F., Motch, C., Buckley, D. A. H., Zickgraf, F.-J., & Pietsch, W. 1997, A&A, 326, 662
Haberl, F., Motch, C., & Pietsch, W. 1998, Astronomische Nachrichten, 319, 97
Haberl, F., Motch, C., Zavlin, V. E., Reinsch, K., Gänsicke, B. T., Cropper, M., Schwope, A. D., Turolla, R., & Zane, S. 2004, A&A, in press, (astro-ph/0405485)
Haberl, F., Pietsch, W., & Motch, C. 1999, A&A, 351, L53
Haberl, F., Schwope, A. D., Hambaryan, V., Hasinger, G., & Motch, C. 2003a, A&A, 403, L19
Haberl, F., Zavlin, V. E., Trümper, J., & Burwitz, V. 2003b, A&A, in press, (astro-ph/0312413)
Habets, G. M. H. J. & Heintze, J. R. W. 1981, A&AS, 46, 193
Haensel, P. 2001, A&A, 380, 186
Hailey, C. J. & Mori, K. 2002, ApJ, 578, L133
Halpern, J. P., Camilo, F., Gotthelf, E. V., Helfand, D. J., Kramer, M., Lyne, A. G., Leighly, K. M., & Eracleous, M. 2001, ApJ, 552, L125
Halpern, J. P. & Holt, S. S. 1992, Nature, 357, 222
Halpern, J. P. & Tytler, D. 1988, ApJ, 330, 201
Hambaryan, V., Hasinger, G., Schwope, A. D., & Schulz, N. S. 2002, A&A, 381, 98
Hansen, B. M. S. & Phinney, E. S. 1997, MNRAS, 291, 569
Harrus, I. M., Hughes, J. P., Singh, K. P., Koyama, K., & Asaoka, I. 1997, ApJ, 488, 781
Harrus, I. M., Hughes, J. P., & Slane, P. O. 1998, ApJ, 499, 273
Hartman, J. W., Bhattacharya, D., Wijers, R., & Verbunt, F. 1997, A&A, 322, 477
Hasinger, G., Burg, R., Giacconi, R., Schmidt, M., Trümper, J., & Zamorani, G. 1998, A&A, 329, 482
Haslam, C. G. T., Salter, C. J., & Pauls, T. 1980, A&A, 92, 57
Heger, A., Fryer, C. L., Woosley, S. E., Langer, N., & Hartmann, D. H. 2003, ApJ, 591, 288

Helfand, D. J. 1981, in IAU Symp. 95: Pulsars: 13 Years of Research on Neutron Stars, 343–350

Helfand, D. J. 1984, Advances in Space Research, 3, 29

Helfand, D. J. & Becker, R. H. 1984, Nature, 307, 215

Helfand, D. J., Collins, B. F., & Gotthelf, E. V. 2003, ApJ, 582, 783

Hertz, P. & Grindlay, J. E. 1988, AJ, 96, 233

Hester, J. 2000, Bulletin of the American Astronomical Society, 32, 1542

Hester, J. J., Graham, J. R., Beichman, C. A., & Gautier, T. N. 1990, ApJ, 357, 539

Heyl, J. S. & Hernquist, L. 1998a, MNRAS, 298, L17

—. 1998b, MNRAS, 297, L69

Heyl, J. S. & Kulkarni, S. R. 1998, ApJ, 506, L61

Hill, E. R. 1967, Proceedings of the Astronomical Society of Australia, 20, 297

Hirata, K., Kajita, T., Koshiba, M., Nakahata, M., & Oyama, Y. 1987, Physical Review Letters, 58, 1490

Ho, W. C. G. & Lai, D. 2003, MNRAS, 338, 233

—. 2004, ApJ, 607, 420

Ho, W. C. G., Lai, D., Potekhin, A. Y., & Chabrier, G. 2003, ApJ, 599, 1293

Hobbs, G. B. & Manchester, R. N. 2003, ATNF Pulsar Catalogue, v1.2, (available on the World-Wide-Web at http://www.atnf.csiro.au/research/pulsar/psrcat/)

Holtzman, J. A., Hester, J. J., Casertano, S., Trauger, J. T., Watson, A. M., Ballester, G. E., Burrows, C. J., Clarke, J. T., Crisp, D., Evans, R. W., Gallagher, J. S., Griffiths, R. E., Hoessel, J. G., Matthews, L. D., Mould, J. R., Scowen, P. A., Stapelfeldt, K. R., & Westphal, J. A. 1995, PASP, 107, 156

Hoogerwerf, R., de Bruijne, J. H. J., & de Zeeuw, P. T. 2001, A&A, 365, 49

Hughes, J. P., Ghavamian, P., Rakowski, C. E., & Slane, P. O. 2003a, ApJ, 582, L95

Hughes, J. P., Hayashi, I., Helfand, D., Hwang, U., Itoh, M., Kirshner, R., Koyama, K., Markert, T., Tsunemi, H., & Woo, J. 1995, ApJ, 444, L81

Hughes, J. P., Rakowski, C. E., Burrows, D. N., & Slane, P. O. 2000, ApJ, 528, L109

Hughes, J. P., Slane, P. O., Burrows, D. N., Garmire, G., Nousek, J. A., Olbert, C. M., & Keohane, J. W. 2001, ApJ, 559, L153

Hughes, J. P., Slane, P. O., Park, S., Roming, P. W. A., & Burrows, D. N. 2003b, ApJ, 591, L139

Hulleman, F., Tennant, A. F., van Kerkwijk, M. H., Kulkarni, S. R., Kouveliotou, C., & Patel, S. K. 2001, ApJ, 563, L49

Hulleman, F., van Kerkwijk, M. H., & Kulkarni, S. R. 2000, Nature, 408, 689

Hurford, A. P. & Fesen, R. A. 1996, ApJ, 469, 246

Hurley, K. 2000, in Gamma-Ray Bursts: 5th Huntsville Symposium, ed. R. M. Kippen, R. S. Mallozi, & G. J. Fishman, 763, (astro-ph/9912061)

Ibata, R. A., Wyse, R. F. G., Gilmore, G., Irwin, M. J., & Suntzeff, N. B. 1997, AJ, 113, 634

Ibrahim, A. I., Markwardt, C., Swank, J., Ransom, S., Roberts, M., Kaspi, V., Woods, P., Safi-Harb, S., Balman, S., Parke, W., Kouveliotou, C., Hurley, K., & Cline, T. 2003, ApJ, submitted, (astro-ph/0310665)

Illarionov, A. F. & Sunyaev, R. A. 1975, A&A, 39, 185

James, D. J., Jardine, M. M., Jeffries, R. D., Randich, S., Collier Cameron, A., & Ferreira, M. 2000, MNRAS, 318, 1217

Jarrett, T. H., Beichman, C. A., van Buren, D., Gautier, N., Jorquera, C., & Bruce, C. 1994, in Infrared Astronomy with Arrays, The Next Generation, ed. I. S. McLean (Dordrecht: Kluwer Academic Publisher), 293

Johnston, S. 2003, MNRAS, 340, L43

Johnston, S. & Galloway, D. 1999, MNRAS, 306, L50

Joncas, G., Roger, R. S., & Dewdney, P. E. 1989, A&A, 219, 303

Jorgensen, I. 1994, PASP, 106, 967

Juett, A. M., Marshall, H. L., Chakrabarty, D., & Schulz, N. S. 2002, ApJ, 568, L31

Kaminker, A. D., Haensel, P., & Yakovlev, D. G. 2001, A&A, 373, L17

Kaminker, A. D., Yakovlev, D. G., & Gnedin, O. Y. 2002, A&A, 383, 1076

Kaplan, D. L., Frail, D. A., Gaensler, B. M., Gotthelf, E. V., Kulkarni, S. R., Slane, P. O., & Nechita, A. 2004, ApJS, in press, (astro-ph/0403313)

Kaplan, D. L., Kulkarni, S. R., & Murray, S. S. 2001a, ApJ, 558, 270

Kaplan, D. L., Kulkarni, S. R., & van Kerkwijk, M. H. 2002a, ApJ, 579, L29

—. 2003a, ApJ, 588, L33

Kaplan, D. L., Kulkarni, S. R., van Kerkwijk, M. H., & Marshall, H. L. 2002b, ApJ, 570, L79

Kaplan, D. L., Kulkarni, S. R., van Kerkwijk, M. H., Rothschild, R. E., Lingenfelter, R. L., Marsden, D., Danner, R., & Murakami, T. 2001b, ApJ, 556, 399

Kaplan, D. L., van Kerkwijk, M. H., & Anderson, J. 2002c, ApJ, 571, 447

Kaplan, D. L., van Kerkwijk, M. H., Marshall, H. L., Jacoby, B. A., Kulkarni, S. R., & Frail, D. A. 2003b, ApJ, 590, 1008

Kargaltsev, O., Pavlov, G. G., Sanwal, D., & Garmire, G. P. 2002, ApJ, 580, 1060

Kaspi, V. M. 1996, in ASP Conf. Ser. 105: IAU Colloq. 160: Pulsars: Problems and Progress, ed. S. Johnston, M. A. Walker, & M. Bailes (San Fransisco: ASP), 375

Kaspi, V. M., Gavriil, F. P., Woods, P. M., Jensen, J. B., Roberts, M. S. E., & Chakrabarty, D. 2003, ApJ, 588, L93

Kaspi, V. M., Gotthelf, E. V., Gaensler, B. M., & Lyutikov, M. 2001, ApJ, 562, L163

Kaspi, V. M. & Helfand, D. J. 2002, in ASP Conf. Ser. 271: Neutron Stars in Supernova Remnants, ed. P. O. Slane & B. M. Gaensler (San Fransisco: ASP), 3, (astro-ph/0201183)

Kaspi, V. M., Manchester, R. N., Johnston, S., Lyne, A. G., & D'Amico, N. 1996, AJ, 111, 2028

Katsova, M. M. & Cherepashchuk, A. M. 2000, Astronomy Reports, 44, 804

Kifonidis, K., Plewa, T., Janka, H.-T., & Müller, E. 2003, A&A, 408, 621

Kim, D.-W. & Fabbiano, G. 2003, ApJ, submitted, (astro-ph/0312104)

Kinugasa, K. & Tsunemi, H. 1999, PASJ, 51, 239

Kirshner, R. P. & Chevalier, R. A. 1978, Nature, 276, 480

Kodama, T. & Bower, R. 2003, MNRAS, 346, 1

Koekemoer, A. M., Alexander, D. M., Bauer, F. E., Bergeron, J., Brandt, W. N., Chatzichristou, E., Cristiani, S., Fall, S. M., Grogin, N. A., Livio, M., Mainieri, V., Moustakas, L. A., Padovani, P., Rosati, P., Schreier, E. J., & Urry, C. M. 2004, ApJ, 600, L123

Koester, D. 2002, A&A Rev., 11, 33

Konenkov, D. Y. & Popov, S. B. 1997, Pis'ma Astron. Zh., 23, 569

Koptsevich, A. B., Pavlov, G. G., Zharikov, S. V., Sokolov, V. V., Shibanov, Y. A., & Kurt, V. G. 2001, A&A, 370, 1004

Kotani, T., Kawai, N., Matsuoka, M., & Brinkmann, W. 1996, PASJ, 48, 619

Kothes, R., Uyaniker, B., & Pineault, S. 2001, ApJ, 560, 236

Kramer, M., Lyne, A. G., Hobbs, G., Löhmer, O., Carr, P., Jordan, C., & Wolszczan, A. 2003, ApJ, 593, L31

Kulkarni, S. R., Clifton, T. C., Backer, D. C., Foster, R. S., & Fruchter, A. S. 1988, Nature, 331, 50

Kulkarni, S. R. & Hester, J. J. 1988, Nature, 335, 801

Kulkarni, S. R., Kaplan, D. L., Marshall, H. L., Frail, D. A., Murakami, T., & Yonetoku, D. 2003, ApJ, 585, 948

Kulkarni, S. R., Predehl, P., Hasinger, G., & Aschenbach, B. 1993, Nature, 362, 135

Kulkarni, S. R. & van Kerkwijk, M. H. 1998, ApJ, 507, L49

Kuster, M., Kendziorra, E., Benlloch, S., Becker, W., Lammers, U., Vacanti, G., & Serpell, E. 2002, in New Visions of the X-ray Universe in the XMM-Newton and Chandra Era, (astro-ph/0203207)

Lai, D. 2001, Reviews of Modern Physics, 73, 629, (astro-ph/0009333)

Lai, D. & Ho, W. C. G. 2003, ApJ, 588, 962

Landecker, T. L., Routledge, D., Reynolds, S. P., Smegal, R. J., Borkowski, K. J., & Seward, F. D. 1999, ApJ, 527, 866

Landolt, A. U. 1992, AJ, 104, 340

Large, M. I., Vaughan, A. E., & Mills, B. Y. 1968, Nature, 220, 340

Lasker, B. M., Sturch, C. R., McLean, B. J., Russell, J. L., Jenkner, H., & Shara, M. M. 1990, AJ, 99, 2019

Lattimer, J. M. & Prakash, M. 2000, Phys. Rep., 333, 121

Lattimer, J. M., Prakash, M., Pethick, C. J., & Haensel, P. 1991, Physical Review Letters, 66, 2701

Lazendic, J. S., Slane, P. O., Gaensler, B. M., Plucinsky, P. P., Hughes, J. P., Galloway, D. K., & Crawford, F. 2003, ApJ, 593, L27

Leahy, D. A. & Aschenbach, B. 1995, A&A, 293, 853

Leahy, D. A., Naranan, S., & Singh, K. P. 1986, MNRAS, 220, 501

Leahy, D. A., Nousek, J., & Hamilton, A. J. S. 1991, ApJ, 374, 218

Leahy, D. A. & Roger, R. S. 1991, AJ, 101, 1033

Levenson, N. A., Graham, J. R., & Walters, J. L. 2002, ApJ, 576, 798

Lewin, W. H. G., van Paradijs, J., & Taam, R. E. 1993, Space Science Reviews, 62, 223

Lewis, K. T., Burrows, D. N., Hughes, J. P., Slane, P. O., Garmire, G. P., & Nousek, J. A. 2003, ApJ, 582, 770

Long, K. S. & Blair, W. P. 1990, ApJ, 358, L13

Lorimer, D. R. 2003, in ASP Conf. Ser.: IAU Symposium 218: Young Neutron Stars and Their Environments, ed. F. Camilo & B. M. Gaensler (San Fransisco: ASP), (astro-ph/0308501)

Lorimer, D. R., Bailes, M., & Harrison, P. A. 1997, MNRAS, 289, 592

Lorimer, D. R., Lyne, A. G., & Camilo, F. 1998, A&A, 331, 1002

Lorimer, D. R. & Xilouris, K. M. 2000, ApJ, 545, 385

Lozinskaya, T. A. 1981, Soviet Astronomy Letters, 7, 17

Lu, F. J. & Aschenbach, B. 2002, to be submitted

Lyne, A. G. 2004, in ASP Conf. Ser.: IAU Symposium 218: Young Neutron Stars and Their Environments, ed. F. Camilo & B. M. Gaensler (San Fransisco: ASP)

Lyne, A. G., Burgay, M., Kramer, M., Possenti, A., Manchester, R. N., Camilo, F., McLaughlin, M. A., Lorimer, D. R., D'Amico, N., Joshi, B. C., Reynolds, J., & Freire, P. C. C. 2004, Science, 303, 1153

Lyne, A. G., Camilo, F., Manchester, R. N., Bell, J. F., Kaspi, V. M., D'Amico, N., McKay, N. P. F., Crawford, F., Morris, D. J., Sheppard, D. C., & Stairs, I. H. 2000, MNRAS, 312, 698

Manchester, R. N., Johnston, S., Kaspi, V. M., Lyne, A. G., & D'Amico, N. 1991, MNRAS, 253, 7P

Manchester, R. N., Lyne, A. G., Camilo, F., Bell, J. F., Kaspi, V. M., D'Amico, N., McKay, N. P. F., Crawford, F., Stairs, I. H., Possenti, A., Kramer, M., & Sheppard, D. C. 2001, MNRAS, 328, 17

Manchester, R. N. & Taylor, J. H. 1977, Pulsars (San Francisco : W. H. Freeman, c1977.)

Marino, A., Micela, G., & Peres, G. 2000, A&A, 353, 177

Maron, O., Kijak, J., Kramer, M., & Wielebinski, R. 2000, A&AS, 147, 195

Marsden, D., Lingenfelter, R. E., Rothschild, R. E., & Higdon, J. C. 2001, ApJ, 550, 397

Marshall, H. L., Edelson, R. A., Vaughan, S., Malkan, M., O'Brien, P., & Warwick, R. 2002, ApJ

Marshall, H. L. & Schulz, N. S. 2002, ApJ, 574, 377

Martin, C., Halpern, J. P., & Schiminovich, D. 1998, ApJ, 494, L211

Matsushita, K., Makishima, K., Awaki, H., Canizares, C. R., Fabian, A. C., Fukazawa, Y., Loewenstein, M., Matsumoto, H., Mihara, T., Mushotzky, R. F., Ohashi, T., Ricker, G. R., Serlemitsos, P. J., Tsuru, T., Tsusaka, Y., & Yamazaki, T. 1994, ApJ, 436, L41

Matthews, H. E., Baars, J. W. M., Wendker, H. J., & Goss, W. M. 1977, A&A, 55, 1

Matthews, K. & Soifer, B. T. 1994, in Infrared Astronomy with Arrays, The Next Generation, ed. I. S. McLean (Dordrecht: Kluwer Academic Publisher), 239

Mavromatakis, F., Boumis, P., Papamastorakis, J., & Ventura, J. 2002, A&A, 388, 355

McAdam, W. B., Osborne, J. L., & Parkinson, M. L. 1993, Nature, 361, 516

McGowan, K. E., Kennea, J. A., Zane, S., Córdova, F. A., Cropper, M., Ho, C., Sasseen, T., & Vestrand, W. T. 2003, ApJ, 591, 380

McLaughlin, M. A., Cordes, J. M., Deshpande, A. A., Gaensler, B. M., Hankins, T. H., Kaspi, V. M., & Kern, J. S. 2001, ApJ, 547, L41

McLaughlin, M. A., Cordes, J. M., Hankins, T. H., & Moffett, D. A. 1999, ApJ, 512, 929

McLaughlin, M. A., Kaspi, V. M., Stairs, I. H., Lorimer, D. R., Lyne, A. G., Kramer, M., Manchester, R. N., Faulkner, A. J., Hobbs, G., Camilo, F., Possenti, A., & D'Amico, N. 2003, in ASP Conf. Ser.: IAU Symposium 218: Young Neutron Stars and Their Environments, ed. F. Camilo & B. M. Gaensler (San Fransisco: ASP), (astro-ph/0310455)

McLaughlin, M. A., Stairs, I. H., Kaspi, V. M., Lorimer, D. R., Kramer, M., Lyne, A. G., Manchester, R. N., Camilo, F., Hobbs, G., Possenti, A., D'Amico, N., & Faulkner, A. J. 2003, ApJ, 591, L135

Mereghetti, S. 2000, in The Neutron Star - Black Hole Connection, ed. V. Connaughton, C. Kouveliotou, J. van Paradijs, & J. Ventura (NATO Advanced Study Institute), (astro-ph/9911252)

Mereghetti, S. 2001, astro-ph/0102017

Mereghetti, S., Chiarlone, L., Israel, G. L., & Stella, L. 2002a, in Neutron Stars, Pulsars, and Supernova Remnants, ed. W. Becker, H. Lesch, & J. Trümper, 29, (astro-ph/0205122)

Mereghetti, S., Tiengo, A., & Israel, G. L. 2002b, ApJ, 569, 275

Migliazzo, J. M., Gaensler, B. M., Backer, D. C., Stappers, B. W., van der Swaluw, E., & Strom, R. G. 2002, ApJ, 567, L141

Mignani, R. P. & Caraveo, P. A. 2001, A&A, 376, 213

Mignani, R. P., De Luca, A., & Caraveo, P. A. 2000, ApJ, 543, 318

Milne, D. K., Goss, W. M., Haynes, R. F., Wellington, K. J., Caswell, J. L., & Skellern, D. J. 1979, MNRAS, 188, 437

Miyaji, S., Nomoto, K., Yokoi, K., & Sugimoto, D. 1980, PASJ, 32, 303

Miyata, E., Ohta, K., Torii, K., Takeshima, T., Tsunemi, H., Hasegawa, T., & Hashimoto, Y. 2001, ApJ, 550, 1023

Miyata, E., Tsunemi, H., Kohmura, T., Suzuki, S., & Kumagai, S. 1998a, PASJ, 50, 257

Miyata, E. et al. 1998b, PASJ, 50, 475

Moffett, D., Gaensler, B., Green, A., Slane, P., Harrus, I., & Dodson, R. 2002, in ASP Conf. Ser. 271: Neutron Stars in Supernova Remnants, ed. P. O. Slane & B. M. Gaensler (San Fransisco: ASP), 221

Monet, D. E. A. 1998, in The PMM USNO-A2.0 Catalog (U.S. Naval Observatory, Washington DC)

Morii, M., Sato, R., Kataoka, J., & Kawai, N. 2003, PASJ, 55, L45

Motch, C. 2001, in AIP Conf. Proc. 599: X-ray Astronomy: Stellar Endpoints, AGN, and the Diffuse X-ray Background, 244, (astro-ph/0008485)

Motch, C. & Haberl, F. 1998, A&A, 333, L59

Motch, C., Haberl, F., Zickgraf, F.-J., Hasinger, G., & Schwope, A. D. 1999, A&A, 351, 177

Motch, C., Zavlin, V. E., & Haberl, F. 2003, A&A, 408, 323

Mulchaey, J. S., Davis, D. S., Mushotzky, R. F., & Burstein, D. 2003, ApJS, 145, 39

Murphy, D. C., Persson, S. E., Pahre, M. A., Sivaramakrishnan, A., & Djorgovski, S. G. 1995, PASP, 107, 1234

Murray, S. S., Ransom, S. M., Juda, M., Hwang, U., & Holt, S. S. 2002a, ApJ, 566, 1039

Murray, S. S., Slane, P. O., Seward, F. D., Ransom, S. M., & Gaensler, B. M. 2002b, ApJ, 568, 226

Mushotzky, R. F. 2003, in Carnegie Observatories Astrophysics Series, Vol 3: Clusters of Galaxies: Probes of Cosmological Structure and Galaxy Evolution, ed. J. S. Mulchaey, A. Dressler, & A. Oemler, (astro-ph/0311105)

Mushotzky, R. F., Cowie, L. L., Barger, A. J., & Arnaud, K. A. 2000, Nature, 404, 459

Nakajima, T., Iwamuro, F., Maihara, T., Motohara, K., Terada, H., Goto, M., Iwai, J., Tanabe, H., Taguchi, T., Hata, R., Yanagisawa, K., Iye, M., Kashikawa, N., & Tamura, M. 2000, AJ, 120, 2488

Narayan, R. 1987, ApJ, 319, 162

Narayan, R., Barret, D., & McClintock, J. E. 1997, ApJ, 482, 448

Narayan, R. & Ostriker, J. P. 1990, ApJ, 352, 222

Nelan, E. et al. 2003, Fine Guidance Sensor Instrument Handbook, version 12.0 edn. (Baltimore: STScI), http://www.stsci.edu/instruments/fgs/handbook/Cy13/cover.html

Neuhäuser, R. & Trümper, J. E. 1999, A&A, 343, 151

Nomoto, K. 1984, ApJ, 277, 791

—. 1987, ApJ, 322, 206

Odegard, N. 1986, ApJ, 301, 813

O'Donnell, J. E. 1994, ApJ, 422, 158

Oke, J. B., Cohen, J. G., Carr, M., Cromer, J., Dingizian, A., Harris, F. H., Labrecque, S., Lucinio, R., Schaal, W., Epps, H., & Miller, J. 1995, PASP, 107, 375

Olbert, C. M., Clearfield, C. R., Williams, N. E., Keohane, J. W., & Frail, D. A. 2001, ApJ, 554, L205

Ostriker, J. P., Rees, M. J., & Silk, J. 1970, ApL, 6, 179

Paczyński, B. 2001, astro-ph/0107443

Paerels, F., Mori, K., Motch, C., Haberl, F., Zavlin, V. E., Zane, S., Ramsay, G., Cropper, M., & Brinkman, B. 2001, A&A, 365, L298

Page, D. 1998, in NATO ASIC Proc. 515: The Many Faces of Neutron Stars., ed. R. Bucchieri, J. van Paradijs, & M. Alpar, 539

Page, D., Lattimer, J. M., Prakash, M., & Steiner, A. W. 2004, ApJ, submitted, (astro-ph/0403657)

Patel, S. K., Kouveliotou, C., Woods, P. M., Tennant, A. F., Weisskopf, M. C., Finger, M. H., Göğüş, E., van der Klis, M., & Belloni, T. 2001, ApJ, 563, L45

Pauls, T. 1977, A&A, 59, L13

Pauls, T., van Gorkom, J. H., Goss, W. M., Shaver, P. A., Dickey, J. M., & Kulkarni, S. 1982, A&A, 112, 120

Pavlov, G. G., Kargaltsev, O. Y., Sanwal, D., & Garmire, G. P. 2001a, ApJ, 554, L189

Pavlov, G. G., Sanwal, D., Garmire, G. P., & Zavlin, V. E. 2002, in ASP Conf. Ser. 271: Neutron Stars in Supernova Remnants, ed. P. O. Slane & B. M. Gaensler (San Fransisco: ASP), 247, (astro-ph/0112322)

Pavlov, G. G., Sanwal, D., Kızıltan, B., & Garmire, G. P. 2001b, ApJ, 559, L131

Pavlov, G. G., Sanwal, D., & Teter, M. A. 2003, in ASP Conf. Ser.: IAU Symposium 218: Young Neutron Stars and Their Environments, ed. F. Camilo & B. M. Gaensler (San Fransisco: ASP), (astro-ph/0311526)

Pavlov, G. G., Welty, A. D., & Córdova, F. A. 1997, ApJ, 489, L75

Pavlov, G. G. & Zavlin, V. E. 1999, IAUC, 7270, 1

Pavlov, G. G., Zavlin, V. E., Aschenbach, B., Trümper, J., & Sanwal, D. 2000, ApJ, 531, L53

Pavlov, G. G., Zavlin, V. E., & Sanwal, D. 2002, astro-ph/0206024

Pavlov, G. G., Zavlin, V. E., Sanwal, D., Burwitz, V., & Garmire, G. P. 2001c, ApJ, 552, L129

Pavlov, G. G., Zavlin, V. E., Sanwal, D., & Trümper, J. 2002, ApJ, 569, L95

Pavlov, G. G., Zavlin, V. E., & Trümper, J. 1999, ApJ, 511, L45

Pavlov, G. G., Zavlin, V. E., Trümper, J., & Neuhäuser, R. 1996, ApJ, 472, L33

Pellizzoni, A., Mereghetti, S., & De Luca, A. 2002, A&A, 393, L65

Perna, R. & Hernquist, L. 2000, ApJ, 544, L57

Perna, R., Hernquist, L., & Narayan, R. 2000, ApJ, 541, 344

Perna, R., Heyl, J., & Hernquist, L. 2001, ApJ, 553, 809

Perna, R., Narayan, R., Rybicki, G., Stella, L., & Treves, A. 2003, ApJ, 594, 936

Persson, S. E., Murphy, D. C., Krzeminski, W., Roth, M., & Rieke, M. J. 1998, AJ, 116, 2475

Petre, R., Kriss, G. A., Winkler, P. F., & Canizares, C. R. 1982, ApJ, 258, 22

Petre, R., Kuntz, K. D., & Shelton, R. L. 2002, ApJ, 579, 404

Petruk, O. 1999, A&A, 346, 961

Pfahl, E., Rappaport, S., & Podsiadlowski, P. 2002a, ApJ, 573, 283

Pfahl, E., Rappaport, S., Podsiadlowski, P., & Spruit, H. 2002b, ApJ, 574, 364

Pfeffermann, E., Aschenbach, B., & Predehl, P. 1991, A&A, 246, L28

Phinney, E. S. & Blandford, R. D. 1981, MNRAS, 194, 137

Pisarski, R. L., Helfand, D. J., & Kahn, S. M. 1984, ApJ, 277, 710

Pivovaroff, M. J., Kaspi, V. M., & Camilo, F. 2000, ApJ, 535, 379

Pons, J. A., Walter, F. M., Lattimer, J. M., Prakash, M., Neuhäuser, R., & An, P. 2002a, ApJ, 564, 981

—. 2002b, ApJ, 564, 981

Possenti, A., Cerutti, R., Colpi, M., & Mereghetti, S. 2002, A&A, 387, 993

Potekhin, A. Y. 1998, Journal of Physics B Atomic Molecular Physics, 31, 49, (physics/9710046)

Predehl, P. & Schmitt, J. H. M. M. 1995, A&A, 293, 889

Press, W. H., Teukolsky, S. A., Vetterling, W. T., & Flannery, B. P. 1992, Numerical recipes in C. The art of scientific computing (Cambridge: University Press, —c1992, 2nd ed.)

Psaltis, D., Özel, F., & DeDeo, S. 2000, ApJ, 544, 390

Rankin, J. M. 1993, ApJ, 405, 285

Ransom, S. M. 2001, Ph.D. Thesis

Ransom, S. M., Gaensler, B. M., & Slane, P. O. 2002, ApJ, 570, L75

Raymond, J. C. & Smith, B. W. 1977, ApJS, 35, 419

Reed, B. C. 2000, AJ, 120, 314

Reed, J. E., Hester, J. J., Fabian, A. C., & Winkler, P. F. 1995, ApJ, 440, 706

Rho, J., Dyer, K. K., Borkowski, K. J., & Reynolds, S. P. 2002, ApJ, 581, 1116

Rho, M. 2000, nucl-th/0007073

Roberts, M. S. E., Hessels, J. W. T., Ransom, S. M., Kaspi, V. M., Freire, P. C. C., Crawford, F., & Lorimer, D. R. 2002, ApJ, 577, L19

Roberts, M. S. E., Tam, C. R., Kaspi, V. M., Lyutikov, M., Vasisht, G., Pivovaroff, M., Gotthelf, E. V., & Kawai, N. 2003, ApJ, 588, 992

Rodgers, A. W., Campbell, C. T., & Whiteoak, J. B. 1960, MNRAS, 121, 103

Roger, R. S. & Costain, C. H. 1976, A&A, 51, 151

Romani, R. W. 1987, ApJ, 313, 718

Romani, R. W. & Ng, C.-Y. 2003, ApJ, 585, L41

Romani, R. W. & Yadigaroglu, I.-A. 1995, ApJ, 438, 314

Rosado, M., Ambrocio-Cruz, P., Le Coarer, E., & Marcelin, M. 1996, A&A, 315, 243

Ruderman, M., Zhu, T., & Chen, K. 1998, ApJ, 492, 267

Rutledge, R. E., Fox, D. W., Bogosavljevic, M., & Mahabal, A. 2003, ApJ, 598, 458

Ryan, E., Wagner, R. M., & Starrfield, S. G. 2001, ApJ, 548, 811

Salpeter, E. E. 1955, ApJ, 121, 161

Sanwal, D., Pavlov, G. G., Zavlin, V. E., & Teter, M. A. 2002, ApJ, 574, L61

Schaefer, B. E. 1995, AJ, 110, 1793

Schlegel, D. J., Finkbeiner, D. P., & Davis, M. 1998, ApJ, 500, 525

Schwope, A. D., Hasinger, G., Schwarz, R., Haberl, F., & Schmidt, M. 1999, A&A, 341, L51

Searle, L. 1971, ApJ, 168, 41

Seiradakis, J. H. 1992, IAUC, 5532, 1

Seward, F. D., Schmidt, B., & Slane, P. 1995, ApJ, 453, 284

Seward, F. D., Slane, P. O., Smith, R. K., & Sun, M. 2003, ApJ, 584, 414

Seward, F. D. & Wang, Z. 1988, ApJ, 332, 199

Shakura, N. I. & Sunyaev, R. A. 1973, A&A, 24, 337

Shapiro, S. L. & Teukolsky, S. A. 1983, Black holes, white dwarfs, and neutron stars: The physics of compact objects (New York: Wiley-Interscience)

Sheinis, A. I., Bolte, M., Epps, H. W., Kibrick, R. I., Miller, J. S., Radovan, M. V., Bigelow, B. C., & Sutin, B. M. 2002, PASP, 114, 851

Skrutskie, M. F., Schneider, S. E., Stiening, R., Strom, S. E., Weinberg, M. D., Beichman, C., Chester, T., Cutri, R., Lonsdale, C., Elias, J., Elston, R., Capps, R., Carpenter, J., Huchra, J., Liebert, J., Monet, D., Price, S., & Seitzer, P. 1997, in ASSL Vol. 210: The Impact of Large Scale Near-IR Sky Surveys, 25

Slane, P., Seward, F. D., Bandiera, R., Torii, K., & Tsunemi, H. 1997, ApJ, 485, 221

Slane, P., Zimmerman, E. R., Hughes, J. P., Seward, F. D., Gaensler, B. M., & Clarke, M. J. 2004, ApJ, 601, 1045

Slane, P. O., Helfand, D. J., & Murray, S. S. 2002, ApJ, 571, L45

Smith, J. A., Tucker, D. L., Kent, S., Richmond, M. W., Fukugita, M., Ichikawa, T., Ichikawa, S., Jorgensen, A. M., Uomoto, A., Gunn, J. E., Hamabe, M., Watanabe, M., Tolea, A., Henden, A., Annis, J., Pier, J. R., McKay, T. A., Brinkmann, J., Chen, B., Holtzman, J., Shimasaku, K., & York, D. G. 2002, AJ, 123, 2121

Smith, R. C. 1997, AJ, 114, 2664

Sollerman, J., Lundqvist, P., Lindler, D., Chevalier, R. A., Fransson, C., Gull, T. R., Pun, C. S. J., & Sonneborn, G. 2000, ApJ, 537, 861

Spinrad, H., Stauffer, J., & Harlan, E. 1979, PASP, 91, 619

Spruit, H. C. & Phinney, E. S. 1998, Nature, 393, 139

Staelin, D. H. & Reifenstein, E. C. 1968, Science, 162, 1481

Stairs, I. H., Lyne, A. G., & Shemar, S. L. 2000, Nature, 406, 484

Stelzer, B., Huélamo, N., Hubrig, S., Zinnecker, H., & Micela, G. 2003, A&A, 407, 1067

Stephenson, F. R. 1971, QJRAS, 12, 10

Stephenson, F. R. & Green, D. A. 2002, Historical supernovae and their remnants (Clarendon Press: Oxford)

Stetson, P. B. 2000, PASP, 112, 925

Strom, R. G. 1994, MNRAS, 268, L5

Stys, D. J., Walborn, N. R., Busko, I., Goudfrooij, P., Proffitt, C., & Sahu, K. 2002, American Astronomical Society Meeting, 200, 0

Tananbaum, H. 1999, IAUC, 7246, 1

Tauris, T. & Kjær, K. 2003, in ASP Conf. Ser.: IAU Symposium 218: Young Neutron Stars and Their Environments, ed. F. Camilo & B. M. Gaensler (San Fransisco: ASP)

Tauris, T. M. & Konar, S. 2001, A&A, 376, 543

Tauris, T. M. & Manchester, R. N. 1998, MNRAS, 298, 625

Taylor, A. R., Gibson, S. J., Peracaula, M., Martin, P. G., Landecker, T. L., Brunt, C. M., Dewdney, P. E., Dougherty, S. M., Gray, A. D., Higgs, L. A., Kerton, C. R., Knee, L. B. G., Kothes, R., Purton, C. R., Uyaniker, B., Wallace, B. J., Willis, A. G., & Durand, D. 2003, AJ, 125, 3145

Thompson, C. & Duncan, R. C. 1995, MNRAS, 275, 255

—. 1996, ApJ, 473, 322

Thompson, D., Beckwith, S. V. W., Fockenbrock, R., Fried, J., Hippelein, H., Huang, J.-S., von Kuhlmann, B., Leinert, C., Meisenheimer, K., Phleps, S., Röser, H.-J., Thommes, E., & Wolf, C. 1999, ApJ, 523, 100

Thompson, D. J., Fichtel, C. E., Hartman, R. C., Kniffen, D. A., & Lamb, R. C. 1977, ApJ, 213, 252

Thorsett, S. E., Benjamin, R. A., Brisken, W. F., Golden, A., & Goss, W. M. 2003, ApJ, 592, L71

Thorsett, S. E. & Chakrabarty, D. 1999, ApJ, 512, 288

Torii, K., Tsunemi, H., Dotani, T., & Mitsuda, K. 1997, ApJ, 489, L145

Toropina, O. D., Romanova, M. M., Toropin, Y. M., & Lovelace, R. V. E. 2003, ApJ, 593, 472

Toscano, M., Britton, M. C., Manchester, R. N., Bailes, M., Sandhu, J. S., Kulkarni, S. R., & Anderson, S. B. 1999, ApJ, 523, L171

Townsley, L. K., Broos, P. S., Nousek, J. A., & Garmire, G. P. 2002, Nuclear Instruments and Methods in Physics Research A, 486, 751, (astro-ph/0111031)

Trauger, J. T., Vaughan, A. H., Evans, R. W., & Moody, D. C. 1995, in Calibrating Hubble Space Telescope. Post Servicing Mission. Proceedings of a Workshop held at the Space Telescope Science Institute, in Baltimore, Maryland, May 15-17, 1995. Editor(s), Anuradha Koratkar, Claus Leitherer; Publisher, Space Telescope Science Institute, Baltimore, Maryland, 1995. LC #: QB500.268 .C34 1995. ISBN #: NONE., p.379, 379

Treves, A. & Colpi, M. 1991, A&A, 241, 107

Treves, A., Turolla, R., Zane, S., & Colpi, M. 2000, PASP, 112, 297

Troland, T. H., Crutcher, R. M., & Heiles, C. 1985, ApJ, 298, 808

Tsuruta, S. & Cameron, A. G. W. 1965, Nature, 207, 364

Tsuruta, S., Canuto, V., Lodenquai, J., & Ruderman, M. 1972, ApJ, 176, 739

Tsuruta, S., Teter, M. A., Takatsuka, T., Tatsumi, T., & Tamagaki, R. 2002, ApJ, 571, L143

Tuohy, I. & Garmire, G. 1980, ApJ, 239, L107

Turolla, R., Zane, S., & Drake, J. J. 2004, ApJ, 603, 265

Ueda, Y., Ishisaki, Y., Takahashi, T., Makishima, K., & Ohashi, T. 2001, ApJS, 133, 1

Umeda, H., Nomoto, K., Tsuruta, S., & Mineshige, S. 2000, ApJ, 534, L193

van den Bergh, S. & Kamper, K. W. 1983, ApJ, 268, 129

van den Bergh, S. & Pritchet, C. J. 1986, ApJ, 307, 723

van der Klis, M. 2000, ARAA, 38, 717

van der Swaluw, E. 2003, A&A, 404, 939

van der Swaluw, E., Achterberg, A., Gallant, Y. A., & Tóth, G. 2001, A&A, 380, 309

van der Swaluw, E., Downes, T. P., & Keegan, R. 2003, A&A, submitted, (astro-ph/0311388)

van Kerkwijk, M. H., Kaplan, D. L., Durant, M., Kulkarni, S. R., & Paerels, F. 2004, ApJ, in press, (astro-ph/0402418)

van Kerkwijk, M. H. & Kulkarni, S. R. 2001a, A&A, 380, 221

—. 2001b, A&A, 378, 986

van Straten, W., Bailes, M., Britton, M., Kulkarni, S. R., Anderson, S. B., Manchester, R. N., & Sarkissian, J. 2001, Nature, 412, 158

Vasisht, G. & Gotthelf, E. V. 1997, ApJ, 486, L129

Vasisht, G., Gotthelf, E. V., Torii, K., & Gaensler, B. M. 2000, ApJ, 542, L49

Vikhlinin, A., Forman, W., & Jones, C. 1999a, ApJ, 525, 47

Vikhlinin, A., McNamara, B. R., Hornstrup, A., Quintana, H., Forman, W., Jones, C., & Way, M. 1999b, ApJ, 520, L1

Vink, J., Bocchino, F., Damiani, F., & Kaastra, J. S. 2000, A&A, 362, 711

Vink, J., Kaastra, J. S., & Bleeker, J. A. M. 1997, A&A, 328, 628

Vivekanand, M. & Narayan, R. 1981, Journal of Astrophysics and Astronomy, 2, 315

Vlemmings, W. H. T., Cordes, J. M., & Chatterjee, S. 2004, ApJ, in press, (astro-ph/0403686)

Voges, W., Aschenbach, B., Boller, T., Brauninger, H., Briel, U., Burkert, W., Dennerl, K., Englhauser, J., Gruber, R., Haberl, F., Hartner, G., Hasinger, G., Kurster, M., Pfeffermann, E., Pietsch, W., Predehl, P., Rosso, C., Schmitt, J. H. M. M., Trümper, J., & Zimmermann, H.-U. 1996, IAUC, 6420, 2

Vranesevic, N., Manchester, R. N., Hobbs, G. B., Lyne, A. G., Kramer, M., Lorimer, D. R., Camilo, F., Stairs, I. H., Kaspi, V. M., D'Amico, N., & Possenti, A. 2003, in ASP Conf. Ser.: IAU Symposium 218:

Young Neutron Stars and Their Environments, ed. F. Camilo & B. M. Gaensler (San Fransisco: ASP), (astro-ph/0310201)

Vrtilek, S. D., Raymond, J. C., Garcia, M. R., Verbunt, F., Hasinger, G., & Kurster, M. 1990, A&A, 235, 162

Walter, F. M. 2001, ApJ, 549, 433

Walter, F. M. & Lattimer, J. M. 2002, ApJ, 576, L145

Walter, F. M. & Matthews, L. D. 1997, Nature, 389, 358

Walter, F. M., Wolk, S. J., & Neuhäuser, R. 1996, Nature, 379, 233

Wang, J. C. L. 1997, ApJ, 486, L119

Wang, Q. D. & Gotthelf, E. V. 1998, ApJ, 509, L109

Wang, Q. D., Gotthelf, E. V., Chu, Y.-H., & Dickel, J. R. 2001, ApJ, 559, 275

Wang, Z. & Chakrabarty, D. 2002, ApJ, 579, L33

Watson, M. G., Willingale, R., Grindlay, J. E., & Seward, F. D. 1983, ApJ, 273, 688

Weidemann, V. 1987, A&A, 188, 74

—. 2000, A&A, 363, 647

Weiler, K. W. & Panagia, N. 1978, A&A, 70, 419

Weisskopf, M. C., Tananbaum, H. D., Van Speybroeck, L. P., & O'Dell, S. L. 2000, in Proc. SPIE: X-Ray Optics, Instruments, and Missions III, ed. J. E. Trümper & B. Aschenbach, Vol. 4012, 2–16

Westerlund, B. E. 1969, AJ, 74, 879

White, D. A., Jones, C., & Forman, W. 1997, MNRAS, 292, 419

Whiteoak, J. B. Z. & Green, A. J. 1996, A&AS, 118, 329

Wilkin, F. P. 1996, ApJ, 459, L31

Wolszczan, A., Cordes, J. M., & Dewey, R. J. 1991, ApJ, 372, L99

Woods, P. M., Kouveliotou, C., Göğüş, E., Finger, M. H., Swank, J., Smith, D. A., Hurley, K., & Thompson, C. 2001, ApJ, 552, 748

Woosley, S. E., Heger, A., & Weaver, T. A. 2002, Reviews of Modern Physics, 74, 1015

Yakovlev, D. G., Gnedin, O. Y., Kaminker, A. D., Levenfish, K. P., & Potekhin, A. Y. 2003, in High Energy Studies of Supernova Remnants and Neutron Stars: 34th COSPAR Scientific Assembly, ed. W. Becker & W. Hermsen, (astro-ph/0306143)

Yakovlev, D. G., Gnedin, O. Y., Kaminker, A. D., & Potekhin, A. Y. 2002a, in Neutron Stars, Pulsars, and Supernova Remnants, ed. W. Becker, H. Lesch, , & J. Trmper, 287

Yakovlev, D. G. & Haensel, P. 2003, A&A, 407, 259

Yakovlev, D. G., Kaminker, A. D., & Gnedin, O. Y. 2001, A&A, 379, L5

Yakovlev, D. G., Kaminker, A. D., Haensel, P., & Gnedin, O. Y. 2002b, A&A, 389, L24

Yamauchi, S., Koyama, K., Tomida, H., Yokogawa, J., & Tamura, K. 1999, PASJ, 51, 13

Young, M. D., Manchester, R. N., & Johnston, S. 1999, Nature, 400, 848

Yusef-Zadeh, F., Shure, M., Wardle, M., & Kassim, N. 2000, ApJ, 540, 842

Zampieri, L., Campana, S., Turolla, R., Chieregato, M., Falomo, R., Fugazza, D., Moretti, A., & Treves, A. 2001, A&A, 378, L5

Zane, S., Haberl, F., Cropper, M., Zavlin, V. E., Lumb, D., Sembay, S., & Motch, C. 2002, MNRAS, 334, 345

Zane, S., Turolla, R., & Drake, J. J. 2003, astro-ph/0302197

Zavlin, V. E. & Pavlov, G. G. 2002, in Neutron Stars, Pulsars, and Supernova Remnants, ed. W. Becker, H. Lesch, , & J. Trmper, 263, (astro-ph/0206025)

Zavlin, V. E., Pavlov, G. G., & Sanwal, D. 2004, ApJ, 606, 444

Zavlin, V. E., Pavlov, G. G., Sanwal, D., & Trümper, J. 2000, ApJ, 540, L25

Zavlin, V. E., Pavlov, G. G., & Shibanov, Y. A. 1996, A&A, 315, 141

Zavlin, V. E., Trümper, J., & Pavlov, G. G. 1999, ApJ, 525, 959

Zharikov, S. V., Shibanov, Y. A., Koptsevich, A. B., Kawai, N., Urata, Y., Komarova, V. N., Sokolov, V. V., Shibata, S., & Shibazaki, N. 2002, A&A, 394, 633